LA-UR-89-2675-v.1
C.3

Inertial Confinement Fusion at Los Alamos

Progress Since 1985

Volume I - September 1989
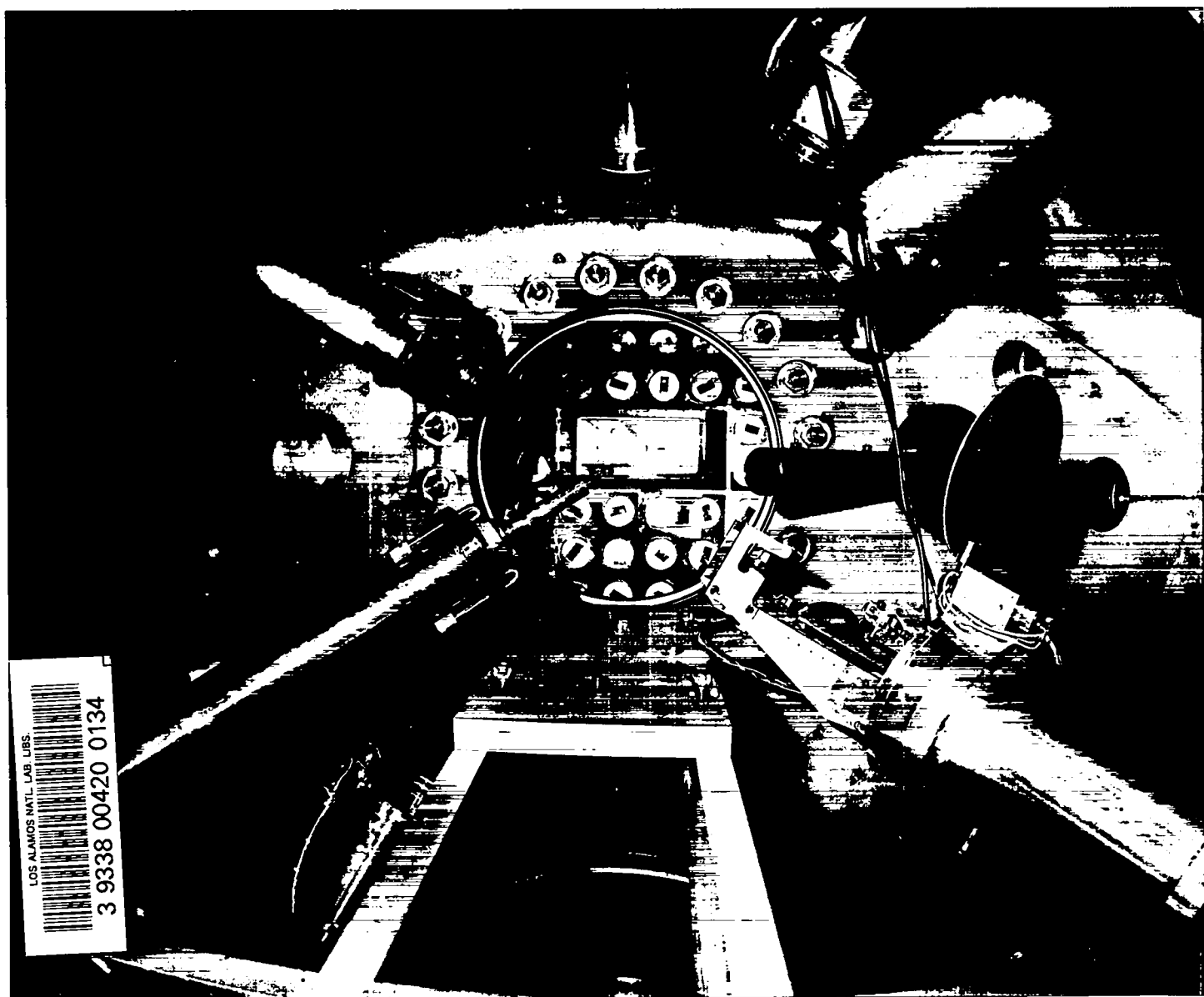
Los Alamos

Acknowledgements

Front Cover
Interior of AURORA target chamber looking directly through the center of the target chamber toward the lens cone. The array of white circles containing rectangular red stripes in the center of this photograph is a portion of the lens plate, some three meters behind the target chamber which focuses the 48 laser beams onto the target. The small yellow sphere in the center of the chamber is an optical reference target used for optical alignment of the laser beams. The yellow tube entering the chamber from the upper left is part of the x-ray diagnostics system. The aluminum colored device in the lower right foreground is the target insertion mechanism

Inertial Confinement Fusion at Los Alamos

Volume I:

Progress in Inertial
Confinement Fusion Since 1985

Compiled by
David C. Cartwright
ICF Program Director

Los Alamos

Contents

I. Introduction

Photograph of actual laser fusion experiment.

I. INTRODUCTION

David C. Cartwright and Thomas E. McDonald

Nuclear fusion, the process that produces the energy in all stars, has been the goal of U.S. laboratory experiments since the magnetic confinement fusion program was initiated in 1952. The national Inertial Confinement Fusion (ICF) program began in earnest in the early 1970s and currently has six participants: Los Alamos, Livermore and Sandia National Laboratories; KMS Fusion; the University of Rochester; and the Naval Research Laboratory.

The ICF mission statement for the Los Alamos National Laboratory is as follows:

> *The Los Alamos ICF program is one of the main efforts by the Department of Energy (DOE) to evaluate the scientific feasibility of inertially confined fusion, using intense lasers or particle beams to compress and heat small masses of deuterium-tritium fuel to thermonuclear burn conditions. The goals of the national program are to support research in high energy-density science and to conduct research on the potential of inertial fusion for energy production.*
>
> *The key technical elements within the ICF program are*
> * *the design and performance of fuel-filled targets requiring minimum input energy and*
> * *the development of a laboratory driver suitable for driving such targets at an acceptable cost.*
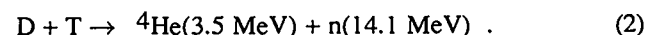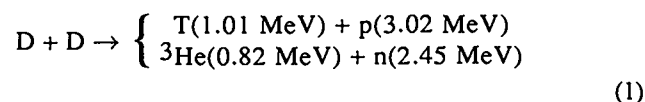
In their 1986 report on the US ICF Program, the National Academy of Sciences recommended that the ICF program be continued at the 1985 level of effort for about five years and then be reevaluated with respect to the progress it had made toward achieving its technical goals. The purpose of this report, Volume I of a two-volume series, is to document the technical progress made by Los Alamos since 1985 in four areas:

* materials technology for ICF,
* laser-matter interaction,
* KrF laser development for ICF applications, and
* plasma theory support of the Sandia light ion program.

A brief overview of the contents of this volume is presented in the following paragraphs.

GENERAL REQUIREMENTS FOR ICF

Inertial confinement fusion attempts to mimic, on a miniature scale, the process by which stars generate their energy. A small amount of deuterium and tritium (DT) fuel is heated rapidly to temperatures high enough to promote fusion reactions in the fuel and at the same time, the fuel is compressed to densities high enough to facilitate reaction of a large fraction of the fuel before it is cooled by hydrodynamic expansion. In the sun, the primary fusion reaction occurs between two nuclei of the lightest isotope of hydrogen, ^1H. The rate at which this reaction proceeds makes it impractical for utilization in a reactor. The other two isotopes of hydrogen, deuterium (^2H or D) and tritium (^3H or T) are the favored fuel elements for a fusion reactor because they react faster. Deuterium occurs naturally in nature. The natural source of deuterium is ordinary water for which there is one molecule of heavy water, HDO, in every 6500 molecules of normal water. Tritium would have to be produced in the fuel cycle of the fusion reactor because it does not occur naturally. The two nuclear reactions of interest for fusion are:

$$D + D \rightarrow \begin{cases} T(1.01 \text{ MeV}) + p(3.02 \text{ MeV}) \\ ^3He(0.82 \text{ MeV}) + n(2.45 \text{ MeV}) \end{cases}$$

$$ \tag{1}$$

$$D + T \rightarrow \ ^4He(3.5 \text{ MeV}) + n(14.1 \text{ MeV}) \ . \tag{2}$$

Both of these fusion reactions are very energetic, but the DT reaction is preferred because of the greater neutron kinetic energy. It is also easier to initiate the DT reaction because the temperature required to ignite the fusion fuel is lower by approximately a factor of 5 than for the DD reaction. If one could convert all the deuterium in one gallon of heavy water to fusion energy, it would be equivalent to 250 gallons of gasoline. If one also utilizes lithium in the fuel cycle to produce the tritium, then the
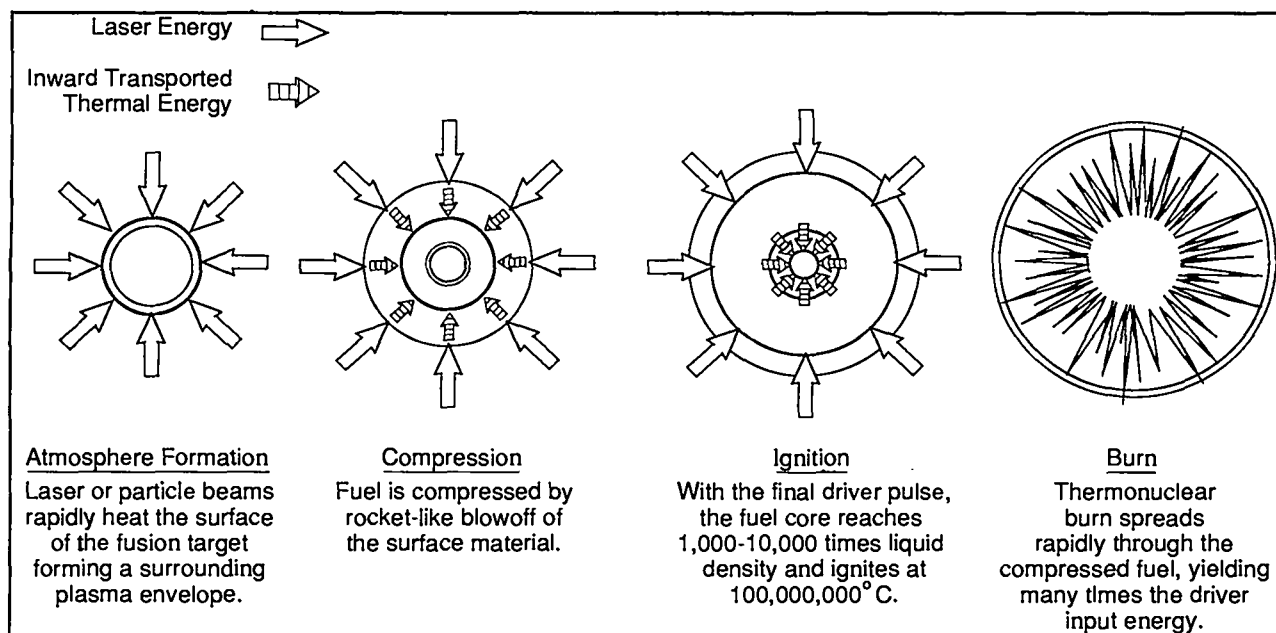
Fig. 1. Processes in DT burn in ICF.

deuterium in this one gallon of water would have the energy equivalent to 850 gallons of gasoline.

The basic problem in producing the fusion reaction is to have the deuterium and tritium nuclei collide with sufficient energy to overcome their repulsive potential barrier. The basic concept is to heat a mixture of DT to a temperature of 10^8 K (or 10 KeV) and confine it long enough that sufficient fusion reactions occur and the energy yield is greater than the energy required to prepare the fusion fuel. This translates to a requirement first enunciated by Lawson (1957) that the product of the density (n) and the confinement time (τ) should be $n\tau \, 10^{15}$ nuclei s/cm^3.

Figure 1 shows schematically the various steps required to convert the incident laser energy into hydrodynamic compression of the fuel. Information on atmospheric formation and compression is being obtained using laboratory drivers, but information about ignition and burn requires new and more powerful drivers before they can be studied in the laboratory. Because the objective is net energy gain from the fusion reaction, it is important to achieve as large an energy conversion efficiency as possible at each step in the sequence. Because we know that ICF will work at some large drive energy, it is important to determine the energy conversion efficiencies and energy requirements for each individual step as the figure of merit for judging the potential for success of the various laboratory drivers.

The temperature and density-confinement time product requirements for ICF are the same as those required for magnetic confinement. In ICF, one increases the density many orders of magnitude, and thus decreases the required confinement time. Basically, the concept is that if the density is high enough then the fuel can burn before the internal energy from the burning causes it to disassemble. Figure 1 illustrates the processes that are used to achieve DT burn in inertial confinement fusion. A spherical mass of fuel is heated by energy impinging on the outside of the sphere. The hot plasma, which expands outward, produces a compression wave that propagates toward the center of the fuel. The compression of the DT is designed so that the final fuel density is 1000 to 10,000 times the original liquid liquid density of DT, 0.2 gm/cm^3. In DT at 1000 times the density of liquid DT, the number density is 3×10^{25} nuclei/cm^3. Therefore, a confinement time of only 30×10^{-12}s satisfies the Lawson criteria. The diameter of the superdense compressed DT mixture is ~100 μm, and at the burn temperatures of 20-50 keV, the free expansion time of the material is on the order of tens of picoseconds (10^{-12} s).

The difficulty in accomplishing this in the laboratory arises from the requirement to contain the maximum energy released by the fusion reaction; this can be accomplished only if the mass of fuel is sufficiently low. For small fuel masses to support a thermonuclear burn in which the energy produced by fusion reaction sustains the burn, the fuel must be condensed to high density. A fundamental scaling parameter for ICF is the product of fuel density ρ and the radius R of the column containing the fuel. It can be shown that the density to which the fuel

must be compressed increases as the reciprocal of the square root of the fuel mass, that is, $\rho \approx 1/\sqrt{M}$. Achieving the required compression for small fuel masses without expending excessive energy from the driver is the basic requirement of ICF.

The fundamental nature of the quantity can be learned by deriving the expression for the burn efficiency, ϕ, of a uniform spherical mass of DT fuel (Evans 1985; Ahlstrom 1985). The burn efficiency is defined as follows:

$$\phi = \frac{\text{Energy released}}{\text{Energy available}} \tag{3}$$

For DT, this expression becomes:

$$\phi = \frac{\int\int n_D n_T \langle \sigma v \rangle Q_{DT} DV dt}{nV Q_{DT}} \tag{4}$$

where n is the number density of the fuel, $\langle \sigma v \rangle$ is the Maxwell-averaged cross section for the DT reactions, and Q_{DT} is the 17.6 MeV of energy released per reaction. Assuming an equimolar mixture of DT and that the confinement time is the radius of the pellet divided by twice the ion sound speed, $r/2c_i$, evaluation of the integral gives:

$$\frac{\phi}{1 - \phi} = \frac{nr \langle \sigma v \rangle}{2 c_i} \tag{5}$$

For efficient burn, the fuel will be heated by the trapping of the 3.5-MeV alpha particles to temperatures of 20-50 keV where $\langle \sigma v \rangle / c_i$ is approximately constant. Evaluating this constant leads to a simple expression for burn efficiency:

$$\phi = \frac{\rho r}{\rho r + 6} , \tag{6}$$

where $\rho r = g/cm^2$ and
ρ is the mass density.

If we use a pellet containing a DT mixture at a density of 0.2 g/cm^3 (the liquid density of DT), then a 33% burnup of the fuel would require a pellet with a 15-cm radius containing about 3 kg of DT. If this pellet is heated instantaneously to the fusion ignition temperature of > 5 keV, it would then release 60 kilotons equivalent TNT of fusion yield. At the 5-keV ignition temperature, the fuel starts to burn vigorously and the alpha particles deposit their energy in the fuel causing the temperature to rapidly rise to 20-50 keV and producing efficient burn in a properly designed capsule. Even if we scale down from

this efficient burnup of the fuel to an output energy approaching the amount of laser energy required to heat this 3-kg mass of fuel, the output energy is still of the order of tens of GJ. For practical energy production, we must also account for the efficiency of the laser, the coupling, and the heating process. Therefore, the beauty of the spherical compression to high density is that we reduce the yield required from the pellet. Most importantly, it lowers the energy required from the laser driver to a sensible value, ~1 MJ .

MATERIALS TECHNOLOGY

Fusion targets, whether for the laser program or the particle beam program, are not difficult to picture because they are simply a series of concentric spherical shells. Yet fabrication of these spheres poses extraordinary difficulties. The targets are small, less than a millimeter in diameter overall. Each shell must possess specific properties ranging from high strength at low densities to high atomic number and density for improved compression. The tolerances are exacting 10 times more stringent than those common in the aerospace industry. Every effort must be expended to meet the designers' demands, because, for their theories and computer codes can be verified only by experiments with real targets.

We have had considerable success in target fabrication, in developing new technologies, new materials, and new tools. We will outline some of these developments and then briefly indicate the value of our efforts to other areas of technology.

It is not surprising that our efforts on the multifaceted task of target fabrication have led to materials and technologies of interest and benefit to other research and development programs. We mention briefly a few of these other applications to indicate the variety of fields in which materials science plays a fundamental role.

- The polymeric foams developed for the cushion layer of targets may benefit biomedical research. The synthetic vascular prostheses currently in use, primarily woven Dacron and Teflon structures, have pores that vary widely in size. In contrast, the cells of the foam produced by the inverse phase separation process are remarkably uniform and can be made in the range of 25 μm in diameter, the size believed to be most desirable for biological uses.

- A process called chemical infusion, which was developed for smoothing polymeric surfaces, may also benefit biomedical research. Experiments on laboratory animals

have indicated that silicone rubber veins infused by this process with stearate ions may be rejected less often than untreated artificial veins.

- Miniature coaxial cables fabricated for inertial confinement fusion experiments may simplify surgical removal of brain tumors. With the high-frequency electrical signals transmitted through such a cable, which is less than 0.1 mm in diameter, cancerous cells may be destroyed without damage to surrounding tissue.

- Laser welding, the method used to braze fill tubes onto tampers, may greatly simplify the fabrication of radioactive components.

- High-strength single-crystal whiskers, which were fabricated and studied for possible use as support structures in laser fusion targets, are now the key component in the Los Alamos structural ceramics program. These whiskers of silicon carbide or silicon nitride have tensile strengths approaching 4,000,000 psi. Composites of such whiskers and ceramic materials have very high tensile strengths and high resistance to fracture.

Clearly, target fabrication and the associated research and development encompass many diverse endeavors. Formerly these were pursued at several scattered Laboratory sites. But since the fall of 1983, most of our activities have been gathered in a single, specially designed building, the Target Fabrication Facility. This facility includes clean rooms for target assembly; a laboratory in which the targets are filled with the deuterium-tritium fuel; a machine shop; and laboratories for electroplating and physical and chemical vapor deposition, for developing and producing polymer foams, for laser welding and solid-state bonding, and for characterizing the various target components. Beyond the obvious advantages of space and equipment, the facility allows greater ease of communication among those involved in materials science, fabrication technology, and materials characterization.

KrF LASER ISSUES FOR FUSION APPLICATIONS

The objective of the Los Alamos KrF development program is to determine if KrF lasers can be economically scaled to sizes and efficiencies of interest for the ICF application. Producing an ICF driver at an acceptable cost *is* the primary issue.

Based on the evidence available, it appears that KrF lasers can be constructed on a large scale, with operating electrical efficiencies between 5% and 10%, and at an acceptable cost (< $100/joule, FY89 dollars). As gas lasers, they have the capability of being operated at repetition rates appropriate to reactor concepts.

In addition, it appears that the 248-nm wavelength and relatively broad bandwidth of the KrF laser is near optimum for target coupling in that

- absorption of the laser radiation in the target is high;
- hot electrons are reduced to a very low level;
- the conversion of laser radiation to X-rays is high; and
- instabilities produced by laser-plasma interactions are reduced.

Some characteristics of a high-power KrF laser for ICF application are summarized in the following paragraphs.

Pulse-shaping flexibility is required for optimum target performance and is obtained by using a mode-locked dye laser for the high-frequency component needed in the pulse. The required pulse shape is synthesized by close stacking spike replicas from beam-splitter stacks that have the requisite intensity profiles. Also, in the dye-laser frequency range, Pockels cells are of sufficient quality to allow direct pulse shaping by the degree of switch opening.

Pulse propagation will depend on the overall quality of amplifier engineering, including homogeneity of the e-beam energy deposition. Energy extraction from the amplifier becomes one of the most important processes in achieving overall high efficiency. In large, well-pumped KrF lasers, the gain is sufficiently high to cause spontaneous emission to be amplified significantly in a distance smaller than a laser dimension. This amplification is parasitic upon the desired energy-extraction scheme. Amplifier saturation and sequencing are the tools to be used in suppressing parasitics after all the surfaces are treated to obtain minimum reflectivity.

Optical system cost is one of the two major cost components in a large fusion system. A key innovation in mirror substrates has already reduced the cost of those elements by a factor of four. The technique involves the use of Pyrex tubing and plate to form a lightweight sandwich that is then fused together at the contact surfaces. Improved resistance to optical damage has a large impact on system cost up to a fluence near 10 J/cm^2, and 4 J/cm^2 has already been exceeded. Substantial progress has been made in the general area of KrF laser radiation and flourine damage resistance.

THE FUTURE

Over 15 years of research have taught us a great deal about ICF on a laboratory scale, and it is certainly more difficult than originally envisioned. Inefficiencies in all the steps between providing the incident energy on the ICF target and igniting a fuel have slowed the program. However, there exists the certainty that ICF works well on some energy scale, and in our quest to provide energy by control of fusion, ICF should be a very strong candidate. Although the process is still some distance from any practical use, the promise warrants a substantial national effort.

REFERENCES

Ahlstrom, H. G., "Physics of Laser Fusion, Vol. II, Diagnostics of Experiments on Laser Fusion Targets at LLNL, Lawrence Livermore National Laboratory, January 1982.

Evans, "The Basic Physics of Laser Fusion," Can. J. Phys. 64, 893-899 (1985).

Lawson, J. D. "Some Criteria for a Power Producing Thermonuclear Reactor," Proc. Phys. Soc. B. 70, 6 (1957).

II. ICF Contributions to Science and Technology
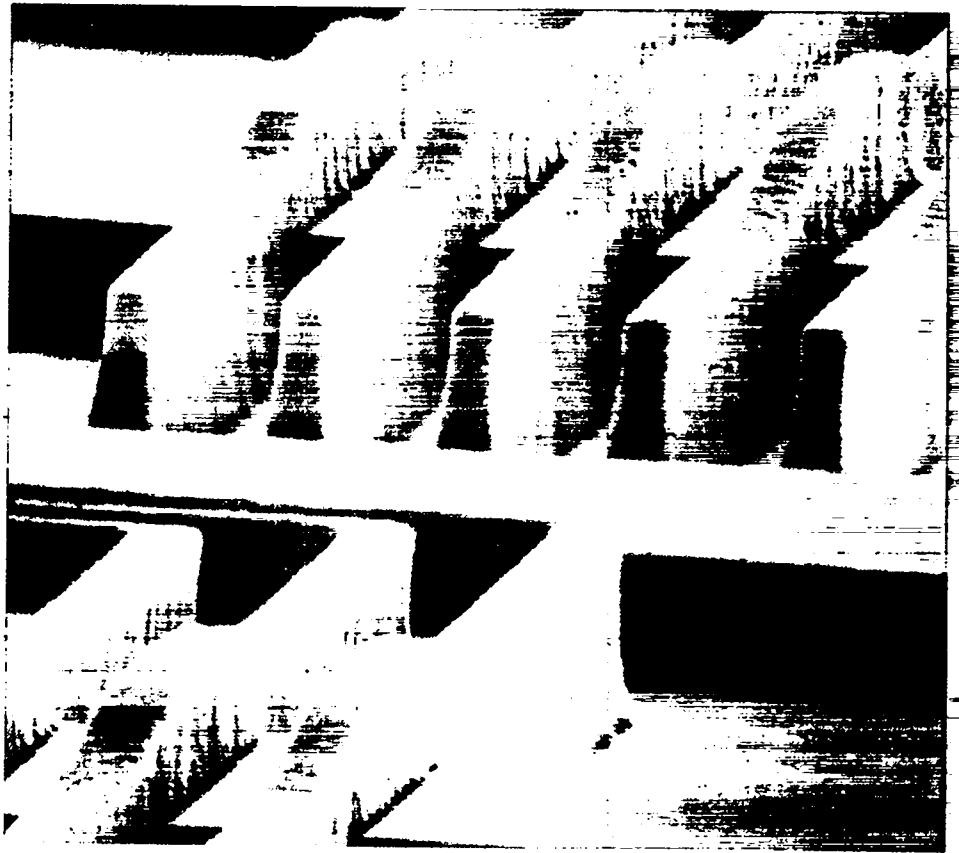
An example of relief structure produced in x-ray resist with a laser plasma source. The resist ridges ride over 0.5-micron-high silicon dioxide steps on a silicon substrate.

II. ICF CONTRIBUTIONS TO SCIENCE AND TECHNOLOGY

Allen A. Hauer and Irving J. Bigio

In addition to its central contributions to fusion physics, the laser-driven Inertial Confinement Fusion (ICF) program has spawned a rich diversity of technological advances and applications ranging from advances in laser/optical technology itself to applications in fields such as biology and materials science, as well as the more obvious plasma and atomic physics. Los Alamos has pursued a number of these applications (and has assisted others in transferring technology), which has led to valuable contributions to science and technology. In some cases, the technology has been commercialized and has led to the formation of companies in the private sector. Examples of some of these "spin-off" technologies and applications are the following.

Laser/Optical Technology:

- development of large-aperture laser optics: NaCl, fused silica, and copper, as well as honeycomb-core large-area mirrors;
- diamond turning of metal mirrors;
- high-damage-threshold transmissive and reflective coatings for optics at 10 μm and 0.25 μm;
- automated computer-controlled optical alignment systems;
- pulse-slicing techniques using Pockels cells, fast detectors, and oscilloscopes;
- various technologies utilized in ultrahigh brightness laser systems (Bright Source);
- optical phase conjugation in the infrared and ultra-violet regions;
- injection locking of unstable resonator lasers;
- various technologies for large-aperture lasers.

Applications of ICF technology to other fields:

- utilization of laser plasma generated x-ray pulses (both coherent and incoherent) for materials science and biological applications;
- laser plasma sources for x-ray lithography;
- development of concepts for laser plasma particle accelerators and the use of lasers for various advanced particle accelerator schemes;
- use of laser generated high-energy particles;
- use of computational tools developed for fusion problems for applications in basic and applied plasma and atomic physics;
- laser initiated switching and control of pulsed power.

Many of the spin-offs are described in various Los Alamos publications. Examples of publications describing contributions in the laser/optics area are Bergmann et al. (1978) and Bigio and Slatkine (1978), whereas several of the applications in other areas are dealt with in Hauer et al. (1988).

One example of new programmatic activities made possible by technological developments in the ICF program is the significant effort that was funded for several years [mainly from Department of Defense (DoD) sources] in the area of vulnerability, lethality, and effects (VL&E). A variety of ICF lasers have been used for these measurements. Some of the best data, both at mid ir and uv wavelengths, have been generated at Los Alamos, providing the nucleus of a data base that is used for a variety of purposes.

The development of injection-locking techniques and nonlinear phase conjugation have been of great value to several other programs and have even made their way into commercial products such as lasers and detectors. There are a number of DoD programs that depend on these techniques for key elements in their systems. These programs include the Tactical Airborne Laser Communicator and the Satellite Laser Communication program, as well as a variety of components of the Strategic Defense Initiative (SDI) program.

As a more recent example, Los Alamos is currently building a collaborative program in biomedical applications of lasers. This will be a joint effort among Los Alamos, the University of New Mexico School of Medicine, and the Lovelace Research Foundation. A broad range of capabilities in lasers and optics, many deriving from developments in the

ICF program, will be brought to bear upon a variety of medical problems.

There have also been significant technology transfers from ICF to other programs; these are discussed in the classified section of this report.

To give a more detailed view of the importance of the spin-offs from ICF to other areas, we present here brief reviews of two of the significant contributions: the utilization of laser generated x-ray sources and the utilization of laser technology in advanced particle accelerator research.

USE OF LASER GENERATED X-RAY SOURCES

The laser generated plasma (LP) can be an efficient, bright, and versatile source of x rays. In some situations, as much as 70% of the absorbed laser light can be re-emitted as x rays.

With the variations in irradiance and wavelength that are allowed by present laser technology, x-ray photon energies can range across the spectrum up to several hundred keV. The x-ray emission also has very interesting temporal characteristics. In many cases, the temporal profile follows the envelope of the laser itself. This in turn implies pulse durations ranging from a few picoseconds (or less) to tens of nanoseconds. The LP can thus be a very high peak-power x-ray source and for many applications is quite competitive with a synchrotron.

Controllability is another very valuable characteristic of LP x-ray sources. Because laser-initiated electronic and pulsed-power switching has become highly developed, the x-ray source can be accurately synchronized with respect to a wide variety of instruments (for example, ultrafast optical and x-ray streak cameras and shutters). In addition, the laser itself is often used to stimulate an event (such as a material phase transition), which can then be probed with an x-ray burst. The spatial distribution of x-ray emission can be varied from a point source (as small as 10 μm) to distributed emission (as large as several millimeters) by simply varying the laser focal conditions.

The physical mechanisms responsible for kilovolt plasma formation and subsequent x-ray emission show a marked variation with laser wavelength. Shorter wavelengths ($\lambda < 1$ μm) are more efficient for producing quasi-thermal plasma emission (Yaakobi et al. 1981). Longer wavelength ($\lambda > 10$ μm) laser interactions have the additional feature of producing large numbers of suprathermal electrons that in turn produce hard x-ray line radiation and bremsstrahlung (Hauer et al. 1984).

X-ray generation mechanisms can thus be divided into two broad categories: thermal and suprathermal. The absorbed laser energy can be channeled into either thermal electrons, which produce thermal plasma heating and x-ray emission, or suprathermal electrons, which tend to escape or deposit deeply in cold material and create harder x-ray emission. We will divide the discussion into two sections dealing with thermal and suprathermal x-ray generation. A schematic diagram of the laser absorption and x-ray emission process is shown in Fig. 1.
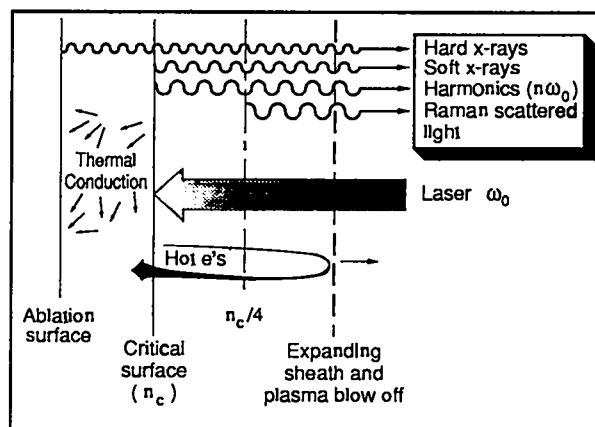
Fig. 1. Laser plasma interaction - absorption/transport phase.

In Table 1 we show some of the characteristics of thermal x-ray emission from LPs and relevant applications that take advantage of these properties. We define the following efficiency parameter:

η = x-ray energy in a particular photon energy band (which is noted) into 4π/incident laser energy.

In many applications in materials science and biology, a pulse width of 1-10 ns is adequate for the study of transient phenomena. This pulse width must be balanced against the need to deliver energy fast enough (high laser power) so that high ionization states can be reached and thus relatively short wavelength x-ray radiation generated (before cooling by thermal conduction, hydrodynamic expansion, and radiation occurs). Radiography of dense plasmas often requires bursts of 100 ps or shorter. This in turn requires the use of shorter wavelength laser irradiation of the x-ray source.

When an application requires very hard x-ray emission, the suprathermal mechanisms must be utilized. The generation of suprathermal x-rays is a very different phenomena from thermal emission (Priedhorsky et al. 1981; Burnett et al. 1984; Hauer et al. 1984; Forslund and Goldstone 1985). In essence, the process amounts to the use of the absorbed laser energy to produce an electron beam, which in turn has many similarities to a classical x-ray tube.

TABLE 1. Characteristics of Thermal x-ray Emission from Laser Plasmas.

X-ray Emission Parameters	Characteristics of X-ray Generation (for laser wavelength and intensity (I)	Applications
Broadband subkilovolt 0.05-1.0 keV	• for given I considerable increase of η with decreasing λ	• photo lithography
	• peak efficiencies $\lambda = 0.35$ μm, $\eta \sim 0.55$ @ I $\sim 10^{14}$ W/cm^2	• surface studies
Thermal line radio-radiation hv $\sim$ 2 keV (He-like emission for elements like Al)	• $\lambda = 0.35$ μm, $\eta \sim 0.02$ @ I = 5 $\times 10^{14}$ W/cm^2	• x-ray graphy • (e.g., biology)
	• $\lambda = 1.06$ μm, ~ 0.006 @ I = 5 $\times 10^{14}$ W/cm^2	• transient diffraction from biological structures
$\Delta v \sim$ 10 eV	• recombination rates generally cause x-ray pulse > laser pulse (for $\tau_L <$ 100 ps)	
Thermal line radiation hv $\sim$ 5 keV (He-like emission for elements like Ti)	• $\lambda = 0.35$ μm, $\eta \sim 0.006$ @ I = 5 $\times 10^{14}$ W/cm^2 • $\lambda =1.06$ μm, $\eta \sim 4 \times 10^{-4}$ @ I = 5 $\times 10^{14}$ W/cm^2 • x-ray pulse usually closely follows laser pulse	• transient diffraction in materials science and biology

x-ray source that combines all of the following characteristics:

- high photon energy up to at least 30 keV,
- small source size <100 μm,
- flexibility in changing source configuration by changing focal conditions, and
- intense fast $\gamma <$ 1-ns pulsed bursts.

In addition, the technology of CO_2 lasers has progressed to the point where compact kilojoule, high repetition rate (> 0.01 Hz) systems can be planned.

TABLE 2. Characteristics of Suprathermal x-ray Emission from Laser Plasmas.

X-Ray Emission Parameters	Characteristics of X-ray Generation (for laser wavelength and intensity (I)	Applications
Characteristics line emission hv > 8 keV Δhv~5 eV	• $\lambda = 10.6$ μm $\eta \sim 4 \times 10^{-5}$ @ I $\sim 3 \times 10^{15}$ W/cm^2 • x-ray pulse follows laser pulse for $\tau_L \sim$ 1 ns	• Transient diffraction from small 2-D spacing crystals •Radiography of very dense plasmas
Bremsstrahlung continuum 10-500 keV (measured)	• $\lambda = 10.6$ μm @ I $\sim 3 \times 10^{15}$ W/cm^2 $\eta \sim 10^{-3}$ (for total spectrally integrated Bremmsstrahlung)	• Transient powder diffraction • Absorption spectra from very dense plasmas. • Transient effects with respect to radiation damages in solids

Detailed measurements have been made of the absolute yields of both bremsstrahlung continuum (Priedhorsky et al. 1981) and inner-shell line radiation. Table 2 gives a review of some parts of these data in the context of potential applications. As can be seen from Table 2, suprathermal x-ray generation is quite inefficient (as is an ordinary x-ray tube). It is, however, one of the few ways to produce an

The unique potential of LP x-ray sources in non-fusion applications has been recognized for some time (Hauer 1976; Mallozzi et al. 1979). Considerable improvement in parameters such as repetition rate and reliability for Nd:glass, CO_2, and KrF lasers has led to a substantial amount of work on nonfusion applications in recent years (Eason et al. 1986; Yaakobi et al. 1986; Hauer 1988).

Most of the applications make use of the fast intense x-ray burst that can be produced with LPs. The energy available in a single burst is often adequate for detection and recording. LP x-ray sources are thus (in contrast to synchrotron radiation) uniquely suited to the study of nonrepetitive or irreversible events (such as some types of materials phase changes). Laser systems suitable as x-ray sources will soon be capable of >1-Hz repetition rate, and thus LPs will even be competitive on a quasi-cw basis. X-ray fluence available with existing laser systems ranges up to 10^{16} keV/keV/steradian with photon energies up to 10 keV or greater.

The applications discussed here fall into three broad categories: x-ray diffraction from transiently strained crystals, pulsed x-ray radiography and lithography, and absorption spectroscopy.

The fast burst of x-ray emission that is available from LP sources is uniquely suited to transient x-ray diffraction (Förster et al. 1984; Shäfer et al. 1984; Hauer 1976). Using currently available lasers, investigators can record diffraction patterns from a wide variety of crystalline materials on a single shot.

The basic idea is that when the crystal is irradiated by the laser, it heats up; the lattice spacing then increases by an amount determined by the coefficient of thermal expansion. Any x-ray radiation incident on the crystal is thus diffracted at a lower angle than that for unheated material. The x-rays from a LP allow such a Bragg diffraction pattern to be recorded on a single-shot basis with a probe time as low as 50 ps. (Similar techniques utilizing synchrotron radiation need multiple shots.) With such a technique it is possible to measure the actual temperature depth profile in a heated material. This is valuable, for example, in analyzing the process of laser material annealing. Such a temperature depth plot from an actual experiment is shown in Fig. 2.
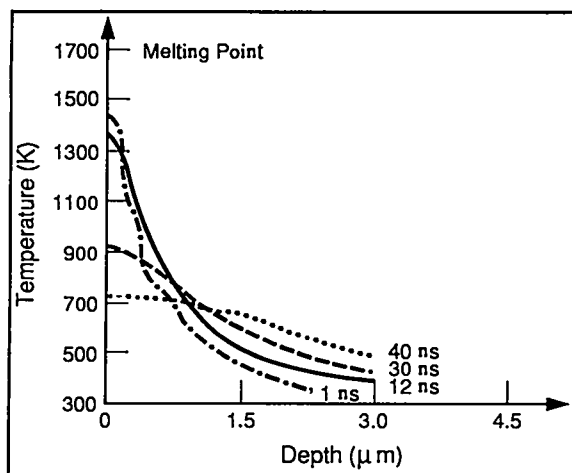

Fig. 2. Temperature-depth profiles within a laser-heated crystal at various probe times.

Transient diffraction studies can be performed on a subnanosecond time scale (Wark et al. 1986). The first motivation in this work was to investigate the possibility of laser heating as a method for x-ray switching and shuttering. This is illustrated in Fig. 3. In Fig. 4, we show the results from an experiment in which diffraction from a crystal was interrupted on a subnanosecond time scale. Analysis of this data shows that the effective crystal reflectivity changes from the order of 10^{-5} to 5×10^{-2} in less than 200 ps.

Transient diffraction techniques have also been applied to the study of shock waves in various materials (Wark et al. 1987). Laser generation of multikilobar shocks has several applications to the study of high explosives (Yang 1974), high-velocity impacts (Pirri 1977), the alteration of the mechanical properties of certain alloys and ceramics (Fairand et al. 1972), and solid-state phase changes.

Probing of the surface of a shocked material by short pulse x-ray diffraction offers many advantages over conventional techniques. The brightness and duration of the x-ray pulses from LPs allow unique measurements of the density in the shocked region. An arrangement for such measurements can be quite similar to heating studies shown in Fig. 4. If a crystal is coated with a thin layer of metal, the laser light will be absorbed in this layer and the crystal will be perturbed purely by a shock wave (and no heating). The results from such a study of shock waves in solids is shown in Fig. 5.

These experiments open up unique possibilities for the study of transient phenomena within matter. These techniques have recently been applied to the time-resolved study of phase changes and the properties of materials within the elastic-plastic transition, as well as the dynamics of materials in a high-radiation flux environment.

X-ray diffraction is not the only way to obtain information about the interatomic spacings within a material; another method is to observe the extended x-ray absorption fine structure (EXAFS). In this technique, the x-ray absorption coefficient of the material of interest is studied as a function of energy just above the K, L, or M absorption edge. As the name suggests, on the high-energy side of the edge, fine structure in the absorption coefficient exists, and this structure can yield information about the local environment surrounding an atom.

The advantage of the LP source is the availability of high temporal resolution, which allows bond lengths and coordination numbers to be measured in materials undergoing transient changes on a subnanosecond time scale.
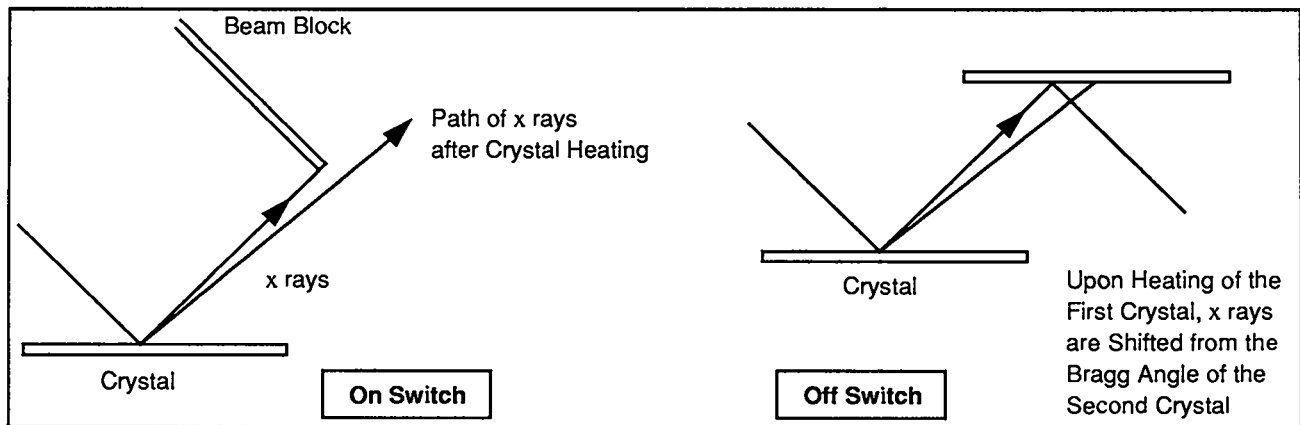
Fig. 3. Concepts for producing x-ray switching and shuttering.
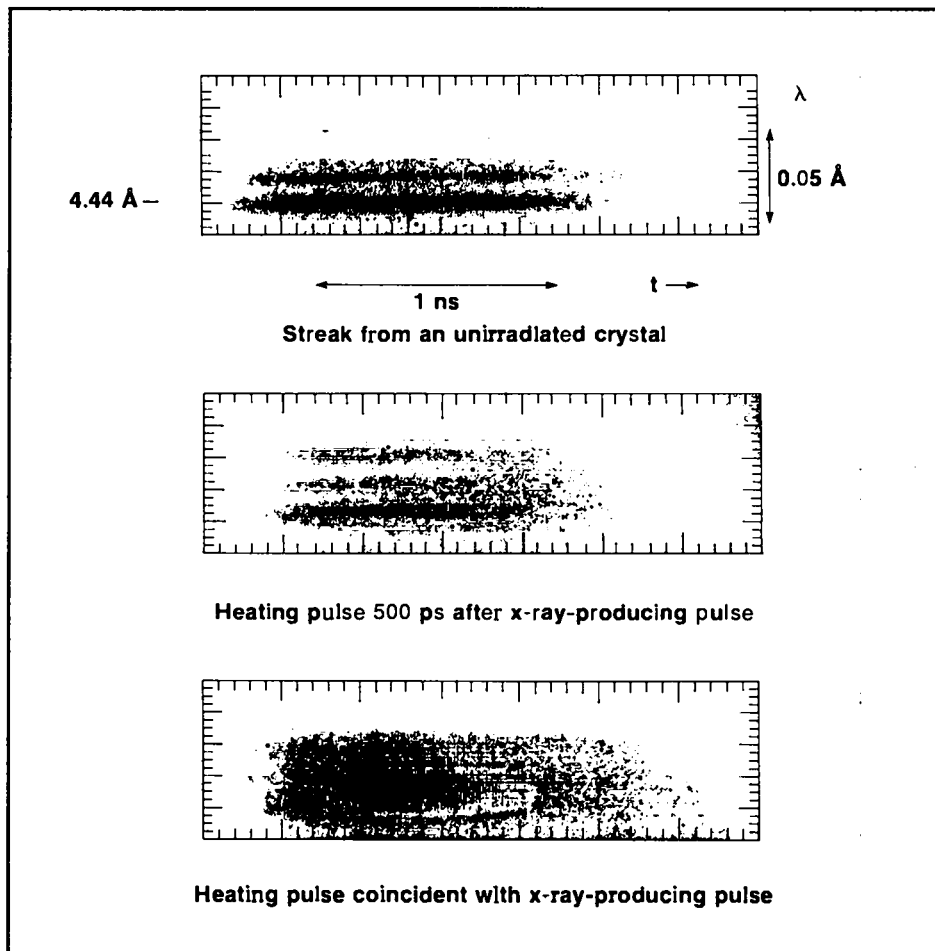
Fig. 4. (a) Time-resolved x-ray spectrum from a crystal with no heating pulse, (b) heating pulse 500 ps after x-ray-producing pulse, and (c) heating and x-ray-producing pulses coincident.

LP x-ray diffraction and radiography have also been applied to biological samples. The study of living cells is of obvious fundamental importance in medical and biological research. Although much can be learned using conventional microscopy in the optical region, a basic limitation is placed on the maximum spatial resolution by the wavelength of the light used. The resolution can be improved by probing with shorter wavelengths, that is,
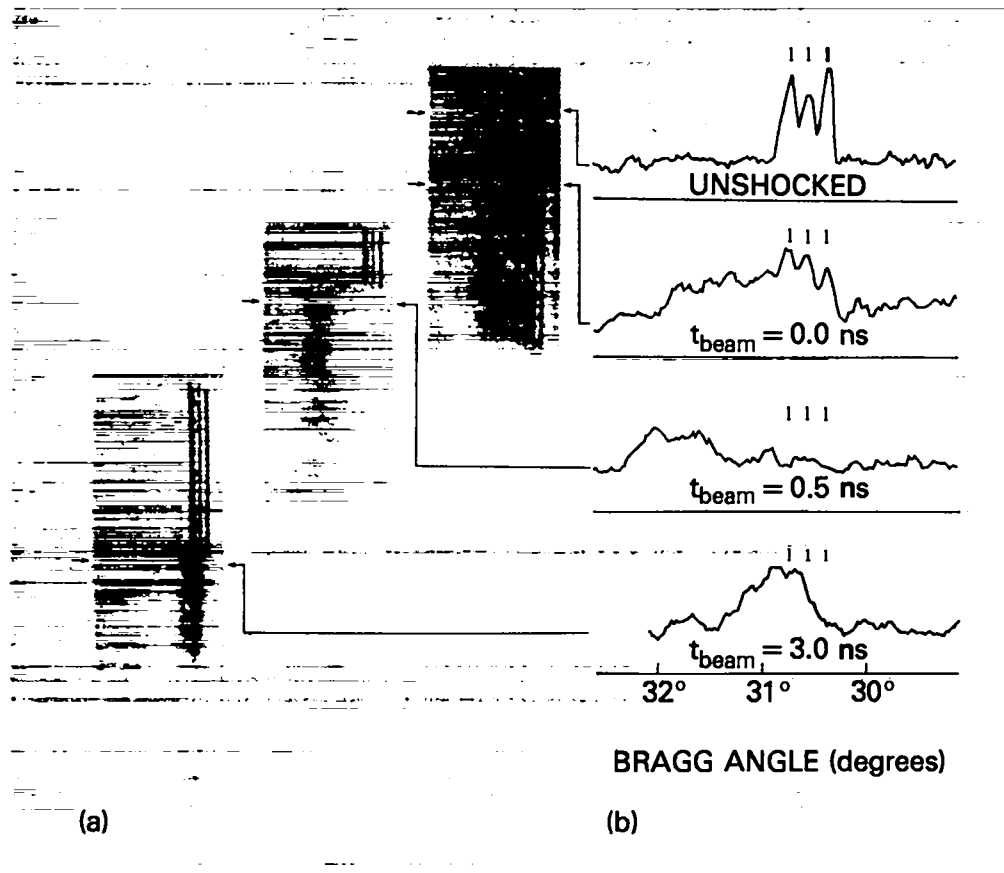
Fig. 5. (a) X-ray line spectra diffracted from silicon shocked at an incident laser energy density of 4 ±0.3 J cm^{-2} (an irradiance of 4 × 10^9 W/cm^2) are shown adjacent to reference lines simultaneously diffracted by the unstrained silicon lattice from a series of beam delays. Each photograph represents a separate shot and beam delay. (b) Densitometer scans, taken at indicated locations through the spectra in (a), are shown for a typical unshocked spectrum and shocked spectra at 0.0-ns, 0.5-ns, and 3.0-ns beam delays.

electron microscopy or soft x-ray contact microscopy. However, in electron microscopy, the sample must be dried and coated before observations can be made; the cell is thus killed and the sample may appear vastly different than its living counterpart. Similar problems occur with x-ray microscopy when a conventional x-ray source is used. A contact print of the sample is taken by irradiating it with x rays over a period of several hours. During this time, the cell suffers severe radiation damage and is killed during the course of the exposure. If a 1-ns burst of LP x-rays is used as the source, this problem is overcome; the radiation damage occurs on a microsecond time scale; thus a print of the living cell is obtained before cell death occurs. Laser plasma x-ray sources have thus made possible a valuable new technique for biological research.

The last few years have seen an increased interest (mainly by industry) in the utilization of x-ray lithography for 1:1 shadowgraphy printing of a patterned mask in

semiconductor circuit manufacturing. This interest results from the diffraction limitation on the resolution achievable with optical lithography, as well as problems associated with the small depth of field. X-ray lithography is the logical extension of the current optical lithography to sub-micron printed circuit manufacturing. A variety of x-ray sources have been used in lithography development. X-ray tubes are beset by low fluence, requiring impracticably long exposure times. This is particularly so because the relatively large focal spot requires a large working distance. Synchrotron storage rings have the advantages of being powerful and collimated but are exceedingly expensive and complex for industrial application. Laser irradiated targets have the advantages of a very small source (hence, good resolution even at close distances) and the possibility of scaling to a high repetition rate industrial laser. Additional characteristics are the reproducibility of source positioning (to a few micrometers), almost complete freedom in

choosing the target material (which affects the spectral characteristics), and mechanical stability in single-pulse operation. An example of relief structure produced in x ray resist with a laser plasma source is given on the first page of this chapter.

Recently, powerful LP-generated x-ray pulses with a duration of about 1 ps have been produced. Once again, the lasers used in such experiments had their original in the ICF program. In one test (Cobble et al. 1989), powerful bursts of kilovolt line radiation with ~1-ps pulse duration were measured. Such sources will be quite valuable in basic atomic physics research and in technological applications such as calibration of ultrafast x-ray instruments.

Versatile x-ray sources for a wide variety of applications are thus an important example of the technological applications of laser fusion research.

LASER-DRIVEN PARTICLE ACCELERATORS

Laser-driven accelerator schemes place unique demands on the specifications of the invoked laser systems. Selecting one such scheme, we review the laser requirements for driving open microstructures. This approach is the focus of a Brookhaven/Los Alamos collaboration on a proof-of-principle experiment. The specific advantages and disadvantages that lasers bring to this scheme are listed, and the appropriateness and scalability of existing technology is discussed. Much of the laser technology used in these early experiments (Bigio et al. 1987) is a result of earlier developments in the Los Alamos ICF program.

Laser-driven particle accelerators will have specifications that demand laser capabilities beyond what is currently available. Proof-of-principle demonstrations notwithstanding, the ultimate practicality of any of the schemes may well depend on the realities of laser development. It is interesting to note, therefore, that in projecting from the laser requirements of a demonstration experiment to those of a scaled system, probably fewer "leaps of faith" are required in the case of open structures than for many of the other currently proposed schemes. The fact that open structures can potentially be used as powerful focusing or bending elements (Palmer and Giordano 1985), wherein power-conversion efficiency is essentially unimportant, also adds attractiveness to the scheme. The conceptual design of the open structure or "grating" scheme is described in detail in Palmer (1982).

Requirements

The above statements require some justification. Table 3 lists the laser specifications as required by the initial demonstration experiments and also as envisioned for a replicated subunit of a scaled system. It should be noted that since many of the specifications of an imagined future generation accelerator are not well defined, some of the laser specifications are consequently nebulous. Nonetheless, the intent is to bolster the argument that we already have a technology base from which to extrapolate future development, and that much of that base is a result of the Los Alamos ICF program.

TABLE 3. Comparison of Short-Term and Long-Term Laser Requirements.

	Initial Experiments	Longer-range Requirements
λ	10 μm	10 μm ? longer ?
E	10 - 100 mJ	$\geq$1 J (depends on staging)
$\Delta\tau$	1 - 5 ps	1 ps
BQ	near diff. lim.	near diff. lim.
PRF	1 Hz	PRF of the accelerator (limit ~1 kHz)
ΔT	1 - 5 ps	1 ps
η	unimportant	$\geq$10%

($\Delta\tau \equiv$ pulse duration, BQ $\equiv$ beam quality, PRF $\equiv$ pulse repetition frequency, ΔT $\equiv$ synchronization jitter wrt accelerator pulse, $\eta \equiv$ efficiency.)

In the case of the requirements for the initial experiments, all of the specifications can either be met or exceeded by the system currently under construction. (It should be noted, however, that the optimum wavelength may be somewhat longer than 10 μm, but that the actual value has not yet been established.) Moreover, viable techniques to generate the critically specified short CO_2-pulse duration have already been demonstrated by others (Corkum 1983). The most difficult specifications to extrapolate to future requirements are the PRF (pulse repetition frequency) (with good beam quality) and the efficiency, η, especially if the requirements exceed 1 kHz and

10% respectively. Both of these requirements are readily within theoretical limits, and the predominant issues are ones of engineering development. However, much engineering is involved and would require a significant investment. Nonetheless, it is refreshing to note that extrapolation to as yet unconceived lasers is not required.

Advantages and Disadvantages

The following lists of advantages and disadvantages refer mainly to the differences that obtain when driving accelerator structures (resonant cavities) with optical lasers rather than with microwave sources. The end result with any viable laser-driven accelerator scheme, and the primary motivation for any of them, is that much higher accelerating gradients are obtained, promising the possibility for building accelerators of much shorter lengths and/or bending and focusing elements of previously unavailable power.

Advantages:
• Electrical breakdown thresholds (for continuous-wave operation) increase with frequency. Thus, there is an improvement of a factor $\simeq 40$ in going from 10 cm to 10 µm in the exciting wavelength.

• Additionally, the higher frequency (and consequently the broader bandwidth) available with lasers permits operation at very short pulse durations. Breakdown thresholds also increase as pulse durations get shorter, resulting in an advantage of several orders of magnitude for picosecond CO_2 laser pulses over continuous or long-pulse microwaves. In this regime, one generally speaks of "optical damage" power-density limits for surfaces and structures. In our case, those limitations are likely to result in maximum accelerating fields of less than 10^8 V/cm, if no surface wear of the structure is tolerated. This is nonetheless a remarkably large gradient.

• The smaller volume of the structures, as well as the short pulse duration, result in a much smaller stored energy per unit of energy transferred to the beam. One consequence is that as the accelerator pulse repetition rate decreases, the system efficiency changes very little. Although not generally invoked for high-energy physics experiments, low duty cycle or "single-shot" operation may useful for other applications, and under such conditions laser-driven devices may prove the most efficient.

• At 10 µm, a picosecond pulse contains only 30 waves. One consequence of such a short duration driving pulse is that there is no reason for the q-factor of the cavities to be

better than a value of about 100. It then follows that the manufacturing tolerances of the accelerating structures can be fairly loose. Surface accuracies on the order of 1% are acceptable.

Disadvantages:
• There is no mechanism yet identified for recapturing any unused optical energy. Thus, unless the transfer efficiency of optical energy to a single electron bunch is quite high, overall system efficiency may be limited to unacceptable levels for full-scale accelerators.

• Under the best of circumstances, and regardless of the transfer efficiency of laser energy to beam energy, the efficiency of the laser system itself is not likely to exceed 20%. Intrinsic efficiencies of free-electron lasers (FELs) can surpass that value, but FELs pose other problems that may be insurmountable for open structure schemes.

PLANS AND STATUS OF EXPERIMENTAL COLLABORATION

With CO_2 lasers the shortest pulse that can normally be obtained with mode-locking techniques is about 1 ns. This is due to the fact that the typical gain bandwidth of the CO_2 laser is too narrow to support shorter pulses. Increasing the bandwidth with pressure broadening generally results in a device whose gain duration is too short for effective mode locking. Such a pressure-broadened device, however, will work well as an amplifier if a picosecond oscillator pulse is available for amplification. This is the basis of our system design.

In our system we plan to take advantage of isotopic shifts in the gain profile that occur for different combinations of carbon and oxygen isotopes in the CO_2 molecule. By mixing different isotopic combinations in the same laser gas mix (Gibson et al. 1979) we obtain adequate gain broadening at pressures in the range of 3 to 4 atm.

To provide a picosecond seed pulse for amplification, a small piece of a longer CO_2 oscillator pulse is switched out by means of a transient plasma mirror at the surface of a slab of semiconductor material. The basic features of this technique have also been demonstrated by Corkum (1983), and the specific design for our system is illustrated in Fig. 6. A picosecond pulse at 1.06 µm, obtained by compressing and amplifying a pulse from a mode-locked Nd:YAG laser, is used to generate a plasma of free carrier pairs in the surface volume of a slab of germanium. The risetime of the free carrier density can be almost as fast as the risetime of the pulse from the YAG laser and the plasma density quickly becomes sufficient to be highly reflecting at 10 µm.
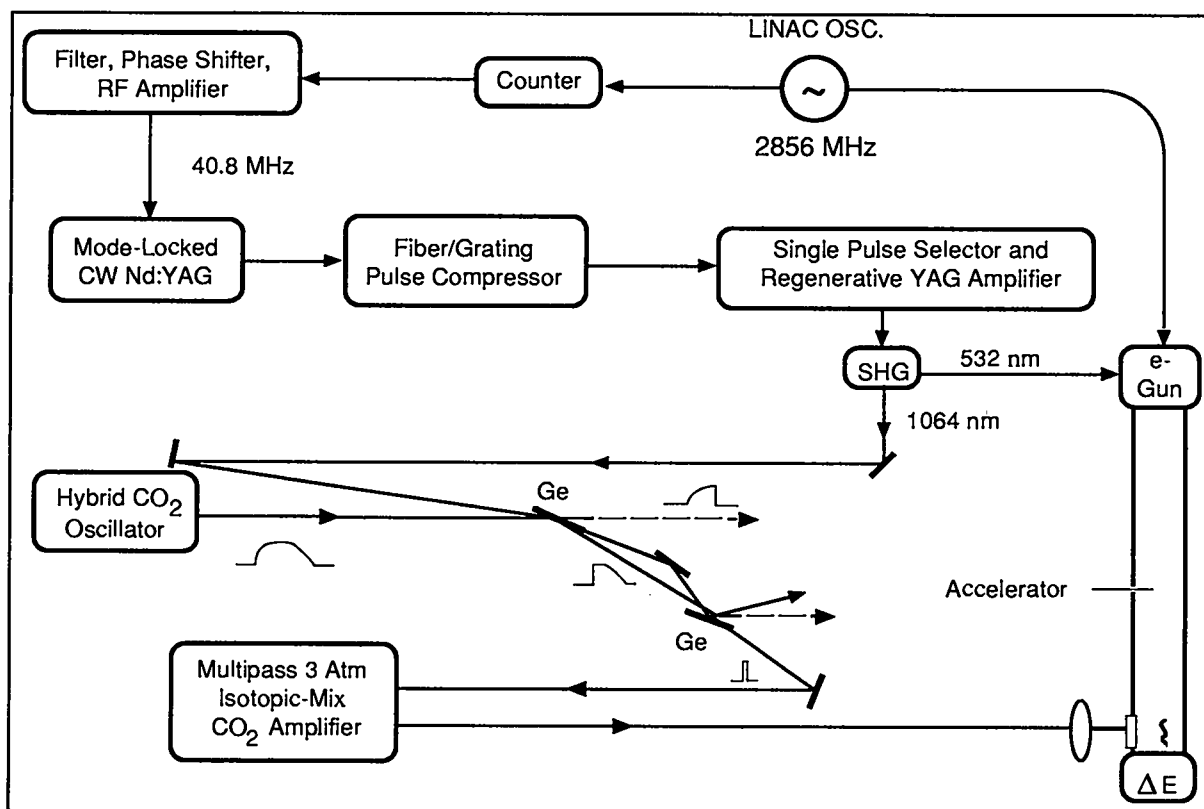
Fig. 6. Schematic of the picosecond CO_2 laser source. SHG represents the second-harmonic generator and Ge denotes the germanium semiconductor slabs used as the fast optical switches.

Thus the reflected portion of the pulse from the oscillator has a very sudden risetime. However, the decay time of the free carriers is too slow for our purposes, so the fast fall of the pulse is generated by using a second germanium slab in the transmission mode. In this case the unwanted tail is removed by plasma reflection, and the remaining transmitted pulse has both the short rise and fall times. This short pulse is then sent to the isotopic mix amplifier before proceeding to the experimental area.

The oscillator is a hybrid composed of two parts: a transverse fast discharge and a low pressure discharge. The result is a smooth single-longitudinal mode pulse, about 100-ns long, and with good pulse-to-pulse reproducibility. The amplifier has a discharge volume of 2.5 × 5 × 120 cm, and it runs at 3 - 4 bar. A closed-cycle gas-handling system with catalytic cleanup is used to avoid loss of the less common components of the isotopic mix.

Perhaps the most interesting feature of the design is the method of highly accurate synchronization of the short 10-μm pulse to the arrival of the electron bunch from the LINAC. This timing is very critical, and jitter of more than 1 - 2 ps cannot be tolerated. The scheme, as illustrated in Fig. 6, utilizes the same picosecond YAG pulse that

generated the plasma mirrors to produce the initial electron bunch at the e-gun injector of the LINAC. This is accomplished by first frequency doubling the 1064-nm light to the green at 532 nm with a second-harmonic generator (a passive, bi-refringent, nonlinear crystal) and then directing the picosecond pulse of green light to the surface of a photocathode material used as the electron source in the injector. All elements are passive, and the ultimate jitter between the CO_2 light pulse and the electron bunch at the experimental station depends mainly on the accuracy of the phasing with respect to the rf wave in the LINAC. We expect the end result to be a jitter of ≤2 ps.

At the time of this writing, the laser system is essentially complete, and integration into the advanced accelerator test facility at Brookhaven National Laboratory is underway.

REFERENCES

Bergmann, E. E., I. J. Bigio, B. J. Feldman, and R. A. Fisher, "High-Efficiency Pulsed 10.6-μm Phase-Conjugate Reflection via Degenerate Four-Wave Mixing," Optics Lett. 3, 82, 1978.

Bigio, I. J., and M. Slatkine, "Injection-Locking Unstable Resonator Excimer Lasers," IEEE J. Quant. Elect., QE-19, 1426, 1983.

Bigio, I. J., N. A. Kurnit, R. F. Harrison, and T. Shimada, "Lasers for Open Structures," in Advanced Accelerator Concepts, F. E. Mills, Ed., A.I.P. Press, New York, 1987.

Burnett, N. H., G. D. Enright, A. Avery, A. Loen, and J. C. Kieffer, "Time Resolved K α Spectra in High-Intensity Laser Target Interaction," Phys. Rev. A 29, 2294, 1984.

Cobble, J. A., G. A. Kyrala, A. A. Hauer, A. J. Taylor, C. C. Gomez, N. D. Delamater, and G. T. Schappert, "Kilovolt X-ray Spectroscopy of a Subpicosecond-Laser-Excited Source," Phys. Rev. A, 39, 454, 1989.

Corkum, P. B., "High-Power Subpicosecond 10-μm Pulse Generation," Opt. Lett. 8, 514, 1983.

Eason, R. W., P. C. Cheng, R. Feder, A. G. Michette, R. J. Rosser, F. O'Neill, Y. Owadano, P. T. Rumsby, M. J. Shaw, and I. C. E. Turcu, "Laser X-ray Microscopy," Opt. Acta 33, 501, 1986.

Fairand, B. P., B. A. Wilcox, W. J. Gallagher, and D. N. Williams, "Laser Shock-Induced Microstructural and Mechanical Property Changes in 7075 Aluminum," J. Appl. Phys. 43, 3893, 1972.

Forslund, D. W. and P. D. Goldstone, "Photon Impact, High-Energy Plasma Physics with CO_2 Lasers," Los Alamos Science 12, 2, 1985.

Förster, E., K. Goetz, K. Schäfer, and W. D. Zimmer, "Laser-Generated Plasma as a Source for Real-Time Studies in X-ray Crystal Research. I. Fundamental Remarks about Source Characteristics and Requirements," Laser and Particle Beams 2, 167, 1984.

Gibson, R. B., K. Boyer, and A. Jovan, IEEE J. Quant. Elect. QE-15, 1224, 1979.

Hauer, A. "Interaction of X-rays and Acoustic Waves in Solids," Ph.D Thesis, University of Rochester, University Microfilms, Inc., Ann Arbor, MI, 1976.

Hauer, A., R. Goldman, R. Kristal, M. A. Yates, M. Mueller, F. Begay, D. VanHulsteyn, K. Mitchell, J. Kephart, H. Oona, E. Stover, J. Brackbill, and D. Forslund, "Suprathermal Electron Generation Transport and Deposition in CO_2 Laser Irradiated Targets," in Laser Interaction and Related Plasma Phenomena, Vol. 6, H. Hora and G. H. Miley, Eds., Plenum Pub. Co., New York, 1984.

Hauer, A. A., D. W. Forslund, C. J. McKinstrie, J. S. Wark, P. J. Hargis, Jr., R. A. Hamil, J. M. Kindel, "Current New Applications of Laser Plasmas," LA-11296-MS, Los Alamos National Laboratory, Los Alamos, NM, 1988.

Mallozzi, P. J., H. M. Epstein, and R. E. Schwerzel, "Laser-Produced Plasmas as an Alternative X-Ray Source for Synchrotron Radiation Research and for Microradiography," in Advances in X-ray Analysis, G. J. McCarthy, C. S. Barrett, D. E. Leyden, J. O. Newkirk, and C. O. Rund, Eds. Plenum, New York, 1979.

Palmer, R. B., and S. Giordano, "Preliminary Results on Open Accelerating Structures," in Laser Acceleration of Particles, C. Joshi and T. Katsouleas, Eds., A.I.P. Press, New York, 1985.

Palmer, R. B., "Near Field Accelerators," in Advanced Accelerator Concepts, F. E. Mills, Ed., A.I.P. Press, New York, 1982.

Pirri, A. N., "Theory for Laser Simulation of Hypervelocity Impact," Phys. Fluids 20, 221, 1977.

Priedhorsky, W., D. Lier, R. Day, and D. Gerke, "Hard X-ray Measurements of 10.6-μm Laser-Irradiated Targets," Phys. Rev. Lett 47, 1661, 1981.

Schäfer, K, and W. D. Zimmer, "Laser-Generated Plasma as a Source for Real-Time Studies in X-Ray Crystal Research. II. In Search of an Optimum Choice of Laser Plasma Coupling Conditions, Laser and Particle Beams 2, 187, 1984.

Wark., J. S., A. Hauer, and J. D. Kilkenny, "Studies of X-ray Switching and Shuttering Techniques," Rev. Sci. Instrum. 57, 2168, 1986.

Wark, J. S., R. R. Whitlock, A. Hauer, J. E. Swain, and P. J. Salone, "Shock Launching in Silicon Studied with Use of Using Pulsed X-ray Diffraction," Phys. Rev. B 35, 9391, 1987.

Yaakobi, B., P. Bourke, Y. Conturie, J. Deletrez, J. M. Forsyth, R. D. Frankel. L. M. Goldman, R. L. McCrory, W. Seka, J. M. Soures, A. J. Burek, and R. E. Deslattes, "High X-ray Conversion Efficiency with Target Irradiation by a Frequency Tripled Nd:Glass Laser," Opt. Comm. 38, 196, 1981.

Yang, L. C. "Stress Waves Generated in Thin Metallic Films by a Q-Switched Ruby Laser," J. Appl. Phys. 45, 2601, 1974.

III. Target Fabrication
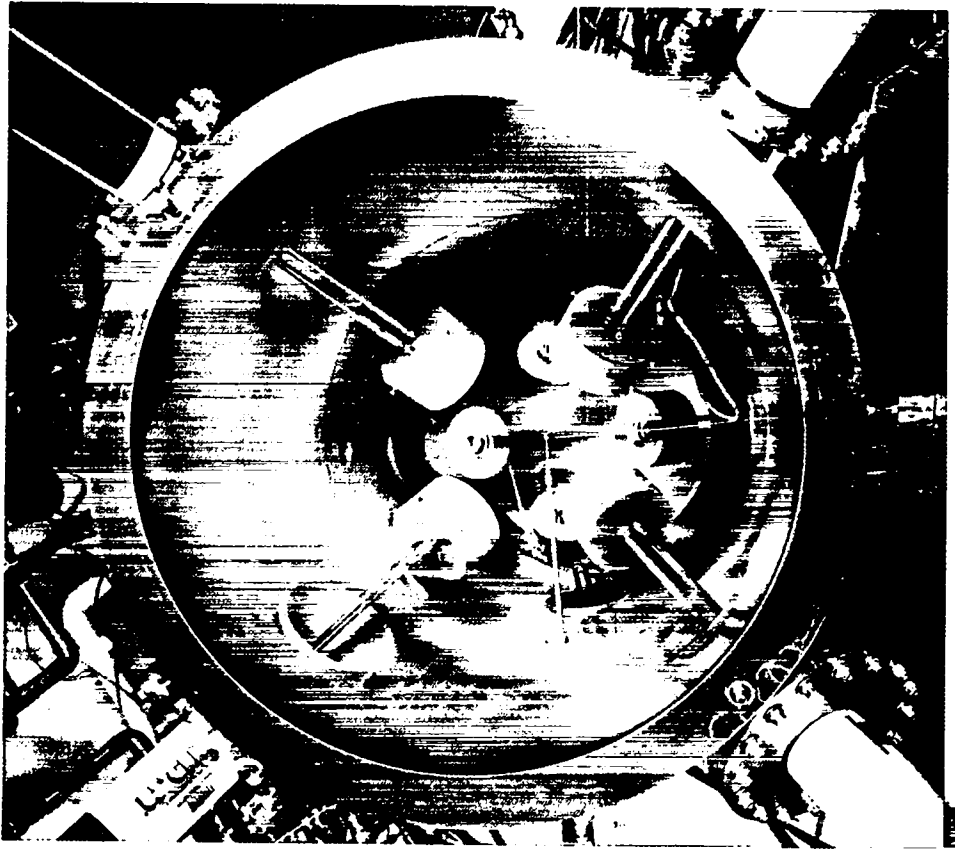
Interior view of the eight-beam coating device used to manufacture certain ICF targets.

III. TARGET FABRICATION

Larry Foreman

INTRODUCTION

The story of laser fusion fabrication in the past four years is the story of a program in decline. Compared to the fabrication effort of 1984, when the Helios CO_2 laser was consuming targets at the rate of 600 per year, the current effort is less than skeletal. There is only one reason for this decline: Los Alamos does not have a laser fusion driver. Our experimenters are working hard to accomplish a reduced program using drivers at other institutions. The fabricators have provided them with the targets they need for this work, but this effort currently consumes only 25 to 50 shots per year.

Even this reduced program has produced some fabrication challenges and milestones which appear below. These accomplishments occur in the areas of metal coatings, foam fabrication and invention, micromachining, assembly, characterization and cryogenic technology.

PROGRESS IN TECHNOLOGICAL DEVELOPMENT

Metallic Coating

Metallic coatings are useful in target fabrication for a number of reasons. When a metallic layer heats and ionizes in a laser induced plasma, it emits x rays characteristic of its atomic number (Z). With proper filtering of the x-ray emission, a metallic layer in the target can provide information about the implosion symmetry. An open shutter image gives information on compression and streaking the filtered image records the implosion or the ablation history.

We broke new ground in the deposition of metallic coatings on laser targets during the last four years, driven by more stringent requirements on layer thickness and uniformity. Thin layers keep the metal from perturbing the implosion. Uniform coatings simplify the interpretation of the implosion data. For example, targets to measure heat transport in low density plasmas required aluminum layers 0.1-μm thick that were uniform to within 10%. Forming these layers was challenging in 1985-1986. With care, we were able to produce them by a physical vapor deposition (PVD) process using a two-axis rotator. Characterizing the layer thickness at the 100Å level on the spherical surface was impossible. We eventually settled for a resolution of 300Å on the equator, 90° from the stalk attachment.

The quest for uniform, thick coatings draws motivation from the need for small, metallic gas containers. We have developed (McCreary et al. 1986, 1988) an eight-gun, planar magnetron sputter coater (Fig. 1) to produce gas-tight vessels by coating onto shaped mandrels and then dissolving the mandrels to leave a hollow container. The eight guns in this PVD system reside at the corners of a cube as shown on the first page of this chapter. The substrate rests in the center of the cube and can rotate about either a vertical or a horizontal axis. This arrangement leads to uniform coating of the substrate with a high average angle of incidence of the vapor flux. Coatings made by this gun geometry, and using the technique of reactive gas pulsing, are strong and specular. They show none of the weakness in the polar regions that plagued previous attempts to coat thick aluminum onto a sphere. The system coats aluminum at a rate of 0.5 to 0.6 μm/hr, accomplishing the coatings we need in a few hours. The eight-gun sputter coater allows even coverage of all geometries except toroidal or other re-entrant forms. The coater is being duplicated for dedicated beryllium coating operations which require special safety and ventilation considerations.

Backlighter production orders motivated research into coating new materials by PVD. A heavy metal backlighter appeared promising for unstable hydrodynamic experiments and we tried a number of materials. We successfully deposited cesium iodide, but preserving the integrity of CsI coatings required extraordinary measures because of their affinity for water. Bismuth coatings were the most

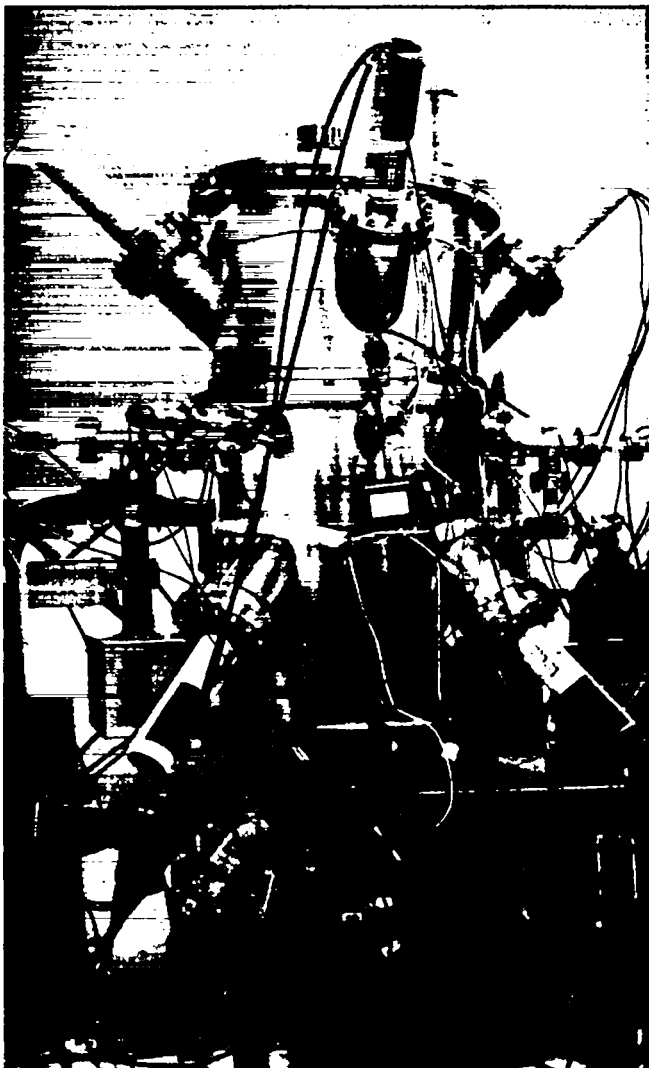successful both in the coating process and in performance as a backlighter.

Fig. 1. Eight-gun coater

In 1988, we adapted a coater to deposit uranium 238. This element requires special handling because it is both highly toxic and pyrophoric (that is, it catches fire on exposure to air). Uranium is a very desirable high-Z backlighter, but it would not adhere well to the carbon fiber substrates used in this work. However, for high-Z conversion efficiency experiments, we successfully coated uranium 238 onto plastic spheres of various sizes. Codeposition of 0.5 wt% of Ti decreased the tendency of the Uranium to oxidize on exposure to air. A thin coating of Cr on the plastic substrates greatly increased their adhesion (Gobby et al. 1989). Finally before exposing the coatings to air, they were overcoated with 400Å of Al to further

protect them from oxidation. (See Silicon/Aluminum/CH Targets for NOVA for more details).

Foam Fabrication

Foams are used in fusion targets to simulate a fuel-filled capsule, to provide hot-electron insulation, or to form a cushion layer. For ICF work, foams must be open-celled with densities in the range of 0.01 to 0.1 gm/cm^3 and have pore sizes of less than 5 μm.

Historically, foam fabricated of poly (1,4) methylpentene (TPX) dissolved in bibenzyl (Young 1987) provided material that fulfilled the density and pore size requirements. TPX foam can be machined into cylinders and spheres. This foam results from cooling a hot solution of TPX in bibenzyl through the phase-separation point. Below this transition the TPX forms a continuous phase surrounding isolated droplets of bibenzyl. Further cooling to room temperature solidifies the bibenzyl. The resulting solid mixture is sufficiently strong to machine to shape. Leaching with methanol extracts the bibenzyl from the polymer matrix and leaves an open celled TPX foam. This process has several disadvantages:

- The leaching process produces a variable shrinkage in the foam which depends on the solvent used to remove the bibenzyl. Thus the results machining the unleached mixture to dimension were unpredictable.
- The pores grow as the density of the material decreases so that foams less than 25 mg/cm^3 have pores that are too large.
- The low-density, large-pore material is mechanically weak.

The search for an alternative foam led researchers at AWE, Lawrence Livermore National Laboratory (LLNL), and Case Western Reserve, as well as at Los Alamos, to a polystyrene emulsion foam. The production process was discovered and patented earlier by Unilever (Barby and Haq 1982) in the UK. At Los Alamos, an adaptation of this process forms foam by polymerizing styrene in an airless, water-in-oil emulsion (Williams and Wrobleski 1988; Williams 1988). The styrene is the continuous phase formed around an internal water phase of at least 90%. These foams (see Fig. 2) have a distinct ringlet appearance. They are stronger than TPX because essentially all the polymer is load bearing. Moreover, they have smaller pore sizes than TPX foam at the same density. Polystyrene emulsion foams in the 25 mg/cm^3 range can be readily machined using high-speed cutting techniques.
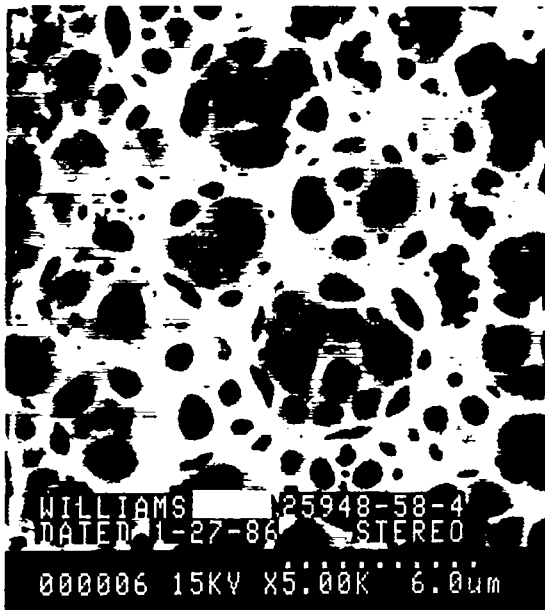
Fig. 2. Polystyrene foam.

Foam materials have been candidates for liquid DT fuel sponges in a number of reactor target designs (Sacks and Darling 1986). In this application foam, pore size takes on an increased significance. Cryogenic targets for an ICF reactor must accelerate to high velocity for insertion into the target chamber. Pore sizes less than 1 μm keep the liquid fuel in place under these high accelerations. A composite foam developed at Los Alamos (Nyitray et al. 1988) combines the strength of the polystyrene emulsion foam with the extremely small pore sizes of the resorcinol-formaldehyde (RF) systems. RF foams have pores smaller than 1 μm at low densities, but very little strength. The Los Alamos approach is to backfill a polystyrene foam with RF foam. Thus the voids in the strong polystyrene foam are filled with the high-porosity, small-pore, but mechanically weak RF foam. The composite product retains the high strength of the polystyrene emulsion foam and small pores of the RF foam; this results in a strong, high-porosity, composite structure. This product has extremely promising application as a fuel-containing layer for a cryogenic, liquid-layer reactor target.

Micromachining

Mechanical Micromachining

A major component of a strong target fabrication capability is fast and effective reaction to requests for out of the ordinary targets. The Los Alamos effort fosters this capability by maintaining a strong micromachining group in the same building that houses the rest of fusion target fabrication. This arrangement makes the machinist part of the interactive design team in an immediate way.

Our capabilities include: CNC diamond turning for optical surface finishes; lapping capability for spherical targets and mandrels; microscopic machining operations and hole drilling for target components of 0.1-mm size; electro-discharge machining (EDM), which allows machining of delicate pieces without deformation; and a CNC milling machine for limited run production pieces. These machining facilities are complemented by a well-equipped inspection group with large optical comparators, a Moore Precision Measuring Machine, and microgram balance. This shop is manned with some of the world's best machinists. It has the capability for safely carrying out hazardous operations such as Be machining and work on DT containing components.

ICF targets require many materials which are products of development efforts. Finding effective machining operations for these new materials is a development effort in itself. It is extremely effective to have a group with this machining capability in hourly contact with the target fabrication supervisor. This operation has been proven in the Centurion program. We are anxious to put it to the test in the fabrication of targets for AURORA.

Laser Micromachining

Laser micromachining is an integral part of our target fabrication capability. Our dye laser can bore micron-sized holes and hole arrays in a variety of substrates including glass, plastics, and metals. Holes of this size in metal foils

are useful as diagnostic pinholes or, when cut repeatedly along a line, as slits. The metal foil can be selected from any region of the periodic table depending on the Z number required. The technique is useful also in making coating masks for PVD processes. Microshell targets can fill rapidly with diagnostic gases, argon or krypton for example, through a small laser-drilled hole. Filling targets with these relatively heavy gases by the diffusion techniques used for hydrogen isotopes may take months. These small holes can be plugged with epoxy to contain the gases. Finally, targets can be backfilled with epoxy through a laser drilled hole to strengthen them before sectioning for layer characterization on the scanning electron microscope.

At lower areal power density small lasers are useful for photoablation. The defocused laser will blow away a thin metal coating, leaving the plastic or glass substrate unharmed. Our laser machining station has a full complement of target manipulation equipment. A cylindrical or spherical target can be rotated under the stationary beam. Combining this motion with our computer-controlled X and Y stages allows creation of almost any pattern on a substrate. We simply remove the coating where it does not belong. Figure 3 shows a unique target fabricated with these methods (Foreman et al. 1988b).

A CO_2 laser at our disposal with similar target trepanning capability is useful for cutting quartz into complex shapes. Our Nd:YAG glass laser provides efficient microwelding and joining capabilities for metals. These capabilities round out the noncontact machining suite and can often make possible the fabrication of targets with complex geometric features.

We recently received a long-term loan of a KrF excimer laser. We hope to adapt it to the photoablation of polymeric materials and foams.

Assembly

Targets produced in 1985 for Antares were generally complex structures. Most required specialized jigs and fixtures to aid in their construction. As the Los Alamos experimental effort moved to other laser facilities, the targets became less complicated. Direct illumination schemes at Rochester and Rutherford resulted in simpler targets. At NOVA, for indirect illumination, much of the final target preparation occurs onsite by people familiar with the target chamber requirements. In these experiments, we supplied the essential target and the resident fabrication group added the shields and backlighters that made the target chamber-ready. Another difference between targets produced in 1985

and those produced more recently is the size of the target support. Targets for Antares had to survive handling in a target insertion mechanism that subjected them to significant mechanical stress. Moreover, the targets were themselves characteristically 500 to 600 µm in diameter, larger by a factor of 3 than those produced for Helios. These two factors contributed to larger target losses on insertion into the target chamber on Antares. Fabricators adapted to these target losses by making the target stalks and glue joints more robust. The experimenters objected to the increased perturbations created by these larger appendages, but the result was larger supports.

Our current targets are mounted on carbon fibers 7 to 10 µm in diameter and a few millimeters long. These attach to the drawn glass stalks that formerly served as the complete stalk. The result is a target with a much smaller perturbation at the point of stalk contact than previously.

A variation on this theme is useful for holding targets temporarily during several processing steps. We coat the glass stalk and fiber with RTV silicone rubber. When this material cures, it retains an aggressive surface adhesion, gripping objects securely with just a touch. We found that this method would secure spherical shell targets through vacuum coating operations and other postprocessing steps. When all target processing was completed, the target could be pulled off the stalk without damaging the target surface. Temporary processing stalks made in this manner are extremely useful for many target fabrication related operations (Foreman et al. 1988b).

Characterization

Microradiography

X-ray techniques are used on ICF targets to measure coating and wall thicknesses, variations in coating and wall thickness, gas fill pressures, and elemental composition. These techniques also measure the density and thickness uniformities of bulk materials from which smaller ICF targets are made. They are equally useful for both opaque and transparent materials. Microradiographic gauging, a development specifically for ICF target characterization, measures thicknesses and thickness variations in coatings. Standard x-ray fluorescence techniques detect gas fill pressures and elemental composition. Standard x-ray and gamma-gauging techniques provide information about both the absolute density and thickness and their uniformities for bulk samples.
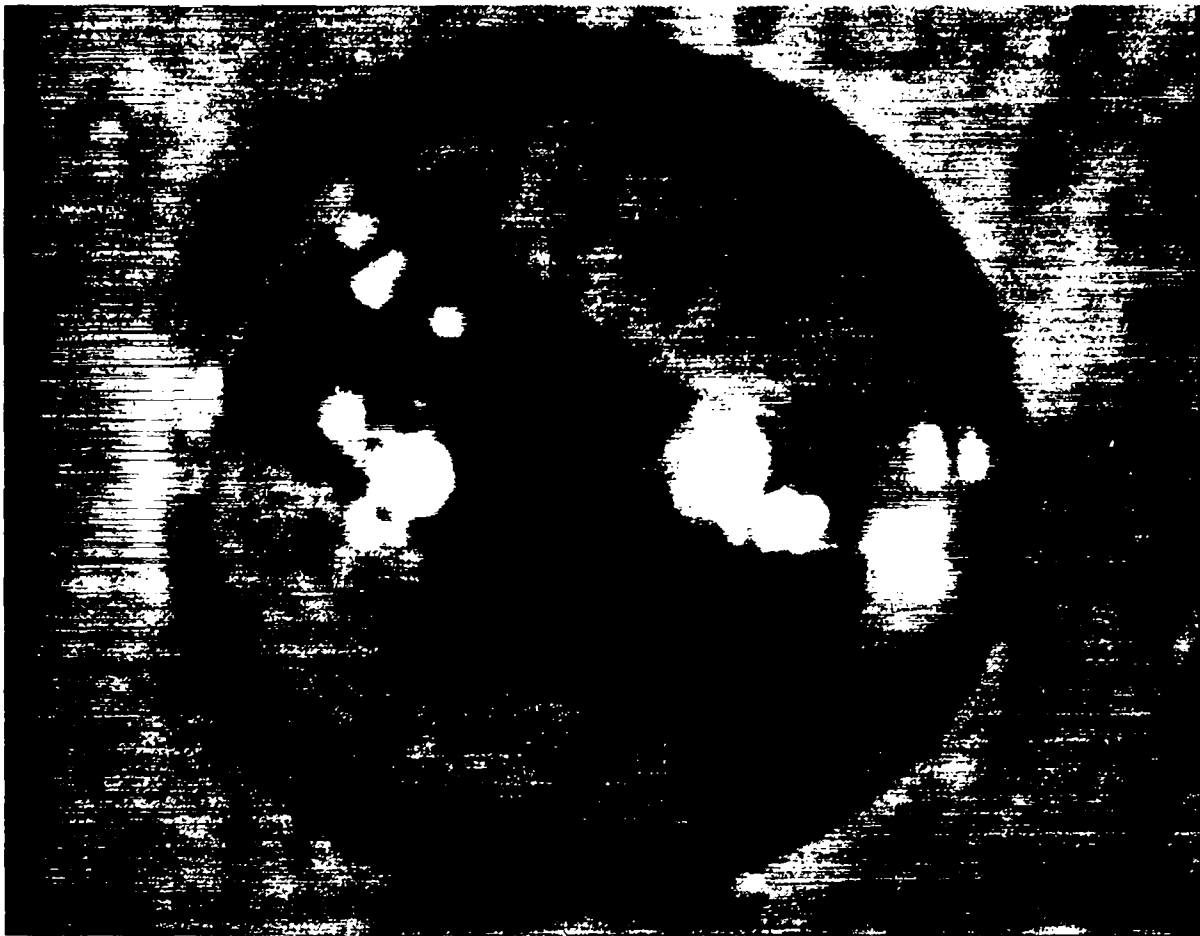
Fig. 3. Banded target.

Standard radiographic gauging involves placing the targets to be measured in near contact with a photographic emulsion. A uniform beam of x rays passing through the targets creates x-ray images on the emulsion. These images are as small as the targets and require microscopic examination to determine target quality. Three general forms of target defects that can be detected by contact radiography appear in Fig. 4.

Improvements on this standard technique have been made on many fronts. The film density data can be digitized and a fast Fourier transform taken to extract concentric and elliptical defects (Stupin 1987a). Concentric and elliptical defects at the 1% level destroy implosion symmetry, but fortunately they are detectable at this magnitude. A statistical test detects short wavelength wart and dimple defects. Wart and dimple defects must be less than 0.1% of wall thickness. This is beyond the sensitivity of photographic methods; however, advanced techniques now being developed should provide this level of sensitivity and

more. Point projection radiography, using an x-ray sensitive television camera and digital image processing, can give the signal-to-noise ratios of 700 or more required for dimple and wart detection at the 0.1% level. The x-ray shadow is magnified by the geometry of the exposure until the defect size matches the camera resolution (Fig. 5). Digitally summing image frames until signal-to-noise ratio increases to the desired level (Stupin 1987b) will give the necessary sensitivity.

A further increase in sensitivity results from digital image subtraction (Stupin et al. 1988). Averaging an image of one view of the target and then digitally subtracting from it the average of an orthogonal view of the target leaves only the differences in the two views. This method removes fixed pattern noise, that is noise introduced by the television camera. This method has detected 2 μm tungsten wires radiographically and a 0.1% area density change in an aluminum step wedge.

Fig. 4. Defects radiography.
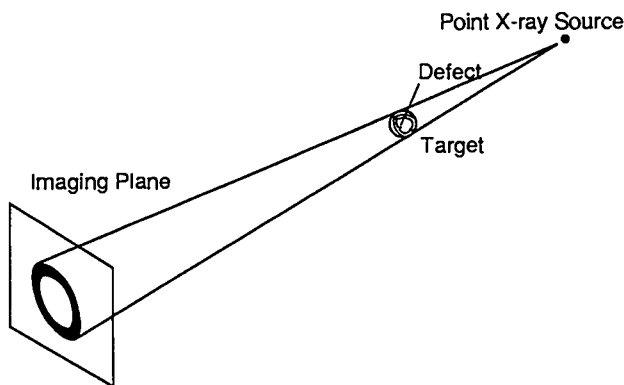
Fig. 5. Point projection radiography.

Scanning Electron Microscopy

Scanning electron microscopy (SEM) is a well-used tool in laser target characterization. Popularity of the SEM can be attributed to three characteristics of a SEM image:
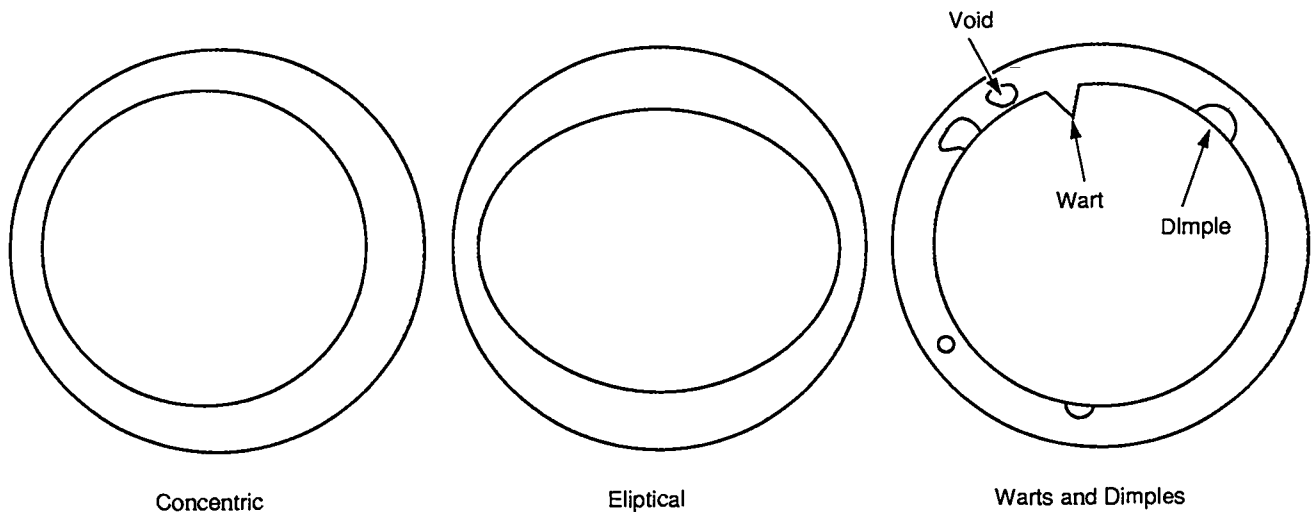
- its extraordinary depth of field, because of the small divergence of the electron beam;
- its high resolution owing to the short wavelength of the electrons; and
- its life-like, three dimensional quality, easily interpreted (Foreman et al. 1988a).

Versatility should probably be added to the list. For example, the SEM can act as a source for x-ray microradiography. Using the small electron spot size and converted soft x rays, which would not travel far in air, one can characterize very low-density materials.

We have acquired two Hitachi, S520 SEMs. One uses a standard tungsten hair-pin electron source, the other has a L_aB_6 long-lifetime source with improved stability. Also we have a Phillips APD 3720 x-ray defractometer that can provide information on the crystallinity of samples.

X-ray Fluorescence

Thickness measurement by x-ray fluorescence is another example of SEM versatility. Reported first in 1982 (Elliott et al. 1982) for Au-metallized, glass microspheres, the technique operates as follows: electrons impinge on the sample, penetrate the Au layer, and stop in the glass, producing Au and Si x-radiation. The ratio of Au/Si flux detected is proportional to the gold layer thickness. The original technique described by Elliott et al. (1982) required some extraordinary measures to circumvent beam stability problems with the SEM in use at the time. With the improvement in beam stability afforded by the Hitachi microscopes, we can calibrate with bulk samples of the coated material. Moreover, we can measure compounds in addition to single elements.

Cryogenic Targets

High-gain target designs for an ICF fusion reactor rely on cryogenic fuel for their high calculated performance. Recent developments in the physics of solid DT layers has made possible the fabrication of cryogenic targets in mm-sizes suitable for reactor-type yields.

Solid DT self-heats because of the beta decay of tritium and the subsequent reabsorption of the beta particle (electron) in the frozen DT. Heat production at the rate of 0.3 W/gm of T is measured. The implication of this phenomenon for the formation of uniform, cryogenic layers was first pursued by John R. Miller (LASL 1976). The radioactively deposited energy drives selective sublimation in the frozen fuel.

Regions where the DT-ice layer is thick have warmer interiors than regions where the layer is thin. Thus material sublimes from the thick regions and coats out on the regions where the ice is thin. This process proceeds exponentially with a characteristic time constant for DT of about 30 minutes.

Researchers at Los Alamos set out to verify that the process takes place as predicted. Experiments in a cylindrical geometry for pure T_2 (Hoffer and Foreman 1988) produced a symmetrization time constant for that material of 14.8 minutes. Later measurements on DT (Hoffer and Foreman 1989) confirmed the model for fresh DT (see Fig. 6), and also measured a slowing of the process that increased as the sample aged; each day of sample age added 12 minutes to the symmetrization time constant. Apparently ^{3}He, a non-condensable product of the beta decay of T, accumulates in the target interior and impedes the mass flow of the DT across the target. Further work on this phenomenon is in progress, but the beta layering process appears to provide thick, symmetric layers of solid DT. Designs of beta-layered targets for the ICF reactor and means of fabricating them have been published (Foreman and Hoffer 1988, 1989).

Specific Targets that Illustrate Fabrication Technology

Plasma physicists at Los Alamos have had to perform their work at other institutions since the closing of Antares in the summer of 1985. Targets for experiments at other institutions are still prepared at Los Alamos; however, the final steps are left for the fabricators at the laser facility where the experiment is performed. For example at NOVA, the Los Alamos fabricators make the target components and characterize them. The Livermore fabricators assemble the target, the hohlraum, backlighters or alignment fiducials into an assembly ready for the target chamber. In what follows, we describe specific target designs for experimental campaigns performed at other institutions.
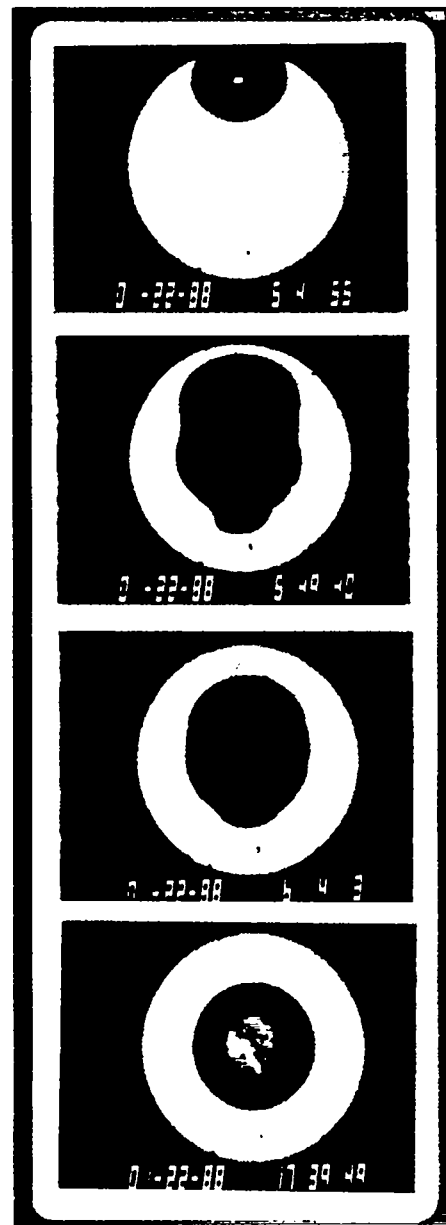
Fig. 6. β layering for DT. Symmetrization driven by β activity in solid DT. The figure shows an axial view through a cylinder 5.74 mm in diameter. The cell is back lit, and the photos show the clean optical path through the DT in the cell. 6a shows the cell nearly filled with liquid DT. The cell was filled completely and then frozen. 6b shows the shape of the DT layer at the instant that freezing was complete. DT contracts 13% on freezing and forms the large irregular void (vapor space) in the center 6c: after 35 minutes, the void has symmetrized noticeably. 6d: at 110 minutes elapsed, the symmetrization is nearly complete.

Targets for UR/LLE

Thermal Transport Targets

Targets for this experiment consisted of layers built on solid spheres as shown in Fig. 7. The thin aluminum layer functioned as an emission marker. When the aluminum lines appeared in the target emission spectra, the aluminum had heated to ionization. A measurement of thermal transport in the low-Z plasma resulted from placing the layer at various depths below the target surface and timing the appearance of the aluminum radiation.

Al layer
(0.05 μm)

CH Coating

OR

75 μm
150 μm
300 μm

Glass Sphere
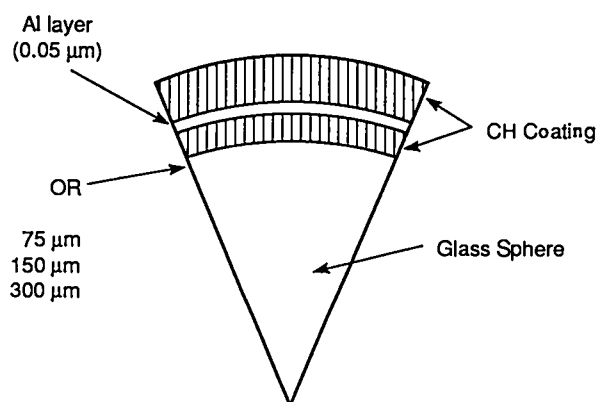
CH Coating Thicknesses	
Inner (μm)	Outer (μm)
1.5	2.0
2.5	4.0
4.0	6.0
	8.0
	12.0

Fig. 7. Transport target pie.

The targets were difficult to make for several reasons. First, the plastic (CH) layers required precise thicknesses. We used a parylene coater to apply the CH, but we had difficulty controlling the absolute thickness of the two layers. Rapid characterization was all-important; we used mounted glass microballoons (GMB) as coating witnesses, putting several in each coating run. These could be quickly characterized by interferometry to determine the thickness of the parylene coating. (This is a transmission measurement which was not possible through a solid glass sphere). Complete characterization of the targets was done by potting and sectioning samples, and examining the plastic and aluminum coating thicknesses in the SEM as a function of azimuth. We found during this experiment that our parylene coater needed some refinement (Williams and Rowen 1987) and that we needed to re-establish a low-pressure plasma polymerization capability for more control of the thinner (< 1 μm) coatings. Thus, we began a coating round-robin experiment (Williams and Foreman 1987) involving target fabrication groups in the US and UK.

The transport targets seemed easy enough to produce at the outset; however, tight specifications on the layer thicknesses made that order difficult to fill. The characterization required to ensure the product met specification was formidable. Moreover, imperfect control on the thin layers formed by the parylene process caused many targets to fail inspection. Our experience with this target forced the development of new characterization methods and prompted improvements to both our parylene and our LPP systems.

High-Z Conversion Efficiency

Targets for two experiments designed to measure x-ray conversion efficiency in high-Z elements required thin, well-characterized coatings of Au, Bi, Tu, and U on solid plastic and glass spheres. For a number of reasons these targets pushed current technology.

The first series required Au coatings varying in thickness from several μm to 160Å. All targets were coated in stainless steel vacuum chambers by an electron gun evaporator. They were stalk mounted and rotated with a 4π–rotation fixture (Reeves 1982). Characterizing layers less than 0.05 μm (500Å) is difficult. Targets with the thinnest layers required x-ray fluorescence for thickness characterization. There were several in an intermediate thickness region which could be characterized both by sectioning and SEM inspection, and x-ray fluorescence. The techniques agree in their thickness determination, but the error bars are large where the techniques overlap.

The second high-Z series explored other materials (Gobby et al. 1989). In particular uranium proved a problematic material to coat; first it is pyrophoric (oxidizes readily); second, it does not adhere well to the substrates. We fixed these problems by precoating the substrates with a 100Å coating of chromium to improve the adhesion and by coating an alloy of U with 5% Ti and then overcoating with 400Å of aluminum in the same coating chamber to cure the

oxidation problem at the expense (acceptable) of adding another material to the spectrum.

Targets for this high-Z series also were fabricated of gold smoke. A metal smoke forms in a vacuum chamber at relatively high pressure (although still subatmospheric). In this case 2 to 10 torr of argon in dynamic equilibrium with the pumping system provides the background pressure. The metal vapor partially condenses in the vacuum chamber itself and is conveyed to the target by the through flow of argon. The coating arrangement appears in Fig. 8. The coated material has the appearance of soot, with a density of between 1 to 10% of the density of the bulk metal. Smoke density on the targets was measured radiographically at $1.5 + 0.4\%$ of bulk gold, low, but acceptable. More importantly, initial runs had significant fractions of tungsten from the evaporation boat in the gold. The explanation was that the tungsten reacted with an O_2 impurity in the target chamber gas and formed WO_3, which has a high vapor pressure and would condense in the smoke. Switching to carbon (graphite) boats solved the problem.
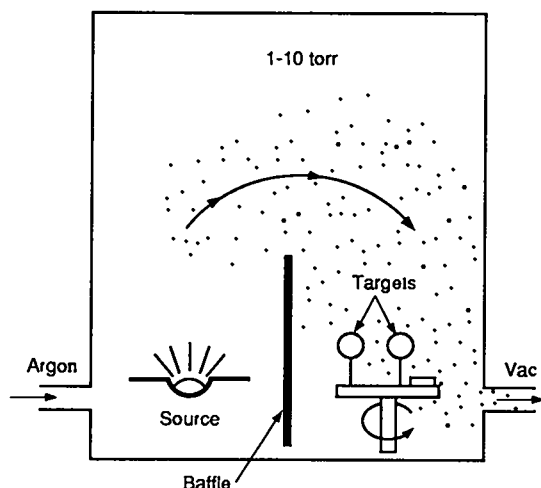
Fig. 8. Au smoke coater.

Targets for NOVA

Silicon/Aluminum/CH Targets for NOVA

These targets, shown in Fig. 9 below, consisted of single crystal <111> silicon rectangles, 15 - 50 mm, half coated with 0.1 μm Al and half of the Al further coated with 30 μm of parylene. We used a rather complicated procedure to fabricate these targets because of an inherent problem with parylene coatings. Parylene deposits on all surfaces in the deposition chamber; it is difficult to selectively remove

without also lifting the coating from the areas where it is intended to remain. This procedure avoided the problem by depositing parylene only where it was required.
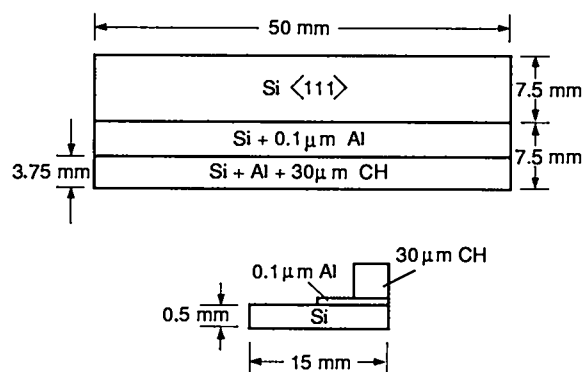
Fig. 9. Si, Al, Cu targets.

The 50-m lengths of silicon were first scribed and broken into two pieces 3.75 and 11.25 m in width. The narrow piece was epoxied to a glass slide, and the wide piece was glued down on the slide next to its brother with radio cement. The targets were then masked and the 0.1 μm of aluminum was deposited. The wide piece was then removed from the glass slide with acetone and put aside; while the narrow piece still attached to the glass slide went into the parylene coater. After it was coated with parylene, the wide piece was again placed next to its brother, but this time epoxied in place. This completed the target.

Targets for Rutherford Appleton Laboratory

Rutherford Filamentation Targets

The Rutherford filamentation targets delivered in the summer of 1987 consisted of two basic types—polymer foam cylinders and thin films. The CH, chlorinated CH, and aerogel cylinders were all 0.2 mm in diameter and 1.0 mm in length. The thin films of CH and chlorinated CH were 1.0 μm thick and measured 0.2 × 1.5 mm.

The CH and chlorinated CH targets were formed from polystyrene and chlorinated polystyrene foams, respectively, into foam cylinders using the phase separation process. They were cast into 0.2-mm holes drilled into a 1.0-mm-thick aluminum plate. The foam was leached in cold methanol (-5°C) for 20 minutes and then placed in a CO_2 extractor to remove the methanol. Each foam cylinder could then be pushed from the aluminum mold with a hair probe. Densities of 0.1 and 0.05 gm/cc foam cylinders were

Nyitray, A., J. M. Williams, and M. Wilkerson, "Composite Foams," Proc. 6th Annual Target Fabrication Specialists Meeting, Los Alamos, NM, June 20-24, 1988.

Progress Report on Laser-Fusion Program at LASL July 1-December 31, 1975, LA-6245-PR, p. 82, Los Alamos Scientific Laboratory, Los Alamos, NM. Patent No. 4292340 to John R. Miller in 1978.

Reeves, G. A., "Physical Deposition onto Small Spheres," Proc. Conference on Lasers and Electro-Optics/ICF, Feb.26-28, San Diego, CA, 1980.

Sacks, R. A., and D. H. Darling, "Direct Drive Cryogenic ICF Capsules Employing D-T Wetted Foam," Nucl. Fusion 27, 447, 1987.

Stupin, D. M., "Filmless Radiographic Detection of Microscopic Wires and Very Small Areal Density Variations," Materials Evaluation 45, 1315, 1987a.

Stupin, D. M., "Radiographic Detection of 100 – Thickness Variations in 1 ≤μ Thick Coatings on Submillimeter-diameter Laser Fusion Targets," in Review of Progress in Quantitative Nondestructive Evaluation, Vol 6B, D. O. Thompson and D. E. Chimenti, Eds., Plenum Publishing Corp., New York, 1987b.

Stupin, D. M., G. H. Stokes, J. Steven-Setchell, "Near-Real-time Radiogrpahy Detects Very Small Wires and Thickness Variations," LA-UR-88-202, Los Alamos National Laboratory, Los Alamos, NM, 1988. (Also published in International Advances in Nondestructive Testing, W. J. McGonnagle, Ed., Gordon and Breach Science Publishers, Montreux, Switzerland, 1989.)

Williams J. M., "Torodial Microstructures from Water-in-Oil Emulsions," Langmuir, 4, 444, 1988.

Williams, J. M., and D. A. Wrobleski, "Spatial Distribution of the Phases in Water-in-Oil Emulsions. Open and Closed Microcellular Foams from Cross-Linked Polystyrene ," Langmuir 4, 656, 1988.

Williams, J. M., and L. R. Foreman, "Parylene Coated Microspheres-Operational Parameters and Round Robin Results," LA-UR-11304-C, Los Alamos National Laboratory, Procs. JOWOG 28 Meeting/Organic Coatings, Los Alamos, NM, October 6-8, 1987.

Williams, J. M., and J. T. Rowen, "Diagnosis and Treatment for a Recalcitrant Parylene Coater," J. Vac. Sci. Technol. A 5, 2760, 1987.

Young, A. T., "Polymer-Solvent Phrase Separation as a Route to Low Density, Microcellular Plastic Foams," J. Cellular Plastics 23, 55, 1987.

IV. Laser-Target Interaction
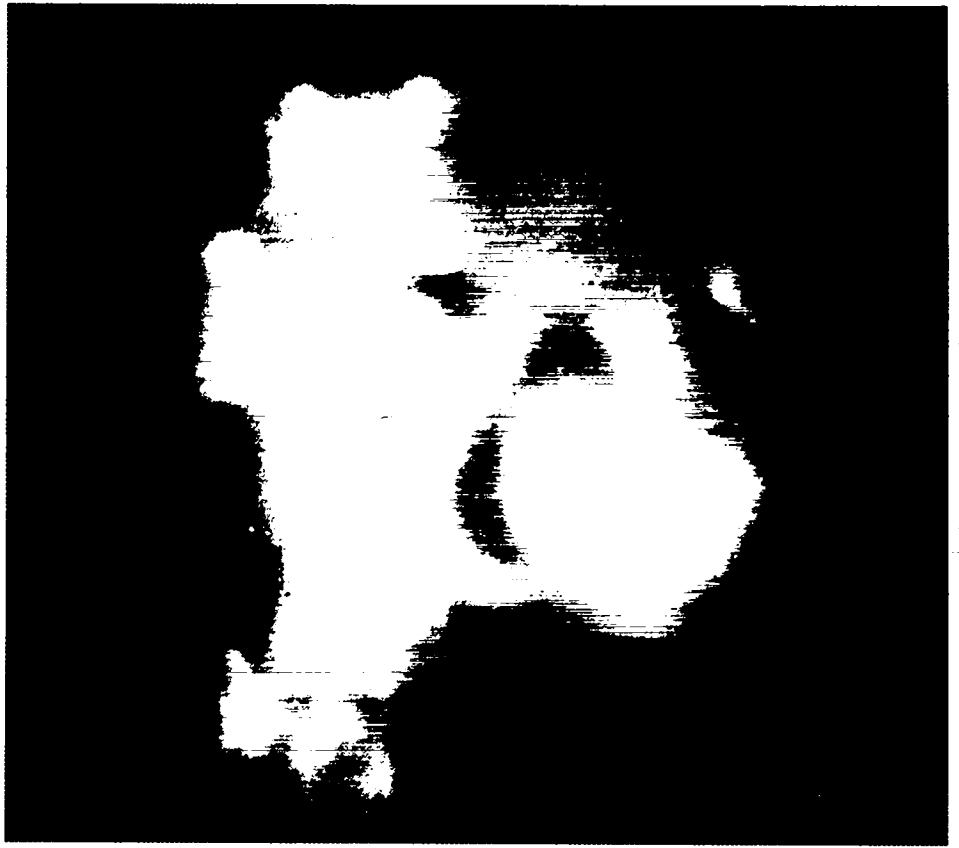
X-ray photograph of intense laser beams striking a spherical fusion target.

IV. LASER-TARGET INTERACTION

Allen A. Hauer, William C. Mead,
Philip D. Goldstone

INTRODUCTION

As illustrated in Fig. 1, use of laser-driven compression for the production of the dense plasma conditions needed in ICF involves a controlled sequence of many physical events. Production of high target gain requires attention to these and many other aspects of laser-plasma interaction and fluid dynamics. This places significant demands on the target design and driver characteristics. We present here a brief introduction to some aspects of ICF theory and experiments.

In order to have confidence in theoretical predictive capabilities, one must constantly compare the modeling tools with well-diagnosed experiments. A detailed overview of laser plasma diagnostics can be found in a recent Los Alamos report (Hauer and Baldis 1988). In Figs. 2 and 3, we diagram the spatial structure of the two important phases of laser plasma interaction that are involved with direct drive fusion. This structure starts from the absorption and scattering of incident laser energy and proceeds through the transport of this energy to denser regions and the resulting ablation pressure, which is used to drive implosions. The structures indicated in Figs. 2 and 3 and their characteristic parameters (temperature, density gradient scalelengths, etc.) are evolving on time scales varying from tens of picoseconds to many nanoseconds. The basic progression of interaction (from absorption through compression) is, however, preserved. In recent years, research has revealed a strong dependence of absorption and scattering processes on the laser wavelength (Garban-Labaune et al. 1985; Turner et al. 1985). For example, the strength of plasma instabilities that generate deleterious hot electron preheat scales as λ^2 or stronger. This had led the laser fusion community to place considerable emphasis on short wavelength interaction studies. At Los Alamos the response to this wavelength

scaling has been to pursue the use of excimer lasers that can operate far into the ultraviolet regime (0.248-0.193 µm) and have other very desirable characteristics. We also indicate in Figs. 2 and 3 some of the techniques used to diagnose the plasma/fluid conditions.

With reference to Fig. 2, laser light is often absorbed by the collisional process of inverse bremsstahlung up to a region near the critical surface (where the local plasma frequency equals the laser frequency) where it is either reflected or absorbed (or scattered) by parametric processes. Brief reviews of the possible absorption and scattering processes can be found in the aforementioned Los Alamos Report (Hauer and Baldis 1988) and in Cairns (1983). In the region from the critical surface outward toward the laser, optical diagnostics provide the preponderance of information. Scattered (shifted-frequency) and harmonic light offer a rich source of information on both the absorption processes and the local plasma conditions. In spanning the range of irradiance from 10^{12} to 10^{16} W/cm^2, the background T_e varies from a few hundred eV to several keV. The critical (electron) density for a given laser wavelength is given by: $n_c \sim 10^{21}/\lambda^2$ cm^{-3} (λ is in microns). The aforementioned trend toward short wavelength research thus implies investigation of plasma processes at much higher density where collisional effects will be emphasized. The critical densities for some common laser wavelengths are shown in Table 1.
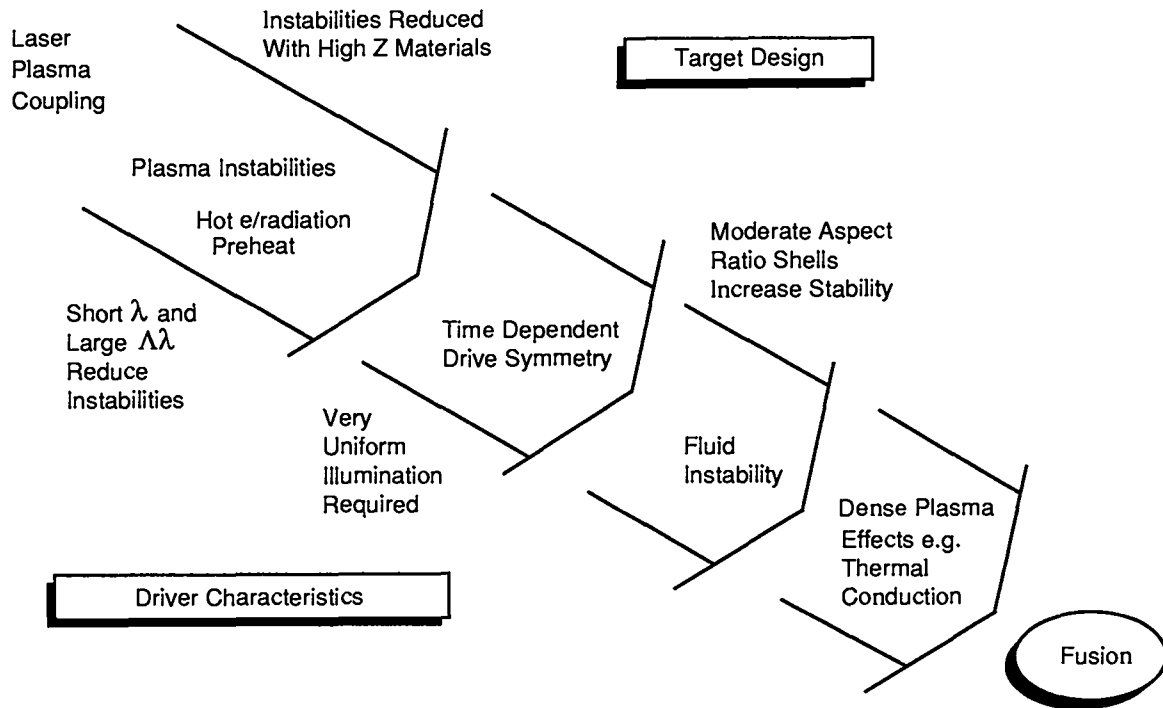
Fig 1. Illustration of the progression of physical processes involved in the production of fusion conditions with lasers.

TABLE 1. Critical Densities for Some Important Lasers

Laser	Wavelength (μm)	n_c (cm^{-3})
CO_2	10.6	10^{19}
Nd glass (ω_o)	1.06	10^{21}
Nd glass ($3\omega_o$)	0.35	9×10^{21}
KrF	0.25	1.6×10^{22}

In the region from below the quarter-critical density ($n_c/4$) to the critical density (n_c), various absorption and scattering processes can result in the generation of suprathermal electrons. An example of these processes is stimulated Raman scattering (SRS) where the laser wave is coupled to an electron plasma wave and a shifted electromagnetic wave. The strongly driven plasma wave can accelerate electrons to very high energies. These electrons can follow a variety of trajectories depositing their energy in dense material or penetrating the sheath potential and escaping.
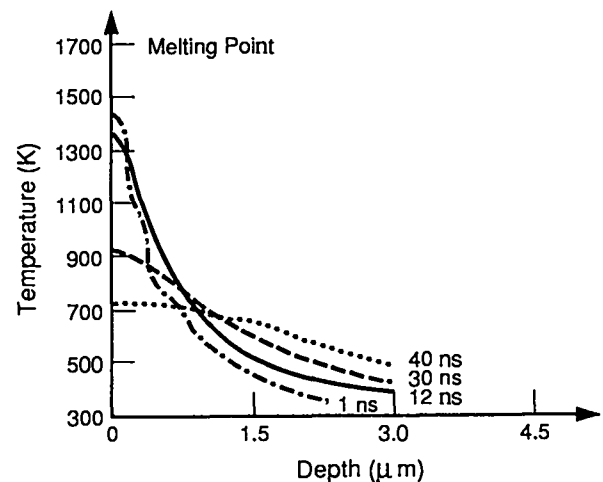
Fig. 2. The absorption/transport phase of laser-plasma interaction.
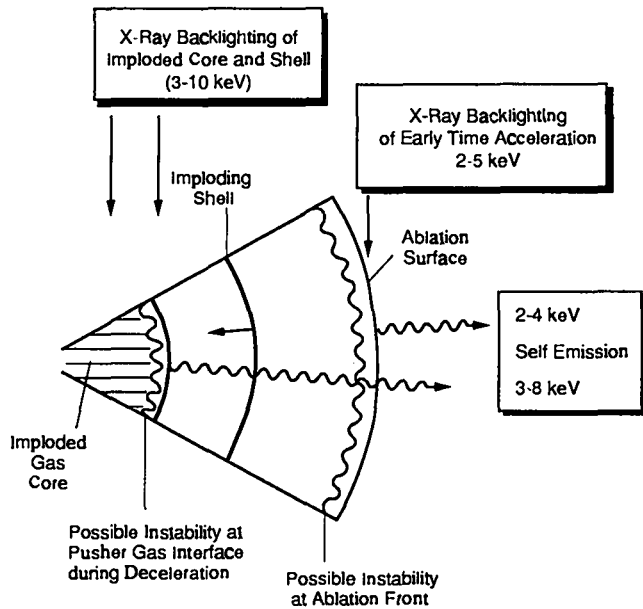
Fig. 3. The acceleration/implosion phase of laser plasma interaction.

These suprathermal electrons can be very detrimental to efficient laser-driven compression, and their prediction and minimization at shorter wavelengths is an important current research topic.

The large laser systems required for significant gain will produce very long scalelength plasmas. The suppression of plasma instabilities under these conditions is one of the principal concerns of laser fusion and points to several desired characteristics of the laser driver.

In addition to plasma physics issues, several problems in basic fluid dynamics must be addressed. These are illustrated in Fig. 3. Raleigh Taylor instability may cause breakup of the imploding shell and thus poor compression. This problem is minimized by proper target design (such as limiting the aspect ratio of the shell) and the use of very (spatially) uniform laser illumination. It is presently thought that direct drive fusion will require more than 1% spatial uniformity early in the drive pulse. Production of such conditions once again places stringent requirements on the laser driver.

To investigate the use of short wavelength excimer lasers as ICF drivers, Los Alamos has recently completed the AURORA KrF facility. AURORA can irradiate targets with 48 f/26 beams arranged in an f/2 cluster. At present the total energy is limited to 5 kJ in a 2- to 5-ns pulse, but the laser can be upgraded to 10 kJ in the 48 beams. AURORA will be able to demonstrate many of the advantages of excimer lasers such as the use of beam spatial smoothing techniques that require substantial bandwidth.

One of the applications will be the study of hydrodynamic stability of foils accelerated by very uniform laser drive. Another area of study, utilizing the high degree of spatial uniformity, will be the investigation of plasma instabilities in the long scalelength, long laser pulse regime that is particularly appropriate for the AURORA laser. Excimer lasers have many advantages for direct drive laser fusion. The large inherent bandwidth at short wavelength makes possible several types of beam smoothing techniques that are needed to supply the very stringent beam uniformity requirements of direct drive. The two most prominent techniques that have been developed for laser beam smoothing, induced spatial incoherence (ISI) (Lehmberg and Obenschain 1983) and distributed phase plates (Kato et al. 1984), are both readily achievable with a KrF laser. Some target designs for direct drive show promise but the margin for error is small and a driver needs to be chosen that gives the highest probability of success with respect to all the critical design parameters. Some of the tradeoffs that must be considered in direct drive design are illustrated in Fig. 4. Experiments on the AURORA laser will help to demonstrate excimer advantages with respect to both smooth uniform drive and reduction of plasma instabilities.

Fig. 4. Illustration of the tradeoffs involved in direct drive laser fusion target design.

THEORY AND SIMULATION

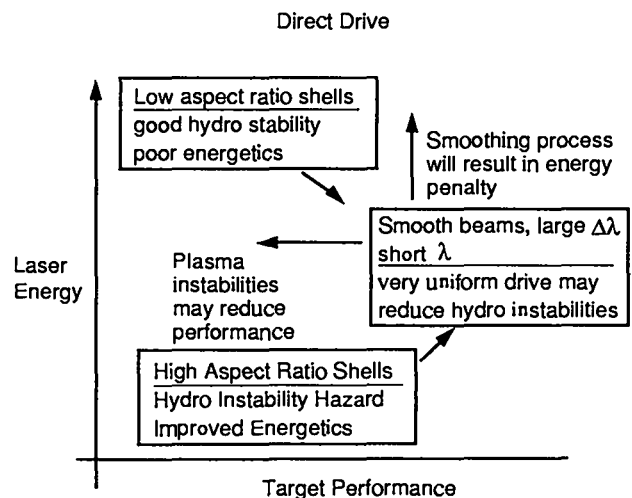We present here a brief review of some aspects of theory that are applicable to the unclassified experiments described later and to direct drive fusion in general.

The inertial fusion program has been well-balanced with considerable strength in both the theoretical and experimental areas. Because of the complexity of the physics, it has been at the forefront in developing new theoretical tools as well as experimental techniques. The phenomena of interest change over time scales of picoseconds; the entire experiment occurs in about a nanosecond. Spatial resolution required to study the physics of targets measured in hundreds of micrometers to millimeters typically approaches a few microns.

Because much of the truly microscopic (submicrometer, subpicosecond) phenomena cannot be readily measured but strongly influence the macroscopic behavior, computer simulation is relied on heavily to couple the microscopic phenomena to macroscopic observables. An important example of such simulation tools is the WAVE code, a 2D particle simulation code that solves Maxwell's equations and the relativistic Newton's laws for the particles in the self-consistent three-component electric and magnetic fields. It typically advances 10^6 particles on a grid of 10^5 cells for 10^4 time steps to determine the processes that absorb the laser light and transport the energy from the low-density, hot-plasma regions to the denser regions. Only a portion of the physical problem can be modeled because one must limit the time step to a small fraction of the laser period and the gird size to the distance light travels in one time step. Consequently, the time that can be covered is only a few picoseconds and the distance is only about 10 to 100 wavelengths of light. Because of the limited time and space scale, the boundary conditions and initial conditions for fields and particles are unknown and must be estimated. Much of the skill in using the code involves guessing the right boundary and initial conditions that appear to be consistent with themselves, with hydrodynamic calculations, and with experiment.

An implicit form of the code, called VENUS (Brackbill and Forslund 1982) has enabled one to greatly increase the time step and grid size (at the expense of some high-frequency phenomena) to consider realistic spatial scales, which allows the study of the central role of self-generated magnetic fields in electron transport and fast-ion emission. After their development by the ICF program, these new-generation codes rapidly spread to the magnetic fusion and space physics communities and represent a significant contribution of ICF to general science and technology. Although quantum mechanical and atomic physics process

are not included in these codes, they can accurately describe the fully developed strong turbulence that can occur in laser-plasma interactions, limited only by the computer resources. To better utilize the results of these codes, we test and evaluate various models to obtain scaling laws that can be reliably extrapolated into new regimes. For example, the accuracy and range of validity of simplified models of the propagation and absorption of light in the plasmas have been verified with the WAVE code. In the last decade, the improvement in the scale of problems that are accessible has increased by a couple of orders of magnitude because of improvements in computer hardware speed and in numerical algorithms (VENUS). This has greatly increased our understanding of the physical processes occurring in laser-produced plasmas. A good review of laser plasma modeling and its applications can be found in Forslund and Goldstone (1985).

Absorption of a significant fraction of the laser light by plasma instabilities can generate an unacceptable level of hot electrons. These long mean-free-path electrons penetrate the gas fuel of the target and cause an inefficient implosion. A rough rule for the level of hot electron generation that is acceptable is:

$$f_H < 7\% \text{ for } T_H < 30 \text{ KeV}$$

$$\text{and } f_{SH} < .3\% \text{ for } T_{SH} < 100 \text{ KeV}.$$

In the above formulas the symbols H and SH stand for "hot" and "superhot" and represent two Maxwellian distributions that can often characterize hot electron generation. For many direct drive target designs, the level of anticipated hot electron generation is very close to or exceeds the levels indicated above. It is generally thought that the use of higher-Z materials will reduce the level of hot electrons through introducing a greater degree of collisionality into the plasma. Many direct drive designs, however, require the use of plastic or other low-Z material in the laser absorption region. A good indication of the level of concern with plasma instabilities can be obtained by plotting the threshold for various modes as a function of laser intensity. Figures 5 and 6 present a series of such plots that give an indication of the intensity regimes that are acceptable for target design. We also show the effect of driver parameters such as laser wavelength and bandwidth in the instabilities.

.25 microns, Z=4   .25 microns, Z=13   .25 microns, Z=50
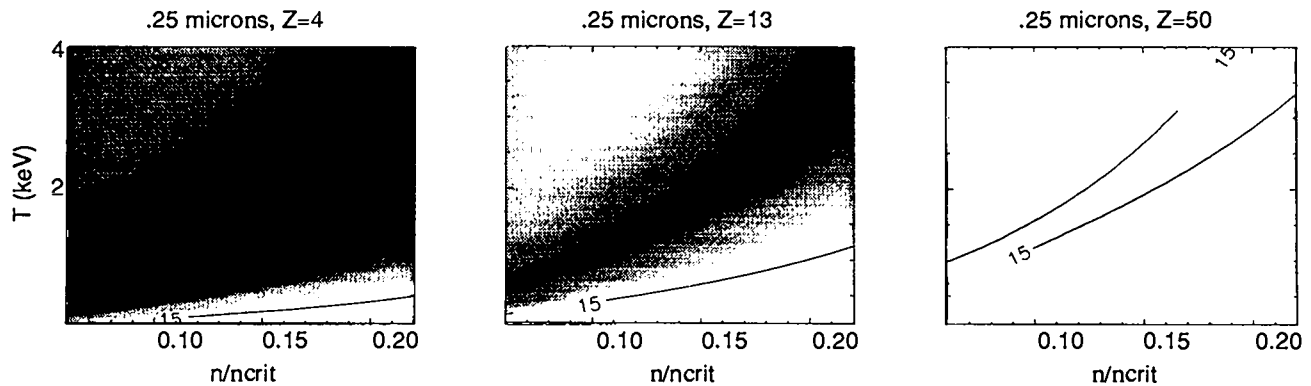
Fig. 5. Comparison of the SRS thresholds as a function of temperature and density for three different average charge (Z) plasmas.

.25 microns, Z=4 band=0   .25 microns, Z=13 band=0.25%   .25 microns, Z=50 band=0.5%
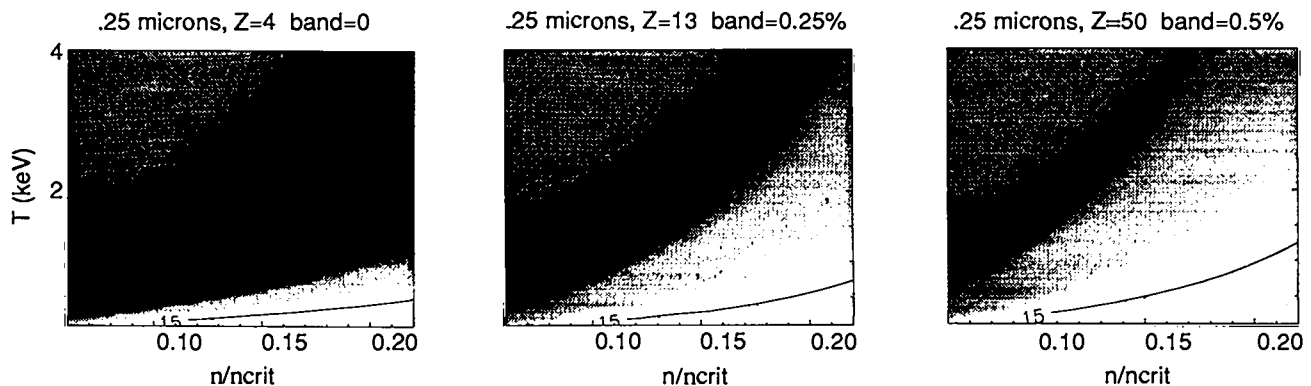
Fig. 6. Variation of SRS thresholds with laser wavelength and bandwidth.

Figures 5 and 6 show calculations of the threshold intensities for stimulated Raman backscatter. The contours represent the intensity thresholds for the particular conditions of temperature and density. In Fig. 5 the thresholds are plotted for three different atomic number materials. This illustrates that there is considerable variation in the thresholds with atomic number. In the higher materials, there is considerable collisional damping of the plasma waves. Many direct drive target designs require low- Z materials to be present in the laser absorption region, which causes some danger of plasma instabilities. In Fig. 6 we show the effect of laser wavelength and bandwidth on the instability thresholds. Changing from a laser wavelength of .35 μm and small bandwidth to a wavelength of .25 μm and significant bandwidth produces a substantial increase in the intensity threshold for SRS. Considerations such as this favor the use of excimer lasers that naturally operate at short wavelength and broad bandwidth.

Typically, the overall laser-matter interaction is modeled with hydrodynamic codes such as LASNEX (Zimmerman and Kruer 1975). A complete description of the physics

contained in such large models is outside the scope of this report (see Mead et al. 1983), but a brief review may be helpful, especially in describing the relationship to experimental diagnostics.

The first step is formulation of a model for the laser absorption and scattering process, such as inverse bremsstrahlung and refractive losses. Electron thermal transport is usually modeled by flux-limited diffusion, although more complex treatments such as semi-empirical treatments of nonlocal deposition have been used. LASNEX uses a one- or two-dimensional Lagrangian formulation for the hydrodynamics. Radiation transport is often handled by multigroup flux-limited transport, but more sophisticated schemes are also employed. Atomic radiation is most often handled using an average ion modeling of the atomic processes (Lokke and Grasberger 1976). This calculation is done in real time and the results are fed back into the hydrodynamic calculation. More sophisticated treatment of atomic radiation effects (Lee 1987) have also been incorporated into the comprehensive model and have been particularly helpful in modelling diagnostic signatures (Willi

et al. 1989). Some x ray diagnostic techniques, such as continuum slopes, can be obtained directly from the overall laser interaction/hydrodynamic modeling. More detailed diagnostic information such as atomic radiation (spectroscopic) line shapes and intensities require the more models described above.

Comprehensive modeling has also been applied to imaging diagnostics. Models have been constructed that use input information such as density, temperature, opacity, functions of space, and time from a hydrodynamic simulation code. The models then perform line-of-sight integrations through the plasma (at various photon energies) to produce a prediction of the observable output emission. Such predictions of observable diagnostic emission have provided a valuable feedback to check many aspects of the simulation itself.

EXPERIMENTS

In this section we first describe typical experiments performed by Los Alamos in three areas that are crucial to the design of high gain targets. This is not meant to be a comprehensive review of experimental work; rather, it is intended to provide insight into the experimental measurements that are necessary for the resolution of the crucial target questions. The section is concluded with a description of early tests on the AURORA laser system and projections for work that will be done there in the near future.

X-ray Conversion Efficiency

Conversion of laser light to x rays is very important to indirect drive. We have recently completed a series of experiments that measures x-ray conversion efficiency in a very controlled and accurate manner (Goldstone et al. 1987). This has enabled us to place accurate bounds on the conversion efficiency that can be assumed and has also revealed other important characteristics of the conversion process.

The efficiency with which energy absorbed in laser-produced high-Z plasmas is converted to soft x rays increases markedly at shorter laser wavelengths (Nishimura et al. 1983; Mead et al. 1983; Kodama et al. 1986; Mochizuki et al. 1986). This results from laser-light deposition at higher plasma densities, yielding cooler plasmas with lower hydrodynamic losses, and this characteristic can be important for some approaches to inertial confinement fusion (Gardner and Bodner 1981). A similar increase in conversion efficiency is expected at lower laser intensities. However, early experiments with planar Au targets (Nishimura et al.

1983; Mead et al. 1983) showed a decrease of x-ray emission at low intensities, whereas the LASNEX (Zimmerman and Kruer 1975) simulations code predicted an increase, indicating that high-Z plasmas were not well understood. Thus we have sought more specific observations of the hydrodynamic, energy-transport, and atomic processes that affect x-ray emission.

The tests described here were the first measurements of x- ray conversion performed in spherical geometry. This pseudo one-dimensional experiment simplifies integration of measurements over solid angle and allows a test of whether two-dimensionality inherent in previous planar experiments might have affected the results.

We have examined the dynamics of high-Z plasmas and the processes that affect x-ray emission, including the material depths associated with energy transport and x-ray generation and the time dependence and spectra of the x-ray emission, at intensities of 4×10^{12} to 4×10^{15} W/cm^2.

We have investigated some of the changes in plasma conditions that are expected as the $\lambda_L = 0.35$ μm irradiance is decreased from 4×10^{14} to 4×10^{13} W/cm^2 (where the emission discrepancy was first noted). At 4×10^{14} W/cm^2, radiation cooling is weaker than laser deposition in the underdense plasma. Hence the corona temperature rises, reducing the inverse-bremsstrahlung absorption opacity, so that the laser penetrates to the critical surface and deposits its energy locally. This produces strong steepening of the density and temperature profiles near the critical density. The x-ray emission originates in a localized region near and above the critical density, with electron transport carrying energy from the absorption region to the emitting region. At 4×10^{13} W/cm^2, radiation cools the corona at a rate nearly equal to the laser deposition, so that the deposition and the x-ray emission occur in an extended plasma well below the critical density. Electron transport is relatively unimportant in this case.

Specific predictions of the features of the x-ray emission region are shown in Table 2. The one-dimensional (1D) LASNEX modeling used for this work includes inverse bremsstrahlung laser deposition, Lagrangean hydrodynamics, thermal electron diffusion with flux limit of $f_e = 0.03$ (as in previous work) or 0.08 (best fit for this and related low-Z spherical work (Hauer et al. 1984), and multigroup flux-limited x-ray diffusion. The modeling includes nonlocal thermodynamic-equilibrium atomic and radiation physics, with a time-dependent solution of the average-atom hydrogenic collisional and radiative rate equations, neglecting subshell energy splittings and transitions.

Experiments to study these phenomena were performed using the 0.35-μm OMEGA multibeam laser facility. The laser initially provided 250 - 300 J in six beams, and later

1600 J in all 24 beams, in a nominal τ_L = 650-ps FWHM pulse. To obtain good uniformity, the beams were focused beyond the target, so that the beam edges were tangent to the initial surface. Illumination nonuniformities were ~ 50% rms (with 2:1 large scale variation) for six-beam irradiations but only ~ 20 % rms for 24-beam experiments.

TABLE 2. Calculated (f_e = 0.08, λ_L = 0.35, τ_L - 650 ps) Characteristics of the Subkiloelectronvolt X -ray Emission

	4×10^{13} W/cm^2	4×10^{14} W/cm^2
Radial extent (μm)	40	8
Density	(0.04 - 0.5)n_c	(0.3 - 1.8)n_c
Electron temperature (keV)	0.1 - 0.5	0.3 - 1.2
Average Z	25 - 30	35 - 45
E_{rad}/E_{abs}	0.85	0.72
E_{MLines}/E_{rad} (%)	<1	5

Absolute x-ray emission measurements were obtained with a four-channel Al photocathode x-ray diode (XRD) spectrometer covering 0.1 - 2 keV with 300-ps time resolution (Pien et al. 1986) An x-ray transmission-grating/streak-camera spectrograph provided time-resolved (15-ps) spectra from 0.5 to 3 keV. For the 24-beam experiments, a time-integrating transmission grating spectrograph provided 0.1- to 3-keV spectra with ~ 2 Å resolution. X-ray microscopes imaged the plasma's kiloelectronvolt emission. M- and N-line emission spectra (Richardson et al. 1985) were studied with time-integrated and time-resolved crystal spectrographs (Henke and Jaanimagi 1985). Gold M-line emission (near 2.5 keV) was present above 10^{14} W/cm^2 and absent at lower intensities, as predicted. The hard x-ray bremsstrahlung (10 to 100 keV) was measured and implied negligible levels of instability-produced superhot electrons (<$10^{-4}E_{laser}$).

Some particularly important data from these experiments are shown in Fig. 7. This information indicates that there is a significant increase in the conversion efficiency when there is a smooth spatial profile for the laser irradiation. Such an effect has also been observed in other experiments. This indicates that there is considerable advantage in employing laser driver schemes that are amenable to a high degree of spatial smoothing. These studies are continuing to obtain an even more detailed understanding of x-ray conversion and its optimization.
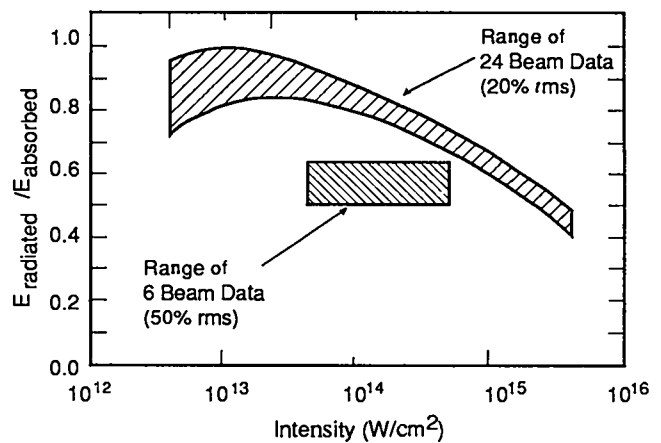
Fig. 7. Experimental measurements of the variation of x-ray conversion efficiency with laser irradiance and beam spatial smoothness.

Stability of Laser-Driven Implosions

One of the most crucial issues for the ultimate success of ICF is the stability and uniformity of the imploding pusher shell. The uniformity could be disrupted by classical hydrodynamic instabilities (such as Rayleigh-Taylor) that occur at the interface between different density materials. Disruption of the symmetry could also be caused by other effects such as nonuniformities in the ablation drive. Asymmetrics in drive can also "seed" the classical instability mechanisms. Los Alamos has had an ongoing series of experiments to investigate hydrodynamic stability in the ICF context. We will describe here some early work using CO_2 lasers. Later we will also describe projected hydrodynamic work for the AURORA laser.

The experiments can be divided into two general categories: acceleration and deceleration phase experiments that study breakup and instability early in the implosion and near stagnation, respectively.

Acceleration Phase Stability

The acceleration phase work has been done with cylindrical-shell targets that have been imploded with relatively uniform eight-beam CO_2 laser illumination. Typically, about 5 kJ was incident on target. Cylindrical configurations offer many advantages in stability experiments. The open geometry facilitates diagnosis when the effects of implosion convergence are measured. The cylindrical geometry is also convenient for comparison with some types of theoretical modeling.

In the present work, the targets were cylindrical shells of copper and aluminum with and without plastic coating. The

basic target configuration is illustrated in Fig. 8. The targets were about 200-μm thick. The uncoated shells behaved much like explosive pushers, whereas the plastic-coated targets behaved similarly to the quasi-ablative targets used in many implosion experiments.
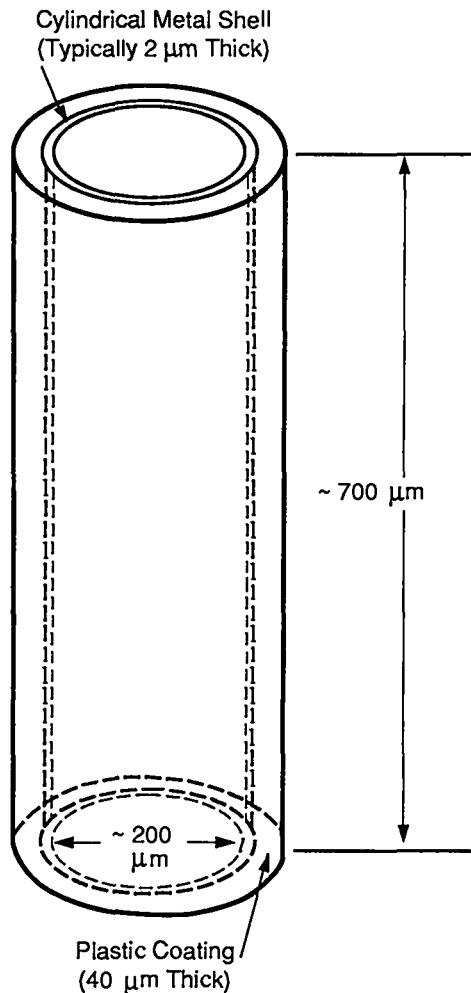
Fig. 8. Basic target configuration used in cylindrical stability experiments.

Eight laser beams were independently targeted (and defocused) around the cylindrical surface of the targets.

In addition to the simple shells, some of the targets had initially imposed perturbations, as shown in Fig. 9, which were arranged to maintain a constant wall thickness. The period of the perturbations was about 25 μm with an amplitude of 0.5 μm. The axial perturbations (Fig. 9) are compatible with the cylindrical symmetry in LASNEX, which permitted the results from LASNEX calculations to be used for some preliminary scoping of the types of growth expected.
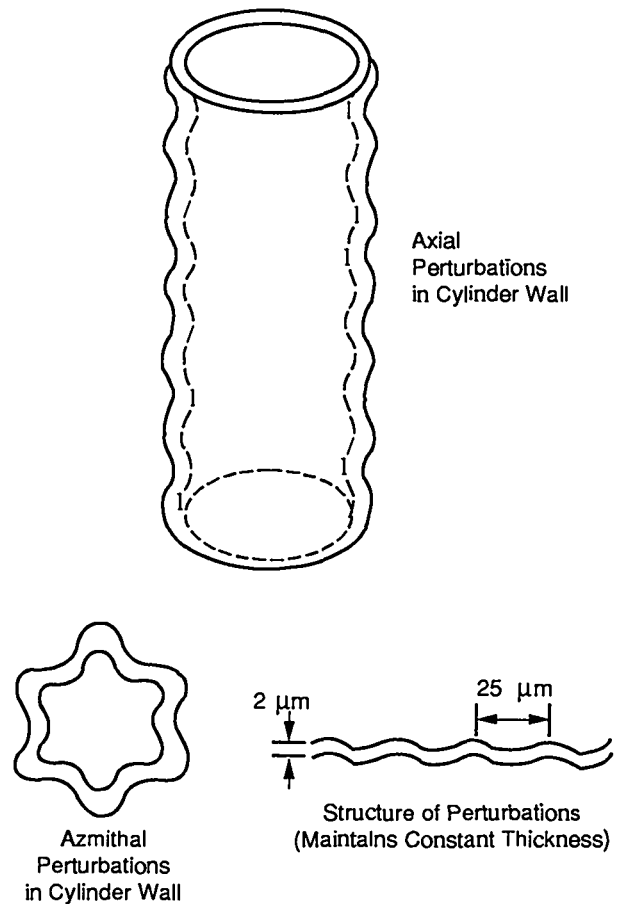
Fig. 9. Perturbations imposed on cylindrical targets.

The implosions were diagnosed primarily with x-ray imaging of self-emission. Several pinhole cameras were arranged to provide imaging along, and perpendicular to, the cylindrical axis. In Fig. 10, we show a comparison between the implosions of coated and uncoated cylindrical shells (viewing along the cylindrical axis) made from images that were filtered for ~ 1.5-keV radiation. The comparison between the implosions of coated and uncoated cylindrical shells (viewing along the cylindrical axis), made from images that were filtered for about 1.5-keV radiation. The comparison here is very similar to the explosive versus semiablative studies done in the high-density series of spherical implosion experiments. Also shown in Fig. 10 is an image taken with a view perpendicular to the axis, which confirms that it is possible to obtain a relatively uniform implosion all along the cylindrical axis. (That is, the views in Fig. 10a and 10b are not end effects.)

Thin Shell (Explosive)   Plastic Coated Shell (Ablative)

View Along Axis (a)   View Along Axis (b)

View Perpendicular to Axis (c)
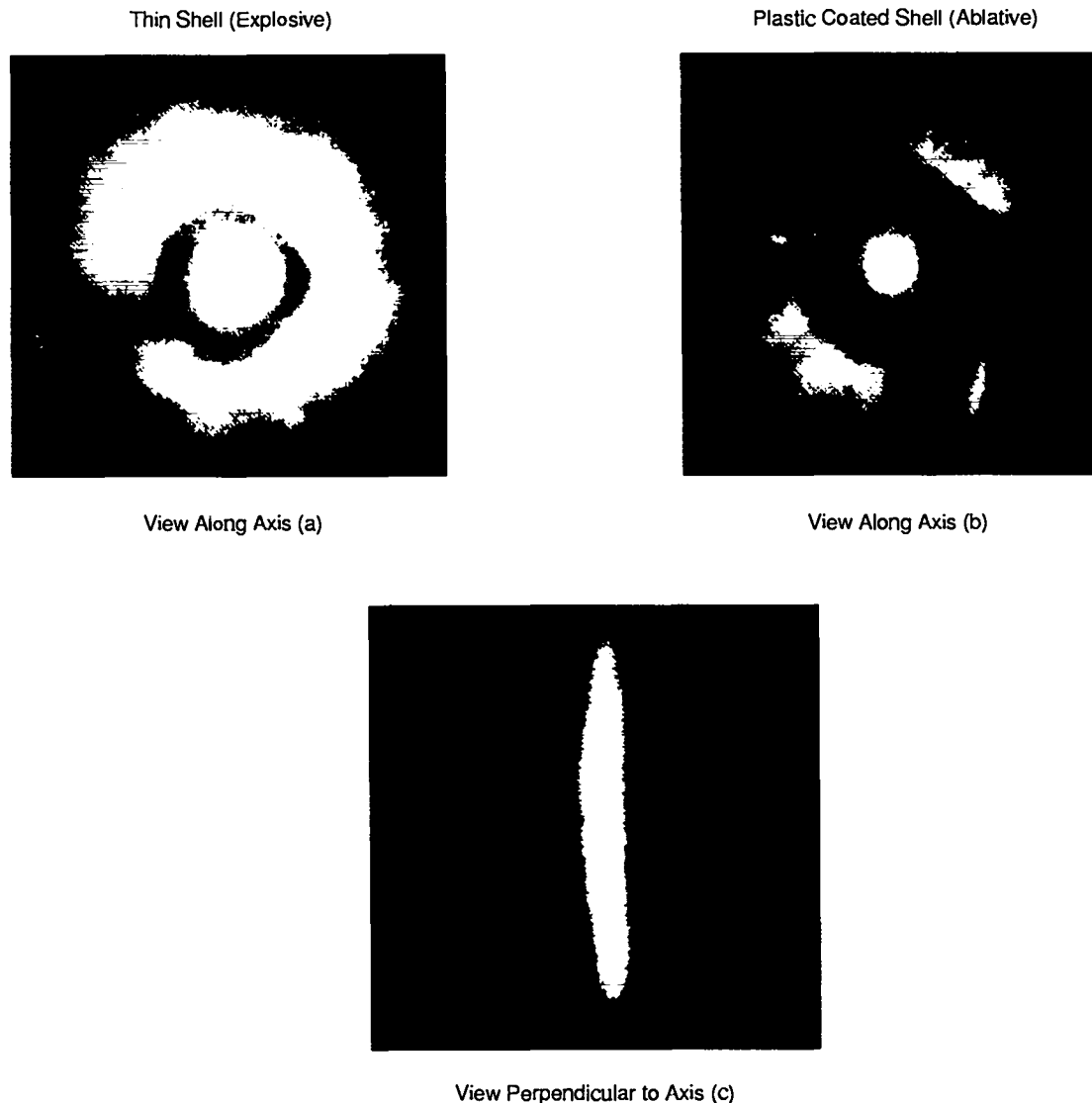
Fig. 10a,b, and c.   X-ray images of the implosion of coated and uncoated cylindrical shells.

We now turn to the targets that contained prearranged perturbations. Targets that continued perturbations were always coated with plastic, so that perturbed versus unperturbed comparisons are only made for the semiablative case. In Fig. 11, we show a comparison of end-on pinhole camera views for unperturbed and perturbed cases. In all cases where perturbations were present, the compressed core is significantly larger (weaker compression) and is surrounded by a halo of radiating material that, in many cases, contains a periodicity. The print in Fig. 11 does not adequately show this periodicity. The nature of this structure is being analyzed further.

The basic conclusions from these preliminary experiments are as follows:

- Strong, uniform cylindrical implosions can be produced. The CO_2 laser actually has an advantage because it gives added symmetrization.
- Evidence of shell breakup was observed in the case of initially perturbed cylindrical targets.
- Cylindrical configuration experiments offer a number of advantages in stability/shell breakup experiments.

Compression Phase Stability

Compression phase stability studies have also been performed. This series of experiments was designed to be a first test of diagnostic techniques appropriate for studying the breakup of imploding shells. Figure 12 shows the basic target configuration used in these tests. *Glass shells (about*

Without Perturbations   With Perturbations

Fig. 11. X-ray images of ablative cylindrical implosions with and without imposed perturbations.

350 μm in diameter) were filled with about 12 atm of DT. In some of the targets, the DT was seeded with about 0.2 - 0.2 atm of argon. Some of the shells were then coated with about 0.5 μm of potassium chloride. Other targets contained no potassium chloride coating but were fabricated from glass shells with a high content of calcium and potassium. Finally, the targets were coated with about 40 μm of plastic.
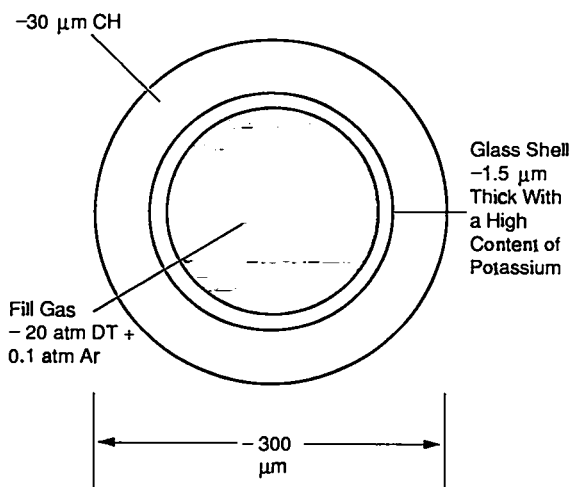
Fig. 12. Target configuration used in spherical shell breakup experiments.

When such targets are imploded, there are typically large temperature gradients in the compressed cores. These gradients can be utilized in the diagnosis of shell stability.

Spectroscopic observation of potassium and chlorine radiation served as the signature of shell breakup. These species could only radiate if they penetrated into the central high-temperature regions of the compressed core. If the potassium chloride remains in the outer portions of the shell, previous experimental measurements and theoretical calculations show that it would be at too low a temperature for efficient excitation of hydrogen- or helium-like potassium and chlorine lines. The argon lines are used to accurately characterize the compressed core conditions. After careful spectral analysis, this information will allow a determination of the amount of shell material mixed into the core.

The chosen targets were slightly larger than those in the high-density series, and this produced a weaker compression. Because in this series we were primarily interested in development of the measurement technique, we wanted a larger compressed core that could be more easily diagnosed (for example, easier x-ray imaging).

The eight beams of the laser were focused 300 mm beyond center, giving a T_{hot} (determined from x rays) of about 100 keV. In Fig. 13 we show a typical spectrum obtained in these experiments. The argon lines show an implosion of modest density ($n_e \sim 2 - 3 \times 10^{23}$ cm^{-3}) with a temperature of about 600 eV. This temperature would be more than adequate to strongly excite chlorine lines. The most striking feature of the spectrum in Fig. 13 is, however, the strong chlorine and potassium absorption features. These features indicate that most of the potassium chloride has remained in the cold outer regions of the shell; in other words, there is little evidence of shell breakup. The spectra remained very similar to that in Fig. 13 throughout this experiment. In Table 2, we summarize the parameter variation present in this series of experiments. Over the range of parameters in Table 3, no evidence of breakup was observed.
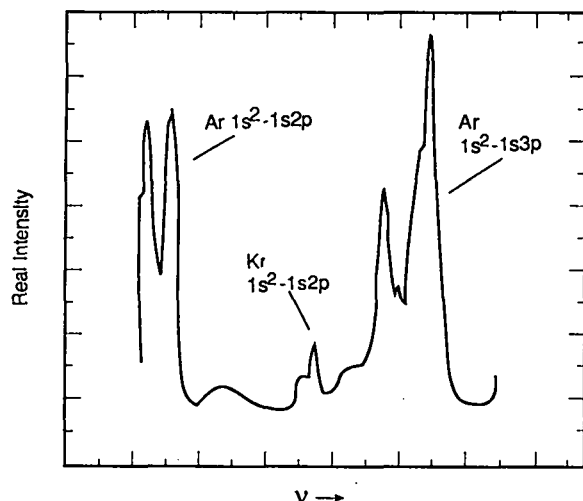
Fig. 13. Typical x-ray spectrum obtained from the implosion of a target similar to that in Fig. 12.

Some evidence of breakup was observed in the following case:
- the target had no potassium chloride coating but had a high concentration of potassium in the glass shell itself; and
- there was significant laser beam imbalance.

In Fig. 14 we show an example of this case, and a definite potassium emission feature is noted. There is also some evidence of weak absorption features to the left of the potassium line. Potassium would thus have been seen in both absorption and emission, which indicates partial shell breakup. This is the type of information that we hope to quantify in future experiments.
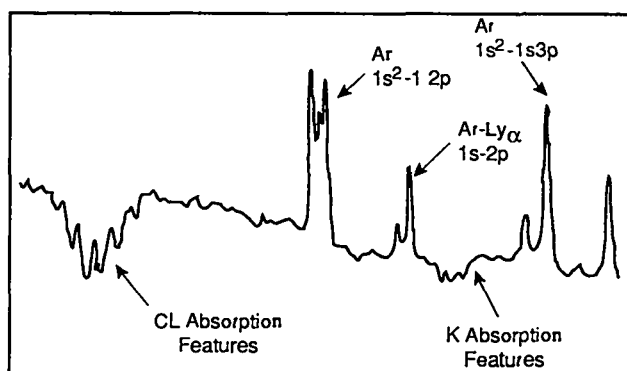
Fig. 14. X-ray spectrum showing potassium emission feature indicative of shell breakup.

The initial aspect ratio (pusher thickness/diameter) in these experiments was relatively low (~ 4). In future experiments we should strive to increase this. This may require replacing the plastic layer with a thin metal layer (to increase the aspect ratio). This, in turn, may favor the use of backlighting to diagnose the compressed core.

TABLE 3. Experimental Parameters

Inner (glass shell wall, t)	$0.8~\mu m < t < 1.8~\mu m$
Number laser beams (b)	$6 < b < 8$
DT gas fill pressure P (atm)	$8 < P, 15$

The Use of Backlighting and Absorption Spectroscopy

In the diagnosis of very dense implosions, the temperatures may sometimes be inadequate for self-emission to be a useful diagnostic. In such cases one can use an external source of radiation (such as another laser-irradiated target) to backlight the imploding target. In a more sophisticated sense, it is also possible to use an external source of radiation to perform absorption spectroscopy and obtain more detailed information than could be obtained with a simple shadowgraph. This is in fact already demonstrated by the spectrum shown in Fig. 13.

The absorption spectra represent "self-backlighting," with radiation from the core passing out through the cold absorbing layers. The information is, however, the same as would be obtained if the probing radiation were from a completely external source. As an example of the type of information that can be obtained from spectra such as that in Fig. 13, we consider a simple analysis to obtain the average ρR of the potassium chloride layer.

For one of the absorption features (which corresponds to a particular ionization state) we can write

$$\int K_v~dv = \frac{\pi e^2}{mc} Nf \quad , \tag{3}$$

where
  K = absorption coefficient,
  N = number of ions in the ground state, and
  f = average oscillator strength for the transitions
      involved,
We note that

$$I = I_0~e^{-Kr} \quad , \tag{4}$$

where R is the path length through the absorbing medium. Combining Eqs. (3) and (4), we can write approximately

$$\int \ln \left[\frac{I_0(v)}{I(v)} \right] dv \equiv \frac{\pi e^2}{mc} f[\rho R] \quad .$$

(5)

Using Eq. (5) for the spectrum in Fig. 13, we obtain an average value of rR of about 10^{-4} g/cm^2. This is consistent with values predicted by hydro simulation.

In the near future, absorption and backlighting techniques should provide a wealth of implosion diagnostic information that is particularly relevant to hydrodynamic instability studies.

Convergent geometry radiation-driven fluid stability studies have also been performed in joint Los Alamos - Lawrence Livermore National Laboratory experiments. Shells with thin high opacity tracer layers have been imploded using hohlraums heated by the NOVA system. The shells are backlit by creating a distributed x-ray source using one of the NOVA beams. The backlit image of the tracer (at characteristic times during the implosion) can provide information on the integrity of the shell and possible breakup because of fluid instabilities. Details of these experiments are presented elsewhere.

Long Scalelength Plasma Experiments

As mentioned above, the suppression of plasma instabilities in very long scalelength plasmas is a central concern of laser fusion research. In this section we describe one experiment that illustrates some of the techniques that are being developed to diagnose long scalelength plasma phenomena. The experiment was conducted jointly by staff from Los Alamos, Imperial College, and the Rutherford Appleton Laboratory.

In Fig. 15 we show the general configuration of these experiments performed on the Vulcan laser at Rutherford. The primary approach in this work was to produce long scalelength plasmas by exploding targets (heating them rapidly with short pulse moderate power beams) and then propagating an "interaction" beam down the cylindrical axis. The interaction beam was at high enough power to exceed the threshold for the filamentation instability. Three varieties of targets were used in these experiments: thin foils of Cl containing plastic (CH), chlorinated plastic foam, and free-standing thin Al foils.
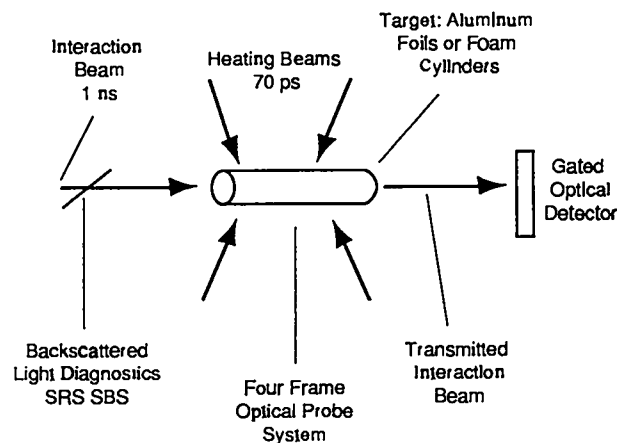
Fig. 15. Experimental configuration used in long scalelength plasma experiments.

The experiment can be thought of as a two-step process. The first step is the creation of the "target" long scalelength plasma with heating from the six short pulse beams. The second step is heating because of the "interaction" or seventh beam. The second stage of the interaction could result in processes such as filamentation (in the long scalelengths), which in turn could result in very elevated temperatures.

Both optical and x-ray diagnostics were used in these experiments. As shown in Fig. 15, a four-frame (15 ps), optical probe beam system produced a longitudinal shadow or schlieren or interferometric picture of the plasma. The transmitted interaction beam was photographed with a gated image intensifier.

The scattered light diagnostics on this set of experiments included observation of stimulated Raman scattering (SRS) (forward and backward) and stimulated Brillouin scattering (SBS) (backward only) of the interaction beam. These diagnostics provide important information on the physics taking place in the filament. SRS is of particular importance because it can tell us something about the hot electrons generated in the filaments, which are of considerable concern to its ICF target design.

X-ray diagnostic development consisted of two primary techniques: streaked (time-resolved) x-ray crystal spectroscopy and gated x-ray imaging. Streaked spectroscopy was intended to provide time-resolved measurements of electron temperature. Because of the expected large temperature difference between the background and the filament, we expect the spectrum due to the filament to be different and, in some regions, dominate that of the background. A gated x-ray imager can provide a time-resolved image with a gate time of 100 ps (FWHM) and an active area of 25 mm. This camera, coupled with an appropriately filtered pinhole array, can provide information on the electron temperature in the

filament. The short gating time is required to reject the significant radiation from the early plasma; also, a longer gate time would yield a washed-out image because the filament conditions change on this time scale.

In Fig. 16 we show data from one of the x-ray diagnostics. At t = 0 the plasma has been heated by the short pulse laser beams. At t = 400 ps, the heating beams are off and the plasma has begun to expand and cool. At t = 800 ps, the interaction beam has come on and very strong heating is observed. Even though the irradiance of the interaction beam is the same as the heating beams, much stronger heating and higher temperatures are observed. Before the interaction beam turns on, the x-ray spectrum is dominated by He-like emission. After the interaction beam turns on, the spectrum exhibits strong H-like emission, indicating higher electron temperatures. However, the strength of the He-like lines is not greatly diminished, suggesting that the high temperature region generating the H-like emission is localized in the plasma. This may be due to the presence of filamentation of the interaction beam in the preformed plasma.

Evidence of filamentary behavior was also observed in the optical probe beam data and in the transmitted interaction beam. In Fig. 17 we show a schlieren photo of the plasma formed from a cylindrical foam target. The strong density gradient observed down the cylindrical axis is consistent with the formation of a filament. In Fig. 18 the data from the transmitted interaction beam are shown. The beam develops structure and breakup as a function of time, phenomena once again consistent with filament development.

Figure 19 shows the backscattered SBS spectrum during the interaction pulse. The SBS spectrum is produced by the scattering of laser light from ion-acoustic waves in the plasma. The lower feature is the unshifted laser light while the upper feature is the SBS signal. Two features are of importance. The first is the size of the shift that comes from a plasma with an electron temperature well above 1 kV, relative to a background electron temperature on the order of 350 eV. The second is the abrupt, delayed turn on relative to the start of the interaction pulse. Both of these effects are consistent with the emission coming from a high temperature region of the plasma, such as would be present during thermal filamentation. The diagnostic techniques developed in these studies will soon be applied to further studies of long scalelength plasma phenomena both at AURORA and other laser systems.
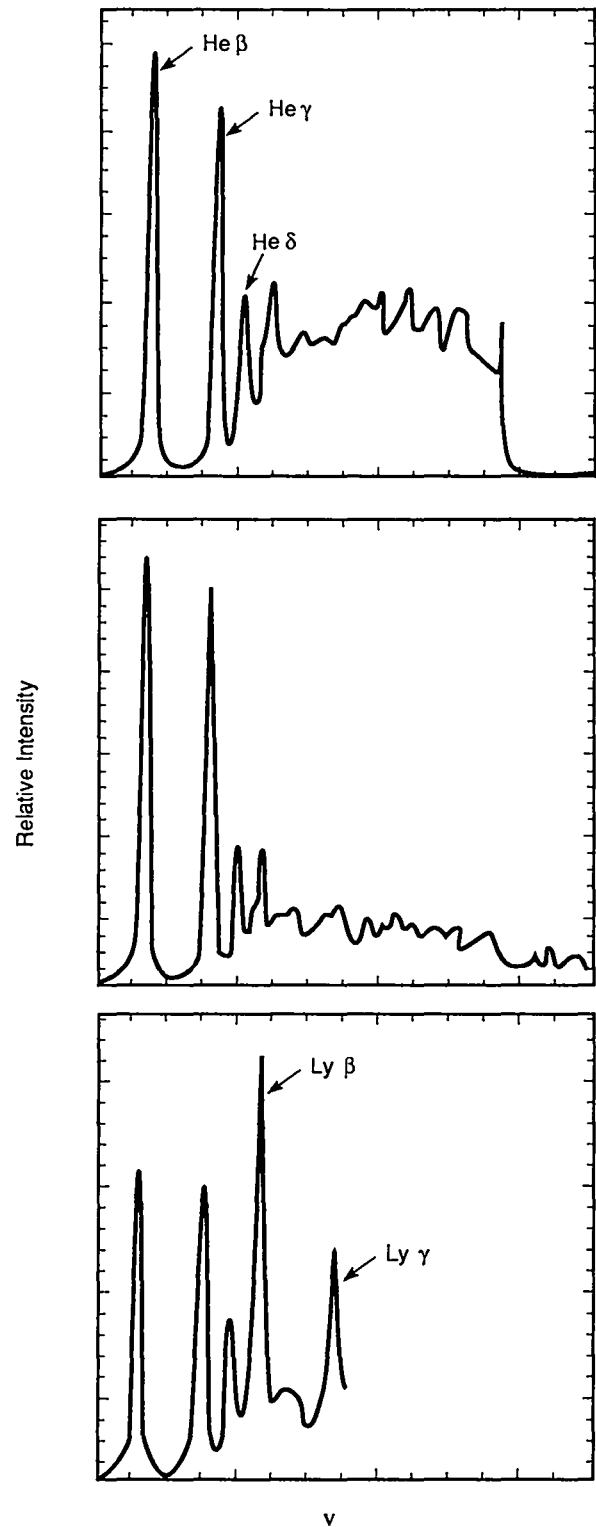
Fig. 16. X-ray spectra taken at three characteristic times in the evolution of and propagation through a long scalelength plasma.

Target: CH foam cylinder
d = 80 μm × 750 μm r = 0.1 gm/cm³

Probe pulse length 15 ps

Interaction Beam

Fig. 17. Evidence of constriction in the propagation of the interaction beam through a long scalelength plasma. This schlieren image was taken with the 15-ps probe beam and was orthogonal to the cylindrical axis.

Experiments on the AURORA KrF Laser

Since the last review of ICF by the National Academy of Sciences in 1985, Los Alamos has (out of operating funds alone) completed construction of the AURORA laser experimental facility, improved many of its components, and achieved several major milestones. In December 1988, AURORA delivered 2.5 KJ in a fully integrated multiplexed mode. In May 1989, target interaction experiments were begun at the ~ 40 TW/cm² irradiation level.

The utility of operating AURORA for physics research in support of national program goals was first acknowledged by DOE in 1987. The near-term goals of AURORA target experiments include the validation of KrF systems for target physics research and investigation of their unique advantages

as an ICF driver. In addition, we will begin to address issues of importance to the feasibility of an LMF using either direct or indirect drive. Longer-term research will increasingly support weapons-related physics.

Target: Al stripe
Framing window 120 ps
Frames represent three consecutive shots

Time from beginning of interaction beam

100 ps

400 ps

600 ps

Fig. 18. Observation of the transmission of the interaction beam through the plasma at three characteristic times.

For the near term, AURORA target experiments will have two major objectives:
- demonstration of the utility some of the unique capabilities of excimer lasers as laser fusion drivers, such as (i) the combination of short wavelength and large bandwidth, (ii) the use of large bandwidth for beam spatial smoothing on a very fast time scale, and (iii) flexible, sophisticated pulse shaping; and
- performance of weapons-related physics experiments.

A more detailed description of the AURORA target irradiation geometry, the target chamber, and the initial diagnostic array is given in the Target Irradiation Section of Chapter V. For continuity, some aspects of the target experiment configuration are repeated here.

Target: Al stripe 200μ x 1.3 mm x 300 nm
Back lighter delay = 800 ps
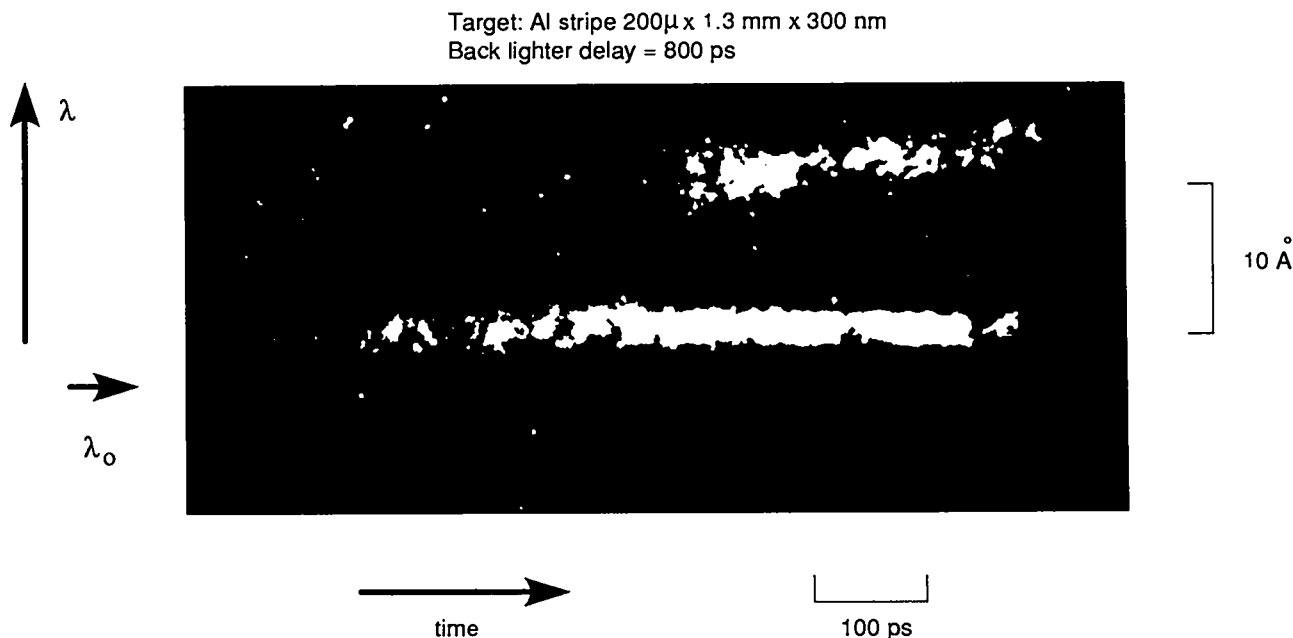
Fig. 19. Temporal evolution of backscattered light in a long scalelength plasma experiment.

Initial Operational Capability

The initial configuration for AURORA emphasizes the cost-effective test and integration of the laser to a "target-qualified" status; in particular, only 48 of the 96 multiplexed beams are time decoded to produce a simultaneous pulse on target. These 48 beams are focused to the target from one side by a set of f/26 focusing lenses arranged in a f/2 cone

AURORA is configured for planar direct drive and exploding foil experiments, and thus is suited for both long scalelength plasma physics and basic hydrodynamic studies. The beam spot size may be varied by moving the plate containing the focusing lenses and repointing the beams so that they overlap in the target plans. The focusing mechanism can be set to ~10 μm.

Initially AURORA will irradiate targets with 5-ns pulses at energy levels of ~1 to 3 kJ (in 48 beams). Beam pointing and focusing will be controlled sufficiently to produce a spot 400 μm in diameter including all of the beams. (The minimum spot size of the individual beams will be limited by the few times diffraction limited optics to ~70 μm on an average beam.) It will be possible to defocus the beam spot on target to ~4.5 mm. As more operational experience is gained with the final focusing system, a minimum spot (containing 48 beams) with a 200-μm diameter is the goal. This will enable access to laser-plasma interactions at $>10^{15}$ W/cm^2.

Initial Experiments

Initial experiments at AURORA have focused all 48 beams to a spot of the order of 400 μm on a flat plate target. In Fig. 20 we show typical x-ray images of the plasma created by such irradiation. The six spots are all images of the same shot but filtered differently to pass different photon energy bands. Strong emission in the region of ~1.5 KeV indicates significant plasma heating (>500 eV). The incident flux on target on this shot was of the order of 30 TW/cm^2. AURORA has thus been shown (in its fully multiplexed and integrated mode) to produce on-target fluxes that are relevant to inertial fusion work.

In Fig. 21 we show a soft x-ray spectrum obtained on another shot very similar to the one that produced the x-ray images in Fig. 20. This spectrum indicates intense soft x-ray emission (of a few hundred joules). These tests thus begin the very important studies of conversion of laser light to x rays with ultraviolet lasers.

The x-ray images shown in Fig. 20 indicate relatively smooth spatial profiles. Although no work has been done on optimization (or on utilization of special techniques such as ISI), the initial quality is encouraging.

~500 μm

~1.3 KeV x-rays

~1.8 KeV x-rays
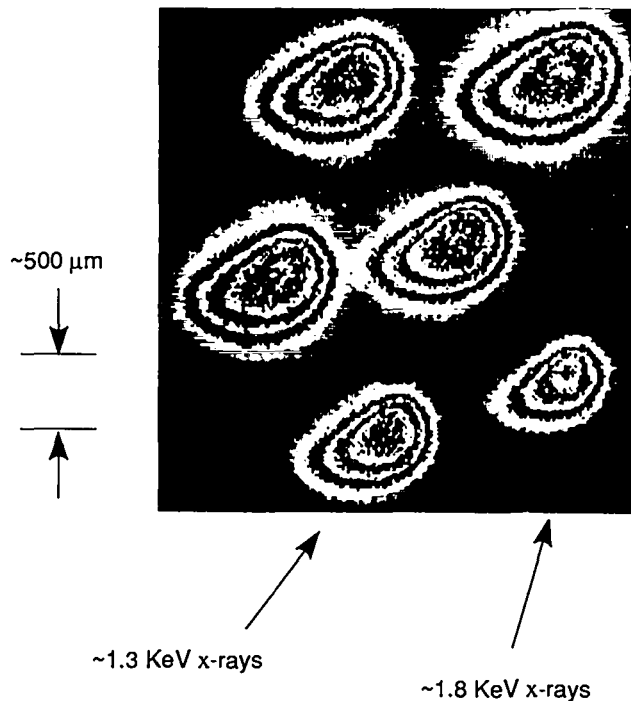
Fig. 20. X-ray images (showing equal intensity contours) of the plasma created by the interaction of ultraviolet light from the AURORA laser with a flat gold target.

Projections for Future Experimental Work at AURORA

Much of AURORA's experimental effort will be devoted to the study of processes relevant to indirect drive targets, which is discussed elsewhere.

With its ability to produce smooth spatial beam profiles, AURORA will be very useful in direct drive unstable hydrodynamic experiments. In Fig. 22 we illustrate some of the conditions that can be achieved with typical AURORA parameters. This is a promising parameter regime of hydrodynamic experiments.

In Fig. 23 we show the parameter regime relevant to long scalelength plasma studies that is accessible with AURORA. The ability of AURORA to operate with widely varying pulse shapes and lengths should be extremely useful in this work.

AURORA will initially operate with 5-ns pulses generated either with a Los Alamos built front end or a special oscillator supplied by the Naval Research Laboratory. Shorter pulse capability should be available soon after.

Because the interpulse spacing in the amplifiers is 5 ns, multiplexing this front end pulse maintains a roughly continuous loading on the amplifier. The Los Alamos oscillator is capable of injecting both shorter, longer, and shaped pulses. Because the storage time in the large KrF amplifiers is several nanoseconds, 2-ns pulses will extract essentially the same energy as the nominal 5-ns pulse. Kinetics calculations also indicate that ASE lasers will not significantly deplete the available energy.

Laser propagation/energy extraction calculations also indicate that propagation of shaped pulses in multiplexed, saturated laser chains like AURORA is straightforward. Figure 24 shows a sample model calculation of a 4-ns Gaussian pulse with a 30-ns low-level "foot" propagated through such a laser chain. Only a small fluctuation is imposed on the "foot" due to energy extraction competition with previous pulses in the multiplexed chain. The short-pulse capability of AURORA will be tested in early experiments to benchmark the kinetics code predictions and increase the confidence in the shaped-pulse propagation calculations.

AURORA should thus be able to perform a large variety of pulse-shaped experiments while at the same time having the flexibility to do experiments in a wide range of irradiances.
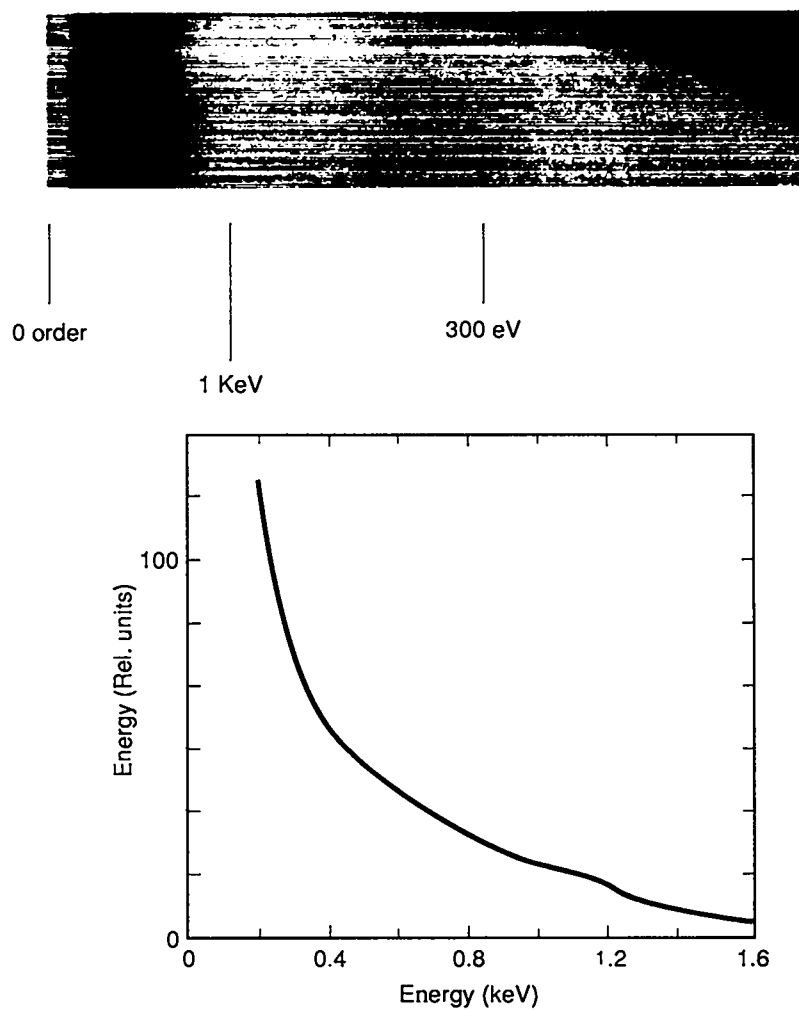
Fig. 21. Intense soft x-ray spectrum produced in a laser target experiment on the AURORA laser system.

CH Disk
$e_0 = 1 g/cm^3$

0.1 cm
(dia.)

Uniform Laser Beam:

$E_{IN} = 5 kJ$

$T_L = 5$ ns FWHM (ins rise & fall)

$P_{MAX} = 1$ TW

$T_{MAX} = 1.3 \cdot 10^{14}$ W/cm^2

Foil Thicknesses

$d_e = 20, 30, 50, 70 \mu m$

- Flat-topped Gaussian pulse is fine.
, 5-kJ, 5-ns KrF pulse produces interesting conditions.

$D_s = 0.1$ cm

$I \approx 10^{14}$ w/cm^2 $V_{MAX} > 2 \ 10^7$ cm/s

$P_A \approx 10 - 20$ Mb $a \approx 10\dot{1}6$ cm/s2

Acceleration history should drive ~9 e-foldings
of Rayleigh-Taylor growth, classically.

$\Rightarrow$ Promising Parameter Space

Fig. 22. Illustration of a typical AURORA parameter regime relevant to basic hydrodynamic studies.

Fig. 23. Plasma parameter regime accessible with the AURORA laser.

Fig. 24. Model calculation of the propagation of a highly shaped pulse through the AURORA laser chain. Such performance should be very useful in early shaped pulse shock and foil acceleration studies.

REFERENCES

Brackbill, J. U., and D. W. Forslund, "An Implicit Method for Electro-Magnetic Plasma Simulation in Two Dimensions," J. Comp. Phys. 46, 271, 1982.

Cairns, R. A., "An Introduction to the Absorption of Laser Light in Plasmas," Laser Plasma Interactions 2, R. A. Cairns, Ed., SUSSP Publications, Glasgow, Scotland, 1983.

Garban-Labaune, C., E. Fabre, C. Max, R. Amiranoff, R. Fabro, J. Virmont, and W. C. Mead, "Experimental Results and Theoretical Analysis of the Effect of Laser Wavelength

on Absorption and Hot Electron Generation in Laser-Plasma Interaction," Phys. Fluids, 28, 2580, 1985.

Forslund, D. W., and P. D. Goldstone, "Photon Impact, High Energy Plasma Physics with CO_2 Lasers," Los Alamos Science, 12, 2, 1985.

Gardner, J. H. and S. E. Bodner, "Wavelength Scaling for Reactor-Size Laser-Fusion Targets," Phys. Rev. Lett. 47, 1137, 1981.

Goldstone, P. D., S. R. Goldman, W. C. Mead, J. A. Cobble, G. Stradling, R. H. Day, A. Hauer, M. C. Richardson, R. S. Marjoribanks, P. A. Jaanimagi, R. L. Keck, F. J. Marshall, W. Seka, O. Bamouin, B. Yaakobi, and S. A. Letzring, "Dymanics of High-Z Plasmas Produced by a Short-Wavelength Laser," Phys. Rev. Lett. 59, 56, 1987.

Hauer, A., and H. Baldis, "Introduction to Laser Plasma Diagnostics," LA-11178-MS, Los Alamos National Laboratory, Los Alamos, NM, 1988.

Hauer, A., W. C. Mead, O. Willi, J. D. Kilkenny, D. K. Bradley, S. D. Tabatabaei, "Measurement and Analysis of Near-Classical Thermal Transport in One-Micron Laser-Irradiated Spherical Plasmas," Phys. Rev. Lett. 53, 2563, 1984.

Henke, B. L., and P. A. Jaanimagi, "Two-Channel Elliptical Analyzer Spectrograph for Absolute, Time-Resolving Time-Integrating Spectrometry of Pulsed X-Ray Sources in the 100-10,000-eV Region," Rev. Sci. Instrum. 56, 1537, 1985.

Kato, Y., K. Mima, N. Miyanaga, S. Arinaga, Y. Kitagawa, M. Nakatsuka, and C. Yamanaka, "Random Phasing of High-Power Lasers for Uniform Target Acceleration and Plasma-Instability Suppression," Phys. Rev. Lett. 53, 1057, 1984.

Kodama, R., K. Okada, N. Ikeda, M. Mineo, K. A. Tanaka, T. Mochizuki, and C. Yamanaka, "Soft X-Ray Emission from ω_0, $2\omega_0$, and $4\omega_0$ Laser-Produced Plasmas," J. Appl. Phys. 59, 3050, 1986.

Lee, Y. T., "A Model for Ionization Balance and L-Shell Spectroscopy of Non-LTE Plasmas," J. Quant Spectrosc. Radiat. Transfer 38, 131, 1987.

Lehmberg, R. H., and S. P. Obenschain, "Use of Induced Spatial Incoherence for Uniform Illumination of Laser Fusion Targets," Opt. Commun. 46, 27, 1983.

Lokke, W. A., and W. H. Grasberger, "X S N Q-U - - A Non-LTE Emission Absorption Coefficient Subroutine," UCRL-52276, Lawrence Livermore National Laboratory, Livermore, CA, 1976.

Mead, W. C., E. M. Campbell, W. L. Kruer, R. E. Turner, C. W. Hatcher, D. S. Bailey, P. H. Y. Lee, J. Foster, K. G. Tirsell, B. Pruett, N. C. Holmes, J. T. Trainor, G. L. Stradling, B. F. Lasinski, C. E. Max, and F. Ze, "Characteristics of Lateral and Axial Transport in Laser Irradiations of Layered-Disk Targets at 1.06 and 0.35 μm Wavelengths," Phys. Fluids 27, 1301, 1984.

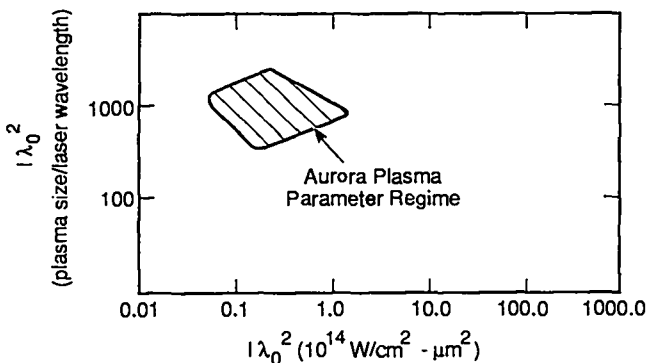Mead, W. C., E. M. Campbell, K. G. Estabrook, R. E. Turner, W. L. Kruer, P. H. Y. Lee, B. Pruett, V. C. Rupert, K. G. Tirsell, G. L. Stradling, F. Ze, C. E. Max, M. D. Rosen, and B. F. Lasinski, "Laser Irradiation of Disk Targets at 0.53 μm Wavelength," Phys. Fluids 26, 2316, 1983.

Mochizuki, T., T. Yabe, K. Okada, M. Hamada, N. Ikeda, S. Kiyokawa, and C. Yamanaka, "Atomic-Number Dependence of Soft X-Ray Emission from Various Targets Irradiated by a 0.53-mm-Wavelength Laser," Phys. Rev. A 33, 525, 1986.

Nishimura, H., F. Matsuoka, M. Yagi, K. Yamada, S. Nakai, G. H. McCall, and C. Yamanaka, "Radiation Conversion and Related Ablation Behavior of a Gold-Foil Target Irradiated by 0.35, 0.53, 1.06, and 1.06 μm Lasers," Phys. Fluids 26, 1688, 1983.

Pien, G., M. C. Richardson, P. D. Goldstone, R. H. Day, F. Ameduri, and G. Eden, "Computerized 3-GHz Multichannel Soft X-Ray Diode Spectrometer for High Density Plasma Diagnosis," Nucl. Instrum. Methods B 18, 101, 1986.

Richardson, M. C., G. G. Gregory, S. A. Letzring, R. S. Marjoribanks, B. Yaakobi, B. L. Henke, P. A. Jaanimagi, and A. Hauer, "Time-Resolved X-Ray Spectrographic Instrumentation for Laser Fusion and X-Ray Laser Studies," Proc. SPIE (International Society for Optical Engineering), Vol. 569, San Diego, CA, August 22-23, 1985.

Turner, R. E., K. Estabrook, R. L. Kaufman, D. R. Bach, R. P. Drake, D. W. Phillon, B. F. Lasinski, E. M. Campbell, W. L. Kruer, E. A. Williams, "Evidence for

Collisional Damping in High Energy Raman-Scattering
Experiments at 0.26 Micron," Phys Rev. Lett., 54, 189,
1985.

Willi, O., S. D. Tabatabaei, D. Riley, A. Hauer, N.
Delamater, C. Chenais-Popovics, P. Apte, and A. Cole,
Measurements of Laser Plasma Coronal Conditions and
Thermal Transport with Time-Resolved X-Ray
Spectroscopy," Phys. Rev. A 39, 6090, 1989.

Zimmerman, G. B., and W. L. Kruer, "Numerical
Simulation of Laser-Initiated Fusion," Comments Plasma
Phys. Controlled Fusion 2, 51, 1975.

V. KrF Laser Development
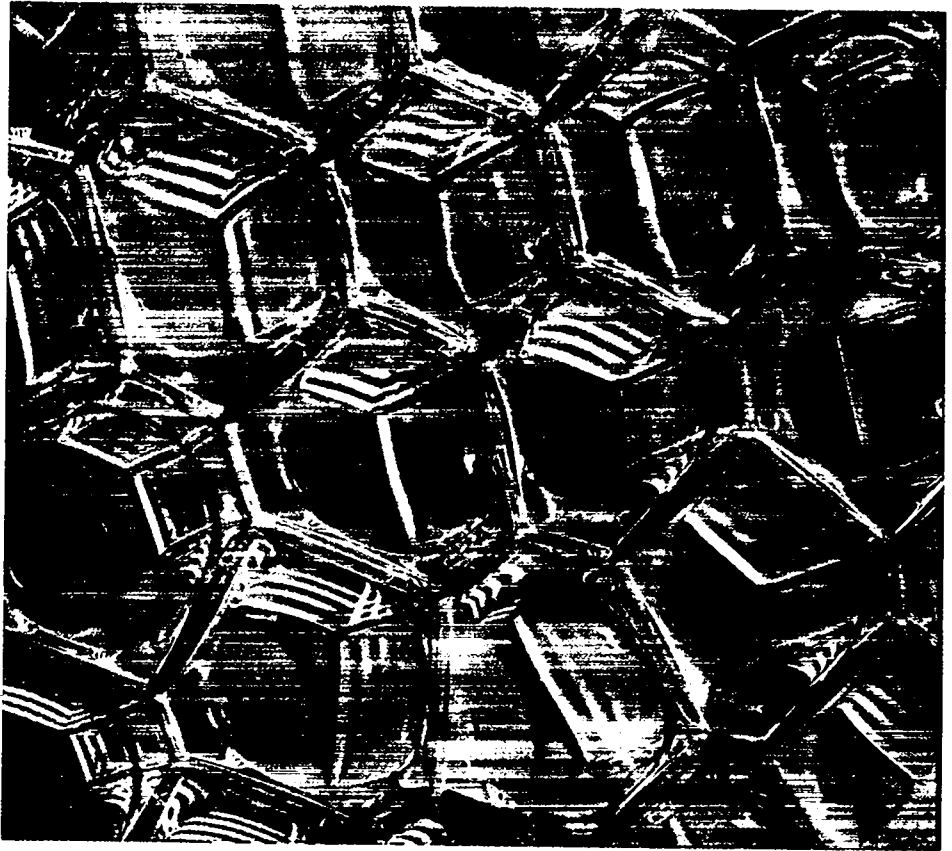
Photograph of the mosaic structure in new lightweight optics.

A. History of KrF Laser Development

B. The AURORA Laser Facility

C. AURORA System Performance

D. The AURORA Target Irradiation System

A. HISTORY OF KrF LASER DEVELOPMENT

Joseph F. Figueira

The Los Alamos National Laboratory has been actively engaged in the development of high-power gas lasers for inertial confinement fusion applications for twenty years. The Los Alamos invention of a scalable electron-beam pumping technology by Boyer, Fenstermacher, Leland, Nutter, and Rink in 1969 (Fenstermacher et al. 1971) revolutionized the scalability limits of gas lasers and allowed the construction of large-aperture, multikilojoule devices. The Los Alamos program began with highly efficient long wavelength molecular lasers based on CO_2. This very successful laser development program culminated in the operation in 1983 of the Antares laser at the 35-kilojoule level (40 TW of power). Based on results from the target experimental programs in the early 1980s, a national shift in the required laser wavelength occurred, and the Los Alamos ir laser program was terminated in favor of the short wavelength KrF gas laser.

The KrF laser is relatively new to the ICF community; it was demonstrated in 1975 (Brau and Ewing 1975), followed immediately by other confirmations of spectroscopy and lasing (Brau 1975; Ewing and Brau 1975; Ault et al. 1975; Mangano and Jacob 1975; Searles and Hart 1975; and Tisone et al. 1975). The development of high peak power KrF laser technology for Inertial Confinement Fusion (ICF) applications is actively in progress throughout the world with major facilities underway in Japan, Canada, England, the USSR, and the US. Because of the newness of the technology, most of these efforts are a strong mixture of facility engineering, advanced technology research and development, and advanced conceptual design studies. The Los Alamos National Laboratory KrF laser development program is probably the largest effort in the world. It addresses both near-term integrated laser demonstrations and longer-term advanced design concepts and technology advancements required for larger fusion laser systems. In this section we will review the basic features of the KrF lasers, describe the status of the worldwide KrF technology

program, provide an overview of the Los Alamos laser development program, describe current progress on the near-term technical activities, and discuss the future directions of the Los Alamos KrF laser development program.

BASIC FEATURES OF THE KrF LASER

KrF lasers operate by electrically pumping high-pressure gas mixtures of krypton (Kr), fluorine (F_2), and a ballast gas such as argon (Ar) with self-sustained electrical discharges or with high-energy electron-beams. The electrical excitation initiates a complex chain of reactions that result in the production of the krypton fluoride (KrF*) molecule and various absorbers. The KrF* molecule can then lase to the unbound lower level, emitting a photon at 248 nm. The upper state lifetime is very fast in the excited KrF molecule, and storage times are limited to approximately 5 ns by quenching and spontaneous emission. KrF is the second most efficient member of a class of excimer lasers that also include the well-studied XeCl (lasing at 308 nm), XeF (lasing at 351 nm), and ArF (lasing at 193 nm), which is the most efficient.

A unique combination of features appears to make the KrF laser well suited as a driver for inertial confinement fusion drivers. These features are summarized below. They will be discussed in more detail in the following sections of this chapter.

- The laser directly operates at 248 nm, optimizing the ICF target efficiency without added wavelength conversion complexity.
- Unlike other ICF lasers, the KrF laser is basically not a storage laser; it prefers to operate in the continuous energy extraction mode. Because of this feature, loaded KrF amplifiers tend to be very linear with little temporal pulse shape distortion. This allows for very robust

pulse-shaping capability that may prove absolutely essential for efficient target performance.

- Electron-beam pumped KrF lasers are scalable to large energies in a single module. This feature has been clearly demonstrated by amplifier architectures now under development. The AURORA large aperture module has already demonstrated 10 KJ extracted from a 2000:1 volume, and advanced Los Alamos designs will explore the 50-KJ to 250-KJ region.

- The laser operates with a broad lasing bandwidth in excess of 200 cm^{-1} that allows the use of spatial and temporal smoothing techniques for both direct and indirect target drive applications.

- Although all of the current ICF related KrF laser technology development programs are emphasizing single-shot facilities, the basic design features of the KrF gas laser will permit extensions to repetitively pulsed devices in the future, if commercial energy applications are pursued.

- The laser medium is a nondamaging gas, eliminating the need for extensive protection systems to insure the survivability of the laser medium. This feature also allows KrF to readily adapt to multiple-pulse operation for commerical applications.

WORLDWIDE PROGRESS

Since their invention in 1975 by Brau and Ewing, excimer lasers have been the subject of steady and increasing interest. Major progress has been made in the commercial development of high average power devices, with 1-KW devices being actively developed on several continents through private companies or industrial consortia. More recent interest has centered on the development of high peak power devices as potential replacements for harmonically converted glass lasers in inertial confinement fusion and atomic physics applications. Active research and technology programs are in progress in the United States and competitive programs are being pursued in Japan, Canada, Germany, the United Kingdom, and the Soviet Union. These programs have led to a series of first-generation, integrated laser-target systems that are in design, construction, or testing. Table 1 shows a current compilation of these laser systems. The Lawrence Livermore National Laboratory (LLNL) RAPIER system was operated briefly in the early 1980s and then decommissioned. The SPRITE laser, built at the Rutherford-Appelton Laboratories in the United Kingdom, was the first truly high-power KrF facility in operation. The UK government has approved an upgrade of this facility to the 3-KJ level and designs are currently in progress for

the 100-KJ Euro-laser. The Naval Research Laboratory (NRL) is the other DOE US participant in the KrF laser development program. NRL has started construction of the NIKE laser that will produce 2 - 4 KJ. The University of Alberta at Edmonton is proposing to build a 1-KJ facility, utilizing some of the components from the LLNL RAPIER laser that have been provided by the DOE through a joint US/Canada protocol. Several Japanese universities are actively involved in the pursuit of KrF LASERS; the major operating facility in operation is the ASHURA laser at the Electro-Technical Laboratory of the University of Tokyo. In addition, the Kurchatov Institute of the USSR is constructing a KJ-class KrF facility in collaboration with Evremov Electro-Technical Institute and is pursuing conceptual designs for a 10-KJ class device. All of these facilities are based on electron-beam pumped KrF laser technology; they employ several different optical architectures and different design philosophies. This broad array of activities will continue to enrich the technology available to KrF lasers and to improve the performance and reduce the cost of many system components.

TABLE 1. KrF Laser Technology Is Being Pursued Internationally for ICF Applications

Laser System	Status	Energy	Power
Rapier (LLNL)	1982	800J	1×10^{10}W
SPRITE (Rutherford)	1983	200J	3×10^{9}W
Euro-Laser (Rutherford)	~1996	100kJ	variable
AURORA (Los Alamos)	1985	10kJ	2×10^{10}W
	1988	1kJ	2×10^{11}W
	1989	4kJ	10^{12}W
Nike (NRL)	1989	10J	——
	~1993	2kJ	——
Rapier B (U of Alberta)	1988 (proposed)	100J	——
		1kJ	——
Ashura (Electro-Technical Lab, Japan)	1988	500J	5×10^{9}W
	(future)	1kJ	2×10^{11}W

OVERVIEW of KrF LASER DEVELOPMENT PROGRAM

In the preceding sections we have discussed both the potential advantages of KrF lasers and the international effort now underway in KrF laser technology. The potential advantages of the laser are well recognized, but they must be demonstrated at current scale size in integrated laser-target systems. More importantly, these advantages must be shown to scale economically to the 100-KJ to 10-MJ sizes required for future progress in the ICF program. The Los Alamos laser development program is composed of three major elements that are intended both to aggressively address near-term feasibility of the KrF laser concept and to show the way to the cost and performance improvements required for future laser facilities.

- The AURORA Laser Facility is a 1-TW KrF laser designed as an integrated performance demonstration of a target-qualified excimer laser system.
- An advanced design effort evaluates the concepts that offer the improved performance and lower cost that will be essential for the construction of future lasers in the 0.1- to 10-MJ class.
- A laser technology program addresses both performance and cost issues that will be important in advanced laser system designs.

Each of these programs is briefly described in this section and will be described in much more detail later in this chapter.

AURORA

The near-term goal for Los Alamos is the successful integration and operation of the of the AURORA Laser Facility at the multikilojoule level with powers approaching 1 TW. AURORA is a short-pulse, high-power, krypton-fluoride laser system. It serves as an end-to-end technology demonstration prototype for large-scale excimer laser systems of interest to short wavelength ICF investigations. The system employs optical angular multiplexing and serial amplification by electron-beam driven KrF laser amplifiers to deliver multikilojoule laser pulses of 248 nm and 5-ns duration to ICF relevant targets. The design goal for the complete system is 5 KJ in 48 laser beams. Figure 1 (on the following page) shows a schematic diagram of the laser system.

Substantial progress has been made on the facility in the last several years including the following highlights:

- Demonstration of 96-beam multiplexing and amplified energy extraction, as evidenced by the integrated operation of the front end, the multiplexer (12-fold and 8-fold encoders), the optical relay train, and three electron-beam driven amplifiers;
- Assembly and installation of the demultiplexer optical hardware, which consists of over 300 optical components ranging in size from several centimeters square to over a meter square;
- Completion of pulsed-power and electron-beam pumping upgrades on the LAM (Large Aperture Module), PA (Pre-Amplifier), and Small Aperture Module (SAM). The SAM shows a 40% increase in deposited electron beam energy, and the PA deposited energy has been increased by a factor of two; and
- Integration of the entire laser system; the extraction of 4 KJ from the laser in 96 beams; and the delivery of 1.2-KJ, 5-ns pulses to the target chamber in 36 beams with intensity of 100 TW/cm^2 on target.

ADVANCED LASER SYSTEM DESIGN

In the longer term, the national ICF program will continue to plan for the construction and operation of the next generation driver for ICF physics experiments. To determine the applicability of KrF laser technology to future generations of fusion drivers, Los Alamos has begun a design effort to explore systems in the 100kJ to 10MJ range. This Advanced KrF Laser Design effort provides information to the KrF program on the design and cost of future KrF laser-fusion systems and provides directions and goals to the KrF technology development effort. Because no current ICF driver has demonstrated both the required cost and the performance scaling, and because uncertainties exist in laser-matter interactions and target physics, Los Alamos is currently pursuing a range of advanced KrF laser design activities: work is currently in progress to scope a 10-MJ Laboratory Microfusion Facility (LMF), a 720-kJ LMF Prototype Beam Line, a 250-kJ Amplifier Module (AM), and a 100-KJ Laser Target Test Facility.

The purpose of the Department of Energy sponsored scoping study for a Laboratory Microfusion Facility is to examine a facility with a capability of producing a target yield of 1000 MJ in a single-pulse mode. An example of a KrF design that requires only minor extrapolations in pulsed-power technology is shown in Fig. 2. This system uses angularly multiplexed amplifier modules 1.3 × 3.9 × 3.8 m^3, each of which produces 250 kJ of 248-nm radiation. These units are then arranged in a trifold
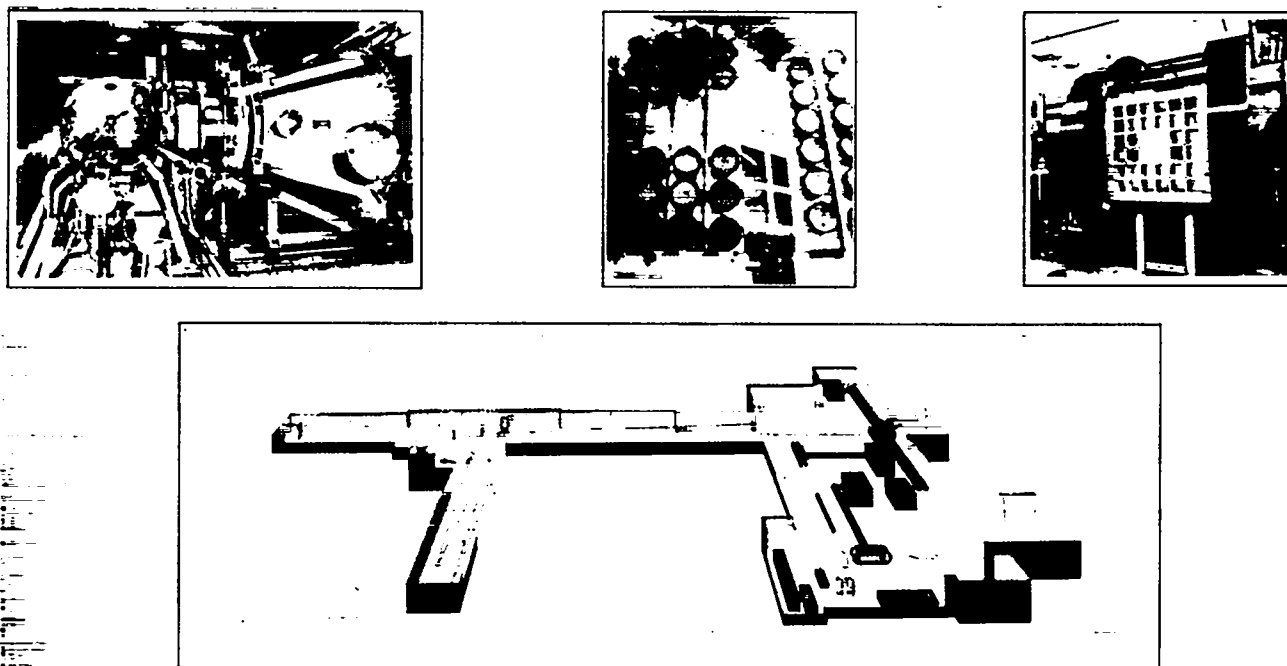
Fig. 1. Schematic of the three major AURORA subsystems: target, optics, and amplifier (l to r).
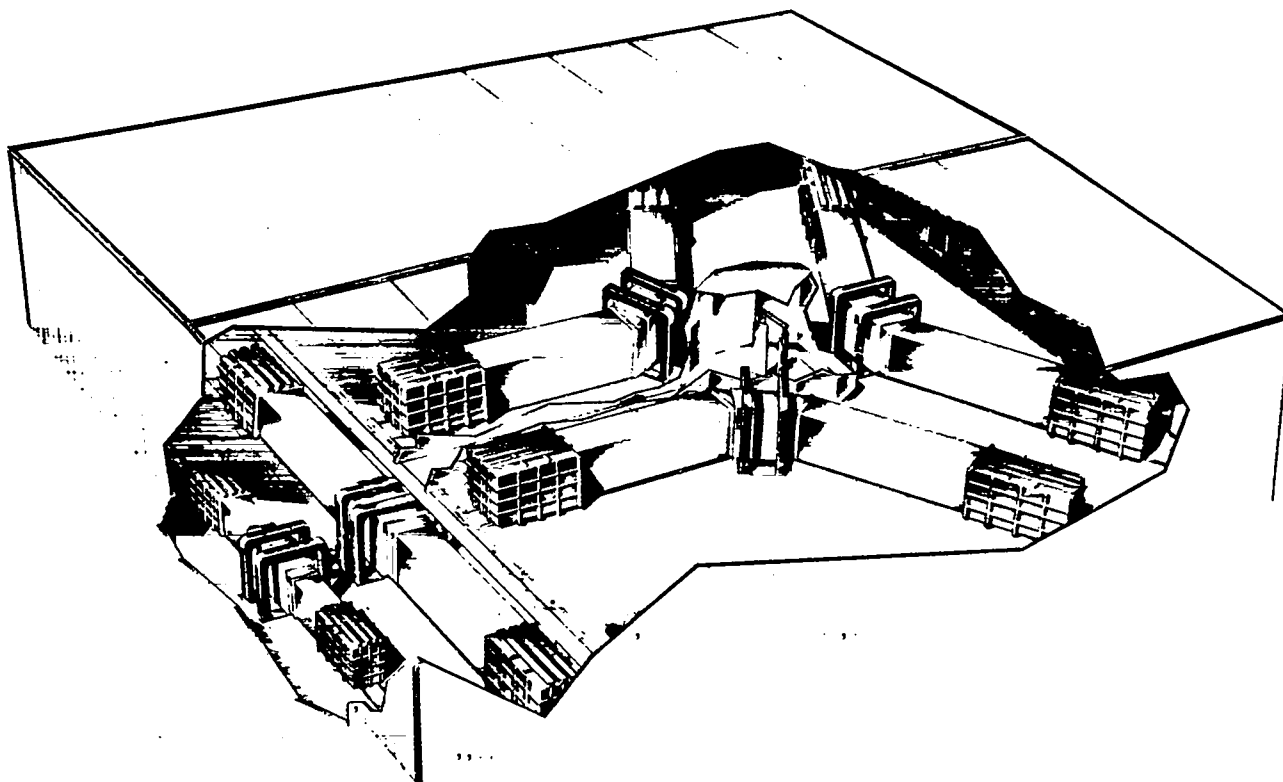
Fig. 2. LMF beam line showing a tri-fold array of 240-kJ modules.

cluster, to form an LMF beam line that produces 720 kJ. These beam lines can then be arranged to produce the required energy ranging from 720 kJ to 10 mJ.

KrF TECHNOLOGY

The current costs of all laser drivers are unacceptable for an LMF scale system. To reduce these costs to an acceptable level, we are currently structuring our advanced technology programs to address the major cost drivers identified by the design studies. Figure 3 shows the laser driver cost by system for a design based on current AURORA technology, compared to the design using the 250-kJ laser module described above. The optics and pulse power account for 60% of the total cost for the AURORA-based designs; this produces an unacceptably high laser system cost. Advanced design concepts have identified technology areas that can be improved to reduce the overall system costs. The optics and pulse power costs have been reduced to 19% of the total system cost, and the total system cost is reduced by a factor of 5. The KrF laser technology development program addresses performance improvements and cost reductions for the LMF designs in the areas of optics, pulse power, and laser performance, as well as those technical issues effecting system reliability and modeling accuracy. Figure 4 illustrates the cost goals for advanced KrF drivers, including the LMF. Also shown are cost estimates from several system studies performed over the last four years. These technology and cost reduction programs will utilize a mixture of industrial, university, and government laboratory involvement and will lead to subscale technology demonstrations that are described in more detail later in this chapter.

CONCLUSION

High-energy, high peak power KrF lasers represent a promising new technology for inertial confinement fusion applications. To evaluate this technology, Los Alamos is conducting a series of integrated system demonstrations with the AURORA Laser Fusion facility. Future applications of this laser are being evaluated by a coordinated program of advanced designs and technology development. If these evaluations are successful, KrF lasers will provide the national ICF program with an attractive future driver candidate for the Laboratory Microfusion Facility in the late 1990s.
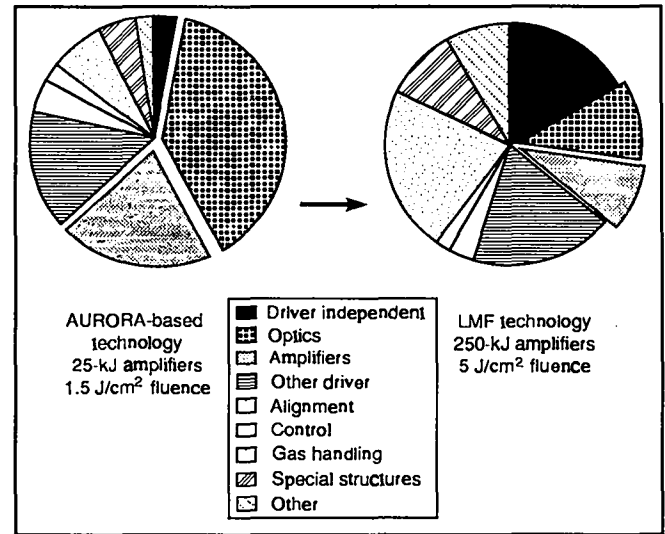
Fig. 3. Distribution of costs for current (AURORA) and future (LMF) technologies.
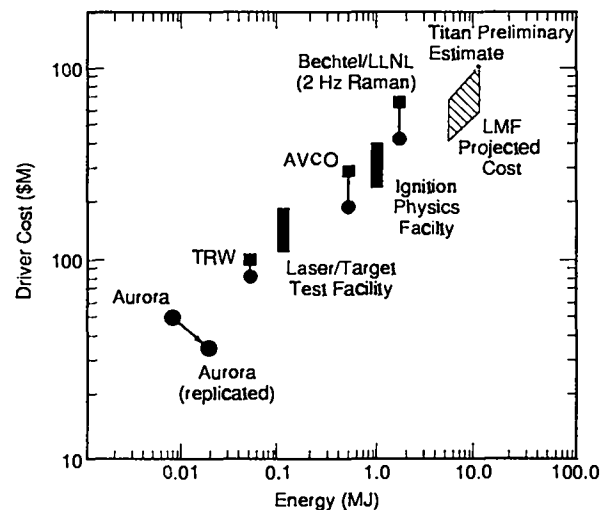
Fig. 4. Estimated driver costs for KrF lasers designed for ICF requirements.

REFERENCES

Ault, E. R., R. S. Bradford, Jr., M. L. Bhaumik, Appl. Phys. Lett. 27, 413, 1975.

Brau, C. A., J. J. Ewing, Appl. Phys. Lett. 27, 435, 1975.

Ewing, J. J., Brau, C. A., Appl. Phys. Lett. 27, 350, 1975.

Fenstermacher, C. A., M. J. Nutter, J. P. Rink, and K. Boyer, "Electron Beam Initiation of Large Volume Electric Discharges in CO_2 Laser Media," Bull. Am. Phys. Soc., 16: 42, Jan. 1971.

Mangano, J. A., J. H. Jacob, Appl, Phys. Lett 27 495, 1975.

Searles, S. K., G. A. Hart, Appl. Phys. Lett. 27, 243, 1975.

Tisone, G. C., A. K. Hays, J. M. Hoffman, Opt. Commun. 15, 188, 1975.

B. THE AURORA LASER FACILITY

Louis A. Rosocha

INTRODUCTION

Because of the attractiveness of short wavelength lasers for inertial confinement fusion (ICF), the Los Alamos National Laboratory (LANL) is investigating the feasibility of high power rare-gas excimer lasers for ICF applications.

The prototype for this demonstration is the AURORA KrF laser system (described in detail by Rosocha et al. 1987, Hanlon and McLeod 1987, and McLeod 1987), whose goal is to demonstrate the applicability of optical angular multiplexing and serial amplification by large electron-beam driven KrF laser amplifiers to large-scale fusion drivers. Multiplexing is a technique for matching the energetic component (~5 ns) of the required target laser pulse to the longer electrical pulse time (~500 ns) required for practical, efficient large-scale KrF laser amplifier operation.

AURORA uses a multiplexed 96-element train of 5-ns pulses, which is amplified and passed through a demultiplexer, where all pulses in the train are stacked in time by using suitable time-of-flight delays. The laser system is presently configured to deliver 48 stacked 5-ns pulses to the target at multikilojoule energy levels. It is possible to extract energy levels approaching 10 kJ from the final AURORA amplifier for a power level of 1 TW.

This article describes the design and performance of the front end, the amplifiers and the optical train, proposed amplifier improvements, and the delivery of demultiplexed pulses to the target plane.

The AURORA prototype excimer laser will demonstrate critical technologies involved in developing KrF drivers for fusion and will serve as a test-bed for some technological aspects of larger laser fusion systems. In particular, AURORA will examine
- uniform electron beam pumping of large laser volumes;

- optical angular multiplexing and demultiplexing systems that are scalable to large system designs;
- staging of large KrF amplifiers;
- uv pulse propagation over long paths;
- alignment of multibeam systems; and
- novel approaches to optical hardware that can lead to cost reductions for even larger systems.

The integrated AURORA laser chain was fired for the first time in December 1988. During the firing, a 96-beam multiplexed pulse train containing approximately 2.5 kJ was extracted from the final amplifier, and nearly a kilojoule of this energy (780 J) was delivered to the target chamber in 48 beams. For this first series of experiments, a smaller LAM mirror was used to extract energy from the central 20% of the full amplifier optical aperture. The full-sized back mirror was installed in June 1989, and preliminary target irradiation experiments were completed in August. The integrated system performance produced laser energies in excess of 4 kJ; it transported and focused 1.2 kJ in 36 beams to 100 TW/cm^2 in the target plane.

KrF lasers are promising candidates for ICF because they have the following specific target-relevant and operational advantages:
- short wavelength (which couples more efficiently to fusion targets than either infrared or visible lasers);
- decreased superthermal electron production;
- broad bandwidth (which decreases deleterious nonlinear plasma processes);
- robust pulse shaping capability;
- relatively high intrinsic laser efficiency;
- high energy scalability;
- potential for repetitive operation; and
- nondamaging gaseous media.
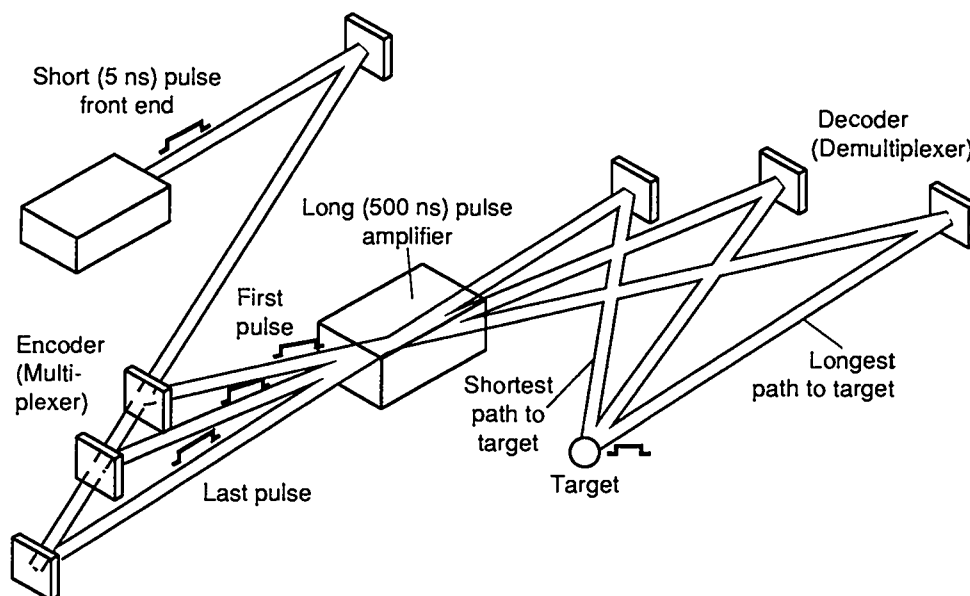
Fig. 1. Angular optical multiplexing allows for efficient energy extraction of long pulse amplifiers. A single 5-ns pulse is split and delayed and feed through the 500-ns amplifier. After amplification the angle encoded time channels are recombined in syncronism at the target. In the schematic shown this technique allows a power multiplication of ×100.

At Los Alamos optical multiplexing has been used to convert a –500-ns amplifier pulse into 96 5-ns laser pulses, because it utilizes existing designs and conventional optical methods, as shown in Fig. 1.

An artist's rendering of the AURORA system is shown in Fig. 2. In this system, the front end laser output is replicated by means of aperture slicers, beam splitters, and mirrors to produce a train consisting of 96 individual 5-ns pulses. These time-encoded (multiplexed) pulses, which are spatially separated, are individually adjusted at the entrance pupil of an optical relay system. At this point, the beams are angle-encoded (multiplexed) in one-to-one correspondence to their time position in the beam train. The beam train is then relayed through two single-pass amplifiers, the Preamplifier (PA) and the Intermediate Amplifier (IA), a double-pass amplifier (LAM), and then demultiplexed by the decoder before being delivered to the target chamber. Three automated alignment systems are employed to maintain optical alignment: these are located at the input pupil, the LAM (and its associated feed array), and at the final aiming mirrors. To deliver short-pulse KrF laser energy to the targets, a decoder (demultiplexer) optical system compresses the multiplexed beam train into a single 5-ns pulse at the target chamber. The decoder optics, the target system, and the target diagnostics for 48-beam energy delivery are operational. We have chosen to use only 48 of the 96 beams to demonstrate the principle of angular multiplexing on AURORA to reduce system cost.

FRONT END DESIGN AND PERFORMANCE

The first baseline design for the AURORA front end employed double Pockels cell switches to slice out 5-ns pulses from the 25-ns output pulse of a Lambda Physik Model EMG-150 KrF laser. The contrast ratio of this system was not suitable for target experiments because it had too much prepulse, and the Pockels cells limited the repetition rate that could be used for final alignment to 1/min. An advanced system incorporating a phase conjugatemirror that had been shown to have some beneficial properties was chosen to replace the Pockels cell system (Kurnit and Thomas 1989; Thomas et al. 1988). This advanced system consists of a stimulated Brillouin scattering (SBS) cell as the return mirror in a two-pass amplifier. Because the SBS medium is not a mirror until threshold is reached, the prepulse originating from the oscillator on the first pass is eliminated. The phase conjugation also improves the beam quality, and a variable duration pulse is generated by attenuating the input to the phase conjugate mirror. Elimination of lossy Pockels cell switches has increased the available output energy and the repetition rate of the AURORA front end. In this report we present some of the details and performance of this front end.
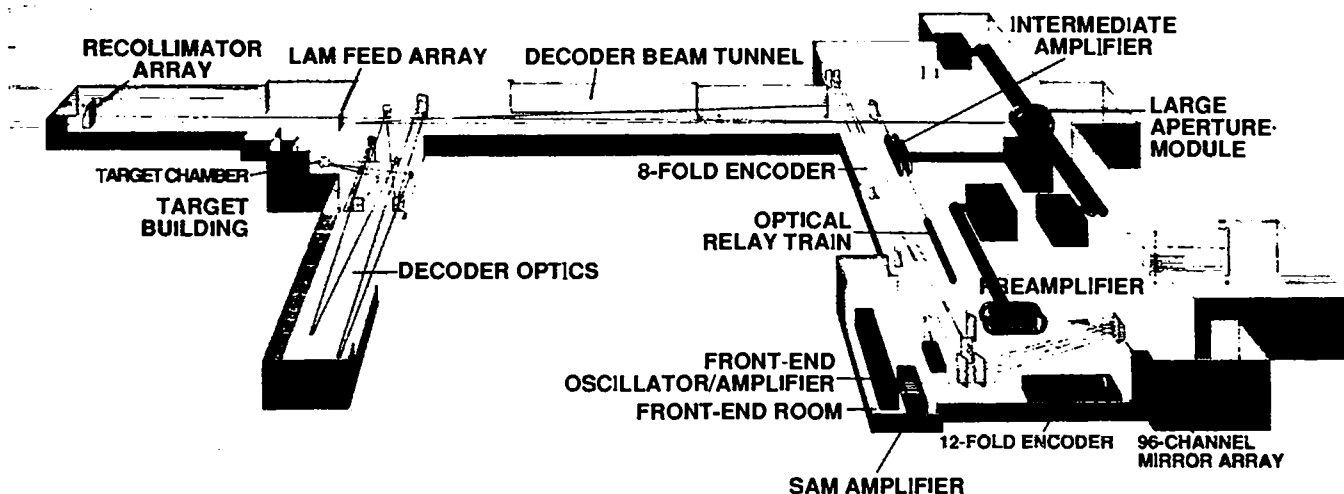
Fig. 2. Artist's rendering of the AURORA laser system. The part of the building on the right contains the front end, the optical multiplexer (encoder), most of the optical relay train, and the amplifiers. The structures on the left house the optical demultiplexer (decoder), final aiming mirrors, and the target facility. To determine the scale, it should be noted that the distance from the Large Aperture Module to the recollimator array is approximately 100 m, and the total flight path from front end to target approaches 1 km. The entire system is now constructed and in the process of high energy operation.

Experimental Setup

The experimental setup is shown schematically in Fig. 3. A modified Lambda Physik Model EMG 150 KrF laser, which contains two commonly switched discharge heads, is used in an oscillator-amplifier arrangement. The oscillator cavity consists of a 10-m concave HR mirror and a 60% flat output coupler, separated by 1.25 m with a 1-mm intracavity aperture, and a single dispersing prism to reduce the bandwidth to ~10 cm^{-1}. The 10-mJ, 20-ns pulse from the oscillator is expanded after it is passed through a clean-up polarizer and then optically delayed to compensate for the built-in delay between the discharge heads. The expanded beam overfills the 1.5- x 3.0-cm cross section of the preamplifier and is injected into the the preamplifier by a 9% reflection from an uncoated wedged beam splitter. An

aperture is placed at the focus of the expanding telescope to prevent the backward ASE pulse from damaging the telescope input lens if the oscillator fails to operate. The ASE is focused at a longer distance and is rejected by the aperture.

After one pass of amplification, the beam is focused by a 25-cm focal length lens into the SBS cell, which contains 20 atm of SF$_6$. A phase-conjugate reflection is produced when the pulse reaches Brillouin threshold; it returns through the preamplifier for a second pass of amplification, and the output is taken through the beam splitter. The output pulse width can be varied by attenuating the oscillator output. This increases the time it takes for the SBS medium to reach threshold and a shorter pulse is reflected. We can presently vary the pulse width from 1-ns to 10-ns FWHM.
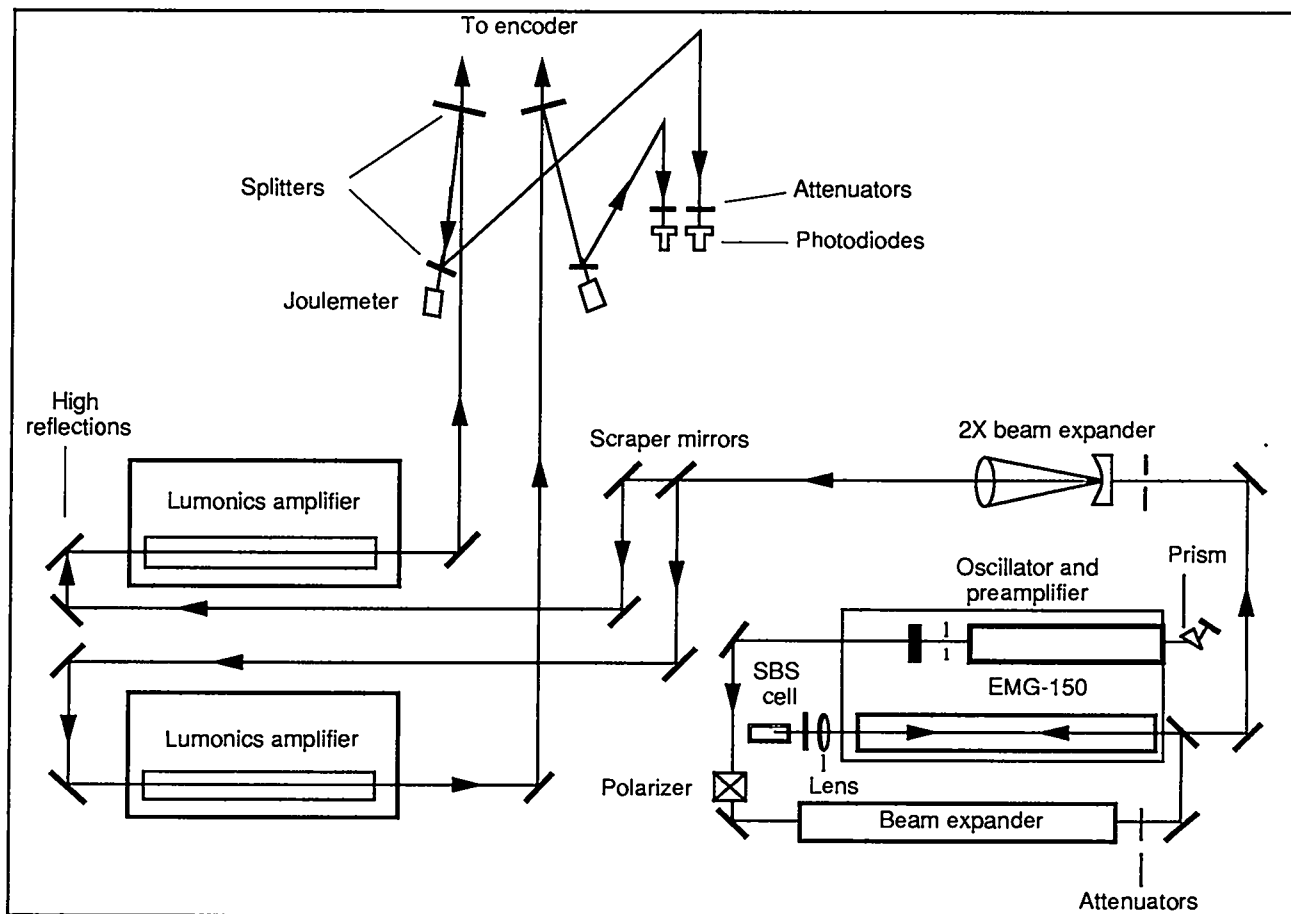
Fig. 3. Schematic of AURORA front end consisting of a Lambda-Physik EMG 150 configured as an oscillator and phase conjugate amplifier, followed by two Lumonics amplifiers.

The 1.5- x 3.0-cm output beam from the EMG 150 is expanded with a 2x telescope to form a 3.0- x 6.0-cm beam. This beam is directed to a pair of scraper mirrors that split it into two 3.0- x 3.0-cm beams. Each beam is then single-pass amplified through a separate Lumonics amplifier and directed to the AURORA encoder section. As each beam leaves the front end room, it passes through an uncoated beam splitter that directs a small percentage of it to a calibrated joulemeter and to a high-speed photodiode where the energy and pulse shape are recorded.

We recently completed a series of performance measurements of the front end, some of which were reported in Thomas 1988. Listed here are some of the important performance characteristics of the new front end.

Output energy: two beams of 475 mj each
          (with a standard deviation of 22 mj) for a 5-ns pulse.
Pulse width: variable from 1 ns to 10 ns.
Bandwidth: variable, presently 10 cm^{-1}.

Prepulse ratio: < 10^{-7} (when ASE is filtered out)
Beam quality: 1.5 x diffraction limited.

Recent measurements were made with a high-speed oscilloscope to look at the output pulse shape and energy when we vary the pulse width. The experiment was performed on one of the output beams, for a short pulse (1 ns) and a long pulse (5 ns). Examples of the input to the Lumonics amplifier and the output after amplification are shown in Fig. 4 for these two pulse widths. The short pulse energy was 409 mJ, and the long pulse energy 505 mJ. The output energy does not go down nearly as much as one might expect with the reduction in pulse width, as a result of saturation and change of pulse shape in the Lumonics amplifier. The output pulse has a spike that is faster than our detection system can resolve. By integrating the pulse, we have estimated the energy contained in the spike to be 20% - 25% of the total energy for the 5-ns pulse. We have several schemes for reducing or

1 ns   5 ns
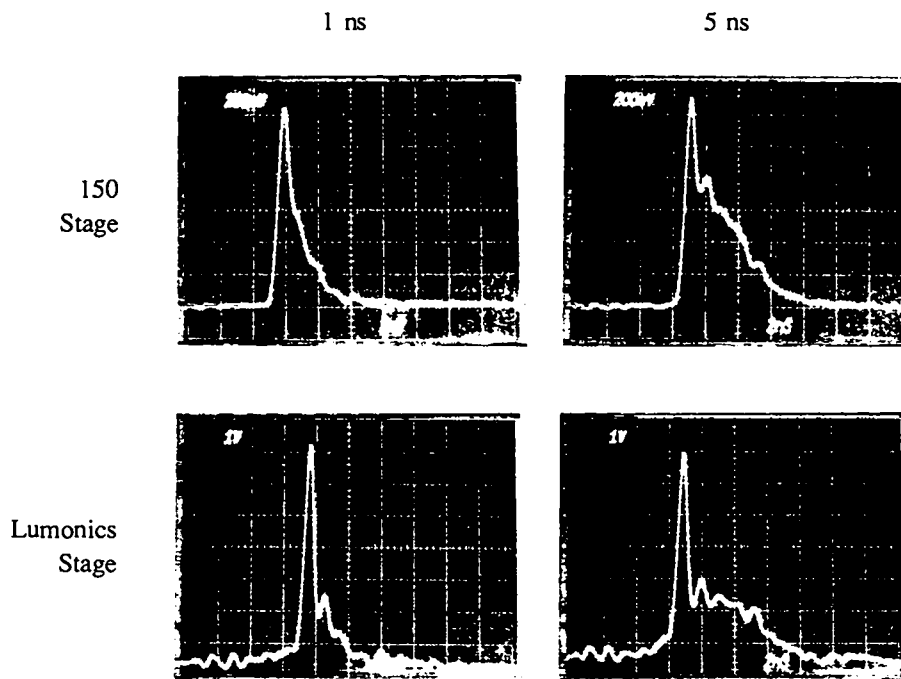
Fig. 4. 1-ns and 5-ns output pulses observed after the EMG 150 and Lumonics amplifiers.

eliminating this spike, each of which requires some research to become system operational. Among these are pre-loading the amplifiers with a longer pulse, and using a saturable absorber to absorb the spike.

Prepulse

The prepulse cannot be measured in the near field of the front end because of the presence of ASE emitted from the Lumonics amplifiers. The beam must be spatially filtered or the measurement done in the far field. We chose to do the experiment in the far field, using the AURORA beam tunnel. One of the front-end beams from the Lambda Physik 150 was propagated 128 m to the end of the beam tunnel, and subsequently to a vacuum photodiode and an oscilloscope. Calibrated attenuators were placed in front of the photodiode, and the pulse was measured. The results are shown in Fig. 5. The beam was attenuated with 6.0 o.d. attenuation, as shown in the top photo. The bottom photo shows the pulse with the attenuator removed. This saturates the photodiode and the preamplifier of the oscilloscope, but still allows accurate measurement of the leading edge of the pulse. We cannot measure any prepulse with this setup, placing an upper limit of $\sim 10^{-7}$ for the prepulse. However, this ratio is severely degraded by the additional small signal gain with the Lumonics amplifier turned on, and a 5- to 10-ns prepulse of amplified ASE (depending on amplifier

timing) is observed with an intensity of 3×10^{-3} that of the main pulse. This will not be a problem with shaped pulses because we will have a toe on the leading edge of the pulse anyway, but it will have to be improved for other experiments by the addition of saturable absorbers (Bigio and Thomas 1986) or Pockels cells. Some recent target experiments have been performed with the Lumonics amplifiers bypassed, and nearly as much system output has been obtained in a cleaner pulse.

(a)
Output pulse
with 6.0 OD attenuator

Vertical
500 mV/div.

Horizontal
5 ns/div.

(b)
Output pulse
with attenuator removed

Vertical
5 mV/div.

Horizontal
5 ns/div.
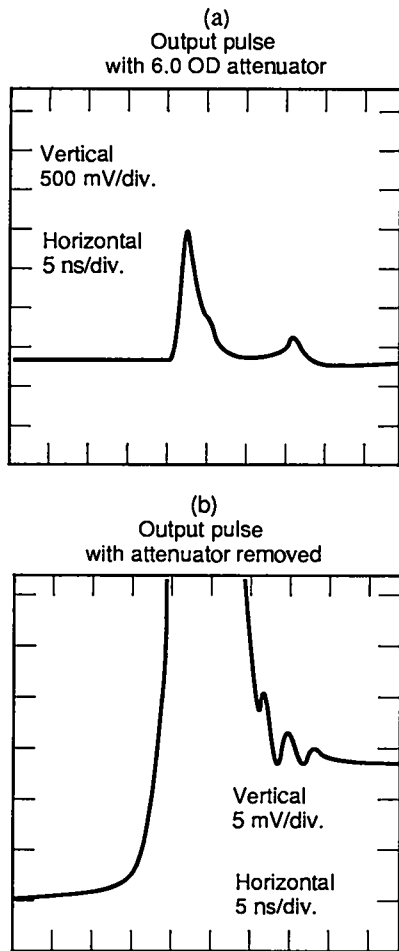
Fig. 5. EMG 150 output observed 128 m downstream with attenuation of 10^6 (a) and attenuation removed (b) to examine leading edge of pulse as trailing pulse in (a) is electrical reflection.

Summary of Front-End Design and Performance

The phase-conjugate front end has provided significant improvements over the previous front end. The operation is a lot simpler, and we have nearly four times the energy and better beam quality. The SBS cell requires almost no maintenance because it is a passive device. Although there are still improvements to be made, this front end has performed well in the initial integration of target shots. Near-term goals include additional control of the pulse shape and further increase in prepulse ratio.

AURORA AMPLIFIERS

The main amplification chain for AURORA consists of four e-beam driven KrF laser amplifiers ranging in aperture

size from 10 cm × 12 cm to 100 cm × 100 cm. these devices are designated as the small aperture model (SAM), the preamplifier (PA), the intermediate amplifier (IA), and the large amplifier module (LAM). The characteristics of these four amplifiers are summarized in Table 1.

The SAM is a double-pass amplifier that is placed between two sections of the encoder (multiplexer) and amplifies a portion (60 ns/12 × 5 ns) of the entire 96-beam pulse train. It was designed to have a stage gain of ~20 and to deliver ~5 J of laser light to the eightfold encoder.

The PA and the IA are single-pass amplifiers with similar design and gain characteristics. Both have large aspect ratios L/D (gain length divided by laser aperture width), operate at high stage gain, are driven by a relatively low fraction of a saturation flux, and are only partially filled by their input laser beams. Assuming a small signal gain (SSG) of 3%/cm, the PA and IA were designed to achieve stage gains of 50 and 40, respectively. For a typical drive energy of 1 J at the PA input, the PA output was designed to be 50 J and that for the IA is designed to be 2 kJ.

The LAM is a lower aspect ratio amplifier (L/D = 2) than either the PA or IA. It is almost completely filled by its input beams, has a high extraction efficiency, and was designed to operate at a fairly low stage gain of 10 because it is driven into the saturated regime by the input laser beams. Assuming optimized performance, the LAM is designed to deliver from 10 to 20 kJ of laser energy when driven with an input of 2 kJ from the IA and operated in a double-pass amplifier configuration. The LAM is the largest amplifier in the AURORA chain and is intended to address many of the scaling issues regarding large aperture KrF lasers. It was first tested as a resonator to understand the physics and engineering issues associated with the operation of so large a device. Configured as a nonoptimized unstable resonator, it produced in excess of 10 kJ of 248-nm laser radiation in the resonator cavity (York et al. 1985).

The assembly drawing in Fig. 6 shows some of the main parts of the LAM. Of particular significance are the laser chamber, the output window, the guide magnets, the water dielectric pulse-forming lines (PFLs), and the electron-gun (e-gun) assembly. Figure 7 is a photograph of the LAM that was taken during the initial construction phase. The LAM is representative of all the amplifiers in the AURORA chain, with the exception that the PA and IA use single-sided e-beam pumping and the SAM does not use a PFL. The pulsed power components for these amplifiers are discussed in a later section.

TABLE 1. Summary of Amplifier/Design Specifications

Unit	PFL Pulse Length (ns)	e-Gun Voltage (kV)	e-Gun J (in gas) (A/cm2)	e-Gun Area (cm2)	Input Light Energy (J)	Output Light Energy (J)	Stage Gain	Clear Aperture (cm)
SAM	100	300	12	12 × 100	0.25	5	20	10 × 12
PA	650	675	10	40 × 300	1	50	50	20 × 20
IA	650	675	10	40 × 300	50	2000	40	40 × 40
LAM	650	675	12	100 × 200	2000	10,000	10	100 × 100
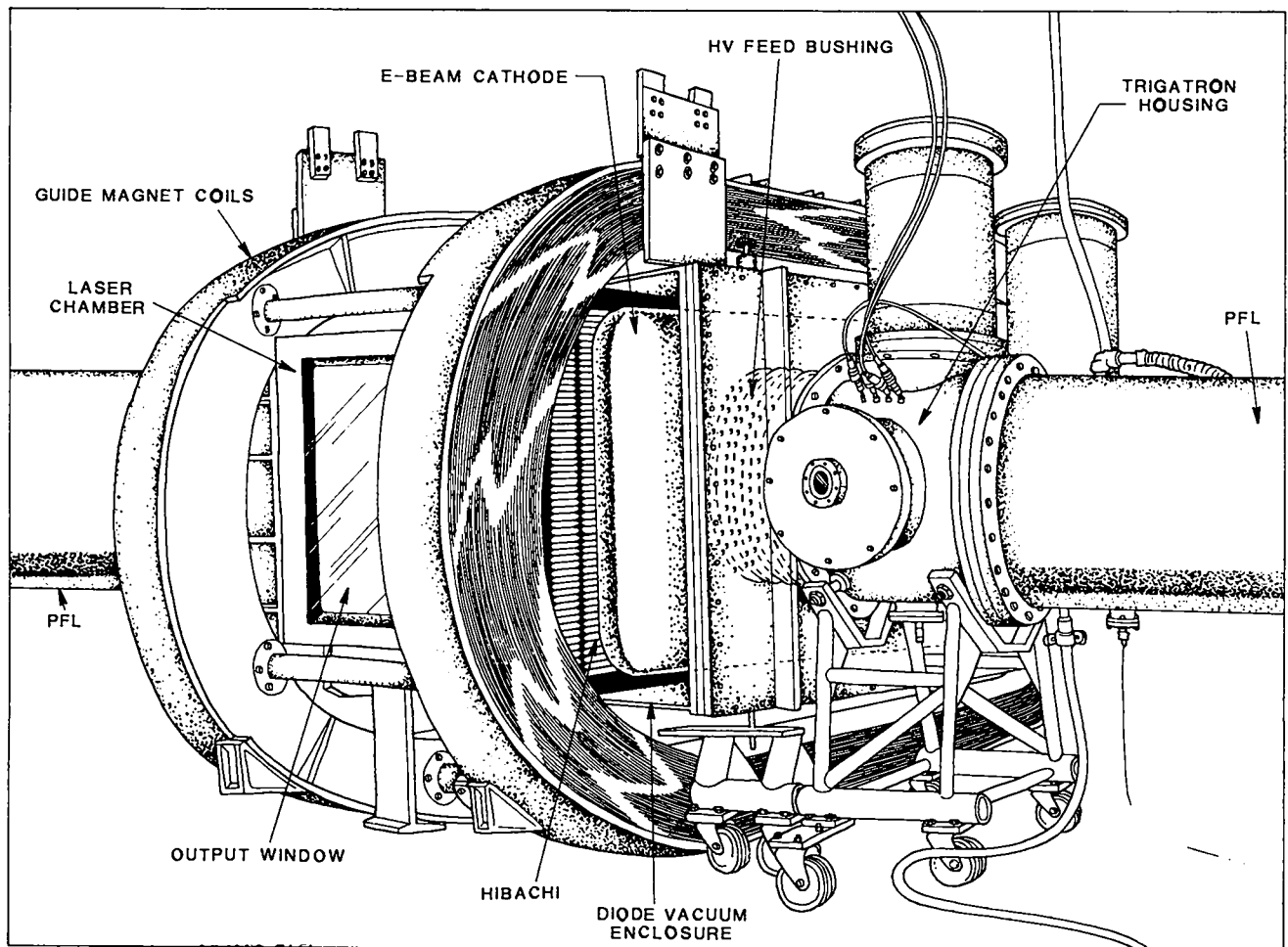
Fig. 6 Assembly drawing of the LAM. Shown are the laser chamber, the output window, the guide magnets, the water dielectric PFLs, and the e-gun assembly. This amplifier is representative of the amplifiers used in the AURORA chain. It is symmetrical in that it uses two sets of PFLs and two e-guns in a double-sided pumping arrangement.

Fig. 7. A photograph showing the AURORA LAM in its initial assembly phase. The main laser cavity, which is pumped by two opposed broad-area cold-cathode e-guns, is located between the coils that provide the guide magnetic field for the e-guns. The e-guns are housed in the vacuum enclosures adjacent to the laser chamber. Each e-gun is powered by a parallel combination of two coaxial water dielectric PFLs, which are clearly visible in the foreground. Each pair of PFLs is charged by a separate Marx generator; the tank visible in the background contains one Marx. On a routine basis, the e-guns deliver ≅ 160 kJ into the laser gas at electron energies of 550 to 600 kV and current densities of 12 A/cm².

The stage gain, extraction efficiency, and ASE characteristics for amplifiers like the PA, IA, and LAM have been designed using a one-dimensional steady-state radiative transport analysis that incorporates bidirectional amplification, nonsaturable absorption, and ASE in a self-consistent manner (Hunter and Hunter 1981). Assumed in the model are a uniform gain region of length L and a square aperture of dimension D on a side. The saturation flux I_{sat} and the ratio of SSG to nonsaturable absorption g_0/α are other parameters necessary for the analysis. The saturation flux is taken to be 1.5 MW/cm². The main result of this model is that the stage gain of the KrF amplifiers increases as the driving flux is reduced. However, as the drive is lowered, more energy is lost as ASE output; therefore, less coherent energy will be extracted at low drive. The single-

pass PA and IA both run at low drive, so they are fairly inefficient. A harder driven double-pass amplifier such as the LAM has relatively low stage gain but a relatively high extraction efficiency. Consequently, there is a required compromise for higher efficiency because double-pass amplifiers will require greater optical complexity. We have chosen to employ single-pass amplifiers early in the amplification chain to minimize the optical complexity of the system and to relax the front-end output requirements. We then use a double-pass amplifier at the high-energy end of the amplification chain to maximize the energy extraction.

Figure 8 shows the predicted performance of the PA, IA, and LAM as calculated using the model mentioned above. The stage gain and extraction efficiency are plotted

as functions of the injection (drive) flux I_{in} for a family of g_oL (gain-length product) values at a given value of g_o/α. We have designed the PA, IA, and LAM to run at injection fluxes of I_{in} @ 0.4% I_{sat}, 4% I_{sat}, and 30% I_{sat}, respectively. These injection fluxes yield stage gains of ~50, 40, and 10 for the parameters indicated on the PA, IA, and LAM graphs, respectively.
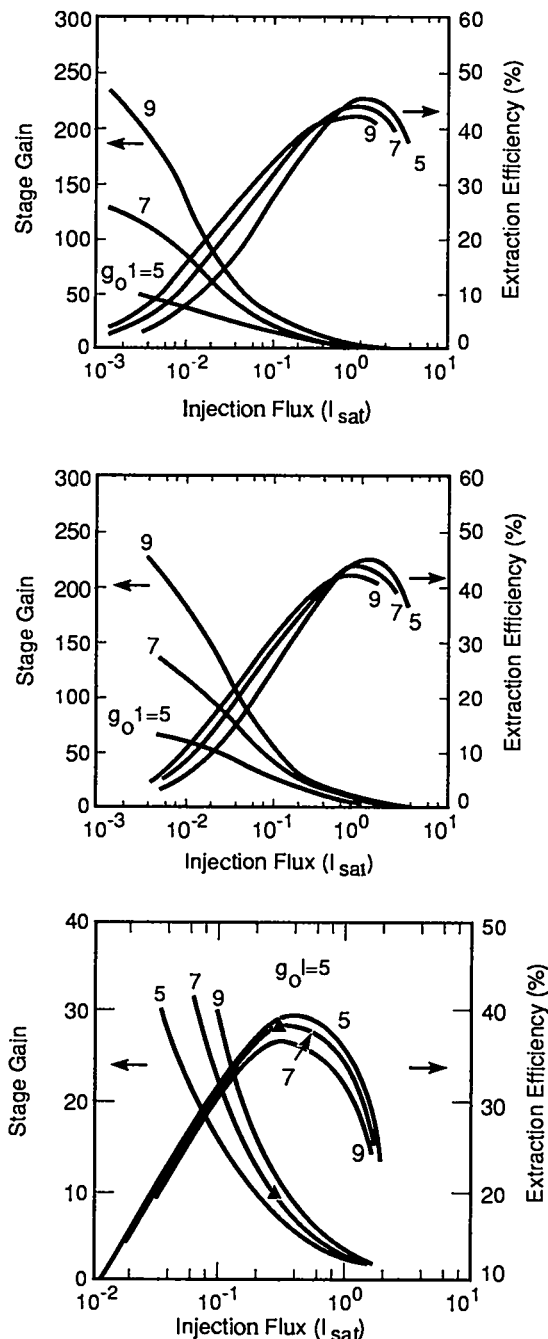
Fig. 8. Stage gains and extraction efficiencies for the (a) PA, (b) IA, and the (c) LAM plotted as a function of the injection flux (expressed in units of I_{sat}). This performance

was calculated by means of model that includes bidirectional amplification, nonsaturable absorptions, and ASE in a self-consistent manner. The ratio of small-signal gain to nonsaturable absorption coefficient g_o/α is taken as ~10; the saturation flux is taken as ~1.5 MW/cm^2. A family of curves for different values of g_oL is shown in the figures. The nominal design points are a stage gain of 50, 40, 10 and extraction efficiencies of ~10, 15, and 40% for the PA, IA, and LAM, respectively.

e-Beam Pumping

Because the laser gain medium is pumped by an e-beam, laser properties are closely linked to the properties of that beam as detailed in Vol. II of this series. If the electron energy deposition in the laser gas is nonuniform, the gain, and hence the optical beam quality, will be nonuniform as well. There are four main sources of electron energy deposition nonuniformities:

- variations in the spatial deposition profile resulting from the energy dependence of the electron stopping power in the laser gas,
- collisional diffusion of the e-beam in the laser gas,
- e-beam pinching in the e-gun diode, and
- temporal nonuniformities in the e-beam energy as a result of diode closure.
  (Diode closure leads to a time-dependent impedance collapse, which in turn results in a diode voltage that decreases in time. This change in electron energy with time results in a change in the spatial e-beam energy deposition.)

The first nonuniformity can be avoided by double-side e-beam pumping, which we employ in the LAM because of its very large aperture. Collisional diffusion and pinching can be countered by the use of a guide magnetic field, which is used in all amplifiers except the SAM. Impedance collapse problems can be countered by proper impedance matching in the diode and pulsed power components.

We have designed the AURORA e-guns to provide reasonably uniform e-beam pumping of all the laser amplifiers using the detailed pumping kinetics described in Vol II, Chapter IV.

For the 20-cm aperture PA, pumping uniformity at 1- to 1.5-amagat laser gas pressures is easily attained with a fairly broad range of voltages. The requirements for the IA are more stringent because single-sided pumping is used for the 40-cm aperture. The IA requires ~650-kV electron energies for 1.5-amagat pressure. For the 1-m LAM

aperture, the required e-gun voltage is in the 600- to 700-kV range for a 1.5-amagat laser gas mix. Double-sided pumping yields a very uniform electron energy deposition profile.

Marx Generators and PFLs

Typically, the e-guns that pump the laser amplifiers are powered by a combination of Marx generators and water dielectric PFLs (Rosocha and Riepe 1987). The LAM used double-sided e-beam pumping and has two PFLs in parallel for each of its two e-guns. The PA and the IA both use single-sided e-beam pumping, and each has a single PFL. The SAM also uses single-sided pumping, but it is an exception in that it employs a Marx with a peaking circuit in place of a PFL. Each Marx generator is of similar design and construction, except for the SAM, which is a commercial device. The SAM is a modified commercial e-beam pumped laser. The PA, IA, and LAM will employ 15-stage Marx generators that erect to an open-circuit voltage of ~1.8 MV and to a voltage of ~1.6 MV when charging the PFLs. These PFLs are coaxial transmission lines that use deionized water as a dielectric. The inner conductor has a 61-cm diameter; the outer conductor has a 91-cm diameter; the length of the line is 10.8 m. The impedance of each line is ~2.7 Ω, the one-way electrical transit time of the line is 325 ns, and the energy storage per line is typically 150 kJ. Each PFL is connected to the e-gun cathode through an SF_6-insulated trigatron output switch and a high-voltage vacuum feed bushing. Depending upon the particular amplifier, the output switches are triggered from 1.2 to 1.8 μs after the Marx erection. When the output switches fire, a voltage pulse of one-half the charge voltage and twice the electrical transit time of the PFL is delivered to the cathode.

e-Gun Assemblies

The e-guns consist of the following main components: diode-feed bushing, cathode-corona shell, emitter, hibachi, and foil. These components are housed in a vacuum enclosure and maintained at a pressure of ~5 × 10⁻⁶ torr. Any of the e-guns (SAM, PA, IA, or LAM) is representative of the design and construction concepts used for AURORA, except that the SAM is considerably smaller than the other three and differs in some details not mentioned here. Figure 9 shows a cross section of the LAM e-guns.
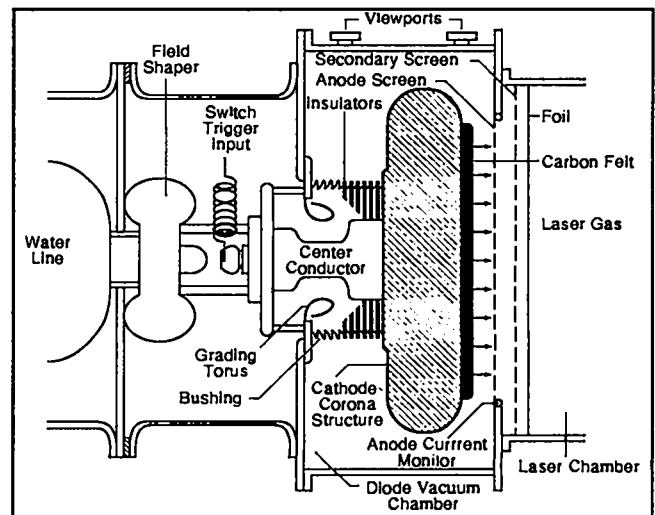
Fig. 9. Cross section for the AURORA LAM e-gun assembly. The LAM e-gun is representative of the major AURORA devices. It employs two parallel-connected PFLs for each of its e-guns in a double-sided excitation arrangement to achieve uniform pumping across its 1-m laser aperture. The laser axis is perpendicular to the plane of the figure. The e-beam emitter dimension is 200 cm along the laser axis and 100 cm transverse to the axis.

The diode-feed bushing electrically interfaces the output switch to the cathode. This bushing is a fairly common high-voltage design using 45°-angled acrylic insulator rings alternating with aluminum field-grading rings. The cathode-corona shell attaches to the end of this bushing, and the graphite felt emitter material is attached to a contoured boss on this shell. Graphite felt is used for the emitter because it exhibits a low ignition voltage and a reasonably uniform spatial distribution of electron emission. The emitter area for the SAM is 12 cm × 100 cm and the anode-cathode (A-K) gap spacing is 3.2 cm, which gives a calculated 6-Ω diode impedance at a nominal voltage of 350 kV. The current density at the cathode is 35 A/cm², with an observed hibachi transmission of 35%. The PA and IA e-guns are almost identical. Both have ~ 8-cm A-K gaps and 40- × 280-cm emitter areas, although the PA beam is masked off to produce a 20-cm-wide beam compatible with its smaller laser aperture. The PA and IA diodes are designed to match the PFL impedance of 2.7 Ω and operate at a nominal cathode voltage of 675 kV and a nominal space-charge-limited current density of 22 A/cm² at the cathode. The LAM cathodes have 100- × 200-cm emitter areas and an A-K gap of ~7.5 cm. The nominal design cathode voltage and current density at the cathode are 675 kV and 25 A/cm², respectively, which matches the 1.35-Ω impedance of two PFLs in parallel.

The interface between the diode vacuum chamber and the laser-gas volume is provided by a titanium or Kapton (registered trademark for polyimide film, E. I. DuPont de Nemours and Company, Inc., Wilmington, Delaware) foil of nominal 25-μm (1-mil) and 75-μm (3-mil) thicknesses, respectively. The foil is supported by an aluminum hibachi structure that typically has a geometrical transmission of 80%. The open-cell hibachi dimensions range from 13.5 cm × 1.6 cm for the SAM to 23.8 × 3.6 cm for the LAM. The laser chambers contain the krypton/F_2/argon laser gas mixtures at typical pressures in the range 600 to 1200 torr. The open-cell sizes and hibachi thicknesses are designed to withstand the mechanical stresses resulting from these pressure differentials. A more detailed discussion of the hibachi design and an e-beam transport analysis is presented in Rosocha and Riepe (1987). The transport of the e-beam from the emitter surface to the pumped laser gas volume depends on many factors. Among these factors are the properties of the cathode emitter (emission uniformity in particular), scattering of the e-beam by the foil and laser gas, energy loss in the foil, obstruction by the hibachi and other mechanical support structures, and the uniformity of the applied guide magnetic field. Typically, the transport efficiency is <50%, although this depends to a large extent on the relative dominance of the previously mentioned factors.

Guide Magnets

Electromagnet coil pairs of quasi-Helmholtz configuration are installed on all amplifiers but the SAM. The coiled pairs are symmetrically placed about the center of the laser chambers and provide nearly uniform magnetic fields parallel to the e-beam paths. These fields stabilize the e-beams against self-pinching and reduce collisional diffusion losses in the laser-gas volume.

The degree of beam pinching is related to the magnitude and direction of the self-magnetic field, which depends on the total beam current and the diode geometry. A device like the SAM has a small self-field that generates little beam pinching; therefore, it does not require a guide magnetic field to overcome the self-field. The PA, IA, and LAM have fairly large self-magnetic fields; thus the use of guide fields for these devices is mandatory. Loss of electrons from collisional diffusion is most important for diffusion perpendicular to the field direction. This diffusion is dependent on the mean-free-path of the electrons in the gas and the radius of the electron gyration about the field lines (Lamor radius). For large magnetic fields, diffusion perpendicular to the field direction is inversely proportional to the field strength.

The main engineering considerations for the guide field are the magnitude of the applied field, the field tilt angle, and the spatial uniformity of the field.

If the guide field is sufficiently strong, it will add with the beam's own self-field in such a way as to produce a resultant field nearly parallel to the beam direction. The electrons within the beam will follow the resultant magnetic field lines in a helical orbit. If the deviation of the field lines from the normal to the cathode is small, the electrons will be transmitted with high efficiency through the hibachi and foil into the laser gas. If the deviation is larger, more beam current is intercepted by the hibachi ribs, which results in inefficient transmission. Once inside the laser-gas volume, the electrons will still be constrained to spiral along the field lines rather than scatter out. Practical experience has shown that the magnitude of the required guide magnetic field is generally a few times that of the self-field. Using a higher magnetic field strength is not advantageous because the closure velocity for the A-K gap increases with increasing applied field strength. This procedure can lead to excessive cathode voltage fall-off and a consequent change in the pumping uniformity if the closure is too fast.

Tilt angle raises two concerns: how transmission of the e-beam through the hibachi is affected and how the size of the beam cross section is reduced. We have designed the guide field tilt at the hibachi to be <5° for all the amplifiers. This keeps the transmission reduction resulting from the tilt <5%. Tilt at the cathode reduces the beam size, which may leave unpumped regions near the edge of the laser cavity. We have designed the guide magnets to allow a tilt at the cathode of ~10°. This tilt results in a beam size reduction of ~8% for the PA, 4% for the IA, and 2% for the LAM.

The spatial variation in the magnitude of the guide field along the laser-cavity optical axis can have two effects: a spatial variation in the guide field can lead to changes in the tilt angle of the resultant magnetic field, which gives a spatial variation in the hibachi transmission; spatial variations in the guide field can lead to spatial variations in the closure velocity. Both of these effects can result in nonuniform electron energy deposition in the laser gas. We have designed the AURORA guide magnets to have a field uniformity of ±10% over the length of the laser cavities. This leads to an ~8% to 10% increase in closure velocity from one end of the laser-gas volume to the other, which is not too severe for our applications.

The PA and IA coils have major and minor diameters of 5.5 m and 1.65 m, respectively; the LAM coils have a major diameter of 4.2 m and a minor diameter of 2.6 m. Typical fields are 0.12 to 1.18 T for the PA and IA, and 0.2 to 0.3 T for the LAM. We found the measured total

deviation in the field from the PA/IA coils to be ~10% along the major axis and ⪆5% along the minor axis. The usual magnet current waveform is a trapezoid with rise and fall times of a few seconds and a few second plateau.

Optical System

The AURORA optical system is representative of typical angularly multiplexed systems. It is designed (Hanlon and McLeod 1987; McLeod 1987) to match the long amplifier electrical excitation pulse time, determined by electrical and laser kinetics considerations, to the much shorter pulse times required for efficient coupling of the laser pulse energy to inertial fusion targets. Angle and time multiplexing are necessary to accomplish this match. Distance is used to provide the time delays needed to time encode a 96-beam pulse train of 5-ns pulses. The 96 pulses are produced by a combination of aperture division (12-fold) and beam splitting (8-fold). These pulses are spatially separated, angle-encoded, and sequentially passed through the KrF laser amplifier chain to produce an amplified 480-ns pulse train. This amplified pulse train is decoded after the final amplifier, using distance to take out the time delays; then all pulses in the train are delivered simultaneously to the fusion target. The major parts of the system are as follows:

1. *an optical encoder* that replicates the 5-ns front-end output pulses to produce a pulse train 480 ns in length consisting of 96 separate beams placed head-to-tail in time;
2. *an angle encoder* that spatially separates the beams through the amplifiers and helps direct them so that they can be decoded;
3. *a centered optical system* that relays the beams through the amplifiers so that they expand and fill the active gain volume;
4. *an optical decoder* to delay the earlier pulses in the pulse train relative to the later pulses so that they all arrive at the target simultaneously;
5. *a set of final aiming mirrors* and focusing lenses that direct the beams onto the target;
6. *isolated beam enclosures* to provide a stable optical environment for the propagation of the uv beams; and
7. *three optical alignment systems* that control the alignment of the encoder, the final amplifier mirror, and the final target chamber aiming mirrors.

Figure 10 on the following page shows a plan view of the optical layout within the AURORA laser building.

Temporal Encoding

The front-end oscillator-amplifiers deliver two 5-ns pulses with two identical apertures to the encoder. The beam sizes are then shaped with prisms to the aspect ratio required for encoding. One beam is delayed by 30 ns with respect to the other, and both are expanded by parabolic-optics telescopes to an aperture size of ~15 × 23 cm. The expanded beams are divided spatially into six parts, each 7 cm × 7 cm in size, with each part given a 5-ns time delay. This division produces a 12-element, 60-ns-long pulse train. The pulse train is then directed through one 10- × 12-cm aperture SAM amplifier in a double-pass mode with the use of 12 flat mirrors, which are part of a 24-element array. After amplification, the pulse train is returned to the second half of the 24-element mirror array, which creates a bundle of 12 parallel beams from the train. The bundle of 12 beams is handled as a unit by three stages of serial 50/50-intensity beam splitters, which produce an 8-fold replication to 96 beams. The time delays required to obtain the final 480-ns composite pulse are obtained by judicious location of the beam splitters. Figure 11 shows photographs of some of the optical elements that comprise the 8-fold encoder sections.

The decision to place the 12-fold aperture division first in the encoding process was based on the following considerations:

- Divergence and aiming problems in the front end are reduced by immediate expansion.
- A convenient station for the input-output array for the SAM amplifier results from this placement.
- Aperture division with a low beam count avoids the use of a very large expansion telescope or the use of several parallel telescopes.
- Intensity division as the second process provides more flexibility in fitting long time delays in the existing building.

The use of a multistage intensity division beam splitter placed stringent requirements on the splitting accuracy of each stage. For three stages, it was necessary to specify a 2% tolerance on the intensity division, even when driving saturated amplifiers. The design of the beam splitters was made even more stringent by both the building constraints and mechanical complexity. It is not possible to pack the beam splitters mechanically in a tight configuration as is done in the mirror arrays because the mounts cannot be hidden behind the optical components. Therefore, to keep the beam array compact, we use large 31- × 45-cm beam-splitting elements, each handling 12 beams.

Aurora Facility
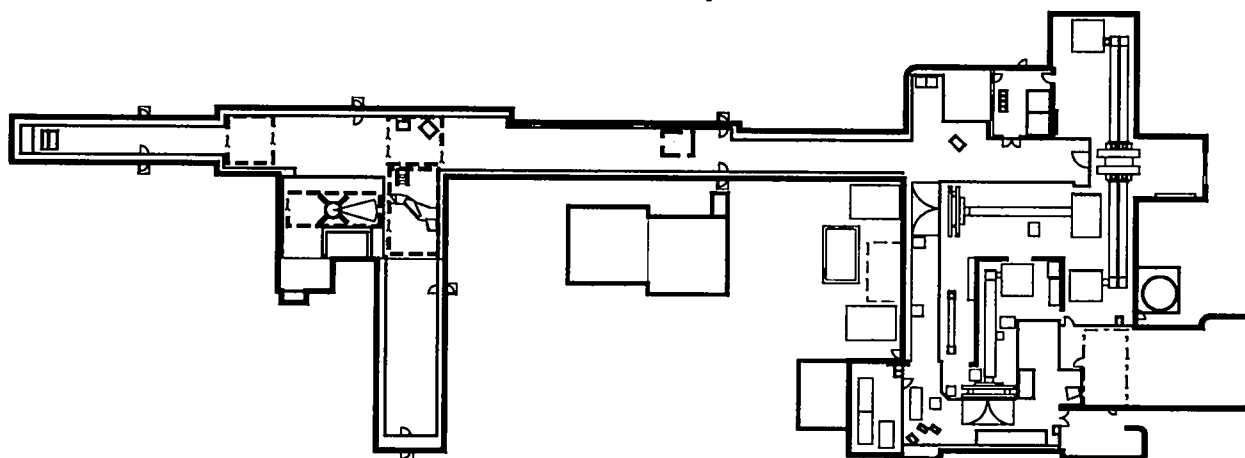
Fig. 10. AURORA system layout plan view (a number of details have been omitted for simplicity of presentation).
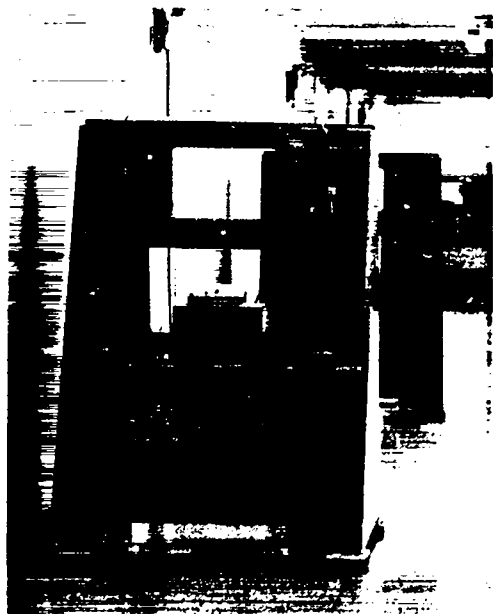
Fig. 11. A photograph showing a portion of the 8-fold encoder. The 8-fold replication of the pulse train from the 12-fold encoder is accomplished with three stages of beam splitters resulting in 96 separate beams. Judicious placement of the beam splitters permits the proper time delays to obtain the 480-ns pulse train. Each of the beam-splitter elements is a coated fused-silica slab 30 cm ×46 cm ×8 cm in thickness and has a 50:50 ±2% splitting ratio. The beam splitters are held in a motorized mount that is attached to the heavy stands.

Angular Multiplexing

In the temporal encoder, the beams are collimated and spatially distinct. They follow parallel paths to an 8 × 12 array of 96 separate flat mirrors called the input pupil array (shown in Fig. 12). It is here that the individual beams are angularly multiplexed; i.e., the beam paths are now slightly separated in angle. The angle of an extreme chief ray is 6.5° from the bundle centerline, whereas the channel-to-channel beam separation is ~1° Each beam is a square cross section, 7 cm on an edge. The input pupil is a small square, 4 cm on an edge. Therefore, the beams are 1.5-cm oversize, which allows for a generous tolerance for alignment and diffraction losses. This allowance also provides reasonable dynamic range for the target alignment control system, which must introduce offsetting pointing errors to compensate for real errors that occur in the form of physical changes elsewhere. The computer-based alignment control system that controls the pointing of these beams, is described later in this chapter. Each of the 96 mirrors that comprise the input pupil array is controlled by a pair of stepper motors that are interfaced to the computer-controlled servo-alignment system. The chief ray of each beam in the array is independently aimed at the input pupil of the centered symmetric optical relay train.

Optical Relay Train

The primary function of the optical relay train (or the centered optical system) is to transport the 96 beams from the 8 × 12 input pupil array through the PA and IA to the 96-element LAM input mirror array. The relay train must interface to the encoder, provide a means to fill the amplifier gain media in an efficient manner, and separate the beams for the decoder. The PA and IA, which are placed toward the front of the amplification chain, are designed as single-pass amplifiers so that the beams use common optical elements throughout the relay train, thereby reducing the complexity and cost of the optical train. Relaying the input pupil through the amplifiers provides the best possible fill factor. The first section of the relay train is a centered symmetric lens train between the input pupil and the PA. This section consists of five lenses that image the input pupil to the output of the PA. From a purely optical design point of view, this is the most complex part of the laser system. Most of the system aberrations are balanced here because the parts are relatively small and inexpensive. The design employs two strong negative power lenses to cancel the positive power of the rest of the lenses, so that the Petzval sum and, consequently, the field curvature at the focal plane behind the LAM input array are nearly zero. This design

allows all the LAM input array mirrors to have a common convex curvature and to be mounted on a plane surface. In this set of lenses, there is an intermediate focus that requires a modest vacuum.

The next section of the relay train images the input pupil from the output of the PA to the output of the IA. It consists of the lenses and a turning mirror. The beams from the PA output are relayed to the second set of relay lenses by the first turning mirror. The first lens in this set has an aspheric surface. These lenses form a pair that provides an intermediate hard focus that can be used for alignment and spatial filtering. The regions of hard focus require a moderate vacuum of ~10^{-3} torr to avoid air breakdown.

At the output of the IA, another lens focuses the beams to a surface behind the 96-element LAM input array. However, to fit the building, a turning mirror is required between the IA and the LAM input array.

There are many factors to consider in this subsystem design. The optical system must fit in and around the mechanically large amplifier hardware, which must be placed in predetermined spaces because of its size. The centered optical subsystem must interface to the encoder, optimally fill the amplifiers, and separate the beams for the decoder. In addition, it must shape the beam envelope in a predetermined space with lenses <60 cm in diameter because larger lenses have prohibitive costs and delivery schedules. The sum of the powers of the lenses must be nearly zero or severe mechanical problems result.

It is convenient to think about the centered optical system as a pupil-relay system. Figure 13, although not to scale, shows the lens shapes and spacing. The first five lenses relay the input pupil (position 2) to the back of the PA (17). The next three lenses relay this pupil image close to the exit of the larger IA (29), and the final lens (30) converges the beams to 5 cm^2 so they will be sized and spaced properly on the final amplifier (LAM) input array. One of the 96 beams is sketched to show a conceptual size and typical path. In addition to relaying the input pupil to the back of the PA, the first five lenses correct most of the aberrations introduced by the entire lens train. Two of these lenses introduce negative power to cancel most of the positive power of the rest of the lenses, so that the focal plane behind the LAM input array will be nearly flat; this allows all the LAM input array mirrors to have the same convex curvature and to be mounted on a plane surface. Between every pupil image is a 96-spot focal plane. Diagram positions 11 and 23 show the focal planes. The focal plane at position 23 is inside a vacuum pipe; otherwise, the amplified beams focused there would break down the air. Positions 20, 32, and 33 are turn mirrors that keep the beam paths inside the building.
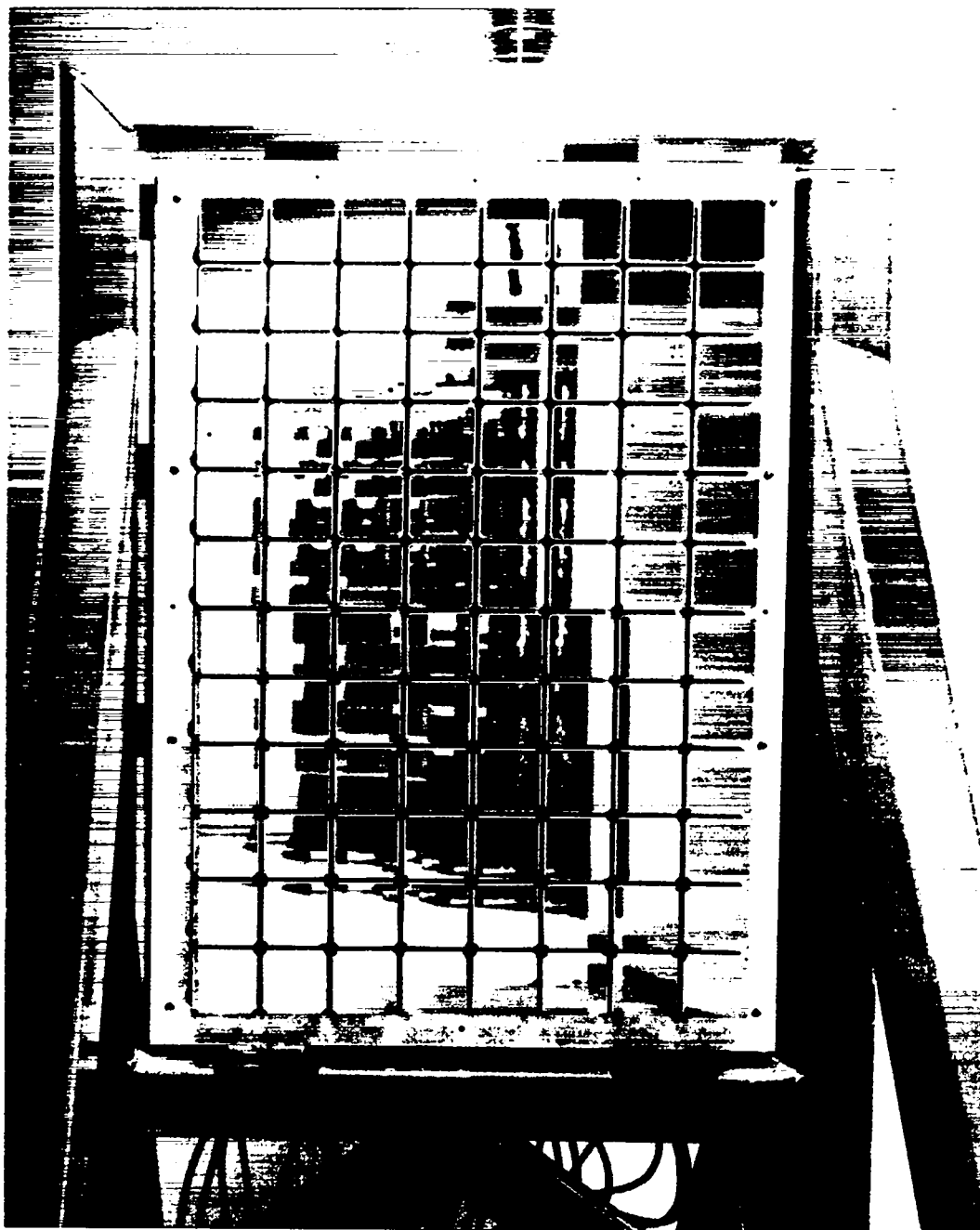
Fig. 12. The 96-element input pupil feed array. This 8 × 12 mirror array angle encodes the AURORA beam train by directing each beamlet through the amplifier chain at slightly different angles relative to the central optical axis. Each mirror is 10 cm on an edge.
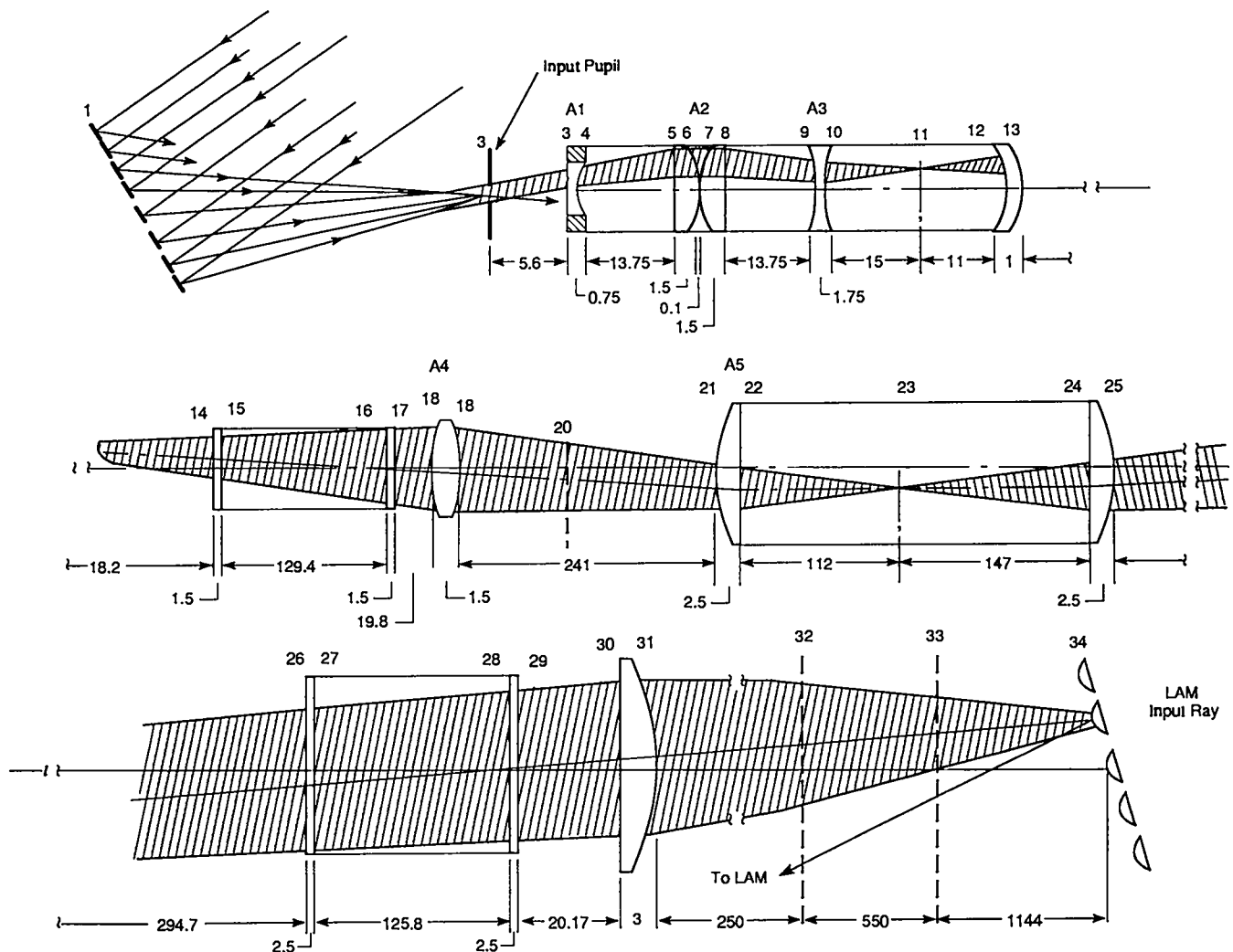
Fig. 13. A conceptual drawing of the centered optical system from the input pupil to the LAM input array. Distances are in inches. Numbers identify the surfaces. Lens surfaces A1 to A5 are mild aspherics.

The YYBAR (DeLano 1963; Shack 1973; Stavroutes 1982) diagram was used to design the AURORA centered optical system first-order layout. YYBAR is an abbreviation for the beam parameters: Y (half the beam diagonal) and YBAR (height of chief ray). It conveniently shows detailed information about the lens system shown in Fig. 13. Figure 14 shows the YYBAR diagram for an extreme angle channel of the AURORA optical system. In contrast to the usual picture of an optical system, shown in Fig. 13, the YYBAR diagram is an end-on projection of beam parameters onto a plane perpendicular to the optic axis. The Y axis of the diagram gives half the beam diagonal, and the YBAR axis gives the height of the chief ray (center ray) from the optic axis. The coordinates of a typical point on the curve plotted in the diagram represent the beam size and chief ray height at the distance down the

beam line that corresponds to the point chosen. The line segments circle around the origin to represent a beam as it progresses through the system. Line segments that are parallel to the YBAR axis represent collimated beams because the beam size in this space, which is given by the Y coordinate, is constant. Line segments that are parallel to the Y axis represent a telecentric space because the chief ray for the beam is parallel to the optic axis. When line segments cross the YBAR axis, the beam size is zero; these points represent focal planes. When line segments cross the Y axis, the YBAR is zero and these points represent pupil positions. The line segment turns clockwise at a positive-powered lens and counterclockwise at a negative-powered lens. Area on the diagram corresponds to the Lagrange invariant times the distance between planes in the real system. On the YYBAR AURORA diagram, the areas that

correspond to the lengths of the two amplifiers are shown crosshatched. The YYBAR diagram proved to be very useful for first-order design for the following reasons:

- The diagram is especially convenient when designing with the tight physical constraints that exist in the AURORA facility.
- The entire system is represented on one convenient diagram, which offers a system point of view.
- The required size for optical elements or containers positioned along the beam path can be read easily from the diagram.
- Component sizes and amplifier fill factors can be read easily from the diagram and adjusted during design.
- After design, the diagram proved to be a useful way to transfer the system requirements to a lens designer and to check if critical first-order properties were disturbed when the lens system was optimized.
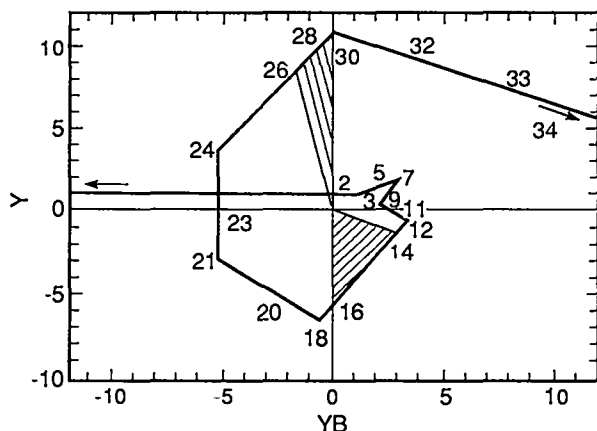
Fig. 14. The YYBAR diagram for the AURORA centered optical system. The numbers correspond to the surfaces identified in Fig. 12. The crosshatched areas correspond to the PA and IA. (Units are given in inches.)

In addition to first-order layout, YYBAR diagrams were also used to analyze single surface reflections from lens surfaces along the centered optical train. These reflections could damage components if the reflected beams were amplified and then focused by the lens train onto an optical element during the return transit. Figure 15 indicates several cases where a lens surface is considered as a reflector. (The surface numbers correspond to those shown in Fig. 13.) AURORA 17 is the YYBAR diagram when surface 17 is a reflector. From 1 to 17, the diagram looks exactly like the AURORA baseline. From 17 back down to 1 is the return path through the PA, the five lenses near the input pupil, and the input pupil. The return beam comes to a focus (Y = 0) between surface 3 and the input pupil. On the

return trip, the beam at 3 is about the same size as the forward-going beam, but now it has been amplified by the PA. This occurrence has two detrimental effects: the return beam robs energy from the amplifier, and it could damage the lens at 3 (which indeed was observed in the AURORA integration process). A plate with holes at the focal plane 11 protects the lens, and the first problem was evaluated during the AURORA integration.

Surface 23 is at the focal plane inside the vacuum pipe in a virtually telecentric space where the chief ray is almost parallel to the optic axis. If a mirror were placed at this position, the chief ray would strike it nearly normally and the beam would return on itself; consequently, at the break points in the curve, the YBAR values and the magnitude of the Y values for the beam coming and going are essentially the same. Therefore, the graph for AURORA 23 is nearly symmetrical.

AURORA 30 shows what happens to the return beam when surface 30 reflects some light. If no precautions are taken, the return beam would be amplified by both the IA and the PA and it would surely damage lens 3 near the input pupil. If a filter plate is placed at 23, the forward beam will focus there and pass through the plate; however, the return beam will be big and almost completely blocked. The filter plate at 23, therefore, is a necessity. Reshaping lens 30 is being considered to eliminate the return focused inside the IA. A computer analysis was also carried out to find potential reflection problems. The YYBAR diagrams offered a convenient summary of those results.

We have also done detailed computer design and analysis of the centered optical system. It has led to choices for the lens shapes, lens splitting, and aspheric placement and constants. The design goal was to have less than ±1 uv wavelength of optical path difference for all field points on a nearly flat field at the focal plane following the centered optical system. This design allows all mirrors in the LAM feed array to have the same radius of curvature and to be mounted on a flat plate.

In the real system, the convex mirror final amplifier feed array intercepts the beams before they reach the focal plane at the end of the centered optical system. However, the array can be set aside to examine experimentally the system beam quality up to this point in the optical train.

Theoretical design of the centered optical system is not the last word. Lens polishing specifications called for no more than a quarter wave peak-to-valley error on the visible transmitted wavefront. Tighter specifications significantly increased the part cost and scheduling. These specifications are sufficient to meet our target plane focused spot goals for all the lenses except possibly for lenses near pupil positions where each beam uses the entire aperture. The smaller
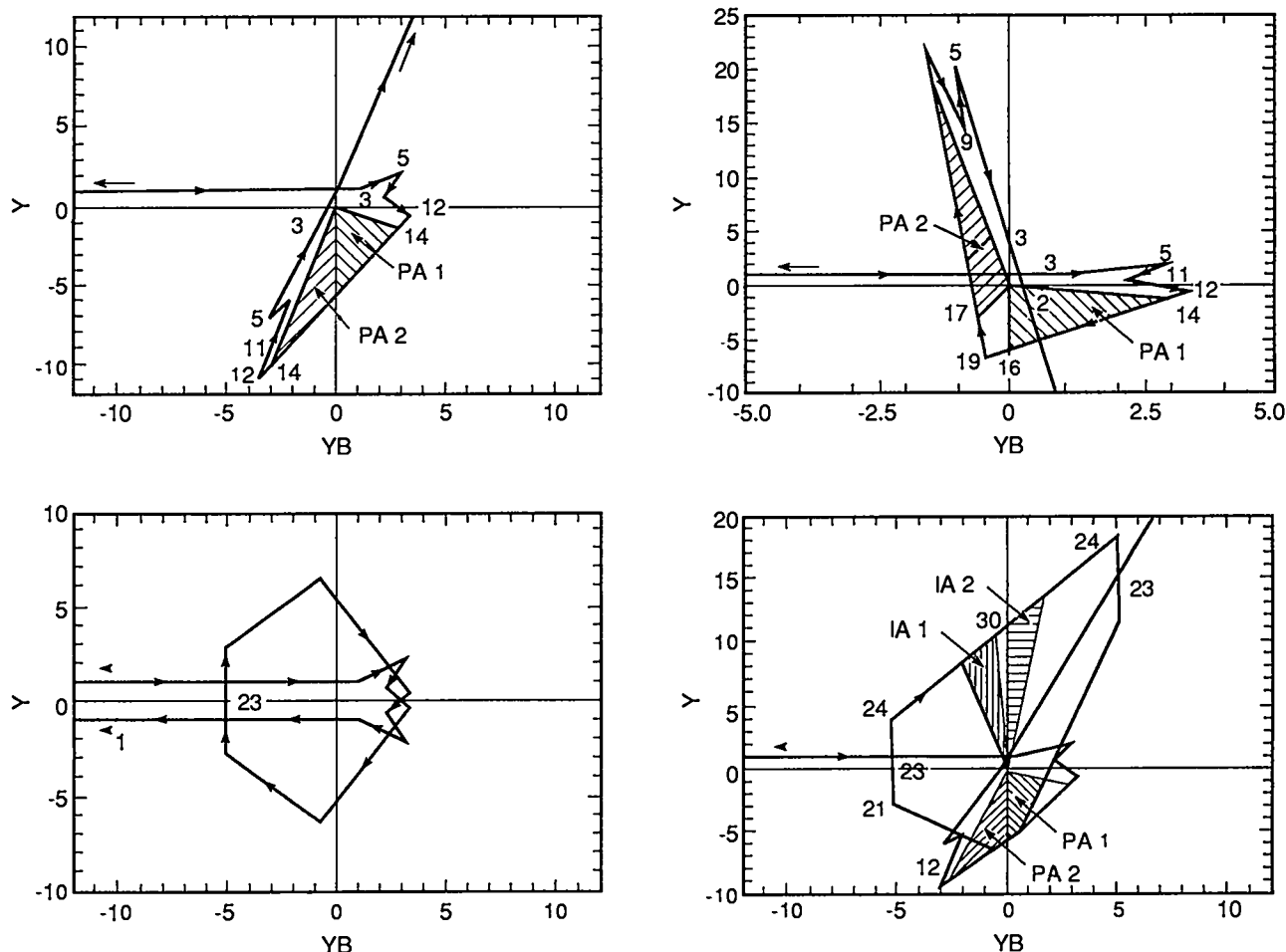
Fig. 15 YYBAR diagrams for the AURORA centered optical system when one of the lens surfaces along the beam line acts as a reflector. These diagrams are useful for understanding the unwanted reflections and also for designing hardware to limit the damage they might cause. (Units are given in inches.)

lenses polished out significantly better than the specification. Pupil lenses met the specification and will be satisfactory at least for initial experiments. The goal is to get 95% of the energy in an ~200-μm spot at the target plane. Spending more time and money for better quality pupil lenses was not considered to be cost-effective during initial AURORA planning. System performance depends on many other factors that were not well known when the lenses were built, for example, front-end oscillator bandwidth, the quality of the air along the propagation path, parasitics, target plane requirements, alignment stability, and the nature of lens polishing errors. So far, the front-end bandwidth has the most influence on system performance. Figure 16 shows spot diagrams for three field angles at three wavelengths separated by ten wave numbers. The plots are scaled as if they were imaged to the target plane without any additional aberrations being introduced. From these plots it

is easy to see that, at the extremes of the bandwidth, the beams are not in focus. This is not necessarily bad because near-field spots are more uniform and tend to smooth out the intensity distribution on the target. However, target designers now want an even broader bandwidth range, ±50 wave numbers, and a similar focal spot. This target consideration will require some color correction for our present design.
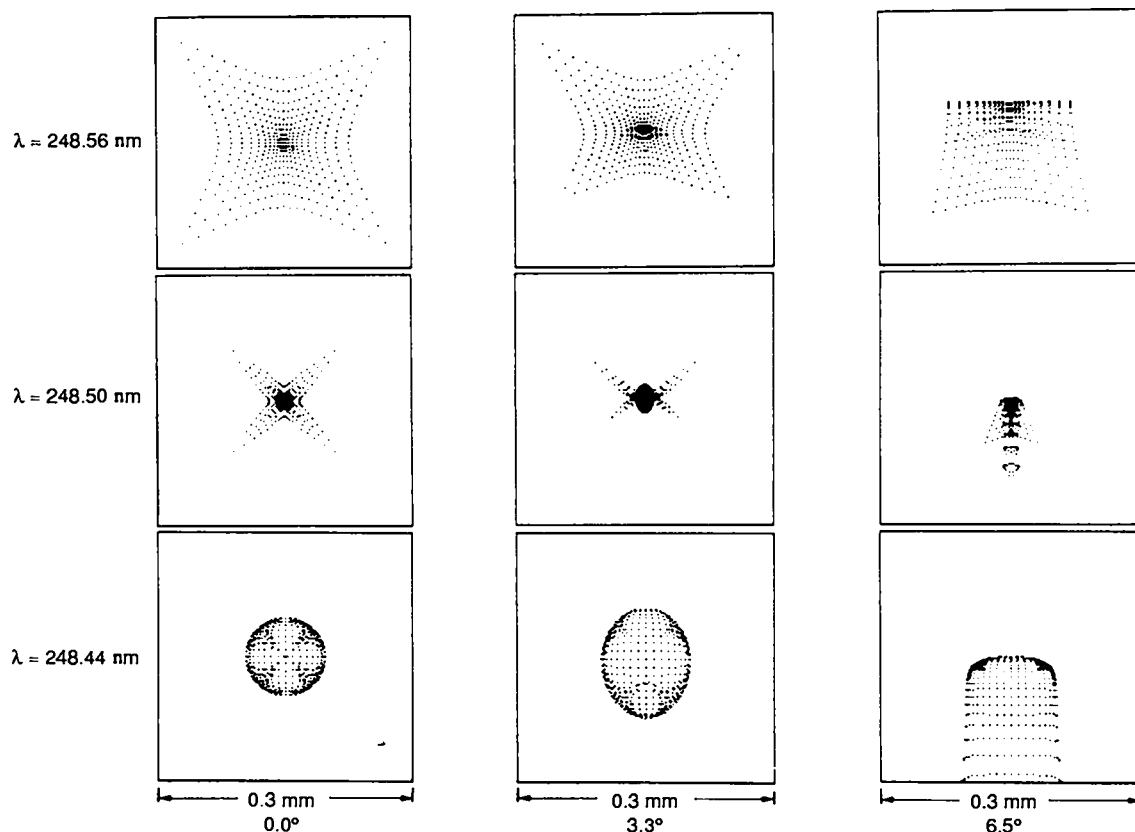
Fig. 16. Focused-spot diagrams for three different field angles at three wavelengths within the ±10 wave number front-end bandwidth.

We have fabricated, set up, and tested the centered optical system in the AURORA system with all elements functioning to first order as expected. The centered optical system was a more difficult subsystem than we first expected for the following reasons:

- The lenses are close to the amplifiers and need to be moved frequently when amplifiers need repair.
- Dispersion in the glass over the required front-end bandwidth requires that the design be color-corrected.
- Parasitics caused by multiple-retroreflections from lens surfaces may be a difficult and expensive problem to correct.

Double passing the amplifiers is just as easy as single passing, may cost less, and solves the problems listed above. If we were able to design this part of the system again, and if building constraints were not a problem, we would probably double-pass all amplifiers; however, glass dispersion over a reasonable front-end bandwidth may fortuitously smooth out the intensity distribution in the target plane in our present system.

LAM Input Array

The AURORA optical design employs a long flight path after the IA to spatially separate the 96 beams. At the end of this path, there is a 96-element array of small convex mirrors. This array consists of an 8 × 12 matrix of small mirrors very similar to the input pupil mirror array. The mirrors in the LAM array are convex to avoid focusing, which would cause air breakdown. The radius of curvature of these mirrors was chosen to cause each beam to fill the full 1- × 1-m LAM aperture. After a double-pass

amplification in the LAM, the beams are then sent to the decoder optics for stacking into a single 5 ns pulse at the target.

Large Amplifier Optics

A large 1.1- × 1.1-m mirror and fused silica window are required for the LAM amplifier. Several large square mirrors have now been fabricated. These optical components pose special problems for polishing shops. The phase I premium quality mirror blank was polished while it was round, but when it was cut square the part sprung about 14 waves, and additional polishing time was required to get the part back into specification. Based on that experience and the possible requirement for refurbishing parts, the next mirror was shaped square first and then polished with good results. A full-size mirror is shown in Fig. 17 in the mount ready for installation into the laser cavity. The mirror mount was built at LANL and is capable of the submicroradian pointing resolution required for demultiplexing.
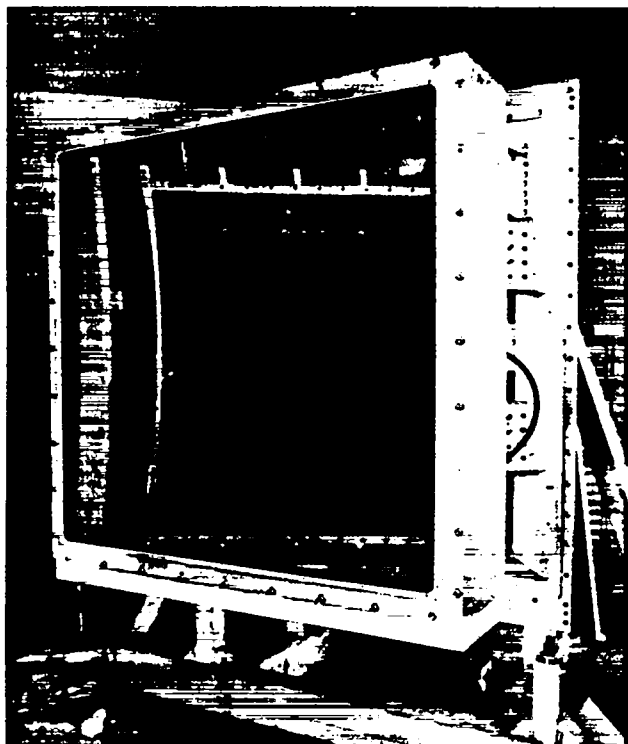
Fig. 17. The LAM primary mirror in large four-bar flexure tilter. The ULE mirror 1.118 m^2 weighs 500 kg. The deeply curved mirror shown was used in preliminary extraction experiments; it was replaced by a 110-m radius mirror for target service.

Materials and Coating Issues

The AURORA optical system requires materials for both transmissive and reflective elements. The transmissive elements consist of lenses and laser windows, both of which require antireflection coatings for 248-nm service. The laser windows are also required to operate in a fluorine environment. The reflective elements are high- and low-power relay mirrors, fold, and turning mirrors, as well as expansion telescopes. These elements require high-reflection coatings for both 248-nm and visible alignment service. Beam splitters have both reflective and transmissive elements.

Pyrex (trade name of Corning Glass Works material, two-phase vitreous) is generally used for small mirrors. Several other materials are being used for other mirrors: Zerodur (trade name of Schott Corporation, two-phase vitreous material with zero expansion coefficient near room temperature) for one turning mirror, Cervit (trade name of Owens-Illinois composite, semivitreous material) for the large LAM mirror, and novel lightweight Pyrex for two other turning mirrors (Hextex Corp.). The novel lightweight Pyrex mirrors employ a sandwich design made from Pyrex flats fused to a honeycomb-shaped array of hexagonal close-packed Pyrex tubes. These mirror blanks are considerably lighter and less expensive than conventional mirrors made from quartz, Zerodur, or ULE (trade name of Corning Glass Works material 7971; synthetic, non-uv transmissive, 7% TiO_2, 93% SiO_2). They cost about the same as blanks of solid BK7 (Borosilicate glass manufactured by Schott Corporation) or equivalents by other manufacturers, but they have considerably better temperature characteristics. The material for transmissive optics is generally synthetic fused silica. Corning 9740, homogeneity grade C, inclusion class II, is a common type used throughout the system (Corning Glass Works, Corning, NY). The LAM output window is the largest piece of this type of material; it is a fused silica monolithic slab with a 1- × 1-m clear aperture and a thickness of ~7cm. Smaller pieces of fused silica are also used for the beam splitters and fold mirrors in the encoder.

Optical component coatings for 248-nm service are a complicated issue because the technology involved in uv coatings is still being developed. AURORA uses various coatings produced by several different vendors: antireflection and high-reflection coatings for use within the fluorine-containing laser environment, 248-nm and visible alignment service high-reflection coatings for high- and low-power relay mirrors, and antireflection coatings for lenses. Antireflection coatings that are not required to withstand fluorine are made with conventional vacuum deposition

coatings. Many of the mirrors in the fluorine-free beam train use an aluminum undercoat to give high reflectance for visible beam alignment.

High-reflection coatings from two different vendors are found to be acceptable for fluorine service. These coatings have damage thresholds in the 0.6 to 10.0 J/cm^2 range, and tested samples appear serviceable after 200 h of exposure to the 0.5% fluorine laser-gas mixture. The material in the highest part of the damage range is ThF_4/MgF_2, whereas that in the lower part of the range is HfO_2/ThF_4. Both have initial reflectivities of ~97%; the smallest reflectivity after fluorine exposure is 93%.

Several sets of antireflection coatings for fluorine service were evaluated. The material with the best fluorine survivability characteristics is HfO_2/ThF_4, with a damage threshold in the 1.6- to 2.5-J/cm^2 range.

Other materials such as ThF_4/MgF_2 and ThF_4/Na_3AlF_6 have reasonable damage thresholds but poor fluorine survivability characteristics. In one test, low-power relay mirror designs used an aluminum film on a Pyrex substrate that was overcoated with a full 248-nm dielectric stack of HfO_2 and SiO_2. The aluminum film was intended to give high reflectance for visible beam alignment. Damage thresholds for these components are in the 1.3- to 1.5-J/cm^2 range. The reflectance is 99% at 248 nm and ~80% at 514 and 633 nm. In the same test, high-power relay mirror designs used a dielectric stack of Al_2O_3 and SiO_2 for uv service. The best samples obtained for these designs give a damage threshold of 4.0 J/cm^2, 99% reflectance at 248 nm, and 90% reflectance at 514 nm. A more detailed description of the AURORA optical materials coatings experience is presented in Hanlon and McLeod (1987).

AUTOMATED ALIGNMENT SYSTEMS

Multiplexer Alignment System

AURORA uses an electronic computer-controlled system that analyzes digitized TV images to position simultaneously the 96 elements of the multiplexed beam train to high accuracy (Kortegaard 1987). This control system is optimal and self-adaptive. Its algorithms constantly determine the optimal number of samples needed to resolve the actual alignment error for each of the beams. A schematic diagram of the multiplexer alignment system is shown in Fig. 18. The input pupil array does the angular portion of the multiplexing task; it must keep each beam aimed in its assigned direction with an accuracy of 30 μrad for first-phase AURORA and an accuracy of 2 μrad for second-phase AURORA. To control the 96 mirrors of the

input array, the beams reflected from these mirrors are sampled and imaged on a TV camera as an 8 × 12 array. The image-plane position of each element of the image has a one-to-one correspondence with the angular position of the associated beam at the PA input pupil. Because each beam overfills the input pupil by a large margin, it is necessary only to control the angular positions of the beams and not their points in space. Positioning error information is obtained by a sophisticated analysis of the video signal produced by the far-field image of the beams at this entrance pupil. Once the positioning error is determined, the optical system is controlled by directing stepper motors to move the input array mirrors until the elements of the image are at the desired coordinates. Parallel processing of the alignment error information for all 96 beams and the use of inherent system noise in the sampling process lead to very short alignment times. Using binary decisions on a noisy sample space permits effective interplating across beam boundary pixels to obtain precise and repeatable measurements of the beam position, without recourse to time-consuming and often unreliable software curve-fitting algorithms.

The alignment of the 96 beams is maintained continuously in real time, until the actual instant of firing. The types of disturbances expected are step displacements and velocity errors. The step errors result from mechanical settling or adjustments and velocity errors may arise from thermal cycling of the building or from drifts in the alignment electronics itself. So far the system has been able to align all 96 beams to a 2-μrad step correction accuracy in ~3 min. Velocity errors of 1 μrad/min or less have been controlled to 5-mrad total error. The velocity correction is predictive, permitting continuous interpolation and correction estimations during the times when the system is an open loop. In addition, the measurement analysis that permits the corrections provides error histories of all the beams, assisting diagnosis of significant disturbances.

By using two dichroic beam splitters, the far-field image is constantly available without interrupting the uv beams. One of these beam splitters inserts a continuous wave visible laser beam before the temporal encoder; the other beam splitter diverts the visible beam at the input pupil. The visible laser is also used to perform an initial necessary manual alignment of the encoder. The encoder optics mounts are designed to hold the required coarse alignment accuracy for long periods of time. The stability of the relay optics that follow the encoder is also adequate for the immediate goal of filling the LAM. A more detailed description of the alignment system and the methods for image analysis have been presented elsewhere (Kortegaard 1987).
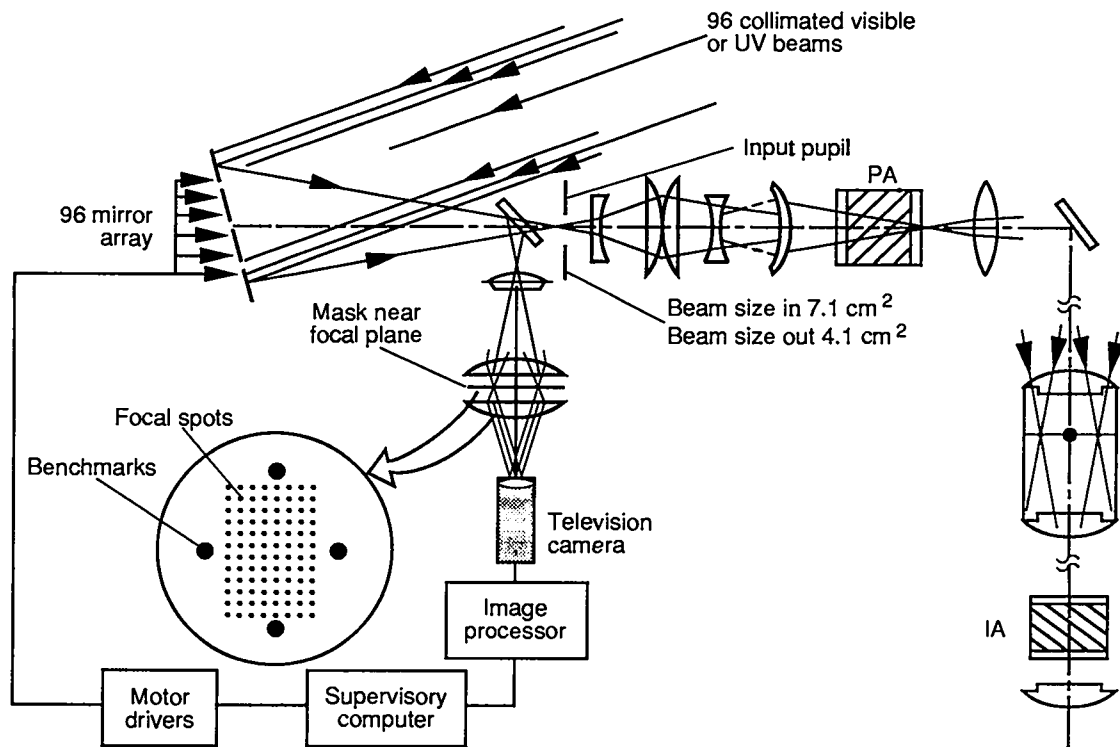
Fig. 18. The input pupil array multiplexer alignment station feedback loop. A dichroic beam splitter in front of the input pupil reflects co-linear visible beams to a 96-spot focal plane on a mask with benchmarks. The spots are image-processed and positioned relative to the benchmarks by driving the input pupil array mirrors.

Power Amplifier Alignment

A second part of the alignment system is concerned with keeping the input mirror array and the main mirror for the final power amplifier (LAM) aligned. The LAM mirror array is similar to the input pupil array, except that the LAM array mirrors are convex rather than flat. The main LAM mirror is a full 1- × 1-m clear aperture concave mirror having a 38-m radius of curvature for first-phase AURORA and a 110-m radius for the second phase. The beams coming from the IA are expanded to fill the LAM by means of the convex mirror array. The main LAM mirror compresses the beams to a manageable size for feeding the decoder. Control of this array is largely static; stepper motors for the 96 mirrors allow the beams to be aligned manually in the initial stages. Real-time control of this mirror array is not required because mount stability and overfill tolerances are adequate to hold the alignment for fairly long periods of time. Static alignment of the main LAM mirrors, however, is not expected to be adequate

because of the following: high-angular error sensitivity at this point in the system; mechanical perturbations caused by, for example, the gas pressure pulse generated when the LAM is fired; the commonality of all 96 channels at the main mirror (any misalignment causes all the beams to be misdirected); and magnetic forces generated by the quick field magnets. Therefore, full-time feedback control of the LAM mirror is designed into the alignment system. This alignment mechanism, shown in Fig. 19, depends on viewing the mirror from its center of curvature; a clear channel for this purpose has been included in the optical layout. A position-sensitive detector and a small laser are placed side by side at the center of curvature; the mirror returns an image of the laser beam onto the detector. Because the LAM mirror radius is large, only small motions at the mirror are required to produce motions at the detector that are easily within the step limits of the main mirror mount control motors. We have finished the installation of this control system and currently intend to use the same TV camera/video analysis system and similar software to what was used in the 96-beam alignment system.
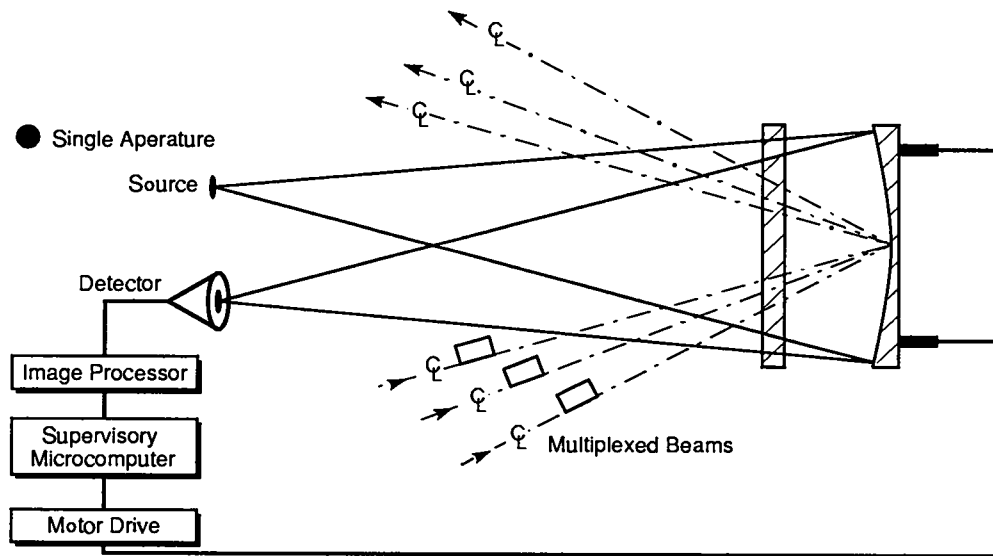
Fig. 19. The aiming of the LAM mirror is accomplished by using closed-loop feedback control.

Optical Demultiplexer System

Because the ICF target requires a short pulse of ~5-ns duration, the 480-ns amplifier pulse must be compressed for delivery to the target. The synthetic long pulse that feeds the LAM consists of a train of 96 separate 5-ns pulses. The 96 pulses have been encoded in the multiplexer to an assigned angle and an assigned time slot in the amplifiers. These assignments are then decoded in the demultiplexer to compress the long-pulse train into a single high-power pulse. This procedure is accomplished by sending the beams along different flight paths to the target. For the AURORA demonstration, only 48 of the 96 beams have been decoded and delivered to the target.

As a result of a deliberate simplification of the encoder design, the pattern of angle assignments naturally divides into four time blocks. Each quadrant of the pattern in space (or angle) is also one-quarter of the pulse train in time. The design of the decoder is also simplified by handling each of these quadrants as a block.

Figure 20 is a diagram that illustrates the demultiplexer (decoder) layout. The diagram is foreshortened drastically in the long dimension for ease of representation. The decoding process starts by recollimating the 96 slightly converging beams from the LAM and dividing them into four quadrants of 24 beams. Two of the quadrants encounter a 240-ns delay in the long separation tunnel after the LAM, which brings the two halves of the 480-ns pulse train into time coincidence. Two 120-ns time delays provided by the shorter beam tunnels at right angles to the main tunnel then

bring all four quadrants into time coincidence. This scheme of decoding by quadrants is illustrated in Fig. 21.

A fine decoding process then provides appropriate 5-ns delays to allow all beams to arrive at the target simultaneously. Each beam must have an entirely separate mirror location within the shorter tunnels. Space is provided behind these mirrors for optical mounts and for the location of final optical diagnostics.

From the fine decoder, the beams are directed to the final aiming mirror array, which then aims the beams through the final focus lenses and onto the target. The precision alignment system required for final aiming is discussed in the next section. A more detailed description of the demultiplexer system is presented in McLeod (1987).

The complicated path crossings produced by angular multiplexing and pulse stacking do not allow isolation of individual beam lines, either for evacuation or the control of air motion; hence, the optical quality of the long beam paths must be controlled. Propagation of the 248-nm light beams over long paths in air is affected by scattering (Rayleigh, aerosol, and Raman); absorption by atmospheric gases; thermal gradients and turbulence; beam alignment; control errors; and optical component figure errors. Practical experience indicates that good beam quality cannot be obtained for modest path lengths (several tens of meters) unless an environmentally isolated beam tube is employed. In Rosocha et al. (1987), we examine how these mechanisms affect beam propagation in the AURORA system, report on experiments performed to characterize air as a practical propagation medium, and describe the construction of a suitable environmentally isolated beam enclosure.
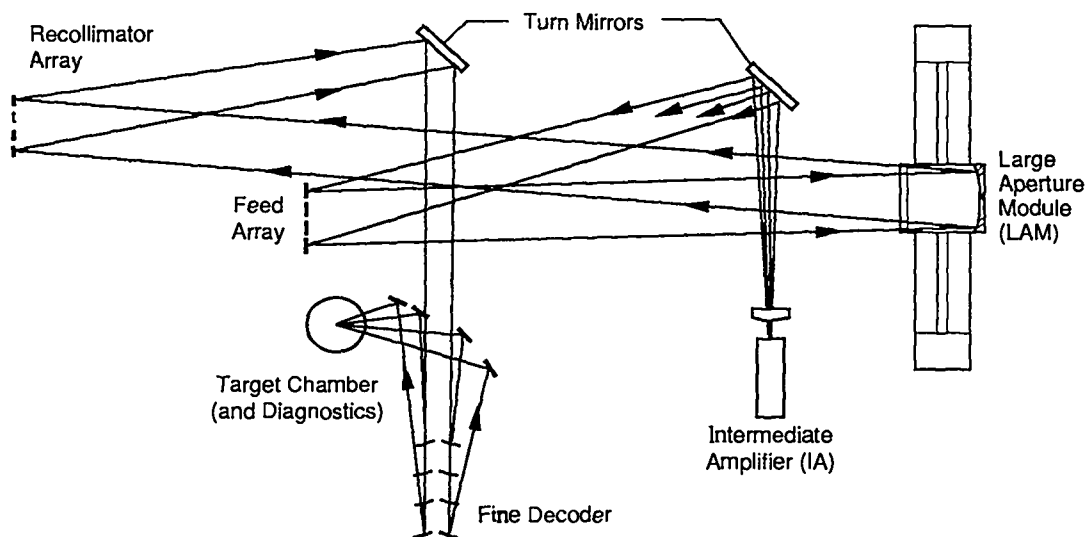
Fig. 20. Current 48-beam layout illuminating only one side of the target—not to scale and with only a few beams show. A 240-ns delay is not required; a 120-ns delay is hidden in turn and grade change from separation tunnel into decoder wing.
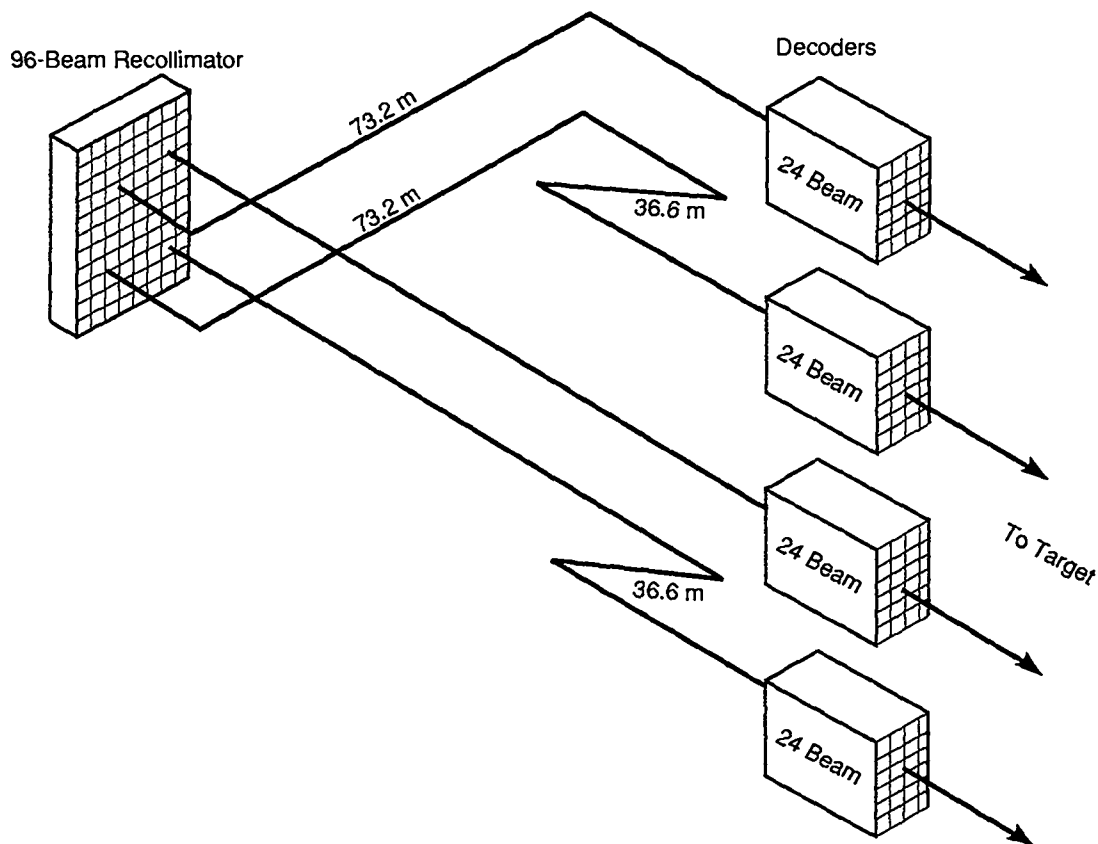
Fig. 21. The pattern of angle assignments in the multiplexer naturally divides the beam train into four time blocks. This enables the scheme of decoding by quadrants to be employed.
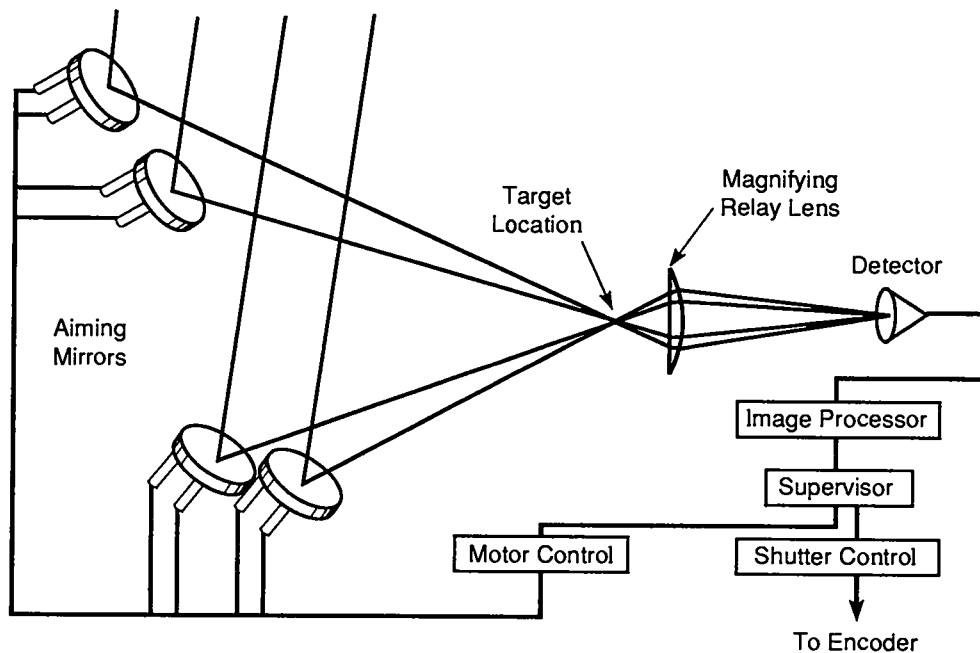
Fig. 22. The final aiming of laser beams on target will employ a third, closed-loop alignment system using data reduction techniques similar to the multiplexer (input pupil) alignment system.

Demultiplexer Alignment

To deliver laser pulses to the fusion target chamber, the beams must be directed from the main LAM mirror and through the decoder to the final aiming mirrors at the target chamber beam cone. Except for the last mirror in each beam path, each remaining decoder mirror needs to be aimed only well enough to direct the light to the next mirror. All optical elements in the decoder have been made oversize to permit several arc seconds of static alignment error at most locations. If necessary, the decoder optical elements can be manually aligned from a remote location by motorized mounts designed into the system.

The last mirror in each beam path is a final aiming mirror, which must be controlled by a third alignment system. This final aiming system does the largest measure of the work in hitting the tiny fusion target. Its accuracy must be one arc second or better, with adjustment steps of an even finer size. An optical system, including an instrument inside the target chamber, will image the focused spot together with fixed optical benchmarks, directly on a similar TV camera/video analysis system as used at the input pupil. Figure 22 shows the final aiming system concept. The software and control schedules for analyzing the properties of these overlapping beams will be very different from those of the input pupil, but similar methods

of high-speed data reduction will be used, and the effects of repositioning each of the beams will be observed to determine velocity errors schedules. The instrument in the target chamber will be withdrawn only seconds prior to delivery of energy to the target, but the velocity measurements will permit continuous error correction interpolation during that interval. (Predictive velocity correction must be used in real time to minimize the average error bounds.)

Because the final aiming mirror system is large and of high mechanical Q, resonance stepper motor control of its pointing schedule may conceivably introduce pointing errors resulting from mechanical vibrations. Therefore, the target alignment system may have to work in conjunction with the input pupil system to minimize any such effects. In total, overall pointing errors of <5 μrad seem attainable with a direct extension of our present methods.

CONCLUSION

We have described the design of the AURORA Laser Facility. This system was conceived as a fully integrated demonstration of the KrF laser for ICF applications.

This evaluation is now beginning with the completion of all the hardware systems described above. Near-term performance has been described by Rosocha and Blair (1988) and Rosocha et al. (1988). In the next section we will

summarize the preliminary data from the AURORA integration tests. A separate section (Kristal) describes the target irradiation apparatus system design and near-term performance.

REFERENCES

Bigio, I. J., and S. J. Thomas, "Effective Saturable Absorber for KrF Lasers," Appl. Phys. Lett. 49, 989, 1986.

DeLano, E., Appl. Opt., 2, 1251, 1963.

Hanlon, J. A. and J. McLeod, "The Aurora Laser Optical System," Fusion Technology, 11, 635, 1987.

Hunter, A. M. and R. O. Hunter, Jr., "Bidirectional Amplification with Nonsaturable Absorption and Spontaneous Emission," IEEE J. Quantum Electron., QE-17, 1879, 1981.

Kortegaard, B. L., "PAC-MAN, A Precision Alignment Control System for Multiple Laser Beams Self-Adaptive Through the Use of Noise," Fusion Technol., 11, 671, 1987.

Kumit, N. A. and S. J. Thomas, "Generation of Variable-Duration KrF Pulses..." IEEE J. Quantum Elec. 25, 2, 1989.

Kumit, N. A., and S. J. Thomas, "Application of a Phase-Conjugate Brillouin Mirror to Generation of High-Quality Variable-Duration KrF Pulses," IEEE J. Quantum Electron, QE-25, 421, 1989.

McLeod, J., "Output Optics for Aurora: Beam Separation, Pulse Stacking, and Target Focusing," Fusion Technol., 11, 654 (1987).

Rosocha, L. A. and K. B. Riepe, "Electron-Beam Sources for Pumping Large Aperture KrF Lasers," Fusion Technol. 11, 576 (1987).

Rosocha, L. A. and L. S. Blair, "Recent Progress on the Los Alamos Aurora ICF Laser System," Proc. of the Intl. Conf. on Lasers '87, p. 164, 1988.

Rosocha, L. A., J. A. Hanlon, J. McLeod, M. Kang, B. L. Kortegaard, M. D. Burrows, and P. S. Bowling, "Aurora Multikilojoule KrF Laser System Prototype for Inertial Confinement Fusion," Fusion Technol., 11, 497, 1987.

Rosocha, L. A., J. McLeod, and J. A. Hanlon, "Beam Propagation Considerations in the Aurora Laser System," Fusion Technol., 11, 624, 1987.

Rosocha, L. A., R. G. Anderson, S. J. Czuchlewski, J. A. Hanlon, R. G. Jones, M. Kang, C. R. Mansfield, S. J. Thomas, R. G. Watt, and J. F. Figueira, "Progress Toward the Delivery of High Energy Pulses with the Aurora KrF ICF Laser System," Proc. of the Intl. Conf. on Lasers '88, p. 154, 1989.

Shack, R. V., Proc. SPIE, 39, 127, 1973.

Stavroutes, D. N., Modular Optical Design, Chap. 2; Springer-Verlag, New York, 1982.

Thomas, S. J. K. W. Hosack, and L. J. Lopez, "Aurora Front-End Ouptut vs Pulse Width," Internal Memo CLS-5-88-330, Los Alamos National Laboratory, Los Alamos, NM, July 20, 1988.

Thomas, S. J., K. W. Hosack, L. J. Lopez, I. J. Bigio, and N. A. Kumit, "Improved Performance of the AURORA Front End with the Use of a Phase-Conjugate Mirror," Proc. CLEO '88, Anaheim, CA, Apr. 26-29, 1988, paper TuM20.

Thomas, S. J., K. W. Hosack, L. J. Lopez, I. J. Bigio, and N. A. Kumit, "Improved Performance of the Aurora Front End with the Use of a Phase-Conjugate Mirror," Digest of Technical Papers, CLEO '88, p. 92,1988.

York, G. W., Jr., S. J. Czuchlewski, L. A. Rosocha, and E. T. Salesky, "Performance of the Large Aperture Module of the Aurora Krypton Fluoride Laser System," Digest of Technical Papers CLEO '85, p. 188, 1985.

C. AURORA SYSTEM PERFORMANCE

Johnny E. Jones, Charles R. Mansfield, Louis A. Rosocha,
Stephen J. Czuchlewski, Thomas P. Turner, and Robert G. Watt

OVERVIEW

The AURORA KrF/ICF laser facility is now operational, and the major activities on the system support laser-target interaction experiments and investigations of the laser physics of large KrF amplifiers.

Development prior to 1985 consisted of construction of the front end, the large aperture module (LAM), and the automated 96-beam input pupil alignment system. Progress in 1985 and 1986 included LAM energy extraction experiments, the construction of additional amplifiers, and the installation of encoder and relay optics.

System integration through the Intermediate Amplifier (IA) was first achieved in March 1987 and led to upgrades to the amplifiers and the front end, followed by amplifier performance studies and reintegration of the system in 1988. The delivery of near-kilojoule level pulses to the target chamber took place in December 1988. Initial beam-focusing and target-relevant experiments commenced in April 1989. Reliable system operation with target irradiance of 100 TW/cm^2 was achieved in August 1989. The system is currently capable of firing several shots per day at this level, and a significant increase in irradiance on target is anticipated in the next few months.

EARLY DEVELOPMENT

Three major portions of the AURORA system were first constructed as tests of the KrF laser technology required for ICF research: the front end, the automated 96-beam input pupil alignment system, and the LAM amplifier.

The original front end used Pockels cells to switch out a 5-ns pulse from a longer 25-ns pulse produced by a commercial electric discharge-pumped, injection-locked KrF oscillator-amplifier system. The 5-ns pulse was then split into two identical pulses that were amplified by two commercial electric discharge KrF amplifiers, resulting in a combined output energy of approximately 350 mJ. This front end was adequate to meet the requirements for proof-of-principle demonstration of the technique of angular multiplexing, although it had an unacceptable contrast ratio for the delivery of energy to fusion targets.

The 96-beam alignment system (Kortegaard 1986, 1985) was constructed early in the program to demonstrate that the perceived alignment difficulties inherent in a multi-beam angularly multiplexed optical system could be overcome. The alignment system at the input pupil to the main e-beam pumped amplifiers aligned all 96 beams simultaneously to a 2-μrad step correction accuracy in approximately three minutes. Drift errors of 1 μrad/min or less were controlled within a 5-μrad total error. This system ultimately received an IR 100 award from *Research and Development* magazine in 1986 as one of the 100 most significant research and development achievements of the year.

The LAM was constructed early in the program to demonstrate the scalability of e-beam pumped amplifiers to large volumes. Its size was chosen to address issues associated with the scaling of these devices to higher energy and lower cost. Its initial performance in an unstable resonator configuration is described below.

The results of these demonstrations of alignment systems and scalable amplifiers have shown conclusively that the basic components of KrF technology can be extended to future system designs with low risk and reduced cost.

LAM Energy Extraction

In April 1985 the LAM was operated as an oscillator with a confocal unstable resonator of magnification M = 2.88 and an aperture of 1 m × 1 m. The pumped volume was 2 m in length, and the resonator length was 2.64 m. The output window was an array of 32 uncoated, fused silica panels with a net geometric transmission of about 60%. The average output fluence was measured with calorimeters at 1.01 J/cm^2. When this value was corrected for the transmission of the uncoated windows and the obstruction of the window mounting structure, the total extracted energy estimate was 10 kJ in a 600-ns pulse. The average small signal gain was estimated to be 2.8%/cm. Details of this experiment were reported by York et al. (1985) and Czuchlewski et al. (1989a,1987).

Electron Gun Performance

During 1985 and early 1986 the Preamplifier (PA) and IA were constructed, and extensive performance experiments were conducted on the amplifier e-guns. It was found that the e-gun voltage, current, and energy deposited in the laser gas were consistent with the Child-Langmuir cold cathode electron diode model (Rosoca and Riepe 1987). The LAM was operated over a range of Marx generator charge voltages from 40 to 60 kV. Typical cathode voltages were 450 to 600 kV with usual cathode current densities of 14 to 25 A/cm^2 measured at the anode plane. Typical electron energy deposited in the laser gas ranged from 80 to 165 kJ, and the corresponding time-averaged specific pump power ranged from 64 to 133 kW/cm^3, as measured by pressure jump calorimetry. Figure 1 shows the energy deposited in the LAM laser gas as a function of Marx generator charge voltage. The solid line on the log-log plot on this graph has a slope of 5/2, which agrees within experimental error with the calculated slope of 5/2 for an ideal Child-Langmuir diode.

Total LAM e-gun current and LAM electron current density on the downstream side of the hibachi and Kapton foil were also measured. Typical current densities in the gas were 10 to 12 A/cm^2 for a total current of 450 kA and a cathode area of 2 × 10^4 cm^2. The overall transmission of the LAM hibachi and Kapton foil was estimated to be 43%. With the more durable 0.002-in. titanium foil, the estimated transmission was reduced to approximately 34%.

In similar experiments, the PA was operated over a range of Marx generator charge voltages from 45 to 55 kV and guide magnetic field strengths of 600 to 1500 G. Typical energy deposited in the laser gas was 5 to 10 kJ, which corresponds to a time-averaged specific pump power

of 75 to 150 kW/cm^3. For low-voltage tests (<500 kV cathode voltage) the measured e-beam current density at the anode was 7 A/cm^2. Figure 2 shows the effect of varying the magnetic field strength on energy deposited in the PA, indicating an optimum field strength of approximately 1200 G.
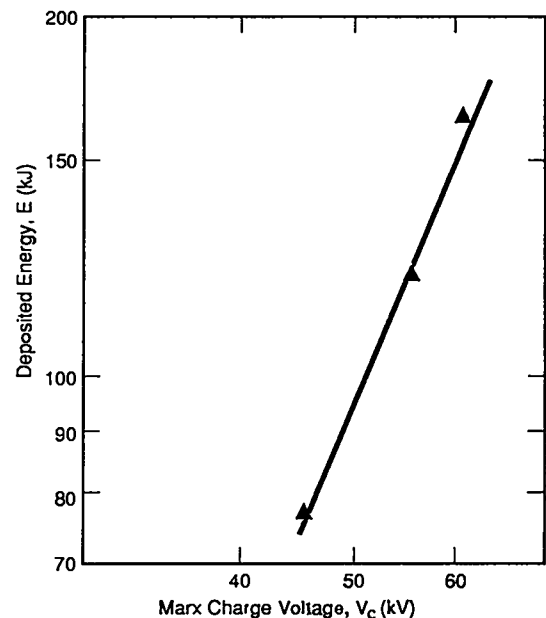
Fig. 1. Measured deposited energy in the LAM laser gas is plotted as a function of the Marx generator charge voltage. The slope of the solid line on the log-log plot is ~5/2, which agrees with an energy versus voltage relationship for a Child-Langmuir diode.
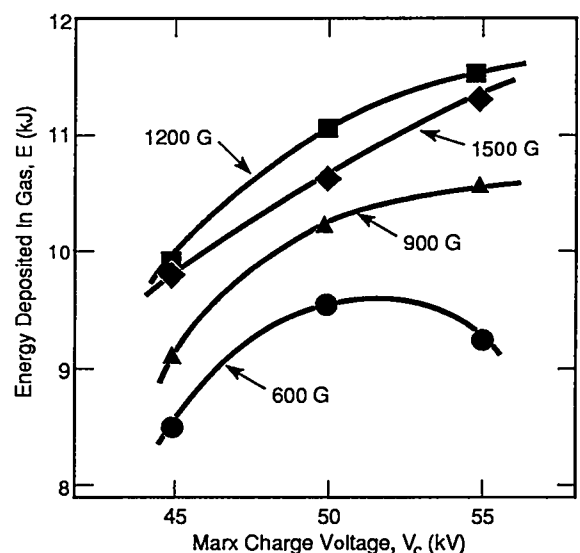
Fig. 2. Measurements of the energy deposited in the PA laser gas versus the Marx generator charge voltage for a family of guide magnetic field values are plotted.

Experiments were conducted on the PA using Faraday cups to determine the spatial distribution of the current density. Additional e-beam uniformity data was collected using e-beam sensitive film mounted parallel to the foil at a distance of 8 cm. Figure 3 shows three densitometer scans of the developed film. The three different scans correspond to different longitudinal cathode positions. These measurements indicate a slight tip in the cathode vertical plane, which was confirmed by mechanical measurements of the anode-cathode gap spacing and was corrected. These experiments showed that e-beam energy deposition was uniform to within ±15%.
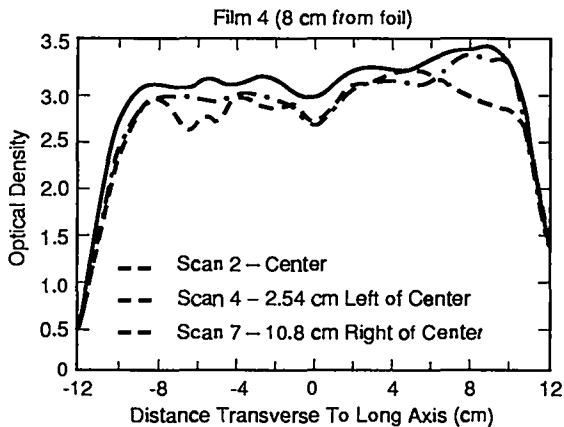
Fig. 3. Densitometer scans of exposed e-beam sensitive film for the PA. This is a single-shot exposure with the film being placed ~8 cm from the foil. The cathode voltage was ~500 kV and the guide field strength was ~1200 G. Each separate trace corresponds to a scan transverse to the long axis of the cathode at a different longitudinal cathode position.

Initial Integration Experiments and System Upgrades

Initial system integration experiments were started on AURORA in July 1986 by coupling the front end to the 12-fold encoder and amplifying the 60-ns, 12-element pulse train with the Small Aperture Module (SAM). These experiments addressed the stage gain of the SAM amplifier; the fidelity of the pulse shapes in the amplification process; and the integration of the front end, 12-fold multiplexer, and one e-beam pumped amplifier (Rose 1987). The input pulse train incident at the SAM is shown in Fig. 4a. The measured average stage gain of the SAM amplifier was approximately 12 for the 12-element pulse train, instead of the original design value of 20. After the 12-fold multiplexing and amplification demonstration was

completed, the 8-fold encoder and input pupil mirror array were integrated into the test effort. The resulting 96-beam pulse train produced by the multiplexer was characterized at the input pupil to the main amplifier chain and is shown in Fig. 4b.
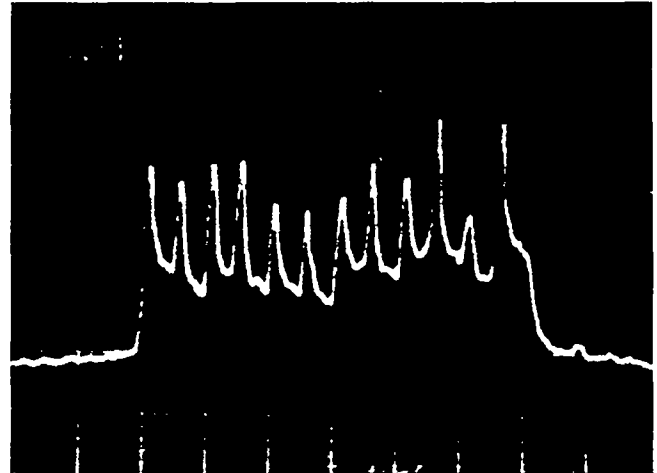
a
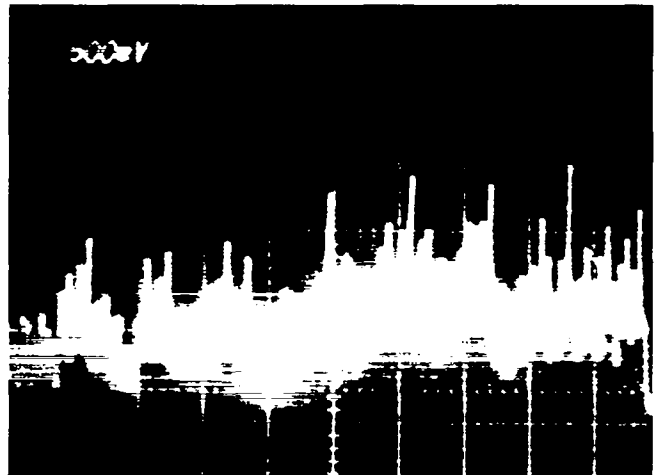
b

Fig. 4. (a) Twelve-element beam train incident at the SAM. (b) Ninety-six element beam train incident at the PA.

Subsequent system integration activities then involved the addition of relay optics and the integration of the PA and IA amplifiers into the AURORA system. System integration through the IA was demonstrated in March 1987 (Rosocha and Blair 1988). This demonstration included the temporal measurement of the incident and amplified pulse trains and the measurement of the small signal gains and the

energy extracted from the PA and IA. The stage gain measured when the PA was loaded with the 96-beam pulse train was approximately 43, compared to the design value of 50. The addition of the IA to the amplifier chain yielded an output energy of 256 J. Although this energy was considerably less than the original design value of 1 kJ, it represented a major step in the integration of the entire AURORA laser system.

The low output in the initial integration experiments led to a series of upgrades to improve the performance of the amplifiers (Kang 1988; Rosocha et al. 1988). The upgrade to the SAM amplifier included the redesign of the hibachi to improve the e-beam transmission from the gun into the laser gas and the addition of a second diverter to improve machine reliability through redundancy. The result was a 37% increase in deposited energy and improved reliability. The PA upgrade consisted of changes in the cathode and hibachi to improve e-beam transmission, which resulted in a doubling of the energy deposited in the laser gas. The LAM upgrade consisted of a redesign of PFLs and bushings with the major objective of improving machine reliability. The new design also improved impedance matching between the PFLs and the diodes and resulted in a 40% increase in deposited energy. Table 1 summarizes the improvements in energy deposition for the SAM, PA, and LAM amplifiers. The original front end was also replaced by the new front end described in detail in the section entitled "The AURORA Laser Facility."

TABLE 1. Electron energy deposition for upgraded amplifiers.

Amplifier Device	Change Voltage (% of maximum)	Electron Beam Energy Deposited in Laser Gas Old	New	Hardware Changes
Small Aperture Module (SAM)	93%	585 J	800 J	Cathode & Hibachi
PreAmplifier (PA)	92%	10 kJ	20 kJ	Cathode & Hibachi
Large Aperture Module (LAM)	83%	125 kJ	>175 kJ	PFLs & Bushings

An IA upgrade was designed to increase the IA deposited energy from the present value of 35 J/l at a cathode voltage of 550 kV to approximately 100 J/l at a cathode voltage of

770 kV and to improve machine reliability and flexibility in laser staging (Kang 1989). This upgrade has not yet been implemented because of the need to avoid interfering with the AURORA shooting schedule but it is scheduled for installation during FY90-91. An additional LAM upgrade to improve e-beam transmission has also been planned.

Amplifier Characterization

A series of experiments was conducted to determine the operating characteristics of the upgraded amplifiers. Extensive measurements were made on the SAM and the LAM, and preliminary measurements were made on the PA.

The SAM small-signal gain (SSG) measurements (McCown et al. 1989a) were made using the front-end beam as a probe beam. The output of the front end was split into five beams: four probe beams and one reference beam. Measurements were made to determine the SAM SSG as a function of vertical position in the laser medium, distance from the foil, fluorine concentration, total gas pressure, and Marx charge voltage. Figure 5 shows the SAM SSG coefficient as a function of gas pressure for two distances from the foil for a Marx charge voltage of 70 kV. Additional measurements were made to investigate the effects of CO_2 contamination on SSG and the fraction of deposited energy lost to fluorescence (McCown et al. 1989b). Experiments were also conducted to determine the optimum timing of the SAM amplifier for maximum energy extraction. With a Marx charge voltage of 70 kV, a gas pressure of 900 torr, a gas mixture of 0.15% F_2, 10% Kr, balance Ar, and an input energy of 100 mJ, the stage gain of the SAM was greater than 20.
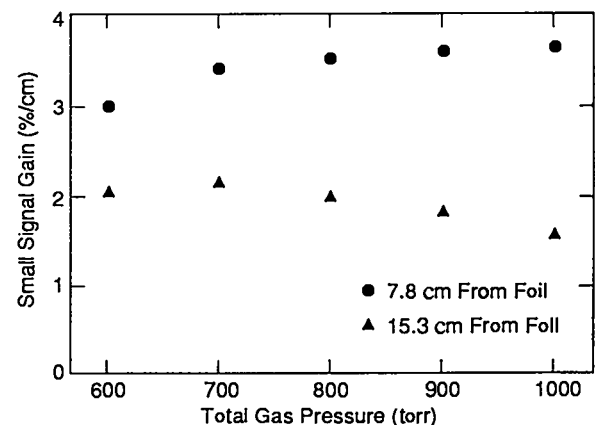
Fig. 5. SAM SG vs total gas pressure for two distances from the foil. Gas composition was 0.3% F_2 10% Kr, balance Ar. Marx charge voltage was 70 kV.

For LAM SSG measurements (Greene and Czuchlewski 1989; Czuchlewski 1989a) a commercial KrF discharge laser was apertured, attenuated, and split into eight beams. Seven of these were used as probe beams with the eighth serving as a reference beam. The seven probe beams were directed through the 1-m × 1-m aperture of the LAM at seven different locations. LAM SSG was measured as a function of horizontal position, vertical position, F_2 concentration, total gas pressure, Marx charge voltage, and CO_2 concentration. Figure 6 shows the LAM SSG as a function of horizontal distance across the aperture for a Marx charge voltage of 50 kV, a gas pressure of 700 torr, and a gas mixture of 0.30% F_2, 10% Kr, balance Ar. As can be seen from the figure, the net small-signal gain was fairly uniform, with an overall average of 1.43%/cm. The highest gain occurred in the center of the chamber, and the north side had slightly lower gain than the south side.
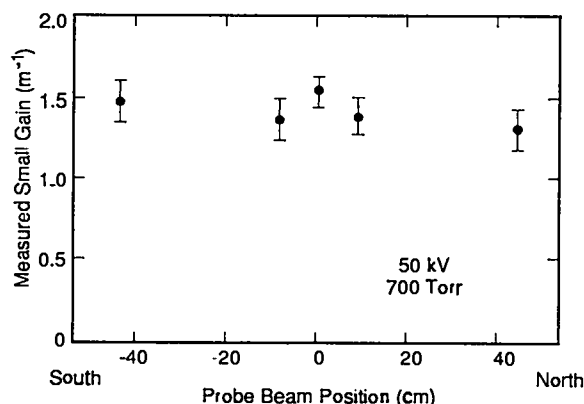
Fig. 6. Horizontal scan of the SSG of the LAM. Gas composition was 0.3% F_2, 10% Kr, balance Ar.

To obtain quantitative information on the amount of amplified spontaneous emission (ASE) inside the LAM chamber, two additional sets of measurements were made. The second set of measurements was made in a restricted volume using two horizontal plates mounted 20-cm apart in the center of the amplifier. This procedure reduced the amount of ASE and, hence, increased the measured SSG to an average of 2.1%/cm for the same conditions. The third set of measurements was made with copper mesh screens intercepting approximately 50% of the e-beam energy and thus cutting the pump power inside the amplifier in half. Because ASE is nonlinear, it was predicted to decrease more than a factor of two, and the SSG with the screens was expected to be more than half the SSG without the screens. Using the screens resulted in a measured SSG of 1.0%/cm and verified the ASE modeling. Figure 7 shows the effects of ASE on the gain of the LAM for the full aperture and the 20-cm restricted aperture cases. The results of the SSG and

ASE studies conducted on the LAM were compared to the calculated LAM performance curves shown in Fig. 7 and were found to be in agreement with the calculations. The anticipated near-term LAM operating range is indicated by the shaded region of Fig. 8.

Gain measurements on the upgraded PA were limited to measurements of the stage gain. With a Marx charge voltage of 50 kV, a gas pressure of 750 torr, an F_2 concentration of 0.3%, and an input energy of 0.5 J, the PA output energy was 65 J for a stage gain of 130.
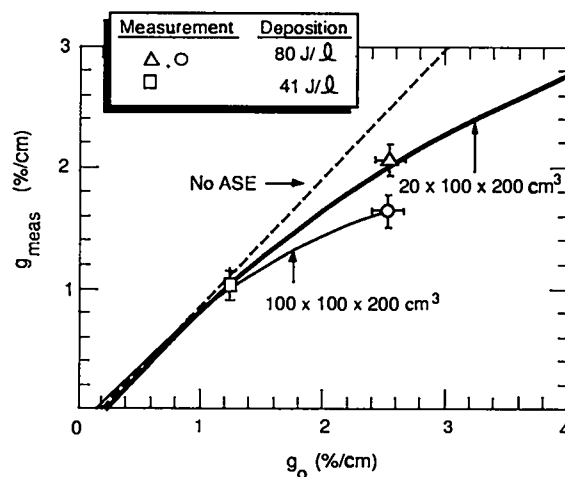
Fig. 7. Gain calculations and measurements for the LAM amplifier, considering the effects of ASE.
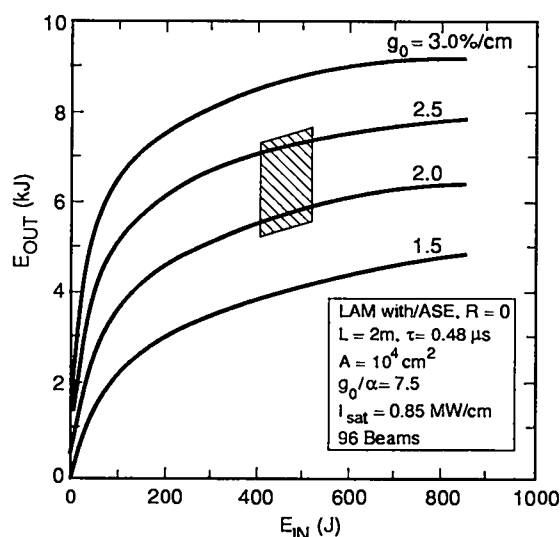
Fig. 8. Plot of LAM ouput energy vs input energy with near-term operating range.

Final System Integration

The goals for the AURORA KrF/ICF laser facility during FY89 were to
- complete the system integration and deliver kilojoule-level energy to target;
- demonstrate reliable system operation; and
- deliver more than 25 TW/cm^2 to the target.

In conjunction with the SAM and PA energy extraction experiments, final system integration began in October 1988. In November, integration was completed through the IA, and 550 J was extracted from the IA. Laser system integration was completed in December 1988 with the extraction of 2500 J from the LAM and the delivery of 780 J to the target chamber lens plate in 48 beams (Rosocha et al. 1988). Table 2 shows amplifier performance on this first fully integrated shot of the AURORA laser system. For this shot the full-size LAM mirror was not available. A down-sized mirror with an area of 20% of the full LAM aperture was used, which resulted in lower LAM output energy and stage gain. Only 48 of the 96 amplified beams are taken to the target area by the present AURORA optics system. The energy delivered to the lens plate on this shot was further reduced by losses on optical surfaces between the LAM and the lens plate (estimated at 15%) and by absorption of energy by impurities in the air in the beam tunnels (estimated at 27% based on absorption measurements) (Rosocha et al. 1987).

TABLE 2. Amplifier performance summary during first full system energy extraction demonstration (December 1988).

Location	Energy In (J)	Energy Out (J)	Stage Gain
Front end	–	0.9	–
Small Aperture Module	0.2	3.5	17
Preamplifier	0.5	65	130
Intermediate Amplifier	65	550	8.5
Large Aperture Module*	520	2500	4.8
Lens Plate**	780	–	–

*Using 1/5-scale mirror in the Large Aperture Module.
**48 beams transported to lens plate.

The full-sized LAM mirror arrived and was installed in May 1989. Tunnel air absorption was reduced to about 10%

by the addition of an air-handling system and filter bank. Damage to the optics in the centered optical system had occurred during the previous shot series that included final integration and the delivery of kilojoule-level light to the lens plate. These damage problems were substantially reduced in the following months, but because a full set of spare optics was not available, the gain of the PA was reduced (by reducing gas pressure) to preserve the damaged optical elements for as long as possible.

System integration was completed in June 1989 with the first full-system shot to target. The shot delivered 770 J to the target in 36 beams in a 7-ns pulse (FWHM), with 80% of the energy in a spot 600 μm in diameter and produced a target irradiance in excess of 30 TW/cm^2.

System Performance During Initial Target Physics Experiments

The first series of target physics experiments using the AURORA KrF/ICF laser facility was conducted during August 1989. The goals of this target shot series, called the "High Intensity Campaign," were to increase the irradiance on target, to check out target physics diagnostics, and to demonstrate the repeatability and reliability of the AURORA laser system. Alignment of the laser system was accomplished using the automatic input pupil alignment system and the automated LAM alignment system. Final beam alignment to target was accomplished manually because the final target alignment system was not yet operational. During this shot series, 36 beams were aligned to target, and the remaining 12 beams were intercepted by calorimeters at the lens plate for diagnostic purposes. The second 48 beams were used for calorimetry and burn patterns at other points in the system. Temporal pulse shapes were also measured at several points in the system. The focal spot size of the 36 overlapped beams on target was measured by visible fluorescence from a uv-sensitive fluor at target center and was confirmed using x-ray images taken with filtered pinhole cameras.

The temporal pulse shape was measured throughout the system using photodiodes with a risetime of 270 ps and 1.35 GSample/s digitizers (742 ps/sample) with typical system risetime resolution limited by analog bandwidth effects to approximately 435 MHz (590 ps rise time resolution). Figure 9 shows the pulse shape at two points in the system for the same shot. For this shot, the pulse width (FWHM) at the output of the SAM amplifier was 2.3 ns, whereas the pulse width at the decoder (following amplification by the PA, the IA, and the LAM) was 3.5 ns. This increase of about 1.3 ns in pulse width has been observed on all system shots. It is believed that this difference in measured pulse widths is due primarily to the difference in beam area used

for the two measurements. The photodiode at the decoder samples the entire beam area, but the one at the SAM output intercepts only the central 20% of the beam area. The data suggests that the pulse duration of the beam center is less than that of the edges. This is consistent with expectations based on the spatial distribution of the gain of the front-end amplifier and was borne out by other pulse-shape measurements at the decoder. This and other pulse-shape data indicates that the entire amplifier chain has good fidelity, and that the shape of the output pulse can be controlled by controlling the front-end pulse shape.
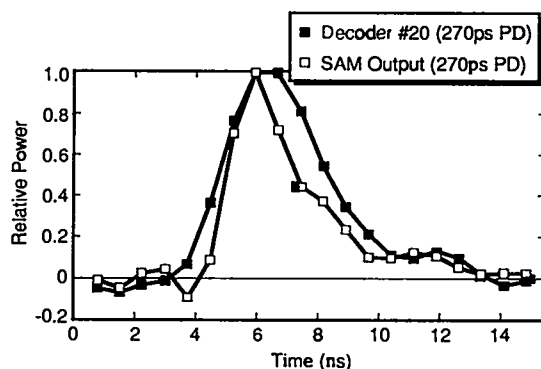
Fig. 9. Pulse shapes measured at the SAM ouput and at the decoder for the same shot with the front end configured for a 3-ns pulse (FWHM).

Optical images from visible fluorescence using the front end only indicated a minimum focal spot diameter of about 350 μm for 36 overlapped beams. Since this technique could not be used for full-energy shots, x-ray pinhole images have been used to estimate the focused spot size. Such images provide an upper limit of the spot size because the plasma producing the x-rays expands to a larger size than the actual focused laser spot. Figure 10 shows a pinhole camera image of x-ray emission from a typical target shot. The FWHM width of this spot is approximately 500 μm. Based on similar data from all target shots, the spot size has varied from 450 to 600 μm, depending on manual alignment and the beam quality of individual beams for a given shot, which is dependent on environmental variables in the beam transport path.

Table 3 lists the energies, pulse durations, and calculated average target irradiances for 11 successful target shots performed during the August campaign. Energies were measured using 12 calorimeters on the lens plate and extrapolated to the 36-beam energy. Pulse durations were measured in the decoder. The irradiances were calculated based on 80% of the energy contained in a focal spot 550 μm in diameter. This produces values for the average irradiance over the focused spot, not values for peak

irradiance at the center of the spot. Because the spot size is less than 550 μm in some cases (and may be less in all cases), the values for irradiance are conservative. The peak irradiance achieved is well over 100 TW/cm^2.
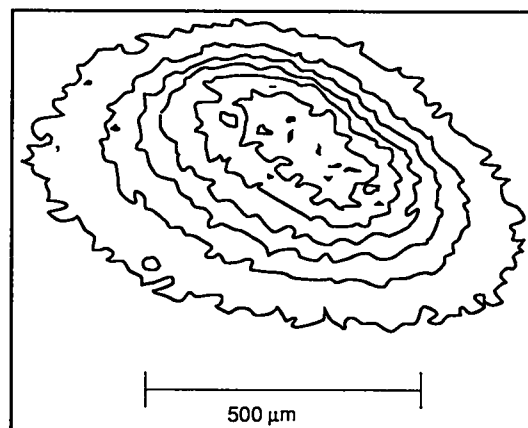
Fig. 10. X-ray pinhole camera image of focused spot on target. 2× camera with 12-μm pinhole and 1.9-mil beryllium filter mounted at 45° to target plane.

TABLE 3. AURORA performance during high intensity campaign (August 15-31, 1989).

Shot Date	36 Beam Energy	Pulse Width FWHM (ns)	Irradiance* (±25%) (TW/cm^2)
8/15	1290	7.0	62
8/16	1300	6.0	73
8/16	1130	7.0	54
8/17	960	4.5	72
8/22	850	5.0	57
8/22	730	3.5	70
8/23	910	3.5	88
8/23	580	4.0	49
8/31	940	3.5	90
8/31	840	3.0	94
8/31	900	3.5	87

*Average irradiance based on 80% energy in a 550 μm diameter spot.

For the first three shots of the series, the front end was operated in its normal configuration with two Lumonics post amplifiers producing a total output energy of 400 to

500 mJ. The amplifier ASE contributed to the total pulse width on target and resulted in a significant tail and increased pulse width. For the remainder of the shots the Lumonics amplifiers were removed. This reduced the front-end output energy to 20 mJ or less, but it caused only a slight reduction in energy on target. This allowed better control of pulse duration, shorter pulses on target, and an increase in target irradiance.

The maximum 36-beam energy delivered to target was 1300 J. This represents a 96-beam energy of 3470 J. Assuming transmission losses of 15% on optical surfaces and 10% to air absorption, the yield of the total LAM output energy was approximately 4500 J.

A high shot rate and good system reliability were successfully demonstrated during the High Intensity Campaign. A total of 13 target shots was fired within 12 working days. Two of these shots are not included in Table 3 because minor problems in the LAM resulted in low energy (<250 J) on target. One of these shots was the first shot fired on August 31. Following that shot, a LAM output switch was replaced, and three successful target shots were fired that day.

ANTICIPATED FUTURE SYSTEM PERFORMANCE

The system has not yet been optimized, and several near-term improvements should result in significant increases in both delivered energy and target irradiance. The most obvious of these is the removal of 12 calorimeters from the lens plate to allow 48 beams to go to target and to increase delivered energy by 33% over the present value. Relatively minor modifications to the front end should result in a 30% increase in output energy. Replacement of damaged relay optics will increase transmission into the PA input by at least 25%. New optics and the further reduction of retropulses and parasitics will allow the PA stage gain to be increased by up to 50% (by operating the PA at the upgrade design levels). Thus far the LAM has been operated at a conservative Marx charge voltage of 50 kV for all system shots. In the past it successfully operated at 60 kV during pulsed power tests. Target alignment has been accomplished manually, but the final automatic target alignment system is nearing operation. It should result in both faster alignment and better beam overlap for a smaller spot. These improvements should allow maximum target irradiance to approach 500 TW/cm^2 within the next six months.

The near-term plans for AURORA include the following activities:

- full characterization of the laser performance of the LAM and other e-beam pumped amplifiers;
- investigations of target prepulse from crosstalk and ASE;
- measurements of energy absorbed by the target and x-ray conversion efficiency;
- studies of the temporal pulse-shaping capabilities of KrF systems; and
- demonstration of the broad bandwidth capability of KrF amplifiers.

Additional performance improvements are planned during the next two years. The installation of IA and LAM upgrades will result in output energies in the 15 - 20 kJ range. Improvements in the optical system and the environmental control of the beam path will allow focal spot diameters of less than 350 μm; the ultimate goal is 200 μm. Target irradiance in excess of 10^{15} W/cm^2 is expected in FY92.

SUMMARY

The development of the AURORA KrF/ICF laser facility shows continual progress in establishing that KrF laser technology is the leading candidate for future ICF drivers. Final integration of the system is complete, and AURORA will soon begin operations as a target physics facility. Recent accomplishments include demonstration of

- high energy, with multi-kilojoule output and the delivery of kilojoule-level pulses to target in 36 beams;
- high intensity, with maximum target irradiance in excess of 100 TW/cm^2; and
- system reliability, with a sustained average shot rate of one shot per day and a maximum shot rate of four per day.

Continued improvements in system performance are anticipated in both the near and far terms, with the goal of achieving routine operation with target irradiance in excess of 10^{15} W/cm^2 in FY92.

REFERENCES

Czuchlewski, S. J., W. T. Leland, M. J. Kircher, D. P. Greene, J. A. Oertel, V. O. Romero, H. S. Steele, "Effect of Volumetric ASE on the Performance of Large KrF Amplifiers," Talk ThP2, Conf. on Lasers & Electro-Optics (CLEO '89), Baltimore, MD, Apr. 24-28, 1989a.

Czuchlewski, S. J., G. W. York, L. A. Rosocha, and B. J. Krohn, "A Large-Aperture 10-kJ KrF Laser," to be

published by Los Alamos National Laboratory, Los Alamos, NM, 1989b.

Czuchlewski, S. J., D. E. Hanson, B. J. Krohn, A. R. Larson, E. T. Salesky, "KrF Laser Optimization," Fusion Technol. 11, 560, 1987.

Greene, D. and S. J. Czuchlewski, "LAM Small Signal Gain and ASE Measurements" in "Development of KrF Lasers for Inertial Confinement Fusion," CLS-Division Annual Report 1988, LA-11600-PR, p. 3, Los Alamos National Laboratory, Los Alamos, NM, 1989.

Jensen, R. J., "KrF for Fusion: An Overview of Laser Issues," Fusion Techn., 11, 481, 1987.

Kang, M., "Aurora Amplifier Upgrades and Performance" in "Development of KrF Lasers for Inertial Confinement Fusion," CLS-Division Annual Report LA-11600-PR, p. 3, Los Alamos National Laboratory, Los Alamos, NM, 1989.

Kang, M., "Design Methodology for E-Beam Pumped KrF Lasers," presented at 1989 CLS-Division Technical Symposium, Los Alamos National Laboratory, Los Alamos, NM, Sept. 21-22, 1989.

Kortegaard, B. L., "PAC-MAN*, a Precision Alignment Control System for Multi-Variable Laser Beams Self-Adaptive through the Use of Noise," LA-UR-86-0726, Los Alamos National Laboratory, Los Alamos, NM, 1986.

Kortegaard, B. L., "Superfine Laser Position Control Using Statistically Enhanced Resolution in Real Time," SPIE 534, 159, 1985.

McCown, A. W., T. P. Turner, B. J. Krohn, S. J. Czuchlewski, R. G. Watt, V. O. Romero, H. S. Steele, "Perfomance of the Small Aperture Module Electron-Beam Pumped Amplifier on the Aurora KrF Laser Facility," Poster TuJ40, Conf. on Lasers and Electro-Optics (CLEO '89), Baltimore, MD, Apr. 24-28, 1989a.

McCown, A. W., T. P. Turner, R. A. Tennant, B. J. Krohn, "Determination of Fluorescence Energy Loss from an Electron-Beam Pumped KrF Laser," Talk ThP1, Conf. on Lasers and Electro-Optics (CLEO '89), Baltimore, MD, Apr. 24-28, 1989b.

Rose, E. A., "Generation of Ninety-Six Angularly Multiplexed KrF Beams at Aurora," Proc. Conf. on Lasers

and Electro-Optics (CLEO '87), p. 110, Baltimore, MD, Apr. 26-May 1, 1987.

Rosocha, L. A., and K. B. Riepe, "Electron-Beam Sources for Pumping Large Aperture KrF Lasers," Fusion Technol. 11, 576, 1987.

Rosocha, L. A. and L. S. Blair, "Recent Progress on the Los Alamos Aurora ICF Laser System," Proc. Intl. Conf. on Lasers '87, Lake Tahoe, NV, Dec. 7-11, 1987, p. 164, 1988.

Rosocha, L. A., J. McLeod, and J. A. Hanlon, "Beam Propagation Considerations in the Aurora Laser System," Fusion Technol. 11, 624, 1987.

Rosocha, L. A., R. G. Anderson, S. J. Czuchlewski, J. A. Hanlon, R. G. Jones, M. Kang, C. R. Mansfield, S. J. Thomas, R. G. Watt, and J. F. Figueira,."Progress Toward the Delivery of High Energy Pulses with the AURORA KrF ICF Laser System," Proc. Intl. Conf. on Lasers '88, Lake Tahoe, NV, Dec. 4-9, 1988.

York, G. W., Jr., S. J. Czuchlewski, L. A. Rosocha, and E. T. Salesky, "Performance of the Large Aperture Module of the Aurora Krypton Fluoride Laser System," Proc. Conf. on Lasers and Electro-Optics (CLEO '85), p. 188, Baltimore, MD, May 21-24, 1985.

D. TARGET IRRADIATION

Richard Kristal

AURORA is a short wavelength (248 nm), 10-kJ KrF laser system designed for use in the ICF program at Los Alamos National Laboratory. It is both an experiment in driver technology and a means for studying target performance using 248-nm KrF laser light. Both features will be used to help evaluate the uv excimer laser as a viable fusion driver.

The system has been designed to employ several electron-beam pumped amplifiers in series, with a fixed aperture of one meter square, to amplify 96 angularly multiplexed 5-ns beamlets to the 10-kJ level. In Phase I, 48 of these beamlets are brought to target by demultiplexing and focusing with f/26 optics. The beamlet ensemble contained within an f/1.8 bundle is focused as a single beam; however, pointing is done individually. Spot size in the target plane is variable from 0.1 to 4 mm, with maximum averaged intensity of $\sim 4 \times 10^{15}$ W/cm^2.

The illumination geometry is designed specifically for several classes of important target physics experiments. These include energy flow, symmetry and preheat studies related to indirectly driven targets; x-ray conversion and plasma coupling characterization on disc targets; and hydrodynamic instability studies in planar geometry.

Much of the technology involved in AURORA is new and state of the art. Some of it, however, is not, and for these applications extensive use has been made of existing equipment and technology from previous laser fusion experiments at Los Alamos.

The entire project was, and still is, an experiment. In recognition of this, it was decided to proceed toward the target irradiation goals in two phases. Phase I entails bringing half of the multiplexed beamlets to target, although all the beamlets are amplified through the entire laser chain. Encouraging results in Phase I would then spur the Phase II effort of bringing the remaining 48 beams to target.

BEAM CONFIGURATION AND IRRADIATION CONDITIONS

The number of beamlets required is determined by the width of the energetic part of the laser gain pulse and the maximum time of interest for depositing the extracted energy on target. When optical architecture considerations are also included, this leads to a total of 96 5-ns beamlets, spending a total of 480 ns per pass in the gain media. As mentioned above, initially only 48 of these are brought to target in Phase I.

In the target chamber the initial 48 AURORA beamlets are arranged in a single tightly packed bundle with a hole in the middle, as shown in Fig. 1. The array is rectangular, eight columns by six rows. The central four columns are separated in the middle to allow diagnostic and alignment system access. The beamlets are each f/26, and the ensemble forms a roughly square bundle of f/1.8 cone angle across the diagonal.

For an f/26 aperture, the diffraction limited focal spot size is ~ 8 μm. However, spot sizes of this order are neither feasible nor desirable from target coronal stability considerations. Spot size is instead determined by surface figure and aberrations from various elements in the beam line. Surface figures of the larger optics are intentionally specified at $\lambda/4$ in the visible, which is less than state of the art. The random addition of these figures, coupled with optical aberrations, are expected to produce an average spot size of ~ 50 μm (for the central 50% encircled energy) with a variation of ~ 20 μm.

With a beamlet energy of 100 J in 5 ns, the expected intensity at best focus is $\sim 3 \times 10^{14}$ W/cm^2 averaged over the central region. The intensity distribution in the superposed spot will depend on the performance capability of the beam aiming system. If all beams were perfectly superposed, then best focus intensity would be

~10^{16} W/cm^2. However, for reasons discussed later, beamlet aiming accuracy is expected to be ~35 μm. This should produce an ensemble central blur spot (50%) of ~120 μm, with 95% of the energy within 200 μm. Under these conditions, the central average intensity for the bundle is expected to be ~4 × 10^{15} W/cm^2.
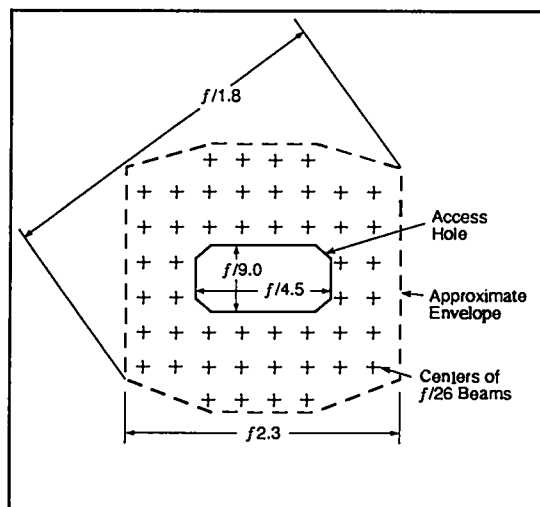
Fig. 1. Beam configuration in target chamber. Beamlets are arranged in rectangular array, with ~3° between beamlet cones. Convergence begins at the lens plate, 180 in. from target.

Fig. 2. Illumination pupil and focusing options. Plane of beamlet superposition (synthesized pupil) is defined as the target plane. Beamlet focal plane position may be varied substantially as shown by moving lens plate.

Superposition of the beamlets need not occur in the focal plane. It actually takes place in the target plane, and the focal plane may be substantially displaced axially as shown in Fig. 2. Focusing of the beamlets is done on the entire bundle as a single unit, with focal plane position anywhere from 2.5 cm in front of the target to 13 cm behind. This capability is designed to allow spot sizes of up to ~4 mm, which are useful for establishing 1D conditions for planar target experiments. With maximum defocusing, aiming system errors are negligible and the large number of beamlets should provide a fairly uniform footprint. The bundle may be pointed off axis by up to 2.5 mm in any direction. A summary of the beam and irradiation parameters appears in Table 1.

TARGET SYSTEM DESCRIPTION

AURORA is composed of a number of nominally distinct functional parts, as noted in Fig. 3: front end section, encoder section, amplifier section, beam tunnel, and target area. These parts are also somewhat spatially localized, as shown in Fig. 4.

TABLE 1. Beam and Irradiation Parameters Each Side

Energy	5 kJ
Pulse width	5 ns
Wavelength	248 nm
Bandwidth	~0.05%
Number of beamlets	48
Beamlet cone	f/26
Beamlet waist	~70 μm
Bundle cone	~f/1.8
Focused spot diameter	
50% of energy	~120 μm
95% of energy	≤ 200 μm
Maximum averaged intensity:	
Beamlet	3 × 10^{14} W/cm^2
Bundle	4 × 10^{15} W/cm^2
Intensity contrast	10^6
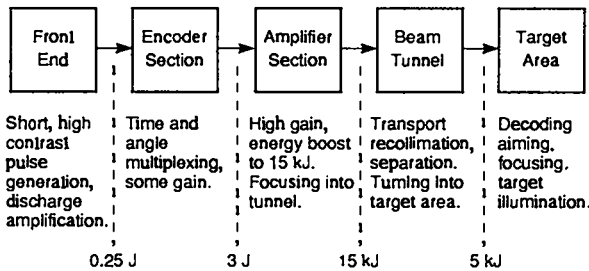
Fig. 3. AURORA functional structure. There are five basic functional parts of AURORA, as shown. Energy levels within each part vary because of optical losses and amplifier gain. Listed values are at boundaries.
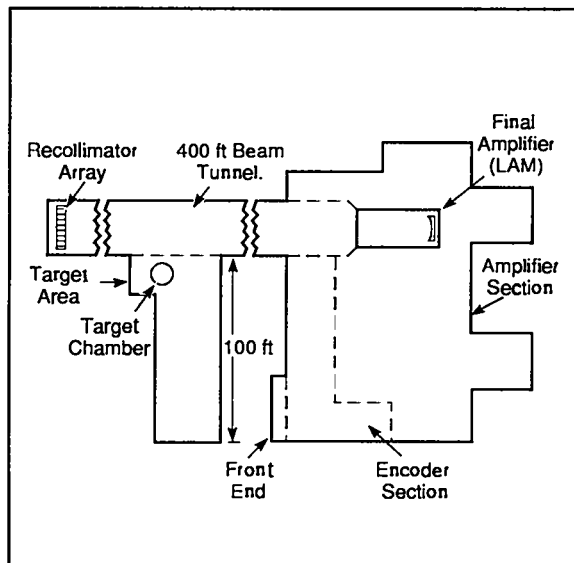
Fig. 4. AURORA physical layout. Front end, encoder, and amplifier sections are all in one building. Tunnel is of double foam wall construction to reduce thermal gradients (and, therefore, index gradients) and turbulence in beam path.

Target Area

The target area contains the target room, aiming mirror gallery, decoder room, and some support areas as detailed in Fig. 5. Essentially all of the large target area hardware has been fabricated and installed. The target room itself contains the basic targeting systems, viz., target chamber, beam cone, lens plate, and related hardware, a photo of which is shown in Fig. 6 (page 4). The aiming mirrors, lens plate, and delay mirror mounts are shown in Fig. 7 (page 5). The target chamber is a stainless steel sphere, 3 in. thick and 62 in. in diameter, composed of two o-ring sealed hemispheres with the seal plane at 35° from horizontal. The target is positioned at the center of the chamber, which is 78 in. above the floor. The chamber has a total of 75 ports, including two opposing 21-in. beam ports to allow for entry of the two f/1.8 beamlet bundles. Target positioning is accomplished using two major subsystems: the target insertion system and the target viewing system. The target insertion system is an airlock single target insertion mechanism used in the Helios CO_2 laser system (Day and Cummings 1978) and modified for use on AURORA. The target is held on the end of a slender stalk, mounted in a cart with a three-axis micropositioner. A dual chain drive transfers the cart across the airlock gate valve and cams it into position on a kinematic base. Positioning reproducibility is 5 μm. The system is operational.
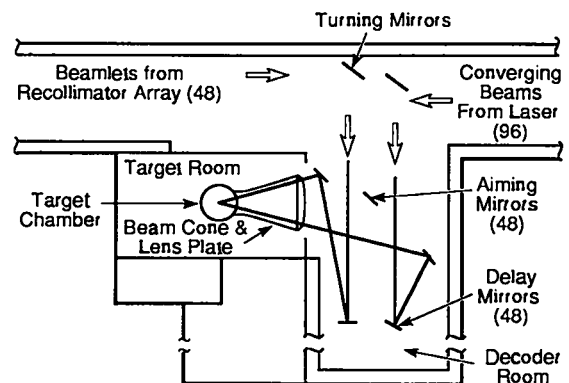
Fig. 5. AURORA target area layout. Target room, aiming mirror gallery, and decoder room are the principal parts of the target area. Remaining 48 beamlets, if brought to target, would require another gallery/decoder on left side of target room.
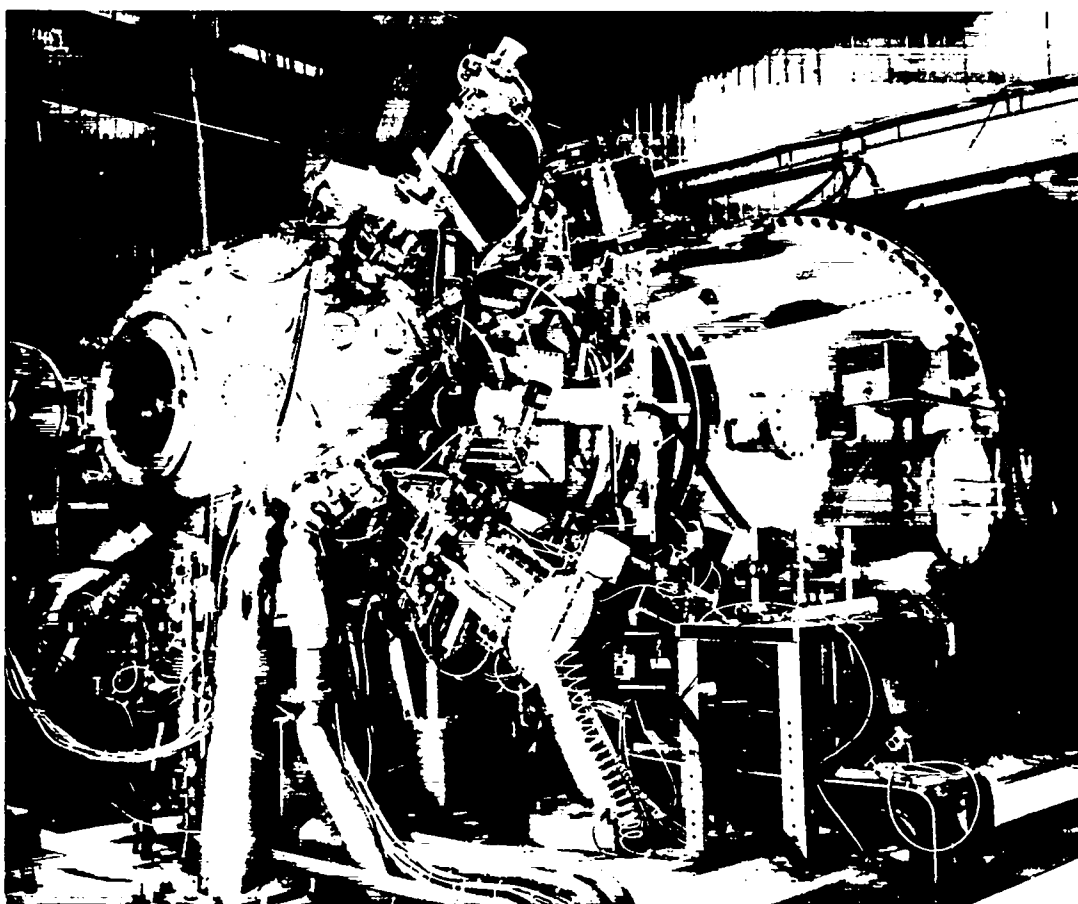
Fig. 6. Photograph of AURORA target system. System axis is 78 in. above floor. Nominal lens plate to target distance is 180 in.

The target is viewed by two telemicroscope systems orthogonally mounted. These systems have a zoom capability of 250 µm to 5 mm over a pan range of 5 mm in any direction. Both systems are operational. The target insertion system and one viewing system are located in the vertical midplane, as shown in Fig. 8 (page 6).

A large gate valve is mounted on the beam port, which serves to isolate the target chamber from the high vacuum (10^{-6} torr) of the beam cone when the former needs servicing at ambient pressure. A person port at the bottom of the chamber permits personnel access to the inside. Vacuum cycle time for the target chamber is less than an hour.

Adjacent to the valve is a beam viewing section containing ample access for parallel ray viewing of the entire beam bundle, e.g., in light scattered by residual gas. Such access may be useful in providing diagnostic data on the whole beam bundle. Just upstream, between the

viewing section and beam cone, is the focus control section. This is composed of a stainless steel bellows across which is mounted a precision, stepper-motor driven, four-point jack screw assembly. This system is heavily geared down, and routinely positions the entire beam cone (~15 tons) under an ambient pressure load of ~8 tons, with an accuracy of 10 µm over the 16-cm focus range. To enable this motion, the beam cone and lens plate are mounted on an undercarriage that rides on a precision low-friction rail system.

Fig. 7a and b. (a) Aiming mirror gallery and lens plate, as viewed from decoder room. Mirror mounts are visible on aiming mirror stand. (b) Array of delay mirror mounts in decoder room.
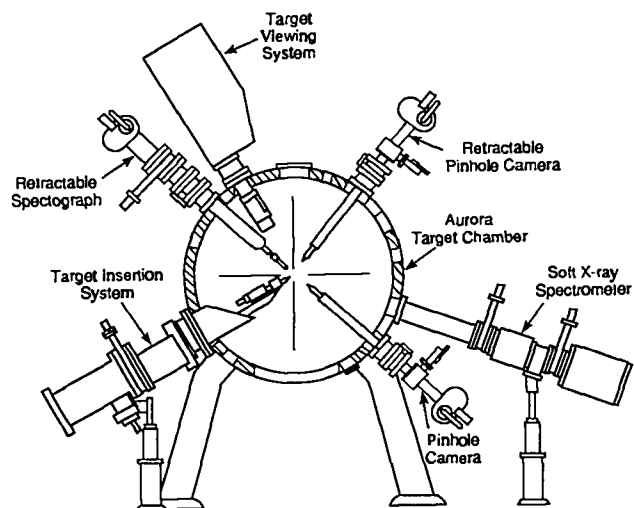
Fig. 8. Target chamber midplane instrumentation. Instrumentation shown except for the target viewing system are all from previous ICF experiments, modified to adapt to AURORA. Diagnostic instruments are all portable and designed to be mounted at other locations on chamber as well.

Fig. 9. Simple beamlet waist model. Shallow beamlet cone (f/26) gives extended waist length.

The lens plate is mounted on the large end of the beam cone and closes the vacuum envelope. It is a reinforced spun spherical dome, 10 ft in diameter, made of 2-in. thick stainless steel. It contains the 48 beamlet ports surrounding a large central rectangular diagnostic port. The lens cells, containing the fused silica condensing lenses, mount on the port flanges. The cells are fixed focus, with the lens also serving as the vacuum window. Spacers under the lens cells accommodate the variation in focal length and port distance to target, and provide an overall initial lens matching of ±125 μm for the worst case. The lenses are plano convex with a focal length of 180 in. They are installed on the lens plate and are operational. Lens matching is only one component of the beamlet focal plane match; the other is beam collimation variation, which may be expected to be of comparable extent. We expect, therefore, to limit the focal plane variation to 250 μm between beamlets.

The effect of this variation is dependent on beamlet behavior in the waist region, which will not be known until it is measured. However, since the focal spot is dominated by figure errors and aberrations, a simple geometric model, as shown in Fig. 9, is useful. Using this model, the expected variation should produce no differences in beamlet average spot size in the nominal focal plane; away from this plane, all beamlet spot sizes should monotonically increase. This only applies, of course, to averages over the profile and the beamlet ensemble. Within each beamlet substantial variations in intensity distribution are expected. These variations will be characterized with the imaging system used for beam aiming, described below.

The beamlets are directed to the lenses by 48 multilayer dielectric mirrors mounted on the large aiming mirror stand. The mirrors are all fabricated and installed. The mounts are controlled in orthogonal directions by stepper motors that provide 17-μm step resolution in the target plane. The mounts will be computer controlled in a closed loop system with error signals generated by an imaging system viewing the target plane. There are two different imaging objectives providing a choice of 90 or 22.5 magnification. Each consists of a retractable catadioptric system located behind the target plane that relays a magnified image of the target plane to a uv-sensitive TV camera system mounted in the center of the lens plate, outside the vacuum envelope. Aiming is accomplished using an auxiliary high repetition rate KrF alignment laser injected at the AURORA front end. Fabrication of the objectives is nearly complete, and assembly of the remaining components is proceeding. Initially, the aiming system will assemble all the beamlet focal spots in as small a circle as possible in the target plane. Short-term beam stability (under normal conditions) is expected to be ≤15 μm, and long-term beam motion will be limited to ~20 μm by the aiming system. This capability, coupled with the 50-μm average spot size, should be adequate for meeting the 200-μm, 95% design goal.

The aiming mirrors are somewhat oversize to allow for lens plate motion. With all the beamlets pointed to the same place in the target plane, movement of the lens plate over its range requires beam repositioning on the mirrors. This is accomplished by open loop remote angle control of the delay mirrors. These mirrors are all located in the decoder room and are spaced such as to provide the requisite path length for each beamlet so that all beamlets arrive at the target plane in synchronism, within 200 ps. The 48 beams incident on the delay mirrors pass through gaps in the aiming mirror stand from a turning mirror array in the beam tunnel, as shown in Fig. 5 and discussed in the next section.

Beam Tunnel

The beam tunnel is a long double wall, heavily thermally insulated structure extending from the LAM power amplifier at its upstream end to an array of recollimator mirrors at the other end. The length of the tunnel, ~400 ft, is determined by the distance needed for physical separation of the multiplexed beams as they converge to their individual virtual focii, while simultaneously limiting coma and astigmatism from off-axis LAM mirror operation. The recollimator mirrors aim the beamlets toward the turning mirrors mentioned above.

The purpose of the double wall structure is to reduce thermally induced gradients and turbulence in the beam path, which would otherwise result in unacceptable beam wander and breakup in the target plane. Because of folded optical paths, the beamlets actually travel more than 1000 ft in the tunnel (including a long path section between the last two amplifiers). Maintaining uv beam integrity over this distance in ordinary room air would be impossible. The tunnel construction, coupled with an absolute minimum of personnel or equipment activity in the tunnel, seems to provide an adequate propagation medium.

INITIAL EXPERIMENTS AND DIAGNOSTICS

Initial experiments will concentrate on absorption, deposition, and x-ray processes, which will be relevant to indirect drive targets. These are important parameters in the establishment of an adequate drive environment, and AURORA will be judged by its ability to produce attractively scalable indirect drive conditions. Key measurements involved in these experiments include time resolved, calibrated, soft x-ray spectrometry; x-ray pinhole photography; x-ray spectroscopy; and scattered light amplitude and distribution.

The time resolved measurement is made with a calibrated seven channel filtered XRD system sensitive on the 20 eV - 2 keV range. This instrument, originally used on Helios experiments (Day 1981; Day et al. 1980), has been modified for use in AURORA. It has a response time of ~200 ps, and will, therefore, also be useful for assessing the temporal superposition of AURORA beamlets. Data from the instrument is analyzed in a number of ways: by folding its response with measured (time integrated) spectra; by comparison with computer code (e.g., LASNEX) prediction; or by use of a simple analytic model for the source spectrum. Presently it uses calibrated aluminum photocathodes. The device contains an airlock so that channel filters can be changed with the target chamber remaining vacuum.

Three ports on the AURORA target chamber have been allocated to this system. They provide a view from -38° off the east-beam line; a view normal to the beam line; and a view from close to the west beam line.

Pinhole photography (van Hulsteyn 1980) is done with a valved, retractable airlock device that transports a small x-ray pinhole camera to the vicinity of the target. The camera is demountable, which permits the use of a variety of pinhole sizes—typically 25 µm—and arrangements—multiple pinholes, each with its own x-ray filter. The film cassette holds a variety of film types as well, and the cassette is replaced after each shot without breaking target-chamber vacuum. This instrument images the target in its own x-ray emission in the range 0.5 to 10 keV. Consequently, it gives important information about the spatial distribution of deposited energy, which depends strongly on the spatial distribution of laser light on target. This is a pivotal measurement when the illuminating beam is composed of 48 individually aimed beamlets. Several of these instruments are available from previous laser fusion experiments at Los Alamos, where they were of inestimable value in interpreting target and laser performance (Yates et al. 1982) Six ports on the AURORA target chamber are designed to accommodate this instrument. Similar considerations concerning view angle apply to this instrument as to the spectrometer, and in some instances, its location is as close to the spectrometer as possible. Soft x-ray (200 - 300 eV) *in-situ* pinhole cameras (Lee et al. 1981) are also available.

X-ray spectroscopy will be done with two types of instruments: a crystal spectrograph (Hauer et al. 1980; Hauer et al. 1986) and a grating spectrograph (Cobble 1981; Sedillo et al. 1985) both available from previous experiments. The crystal spectrograph mounts in the same retractable system as the pinhole camera and provides time-integrated spectra on film over the range of 2 to 20 keV depending on the crystal. The grating spectrograph is more sensitive than the crystal unit and responds to much lower photon energies. It gives time-integrated spectra on film over the range 0.1 to 10 keV. It mounts in an airlock on one of the chamber ports, thereby also permitting rapid film replacement.

These instruments will provide an important complement to the spectrometer by providing the spectral shape to fold with the channel response in determining conversion efficiency. In addition, if the source is bright enough, these instruments can provide a 1D spatial image of the source.

The scattered light measurements, from which target absorption is inferred, will be made with a large number of optical detectors arrayed around the inside of the target chamber and lens plate (Kephart 1980). These will give the total diffuse reflection as well as its angular distribution. The detectors are currently in the prototyping phase. A number of backscatter channels will also be instrumented so that the total reflection can be inferred. The optical detectors can also be filtered to observe Raman-scattered light.

Subsequent experiments will address more subtle, but nonetheless important, issues in indirect drive performance: drive symmetry and instability driven preheat. Instrumentation for these measurements, including a calibrated hard x-ray detection system, x-ray diode arrays and uv spectrographs, are currently in the conceptual design phase.

REFERENCES

Cobble, J., private communication, 1981.

Day, R. H., "Photoemission Measurements for Low Energy X-Ray Detector Applications," AIP Conf. Proc. No. 75, 44, 1981.

Day, R. H., R. Hockaday, F. P. Ameduri, and E. W. Bennett, "Time Resolved Soft X-Ray Spectra of Laser-Fusion Plasmas," BAPS 25, 962, 1980.

Day, R. D. and C. D. Cummings, "LASL Eight-Beam Laser Target Insertion System," in Proc. Topical. Mtg. on ICF (OSA, Washington, DC), 1978.

Hauer, A., R. D. Cowan, B. Yaakobi, O. Bamouin, and R. Epstein, "Absorption-Spectroscopy Diagnosis of Pusher Conditions in Laser-Driven Implosions," Phys. Rev. A. 34, 411, 1986.

Hauer, A., K. B. Mitchell, D. B. van Hulsteyn, T. H. Tan, E. J. Linnebur, M. M. Mueller, P. C. Kepple, and H. R. Griem, "Spectroscopic Measurement of High Density CO_2 Laser Driven Implosion, Phys. Rev. Lett. 45, 1495, 1980.

Kephart, J. F., private communication, 1980.

Lee, P., D. B. van Hulsteyn, A. Hauer, and S. Whitehill, "Low Energy X-Ray Imaging of Laser Plasmas," Opt. Lett. (USA) 6, 196, 1981.

Sedillo, T., J. Cobble, P. D. Goldstone, A. Hauer, G. Stradling, J. Chmielewski, G. Eden, I. V. Johnson, M.

Richardson, G. Gregory, G. Pien, and W. Watson, "Transmission-Grating Spectrograph for 0.1-5 keV," BAPS 30, 1532, 1985.

van Hulsteyn, D. B., private communication, 1980.

Yates, M. A., D. B. van Hulsteyn, H. Rutkowski, G. Kyrala, and J. U. Brackbill, "Experimental Evidence for Self-Generated Magnetic Fields and Remote Energy Deposition in Laser-Irradiated Targets," Phys. Rev. Lett. 49, 1702, 1982.

VI. Advanced KrF Lasers
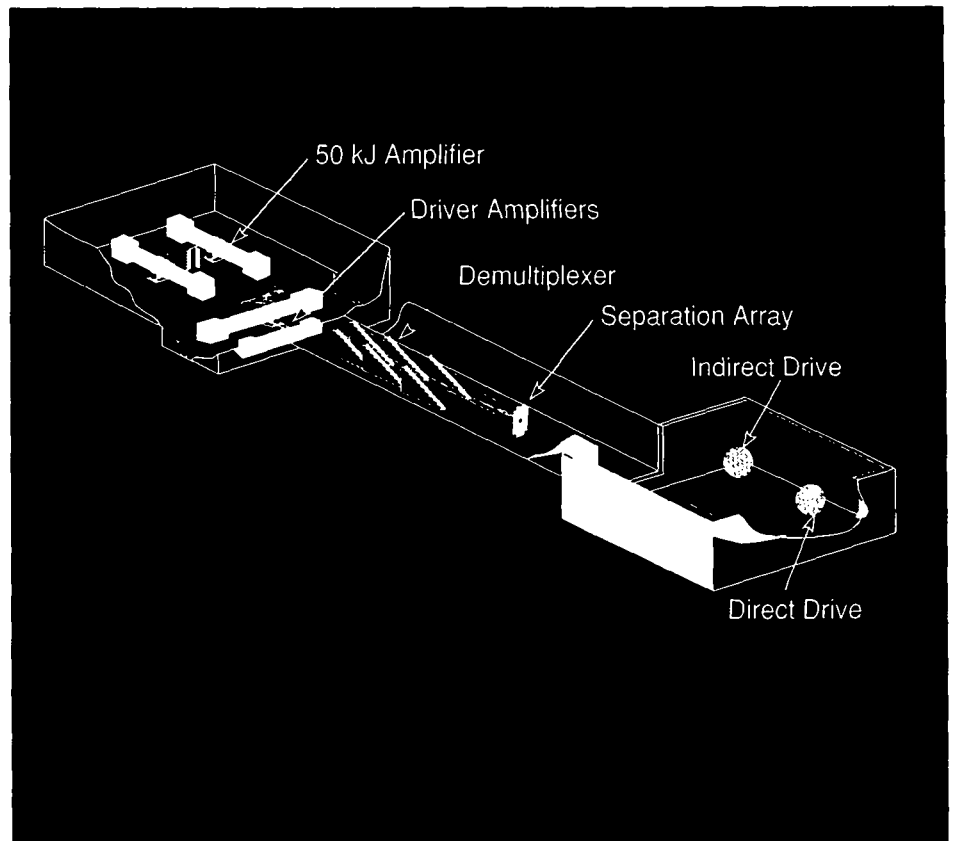
Perspective drawing of the 100-kJ Laser Target Test Facility for Los Alamos.

A. KrF Lasers for the LMF

B. The Laser Target Test Facility

A. KrF LASERS FOR THE LMF

John Pendergrass and David Harris

INTRODUCTION

LMC Scoping Study and LANL Participation

The Inertial Fusion Division of the Office of Weapons Research, Development, and Testing of the US Department of Energy (DOE) is conducting a multiyear scoping study of a proposed facility to develop Inertial Confinement Fusion (ICF) for defense and commercial applications. The requirements, the suitability of extrapolations of existing driver and other technologies, and the costs for the facility are being investigated. The study is called the Laboratory Microfusion Capability (LMC) Scoping Study (DOE/DP-1989) and the facility is referred to as the Laboratory Microfusion Facility (LMF). The LMC Scoping Study is examining both direct drive targets including cryogenic designs and indirectly driven targets. Los Alamos National Laboratory (LANL) is actively participating in the LMC study and is developing a conceptual design for an LMF using a KrF laser driver.

The LMC Scoping Study is the latest in a long line of studies of a single-pulse ICF facility to develop high-gain targets. Such a facility has generally been recognized as a necessary step in the development of ICF for commercial applications such as the production of electric power and process heat and the breeding of fissionable isotopes (Wilke et al. 1979). The LMC Scoping Study emphasizes the use of driver energy and target emissions for defense-related experiments.

The LMC Scoping Study has two phases. The first phase, completed in October 1988, concentrated on the driver-independent aspects of an LMF. These included

- the specific applications for which the LMF would be designed;
- the overall driver and target performances (for example, the driver pulse energy and target yield required for the various applications); and
- a common LMF construction work breakdown structure and common methodologies for estimating target performance and LMF costs. (These are the ground rules that would be used by all study participants during Phase II, so that all LMF concepts could be compared on an equal basis.)

LANL contributed substantially to this process and has followed the LMC Scoping Study ground rules developed in Phase I. The primary objectives of the second phase of the LMC Scoping Study are the development of conceptual designs for the LMF that incorporate the different driver technologies being considered and the formulation of corresponding technology development plans required for a successful LMF.

The participants in the first phase of the study concluded that an LMF should drive targets with yields up to 1000 MJ. The driver pulse energy required to achieve such target yields with a KrF laser driver was estimated to be in the range of 1 - 10 MJ. (The required driver pulse energy varies for the different driver technologies.) This driver energy and target yield would permit

- the development of high-gain targets;
- the performance of experiments of interest to the defense community, such as weapons-physics studies and weapons-effects simulations; and
- the demonstration of some of the technologies required for ICF applications beyond those for which the LMF would be designed.

The LMF is to be designed to accommodate at least one high-yield (100-1000 MJ) shot per week and at least two lower-yield (>100 MJ or less) shots per day. These and other requirements are discussed in more detail below.

Considerable technology development will be required prior to the design of an LMF. The time allotted for this development will be influenced by these two opposing considerations:

— the need to reduce the risks and uncertainties in target performance, driver cost and performance, and target chamber design because of the large extrapolations in technology and physics from existing facilities; and

— the need to have this capability to support defense and energy programs.

Many of the defense-related experiments could be performed in other facilities and in underground tests. The demand for defense-related experimental capability provided by an LMF may be too low to justify proceeding directly to an LMF at this time. Moreover, the extrapolations from today's technology and target physics performance to an LMF target physics performance result in a significant risk. The desire to accept this risk could be altered dramatically by physics or technology breakthroughs or by a nuclear test-ban treaty. At LANL, we believe that one or more facilities intermediate in scale between existing ICF experimental facilities and the LMF will be needed for the following reasons:

— to better understand target physics in order to help validate LMF feasibility and to determine LMF driver requirements such as energy, pulse shape, illumination geometry, etc;

— to demonstrate driver cost scaling, technology improvements, and performance (such as pulse shaping flexibility and accuracy, bandwidth control, and beam quality); and

— to provide a near-term capability to perform defense-related experiments.

In addition to the LMC Scoping study, substantial efforts are underway at LANL to

• establish the requirements for the intermediate facilities,

• develop attractive concepts for them,

• assess the technology advances required to obtain the performance improvements and cost reductions, and

• formulate technology development and cost-reduction programs to achieve these advances as part of a strategy to provide a path to an LMF with lower risk.

Research and development (R&D) path from today's KrF facilities to an LMF that is aggressive but involves acceptable risk is outlined in Fig. 1. The existing AURORA facility (Rosocha et al. 1987) can be viewed as the first step in this process. Various projects have been started to further develop the KrF technologies needed for advanced facilities.
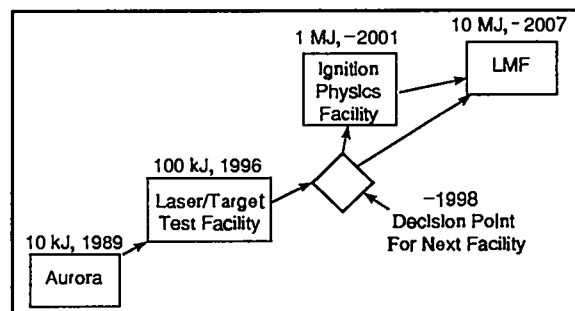
Fig. 1. Aggressive R&D path from today's KrF facilities to an LMF that involves acceptable risks.

The preliminary Los Alamos KrF laser-driven LMF design effort has concentrated on major systems. Those conventional items which contribute significantly to total facility cost or facility performance have also received considerable attention. Those items having leverage for considerable cost reduction or performance improvements have been identified, and technology development programs have been implemented.

Other items have been investigated in less detail; only preliminary estimates of their cost have been prepared. We have identified virtually all the R&D, equipment, structures, and construction and project management activities that are required for successful completion of an LMF. We have assembled descriptions of the general requirements and characteristics of these items in a detailed, comprehensive work breakdown structure (capital-cost account checklist) for an LMF with a KrF laser driver (Pendergrass and Harris 1989). The upper levels of this work breakdown structure without the detailed descriptions and requirements are illustrated in Fig. 2. We are using this breakdown as a guide in deciding when supplementary studies are needed. Thus, we are confident that many of the general characteristics of the present LANL concept will stand the test of time. We also recognize that many of the details must be studied further, and that some will require modification as a result of future studies.

We have assumed that some advances to the state of the art for KrF will be achieved by the time an LMF is built. Where little improvement can be reliably expected, we have been relatively conservative. Worldwide, funding for KrF laser technology development is growing as the important advantages of KrF lasers for ICF drivers become increasingly apparent. Breakthroughs in key technologies, such as pulsed power, electron-beam diodes, optical performance, and optics fabrication technologies and capabilities could significantly alter KrF laser architectures and costs. The design presented here represents an initial starting point prior to significant design verification tests; it

```
                        ┌─────────────────────────────────┐
                        │ Laboratory Microfusion Facility │
                        └─────────────────────────────────┘
```

Facilities	Driver	Experimental Area Equip	Other Special Equipment	Project Office
Land and Land Rights	Low-Power Laser	Target Chamber	Target Fabrication Equip	Construction Facil, Equip, & Services
Conventional Structures & Facil	Major Amplifiers	Target Chamber Shielding	Central Control Room Equip	Architect Engineer Home Office
Special Structures	Major Optics	Target Chamber Vacuum Equip	Applications Fabrication Equip	Architect Engineer Field Office
Misc Facility Equipment	Maintenance Equipment	Target Insertion Systems	Central Computer Facility Equip	Owner's General & Administrative
	Environment Controls	Target Diagnostics	Optics Shop & Laboratory Equip	Contingency Allowances
	Instrument & Controls	Applications Equipment		
	Safety Systems	Target Chamber Cryo, etc. Systems		
	Prototype Module	Target Chamber Maint Equip		
	Spares	Target Chamber Instr & Controls		
		Safety Systems		

Fig. 2. Higher-level accounts in the work breakdown structure for a KrF laser-driven LMF.

is considered preliminary. Regular updates of the LANL LMF concept are planned.

A brief report like this cannot cover all aspects of the very complex LMF. Therefore, we concentrate on descriptions of the two major systems and the structures that house them in the LANL LMF concept: the KrF laser driver and the driver building and the experimental area equipment. We will not discuss more conventional items, such as project administration, site preparation, target fabrication, central computing, optical laboratory, and other equipment and structures. However, we recognize that some of these items are costly and require careful attention in the completion of a successful LMF project. As mentioned above, all these items are covered in our cost estimates.

KRF LASERS AS ICF DRIVERS

KrF laser technology offers several advantages over other driver technologies (Rosocha et al, 1987a; Harris et al,

1987b). Experiments and theory all indicate that the x-ray conversion efficiency (the fraction of incident laser energy that is converted to x rays by a target) increases as the wavelength becomes shorter. At the 248-nm KrF wavelength, the x-ray conversion efficiency is relatively high. The KrF laser bandwidth about the 248-nm line center for the light from a KrF laser can be relatively broad, approaching 1% of the lasing wavelength. A narrow-bandwidth laser light drives several nonlinear processes that produce highly penetrating "hot" or energetic electrons. These hot electrons preheat the fuel and can greatly reduce target gain. Thus, the KrF laser wavelength and bandwidth represent a near-optimum combination for driving ICF targets.

Pulses must be carefully shaped temporally to achieve high gain with ≤10 MJ of KrF laser-driver energy. KrF lasers can deliver complex temporally shaped pulses in two ways. The preferred method is to generate the desired pulse profile in the front end and amplify the pulses without

distortion. Calculations indicate that amplification without distortion is possible because in saturated amplifiers the gain is nearly independent of power throughout the pulse. The alternative method is to adjust the time decoding so that different beams arrive at the target at different times to deliver the desired pulse shape to the target. The front-end pulse shaping method is preferred because flexibility is more easily obtained and more uniform target illumination can be achieved.

The pulse-compression technique used in the LMF design is pure angular multiplexing. Other approaches include the use of nonlinear Raman and Brillouin processes (Ewing 1986). The input energy is converted by nonlinear processes into slightly longer wavelength light in shorter pulses of higher beam quality that are extracted using seed pulses of the correct wavelength. The conversion step involves significant inefficiencies and more than one stage, or the use of a hybrid combination with angular multiplexing to obtain the necessary pulse compression. Nonlinear pulse compression techniques have been studied extensively at LANL and elsewhere for many years and are being used in existing facilities around the world. However, these pulse-compression techniques have not yet proven as efficient, cost effective, simple, flexible, or reliable as pure angular multiplexing at the LMF scale. Therefore, these technologies are not currently being considered for the baseline LANL LMF concept.

In addition to being an ICF R&D facility, AURORA is the first end-to-end integrated-system demonstration of a large-scale angular multiplexed KrF laser driver with a long (approximately 1 km from front end to targets) total ultraviolet optical path length (Rosocha et al. 1987; Hanlon and McLeod, 1987; McLeod 1987; Rosocha and Riepe 1987; Kortegaard 1987; Rosocha McLeod and Hanlon 1987; Bowling et al. 1987). It uses pure angular multiplexing to superimpose 48 5-ns pulses on targets. As the largest and one of the newest KrF laser systems in the world, AURORA was an obvious starting point for the development of the LANL concept for an LMF. Much of the technology and concepts used in AURORA can be utilized. Suitable changes in design details required for the much larger scales and component counts of the equipment in an LMF have been introduced to take advantage of advances in design methods, materials, cost reductions, etc., that can be expected between now and the construction of an LMF. Numerous studies have been conducted at LANL and elsewhere of ways to scale KrF laser technology to higher energies and to assess the potential and impacts of such technology advances to cost reductions (Harris et al. 1985; Harris et al. 1987a). The results of these studies are being

assimilated and applied wherever possible in developing the LANL concept for a KrF laser driver for an LMF.

Differences Between AURORA and the LMF Driver Design

The KrF laser driver in the LANL LMF concept includes several innovations relative to AURORA that can be briefly described. Some of these differences are summarized in Table 1. In AURORA, the number of beams is increased rapidly at low energy and a relatively large number of beams are propagated through much of the amplifier chain. Our studies indicate that for the LMF it is less costly and reduces prepulse to increase the number of beams by roughly the same factor between amplifier stages.

The 10.0% Kr/0.3% F_2/89.7% Ar laser-gas mixture used in AURORA has been changed to 99.7% Kr/0.3% F_2 for the LMF. The change was made primarily because theoretical and experimental studies indicated that higher intrinsic efficiencies could be achieved with Kr-rich mixtures because they eliminated dilution by argon that diverted pump energy from the preferred excitation (Mandl et al. 1987).

A side effect of this change is that the new mixture has a modestly greater stopping power for energetic electrons because of its higher average atomic number. Therefore, a higher diode voltage can be used to pump the same thickness of lasing medium, raising the required diode impedance and reducing the pulsed power rise time and efficiency. Both the AURORA Large Amplifier Module (LAM) and the LMF main amplifiers are designed to operate at or near the local atmospheric pressure to minimize structural requirements. A decision made in scaling the LMF main amplifiers from the 20-kJ AURORA LAM to about a factor of 10 increase in the output energy was that the pulsed-power and electron-beam technologies would not be pushed too far toward higher voltages (1.0 MV for LMF versus 0.7 MV for AURORA). Also, to avoid invoking large extrapolations in window fabrication capabilities, we decided to keep essentially the same diagonal for individual transmissive optics pieces. Thus, the LMF amplifier dimension in the electron-beam direction is not much greater than that of the AURORA LAM (1.3 m for the LMF versus 1.0 m for AURORA).

TABLE 1. Comparison of some LMF main amplifier
parameters with Aurora Large Amplifier Module (LAM)
parameters.

Parameter	Value for Aurora LAM	Value for LMF Main Amplifier
Amplifier inside dimensions (W x H x L)	$1.0 \times 1.0 \times 2.0$	$1.3 \times 3.9 \times 3.8$
Amplifier output energy (kJ)	10	240
Window segment largest dimensions (m)	1.5	1.5
Amplifier pump duration (ns)	500	750
Electron-beam diode dimensions (H x L, m)	1.0×2.0	3.9×3.75
Electron-beam diode voltage (kV)	670	1000
Electron-beam diode current density (A/cm^2)	24	24
Total electron-beam diode current (MA)	0.5	3.6
Energy per pulse-forming-line Marx bank (MJ)	0.2	2.4
Lasing-medium composition (volume % Kr, F$_2$, Ar)	0.0,0.3,89.7	99.7,0.3,0.0
Short-pulse beams per amplifier	96	60
Peak power pulse length to target (ns)	2-10	5-50

The KrF amplifier dimension in the optical direction is
constrained by the optics-damage threshold fluence and laser
intensity limits. Therefore, the LMF main amplifier is
only about twice as long as the AURORA LAM (3.75 m
versus 2.0 m). KrF amplifiers are less constrained in the
third direction, although the increase in parasitic oscillations
with increase in amplifier size and practical limits on
pulsed-power and electron-beam equipment must be
considered. The height of the LMF amplifier is 3.9 m
compared to a height of 1.0 m for the AURORA LAM.
Scaling in this way is attractive because parasitic
oscillations in this direction can be controlled by blackening
the inside of the top and bottom of the amplifier chamber.

The area of the LMF main amplifier window is thus
about five times that of the LAM window. Therefore, if an
LMF main amplifier window is to be made from pieces of
window material of near the same diagonal as that of the
AURORA LAM window, and its span is somewhat greater,
then it will have to be constructed of multiple rectangular
segments, rather than a single square piece as in the
AURORA LAM. Six such segments are required for the
LMF main amplifier windows.

A 3:1 height-to-width ratio allows three LMF main
amplifiers to aperture-share the square input and output
array mirrors and high-intensity downstream optics that
decode the short pulses from the amplifiers and deliver them
to target. The square optics whose apertures are shared are
87 cm diagonally, which is within the current optics
industry fabrication capability. To more efficiently utilize
driver-building floor space, the LMF main amplifiers are
located closer together. The long pulse-forming lines join
the amplifier diode at an angle of 30°. This is described in
more detail in the section, LANL Concept for a KrF Laser-
Driver for an LMF.

The LMF amplifiers are pumped longer (750 ns versus
500 ns for the AURORA LAM), but the target pulses are
longer for the LMF amplifiers (10 ns versus 5 ns for the
LAM). As a consequence, only 60 short pulses are passed
through each LMF main amplifier, instead of the 96 for the
AURORA LAM.

Higher optical fluences were assumed on the
downstream optics for the LMF than are used for
AURORA. Because the cost of these optics is a large
fraction of the total LMF cost, improvements in this
parameter have substantial leverage for reducing LMF costs.
An average fluence of 5 J/cm^2 at 248 nm for 10-ns pulses
for multi-layer dielectric coatings is assumed for the high-
energy optics downstream of the LMF main amplifiers. In
contrast, 1.0 J/cm^2 at 5 ns was used in the design of the
high-intensity optics for AURORA.

The current LMF concept has 45 main amplifiers, each with an output of 240 kJ for a total yield of 10.8 MJ. The 8% excess over 10 MJ is to cover losses in delivering the beams to target. In exploring the possibilities for scaleup from the AURORA LAM to LMF main amplifiers, two concepts at opposite ends of a large range were also considered. The first of the two concepts employed approximately LAM-sized main amplifiers. With a few improvements, the output of LAM-scale amplifiers could be raised to about 24 kJ, so that 450 amplifiers would have a combined output of a little over 10 MJ.

The first case involved a high component count that resulted in concern about reliability and operability. It was observed that the economies of scale would provide a significant cost reduction of larger amplifier modules were used. The second alternative concept involved a scaleup in output energy per amplifier from AURORA by a factor of 100, rather than the factor of 10 for the current concept. Only four 2.4-MJ main amplifiers would be needed to provide the same total output energy. The extremely large amplifier size of the second alternative caused concern about scaleup to this size because some technology and fabrication breakthroughs would be required for their realization. In addition, the projected savings in cost from successful scaleup of the amplifiers to this size are modest, partly because scaleup in size reduces the opportunity for manufacturing-cost learning by decreasing the number of units in a production run. The current LMF concept balances the benefits of size scaling and quantity production discounts.

PERFORMANCE REQUIREMENTS AND COSTS FOR AN LMF

Introduction

Some principal performance requirements for an LMF that have been identified by the ICF community are listed in Table 2, together with some desirable features and parameter values selected for the LANL LMF concept. The reasons for some of these features and parameter values are discussed below.

TABLE 2. Important cost and performance goals, requirements, and overall design parameter values for the Los Alamos LMF concept.

Goal, Requirement, Other Parameter	Value
Total LMF Cost Goal*	$100/J
Driver energy	≥10 MJ
Target yield goal	1 GJ
Shot rate	1 high-yield/week, 2 low-yield/day
Operability	90% availability
Reliability	95% successful driver performance
Maximum downtime for repair or maintenance	2 weeks
Illumination geometry	for 3-sided indirect-drive targets
Pulse shaping	flexible
Peak power pulse length	10 ns
Bandwidth range line	0.1% to 0.5% of center wavelength
Backlighting	required
Main amplifier output pulse energy	240 kJ
Number of beams to target and for backlighting	900

* Using the standard LMF costing methodology.

Cost

This overview concentrates on the design and performance requirements for an LMF with a KrF laser driver. However, the cost of an LMF using any driver technology is expected to be large, so that cost becomes one of the paramount considerations in deciding whether or not to continue to pursue the LMF. Differences in the cost of an LMF with different driver technologies may be more important than small differences in performance. An LMF will not be constructed at any cost if there is not high confidence that it will perform as required. However, if an

LMF can't be shown to perform as required, then it won't be constructed at any cost. On the other hand, if it costs too much, then no matter how well it might perform, it won't be built. Thus, for a successful LMF the right combination of performance and cost must be achieved.

A cost goal of $200/J or less of KrF laser-driver output energy for a complete 10-MJ facility has been adopted for the LANL LMC study as potentially affordable. This upper limit on the unit cost corresponds to a total facility cost of $2B for a 10-MJ facility. LANL is actively exploring cost tradeoffs and technology developments to find ways to further reduce the LMF cost.

There are several reasons to expect a decline in terms of constant dollars for unit costs for the technologies that are required for an LMF. Increased performance from equipment of the same physical size can be anticipated with considerable confidence in several areas. Increased understanding of the physics and engineering of large KrF laser amplifiers obtained during the design, construction, and operation of the experimental R&D facilities that precede the LMF can result in increased efficiency and greater energy densities. In some areas, better performance or lower cost may be developed. An example is pulsed power, in which replacement of pulse-forming lines with pulse-forming networks is a possibility. Continued research into damage mechanisms for optics can lead to much higher fluence capabilities. The R&D to develop materials that cost less and/or have superior properties, such as electron beam foils with high transmission and longer electron-beam lifetime, and optics with improved resistance to attack by fluorine, can help in many areas.

New mass production facilities may be needed because of the scale of the LMF and/or an increase in demand by other customers. These facilities may result in significant cost reductions for the LMF. Overhead, including amortization of capital investments in manufacturing capability per unit of production, is less for larger orders. Favorable scaling of unit costs with size or other measure of capacity is common. Manufacturing learning, which increases efficiency, improves quality and materials, and improves basic fabrication and assembly procedures, is also common. Improved design methods and physics and engineering analysis codes and models can permit designers to reduce safety margins and associated costs. Better fabrication processes and quality control can reduce costs substantially.

We have employed in-house expertise and contracted for independent industry help in preparing estimates of cost based on current technology and manufacturing capabilities and in assessing potential cost reductions from the factors listed above. These activities continue. Because of the

emphasis here on technology rather than costs, we only summarize current results of this cost projection process in Fig. 3. These results do provide encouragement that acceptable unit and total costs for an LMF can be achieved. We are currently examining designs which may result in significant cost reductions from these results.
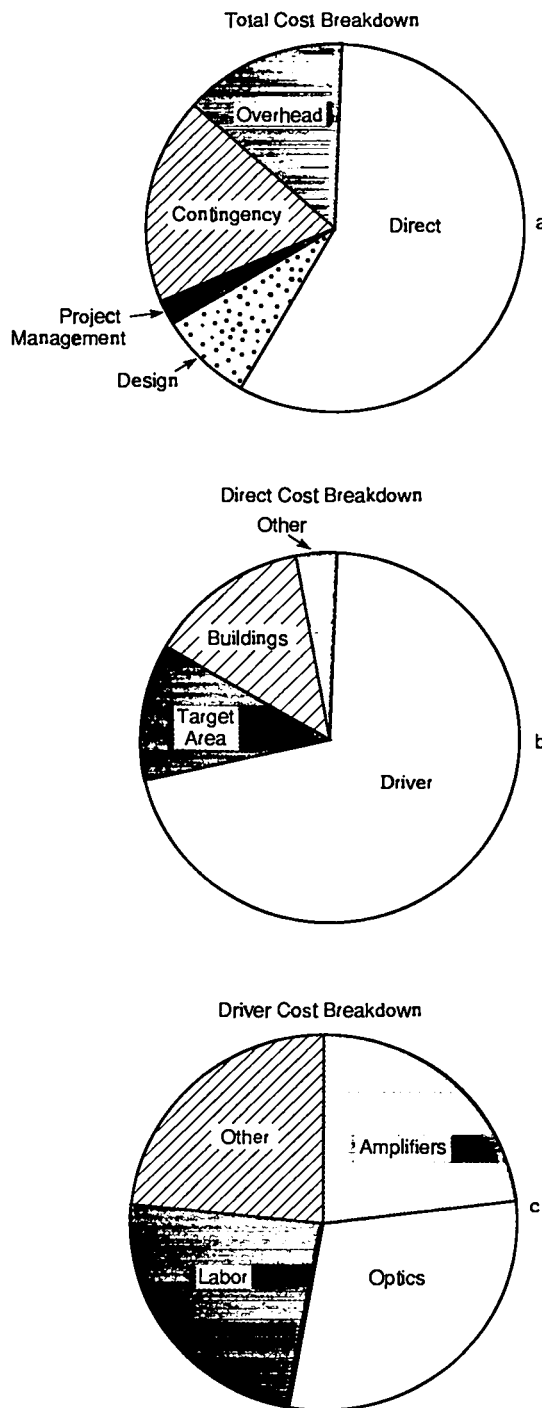

Fig. 3. Summary of results of detailed LMF cost studies in terms of costs for major categories.

Figure 3a shows the total LMF cost breakdown for the initial LMF conceptual design using the standardized costing methodology defined in the LMC Scoping Study Phase I final report (DOE/DP-1989). The preliminary cost estimate for the 10-MJ KrF laser is $1.75 B. Figure 3b shows the breakdown of the direct cost, showing where the leverages lie. Future iterations of the KrF driver for the design such that the high-leverage items are reduced.

Performance

Driver Pulse Energy and Target Yield

The maximum pulse energy that is considered desirable for an LMF driver is based primarily on our current experimental and theoretical understanding of target physics. The ignition and propagation of thermonuclear burn required for target gains ≥ 100 is a primary goal of the LMF. Estimates of the range of driver energies in which the onset of ignition and ever more complete burn propagation occurs involve considerable uncertainty. Nonetheless, the community of target designers appears to have reached consensus on the approximate range of driver energies required to access the ignition regime of target physics: one to a few megajoules.

A driver energy substantially above the estimated ignition range is desirable to ensure that the physics of interest can be accessed and thoroughly explored in the LMF. However, the projected cost of an LMF very large. The higher costs for driver capabilities significantly greater than the estimated ignition range must be weighed against the probability of success in exploring the interesting physics regime.

A secondary consideration in selecting the maximum driver energy for an LMF is the driver energies and target yields required for the various applications experiments that have been suggested. These experiments include nuclear-weapons physics experiments; weapons-effects simulations; studies of intense laser-matter interactions; investigations of the properties of materials; and energy transport at extreme temperatures, pressures, and densities. For these defense-related experiments, target yields up to 1 GJ are considered desirable (Hogan 1988). A driver pulse energy of 10 MJ and a target gain of 100 will give a 1-GJ yield.

Based on these considerations, the following values were selected in the LANL LMF concept: a maximum value of 10 MJ for the driver energy delivered to targets by the KrF laser and a maximum target yield of 1 GJ that must be accommodated by the target chamber. This value for the maximum driver pulse energy gives a reasonable margin of

performance over that believed to be necessary for the development of high-gain targets and is also projected to be affordable.

Types of Experiments and Shot Rate

An LMF service life of 25 years is assumed. The design shot rate for the LMF is based on estimates of the number of shots required to successfully develop high-gain targets, thoroughly explore the target design and physics parameter space, and meet the anticipated demand for applications experiments in a timely way. These deliberations led to a specification of an average of 1 high-yield (100 MJ to 1 GJ) shot per week for a total of at least 1300 and at least 5700 lower-yield (< 100 MJ) shots at 2 per day (Hogan 1988). This schedule could also include some experiments that use the laser without irradiating targets. If other applications experiments, down time for repairs or major-maintenance activities, and long setup times for some experiments are considered, somewhat higher shot rates per week will be desired at times to achieve the specified average shot rates. A breakdown of experiment rates and total experiments for the different classes of experiments that might be conducted in an LMF is given in Table 3.

Experimentation in an LMF following startup to achieve high target gains is expected to proceed roughly as follows. Many shots at various output energies will be required to thoroughly characterize the operation of the driver. Defense-related experiments that utilize only the laser light could begin during the early period of LMF operation and dummy targets could be used to begin to investigate target dynamics. Initially, modest gains and yields would be obtained with targets containing fusion fuel. Such low-gain, low-yield targets could be very useful in examining some of the details of target physics. Not all the defense-related experiments that would utilize target emissions require high yields or gains; low-gain, low-yield experiments could be started during this phase of LMF operation. Eventually, the successful development of targets that give high gains and yields would allow full exploration of ICF target physics, and the performance of other defense-related experiments.

TABLE 3. Experiment rates and total experiments over service life required to make an LMF
an acceptable facility, plus desired rates to make an LMF even more attractive.[†]

Experiment Category	Experiment Rate		Total Number of Experiments		
	All Yields	100 to 1000 MJ	< 10 MJ	10 to 100 MJ	100 MJ 1000 MJ
High-gain target development					
Required	>300/yr	>35/yr	>1000	>300	>100
Desirable	>600/yr	>50/yr			
Weapons-Physics Experiments					
Required	>500/yr	>50/yr	>1000	>3000	>1000
Desirable	>800/yr	>100/yr			
Weapons-Effects Experiments					
Source Development		>10/yr		>200	>100
Tests	>16/yr	>6/yr		>200	>100
Total*					
Required**	>500/yr	>50/yr	>200	>3700	>1300
Desired	>800/yr	>100/yr			

* Not all categories of experiments would be conducted at the same rate thoughout the service life of an LMF. For example, the
development of high-gain targets must precede some of the experiments that require large target yields. Therefore, the total
required rates are somewhat less than the sum of the rates listed for the individual experiment categories. The total
experiments required over the lifetime of an LMF is the sum of the experiments for each category.

**These requirements correspond to approximately 2 low-yield shots per day, 1 high-yield shot per week,
and a 25-year service life based on the requirement for high-yield shots.

†Hogan, 1988.

The primary utility of an LMF for nuclear weapons
related experiments is that it could permit certain
experiments to be performed at lower cost and at a rate that
meets nuclear weapons program needs in a more timely way
than underground tests. Comprehensive parameter studies
that take too long and cost too much with underground tests
may be feasible with an LMF. Measurements could be
made that are not feasible in underground experiments. ICF
offers a potentially important advantage over many other
above-ground experimental techniques for defense-related
experiments: larger objects can be exposed to meaningful
fluxes with a superior match to the spectra of radiations
from nuclear weapons.

Two classes of nuclear weapons related experiments
have received the most attention in developing the LANL
concept for an LMF: weapons-effects and weapons-
vulnerability experiments and weapons physics experiments.
The first class of experiments investigates the effects of the
outputs of nuclear weapons on materials and equipment that
are likely targets of such weapons, especially the
vulnerability of other nuclear weapons. The second class
further clarifies the basic physics of nuclear weapons. The
response of materials to high energy deposition densities and
radiation fluxes would be studied experimentally, especially
the materials inside nuclear warheads and NDEWs at energy
densities typical of nuclear. Properties important to the
theoretical modeling of such responses, including equations
of state and opacities and other radiation transport properties,
would also be measured.

Both of these classes of experiments require that objects
(some with large masses) be located relatively close to
targets, which could result in the generation of potentially
damaging missiles (shrapnel) by the rapid isochoric
deposition of target emissions at high energy density.
Some of these objects would contain fissionable material,
which may greatly add to the induced radioactivity and
complicate the design of the target chamber. More work
needs to be performed on the definition of experiments
before a target chamber concept can be finalized.

The output from ICF targets differs from that of nuclear
weapons, resulting in a requirement for some temporal,
spatial, and spectral modification of ICF target emissions to
approximate the output of nuclear weapons. Protection of
the experiments from the unwanted effects of ICF
microexplosions may also be necessary. It is desirable to
have the capability to make experimental measurements for

relatively long times after target microexplosions and to perform additional *in-situ* post-shot experiments. A preliminary experimental program would be required in an LMF to develop such conversion methods to provide radiation sources that match nuclear-weapons outputs with satisfactory fidelity. Continuing R&D will be needed to provide the measurement capabilities for the new experimental opportunities offered by an LMF.

Operability, Maintainability, and Reliability

The component count and the consequences of failure to meet operating schedules and to operate as intended will be much greater for an LMF than for existing ICF experimental facilities. Also, the operating costs will be much greater for an LMF than for existing ICF facilities. Therefore, an analysis of the operating characteristics of an LMF is essential to a rational assessment of its cost effectiveness. An LMF that is too often unavailable, is too unreliable, or has excessive operating and maintenance costs will not be considered attractive, however low its capital cost. Modest additional expenditures for equipment, maintenance, quality control, training, etc., to increase availability and reliability may greatly enhance the cost effectiveness of an LMF.

In the LANL studies, a great premium is placed on automating LMF operation to reduce the number of operating personnel required. Improvements are being sought in component life before failure, replacement, repair, and maintenance, as well as short down times, easy access, and low maintenance costs. Ways are being explored to achieve fast facility turnaround and setup of targets and applications experiments under ordinary operating conditions as an aid to meeting or exceeding the proposed LMF schedules.

Illumination Geometries

There are two primary families of target concepts: direct drive and indirect drive. The two classes may have different requirements for the optical quality of the beams used to drive them. Fortunately, the KrF laser driver for either drive concept is similar, if not the same.

The fuel capsule in a direct-drive target is illuminated directly on its outside surface by the driver beams. The compressive forces that implode the capsule must be highly uniform to compress the capsule to the densities needed for high gain. If the beams lack uniformity, instabilities develop that can seriously degrade target performance. In general, this means that the beams must have good beam quality and balance and must be distributed throughout the full 4-π solid angle around targets.

A technique called induced spatial incoherence (ISI) has been proposed to smooth beam profiles (Lehmberg and Goldhar 1987). In this technique, a beam cross section is divided into many smaller portions that are made mutually incoherent. Each portion can be made to focus to the same diffraction profile, provided the portions are small compared to the scale of transverse aberrations and to the optical apertures in the laser system. When the small portions of laser light are superimposed on a target, it can't respond on the time scale of the relative delays. The target only responds over a much longer time to the integrated energy deposition, which is much smoother over the beam footprint.

In indirect drive, the hohlraum combines the functions of the regular distribution of beams in 4-π, solid-angle, precise balancing of beam energy and the ISI beam-profile smoothing used with direct drive to obtain the required illumination uniformity. X-ray energy absorbed by the outer layers of the capsule causes it to implode.

One goal for the facilities that precede an LMF is to determine the best target illumination geometry for an LMF, or at least to narrow the number of geometries that must be explored at the LMF driver-energy scale. As facilities approach the LMF scale, the cost of providing more than one illumination geometry becomes increasingly expensive.

For now, we have assumed for the LANL LMF concept that the illumination geometry will be for three-sided indirect-drive targets. If some other illumination geometry is shown to be optimum by experiments in smaller facilities, the present LANL LMF concept can be switched over to that geometry with relatively minor changes. Even if the best geometry is not determined until experiments have been conducted in an LMF, only modest changes are necessary to the existing high-energy optics systems to deliver driver beams to target and to much of the experimental area equipment and structures, for example, the experimental area building and the target chamber. Much of the existing equipment and structures could be used for the new geometry. If ISI must be provided for direct drive, the added cost and complexity of the required equipment is not large.

Pulse Shaping

KrF laser technology offers a significant advantage in easily providing the complex temporal pulse shapes required to efficiently implode ICF targets. Pulse shaping may make the difference in obtaining high gain with affordable driver pulse energies. Other driver technologies have inherent limitations that limit the range of pulse shapes that

can be delivered and/or make flexible changing of pulse shape difficult.

Current theoretical and experimental studies indicate that to implode targets efficiently the shapes of the pulses of energy delivered to fuel capsules should typically include a long low-energy, low-power foot, followed by a smooth steep rise to a narrow high-energy, high-power peak. (This pulse shape can be approximated by a series of stepped pulses.) The details of the optimum shape depend on such factors as the driver energy delivered to the target and the target design.

In the past, it was believed that the best way to shape pulses from a KrF laser driver was to appropriately adjust the times of arrival of many short pulses of similar shape at a target so that their superposition gave the desired longer overall pulse shape. However, recent theoretical analyses at LANL indicate that pulses of the desired overall shape generated with great flexibility at low cost by the low-energy front end can be propagated without significant distortion through a chain of amplifiers of increasingly higher output energies if the amplifiers are operated in a continuously saturated mode. When the amplifiers are saturated, the lower-power portions of a pulse passing through them overlap previous high-power pulses and have the same gain as the higher-power portions of the pulse. If all of the beams delivered to a target have the same pulse shape, better drive symmetry will be achieved and the optical complexity of the system is reduced.

Both types of pulse shaping are being studied further as part of the LANL LMF and intermediate-facility conceptual-design studies. The newer approach to pulse shaping, which is promising when pure angular multiplexing is used for pulse compression, may not be possible with nonlinear pulse compression techniques, such as Raman and Brillouin.

Pulse Length

The length of the individually shaped or superimposed short pulses required to efficiently drive targets is determined by the width of the high-power peak of the complex pulse. Theoretical studies suggest that the optimum short-pulse length increases as the size of the target increases. The appropriate peak-power pulse length for 10-MJ driver pulse energies is estimated to be of the order of 10 ns, and this value was adopted for the LANL LMF driver concept.

Bandwidth

KrF lasers have the potential to deliver light with large bandwidths. Large bandwidths improve the coupling of the driver energy delivered to targets and increase the efficiency with which targets are imploded. Flexibility in varying the

bandwidth is of interest for target development and to determine commercial applications driver requirements. The goal for the LANL LMF driver concept, a bandwidth up to 0.5% or more, is based on preliminary theoretical analyses. More refined analysis and experimental results obtained in the ICF facilities that precede an LMF will determine the bandwidth requirements for a KrF laser driver for the LMF.

Prepulse

Prepulse (energy arriving on targets before the main pulse) can significantly degrade the performance of the target. Prepulse can be produced in several ways, including poor front-end contrast ratio, late-beam to early-beam crosstalk caused by small-angle scattering by optics, and amplified spontaneous emission (ASE).

The principal objective is to keep prepulse low enough to avoid the premature generation of plasma. Current target-design studies indicate that prepulse power should be no more than about 10^7 W/cm^2. By using high contrast front ends, controlling crosstalk by proper optical design, and controlling ASE in the larger amplifiers to acceptable levels by maintaining saturation, the required prepulse limits can be achieved.

Backlighting

One of the most powerful techniques for collecting data on target dynamics is time-resolved photography, in which x rays from an external source are passed through the target, instead of recording only x-ray photons emitted by the target. To be useful, the source of x rays must be very bright, very close to the targets, and light up when the targets are illuminated. At present, the best method of providing such an x-ray source appears to be the use of powerful tightly focused laser beams to heat a small amount of an appropriate material located close to the targets to temperatures at which it radiates strongly at the desired wavelengths. Up to 10% of the total driver energy may be diverted for this purpose in the LANL LMF design.

LANL CONCEPT FOR A KrF LASER DRIVER FOR AN LMF

In developing a conceptual design and estimating costs for a KrF laser driver for an LMF, most of the effort to date was concentrated on theoretical analyses and design tradeoffs, cost, engineering-feasibility, industry-capability, maintenance, and system-operability studies for the larger, more expensive, and often more highly stressed components. In particular, the main amplifiers and their support systems and the large optical components have

received the most attention to date. However, the smaller, less-costly equipment was also considered, and more attention is being paid to it now that some studies of the larger components have yielded significant results.

The equipment and structures required for a complete KrF laser driver at the LMF scale is described below. The facility uses pure angular multiplexing for pulse compression, main amplifiers that are pumped from both sides using electron beams with guide magnets, and a pulse-power system energized by pulse-forming lines. The description begins with the low-energy optical systems and amplifier train that provide the precisely timed and temporally shaped train of pulses that constitute the input to the main amplifiers. A description of the main amplifier systems that produce the high-energy pulses required to drive targets follows, and then a description of the optical systems that demultiplex, transport, and focus the pulses onto targets is given. Next, other driver subsystems, such as laser-gas handling, beam alignment, system control, beam and amplifier diagnostic, and other system instrumentation and equipment, are discussed. We conclude with a discussion of the high-energy beam enclosures, the needed prototyping, spares, and the driver building. Figure 4 is an artist's conception of the initial design of the entire LMF, which shows the main amplifiers located in the driver building, in addition to other major equipment and structures.
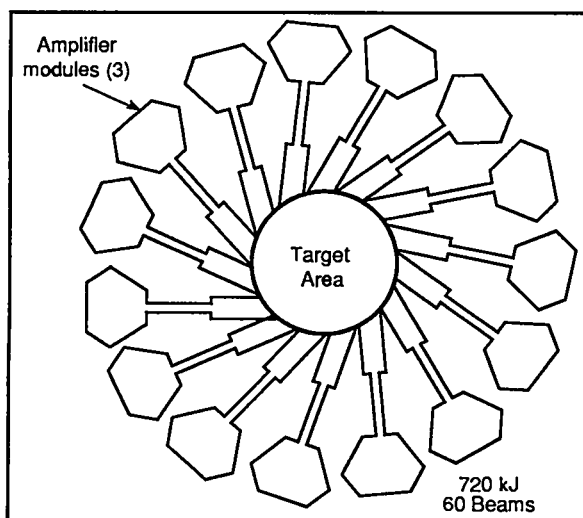
Fig. 4. Artist's conception of initial design of the entire LMF.

Low-Energy Laser Equipment

The low-energy driver systems begin with the front-end equipment that provides the input pulses for the entire driver system. A variety of optical components divide the pulses from the front end, angularly encode them, separate them spatially, time-encode them to form a train of head-to-tail short pulses, expand them to fill amplifier apertures, and relay them through a chain of amplifiers. Larger amplifiers downstream boost the pulse energies to the levels required for the inputs to the main amplifiers. All these systems require appropriate alignment, diagnostic, and controls systems.

Front End

The front end consists of a master oscillator and pulse-switchout, pulse-shaping, and bandwidth-broadening, equipment. Small amplifiers that boost the energy of the pulses from the master oscillator are also considered as part of the front end. The master oscillator is a small, precisely controlled laser that generates light at the 248-nm KrF wavelength or at a wavelength that can be transformed into the required wavelength. The short (10-ns) seed pulses required from the front end are extracted from the master oscillator by electro-optical pulse-switching equipment.

Equipment may be required in the front end to alter the frequency of the laser-light pulses extracted from the master oscillator, to adjust their bandwidth, to increase their contrast ratio, to shorten them and their ramp-up and ramp-down times, and to alter their temporal shape. For example, the pulse shapes can be adjusted in the front end by flattening the top of the pulse, by eliminating leading spikes, creating trailing spikes, or in more general ways. Small KrF amplifiers of conventional design can be used to boost the energy of the laser-light pulses from the master oscillator and/or at one or more points among the equipment in the front end.

A good front-end design is important for the success of an LMF with a KrF laser driver. However, the development of a detailed conceptual design for the front end of the LANL LMF driver concept has not received much attention to date. This is because there appear to be many promising options, none of which cost very much. Also, if changes are needed in the front end, even after final design and construction of an LMF, the time and cost required to effect them are not great. The most recent design for the AURORA front end has many of the necessary qualities (Thomas and Kurnit 1989).

TABLE 4. Summary of Los Alamos LMF amplifier staging from the main amplifiers (ultimate gain stage) upstream to the front end.

Gain-Stage Designation	Gain-Stage Amplifier Parameters					Overall Gain-Stage Parameters			
	Input Energy (k)	Output Energy (kJ)	Gain	Pump Time (ns)	Beams	Amplifiers	Input Energy (kJ)	Output Energy (kJ)	Beams
Ultimate (U)	32.7	240	22	750	60	45	432	10800	900
Penultimate (PU)	2.0	42	21	750	60	15	30	630	900
Antepenultimate (APA)	0.124	2.6	21	375	30	15	1.86	39	450
Preantepenultimate (PAPU)	0.024	0.72	21	188	15	5	0.12	3.6	75
Final common (FC)	0.008	0.24	30	188	15	1	0.008	0.24	15
Semifinal common (SFC)	0.0005	0.015	30	63	5	1	0.0005	0.015	5
Front end (FE)	–	0.001	–	10	1	1	–	0.001	1

TABLE 5. Summary of the characteristics, counts, and costs of the small optical components required in the low-energy part of the Los Alamos KrF laser driver concept for an LMF required to produce and deliver the precisely timed, temporally shaped, and wavelength-tailored pulse train used as input to the main amplifiers.

Optics Station Gain Stage and Station	Optical Element	Element	Element Size Diameter (cm)	Element Count Total	Cost of Elements (1000 $) Optics	Mounts	Total
FE01	beam splitters for 5-channel multiplexer	in front-end room of common driver buillding	12.8	4	4.8	1.4	6.2
FE02	beam-direction mirrors (flat)	in front-end room of common driver building	12.8	5	4.0	1.2	5.2
FE03	input-pupil-arrays mirrors (spherical)	in front-end room of common driver building	12.8	5	4.0	1.2	5.2
SFC01	beam splitters for 15-channel multiplexer	in common driver building	12.8	10	10.8	3.3	14.1
SFC02	beam-direction mirrors (flat)	in common driver building	12.8	15	10.8	3.3	14.1
FC01	FC-amplifier input-aray mirrors (spherical)	in common driver building	12.8	15	10.8	3.3	14.1

TABLE 5 (continued)

Optics Station	Optical Element	Element	Element Size	Element Count	Cost of Elements (1000 $)		
Gain Stage and Station			Diameter (cm)	Total	Optics	Mounts	Total
FC02	FC-amplifier window (flat)	front of FC amplifier	31.0	1	5.4	1.1	6.5
FC03	FC-amplifier back mirror (spherical)	back of FC amplifier	31.0	1	4.2	0.8	5.0
FC04	FC-amplifier output-array mirros (spherical)	in common driver building	15.6	15	14.0	4.2	18.2
FC05	beam splitters for 15-channel multiplexer	in common-driver building	15.6	60	79.4	23.8	103.2
FC06	beam-direction mirrors (flat)	in common-driver building	15.6	75	59.6	17.9	77.5
PAPU01	PUPU-amplifier input-array mirrors (spherical)	in PAPU-stage rooms of driver buildings	15.6	75	59.6	17.9	77.5
PAPU02	PAPU-amplifier windows (flat)	front of PAPU amplifiers	62.0	5	102.4	20.5	122.9
PAPU03	PAPU-amplifier back mirrors (spherical)	back of PAPU amplifiers	62.0	5	80.1	16.0	96.1
PAPU04	PAPU-amplifier output-array mirrors (spherical)	in PAPU-stage rooms of driver buildings	16.5	75	64.2	19.3	83.5
PAPU05	beam splitters for 30-channel multiplexers	in PAPU-stage rooms of driver buildings	16.5	375	460.6	138.2	598.8
PAPU06	beam-direction mirrors (flat)	in PAPU-stage rooms of driver	16.5	225	172.4	51.7	224.1
APU01	beam-direction mirrors (flat)	in APU-stage areas of driver-building basements	16.5	225	172.4	51.7	224.1
APU02	APU-amplifier input-array mirrors (spherical)	in APU-stage areas of driver-building basements	16.5	450	321.8	96.5	418.3
APU03	APU-amplifier windows (flat)	front of APU	62.0	15	275.1	55.0	330.1
APU04	APU-amplifier back mirrors (spherical)	back of APU amplifiers	62.0	15	215.3	43.1	258.4
APU05	APU-amplifier output array mirrors (spherical)	in APU-stage areas of driver-building basements	22.0	450	474.6	142.4	617.0
APU06	beam splitters for 60-channel multiplexers	in APU-stage areas of driver-building basements	22.0	450	952.3	285.7	1238.0

TABLE 5 (continued)

Optics Station	Optical Element	Element	Element Size	Element Count	Cost of Elements (1000 $)		
Gain Stage and Station			Diameter (cm)	Total	Optics	Mounts	Total
APU07	beam-direction mirrors (flat)	in APU-stage areas of driver-building basements	22.0	900	885.7	265.7	1151.4
PU01	PU-amplifier input-array mirrors (spherical)	in PU-stage areas of driver-building basements	23.3	900	959.0	287.7	1246.7
PU02	PU-amplifier turning mirrors (flat)	in front of PU amplifiers	196.0	15	719.6	72.0	791.6
PU03	PU-amplifier windows (flat)	front of PU amplifiers	165.1	15	4890.5	489.1	5379.6
PU04	PU-amplifier back mirrors (spherical)	back of PU amplifiers	165.1	15	2554.1	255.4	2809.5

Intermediate Amplifiers

The amplification required to increase the energy of the front-end output pulses to the level needed for the input to the main power amplifiers in the LANL LMF driver concept is accomplished in five stages. The designation adopted for these stages and some important characteristics of the amplifiers at each stage are listed in Table 4. The laser-light pulses are optically divided using beam splitters; then they are angularly encoded, time encoded, cleaned up, relayed between stages, and directed into and out of the amplifiers by mirrors. The required optical stations and their important characteristics are identified in Table 5. The amplifier staging and the required optical stations are illustrated schematically in Figs. 5 and 6.

Each of the first two stages of amplification employs a single amplifier. The output of the second of these amplifiers is split for distribution to the 15 individual driver-building arms; these arms contain the 45 main amplifiers that share optical apertures in groups of three. This is the reason for the designation "common" for the first two amplifier stages and the driver-building area that houses them.

The semifinal common-stage amplifier is single pass. The equipment for this amplifier includes (in addition to the input and output optics) a laser chamber and accessories; an input window and an output window; and laser-gas, pulsed-power diagnostic, instrumentation, and control systems.

The pulsed power for this amplifier features peaking circuits, instead of the pulse-forming lines used for the larger amplifiers in the train, and electron-beam lasing-medium pumping systems without the guide-magnets used for the other amplifiers. Otherwise, a similar concept is used for all the larger amplifiers (including the main amplifiers), for which a more detailed description in provided below.

The rest of the intermediate amplifiers are double pass. Detailed conceptual designs have not yet been prepared for each of the amplifiers that precede the main amplifiers, but their estimated costs are included in the total for the LMF. The main amplifiers are more expensive and call for larger extrapolations from today's technology. Calculations for the main amplifiers indicate that a broad peak in extraction efficiency occurs with a stage gain near 25. For this reason, all the intermediate amplifiers, as well as the main amplifiers, are designed to operate with gains in the range 20 to 30.

Optics

The optics and other equipment for pure angular multiplexing include angle encoding, time encoding, beam cleanup, and image relaying, optics amplifier input and output optics (including beam splitters), mirrors, mounts, supports, alignment actuators, and stepper motors. The corresponding equipment for AURORA has been described in the literature (Hanlon and McLeod 1987).
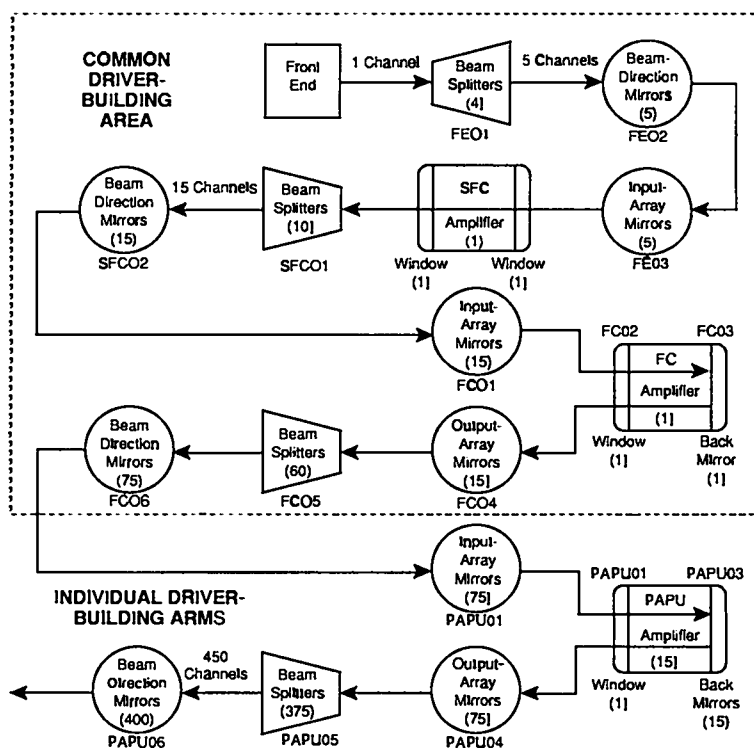
Fig. 5. Amplification stages and optical stations in low-energy part of LANL LMF concept.
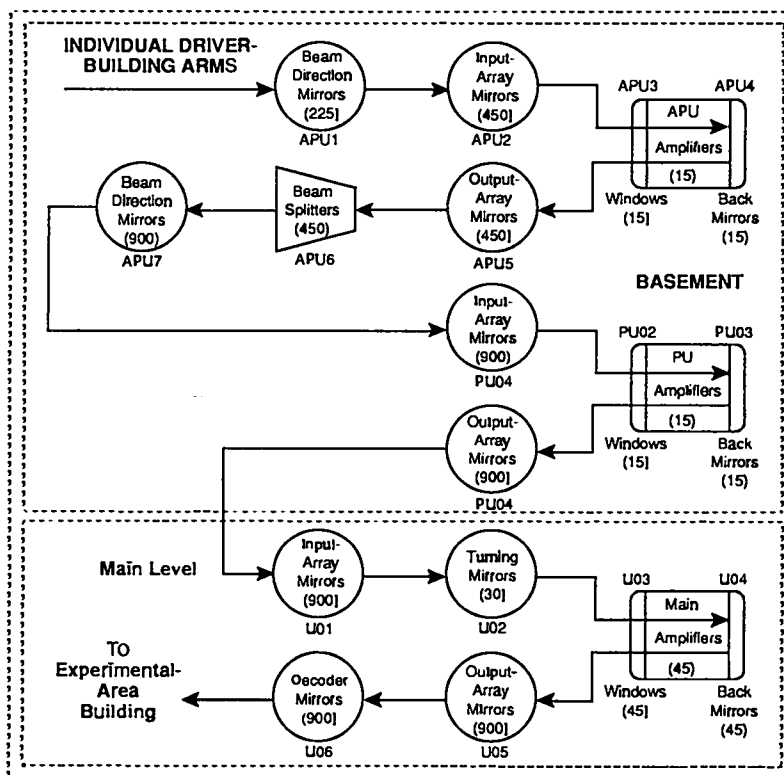

Fig. 6. Amplification stages and optical stations from the low-energy part to the high-energy part of LANL LMF concept.

A low-energy seed pulse with the appropriate temporal shape from the front end is divided by beam splitters into pulses of the same length but with lower energies. Further splitting occurs after all but the penultimate and ultimate gain stage. The number of beam splitters required at each station depends upon the desired increase in the number of channels between amplification stages and the number of beam-splitter stations between gain stages.

Each of the lower-energy beams is directed by mirrors along distinct optical paths (angle encoding) of different lengths. This permits the many short pulses to be delivered consecutively in time (time or temporal encoding) to amplifiers to synthesize the long pulse that can extract laser light energy throughout a long pump period for high efficiency. The short pulses can be delivered with no gaps between them or at intervals small in comparison to the KrF laser upper-state lifetime.

The separate identities of the short pulses are maintained as they are passed through several stages of amplification by directing them through the amplifiers at slightly different angles (angular multiplexing), using arrays of distinct input and output mirrors for each short pulse. The input beams are expanded by weakly powered spherical mirrors to fill the amplifiers whose apertures must be much larger to supply the output energies and to accommodate the output intensities that result from large stage gain.

The input-array mirrors must be located far from the amplifiers to keep the angles small enough so that each short pulse extracts nearly all the volume. Otherwise, amplifier efficiency is decreased in proportion to the fraction of the unextracted volume and by increased ASE in the portions of the unextracted pumped volume. Also, if the optics are located close to the amplifiers, then the aberrations introduced by spherical mirrors, which are preferred because they cost less than aspherical ones, may be too large. In addition, the long flight paths isolate the gain stages to prevent parasitic or retroreflection amplification. On the other hand, the angles must also be large enough to prevent small-angle scattering of laser light by amplifier optical from channels for late pulses into channels for early pulses (crosstalk). Small-angle scattering can result in excessive prepulse being delivered prematurely to targets. These angles (typically only a few thousandths of a radian) play a large part in determining the sizes, relative locations (typically 100 to 200 m from the amplifiers), and feasible groupings of amplifiers and optics. Because of the importance of small-angle scattering in determining optical layouts and the necessity to determine such scattering experimentally, small-angle scattering is being examined in parallel with damage threshold in an experimental program to develop improved optical coatings.

The locations of the mirrors in input and output arrays typically do not correspond in a systematic way to the chronological order of arrival of the short pulses at the arrays. This permits more uniform energy extraction by all beams in time and space of energy from the pumped volume of the amplifier and reduces ASE. In addition, configurations that employ fewer turning mirrors to direct beams have become possible. The input and output mirrors may be interspersed on the same array mount to reduce mount costs.

The beams enter the amplifiers through large flat windows that separate the lasing medium from the helium in which the beams are transported between amplifiers in the LMF. These long focal-length spherical mirrors redirect the beams back through the pumped volume for additional amplification and out the window and reduce the size of the beams delivered to in the output array mirrors. The array of output mirrors must be weakly powered to recollimate the beams for relay (through beam splitters after several of the intermediate amplification stages) to the next amplifier stage. These spherical mirrors are located at approximately the same distance from the amplifiers as the input mirrors. One or more sets of flat mirrors may be required to change the directions of the beams between amplifiers.

The sizes of the optics do not change rapidly from gain stage to gain stage, certainly not in proportion to the gain per stage. This occurs because of the many subdivisions of beam energy as a result of beam splitting and also because the damage threshold is not closely approached in the low-energy part of the laser system. The segmented windows, amplifier back mirrors, and the large turning mirrors required for aperture sharing for the main amplifiers are described in more detail in the Main Amplifier section.

Another guiding principle in the design of the optics for a KrF laser driver is that square optics may be more expensive (per unit area) to make and mount than round optics. Therefore, a round optic with an area not utilized by a square beam may be less expensive than a square optic with little wasted area. That is why the LMF includes round optics in many places.

Main Amplifiers

The 45 KrF main amplifiers in the LANL LMF driver concept are configured in groups of three that share input and output optics. An artist's conception of the overall layout of the three-amplifier groups in the driver building is shown in Fig. 7, and some of the details are given schematically in Fig. 8. Aperture sharing provides an additional stage of beam splitting to reduce from 2700 to 900 the number of beams needed to extract energy from 15

sets of three amplifiers. It makes the number of input and output optics manageable and their size and cost affordable. The additional optics station needed to split and turn the beams involves only a single large component for two out of each group of three main amplifiers—a total of 30 for the entire LMF. This arrangement allows the matching of square optics for input, output, and downstream beam transport to the 3:1 optical aspect ratio of the main amplifiers.

This arrangement also permits more efficient utilization of space within the driver building and results in additional cost savings. The pulse-forming lines must join the electron-beam pumping system at an angle of 30° to maximize the utilization of space within the driver beams.

Pulsed-Power Systems

The main amplifier pulsed-power systems deliver large pulses of high-voltage electrical energy to electron-beam diode that pump the amplifiers from both sides (Rosocha and Riepe 1985; Sullivan 1987). The pulse-power equipment includes an initial energy storage section, a pulse-shortening energy transfer section, an output section, fluids support systems, handling and special maintenance equipment, and diagnostic and triggering systems.

Marx generators provide the initial energy storage of the electrical energy fed to the pulse forming lines.

The pulse-forming lines shorten the electrical pulses from the initial energy-storage section. The pulse-forming line concept used for the main amplifiers of the LANL KrF laser driver is illustrated in Fig. 9. The use of planar central conductors in a rectangular tank of degassed and deionized water makes the maintenance of the pulse-forming lines much easier than for the coaxial geometry used on AURORA. New materials and designs may make pulse-forming networks more cost effective for large KrF amplifiers of the types under consideration. Pulse-forming network technology is being investigated for its potential use in an LMF with a KrF laser driver.

The output sections of the pulsed-power systems consist of short transition sections (including bending and impedance matching) to interface the pulse-forming lines to the bushing and e-beam diode equipment. The transition section with a 30° bend is illustrated in Fig. 8. One option for the output switches are rim-fired, gas-insulated, laser-triggered switches with the laser optics enclosed within the central conductor structure of the transition section. Rail-gap switches are also being considered. Current-return conductors and accessories complete the pulsed-power circuits.

The pulsed-power triggering systems consist of special heavy-duty circuits and electronic equipment to initiate the operation of the switches in the pulsed-power equipment, plus interfaces to the overall driver control systems. The triggering must be synchronous with the triggering of other laser equipment, or with appropriate lead times or delays.

Electron-Beam Pumping Systems

The main amplifier electron-beam pumping systems generate the pulses of high-energy electrons that pump the lasing medium (Rosocha and Riepe 1989; Sullivan 1987). These systems are illustrated schematically in Fig. 10. They include cathode and anode structures, guide-field magnet systems, vacuum housing and pumping systems, supports, and special maintenance and diagnostic equipment. The main amplifiers are pumped from both sides to promote energy-deposition uniformity across the pump volume. The measures taken to ensure acceptable beam uniformity over the cross section of the electron beams in the laser chamber are discussed below.

The e-beam diodes in the conceptual design for the main KrF amplifiers represent a significant extrapolation in area, voltage, and total current from AURORA LAM diodes. A comparison of these design parameters for AURORA and for the LANL LMF concept is presented in Table 1. One of the principal design issues for the main amplifiers is the choice between monolithic cathodes and segmented cathodes in the electron-beam systems. The current choice for the main amplifier cathode in the LANL LMF concept is a monolithic structure with a velvet cold-cathode emitter surface on aluminum and enclosed in a vacuum housing.

The two considerations that drive the interest in monolithic cathodes are a modest cost savings and the possibility of greater system reliability through a reduction in component count and overall complexity. That either or both of these advantages can be realized has not yet been established. A principal issue whether emission over large monolithic cathodes is uniform. One of the primary recommendations of the working groups at a recent workshop (Honig and Kristiansen 1989) that addressed this question was that segmented diodes, with segment areas about the same as the monolithic cathodes in use today, could be used without guide-field magnets. In addition to the information gained from experiments with the AURORA diodes, both external and in-house design and R&D programs have been initiated. Improved emitter surfaces are expected in the near future. The principal improvements sought include longer service life before replacement and reduced exfoliation of fibers. This issue of optimum pump architecture is still unresolved.
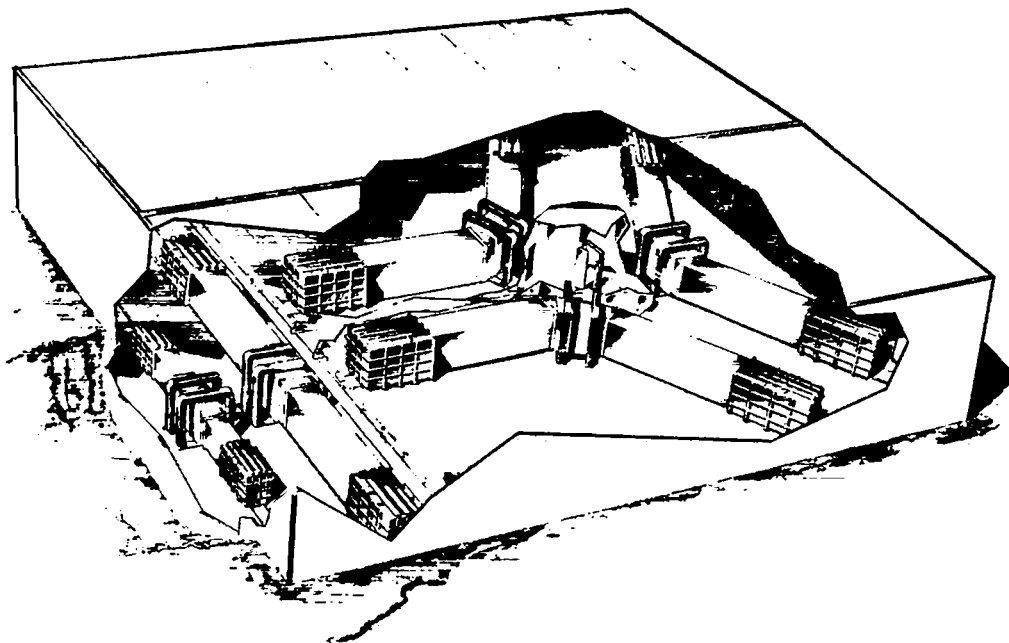
Fig. 7. Artist's conception of three main amplifiers (or ultimate gain stage) that share apertures, together with the single penultimate gain stage and antepenultimate gain stage amplifiers that drive them, in one of the 15 arms of the driver building.
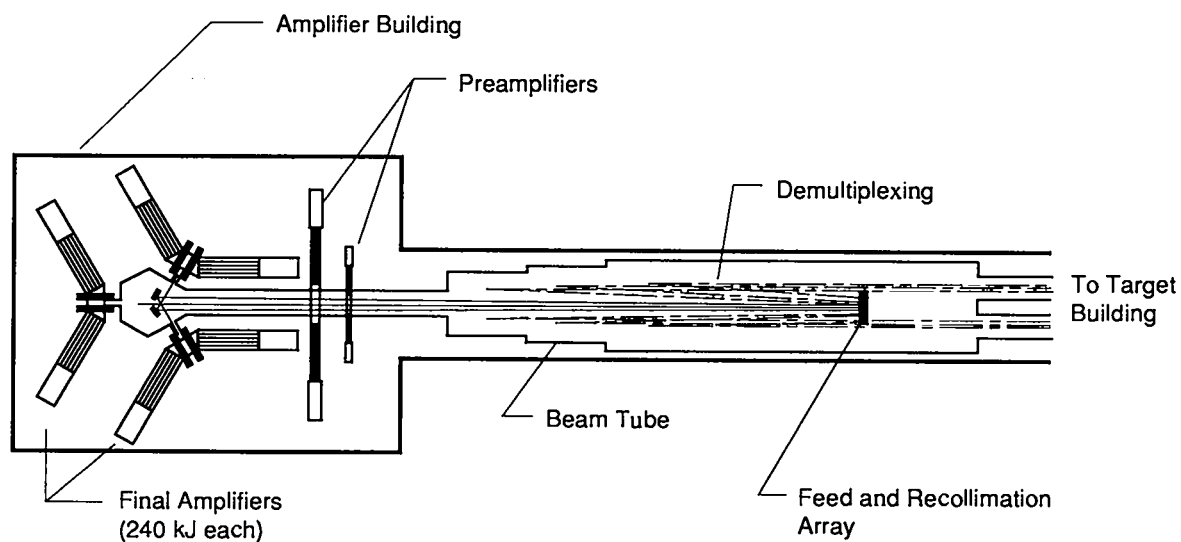

Fig. 8. Details of layout of main amplifiers and time decoder optics in a driver-building arm.
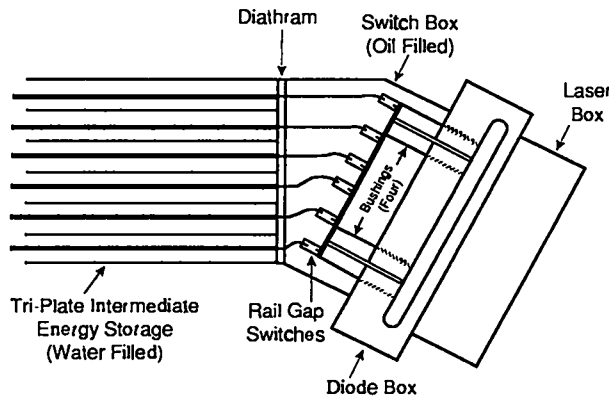
Fig. 9. Transition between main amplifier pulse-forming line and electron-beam diodes showing 30° bend.
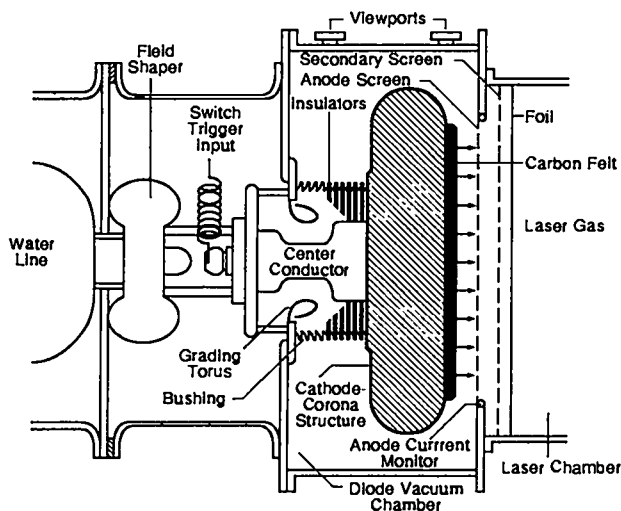
Fig. 10. Main amplifier electron-beam equipment.

The magnetic fields generated by the electron beams from large monolithic cathodes can produce beam pinching. To control this problem, large electromagnetic coils are placed around the electron-beam in the main KrF amplifier to provide an external guide field. These are shown in Fig. 7. The magnetic field generated by such coils must be relatively uniform and very strong (of the order of 0.5 Telsa for the LANL concept). The currents required to generate such fields are large and the cross-section of nonsuperconducting coils to carry this current with acceptable resistive losses is correspondingly large. The coils would be operated in a pulsed mode. The power required during the time the coils are activated is also large.

Chambers

The main KrF laser amplifier chambers in the LANL LMF driver concept are rectangular vessels that must resist both internal and external pressure loading and the loading imposed by the strong fields of the main guide magnets. They are illustrated in an artist's conception in Fig. 7 and schematically in Fig. 10 with more detail. Prior to a shot, the pressure in the laser gas will be approximately that of the local atmosphere. During a shot, the electrical pump energy that is not converted to laser energy will cause a transient pressure rise of a fraction of an atmosphere. When the laser chambers are evacuated to remove the lasing medium, they must be able to resist buckling under an external pressure loading of essentially a full local atmosphere.

The amplifier chambers must provide stable platforms for the optics integral with them, for example, the window at the front of the chamber and the mirror at the back of the chamber. Thus, the support structure for the chambers must be massive and be designed for control of vibrations. When the main guide-field magnets are energized, the back mirrors may move in response to the strong magnetic field that is generated. Their mounts must be designed to allow the real-time realignment that must be accomplished after ramping up the magnetic field. This is currently done on the AURORA Facility, and various similar technologies will be employed. Parasitic oscillations will be controlled by special antireflection coatings and baffles in the shadow of the hibachi structures and on the unoccupied areas of the laser-chamber top and bottom.

Amplifier Optics

Although they are relatively few in number, the main amplifier windows and back mirrors represent a substantial fraction of the total cost of the optics for an LMF. Their costs and some of their characteristics are summarized in Table 6 and illustrated in Fig. 11. The corresponding optics for AURORA have been described in the literature (Hanlon and McLeod 1987; McLeod 1987).

TABLE 6. Summary of the characteristics, counts, and costs of the large optical componenets required to produce the high-energy beams in the main KrF laser amplifiers of the Los Alamos LMF driver concept and to transport, aim, and focus them onto targets from the input of the forty-five main amplifiers configured in three-amplifier modules.

Optics Station	Optical Element	Element Location	Element Parameters	Element Size	Element Count		Cost of Elements (1000 $)	
Gain Stage and Station			Shape, Figure Segments	Diameter or Long Side (cm)	Total	Optics	Mounts	Total
U01	main-amplifier input-array mirrors	ends of driver buildings opposite main amplifiers	1.21:1 rectangle, flat, 1	40.0	900	2,096	419	2,515
U02	main-amplifier turning mirrors	center of three aperture-combined main amplifiers	2.10:1 rectangle, flat, 6	465.0	30	6,381	638	7,019
U03	main-amplifier windows	front of main amplifiers	2.00:1 rectangle, flat, 6	465.0?	270	46,405	4,640	51,045
U04	main-amplifier back mirrors	back of main amplifiers	2.00:1 rectangle spherical, 6	465.07	270	23,347	2,435	26,782
UO5	separation-array mirrors	ends of driver buildings opposite main amplifiers	1.21:1 rectangle, spherical, 1	87.0	900	7,144	1,429	8,573
U06	demultiplexer mirrors	along sides of driver buildings	1.21:1 rectangle, flat, 1	87.0	900	7,144	1,429	8,573
T01	delay mirrors for half of beams	in experimental area building	1.21:1 rectangle, flat, 1	87.0	450	3,828	766	4,594
T02	optical-switchyard mirrors	in experimental area building	1.70:1 rectangle, flat, 1	110.0	900	10,567	1,057	11,624
T03	beam-direction	in experimental area building around chamber	round, flat	110.0	900	10,567	1,057	11,624
T04	beam-aiming mirrors	in experimental area building around chamber	round, flat, 1	95.0	900	8,265	1,653	9,918
T05	vacuum-window focusing lenses	in target-chamber wall	round, lens, 1	87.0	900	47,270	9,454	56,725
T06	final turning mirrors	on inside wall of target chamber	round, flat, 1	180.0	900	24,680	2,467	27,148
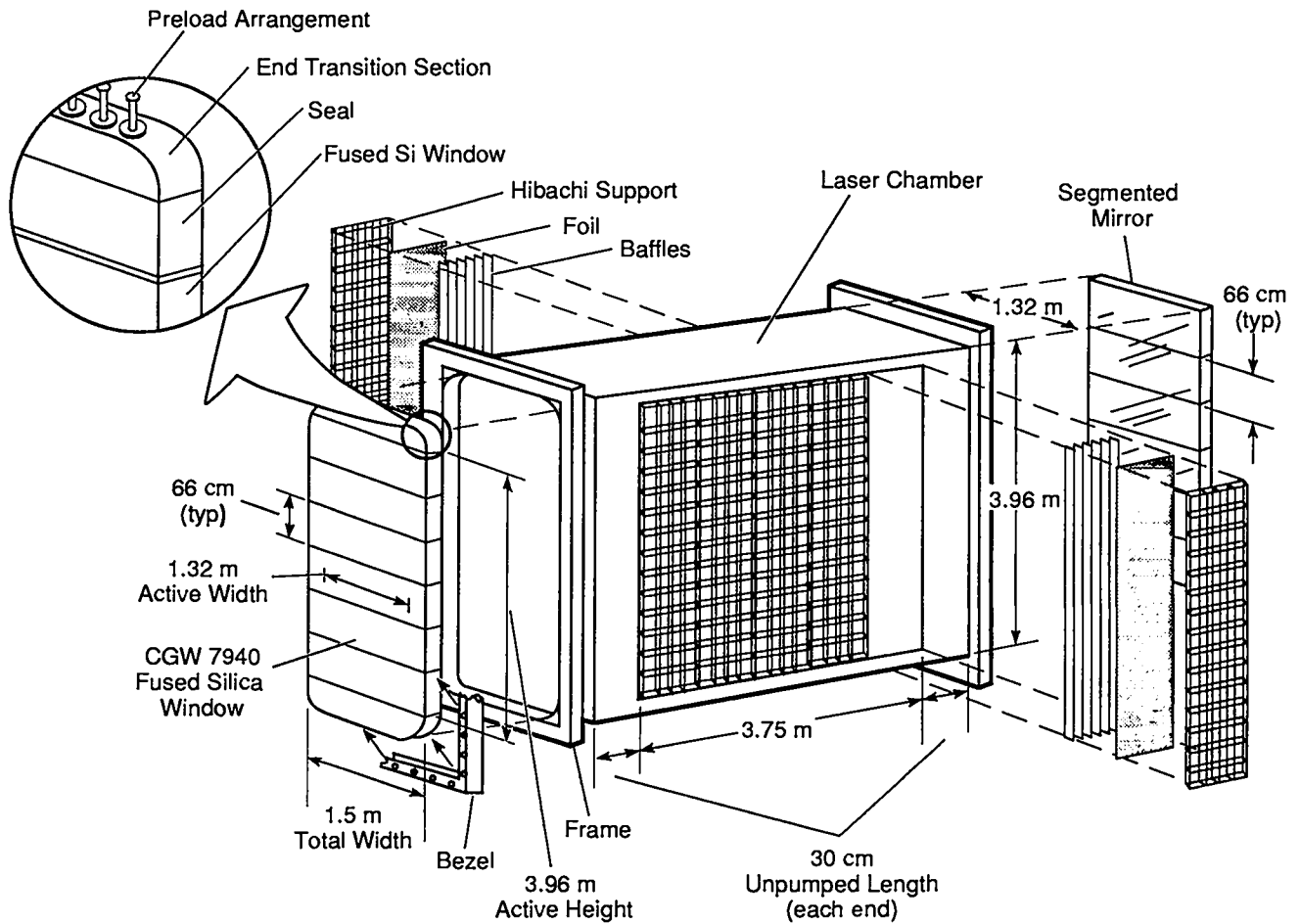
Fig. 11. Main amplifier chamber with interfaces to electron-beam equipment and integral optics.

Low thermal expansion, high strength, and resistance to color center formation are important considerations for the window material. Although fused silica is the current material of choice for the main amplifier windows, other window materials are still being considered. They include single-crystal materials with fluorine as a constituent for better substrate resistance to the lasing medium. These materials can be grown in large-plate geometries by edge-crystallization methods under development in industry and could be available by the time an LMF is built.

Sizes near those currently available for window blanks limitations may persist for the LMP. Therefore, we conservatively assume that the windows and mirrors for the main amplifiers in an LMF would be segmented, and the size would not far exceed the largest size that is currently produced and used on AURORA. The windows are rectangular, with an aspect ratio of 2:1 (1.5-m diagonal); they are about 10-cm thick. For comparison, the length of the diagonal of the AURORA main amplifier window is also about 1.5 m and its thickness is 7 cm.

The mounts for the main amplifier windows must support them without distortion under gravitational loading. The window mounts must also prevent damage to these optics from the one-sided impulsive pressure loading by the lasing medium and the thermal loading caused by deposited laser light energy and thermal energy transferred from the hot lasing medium when the laser is fired. The windows may need to move and expand in response to this loading. Special equipment would then be required to automatically adjust, and perhaps also reseal, the windows after every shot.

The joints between the segments intercept more laser light than their total geometric cross section would suggest because the beams are directed into and out of the amplifiers at an angle and must pass through the windows twice. In addition to the beam energy loss, ASE from unextracted regions in the shadow of the joints is a concern. We have developed a design for the main amplifier windows that does away with thick sashes for mechanical support at the joints. This concept is illustrated schematically in Fig. 11. The pressure loading is supported at the ends of the

segments 1.5 m in length, that span the 1.3-m window opening. The joints require only thin seals.

The back mirrors are also segmented (with the same segmentation as the windows) and must be spherically figured. However, their design in many respects is not so difficult as that of the windows. The substrates can be made of any suitable low-expansion mirror material. The high-reflection dielectric coatings require many more layers than the windows, but they also provide more protection for the substrate from attack by the laser-gas mixture. The joints need not be sealed against a pressure differential. They are exposed to beams passed through the amplifier only once and at only one surface.

Laser-Gas Systems

The amplifiers must be supported by equipment to receive, store, and mix the chemically aggressive and hazardous lasing medium and to fill and empty the laser chambers. A single central laser gas facility could serve all the smaller amplifiers and all of the main amplifiers, but a separate module to serve the amplifiers in each laser-building arm makes more sense. A schematic of the major items needed, all relatively conventional process equipment, is presented in Fig. 12. A detailed study of the requirements, equipment, and costs for the gas systems for the LMF is under way.

Figure 13, in which the measured effects of common contaminants on KrF laser performance are summarized, gives an indication of the necessity for constraining the contaminants in the lasing medium at very low levels to achieve high laser efficiency. Also, organics, such as the vapors from lubricants and plasticizers outgassing from polymeric materials, must not be allowed to contaminate the laser gas.

The resources, sources, quantities, and costs for some of the gases required for operation of an LMF, including the lasing-medium constituents, are given in Table 7. The estimates of the annual consumptions are based on reasonable assumptions of the amounts required to fill LMF equipment, such as the smaller amplifiers and the laser-gas support systems, and to the main amplifiers. Losses during purification, ordinary leakage, and losses when access for maintenance is required are also accounted for. The quantities of fluorine required are small and it is less expensive to dispose of it in an approved manner than to repurify and recycle it. The krypton requirement is relatively large in comparison to current production rates, and it has a high unit cost. However, krypton is relatively easy and inexpensive to separate, clean up, and reuse , and production rates could be increased substantially if the demand were there.

Main Amplifier Input and High-Energy Output, Decoder, Transport, and Targeting Optics

The high-energy optics consist of a large number (several stations for each of 900 beams) of large (approximately 1-m diagonal) optics. The high-energy optics as a group operate at the highest average fluences (≤ 5 J/cm^2) in the laser system. Much of the published discussion of the corresponding optics for AURORA applies to the LMF optics (McLeod 1987). This fluence is a reasonable extrapolation from today's values, based on recent increases in coating damage thresholds. The number of channels in this section of the driver optics could be reduced significantly only if the conservative size assumed for these optics could be substantially increased. The size of the optics that can be produced cost effectively at the time the LMF is built cannot be predicted now. We also discuss here briefly the input optics for the main amplifiers, including the turning mirrors used to split the main amplifier input beams and direct them into the amplifiers.

The total cost for these optical components is so large that extensive efforts have been made to find ways to substantially reduce their cost. A summary of some of the important characteristics of the optics in this group and an estimate of their costs are presented in Table 6. The optics are illustrated in Fig. 14. The cost estimates in Table 6 are for the equipment only and don't include installation, integration, and indirect costs. In preparing the cost estimates, all the possibilities for cost reduction mentioned in the Introduction were considered.

The cost estimates for the high-energy flat mirrors also assume that they are of a novel lightweight design (Hextek) developed over a period of several years at the Mirror Fabrication Group of the Astronomy Department at the University of Arizona. The mirror blanks are fabricated by fusing at high temperature short sections of Pyrex tubing in a closest-packing array to one side of a flat Pyrex plate. The plat is much thinner than a conventional monolithic mirror blank of the same stiffness as the Hextek mirrors. The weight of the completed blank is much less than that of an equivalent monolithic blank. The blanks have been successfully polished and coated to produce mirrors of high quality that are currently in use on AURORA.
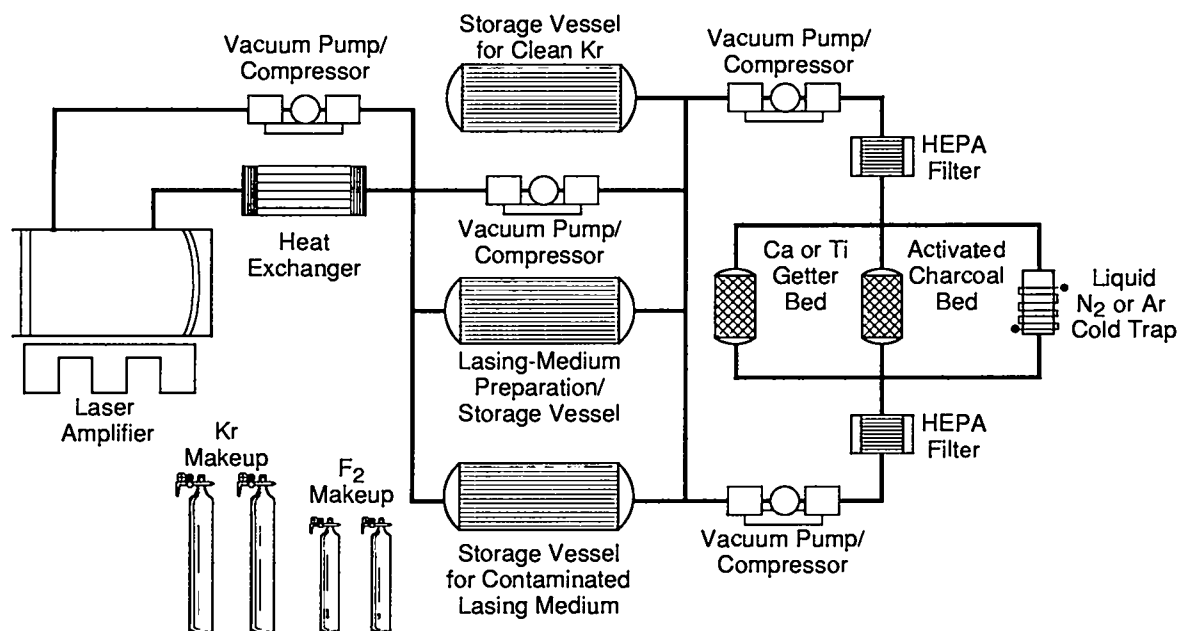
Fig. 12. Laser gas equipment.

TABLE 7. Resources, stockpiles, production rates, and annual sales versus LMF requirements and costs and delivered purity for helium, krypton, and fluorine (1985 sales, resources, and stockpiles; 1988 delivered costs).

Gas	Initial Requirement and Annual Makeup (std m³)	U.S. Combined Domestic and Export Annual Measured Sales (std m³)	Cost of U.S. Government Resource (std m³)	U.S. Purity as Stockpile (std m³)	Initial Inventory & Supplied (%)	Unit Cost ($/std m³)	Annual Makeup (M$)
helium (He)	3.30×10^5 2.63×10^5*	5.30×10^8 (3,3,5,23, 1,1 ppm of H_2O, O_2, N_2, Ne, H_2, THC)	6.76×10^9 0.526	1.04×10^9	99.997	2	0.660
krypton (Kr)	1,600 160**	2,500	1.14 ppm in air	99.995 (3,3,5,25, 3,1 ppm of H_2O, O_2mN_2, (Xe,CO_2,THC)	1500	2.400 0.240	
fluorine (F_2)	5 60***	40,000	3 to 4% in phosphate rock	98	100	0.001 0.006	

* Assumes 0.1%/day normal leakage and 1% loss/maintenance access every 10 days.
** Assumes 10% loss/year.
*** Assumes 100% turnover per month.
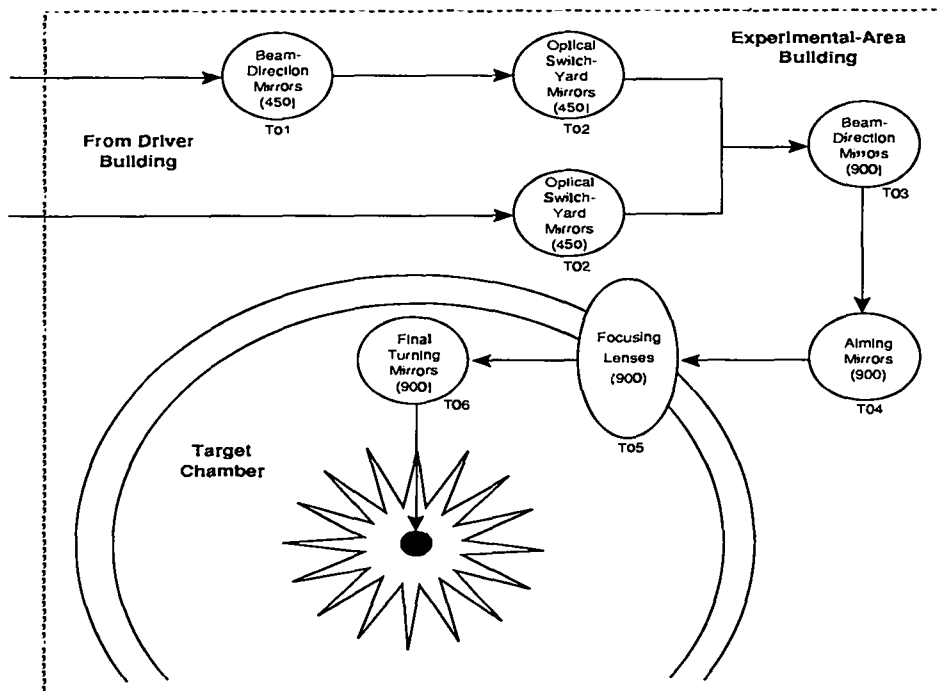
Fig. 14. Optical stations in experimental area of LANL LMF concept.
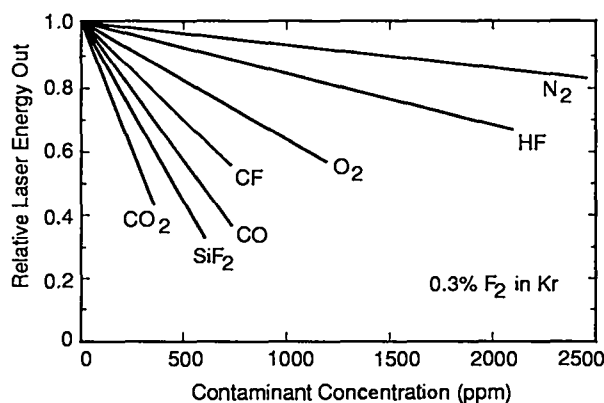
Fig. 13. Effects of common lasing medium contaminants on KrF laser performance.

In order for three LMF main amplifiers to share apertures with the input and output mirror arrays, they must have matching aspect ratios. The square beams directed toward the amplifiers must be split into three equal vertical strips three times as high as they are wide to match the aspect ratio of the amplifier windows. As illustrated in Figs. 6 and 7, this is accomplished using two mirrors (for an LMF total of 30) of the same height as the amplifiers but wider, because the input beams must strike them at a 60° angle. These mirrors intercept and redirect into two amplifiers one-third of each input beam from both sides. The central portion of the input beam passes between the

two turning mirrors into the third amplifier of the group of three. Thus, for a set of three main amplifiers, 60 square input beams are split into 180 3:1 aspect-ratio beams, and 60 are passed through each main amplifier. The rectangular beams emerging from the main amplifiers are then recombined into 60 square output beams by the same mirrors and sent to the recollimator arrays.

The 900 recombined and recollimated main amplifier output beams are directed by the output array along the arms of the driver buildings in the general direction of the amplifiers. A separate Hextek mirror located along the outside walls of the beam enclosures provides an optical path of different length for each short pulse; the path reduces some of the time differences introduced by time encoding. Not all of the time decoding is done here because the optical paths for delivery of beams to targets from different sides and at different angles are of different length. The decoder mirrors direct the beams back down the driver-building arms toward the central experimental area building.

Half (450) of the beams entering the experimental area building, shown in Fig. 5C, are sent directly to an optical switchyard with a mirror for each beam to be routed as required for delivery to target. The other half of the beams entering the experimental area building pass to the opposite side of the building from where they enter. There, a mirror sends the beam to an optical switchyard. In this optical switchyard (as in the other switchyard), each of these 450 beams is directed by a separate fixed mirror. A mirror for each of the 900 beams located around the outside of the

target chamber in the experimental area building turns that beam toward a separate aiming mirror that can be adjusted by the automatic targeting system. This mirror aims it at an angle of approximately 60° from the normal to the spherical target-chamber surface toward a lens for each beam that is mounted in the target chamber wall.

The lens, which is located in a cylindrical penetration through the target chamber wall, is shielded to protect the lens from target emissions. The lens is moved by the targeting system to focus the beam for delivery to target. The lens also serves as the vacuum barrier for the beam line interfacing with the evacuated target chamber. Each beam then strikes a final mirror inside the target chamber that turns the beams toward the targets. This last mirror must be in the direct line-of-sight to the targets. The last two optics in the high-energy chain that delivers the driver energy to target are illustrated schematically in Fig. 15. More discussion of the reasons for this arrangement and the methods adopted to protect the lenses from target emissions are presented in the section on the LANL experimental area concept for an LMF with a KrF laser driver.

Alignment

Alignment and focusing systems must rapidly counter any drift of alignment in the driver optical components, eliminate the disturbances resulting from the effects of firing the laser and target microexplosions, and aim and refocus the driver onto new targets. The following equipment is required for alignment and focusing of optics: beam-position sensors, stepper motors, low-backlash micropositioners and mechanical linkages on selected adjustable optical components, low-power alignment lasers, beam-position sensors, microcomputers and peripherals, displays, oscilloscopes, image analyzers, data-transmission lines, control systems, and interfaces to the driver control systems.

The optics at many of the stations are aligned only infrequently, after which they are fixed in position. Arrays of optics typically will be mounted on a single rigid frame that preserves their relative locations for long periods of time so that the optics can be manipulated as a single unit. Adjustable mounts with microradian pointing accuracies that meet all requirements have been designed at LANL.
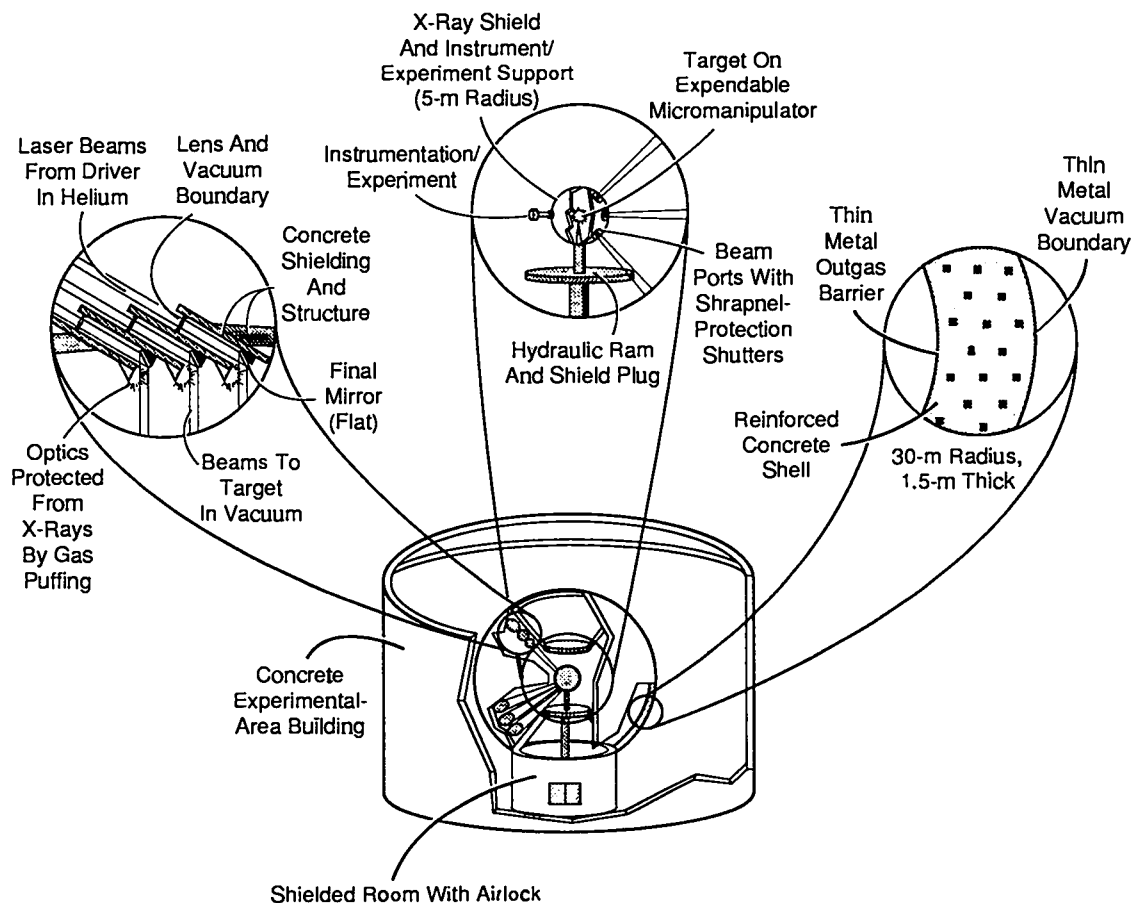

Fig. 15. LANL LMF target-chamber optical layout concept in experimental area building.

An award-winning microcomputer-controlled alignment-system design was developed at LANL for AURORA to automatically align a large number of optical channels in a short time and then update the alignment periodically thereafter (Kortegaard 1987). The sophisticated software to operate it also was developed at LANL. This alignment system design uses inexpensive electro-optical components in innovative ways to achieve outstanding results. There is a continuing project at LANL to improve this concept to meet the even more stringent requirements for future ICF drivers.

Diagnostics Systems

Diagnostic systems, in addition to the ordinary instrumentation needed for operation, are required to continuously monitor the status of much of the driver equipment (Rosocha and Riepe 1987). A record of the performance of the driver as a whole and its subsystems individually can aid in diagnosing malfunctions and substandard performance and determining when preventative maintenance is required.

For the pulsed-power subsystem, the parameters of interest include stage and overall voltages, stored energy, inductance, series resistances, jitter, actual peak current and charge transfer, and short-circuit current and charge transfer. For the electron-beam systems, vacuum, charges, voltages, currents, jitter, and electric and magnetic fields are parameters of interest. Prior to shots, the lasing medium in amplifiers must be monitored for composition, including impurities, plus thermal uniformity. After a shot is triggered, it will be desirable to also measure and record the variables needed to analyze laser-gas composition, pressure, temperature, volumetric energy deposition and power, pumping efficiency, extraction efficiency, gain, ASE, parasitic oscillation, etc., as functions of time and position after triggering a shot. Some of these measurements are extremely difficult to obtain and will require sophisticated and expensive equipment.

Beam Enclosures

Special enclosures are needed to provide stable, uniform low-loss paths for the propagation of the laser beams. Some of the issues as they apply to AURORA have been discussed in the literature (Bowling et al. 1987). The enclosures are relatively small, simple, and inexpensive in the low-energy portion of the amplifier chain, but they are larger and more expensive in the high-energy part of the driver and targeting systems. The enclosures include tubes,

ducts, halls, rooms, and other structures that are insulated to stabilize temperature distributions within them. The required equipment includes special environment-control systems, such as heat exchangers, baffles, gas flow directing equipment, blowers, fans, drives, instrumentation and controls, etc., to maintain the interior of the enclosures at uniform temperatures. Special provisions must also be made for visual inspection from outside, access for repair and maintenance, and control of access to the enclosures that contain unbreathable atmospheres.

Large beam energies must only be transported from the output of the main amplifiers to the targets. The average pulse fluences there are ≤ 5 J/cm^2, with localized peaks of up to three to four times the average. Transport in air of such intense beams over the long beam paths required for time decoding and delivery of the beams to the target chamber is not a viable option because of rotational Raman and Rayleigh scattering losses.

Transport in a soft vacuum (up to few torr) of the high-energy beams from the main amplifier output windows to the target chamber windows is possible. However, the structural requirements for large cross section vacuum beam enclosures, which must resist buckling from external pressures near one local atmosphere with an appropriate safety margin, appear to introduce unacceptable costs.

The option selected for the transport of high-energy KrF laser beams in the LANL LMF concept is high-purity helium (He) gas at small overpressures in light, insulated beam enclosures within buildings in which the temperatures are carefully controlled. As a high-energy beam-transport medium, a monoatomic, inert gas offers the advantages of small Rayleigh-scattering losses, no rotational Raman scattering, and ease of purity maintenance. The Rayleigh-scattering losses with helium as the transport medium are negligible. Helium offers the additional benefit of easy control of refractive-index variation, because it has a low refractive index (1.000036 @ STP) to begin with and superior thermophysical properties that facilitate the control of temperature gradients.

The basic concept is illustrated schematically in Fig. 16. The enclosure shown is for a relatively empty section through which high-energy beams are transported for time decoding or delivery to the target building. While similar in principle, the enclosures surrounding amplifiers and concentrations of large optical components and those involving changes in elevation inside the target building will be more complex. The magnitude of the problem is indicated by the illustrations of the LANL LMF concept in Figs. 4 through 7, which show something of the driver-

building arms, the enclosures and their shapes and contents, and the many beams that must be delivered to target.
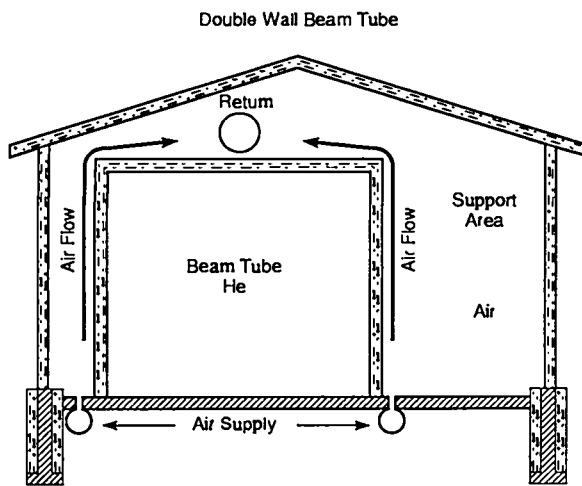
Double Wall Beam Tube

Fig. 16. LANL high-energy beam-enclosure concept.

An obvious design goal is to keep the total volume inside the beam enclosures as small as possible to reduce the amount of expensive inert gas that is required; nevertheless, there must be convenient access to enclosed equipment for inspection, replacement, repair, and maintenance Another design goal is to make the surface-to-volume ratio of the beam enclosures small to reduce the cost of the enclosures, the potential for leakage, and the requirements for temperature control.

The economics of the use of helium for the high-energy beam-transport gas in an LMF depend on several factors, including

- the amount required to fill all of the beam enclosures;
- the form in which the helium is delivered and stored and the on-site storage requirements;
- the purity at which the helium is delivered, the purity that is required for normal operations, and the cost of owning and operating any on-site purification equipment that may be required to prepare the as-delivered helium for service and to maintain the helium in the enclosures at the required purity;
- the loss rates for helium during normal operations and maintenance;
- the cost of achieving a specified loss rate; and
- the costs associated with the safe operation and maintenance of the LMF facility that uses a nonbreathable atmosphere in the enclosures.

Accurate estimates of the volume of helium required to fill all the complex high-energy beam-transport enclosures will not be possible until the design is completed.

However, a rough estimate can be obtained by estimating the average total cross section of the enclosures required to transport all the beams, with due allowance for a workable design of separation and clearance around the beams, and then multiplying that sum by the average length of the optical path from the main amplifiers to the target chamber. Based on a pulse energy of 10 MJ at an average fluence of 5 J/cm^2, a separation and clearance factor of 3, and an average optical path length of 600 m, approximately 3.6×10^5 std m^3 of helium is required.

The identified US helium resource, the amount of helium in the national stockpile, the annual US domestic and foreign sales of helium, and the as-delivered purity and unit cost of helium are listed in Table 7. The amount and cost of helium required annually, based on listed assumptions about leakage during operation and losses during access for maintenance, are also given in Table 7.

The long-term storage of the high-purity helium required for an LMF is more expensive per unit mass than the helium itself. Therefore, reductions in the requirements for storage of helium onsite is one way to improve the helium economy for an LMF. The largest reduction in on-site helium storage requirements can be achieved through use of the high-energy beam-transport enclosures as the primary storage for helium, and we have assumed this for the LANL LMF concept. Some additional storage of helium on the site is required to make up leakage during normal operations and losses incurred when enclosures are entered for repairs or routine maintenance of equipment. Long-distance transport and long-term storage of helium as a liquid are less expensive than storage as a gas at high pressure; and we have assumed this for the LMF.

Control Systems

The driver control systems must address an unusual, but by no means unique, combination of requirements. Data acquisition and control systems for AURORA have been described in the literature (Bowling et al. 1987). Some of the many operations that must be performed to prepare the driver for a shot, such as final alignment of optics, can't be performed fast enough manually and/or with adequate precision. The assistance of sophisticated servomechanisms and data acquisition, computational, and control systems operated from a central control room is necessary. Also, many driver components must be triggered to operate synchronously to within less than a nanosecond or to initiate operations with similarly precise delays. Some other driver operational parameters also must be controlled within tight limits.

The initiation of driver operation will also trigger actions by other LMF systems whose timing is critical, such as experiment and diagnostic instrumentation. Improper driver operations may result in considerable damage to these systems and/or targets and involve significant costs. Some of this triggering and control is accomplished using passive systems, but active systems are also required.

On the other hand, many of the operations required to prepare the driver, the target chamber, targets, and experiments for a shot do not need to be closely coordinated with operation of the driver, nor do they require such precise timing, or involve such close control. The laser-gas operations, post-shot cleanup, target and experiment setup, and evacuation of the target chamber in preparation for the next shot are examples. Such local, off-line control functions may be provided more efficiently and at lower cost by independent systems, placed throughout the large LMF site.

Therefore, the LANL LMF concept includes a driver-oriented master control system in a screened, central control room at the apex of a complex hierarchy of subsidiary control systems. The authority of the master control system must be supreme. The driver firing and certain important safety procedures would be controlled from this control room. In addition, there may be distributed control rooms, for example, one for the experimental area concerned primarily with target-chamber operations and one for site services.

Safety and Environmental Protection Systems

The driver building would be cleared of personnel shortly before a shot was fired. Some specialized systems will be required to ensure safety during other activities within the driver building and to protect the public and the environment. The principal hazards associated with the operation of the driver include high voltages, stray currents, residual charges, strong electrical and magnetic fields, the fluorine in the lasing medium, energetic electrons, x-ray emissions, energetic laser-light pulses, a nonbreathable atmosphere in the beam enclosures, and high vacuums. A more detailed analysis is presently being conducted of the hazards associated with LMF operation, the safety and environmental-protection equipment and procedures required throughout an LMF, and their costs and impacts on facility operations.

Systems to detect the presence of operating personnel, experimenters, intruders, etc., and to monitor radiation, electric and magnetic fields, chemical hazards, temperatures

and pressures, etc., will be needed. The list of required safety equipment also includes warning signs and displays, visible and audible alarm systems, and special visual and voice communications equipment, etc., to caution and advise personnel in operational areas. Barriers will be needed, such as special doors, walls, fences, and guards, to restrict access to operational areas and equipment. Safety interlocks to centralized and distributed control systems will also be needed to prevent simultaneous occupation of an area and operation of equipment, simultaneous operation of two incompatible systems or pieces of equipment, etc. Miscellaneous safety systems, such as special emergency lighting, local ventilation, electrical grounding, chemical cleanup, injury treatment, respirator, and washing systems, and emergency shelters will also be required. The driver-building ventilation air can be continuously sampled to detect the presence of fluorine and quickly diverted through a charcoal bed if fluorine is detected.

Prototype Amplifier Module

In spite of the experience gained in the design, construction, and operation of the smaller facilities with KrF laser drivers, a prototype of the large laser equipment for an LMF may be needed. The schedule and cost for such a prototype are included in the LANL LMF study. The prototype would consist of a single large amplifier, with the appropriate equipment for pulsed-power, electron-beam pumping, guide-magnet, optical, laser-gas, diagnostics, instrumentation, and control systems, etc., at or near the scale of the LMF main amplifiers. The prototype would provide scale-up confidence before a commitment is made to the full LMF design; permit proposed minor design changes, new materials, etc., to be evaluated under realistic conditions during design of the LMF; and provide an opportunity for hands-on training and experience for operating and maintenance personnel prior to startup of the LMF.

The prototype need not include all of the low-energy systems, for example, the pulse-shaping systems that deliver the input pulses for the LMF main amplifiers. The high-energy beam-transport equipment for delivering focused, shaped pulses to targets need not be provided. Some of the modules of modular subsystems for the main amplifiers for an LMF might be omitted, such as pulsed-power or electron-beam lasing-medium pumping equipment. However, the prototype must be capable of operations that address the critical design issues of the main amplifier and associated equipment for an LMF in sufficient detail, at an adequate scale, and for enough shots to provide the design verification for the LMF. Alternatively, the prototype must

be identical to a main amplifier for the LMF and eventually be installed as such or serve as a spare. Because the prototype would be a first-of-a-kind device, its cost may be higher, but the construction of the LMF main amplifiers would then occur farther down the fabrication-cost learning curve.

Spares

For some of the driver equipment described above, comprehensive and detailed reliability and maintenance studies should be established so that adequate initial inventories of spares are on hand for critical driver components and subsystems that are expected to fail in service. The objectives are to rapidly restore the driver to service and to permit operations and maintenance training with actual equipment. The spares used for failed equipment may be replaced with new units from suppliers. Alternatively, the failed equipment could be repaired and placed in the spares inventory. An initial inventory of critical spares large enough to last the projected service life of the LMF may be desirable if the timely availability of future supplies is in doubt or if the acquisition of spares in the future is predicted to be very expensive, provided such spares have an unlimited shelf life. (Spares may be much more expensive to acquire after an initial order is filled because of the expense of restarting production, limited production runs, and/or competition for the manufacturing capability.) Alternatively, the establishment of on site and/or off site standby manufacturing capability that is dedicated to the LMF or on which the LMF has first call might be warranted. A manufacturing capacity that is sufficient to meet the anticipated average requirement for spares and that operates throughout the service life of the LMF might also be justified.

Driver Building

As illustrated in Fig. 4, the driver building is divided into 15 arms that are tangential rather than radial to a central circle. The outer area of each arm contains on-grade groups of three main amplifiers that share optical apertures and their accessories. Smaller amplifiers are located in basements under each arm. The wider sections of the halls leading from the outer areas contain demultiplexing optics. The narrower sections house beam enclosures for high-energy beam transport; the input and output mirror arrays for the main amplifiers are located at their inner ends.

The requirements for the driver building are not severe. A thick concrete floor is required to provide a stable platform for optical components, including the windows and

back mirrors for the amplifiers. Elsewhere, the building pad can be thinner to save costs, except for walls and roofs and locations where greater thickness is required to support heavy equipment, such as cranes and other lifting equipment. Such thinning of the floor is also contingent on the use of a special design to prevent the transmission of vibrations to the more sensitive areas or the elimination of activities that generate the disturbances during critical times prior to shots and during shots.

Conventional steel industrial-building technology. Relatively low-cost enclosures that resist adequate external loads and provide a stable environment. These loads include those due to weather (wind, rain, snow, ice, sudden temperature variations, etc.), diurnal temperature variations, geologic ground motions, site machinery, and passing vehicles. Provisions must be made for high-capacity traveling overhead cranes and other lifting and transportation equipment required for raising, lowering, and moving heavy driver components during their installation and their disassembly for replacement, repair, and maintenance.

LANL EXPERIMENTAL AREA CONCEPT FOR AN LMF WITH A KrF LASER DRIVER

The experimental area for an LMF includes a target chamber and associated equipment and the building that houses them. The associated equipment includes the systems required to maintain appropriate environments support targets and experiments; to make experimental measurements; to monitor, control, and maintain the experimental area systems; and to protect workers, the public, and the environment from the hazards associated with experimental area operations. The optical systems that direct high-energy laser beams around the experimental area building and focus them onto targets are considered to be part of the driver. They were discussed previously in connection with the driver and are not discussed further here, except where they interface with the target chamber.

Target-Chamber Requirements

The target chamber for an LMF must meet many requirements. The target chamber for an LMF will not be a simple vacuum vessel. The combined requirements for structural, mechanical, heat-transfer, electrical, nuclear, etc., components and systems for an LMF target chamber is unprecedented. These components and systems include first-wall and driver protection systems, for last/optical/components vacuum membranes and structural shells, environment-control systems, chamber

instrumentation and control systems, shielding, penetrations, and supports.

There are also several desirable characteristics of target chambers for an LMF that involve significant cost/performance tradeoffs. These desirable characteristics include low cost, high availability, high reliability, fast turnaround, low risk, easy maintenance, low activation, and easy access for experiments.

The target chamber must be compatible with the illumination geometry required and must interface satisfactorily with the driver, including providing a stable platform for optics. It must provide the environment required for targets and experiments. These include, at a minimum, high vacuum for targets and instruments, a stable platform for targets and instruments, and liquid-helium cryogenic support for targets. The target chamber must provide enough solid-angle and lineal, areal, and volumetric room between beams at locations close enough to the target for diagnostic and experimental instrumentation and for experiments.

The target chamber must contain the products of ICF target microexplosions. It must protect itself and the systems that interface with it, facility personnel, and equipment and structures that are external to it from the consequences of target microexplosions. The target chamber must function satisfactorily for thousands of shots with yields ranging from <100 MJ up to about 1 GJ. Up to approximately one-third of the target yield will be in x rays and debris-ion kinetic energy. The design for a maximum target yield of 1.4 GJ with up to 600 MJ in x ray and ions provides a safety margin for targets that perform beyond expectations.

The chamber must successfully resist impulsive loading, including mechanical and thermal stresses and the reaction to material ablation that results from rapid isochoric deposition of neutron energy in exposed components and x-ray and ion energy at exposed surfaces. Unacceptable reductions in integrity and performance resulting from radiation damage, melting, thermal and mechanical stressing, and material loss by ablation must be prevented. Unprotected, thin, small-radius target-chamber first walls exposed to target x rays and ions will ablate, and/or crack melt, at the front surface, and may spall at the back surface as a consequence of the impulsive loading. Energetic missiles (shrapnel) can be generated from targets and surrounding material that disintegrate in response to shocks produced by the rapid surface deposition of large amounts of energy.

Thus, some method for protecting target-chamber surfaces and components from target emissions must be included in the target-chamber design. The proposed solutions to this problem include renewable or resistant protective layers, large chambers, and gas puffing (Orth 1988; Monsler and Meier 1988; Pitts et al. 1988; Bourque et al. 1989). None of these proposals has emerged as a clear choice for use. The assessment of their relative merits is complicated by the lack of definitive experimental data or convincing theoretical models for the interaction of target emissions with condensed materials. Various theoretical and experimental analyses are being performed at Los Alamos and elsewhere to resolve the issues.

The target chamber must be shielded to reduce the leakage of neutrons and gamma rays when shots are fired and from activated materials between shots so that normal operation and maintenance activities can be carried on conveniently in the experimental area building and to protect personnel, the public, and the environment during shots. The shielding is also required to protect sensitive components from damage by radiation and to reduce long-lived activation by reducing the kinds and amounts of materials exposed to neutrons. Activated target, experiment, instrument, target-chamber gases, and structural materials must be reliably contained. Special measures will be necessary to control radiation streaming through penetrations, which is a particular concern. If a target-chamber design is to be truly low-activation, then considerable attention to the control of neutron streaming is necessary.

Optics other than the final mirrors can be easily and adequately protected from radiation damage, but maintenance becomes more difficult and costly if they become highly activated. The focusing lenses that also serve as vacuum interfaces are apparently the most easily damaged components. They need not be line-of-sight with the targets and they only need to be protected from excessive exposure to streaming neutrons and from materials ablated from exposed target-chamber surfaces. Therefore, to control the exposure of optics and other equipment to streaming neutrons, special materials selection, shielding, bends in the optical paths, and other measures will be needed for a small part of the way along the beam enclosures from the target chamber.

The target chamber must also include some means of protecting the driver optics that are exposed directly to target neutrons, x rays and ions and shrapnel. Surveys of some of the issues of protecting exposed optics and some of the potential solutions have been published (Bourque et al.; Nilson and Woodworth 1989). Protection of these large, expensive optics from gases heated by target emissions and vapors ablated from exposed surfaces is also essential for economical facility operation. Protection of optics from shrapnel is viewed by many as the most difficult

engineering problem for LMF target chambers. With a nominal 1-GJ yield , calculations to estimate the production of shrapnel by x rays striking the surfaces of thin components made of metallic materials and located a few tens of centimeters from targets indicated that shrapnel pieces might range in mass from micrograms up to a few grams and have velocities up to a few kilometers per second (Nilson and Woodworth 1988). It is hoped that by careful design the maximum momentum for any missile produced by target microexplosions can be reduced to the order of a few hundredths of a kg-m/s, for all but those experiments requiring that large masses be placed close to targets. For example, this corresponds to particles of typical densities of the order of 1 mm in diameter travelling at about 10 km/s. Considerable additional investigation that includes the effects of surface deposition of ion energy and volumetric deposition of neutrons will be required to verify that this goal can be achieved and to examine the more severe cases in which large masses are placed near targets.

Unfortunately, the sensitivities of optical coatings expected to be the least damage resistant and the substrates to the various target emissions and hot gases and vapors are not well known. For direct-shine neutrons, the only feasible method for limiting damage is to locate the exposed optics sufficiently far from the source that fluences are reduced to acceptable levels. The only proposed solution for protection from target x rays and ions that is generally considered credible is to puff gases into the optical path just before the driver is fired. Gas puffing may also provide all the protection from hot gases and vapors that is required and can provide some protection from small pieces of shrapnel. Mechanical shutters of various types have been proposed for protecting the final optics from larger missiles. These shutters could also provide increased protection from ablated materials, which would arrive at optics roughly on the same time scale as shrapnel in the absence of gas puffing. Some of these concepts for protecting optics are discussed in more detail below.

Even at tens of meters from a 1-GJ target emitting one-third of its energy release as x rays and ions, the fluence on optical surfaces is of the order of a few J/cm^2. Such x-ray fluences are sufficient to permanently damage optical coatings and the surfaces of uncoated substrates. Gas puffing has been proposed to protect exposed optics in the driver energy-delivery systems from damage by target x-ray and ion emissions. According to calculations and limited experimental evidence, a few tens of torr-meters of an inert gas of moderate to high atomic number puffed between the last optics and targets just before the laser is fired will suffice to protect these optics. The timing is critical: the gas must be introduced before the driver beams are injected

and must not arrive near the targets and certain instrumentation before the target is illuminated. A gas expanding into a vacuum typically requires only a few milliseconds to move to a few tens of meters. The higher atomic-number inert gases, such as xenon, have greater stopping powers for ions and x rays and higher molecular weights mean slower molecular speeds. However, the costs of inert gases with atomic numbers higher than that of argon are much greater, and they provide only modest increases in performance. The gas must be introduced so that inhomogeneities are modest. The low density helps in keeping density variations low. The laser light must not interact strongly with the gas, so that the choice of gases for protection of optics is limited. Some exploratory studies of gas puffing have been conducted (Bourque et al. 1989; Nilson and Woodworth 1988).

Considerable effort has been expended elsewhere in exploring low-activation concepts for the smaller target chambers that may be appropriate for use with other drivers (MacFarlane et al. 1988; Orth 1988; Monsler and Meier 1988; Pitts et al. 1988; Bourque et al. 1989). The yield of fusion neutrons (14.1 MeV when born, but with a spectrum somewhat degraded by interactions in targets), from a single 1-GJ yield target is about 4×10^{20}. Reduced activation or a shift from long-lived radioactivity to only isotopes that decay rapidly can allow better access for experiment setup and maintenance on some parts of the target chamber and associated equipment sooner after shutdown. Hands-on maintenance can replace some remote maintenance. Alternatively, radiation exposures of facility personnel can be reduced. Radwaste processing and disposal while the facility is being operated and the decommissioning of the LMF after its useful service life could be less costly if most of the activated materials can be made to fall into a waste category with much lower treatment and disposal costs.

Some of these low-activation concepts involve considerable complexity, large uncertainties that will require extensive R&D to reduce, the use of relatively expensive materials, and potentially significant impacts on operational schedules. Many of them are not suitable for adaptation for the LANL LMF target-chamber concept because of incompatibility or cost. Some radiation and activation analyses for these concepts reveal that many of the hoped-for benefits are not achieved at all or only to a limited degree (Bourque et al. 1989; Tobin et al. 1988). Complete control over target and close-in instrument and experiment materials to eliminate activation is not possible. The driver optics that must have line-of-sight access to targets can't be shielded from neutrons. We do not believe that the high cost of extreme measures to achieve low activation of some parts of the target chamber is justified when other

components will routinely become highly activated. The severity of the problem will fluctuate with the recent and long-term irradiation, target, and experiment history. Much of the time, access for experiment setup and hands-on maintenance will be constrained, and a worst-case suite of remotely operated equipment must be available. However, when reductions in activation at modest cost and impact on other requirements can be identified, they will be incorporated into the further development of LANL LMF target-chamber concept.

Several target-chamber concepts developed elsewhere for use with other driver technologies in an LMF have been described in the literature , for example, light-ion accelerators and solid-state lasers (MacFarlane et al. 1988; Orth 1988; Monsler and Meier 1988; Pitts et al. 1988; Bourque et al. 1989). The light-ion target-chamber concepts are completely incompatible with laser drivers and won't be discussed further (MacFarlane et al. 1988). In general, the concepts developed for use with solid-state lasers do not appear to be particularly attractive for use with a KrF laser driver at the LMF scale, although some of the ideas incorporated in them are adaptable for use with KrF lasers.

The concept for use with solid-state lasers that has been studied most intensively involves forming a thick layer (2 cm and up) of a low-density (about 0.1 g/cm^3) water frost on panels cooled to 100 K to 150 K with liquid nitrogen over a period of several hours (Orth 1987). The frost protects underlying structures that otherwise would be exposed to target emissions. It reduces impulsive loading of and heat transfer to the first wall. It substitutes vaporization of a relatively benign material for that of structural materials and makes removal of activated target and experimental materials easier. On the other hand, it provides little protection for the cryopanels from large pieces of shrapnel. In addition, the thermal loading (on the required equipment for cryogenic targets up until just before the driver is fired and on the targets during the interval between removing the cryostat and firing the driver) is substantially reduced from that of an ambient-temperature chamber. This characteristic of the target-chamber concept may allow substantially longer target lifetimes before unacceptable degradation after the cryostat is withdrawn. Water evaporated by target emissions eventually recondenses onto liquid water and unmelted frost. Considerable effort was devoted to ways to reduce activation in this concept. The characteristics of this and other LMF target-chamber concepts that may be useful with a KrF laser driver will be mentioned in the discussion of the LANL LMF target chamber concept.

Rotating or explosive shutters have been proposed for the protection of the exposed target chamber optics against

the impact of missiles (Nilson and Woodworth 1988). The current assumed design basis is 0.1-g pieces of shrapnel moving at 10 km/s generated 5 to 10 m away from the shutters, so that they must close within about 0.5 to 1 ms. As noted above, this requirement is not well established. There are, however, substantial experimental and theoretical data bases for the estimation of the thickness of materials required to stop missiles of a given shape, velocity, and material. To stop missiles of the design basis size and speed, steel or aluminum alloy thicknesses of the order of 1 cm are apparently adequate.

The essence of the explosive-shutter concept for protection against damage by shrapnel is to drive plates normal to the beam paths using high-explosive charges to seal off beam ports. To keep shutter sizes down to allow rapid closing with practical equipment, the shutters would be located at radii at which the cross section of focused target beams that start out at approximately 1 m diameter at the final optics are reduced to 10 to 20 cm in diameter. If additional analysis indicates that only slower shrapnel speeds must be dealt with, then less-violent mechanical methods could perhaps be used to drive the plates. There are several concerns with regard to this concept that have led us to reject it. The operating cost estimates are high, long turnaround times are expected, the effect of shutter operation on other systems is of concern, and reliability is an issue.

Rotating shutters are an alternative to explosively driven shutters, and are a concept that we are currently pursuing. This concept uses rotating disks with holes that match beam cross-sections, plus a small allowance that is distributed uniformly around the periphery. The holes pass the beams when they are aligned. The hole closing time is determined by the disk rotation rate, the radial location of the holes, and the hole size. A second, more-slowly rotating disk with matching holes in front of the faster-rotating disks can be used to block the holes in the faster rotating disks when it has rotated through an angle sufficient to align with the next beam path. The rotation rate for the slower disk is determined by the hole size, the faster-disk rotation rate, the number of holes, and the size of the disks. The rotating shutter also protects in the short term against ablated target-chamber materials. A fast-acting, but slower mechanical valve or shutter behind the rotating shutters can be used to provide a long term gas-tight seal if needed.

Our rotating shutter concept does not push conventional flywheel technology. Maximum stresses can be kept well below allowable stresses. The impact of shrapnel is not expected to cause disintegration of the disks, but there are many existing designs for "catchers" for flywheels disintegrating under much more severe conditions. Good vibration isolation will be required to insulate optics from

the effects of the rotation of the large total mass of the shutters required to protect all the final optics.

The rotating shutter assemblies are projected to have modest capital costs, much lower operating costs and shorter turnaround times than explosively driven shutters, to perturb other systems to a much lesser degree, and to offer greater reliability. The reliability issues are different for explosive and rotating shutters. Whether or not an explosive shutter will work can't be determined until much of an experiment is completed and subject to potential destruction. However, firing of the driver may be avoided by monitoring the performance of the explosive shutters after they are fired, but before the driver is fired. The performance of a rotating shutter, on the other hand, can be monitored continuously before firing the driver.

LANL LMF Target-Chamber Concept

A few distinguishing characteristics of the LANL KrF laser driver concept for an LMF led us to investigate a concept for the experimental area that differs significantly from the experimental area concepts that have been proposed for use with other potential LMF driver technologies. These characteristics are the large number of separate high-energy beams (900) delivered to target and the large total area of optics required to do it. Substantial increases in the design fluence and the size of the optics that can be cost-effectively produced would be required to change the situation very much.

The last optical surfaces in the high-energy beam-transport trains will be in direct line-of-sight from the targets. All other optics in the experimental area building can be more or less protected by shielding and various neutron-streaming control schemes, but the only practical way to protect direct line-of-sight optics from rapid damage by fusion neutrons is to locate them far enough away from target microexplosions. Preliminary estimates indicate that locating the last optics approximately 30 m away from targets with yields of 1.5 GJ will suffice to reduce rates of damage by fusion neutrons to acceptable values. The surface area of a sphere with a radius of 30 m is approximately 10^4 m^2. Thus, if all the high-energy beam-transport optics and other equipment that must be near the target chamber are located at a radius of 30 m or more from its center, then there should be enough room for all the optics and equipment, provided the groupings of beams and equipment required for a particular illumination geometry do not create interferences.

The driver beams must be transported to target through a vacuum. If each beam is enclosed in a separate truncated-cone vacuum tube, or even groups of beams enclosed in

larger tubes, the total lateral surface area of the cones reaching from a small spherical target chamber out to a radius of 30 m would exceed the surface area of a sphere of 30-m radius. For example, if 7 of the 900 beams were grouped in a closest-packing arrangement in each tube, and the spherical target chamber had a radius of 5 m, then the lateral surface area of the approximately 129 beam tubes would be about 18,000 m^2, as compared to 10,000 m^2 for the sphere. Each beam tube would have to be vacuum-capable and shielded to prevent the leakage of radiation. The total amount of materials contained in this complex geometry would far exceed the material required for a simple large spherical vacuum vessel with the same thickness of shielding. We also note that at least some of the LMF target-chamber concepts developed for use with other driver technologies include thick concrete radiation shielding at distances of about 30 m from the center of the chamber (Bourque et al. 1989). With such shielding, the experimental area building need not be the primary radiation shielding.

These considerations caused us to seek large target-chamber concepts with features that could lead to costs comparable to or less than those of the much smaller target-chamber concepts. The target-chamber concept illustrated schematically in Fig. 16 has several such features.

We note that the smaller target-chamber concepts often include complex systems to reduce or eliminate the ablation of structural materials and impulsive loading as a result of target emissions impinging on exposed surfaces. Such complications add substantially to the cost of such target chambers. Our target-chamber concept is relatively simple. Whether a higher-capacity vacuum system is needed to evacuate the larger volume of the LANL target-chamber concept is also not clear in view of some of the first-wall protection schemes described above that have been proposed for smaller target-chamber concepts (Orth 1988; Monsler and Meier 1988; Pitts et al. 1988).

The basic structure for the target-chamber concept shown in Fig. 16 consists of a 1.5-m-thick layer of concrete covered by thin layers of metal on the inside and the outside. This concrete is formulated with heavy aggregate to stop gamma radiation, and with boron to absorb neutrons moderated by the water in the concrete. It has a high modulus of elasticity, low thermal expansion, and low elastic and creep deformations. For sufficiently large target chambers, the volumetric energy deposition by neutrons is reduced to values that can be tolerated by concrete shielding, so that shields containing water or other low-atomic-weight fluids to moderate neutrons are not necessary. Concrete containing high atomic-number materials and boron is a better gamma-ray shield and nearly

as good a neutron shield as boronated water or boron carbide. The additional shielding and other measures to reduce neutron streaming along optical paths is not shown in Fig. 16. The geometry of the penetrations for the driver beams through the concrete shell reduces streaming through them. The neutron streaming control structures required outside the chamber are fewer than those associated with some other target-chamber concepts.

The cost of such concrete is higher than that of conventional concrete, but it is still a relatively inexpensive material. As noted above, thick shielding of one sort or another at radii substantially larger than that of the smaller target chambers is needed in other experimental area concepts. For any target-chamber concept with laser drivers, the large optics (for example, windows into the target chamber, either flat or lenses, and mirrors to direct and focus the driver beams) have to be provided with stable supports. The massive concrete construction of the LANL LMF target-chamber concept provides the stable platform needed for the window and targeting optics.

If a target chamber is constructed like a conventional metallic vessel, then a large shell thickness, roughly proportional to the shell radius, would be required to prevent buckling under the external pressure loading of the atmosphere when it is evacuated. (A small target chamber would also have to resist internal impulsive and pressure loading due to the ablation of materials exposed to target emissions.) The effects of these internal loadings become less significant as the target-chamber size is increased and for a chamber radius of 30 m become insignificant. Even for a 30-m target chamber, the thickness required to resist internal loading because of micro-explosions for a simple steel or aluminum shell is only a few centimeters.

The concrete target chamber of the LANL concept would be subjected primarily to external pressure loading, except at locations where modest tensile forces due to the weight of the shell must be countered by reinforcing members. Its wall is thick and the concrete is strong in compression. Therefore, the concrete shell can take up the atmospheric loading when a vacuum is drawn within the chamber. A massive metallic vacuum vessel is not required. For example, a thin layer of steel or aluminum sheets (a few mm at most) easily welded together in place to form a continuous membrane on the outside of the concrete shell serves as the vacuum barrier. A layer of aluminum or other impermeable low-activation material securely attached to the concrete at frequent intervals on the inside provides a barrier to outgassing by the concrete when the chamber is evacuated. The surfaces of penetrations through the chamber walls for driver beams, target and experiment mounting,

etc., also must be lined with a metallic outgassing barrier. All of these materials are inexpensive and easily worked.

As shown in Fig. 16, the chamber would be supported on a thick-walled hollow cylindrical pedestal of similar construction. This pedestal would contain the airlocks required for introduction of targets, experiments, instrumentation, etc., into the chamber and access for maintenance, cleanup after experiments, etc., using various types of remotely operated tools and manipulators. The support structure would also be appropriate for housing many of the target chamber auxiliary systems, such as vacuum equipment, that are expected to become contaminated with radioactive substances generated by fusion-neutron interactions within the target chamber and require shielding. Hot cells for dismantling, decontaminating, treating, studying, storing, repairing, maintaining, etc., radioactive target-chamber equipment, the remains of targets, experiments, instrumentation, etc., would be included within this shielded pedestal.

The inner shell shown in Fig. 16 can be constructed of a purified aluminum alloy or other special material for reduced activation and weight. It need be only as sophisticated and as big as required for a particular series of experiments and could be different for different experimental campaigns. The potential requirement for target chambers of significantly different design for certain classes of nuclear weapons-related experiments was mentioned earlier. The radius of such shells would be only a few meters, with the exact size depending on the requirements for a specific series of experiments. The shell is there for several reasons. To contain gases puffed in for final optics protection, light, inexpensive beam tubes that have little pressure differential could be installed across the walls that run from the inner shell to the outer shell of the target.

The final line-of-sight mirrors inside the target chamber, which deliver the driver beams to the target, must be protected from shrapnel. If mechanical shutters of the types discussed above are used to provide this protection, as in the current LANL target-chamber concept, then the smaller the openings that must be closed, the less massive the equipment required to do so and possibly the lower its cost. Of course, the shutters must close more rapidly (within 0.5 ms at 5 m versus 3 ms at 30 m for particles moving at 10 km/s) when located closer to the targets, but the mass that must be moved to close the holes would also be much less. For example, the area of the opening for a single beam or a cluster of beams at 5 m from the targets would only be 1/36th of the area required at 30 m.

The targets and some other equipment must be fairly close to the targets and must be provided with very stable supports. The inner shell provides this support and also

supports the shrapnel protection equipment. The ablation of material from exposed surfaces by target x rays and ions is substantially reduced for surfaces far from target microexplosions, for example, at 30 m compared to a radii of 5 m. The decrease in material thickness is not significant at a 5-m radius in a structural sense for metallic materials of thicknesses of the order of 1 cm and up, nor is it significant for metallic materials of a thickness of a few mm. The rate of loss for 1 GJ-yield shots will be of the order of no more than a few microns per shot. The inner shell protects the outer shell to prevent any ablation except where it is in line with an openings in the inner shell. Any target-chamber or experimental equipment that is located outside the inner shell away from penetrations will be similarly protected. Thus, a very large volume is available in which to park equipment for protection .

On the other hand, there are concerns about where the ablated material ends up and how its energy is transferred. Hot vapors of metallic or other materials transferring energy to delicate instruments and optical surfaces can damage them by overheating and/or thermally stressing them. Condensation of such materials on optical surfaces can render them useless. These vapors will be trapped inside the inner shell when the shrapnel-protection shutters are closed. They will condense rapidly onto cooler surfaces or homogeneously condense to form aerosols that would be removed by the target-chamber vacuum system. It appears that thicknesses of only a few centimeters can resist the internal impulsive and pressure loading on the inner shell from ablation, but our understanding of the response of materials to intense, pulsed radiation from ICF targets is somewhat limited. Such thicknesses may be less than that required for a simple spherical vacuum vessel of this size to resist the external pressure of the atmosphere. Much greater thicknesses may be needed to provide a stable platform for some heavy instrumentation and other equipment. The inner shell in the LANL LMF target-chamber concept does not have to resist external pressure loading. If, for example, the use of a layer of water frost for one of the first-wall protection schemes described above is shown to be necessary or desirable, then the addition of the required equipment to the inner shell of the LANL LMF target-chamber concept would be relatively easy.

Target support equipment, such as beam-alignment equipment, target and nontarget diagnostic systems, etc., would be withdrawn to protected locations shortly before firing the driver. However, both high-yield and lower-yield shots are expected to irreparably damage parts of target mounts near the target and exposed parts of instruments that require line-of-site access to targets. Much of this equipment would be of robust construction but would

require some repair and replacement after each shot. Debris from damage of this type and from applications nontarget experiments and contamination by material ablated from exposed surfaces may have to be cleaned up after each shot or series of shots. Nontarget experiments and single-use instrumentation must be recovered after each shot. Much of the equipment, debris, and contamination will be highly radioactive. Therefore, to meet the specified facility shot rate, the necessary repair, replacement, cleanup, etc., under difficult conditions must be rapidly completed and new targets and experiments set up. To reduce the facility turnaround time, the inner shell is mounted on a platform that can be raised into position for a shot and then lowered into the shielded airlock beneath the target chamber by a hydraulic ram. There, remotely operated equipment can be used to inspect for damage and contamination, replace and repair damaged components, clean up and decontaminate, and extract experiments, and then set up new targets and experiments. The time constraints on this cycle could be eased by the use of one or more demountable inner shells that can be separated from the hydraulic ram and set aside to be worked on. A shell with a pre-assembled package consisting of a target, its support, diagnostic, and positioning systems, applications experiments, instrumentation, etc., could be set in place without delay.

In the LANL LMF concept, flat mirrors were selected for the final optical surfaces in the train that aims and focuses the driver beams onto targets because this class of optics is generally less expensive than powered mirrors and lenses, less expensive to refurbish or replace, and more resistant to neutron damage than lenses. They would be fixed in place after an initial alignment, so that no optics alignment equipment would be required within the target chamber. The mirrors are not located far enough from the targets to sufficiently reduce their susceptibility to damage by target x rays, but the job of protecting them from x rays is much easier. They must also be protected from energetic (tens to a few hundred keV) target-debris ions. Both types of protection are provided by interposing puffs of an inert gas between the targets and the last optical surfaces just before the laser is fired, as discussed above. Preliminary radiation transport calculations and the results of x-ray damage experiments suggest that 20 to 30 torr-m of argon will provide the necessary protection from target x rays and will not significantly affect the delivery of the driver energy to target by scattering the light or deflecting the beams. This corresponds to a pressure of about 1 torr in the chamber if the gas that is puffed in is distributed uniformly throughout the entire inner wall of the chamber. However, it should be possible to puff gas only into the beam paths initially, thereby reducing the gas required by roughly an

order of magnitude. Much less gas is required to stop the target-debris ions. Analyses and experiments to study this concept have been announced elsewhere (Bourque et al. 1989; Nilson and Woodworth 1988).

The vacuum barrier transmission optics through which the driver beams are introduced into the target chamber can be either windows or lenses. Windows are less expensive than lenses, but another expensive station would have to provide the beam-focusing capability of the lenses. The windows could be fixed in place, whereas the lenses would have to be both movable and reliably sealed against leaks. Thus, the design of the focusing mounts for lenses used as vacuum barriers would have to be fairly sophisticated. In the belief that successful designs for lenses that also serve as vacuum barriers can be achieved, the LANL LMF concept includes such lenses. Although transmissive optics may be more vulnerable to damage by neutrons than reflective optics, these lenses don't need to be in direct line-of-sight from targets and can be shielded.

Other Experimental Area Equipment

Several large scale and many smaller systems are needed to support target-chamber and other experimental area operations in addition to those described above. They include equipment required to set up and conduct target and applications experiments, such as refrigeration systems to support cryogenic targets (and some of the cryogenic first-wall protection schemes, if they prove to be necessary). Also required are a system for rapidly evacuating the large target chamber, systems to position and orient targets, extensive safety and environmental-protection systems, and a wide variety of diagnostic, maintenance, instrumentation and control systems.

Target Systems Associated with the Target Chamber

Optical, electronic, and electromechanical micropositioning equipment is required for determining and adjusting target location and orientation. Target preshot diagnostics systems are needed for viewing and otherwise inspecting and testing targets *in situ* to assure target viability before firing the driver. Target performance must be determined to characterize the output for both target and applications experiments.

Special equipment is required for remotely inserting targets premounted on supports into the inner shell, controlling the target environment, positioning the targets, performing pre-shot diagnostic testing and monitoring of targets in the target chamber, and collecting and recording

target-performance and target-experiment data. Much of this equipment must be
- withdrawn rapidly from near targets just before the driver is fired (perhaps moved outside at least the inner shell of the target chamber);
- provided with protection from target emissions just before the driver is fired (for example, by being positioned behind fixed or movable shielding); or
- be sacrificed.

Some of this equipment would be common to many experiments and available as general facility support. Some of it would be specialized and supplied by facility users for their particular experiments.

Insertion systems introduce targets and the instrumentation required for target experiments into the inner shell of the target chamber. The instrumentation is supported on appropriate mounts in equipment that provides a controlled environment. The required equipment may include these items:
- special transporters, handling fixtures, and target-chamber penetrations;
- interfaces, such as transfer locks, manipulator systems, and glove boxes;
- cryogenic refrigeration systems, thermal shields, and vacuum or inert-gas enclosures, and
- viewing, display, instrumentation, recording, control, etc., systems.

The instrumentation, recording, computing, display, etc., systems for determining target performance and performing target experiments must include equipment to obtain information about the incident driver pulse energy and power, spectral content (bandwidth and distribution), spatial profile, synchrony, and symmetry as a function of time. Driver-target energy-coupling parameters must be determined as a function of time, including
- the driver-to-ablative-surface energy transfer efficiency and symmetry, intensity, spectrum, and conversion to x rays and
- the fuel preheat magnitude and spectral content for electrons, ions, and x rays.

The details of the capsule implosion dynamics are to be determined, such as the motions, symmetry, areal and mass densities, mixing, instabilities, and pre-ignition temperatures and pressures as functions of time and position for the central ignition, main fuel, and pusher regions. The following data are sought: ignition time, the timing and spatial distribution of the burn, and the total, neutron, fusion gamma, fusion charged-particle, and target-debris charged-particle and x-ray yields and yield rates as functions of time. The equipment that provides x rays backlighting of targets is needed to obtain some of this data.

Applications Experiment Systems

Equipment common to many experiments may exist as general facility support for such applications experiments as weapons-effects simulation and weapons-physics experiments (Hogan 1988). Specialized equipment will have to be provided by LMF users. Equipment similar to that discussed for target experiments is required for applications experiments, that is, special systems to remotely insert and mount applications experiment packages into the target chamber, to monitor them prior to shots, to control their environment, to instrument and record their performance. However, nontarget experiments may be physically much larger and the capacity of their support systems larger, but their positions and orientations may be less critical. Equipment to recover, cleanup after, and/or perform post-shot analyses on applications experiments also may be necessary. For post-experiment analysis, special remote equipment for dismantling; sectioning; mechanical, electrical, etc. testing; multiplexing analysis; and chemical analysis in hot and warm cells may be needed.

Cryogenic and Other Heating and Cooling Systems

The liquid-helium system to support cryogenic targets will be relatively conventional and the required capacity relatively small. Some instrumentation and nontarget experiments may have substantially greater requirements for liquid helium. The liquid-nitrogen system for targets would also be relatively small and conventional, but once again instruments and some experiments may require more. Apparently a large liquid-nitrogen system will be required in the experimental area only if a method of protecting the first wall of the inner shell that involves the use of liquid nitrogen is needed and/or cryopanels are used for evacuating the target chamber. In this case the equipment required and its cost would have to be examined in more detail.

The required liquid-helium equipment could include: refrigerator/ liquifiers; compressors, pumps, and drives; ambient and cryogenic piping, valves, fittings, traps, and baffles; heat-exchangers; dewars and other storage vessels; auxiliary equipment, such as initial cool down and purification systems; and instrumentation and controls. The liquid-nitrogen system equipment falls into the same categories. A single liquid-helium or liquid-nitrogen supply system might serve the entire needs of the LMF, but separate systems for different areas, including the experimental area, or only partial sharing of equipment with other areas are options that could reduce costs and increase flexibility.

A need for chilled water for various target-chamber and experimental area operations is anticipated. The equipment required includes chillers, pumps and drives, heat exchangers, water purification and treatment equipment, storage tanks, piping, valves, fittings, insulation, hangers and supports, and instrumentation and controls. A choice will have to be made between a single centralized supply and separate systems for different areas. Other special cooling-water and gas heat transfer systems may be required and would involve similar kinds of equipment, but no such additional requirements have been identified so far.

Target-Chamber Vacuum System

The technology for the target-chamber vacuum system is relatively conventional, but the capacity needed is unusually large. Therefore, we discuss the target-chamber vacuum system in more detail. The target chamber in the LANL LMF concept encloses a very large volume (approximately 10^5 m^3), has a very large internal surface area (around 10^4 m^2), and many penetrations (900 for the windows alone) that must be reliably sealed. It must be evacuated quickly (within a few hours at most) from a starting pressure of ~ 0.1 torr of the inert gas puffed to protect the final mirrors down to a residual pressure of about 10^{-6} torr before every shot. The mass that must be pumped out after each shot is of the order of a few tens of kilograms. The low final pressure is required to reduce condensation on cryogenic targets and for the proper operation of several types of experimental instrumentation.

These unusual requirements do not present significant technological or cost concerns. We find that the vacuum-pumping capacity to meet these requirements can be provided by approximately 10 to 15 large (about 10 m^3/s pumping speed each) commercially available turbomolecular pumps backed by standard mechanical roughing pumps at a total cost of only a few million dollars for a complete vacuum system.

The target chamber vacuum system must handle unburnt tritium and activated materials ablated from exposed chamber surfaces by target emissions that react to produce noncondensing gases, form aerosols, or are adsorbed or absorbed by aerosols. The gases pumped from the target chamber can be passed through high-efficiency filters to remove particulates and charcoal beds to adsorb and/or react with radioactive gaseous contaminates. The inert gas used to protect the final mirrors can then be recycled.

Safety and Environmental Protection

The kinds of equipment and procedures that will be required to ensure the safety of facility personnel, visitors,

and the public and to protect the environment during both normal operations in the experimental area and under emergency conditions are similar to those discussed for the driver. There are substantial hazards associated with operations in the experimental area, but none are really exceptional, and essentially all the equipment required to address the problems that they present is conventional. Even the necessity to cope with 14-MeV fusion neutrons in large numbers requires no new technology, and the associated hazards pale in comparison with those of many other nuclear facilities. Therefore, we will not discuss the required safety and environmental protection equipment and procedures in great detail here. However, we note that because the equipment represents substantial additions to the total LMF capital, operating, and maintenance costs and potentially significant impacts on LMF operations, we are studying in greater depth the relevant regulations, the necessary equipment and their costs, and the effects on operations of safety and environmental-protection procedures.

Systems to clean up the experimental area building atmosphere before discharging circulated air to the environment may be needed during normal operations. Such systems must clean the air in the experimental area building before discharging it to the surrounds after accidental releases of radioactivity and/or toxic chemicals. The required equipment includes special gas circulation, filtration (high-efficiency particulate air-HEPA filters), and/or liquid scrubbing or, more typically, adsorption (activated-charcoal) systems for removing gaseous and particulate radioactive and other hazardous substances from the air. This equipment is all standard in the nuclear power industry.

Target-Chamber Diagnostics

Diagnostic instrumentation is required to monitor the condition of such target-chamber equipment as the gas-puffing systems and the equipment required to protect optics from shrapnel before shots are fired. With the appropriate diagnostics, malfunctions in protective equipment will be detected before the laser is fired so that shots could be aborted and expensive damage avoided. Diagnostics are also needed to record the information during shots to identify causes of improper operation and make decisions regarding maintenance.

Target-Chamber Maintenance

A requirement is anticipated for dedicated general-purpose and special-purpose equipment to perform maintenance operations remotely on activated target-chamber components and systems. Nonactivated experimental area

equipment would be maintained using conventional facility maintenance equipment and facilities. Damage by missiles and interference with functionality by deposited target and experiment debris and ablated target-chamber material are potential sources of trouble. The required equipment may include remote handling and transportation equipment, cutting, welding, and other assembly and disassembly tools, and special equipment for decontamination and radioactive waste treatment and storage dedicated to the target chamber and associated equipment. Most of this equipment is expected to be relatively conventional and hence easily specified once the requirements are established.

The remote-handling equipment that is needed may include floor-mounted, bridge-mounted, and through-the-wall manipulator systems with associated controls, and glove boxes. The required remote-transport equipment may include special-purpose, dedicated cranes, transporters, handling fixtures, and transfer locks, with associated controls. The remote inspection, viewing, and test systems that are needed may include in-chamber and ex-chamber direct-optical, television, and laser systems. Remotely controlled tools may be needed for cutting, welding, and machining activated target chamber equipment and associated equipment for assembly and disassembly and repair in place.

Special decontamination equipment dedicated to the experimental area in addition to central radwaste-facility equipment may be needed to remove surface contamination from the target chamber and associated equipment prior to maintenance or disposal. Such dedicated equipment might include water, steam, and chemical cleaning systems. Special dedicated radioactive waste treatment and disposal equipment also may be required. Such dedicated equipment might be for the handling, cutting, chemical treatment, fixation, compacting, packaging, storing, and shipping of activated and contaminated target-chamber and experiment components and decontamination wastes.

Experimental Area Building

The experimental area consists of the basic building structures, ordinary building services, and any special containment, security, and safety structures required to house the target chamber and its support systems, some target and applications experimental equipment, and some security, safety, and environmental-protection systems. Figure 4 illustrates its location at the center of the arms of the driver building.

Many of the requirements for the experimental area building are essentially those for any structures in which operations involving intense radiation fields are conducted or radioactive materials are contained. However, the LMF experimental area building will not resemble a fission power

plant containment building in that it will not have to cope with continuous large releases of energy, nuclear reactions other than decay that produce highly radioactive isotopes, or high pressures that persist indefinitely.

The experimental area building must be cleared of people when shots are fired to avoid hazards, such as intense electromagnetic fields generated by high voltages and currents, and the intense radiation fields generated during shots. The building must provide some shielding capability to supplement other target-chamber and beam-enclosure shielding to reduce the fluences. The fluences of fusion neutrons and energetic gamma photons that escape from the building during a shot must be kept to very low levels to meet regulatory requirements. Concrete appears to be an appropriate primary construction material for the experimental area building.

How much supplemental shielding must be provided by the building depends on the shielding around the target chamber and beam enclosures in the experimental area and any other shielding internal to the building structure. The shielding around the target chamber is designed to reduce the levels of radiation to levels that permit routine access to the experimental area building by operating personnel and experimenters. Nucleonics and radiation transport calculations have been performed to assess the amount of activation that can be expected and the shielding that must be provided to deal with the target emissions and radiation from activated materials. The equipment and procedures required to ensure safe operation, protect the environment, and meet regulatory requirements and the associated costs are being investigated

The experimental area building also must accommodate in an acceptable manner the externally imposed loads. These were described in the driver building section. The many large optical components in the experimental area for the delivery of high-energy beams to target must be provided with stable platforms. Targets mounted in the target chamber awaiting illumination by the driver beams and some experiment instrumentation must also be protected from vibrations. A lot of room will be required around the large target chamber to direct driver beams to the appropriate places. Therefore, the experimental area building will be large. The thick foundations and other structural components of a very large concrete structure can provide the stable attachments for large optical components within the experimental area building. Additional massive concrete structures to provide stable platforms for large optical components, and one or more operating floors will be required within the building. However, no large optics need be attached to the roof in the LANL LMF concept.

For the three-sided target illumination geometry selected as the reference for the LANL LMF concept, an experimental area building in the shape of a vertical cylinder with a shallow domed roof is convenient. It is located largely below grade to reduce the shielding capability that must be provided by the building structure. The thickness of its walls can be minimized to reduce costs and the below grade location is convenient for interfacing with the driver building, whose main operating floor is located on grade. Because no large optics will be supported by the roof of the experimental area building, and because operating floors within the building provide the shielding to prevent excessive skyshine or radiation escape through the roof, it can be designed for minimum thickness consistent with other requirements. Thin, doubly curved panels with an diameter/height ratio of about 6:1 stiffened by curved radial ribs and a circumferential thrust ring, all poured in place, is one such option. If the roof is supported by columns carefully designed to economize on materials while providing the necessary strength, stiffness, and resistance to transmission of vibrations, then thin precast curtain walls can be used above ground. If the building excavation is in competent rock, the underground walls can be made of concrete reinforced with steel fibers constructed in one step by spraying. If not, then thin precast concrete panels can be used. This simple type of construction has been used successfully for many years to quickly and economically construct much larger enclosed sports complexes and other public buildings.

CONCLUSIONS

LANL has made considerable progress in the development of a credible concept for an affordable LMF with a KrF laser driver that meets the requirements defined in the first phase of the LMC Scoping Study insofar as the major systems are concerned. This concept represents reasonable extrapolations from and modifications of existing AURORA technology. Additional studies are being conducted to fill in the details and to find ways to improve performance and reduce costs to make the LANL LMF concept even more attractive. An R&D path from today's KrF facilities to an LMF with a KrF laser driver that is aggressive, but still involves acceptable risks, also has been defined at LANL.

ACKNOWLEDGMENTS

REFERENCES

Bourque, R. F., E. T. Cheng, R. L. Creedon, K. R. Schultz, and D. L. Sonn, "Innovative Design Concepts for the LMF Target Chamber and Related Systems," GA-A19651, General Atomics, San Diego, CA, June 1989.

Bowling, P. S., L. Burczyk, R. D. Dingler, and R. B. Shurter, "AURORA Inertial Confinement Fusion Laser Control and Data Acquisition System," Fusion Technol. 11, 612, 1987.

DOE, "LMF Laboratory Microfusion Capability Study, Phase I Summary," DOE/DP-0069, U. S Department of Energy, 1989.

Ewing, J. J., J. M. Eggleston, D. D. Lowenthal, and M. J. Kushner, "New Techniques for KrF Laser Fusion Systems," Final Report, Spectra Technology, Bellevue, WA, 1986.

Hanlon, J. H., and J. McLeod, "The AURORA Laser Optical System," Fusion Technol. 11, 634, 1987.

Harris, D. B. R. R. Berggren, N. A. Kurnit, R. G. Berger, J. M. Eggleston, J. J. Ewing, and M. J. Kushner, "KrF Lasers as Inertial Fusion Drivers," Proc. 11th IEEE Symposium on Fusion Engineering, Austin, TX, November 18-22 1985.

Harris, D. B., N. A. Kurnit, D. D. Lowenthal, R. G. Berger, J. M. Eggleston, J. J. Ewing, M. J. Kushner, L. M. Waganer, D. A. Bowers, and D. S. Zuckerman, "Future Developments and Applications of KrF Laser-Fusion Systems," Fusion Technol. 11, 705, 1987a.

Harris, D. B., L. A. Rosocha, and D. C. Cartwright, "Los Alamos National Laboratory View of Commercial Drivers for Laser-Driven Reactors," Proc. 3rd Inertial Confinement Fusion Systems and Applications Colloquium, UWFDM-749, Madison, WI, November 9-11, 1987b.

Hogan, W. J., "Missions and Requirements for a Laboratory Microfusion Facility (LMF)," Proc. 8th Topical Meeting on the Technology of Fusion Energy, Salt Lake City, UT, October 9-13, 1988; also Fusion Technol. 15, Part 2A, 541, 1988.

Honig, E. M. and M. Kristiansen, Co-Chairmen, Workshop on Large Area Electron Beam Diodes, Monterey, CA, June 8-10, 1989. (Proceedings to be published by Los Alamos National Laboratory.)

Kortegaard, B. L., "PAC-MAN, A Precision Alignment Control System for Multiple Laser Beams Self-Adaptive Through the Use of Noise," Fusion Technol. 11, 671, 1987.

Lehmberg, R. H., and J. Goldhar, "Use of Incoherence to Produce Smooth and Controllable Irradiation Profiles with KrF Fusion Lasers," Fusion Technol. 11, 532, 1987.

MacFarlane, J. J., R. R. Peterson, and G. A. Moses, "Analysis of Physical Processes in ICF Target Chambers: Application to the Laboratory Microfusion Facility," Proc. 8th Topical Meeting on the Technology of Fusion Energy, Salt Lake City, UT, October 9-13, 1988; also Fusion Technol. 15, Part 2A, 557, 1988.

Mandl, A. E., D. E. Klimek, and E. T. Salesky, "KrF Laser Studies at High Krypton Density," Fusion Technol. 11, 542, 1987.

McLeod, J., "Output Optics for AURORA: Beam Separation, Pulse Stacking, and Target Focusing," Fusion Technol. 11, 654, 1987.

Monsler, M. J., and W. R. Meier, "A Carbon-Carpet First Wall for the Laboratory Microfusion Facility," Proc. 8th Topical Meeting on the Technology of Fusion Energy, Salt Lake City, UT, October 9-13, 1988; also Fusion Technol. 15, Part 2A, 563, 1988.

Nilson D. G., and J. G. Woodworth, "Final Optic Protection Designs for ICF Containment Chambers," Proc. 8th Topical Meeting on the Technology of Fusion Energy, Salt Lake City, UT, October 9-13, 1988; also Fusion Technol. 15, Part 2A, 578, 1988.

Orth, C. D., "Frost as a First Wall for the ICF Laboratory Microfusion Facility," Proc. 8th Topical Meeting on the Technology of Fusion Energy, Salt Lake City, UT, October 9-13, 1988; also Fusion Technol. 15, Part 2A, 571, 1988.

Pendergrass, J. H., and D. B. Harris, "Work Breakdown Structure for an LMF with a KrF Laser Driver," LA-UR-89-2827, Los Alamos Scientific Laboratory, Los Alamos, NM, 1989.

Pitts, J. H., J. G. Woodworth, and M. Tabak, "Preventing Vaporization and Destructive Shock Waves in ICF Target-Chamber First Walls," Proc. 8th Topical Meeting on the Technology of Fusion Energy, Salt Lake City, UT, October 9-13, 1988; also Fusion Technol. 15, Part 2A, 595, 1988.

Rosocha, L. A., and K. B. Riepe, "Electron-Beam Sources for Pumping Large Aperture KrF Lasers," Fusion Technol. 11, 576, 1987.

Rosocha, L. A., J. A. Hanlon, J. McLeod, M. Kang, B. L. Kortegaard, M. D. Burrows, and P. S. Bowling, "AURORA Multikilojoule KrF Laser System Prototype for Inertial Confinement Fusion," Fusion Technol. 11, 497, 1987a.

Rosocha, L. A., J. McLeod, and J. A. Hanlon, "Beam Propagation Considerations in the AURORA Laser System," Fusion Technol. 11, 624, 1987b.

Sullivan, J. A., "Design of a 100-kJ KrF Power Amplifier Module," Fusion Technol. 11, 684, 1987.

Tobin, M. T., M. S. Singh, and W. R. Meier, "Neutronics Analysis of the Laboratory Microfusion Facility," Proc. 8th Topical Meeting on the Technology of Fusion Energy, Salt Lake City, UT, October 9-13, 1988; also Fusion Technol. 15, Part 2A, 583, 1988.

Willke, T., D. Dingee, M. Bampton, W. Bickford, J. Hartman, A. Rockwood, E. Simonen, V. Teofilo, and T. Frank, "A Plan for the Development and Commercialization of Inertial Confinement Fusion," in Proc. Heavy Ion Fusion Workshop, Sept. 19-26, 1978, ANL-79-41, Argonne National Laboratory, Argonne, IL, 1979.

B. LASER TARGET TEST FACILITY

J. Allan Sullivan

INTRODUCTION

The Los Alamos 100-kJ Laser Target Test Facility (LTTF) is a necessary and logical step prior to committing to a 10-MJ Laboratory Microfusion Facility (LMF). It will serve as both a test bed for the low-cost advanced technologies needed for the LMF and as a necessary check on the target physics. Los Alamos has a target date of October 1989 for completing the conceptual design of this facility. Because we are in the early conceptual phase of the LTTF, this article will be limited in scope to general considerations of facility design, laser architecture, performance parameters, and costs.

PURPOSE AND GOALS

The prime reasons for constructing the LTTF are to demonstrate the scaling of KrF lasers to 100-kJ class devices and to measure target interactions at energies and laser bandwidths of interest, based on predictions of capsule performance for shaped pulses using existing codes. Before a commitment is made to the construction of a 10-MJ LMF or even a 1-MJ prototype for such a facility, the type of drive required can be determined at lower energies. This will result in significant cost reductions for the larger facilities. For the KrF laser, the intermediate step also provides an opportunity for a stepped approach to the needed laser amplifier scaling. The stepped approach will significantly reduce the performance risk inherent in moving to an LMF in a single step.

The baseline design of the facility will incorporate both direct and indirect drive targets with the option for conversion from one irradiation geometry to the other.

The layout of laser amplifiers and the target chamber will be similar to that of a 10-MJ LMF facility except the final amplifier energy for the LTTF will be 50 kJ instead of the 250 kJ that is the baseline design for the LMF. To reach the 100-kJ output energy, two of the 50-kJ amplifiers will be arranged as a doublet in which the outputs are recollimated on a single optic before being demultiplexed and directed to the target. This conceptual design is illustrated in Fig. 1.

The technologies that will be demonstrated on the LTTF are

- the performance of 50-kJ KrF amplifier modules. These units will be within a factor of 5 in energy output of the amplifiers assumed in the current LMF design.
- pulse shape generation in the front end and propagation through the amplifier chain with minimal distortion;
- broad bandwidth generation and propagation;
- interstage encoding that will make possible the use of more compact initial amplifiers that operate with shorter pulse lengths than is possible when the full encoding is accomplished immediately after the front end and first amplifier stage as in the current AURORA laser;
- aperture sharing with two 50 kJ amplifiers;
- the performance of high damage threshold reflective optics; and
- verification of the LASNEX predictions of ignition and gain for shaped pulses.

In addition to the specific technological advances to be achieved, the construction of the LTTF will place the important factor of cost projections for an LMF on a much firmer footing. The initial construction and testing of a 50-kJ amplifier will be completed before an amplifier of this size is placed in the LTTF. The economy of scale for large amplifiers should be born out by the construction of the LTTF.
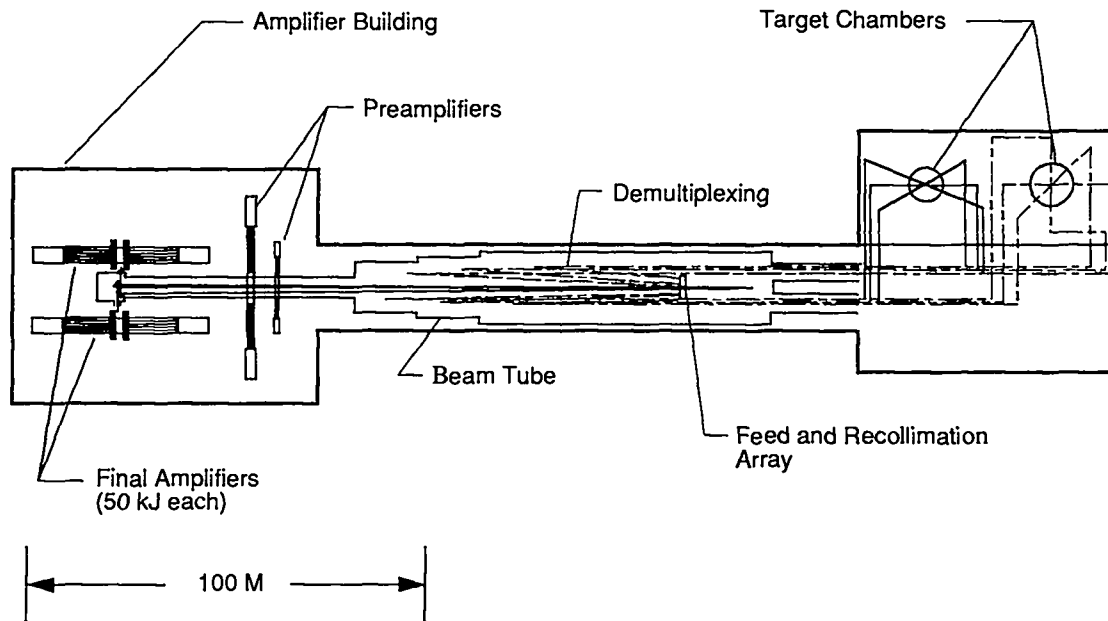
Fig. 1. Conceptual layout of the amplifiers and target chamber for the LTTF.

PERFORMANCE PARAMETERS

At this early stage of the design of the LTTF only general requirements have been fixed. Specific design descriptions of components and the facility and specific performance parameters are not available. The general requirements and specifications that are available are listed in Table 1.

TABLE 1. Design Requirements and Parameters for the Los Alamos KrF Laser Target Test Facility.

Requirement or Parameter	Value
Laser Output Energy	100 kJ
Ultimate Amplifier Stage	50 kJ
Aperture Sharing	Yes
Interstage Encoding	Yes
Laser Wavelength	248 nm
Integrated Laser Shots Per Day	2
Target Shots Per Week	1
Pulse Shaping	Yes
Indirect Drive	Yes
Direct Drive	Yes

The design of the 50-kJ amplifier has been accomplished to the conceptual level. This amplifier unit is a factor of 2.5

higher in output energy than the AURORA LAM class amplifier. However, with the upgrade in design parameters and performance improvement currently being developed, the actual size of the 50-kJ amplifier will be slightly more than a factor of 2 larger than the AURORA LAM. The performance parameters for the 50-kJ amplifier module are compared with an AURORA-class LAM and to an LMF amplifier module in Table 2. A concept of the amplifier is shown in Fig. 2.

FACILITY CONCEPTUAL DESCRIPTION

The conceptual layout of the 100-kJ LTTF (Fig. 1) illustrates the current concept; that is, the facility will have a single 100-kJ laser arm attached to a target building with two target chambers. The plan is to construct the facility so that a later upgrade in energy to the 1-MJ level would be possible with a modest amount of new construction. This plan would allow for true prototyping of LMF equipment at the ignition level and would serve as a test bed for checking the target parameters and laser parameters that were determined from the LTTF. The upgrade will involve the full replacement of the 100-kJ equipment and optics and the addition of laser arms as required to reach the final target energy . An example of the upgraded facility is presented as Fig. 3 for which 100-kJ amplifiers have been assumed as the ultimate gain stage units. An upgrade using 240-kJ amplifiers would require only two laser arms to give a total energy of 1440 kJ.
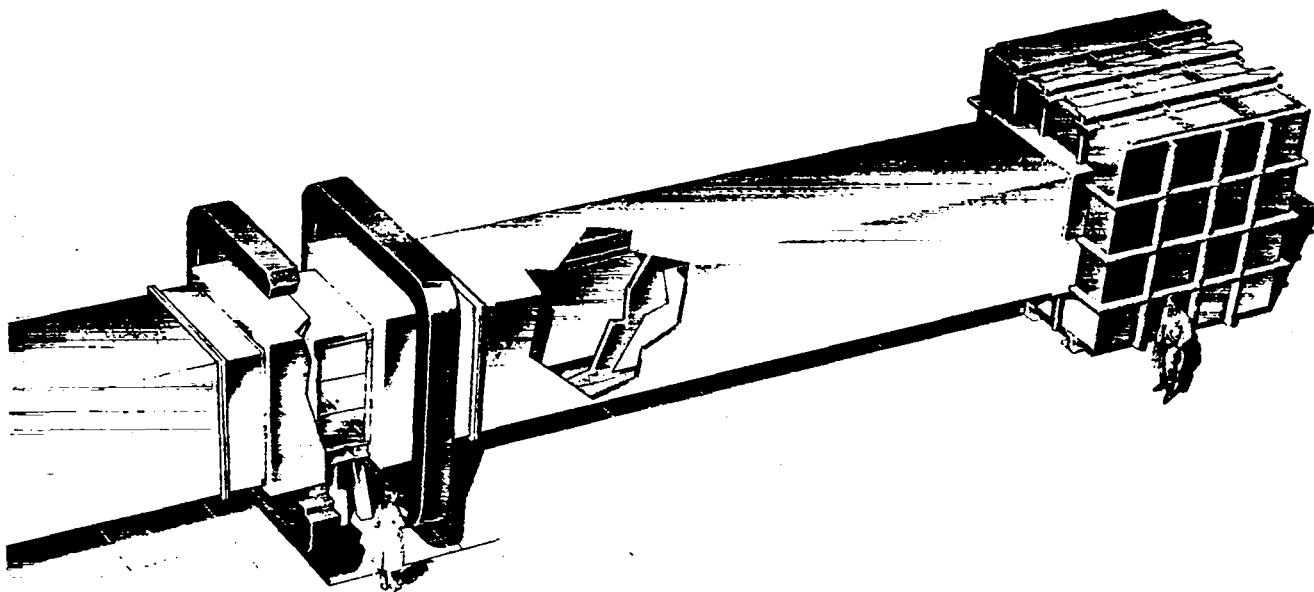
Fig. 2. Concept of the final amplifier for the LTTF.

TABLE 2. Comparison of KrF Amplifiers

Parameter	Units	20 kJ LAM Class	50 kJ Amplifier	240 kJ Amplifier
Pumped width	meters	1.0	1.1	1.3
Pumped height	meters	1.0	2.2	3.9
Pumped length	meters	2.0	2.35	3.75
Unpumped lengths				
each end	meters		0.20	0.20
Pump power	kW/cm^3	81	250	200
Pump duration	ns	500	576	750
E-beam voltage	kVolts	675	800	1000
Current density				
into gas	A/cm^2	6	20	13
Hibachi				
transmission	%	30	50	60
Diode current				
density	A/cm^2	20	40	21.7
Diode current				
per side	MA	0.5	2.07	4.20
Diode impedance	Ω	1.34	0.37	0.32
Intrinsic				
efficiency	%	6.0	11	11
Krypton fraction	%	6	50	70
Argon fraction	%	93.7	49.5	29.7
Fluorine	%	0.3	0.5	0.3
Gas density	Amagat	0.8	1.0	1.0
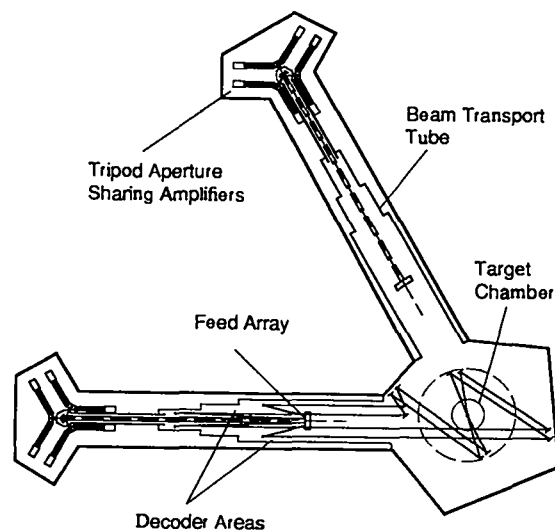
Fig. 3. Upgraded facility for the LTTF.

The LTTF facility will have a front end that delivers a single shaped pulse to the amplifier chain. Each pulse will be amplified and further divided (encoded) until the required number of time slots at the correct energy is achieved at the output of the final amplifier cluster. Pulse shaping will be accomplished in the front end where the optics are small, so that control of the pulse shape will be a matter of changing the shape of a voltage signal to a Pockels cell and inserting or removing saturable absorbers. The grouping of the final

amplifiers to share a common optic at the recollimator location reduces the total number of optic elements as well as the number of alignment elements. To an observer viewing the amplifiers from the feed and collimation array, the two amplifier beams appear as one large beam that is made square by choosing the aspect ratio of the amplifiers as 2:1. The preamplifiers shown in Fig. 1 are located below the main floor level near the doublet of ultimate amplifiers. The output beam from the penultimate amplifier will propagate up to the feed and recollimation array and will progress from there to the ultimate amplifiers where it will be spatially divided into two equal parts. The beams will double pass each amplifier, be brought adjacent to each other, and then travel to the recollimation optics. After recollimation the beamlets will be partially decoded in the areas shown in Fig. 1. The first half of the beam will be handled on one side and the second half on the other side of the center line of the recollimator array and beam transport housing. The beamlets will then be directed to the target building individually where the remaining half pulse width delay of the lower set of beamlets will be removed. The beams will then be directed to aiming mirrors and thence through focusing lenses on the target chamber to the target. The estimated size of the target chamber is 10 m in diameter, and the aiming optics will be located about 10 m from the target.

SUMMARY

The scaling of KrF laser technology to a very large 10-MJ class laser microfusion facility demands the construction of an intermediate facility that will permit the demonstration of the operational viability of the components at an affordable scale. To meet this requirement, an upgradable 100-kJ laser fusion facility is proposed as the next major step in the KrF development program at Los Alamos.

VII. KrF Laser Technology
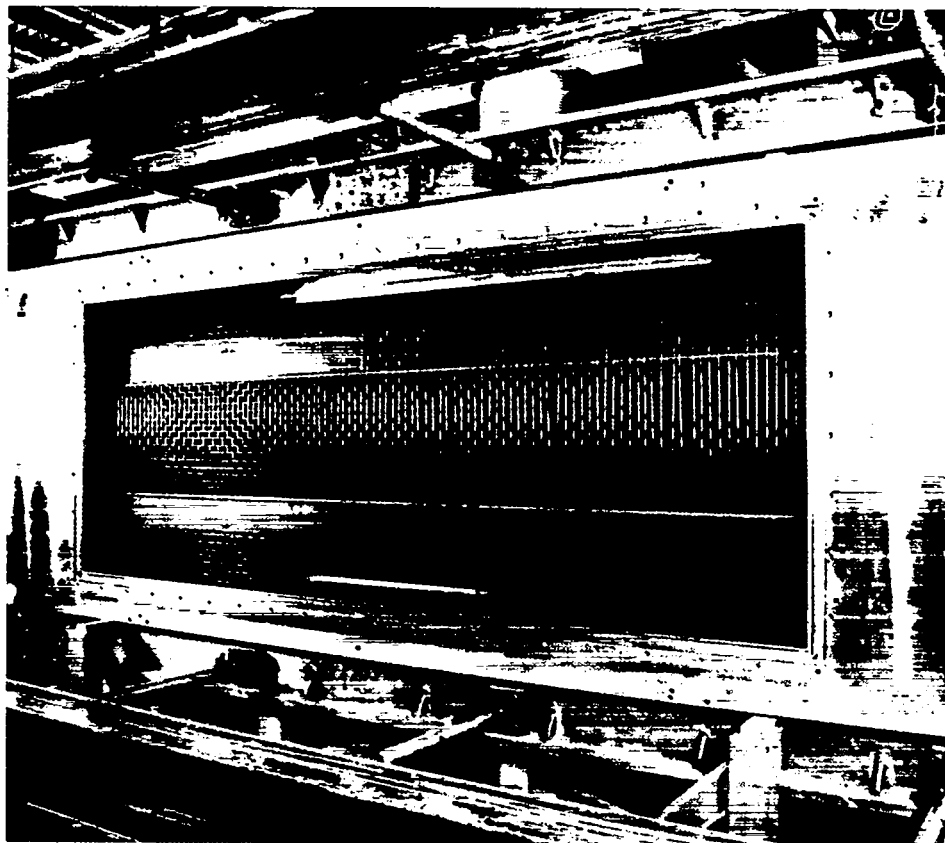
Large-aperture electron-beam diode for the AURORA Laser Facility.

A. Gas Chemistry for KrF Lasers

B. The Plasma Physics of Electron-Beam Diodes for KrF Laser Amplifiers

C. Optics Technology for KrF Lasers

D. Nonlinear Pulse Compression

E. AURORA Front-End Development

F. Electron-Beam Pumping Technology for KrF Lasers

A. GAS CHEMISTRY FOR KrF LASERS

Robert Anderson and Roger Tennant

INTRODUCTION

Gas handling and analytical chemistry in large KrF e-beam lasers present many unique problems that have received considerable attention in the past several years. It has been demonstrated in both discharge and e-beam pumped lasers that very small quantities of gaseous contaminants can have drastic effects on laser performance. These contaminants are generated by fluorine reactions with seals, construction materials, e-beam foils, and optics; they can cause kinetics effects, scattering, and laser beam attenuation. It is important to understand the formation and control of these impurities to minimize the effects on the AURORA system and on future excimer laser systems. The specific areas summarized here include materials compatibility, gas handling and vacuum systems, gas delivery and mixing, rare gas recovery, gas analysis, and laser beam absorption in air.

FLUORINE MATERIALS COMPATIBILITY

The materials that are suitable for use in KrF e-beam lasers have been an issue of study since Los Alamos started working with KrF lasers in 1975. A great deal of applicable information has been accumulated from both the open literature and from in-house empirical studies. The results to date and the on-going areas of study are summarized here in four general areas: the materials suitable for seals, general construction materials, optic substrates, and e-beam foils. Table 1 summarizes the corrosion rate of those materials usually considered for use in KrF lasers. Very high F_2 concentrations (up to 100 times those typically used in KrF lasers) were used to determine the corrosion rates shown.

TABLE 1. Compatibility of Materials with Gaseous Fluorine*

Corrosion Rate mils/year	Temperature, Degrees F			
	>1	>5	5 to 50	>5
Metals				
Nickel	1100	1200	1300	>1300
Aluminum 2024	700	>1000	1000	>1000
Aluminum 5154	700	>1000	1000	>1000
Silver	700			
Monel		1000	750	>1200
Inconel		1000		>750
304 Stainless Steel	400	400	500	>500
316 Stainless Steel	400			
Copper	200	400	800	>800
Bronze	200	400	700	
Brass	200	400	600	>600
Titanium Alloy 16V-2.5A1			300	
Titanium Alloy 6A1-4V	250			
Zirconium		100	400	>700
Tantalum	212		100	>100
Tin	212		100	>100
Lead			100	>100
Beryllium				75
Molybdenum				75
Nonmetals				
Alumina	392	1400		
Teflon	390			>390
Silica		480		>480
Activated Alumina		400		>400
Pyrex	212	400		>400
Soda Glass (HF absent)	212		300	>300
Graphite		75		
Amorphous Carbon			212	>212
Neoprene				All temp

* (From DMIC Memo 201, Battelle Memorial Institute, 1965 as found in Douglas 1967 and NACE 1985.)

Materials for Seals

A seal must be constructed of F_2-compatible material and it must maintain a long-term vacuum and pressure sealing force. Seal materials studied include Teflon, Viton, Kalrez, and Neoprene. As shown in Table 1, Teflon has been found to be the most chemically inert; however, Teflon is porous and it cold lows with time. Hence it is difficult to attain a long-term vacuum and pressure seal with Teflon. Teflon-coated Viton O-rings and Teflon with a central spring to provide a more constant sealing force could be used. Viton, Kalrez, and Neoprene have been studied extensively. Neoprene becomes brittle (seal integrity decreases with time), and a substantial amount of CO_2 is produced as a reaction product (Neoprene + F_2). Of the two remaining types, Kalrez is slightly more chemically inert than Viton. However, Kalrez costs about 30 times as much as Viton. Also, the predominate contaminant from Kalrez is SiF_4 and from Viton, small amounts of CO_2 and CF_4. Figure 1 shows the effect of various gaseous contaminants on KrF discharge laser output. Similar effects are anticipated for KrF e-beam lasers. Because of the need for F_2-compatibility and reasonable cost, there is no clear advantage of using Kalrez over Viton. Therefore, for e-beam KrF lasers with a small O-ring surface area and a large gas volume, Viton is generally the seal of choice.

When the seal surface to gas volume ratio is large (as in spectrophotometer gas analysis cells) or when a very long-term material study is being conducted, metal seals are sometimes used to eliminate the reaction products of the O-rings. Metal seals that have been used with success include the conflat knife edge type with copper or aluminum gaskets, hard silver solder or welded joints, copper or silver alloy wires, and C-seals of various types.

Materials for General Construction

Results from in-house F_2 material interaction studies are consistent with the Battelle data in Table 1. Materials that have been studied at Los Alamos include nickel, aluminum, inconel, stainless steel, copper, brass, titanium , alumina, Teflon, Kel-F, silica, Pyrex, Kynar, PVC, polyethylene, epoxy, plexiglass, lexan, and delrin. For near room-temperature operation outside regions impacted by the e-beam, either aluminum or stainless steel is adequate as a general construction material. A common practical issue to be addressed is weldability. Stainless steel (304 or 316) can be reliably welded. Generally, if aluminum is to be welded, alloys such as 2219 should be used. Other more common alloys (for example, 6061) typically have a weld cracking

problem that leads to serious air leaks. Materials such as nickel, monel, and inconel may be desirable but are not necessary for current applications. In general, plastics should not be used because of gaseous contaminant formation (see Fig. 1). There has been a great deal of concern over the formation of SiF_4 from the reaction between silicon in the metals of construction and F_2. Once the laser system is dry (the water and HF are gone), the SiF_4 formation rate is very slow. Except during the initial conditioning of the lasers with F_2 (which has to be done every time the lasers are opened to air), gas contaminant formation does not appear to be a major problem for operations lasting a few hours.
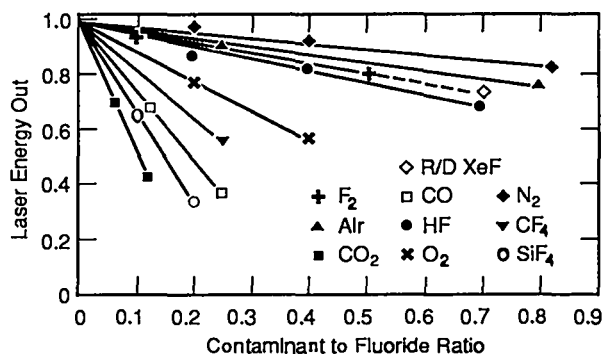

Fig. 1. Effect of various gaseous contaminants on KrF discharge laser output.

Contaminants are still a problem in the recycling of the expensive laser gas. After a system shot, the laser gas is typically pumped through a series of three tanks. The first tank serves as a collection vessel, the second tank is used for long term storage and analysis, and the third is used for mixing and supplying gas to the lasers. The gas in the third tank contains F_2; current data indicates that the shelf life for reuse is about eight weeks. Sometimes a tank contains laser gas for extended periods of time at a pressure below the local ambient pressure. Hence, air leaks are possible. Except for possible air leaks, the main contaminant that gradually accumulates is SiF_4. More exact data on the effects of small amounts of air and SiF_4 on KrF e-beam laser performance is needed.

If the gas in the second tank is not pure enough, it needs to be reprocessed or dumped. Krypton currently costs about $1.50 per standard liter. For the near term, occasional dumping of contaminated gas may be acceptable, but eventually the reprocessing issue must be addressed. The predominate contaminants appear to be air, CO_2, and SiF_4. If air leaks can be prevented and if the F_2 does not have to be removed, then the gas would have to be purified only occasionally. This could be done by pumping the gas through a pressurized liquid nitrogen or liquid argon cooled

trap to regulate the temperature . Such a system could be relatively simple and moderately inexpensive to operate. If air and/or F_2 have to be removed, then a high temperature getter trap would have to be used and it may be necessary to reprocess all of the gas. Such a system is more complicated to build, much more costly to operate safely, and produces a much larger hazardous waste disposal problem (the getter bed material).

Materials for Optical Substrates

Probably the F_2 substrate materials used most frequently for optics in contact with the laser gas are of silica. These substrates are protected by a coating that is highly resistant to F_2 attack. The problem of chemical attack of the substrate is thought to arise largely from pin holes in the optical coating. The primary attacking species is HF, which is formed from the reaction of F_2 with the monolayers of H_2O; HF can produce substantial pits in silica substrates. (Water removal will be discussed later.)

For the long term, more attack-resistant substrate materials are possible for at least some of the optic substrates. For example, mirrors could be coated on metal substrates. Also, there is an effort underway at Harshaw to produce large-diameter calcium fluoride optics that could be used for some of the transmissive optics.

E-beam Foil Materials

In e-beam pumped lasers, a vacuum barrier (foil) is required to separate the pressurized laser chamber from the high vacuum of the diode box. A good e-beam foil material has to meet many technical requirements:
— a thickness/Z-number combination such that e-beam losses are within acceptable limits;
— the tensile strength necessary to support the pressure impulse created by the e-beam;
— compatibility with the laser gas;
— suitable metallurgical properties to minimize problems with pin holes, fatigue, parasitic laser oscillations, etc.;
— sufficient thermal conductivity to prevent failure at the elevated foil temperatures produced by the e-beam.

An e-beam can easily produce peak temperatures of the order of 400^oF on foil surfaces. High peak temperatures on the foil and on the back wall of the laser chamber drive F_2 material reactions much more vigorously than at room temperature and will also reduce tensile strength. As a result, 20 to 30 pulses is enough to produce a virtual snowstorm of particulates from a more reactive foil material such as titanium. Although never completely eliminated, the level of particulate generation is greatly reduced by frequently changing the gas mix (after 3 or 4 shots). The particulates formed from only 3 or 4 shots are still very fine and can be removed by the pumping system and filtered out of the gas before they deposit extensively throughout the laser chamber.

Three general types of metal foils have been investigated for use in KrF lasers. These include titanium alloys, nickel alloys, and aluminum alloys. The nickel and aluminum foils have their utility, but it is currently accepted that, despite its reactivity with fluorine, titanium is the best e-beam foil material. The final foil developed for use on large KrF e-beam amplifiers will probably be titanium coated with a more F_2-compatible metal such as aluminum, copper, or nickel. Further development and testing is currently being done.

Conclusions about Material Compatibility

A great deal of progress has been made in the last 14 years in understanding F_2 material interaction problems in KrF e-beam lasers. The large size (square meters) of some of the AURORA amplifiers creates unique problems not found in smaller KrF lasers. These problems include the availability of large F_2-compatible optical substrates such as calcium fluoride, though this situation may be changing. The production of large F_2-compatible foils that suppress parasitic oscillations is a new issue. Areas requiring additional work include
— determination of the effect of certain contaminant gases on laser performance;
— development and testing of techniques to remove water from laser surfaces to prevent or reduce HF formation;
— development and testing of an optimum foil for long term application in large laser amplifiers;
— refinement of fabrication, cleaning, and conditioning techniques to minimize gaseous contaminant formation;
— refinement and testing of the gas processing system.

GAS HANDLING ISSUES

Several gas handling issues need to be addressed for successful operation of a large KrF laser facility. There are substantial gas-related concerns both inside and outside of the laser systems. These include the filling and evaluating of the laser systems and plumbing; the uniform mixing of the laser gas; the analysis of the laser gas composition to ensure proper concentration and purity; and the providing and maintaining of a uniform and nonabsorbing atmosphere in the beam propagation tunnels. Careful attention to detail in

the above areas has contributed substantially to the recent successful operations of the AURORA laser system.

Gas Handling and Vacuum Systems

Analytical studies have shown that chemical contaminants in the laser chambers can cause significant problems in laser performance. Although there are many contaminants of concern, the foremost has been water. Water is introduced into the system via room air when the system is opened and it occurs in the laser gases themselves. All laser gases used in AURORA are of the highest purity available in the commercial market. The formation of HF from the water/F_2 reactions created a mechanism for the formation of other contaminant species such as SiF_4 and CO_2, thought to be caused by the HF attack on optics, metal surfaces and seals. In a laser system, like AURORA, with miles of piping and very large laser chambers (up to 4700 l), there are literally many tens of square meters of surface area covered with molecular layers of water. To reduce the effects of the water/F_2 reactions, very large and efficient pumping systems are utilized. Rough pumping is accomplished through a central vacuum system consisting of two Leybold DK-200 pumps coupled with two WS 1000 Leybold blowers. Typically this system will evacuate the laser chambers (and the hundreds of meters of connecting plumbing) to <50 m Torr. Each laser chamber is also pumped with a cryotrapped mechanical blower combination capable of pumping the chamber to a suitable operating pressure (<10 m Torr). Some success in system passivation has been achieved by altering purges of the system with dry argon and 0.5% F_2. It has been concluded that it is critical to remove as much water as possible prior to laser operation. Other methods for removing surface water (uv light exposure, heating, plasma) are also being examined.

Because of the high cost ($1.50 per standard liter) and the large volume of krypton gas used in AURORA, the need to reclaim gases is obvious. The integration of gas reclamation into an already complex gas handling system increases the potential for further gas contamination. Dry pumps and compressors are required to reduce the formation of COF_2 and CF_4, both known excimer laser poisons. Extreme caution must be exercised in the fabrication of lines, the selection of hardware, and cleaning methods used in a gas handling system of this magnitude.

Gas Mixing

In addition to the control of contamination, the supplying of a precise, homogeneous gas mix is imperative. A typical gas mix in an AURORA amplifier consists of from 0.15% - 0.3% F_2 in 10% Kr, with a balance of Ar.

Experiments have shown that when supplied in series, the F_2 does not readily mix with the Kr/Ar in the laser chamber. Because the partial pressure of the F_2 is so small, it has been determined that for efficient laser performance, additional mixing must occur. In AURORA this is accomplished by circulating the gas through a filter and a metal bellows pump recirculating system. This method seems to produce a homogeneous mix, but it creates additional potential contaminant and passivation concerns. It has, however, been demonstrated that with adequate passivation measures, the gas can be controlled to within a few percent of desired partial pressures. To eliminate the need for additional mixing pumps, a premix supply tank has been implemented as part of the reclaim and supply system. This 15,000-l nickel tank is equipped with a magnetic coupled F_2-compatible mixing fan. The reclaimed gas is replenished as required, mixed, and then supplied to the laser amplifiers as a premix. Chemical analyses are performed at regular intervals to ensure gas purity. Further studies in gas mixes and their effects on laser performance would be desirable. In particular, the mechanisms/processes which affect the laser kinetics and performance must be understood.

Gas Analysis

To understand and measure the gas mix ratios and system contaminants, an elaborate analytical capability has been established. Early attempts were made to measure F_2 concentrations inside the laser chambers using absorption of the 325-nm HeCd laser (analytical precision ~10%). This technique was later discontinued because of experimental uncertainties caused by optical scattering from particulates generated by interaction of F_2 with the titanium foil and by power fluctuations of the HeCd laser. Subsequently, a method was developed for storing samples of laser amplifier gas in lecture bottles for later chemical analysis. This method was thoroughly tested and proved to be much more accurate (analytical precision ±5%) than previous methods if analysis were performed shortly (2-3 h) after the sample was taken. Adequate passivation of sample cells was found to be critical to precision analysis. The analytical system for AURORA consists of three major analytical instruments: a uv spectrophotometer to measure the F_2 concentration (accurate to ±5%); an IR spectrometer to measure contaminants; and a UTI mass spectrometer to measure Kr/Ar ratios and contaminants. The analytical precision of contaminant measurements depends on several factors. The partial pressure of the contaminants (particularly as compared to the instrument signal to noise ratio) and the accuracy of the measured cross section for the species directly affect the analytical precision. For small partial pressures, the most common analytical problems (for example, pressure

broadening and instrument sensitivity) also affect analysis. For most common contaminant compounds, the analytical precision is ±10%.

Laser Beam Absorption

Considerable progress has been made in understanding the attenuation of the AURORA laser beam by atmospheric impurities in the beam path. Experiments have identified possible uv-absorbing contaminants present in the beam tunnel air. The outgassing properties of many materials used in or near the beam tunnel are also being studied. The impurities that absorb 248-nm photons and degrade the beam are either molecules with high 248-nm cross sections at parts per billion (ppb) concentrations or molecules with low cross sections at part per million (ppm) concentration. When there is no source of contamination, the latter is not a serious problem because air permeation rates will usually reduce impurity concentrations below the ppm range. The high cross section (ppb concentration) contaminants can cause serious effects, especially when long beam paths are necessary, as in the AURORA project. Contaminants of ppb concentrations also create analytical difficulties, and therefore require sophisticated preconcentrating analytical techniques or pressurized long path-length uv cells. Preconcentration techniques not only separate the major components, nitrogen and oxygen, but also separate or eliminate interference from water and carbon dioxide collected by extracting the impurities with heptane. Because the long path-length cells suffer from interference from these contaminants, the preconcentration method is the analytical method of choice.

Preliminary results indicate that the contaminants of most concern are plasticizers (dioctyl phthalate, dibutyl phthalate), transformer oils, and ozone. Studies are looking at submicron particulates as possible air attenuators. Large HEPA (high efficiency particulate air) and activated charcoal filters that have been installed in the AURORA beam tunnels have resulted in a four-fold reduction of the typically observed beam attenuation.

REFERENCES

Douglas Missile and Space Systems, Advanced Propulsion Staff, "Fluorine Systems Handbook," NASA CR-72064 (prepared for National Aeronautics and Space Administration), Santa Monica, CA, 1967.

NACE, Corrosion Data Survey, Metals Section, 6th Edition, D. L. Garver, Ed., National Association of Corrosion Engineers, Houston, Texas, 1985.

B. THE PLASMA PHYSICS OF ELECTRON BEAM DIODES FOR KrF LASER AMPLIFIERS

Michael E. Jones and Vincent A. Thomas

Diode Operation

The design of KrF amplifiers at the 100- to 300-kJ output level, as presently envisioned for the Laboratory Microfusion Facility, requires that the gaseous laser medium (gas) be pumped by electron beams with kinetic energy of approximately 1 MeV and a current density of 20-40 A/cm^2 for about 1 μs. For laser apertures of 3 m^2, the total electron current required can exceed 3 MA.

At Los Alamos, the approach to producing these electron beams has been to utilize monolithic cold cathode diodes fed by the appropriate pulsed power (Rosocha and Riepe 1987). This is shown schematically in Fig. 1 on the following page. These diodes consist of cathodes coated with a material such as felt that forms a plasma in the presence of high electrical stresses. The resulting electron emission is space-charge limited and, in an idealized sense, is simply a Child-Langmuir diode. In this approximation the large planar diode current density is limited only by the space- charge of the beam between the cathode and anode. For voltage below the rest mass of the electron (0.5 MeV) this current density, J, is given by

$$J = k\frac{V^{3/2}}{d^2}$$

(1)

where V is the diode voltage, d is the distance between the anode and the cathode (the A-K gap), and k = 2.34 x 10^6 Amp/Volt $3/2$.

Though the diode behaves approximately as a simple one-dimensional Child-Langmuir diode, other effects can significantly change the character of diode performance. In particular, for diode operation greater than a few hundred nanoseconds, it has been observed that the current in the

diode can increase in time. This phenomenon, known as impedance collapse of the diode, is believed to be associated with the motion of highly conductive plasma from the cathode and/or anode so that the effective A-K gap decreases. Experience has shown that the electrical characteristics of this class of diodes can be successfully modeled by modifying Eq. (1) to include an empirically determined closure velocity v_c

$$J = k\frac{V^{3/2}}{(d-v_ct)^2},$$

(2)

where t is the time. Typically v_c is a few centimeters per microsecond. The dependence of this closure velocity on cathode and anode material, background gas pressure, and applied magnetic field is complex, and only general rules of thumb exist from experimental data.

In addition, at the low impedances envisioned for future KrF lasers, the one-dimensional approximation is not strictly valid because the self-magnetic field produced by the electron beam would cause the electrons to exit the diode at large angles or be completely pinched off if not compensated by an externally applied magnetic field. This effect changes the space charge distribution in the diode and can change the impedance (see Fig. 1). The applied magnetic field, if large enough, will cause the electrons to follow the field lines. However, it has been observed empirically that a larger applied magnetic field tends to enhance the closure velocity. Thus, some compromise in the externally applied magnetic field is required. For externally applied magnetic fields of only one or two times the self field of the beam, the electron beam experiences a significant rotation. Because the foil separating the diode from the laser gas is mounted on a support, referred to as the hibachi, of finite thickness, the spiraling electrons can intersect this support structure

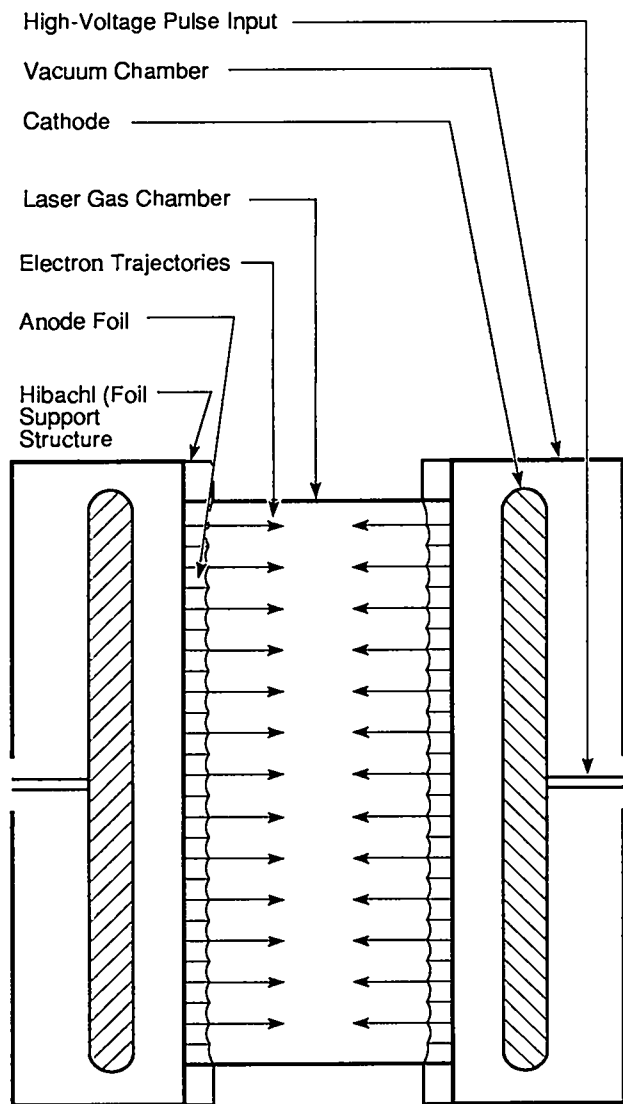and never enter the gas. This effect represents a significant inefficiency in the laser system.

High-Voltage Pulse Input

Vacuum Chamber

Cathode

Laser Gas Chamber

Electron Trajectories

Anode Foil

Hibachi (Foil Support Structure

Fig. 1. Schematic diagram of an electron-beam pumped KrF amplifier showing the anodes, cathodes, and hibachi/foil support structures.

Diode Size

The fundamental question that needs to be addressed before applying the technology is, How large can the diode be made and still maintain uniform pumping of the laser gas. Also, at what point does the externally applied magnetic field become impractical to use?

In addition to limiting the amplifier size by the size of a monolithic diode, it is possible to pump a single amplifier module with multiple or segmented diodes. The idea is to use a number of smaller diodes in parallel, each with a larger impedance to ameliorate the beam pinching problem. Return current paths would be provided between each diode. As a result, the applied magnetic field requirement could be made smaller or even eliminated. The disadvantages of this approach include additional fabrication complexity, potential electrical breakdown associated with the return current paths, and additional diode shaping, which would provide electron flow to fill in the gaps between the diodes to obtain uniform deposition.

Efficiency

At present, the efficiency of energy deposition in the laser medium is only about 25-30% of the electrical pulsed power energy supplied to the diode in any high power KrF laser. This inefficiency arises for several reasons. Much of the loss is attributed to the transmission of the electrons along skewed trajectories through the structure known as the hibachi, which supports the foil separating the diode from the laser gas. A thorough knowledge of the three-dimensional electron trajectories in the self-consistent electric and magnetic fields of the beam would, in principle, allow one to shape the hibachi to optimize this transport. A factor of two in improvement in this area appears possible and would reduce the pulsed power costs by a factor of 2.

Other important areas of energy loss include losses in the foil itself. At the higher energies envisioned for LMF parameters, this effect would be reduced compared with present facilities. Also, it is important to maintain an impedance match between the pulsed power pulse forming network and the diode throughout the pumping. The diode impedance can be a function of the magnetic field, and diode closure caused by cathode plasma expansion or other effects needs to be minimized.

Deposition Uniformity

Another important issue is the uniformity of deposition in the laser gas across the laser aperture. Monolithic cathode designs do not have the gaps in electron flow that must be corrected in segmented cathode designs. Even flat monolithic cathodes can produce nonuniform emission, depending upon the interaction of the self-consistent field with the geometry and the externally applied magnetic field. Also, there is evidence that low impedance diodes may

produce filamented electron beams. The constraints placed upon amplifier scaling by this phenomenon and its dependence on applied magnetic field are not thoroughly understand at present.

Furthermore, because the energy deposition in the gas is a function of electron beam voltage, it is necessary to ensure a correct impedance match. Diode closure will need to be minimized to avoid voltage droop, which could change the deposition profile during the laser pumping.

Modeling

To address these issues and to aid in the design of future KrF systems, particle-in-cell (PIC) methods originally invented for plasma physics applications are being developed. These PIC methods are used to study the issues of electron beam production and transport. The electron trajectories in the self-consistent electric and magnetic fields, including the effects of boundaries for a diode on the E-Gun Test Facility at Los Alamos. This calculation accurately models the geometry by alternatively advancing in time the charged particles representing the electrons and the electric and magnetic fields from the solution of the full set of Maxwell's equations. This procedure allows the study not only of equilibria but dynamic effects in the diode. The geometry of the system is treated by solving Maxwell's equations on a finite difference mesh that conforms to the electrode boundaries. This procedure is particularly suited for studying segmented, expanding-flow diodes.

This technique and its generalization to three dimensions (presently under development), together with careful correlation with experiments, will allow us to study the issues described above and make the necessary advances in technology to achieve our goal of high energy amplifiers.

REFERENCES

Rosocha, L. A., and K. B. Riepe, Fusion Technol. 11, 576, 1987.

C. OPTICS TECHNOLOGY FOR KrF LASERS

Ralph Berggren and James D. Boyer

INTRODUCTION

By improving optical technology, we hope to significantly reduce the costs of optics for a large ICF system. The costs referred to here are the projected costs for optics that will be obtained in the future in immense quantities. The quantities required can easily be estimated. An ICF system that supplies 10 MJ onto a target, using optics that can handle 40 kJ/m^2 (4 J/cm^2), will require 250 m^2 of mirror area for every turn of the beam. If the individual mirrors are on the order of 0.5m^2 square, and there are 6 turns, we would need 6000 of these relatively large mirrors just for the optics between the final amplifiers and the target. More components, but of smaller size, would be needed for other optics feeding the amplifier. Fewer, but larger, components would be needed in the amplifiers themselves.

Working with such projected costs offers both disadvantages and advantages. The disadvantages relate to the difficulty of estimating costs in the future for many components that can not readily be made today. The advantage is the opportunity to specify a complete process that is optimized for the particular requirements; this might reduce cost substantially.

Our current plan is to identify paths that might lead to lower cost and to pursue a few chosen paths. We intend to show small-scale demonstrations of concepts and techniques. Along with those demonstrations we will define the path to be followed to reach desired performance goals for the LMF. Our goal is to show convincing cost projections reduced to about one-half of the current values.

Within the current program of somewhat less than two years' duration, we expect to show results on a small scale and then to begin the scaling process to a larger size.

The first step in the program is to identify the most cost-sensitive areas. This is quite easy, as the largest element of the cost, and one that is reasonably sensitive to technology, is the large quantity of mirrors between the lasers and the targets, as indicated previously. Reductions in the cost of the optical system can then be obtained either by increasing component performance or reducing the specific costs.

The areas chosen for near-term work include:

Optical Damage Threshold. This is the single area in the optics in which an improvement in performance can result in a direct and substantial reduction of the system cost. It is probably true that the cost of the coating will be somewhat insensitive to the performance that is achieved; but the required total area of mirrors varies inversely with the optical damage threshold.

Component Fabrication. This is a major area of study. Various possible improvements, including replication, glass molding, and improvements in "conventional" polishing are being considered.

Component Mounting and Alignment. This area may have an impact on system design and cost. Combining many beams onto single optical elements reduces one measure of the complexity of the system this is our current concept for a "combined-beam" architecture. Because mounting has not been one of the more critical elements, the cost model has not considered the details of mounting and alignment. We intend to obtain a better understanding of the complexity of multiple mirrors and of the actual costs involved.

Small-Angle Scattering. The system design assumes that scattering can be reduced to a satisfactory level. To determine optical damage, we continue to measure scattering. We intend to obtain some long-term reductions and to assure that lower costs of optical fabrication do not reduce the damage threshold or increase scattering.

COMPONENT COST PROJECTIONS

With current projections, the optics for an LMF represent about one-third of the system cost. Table I shows an example of the projected cost for optics for a 0.6-m mirror and the equivalent cost per square meter. (The 0.6-m mirror is assumed to be square. The cost model is based on the largest dimension, diameter or diagonal. It gives the same cost for round or rectangular pieces.)

TABLE 1. Projected Cost of Optical Elements

Item	Cost of	Cost 0.6-m per m^2
Mirror blank	$ 6,000	$16,700
Fabrication	$ 6,100	$17,000
Coating	$11,000	$30,600
Total	$23,100	$64,300

Some historical costs indicate the possibility of reducing the estimates in Table 1. A mirror 0.8-m in diameter was repolished to an accuracy of a few waves at a cost (1983) of $3,000 per m^2. For repetitive work, perhaps pieces could be polished to our requirements at a cost higher than that but much lower than $17,000 per m^2. The same piece was coated with an HR dielectric at 308 nm for $4,000 per m^2. For this too, our requirements are more stringent but can perhaps be met for a cost less than that given in the table.

It appears that significant savings from the currently projected costs may be obtained in all aspects - blank, coating and figuring. There will also be interrelationships between them that must be considered.

OPTICAL DAMAGE THRESHOLD IMPROVEMENT

The need for optical components that could survive intense ultraviolet (uv) radiation was recognized in the early design phase of the Los Alamos KrF/ICF program. A small effort was initiated in 1981 with the goal of assessing damage thresholds of available uv reflectors. The best threshold observed for these off-the-shelf reflectors was 1.5 J/cm^2 at 248 nm with a 15-ns laser pulse. This effort expanded into a survey of the damage resistance of known materials used for reflectors in the ultraviolet. Consequently, the KrF optical damage team became an important element in the development of optical components

for the LAM and later the AURORA. The LAM optics had to be resistant to attacks by the fluorine-containing laser gas mix, as well as to what were then high damage fluences. The team developed test methodology and facilities for both laser damage thresholds and resistance to fluorine attacks. The team contributed significantly to a better understanding of laser-induced damage to optical components and to the design and evaluation of optics included in the AURORA system.

From the beginning of the optical damage program to the end of FY84, the maximum observed damage thresholds for reflectors increased from 1.5 /cm^2 to about 6.5 J/cm^2 peak fluence at 248 nm and a 15-ns pulse length. Los Alamos did not have on-site coating capability and therefore relied on commercial vendors for coating production. The increased damage thresholds were the result of feedback of damage test results to the coating vendors and the vendors' growing experience in producing high fluence optical coatings. In this early round of development, the effort was limited to materials already in use by the coating industry. The database at the end of 1984 included 18 different material combinations. The best observed coatings were quarter-wave stacks of Al_2O_3/SiO_2 for which damage thresholds ranged from 1.5 to 6.5 J/cm^2 (Foltyn and Jolin 1983). Parallel work near the end of this period indicated similar results for Al_2O_3/SiO_2 anti-reflective coatings. At the end of 1984, a typical Al_2O_3/SiO_2 coated optic would withstand a peak fluence of 3-4 J/cm^2 for a 15-ns pulse.

The Los Alamos optical damage team developed a standardized damage test procedure that provided a well-determined definition of damage threshold (Foltyn and Newnam 1981). Damage thresholds had previously been determined in one-on-one tests in which each site was exposed to one pulse at one fluence. The sample was removed from the test fixture and examined for damage, and the threshold was reported as the mean of the highest nondamaging and the lowest damaging fluence. Other experiments had shown that multiple shots of a fixed fluence on each site tested resulted in lower damage thresholds (Bass and Barrett 1971; Gill and Newnam 1978). The optical damage team developed the damage probability, or N-on-M testing procedure. In practice, M sites (typically 10) are tested at each fluence, and each site is irradiated with N shots (about 100). The fraction of sites damaging at each fluence are plotted versus fluence. Generally, the data fall on a straight line that intersects the fluence axis. This intersection provides a spotsize-independent definition of damage threshold (Foltyn 1982). Figure 1 is a typical damage probability plot of recent test data. This new procedure influenced the design of the damage test facility discussed in the following section.
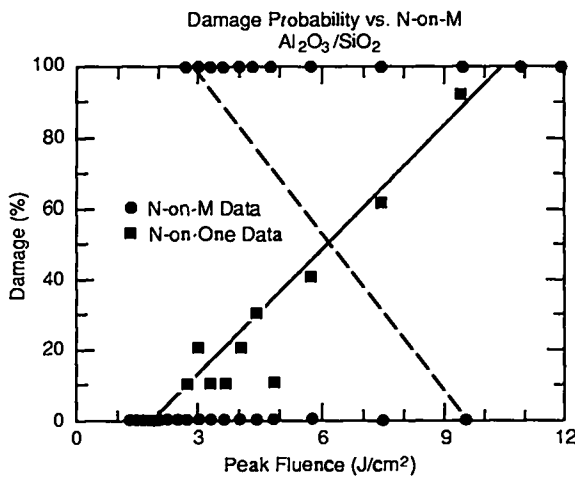
Fig. 1. Typical damage probability plot of recent test data.

Figure 2 diagrams the damage facility in existence at the end of 1984. The laser source was an excimer laser running on a KrF gas mixture at 248 nm. Maximum repetition rate for this system was 35 Hz. In principle, there was real-time monitoring of peak fluence, spatial profile, average power, and temporal pulse shape. In practice, some of these quantities would vary by ±5% during irradiation of each site with its 100 shots, and only average values were known. It is also worthwhile to note that the monitoring was off the main laser beam rather than at the test plane. Correlation of the off-beam diagnostics with test plane fluences was necessary.

The LAM required optics not only resistant to damage by high laser fluences but able to withstand exposure to the fluorine-containing laser gas mix. Even though the fused silica needed for the output window of the LAM is not reactive to molecular fluorine, fused silica rapidly fogs in the presence of moisture because of etching of the surface by HF. In principle the surface can be protected by a nonreactive anti-reflective coating such as Al_2O_3/AlF_3. The LAM mirror is also on a silica-based substrate and subject to attacks by the moisture-generated HF. The damage team developed a test procedure to measure the resistance of a coating to attacks by the laser gas mixture and examined a variety of coating materials for joint fluorine and laser damage resistance (Foltyn et al. 1985). Laser damage resistance was also measured while the optic was exposed to fluorine. It was found that as long as the coating had not visibly degraded, the damage threshold did not change dramatically.
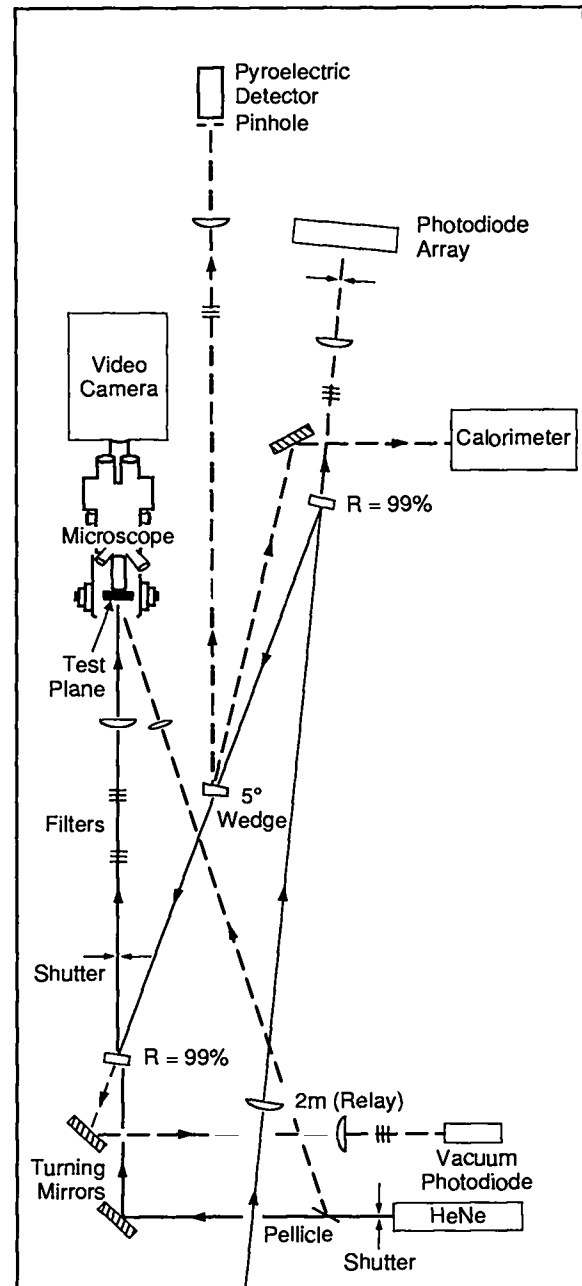

Fig. 2. Diagram of damage facility at the end of 1984.

The optical damage team made several significant contributions to the Los Alamos KrF/ICF program. The team established a performance baseline for high fluence optics operating at 248 nm. It developed a reliable laser damage test methodology. The laser paved the way for understanding the relationship of damage thresholds of laboratory specimens 1 to 2 in. in diameter to that of the large optics needed for AURORA. In addition, the team developed a systematic test for the fluorine resistance of laser cavity optics.

Current Status

We have progressed significantly in several important areas. An optical damage test facility dedicated to the KrF 248-nm wavelength has been in place and operating since the end of 1986. This facility has increased our ability to address KrF/ICF specific problems. The best observed damage threshold at 248 nm is nearly twice that observed through 1984. This progress represents a recent breakthrough, and further progress is expected in the near future. We have also achieved a very significant improvement in the resistance of coated optics to fluorine attack. Interestingly, the coating materials showing the best fluorine resistance (Al_2O_3/AlF_3) are the ones giving the best damage thresholds to date. We have also made progress on scaling issues that relate laboratory damage threshold measurements to system parameters such as pulse length scaling.

The dedicated KrF optical damage facility that has been in operating since 1986 is an extension of the design shown in Fig. 2. The laser is a commercial excimer operating from single shot to 250 Hz and produces a nominal 22-ns pulse at 248 nm. Pulse lengths of 11 and 38 ns have been produced by detuning and pulse stacking, respectively. Fluence at the test plane is now controlled by an angle-tuned dielectric-mirror-based attenuator. A computer is now used to control and monitor beam energy as well as to control sample position and record and display test results. Energy monitoring is still based on a multiple-shot average. We hope to soon have shot-by-shot records of test fluence to account for fluctuations that may be up to 10% for the 100 shots seen by each test site. A recent addition to this facility is the capability of viewing the test optic under low intensity 248-nm laser illumination. We now characterize the test plane beam spatial profile by translating a linear Reticon array across the beam position. With this data we generate 3D and contour plots and also calculate accurate peak to average fluence ratios at the test plane. The latter serves as a crosscheck with our pinhole measurement of peak fluence.

The best damage threshold observed at 248 nm is now a factor of two greater than that seen at the end of 1984. This coating was a Al_2O_3/AlF_3 reflector and both samples from the best coating run had damage thresholds 12.5 J/cm². Figure 3 is a damage probability plot for one of these samples. Note that even at 24 J/cm² only 80% of the tested sites were damaged. We have data on ten runs of this material produced in the same development effort. The worst threshold was 4.5 J/cm² and the mean about 9.0 J/cm². This result is encouraging in that both materials have band edges well below 200 nm. (Previously, AlF_3 had not been

used successfully in a multilayer reflector because of coating process problems.) A Japanese group also reported high damage thresholds for mirrors with similar materials (Al_2O_3/MgF_2, YF_3/MgF_2, and Sc_2O_3/Na_3AlF_6) (Izawa et al. 1988). Development of new coating materials seems to be one key to improved damage thresholds. Current results for anti-reflective coatings on transmitting elements is less encouraging. Other than some strange results with one set of Sol-Gel coatings, the best thresholds have been about 6 J/cm². The thresholds of anti-reflective coatings are probably limited by the substrate surface conditions.
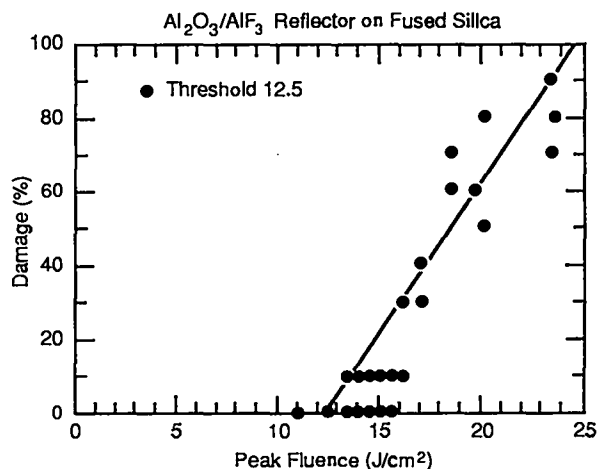

Fig. 3. Damage probability plot for Al_2O_3/AlF_3 reflector.

We have also made significant progress in fluorine-resistant optics. Several of the Al_2O_3/AlF_3 coated reflectors survived for over 1000 hours of exposure to 5% F_2 in argon with no degradation in either the visible or uv. For anti-reflectively coated fused silica windows, the best seen to date is also an Al_2O_3/AlF_3 coating. The better samples typically lasted for a week in 5% F_2 in argon mixture. This is nearly a tenfold increase over the 1984 results if the increased fluorine concentration is taken into account.

We have also made considerable progress in two scaling issues of concern to large KrF laser systems. Pulse-length scaling of laser damage thresholds is of great interest to KrF/ICF system designers in that a typical system will have both short pulse (2-10 ns) and long pulse (300-2000 ns) components. Laser damage testing in the ultraviolet is typically performed with 15- to 25- ns pulse-length excimer lasers. Foltyn and Jolin (1986) report the most current complete set of data covering the 9 ns to 625 ns range, but for 351 nm rather than 248 nm. Recent results at 248 nm for 11-38 ns (Boyer 1987) show similar behavior to the broader-range 351 nm test. Both experiments show an average scaling of damage thresholds with (pulse length)x where x is 0.36 for 351 nm and 0.3 for 248 nm. The

exponent varies over the range 0.2 – 0.5 from coating run to coating run. A second scaling issue arises when damage near threshold fluences is considered. This damage is usually in the form of micron-sized pits in the coating. A frequent question is whether these pits are related to system performance. We attempted to answer this question in a recent experiment in which we determined the damage probability curve on a small area of a sample and then irradiated the remaining sample with a fluence halfway between the microscopic threshold fluence and the higher fluence where more significant damage occurs. In every case, one or more sites initiated growing damage. It therefore appears that the microscopic damage threshold is the related definition of damage.

Current Program Plan

Our current program plan focuses on coating development work with contractors outside Los Alamos. We hope to place critical mass development programs in two major areas: new material development and advanced deposition processes. The new material development contract will focus on deposition of high-quality coating of fluorides and oxides with band edges known to be well below 248 nm. The materials will first be characterized as single layer films and only as multilayer stacks after the single layer deposition process is well understood. The second contract will focus on advanced deposition processes such as plasma plating, ion-beam sputtering, and ion-beam assisted deposition. All these processes offer greater control of the deposition process and have produced superior coatings in all respects except damage thresholds. We believe that with further development these processes will yield coatings with damage thresholds in excess of those possible with the current electron-beam sputtering process. All three advanced processes produce films with near-bulk density and are therefore expected to provide improved fluorine resistance. Other current efforts aim at gaining an understanding of damage mechanisms and at increasing the damage thresholds of transmitting optics.

Our present efforts at understanding optical damage mechanisms are contained in two experiments. From purely geometric arguments, the fluence measured at normal incidence needed to damage an optic at a non-normal incidence should increase by $1/\cos(q)$ where (q) is the angle of incidence. A well-designed experiment has shown that the increase is much slower than predicted by geometric arguments for thin film dielectric coatings (Newnam et al. 1982). The experimental result can be qualitatively explained with two assumptions: damage occurs at defects in the coating rather than in the bulk material and these defects are not point-like or spherical in shape. The first

assumption fits visual observation quite well. If we assume that the defects are cylindrical in shape with the long axis parallel to the coating normal, the angular dependence is explained and the only free parameter is the cylinder diameter. We are testing this model by looking at the angular dependence of the damage thresholds of uncoated dielectrics. We are beginning to identify these defects prior to damage by looking at the coatings under uv illumination prior to exposure to high fluence uv radiation. Previous experiments in this area were encouraging (Moran et al. 1988) but never carried to completion.

The damage thresholds of anti-reflection coated optics are generally below or equal to those of uncoated substrates. We are attempting to obtain a selection of fused silica substrates from a variety of suppliers. These will be ranked by damage threshold. Recently we found that damage thresholds for a given lot are well clustered. By coating samples from each lot in the same coating run, we hope to both test the hypothesis that the substrate damage threshold is limiting and gain insight into how the substrate thresholds might be improved. Preliminary experiments show that a high temperature anneal (1000 C to 1200 C) changes damage thresholds of our fused silica substrates significantly—sometimes increasing by nearly a factor of two, sometimes staying constant, and sometimes decreasing. We hope to learn which element of substrate preparation leads to this behavior. Once we understand the uncoated fused silica, progress in improving the damage thresholds of anti-reflective coatings should accelerate rapidly.

COMPONENT FABRICATION DEVELOPMENT

There are three types of efforts being pursued in this area. Substrate development has as its goal the production of mirror blanks that are satisfactory for our requirements in the 0.5-m to 1.0-m sizes and that are less expensive than conventional solid blanks of low-expansion materials. Efforts in "conventional" fabrication are directed to lowering the production cost of mirrors polished in more or less traditional ways. The third effort, surface replication technology, is an attempt to create a finished optical surface without polishing. Several approaches appear to be possible.

Substrate Development

Major progress has been demonstrated in this area on the AURORA program. For mirrors of .5 m and larger, solid blanks of inexpensive materials such as Pyrex are not adequate. The material is expensive and difficult to obtain

in thick pieces. More importantly, the coefficient of thermal expansion is high, so that the mirror deforms substantially when the temperature is changed because of the thermal gradients. For thick pieces, the time for the temperature to equilibrate is so long that it is difficult either to polish them.

Thus, one conventionally is limited to the use of low-expansion materials such as Corning ULE or Schott ZeroDur. However, these are expensive in large solid pieces and even more expensive when cored out so as to be lightweight.

In AURORA we have made use of the Hextek lightweight borosilicate glass blanks, in sizes up to nearly 1 m (diagonal). The thin plates that are used for the face and back plates are connected by a core structure made from tubes. The entire structure is joined together by a proprietary process called gas fusion. The result is a mirror blank that is light, stiff, and formed to the approximate curve of the desired mirror.

Because the entire structure is made of relatively thin pieces that are exposed to the atmosphere, it comes to thermal equilibrium fairly quickly in response to a temperature change. Because the coefficient of expansion of the material is very uniform, a uniform temperature change results in very little distortion of the figure of the mirror.

At smaller sizes (2 m^2 and smaller) an even simpler and very inexpensive technique has been used. The mirror blanks were simply molded of Pyrex, with an integral hub molded on the back for mounting. The resulting mirrors were very inexpensive and very simple to mount.

Our current program is not specifically directed to substrate development. Instead we will respond to needs for specific new techniques if required by new ideas for fabrication, replication, or coating.

Conventional Fabrication Development

There has been a major reduction in the cost of polishing flat optics during the last decade as a result of the widespread use of planetary polishing. Besides reducing the cost, the technique has made it much easier to polish non-round pieces and lightweight structures. The lightweight, rectangular mirrors done for AURORA are an excellent example of the state of the art.

We can't anticipate any further breakthroughs; therefore, our attention for future improvements is directed to the specific factors involved in polishing a large number of identical parts. We will identify as well as possible the sequence of operations and estimate the production time and cost for large quantities. It seems reasonable to expect that successive pieces would behave similarly so that grinding

and polishing could be done faster and with fewer test cycles.

There will then be interactions with the design of the piece and its mount and with the type of material. It may be possible to polish a final figure faster on a low-expansion material and to accelerate the heating and cooling cycles during coating. Would this overcome the additional cost of the material? We hope to address these issues during the current study.

One obvious need is to specify the figure and surface finish requirements of the mirrors. This is a complex task, because the system architecture for the LMF and the requirements for the beam quality on the target are not yet defined. Thus, we must make one or more sets of assumptions and include these factors explicitly in our cost model.

Based on some of the cost history data and on a subjective estimate of possible gains made by optimizing the design and fabrication cycles, we feel it is reasonable to reduce the projected costs to no more than one-half the values given in the table.

Surface Replication Technology

Of interest here are techniques which create a finished surface directly, by casting, molding, growing, or some other approach, without requiring conventional grinding and polishing. If a good, inexpensive, process is found, it could be used for most of the mirrors in the system. Even if the process is not competitive with improved conventional fabrication for flat mirrors, it could be an effective way of generating aspheric surfaces. Current designs avoid using aspherics, mostly because they are expected to be too expensive to be practical. (Alignment of aspherics is also an issue that must be addressed.) The alternative to using aspherics is to use more mirrors or longer separations between mirrors. Using aspherics could reduce the cost of the system significantly.

Three approaches to replication are being considered and are discussed below: epoxy replication; molding of glass substrates; and CVD growth of silicon carbide. There are certainly other possible approaches. These three are chosen for initial work because they offer approaches to development that seem to have a fair chance of success.

Epoxy Replication

This well-developed technique is used commercially in many applications. Although it is commonly used for small parts of a few cm, we have found a commercial capability currently existing for parts as large as 0.4 m in diameter. Figure accuracy of one-tenth wave is certainly

obtained in small parts and may easily be obtained at the 0.4-m size. Published reports describe a piece 0.5 m in diameter with a replication accuracy of 1/20 wave. In our program we will obtain samples to verify the state of the art, including measurements of figure accuracy and surface roughness. We will also consider designs of the substrate and mount that will provide optimum performance and minimum cost.

Epoxy replication has not been actively considered before because of the thermal limitations and difficulties of coating. Typically, the epoxy must be maintained at a temperature of less than 80 C to 100 C. This makes it difficult to use with a multilayer dielectric coating. The issue of coating is addressed in the following section. There is also a serious question whether the optical damage threshold can reach a reasonable value. A simple thermal analysis shows that even with a very high reflectivity, a short pulse will heat the outer layer of the epoxy above the 100 C threshold. However, there is also some preliminary data indicating that transient heating is much less of a problem, and that the simple thermal pulse heating may not set the limit on the damage threshold.

The coating issue will be addressed two ways. First, there are techniques of coating that can probably provide durable coatings when applied at less than 80° or 100° C. Second, it may be possible to apply a dielectric coating in the same way that simple coatings are now applied. That is, the coating is deposited first on the master, the epoxy is added behind it, and the substrate is pressed against the epoxy. A parting layer assures that the coating separates from the master and comes off with the epoxy. The coatings that are used on replicated parts are typically gold, silver, or silicon dioxide over aluminum. Both approaches will be tried with multilayer dielectrics. The mirrors will be tested for surface finish and damage threshold.

Molding of Glass

This approach has been demonstrated at a size of 10 cm and a figure accuracy of the order of one wave or better. The results were reported for a conventional mirror by Angell and a cylindrical mirror by the Japanese. This work is being carried on by Hextek as an extension of their substrate development work. Even if a perfect figure is not achieved, the process could significantly reduce the cost of conventional polishing of the mirror by eliminating several generating, grinding, and polishing steps.

The techniques will be developed on a very small scale (5 m), with the scattering, surface finish, and figure measured. If successful, scaling to 15 cm and ultimately to 0.5 m to 1 mr will then be attempted. Initial tries will repeat and extend earlier work with Pyrex against a fused

silica master. As with all replication processes, durability of the master will eventually become an issue and a search will be made for more durable masters.

Chemical Vapor Deposition

The goal here is to develop finished SiC mirrors. Using an SiC master, SiC is deposited to form the finished surface and then to build up a lightweight core structure behind the surface. The surface can then be easily coated with a conventional multilayer dielectric. Development of these mirrors is now being supported by the Air Force at Morton Thiokol/CVD. We will monitor this development. After the first stage, involving demonstration of a 0.25-m piece with a good figure, it may be necessary to support some development of mirror structures directly related to ICF requirements, stressing cost more than weight reduction.

The material itself is relatively inexpensive. However, the deposition process is slow using current techniques. For production of a large number of mirrors, the capital cost of furnaces could then be a limiting problem. Thus this process is considered to be something of a "long shot." It has the potential advantage of producing a light, stiff, high conductivity mirror with a very homogeneous coefficient of thermal expansion.

COMPONENT MOUNTING AND ALIGNMENT TECHNOLOGY

The current cost model does not explicitly consider the cost of mounting the elements. Fortunately the AURORA program provides a good basis for further development of mounting techniques. For the array of recollimator mirrors, a very simple two-axis flexure mount was developed that was integrated with the design of the molded Pyrex mirrors. Even with flexure mounts and motorized adjusters, the mounts have been shown to be stable to one or two microradians over temperature variations up to 10 C. With that stability, individual mirrors could be mounted in arrays with only the arrays adjustable. The AURORA program has also demonstrated a novel control technology that maintains the alignment of all 96 beams.

Our program plan calls for simplifying the mount design to yield a stable, low-cost, non-motorized mount, to demonstrate this in a large array of relatively small (15 cm) mirrors, and to scale the concepts to larger sizes. In the process, a good basis for prediction of mount costs will be developed.

SMALL-ANGLE SCATTERING

Small-angle scattering, like the optical damage threshold, is important for the system design as it may strongly affect the cost of the system. If large angles are needed in the multiplexing system, then both the efficiency and the cost of the system are seriously affected. As with damage threshold, the scattering is affected in an unknown way by the fabrication processes being considered.

The scattering coefficient is defined as the fraction of total input powers scattered per steradian as a function of angle. The scattering function has units of steradian^{-1}. Designs for the LMF use a minimum angle between a beams of about 5 milliradians. At that angle, the scattering must be somewhat below one per steradian. The actual number required will depend on target physics and cannot be definitely specified. A value somewhat below unity is thought to be a very safe value.

The AURORA system operates at a much smaller channel to channel angular spacing, but it can tolerate scattering at least an order of magnitude larger than that for an LMF driver.. During the AURORA program, we developed an apparatus for measuring the scattering at the required angles. Tests on fresh surfaces and surfaces exposed to F_2 showed favorable results; that is, the fluorine environment did not seriously change the level of small-angle scattering.

We are now in the process of making some improvements to decrease the background at angle of 2 to 10 mrad. Testing during development of fabrication and coating processes will be used to assure that less expensive processes still yield adequate scattering and to find processes that will minimize the scattering at the desired angle.

CONCLUSIONS

A program is being undertaken that will extend development efforts begun under AURORA and move toward emphasis on cost reduction of a large system. By its very nature, this will have to be considered as an ongoing program. For this beginning phase we have identified some promising areas and have established goals that will show whether progress is possible, using techniques that have a promise of then being scaled to larger or higher-performance components.

REFERENCES

Bass, M., and H. H. Barrett, "The Probability and Dynamics of Damaging Optical Materials with Lasers," NBS Special Publication 356, 76 National Bureau of Standards, 1971.

Boyer, J. D., "Pulse Length Scaling Results at 248 nm," 19th Annual Symposium on Optical Materials for High Power Lasers, Boulder, CO, October 26-28, 1987.

Foltyn, S. R., and B. E. Newnam, "Ultraviolet Damage Resistance of Dielectric Reflectors Under Multiple-Shot Irradiation," IEEE J. Quant. Electron. QE-17, 2092, 1981.

Foltyn, S. R., and L. J. Jolin, "Alumina/Silica Multilayer Coatings for Excimer Lasers," NBS Special Publication 688, 354, National Bureau of Standards, 1983.

Foltyn, S. R., and L. J. Jolin, "Long-Range Pulselength Scaling of 351 nm Laser Damage Thresholds," NBS Special Publication 752, 336, National Bureau of Standards, 1986.

Foltyn, S. R., L. J. Jolin, and G. Lindholm, "Effect of Molecular Fluorine on the Performance of Excimer Laser Optics," NBS Special Publication 746, 403, National Bureau of Standards, 1985.

Foltyn, S. R., "Spotsize Effects in Laser Damage Testing," NBS Special Publication 669, 368, National Bureau of Standards, 1982.

Gill, D. H., and B. E. Newnam, "Optical Performance as a Measure of Damage Threshold: A New 'Practical' Criterion," Paper ThD7, Inertial Confinement Fusion Conference, San Diego, CA, 1978; also LA-UR-78-137, Los Alamos National Laboratory, Los Alamos, NM, 1978.

Izawa, T., Y. Ishiwata, I. Hashimoto, H. Shikakura, Y. Owadano, Y. Matsumoto, and M. Yano, "Laser Damage Thresholds of Optical Coatings at 248 nm," 20th Annual Symposium on Optical Materials for High Power Lasers, Boulder, CO, October 26-28, 1988.

Moran, M. B., R. H. Kuo, and C. D. Marrs, "Scatter Intensity Mapping of Laser-Illuminated Coating Defects," Applied Optics 27, 957, 1988.

Newnam, B. E., S. R. Foltyn, D. H. Gill, and L. J. Jolin, "Angular Dependence of Multilayer-Reflector Damage Threshold," NBS Special Publication 727, 342, National Bureau of Standards, 1982.

D. NONLINEAR PULSE COMPRESSION

Norman A. Kurnit

In view of the recommendations made last year in the report of the DOE KrF Panel, it appears that some elaboration of our reasons for rejection of nonlinear optical pulse compression techniques in favor of optical angular multiplexing is appropriate here. This decision is largely based on the conclusion that for large systems, the size of individual optics downstream from the final amplifiers is already sufficiently large that using nonlinear optics to compress the energy in larger time slots or to combine the outputs of several amplifiers does not result in any cost savings. Furthermore, there are efficiency losses in any nonlinear conversion process, and the process requires additional optical elements that increase the cost. Finally, the nonlinear techniques impose severe constraints on the bandwidth that can be compressed and thus do not provide the bandwidth flexibility that is believed to be desirable for an ICF facility. Although detailed designs have not been done in the context of the LMF, it appears that the following considerations make nonlinear pulse compression techniques noncompetitive with angular multiplexing.

Backward Raman scattering is the technique which has been most intensively pursued for pulse compression. However, the work at LLNL (Jacobs et al. 1980) indicated that obtaining more than a factor of five compression is difficult because of the onset of forward second-Stokes scattering by the compressed pulse, and that conversion efficiencies of more than 70% are also difficult to achieve. Thus, one needs at least two stages of compression (one of which can be angular multiplexing of relatively long pulses in the KrF amplifier) in order to reduce the duration of the amplifier output pulse required for efficient electrical excitation down to the pulse length needed for target illumination. Although backward Raman compression can help to reduce the beam count, it tends to increase the total area of optics required because the area of downstream optics is determined by the total energy and the short-pulse damage fluence, and additional interstage demultiplexing optics and

Raman cell windows are needed. On the other hand, because no angular demultiplexing is required after the Raman cell, fewer optical stations may be needed to bring the pulse to target, and the area of the first-stage demultiplexing optics is somewhat smaller because of the longer pulse length. The cost impact of this trade-off needs to be evaluated in greater detail, but it is doubtful that the optics cost will be any lower. One has, in addition, the extra cost of supplying the extra driver energy needed to make up for Raman conversion losses. The reduction in beam count is not a significant consideration because aperture combination can provide this in the case of amplifiers of the size envisaged for the LMF.

Toward the end of the LLNL work, a proposal was made for a system in which multiple beams were stacked at angles such that they made several bounces off reflective walls in a large Raman cell and were extracted by a two-pass (forward and backward) Stokes beam, possibly achieving higher conversion and larger compression. However, this requires a large area of highly reflective (but not necessarily high quality) optics, which would be a significant cost item. It does not appear that this technique would be useful for pump pulses much longer than 100 ns, so a prior stage of multiplexing would still be needed unless an efficient driver can be developed for pulses this short.

Another problem with backward or small angle Raman scattering is the requirement for narrow linewidth, which may not be desirable from target physics considerations. Also, pulse shapes obtained by backward Raman scattering tend to have a fast leading edge and slow falling edge, and although some pulse shaping is possible by tailoring the input Stokes pulse, the output pulse shape is sensitive to gain variations and may be difficult to control. It is doubtful that a range of precisely tailored pulses of desired shapes can be easily achieved.

We have given some consideration to pulse compression by backward Brillouin scattering as well (Slatkine et al. 1984; Fedosejevs and Offenberger 1985 and

references therein). In this case, higher compression factors can be achieved because there is no forward second-Stokes generation. However, absorption in available media limits the length of the input pulse that can be efficiently compressed, and one tends to get output pulses that are both shorter than desirable and improperly shaped. The laser must also have an extremely narrow bandwidth for efficient compression, which, in addition to possibly being undesirable for target interactions, can lead to transverse Brillouin scattering in windows (Eggleston and Kushner 1987; Murray et al. 1989). (The latter can also be a problem for the bandwidths needed for backward Raman scattering.)

The last nonlinear technique for pulse compression that has been seriously considered (principally at Rutherford (Partanen and Shaw 1986; Shaw et al. 1986), but also in a study done for us by STI (Spectra Technology, Inc. 1987)) is the use of near-forward Raman scattering to slice a long pump pulse into shorter Stokes pulses. In this case, one must either multiplex the same number of beams through the Raman cell as one would have had to through the amplifier (although several amplifiers could be combined in on Raman cell), or multiplex both the amplifier (m times) and the Raman cell (n times), which leads to handling a much smaller number of beams (m + n instead of m × n), but has the disadvantage of two sets of demultiplexing optics (and hence greater optics area). This technique appears to lend itself best to smaller amplifiers where each beamlet would otherwise contain too little energy or to applications where very short pulses are desired. The STI study considered combining small (2.5-kJ) e-beam sustained discharge lasers, and, using fairly optimistic Raman efficiency assumptions, came up with a cost 25% higher than a system based on angular-multiplexed 200-kJ e-beam pumped amplifiers. Although this study did not compare systems composed of the same amplifier elements, it does indicate that there are no magical savings to be had. Bandwidth constraints are somewhat relaxed in this geometry, but not enough to affect target interactions. Pulse shaping would probably be difficult, except by stacking different lengths of square pulses from different directions.

These considerations were discussed at the KrF Workshop held in Santa Fe in April 1989. There appeared to be general agreement among representatives from all of the major laboratories that have addressed these issues in KrF that, although nonlinear compression techniques might present some cost savings in relatively small, short-pulse systems that would otherwise require a large number of beamlets, there were no obvious cost savings in large systems and no workable methods for achieving large

bandwidths, aside from the possibility of generating a comb of multiple narrow frequencies in the front end to drive different amplifiers and Raman cells. We believe this adds unnecessary complexity and may not have as beneficial effect as a truly broadband source.

REFERENCES

Eggleston, J. M. and M. J. Kushner, "Stimulated Briullouin Scattering Parasitics in Large Optical Windows," Opt. Lett. 12, 410, 1987.

Fedosejevs, R., and A. A. Offenberger, "Subnanosecond Pulses from a KrF Laser Pumped SF6 Brillouin Amplifier," IEEE J. Quant. Elect., QE-21, 1558, 1985.

Jacobs, R. R., J. Goldhar, D. Eimerl, S. B. Brown, and J. R. Murray, "High-Efficiency Energy Extraction in Backward-Wave Raman Scattering," Appl. Phys. Lett. 37, 264, 1980.

Lowenthal, D., D. Harris, J. Eggleston, and M. Kushner, "Nonlinear Techniques for Fusion Lasers," Interim Final Report, Contract 9-X65-W1478-1, Spectra Technology, Inc., Bellevue, WA, 1987.

Murray, J. R., J. R. Smith, R. B. Ehrlich, D. T. Kyrazis, C. E. Thompson, T. L. Weiland, R. B. Wilcox, "Experimental Observation and Suppression of Transverse Stimulated Brillouin Scattering in Large Optical Components," UCRL-99914, Preprint, Lawrence Livermore National Laboratory, Livermore, CA, 1989.

Partanen, J. P., and M. J. Shaw, "High-Power Forward Raman Amplifiers Employing Low-Pressure Gases in Light Guides. I. Theory and Applications," J. Opt. Soc. Am. B 3, 1374, 1986.

Shaw, M. J., J. P. Partanen, Y. Owadano, I. N. Ross, E. Hodgson, C. B. Edwards, and F. O,Neill, "High-Power Forward Raman Amplifiers Employing Low-Pressure Gases in Light Guides. II. Experiments," J. Opt. Soc. Am. B 3, 1466, 1986.

Slatkine, M., I. J. Bigio, N. A. Kurnit, and D. E. Watkins, "Pulse Compression of Excimer Radiation by Backward-Stimulated Brillouin Scattering in Gaseous Media," Paper WII7 in Proc. XIII Int. Quantum Electron. Conf., Anaheim, CA, 1984.

E. ADVANCED FRONT-END DEVELOPMENT

Norman A. Kurnit and Scott J. Thomas

INTRODUCTION

The KrF laser possesses a unique combination of intrinsic performance features that can have a major impact on reducing the energy requirements for an LMF. These features include short wavelength, broad bandwidth, pulse-shaping capability, and high spatial-quality beams. Because of the master oscillator/power amplifier configuration used in the KrF laser architecture, it is extremely important to develop master oscillator technology that can reliably produce pulses with the required temporal, spatial, and bandwidth properties. After being temporally multiplexed, the output pulses from this oscillator must be amplified to a level that can be used to drive large e-beam amplifiers. The master oscillator and amplification stages before the temporal multiplexing are generally called the "front end" and typically are expected to produce an energy on the order of several hundred millijoules to one joule.

The initial requirements for the AURORA front end were to produce stable, high beam quality, 5-ns pulses with sufficient energy to drive the subsequent amplifiers in the AURORA chain. In addition to this, Los Alamos has been developing front-end technology to meet the increasingly demanding requirements for target physics experiments and to support advanced facility design concepts. In this section we describe this development program and discuss its implementation in the AURORA laser facility. In particular, we describe our development approach for pulse shaping to produce high contrast-ratio multiple-stepped and continuous-shaped pulses, and bandwidth control to produce outputs in excess of 200 cm^{-1} bandwidth.

Current AURORA Front End

The present front end of AURORA was developed as a response to some severe constraints on space and to improve the performance of components that were already in place. It utilizes phase conjugation by stimulated Brillouin scattering after the first pass of a double-pass high-gain discharge amplifier to both improve the beam quality and reduce the amount of amplified spontaneous emission (ASE) that can reach the target before the desired pulse (Kurnit and Thomas 1989; Thomas et al. 1988). A side benefit found during the development of this system was that it was possible to produce a variable-duration pulse simply by changing the power level incident on the Brillouin cell. The lossy Pockels cells, which had limited the repetition rate of the front end to one pulse per minute because of thermally induced birefringence, could be removed. These changes also resulted in an increase of three to four times in the output energy available from the front end.

This system was installed for the initial stages of AURORA integration and will undergo further improvements in response to the increased needs for some target experiments. ASE initiated in the second pass of the first amplifier must be further reduced for some experiments, and additional control is needed over the pulse shape, which has a fast spike on the leading edge that is undesirable for some experiments. For other classes of experiments, i.e. Rayleigh-Taylor growth rate measurements, the ASE background (or even higher levels that can be produced by pulse stacking) is actually beneficial and will provide a required prepulse to generate the longer scale-length plasma needed for this measurement. In the near term, ozone saturable absorbers (Bigio and Thomas 1986) will be integrated into the system to further suppress ASE and to reduce the leading edge spike, and a Pockels cell switch can be added for some experiments if additional ASE reduction is

necessary. The latter option could, however, limit the rep-rate used for final alignment, because the Pockels cell must be placed after the phase-conjugate amplifier in order to reduce ASE from the second amplification pass, and appreciable energy must be handled at this location. The recent development of low loss beta-barium-borate (BBO) electro-optic crystals for uv applications will help to alleviate this problem, although crystals are presently limited to ~1 cm aperture. In the long term, the recent expansion of the front-end room will allow a more complete redesign of the front end to provide a greater range of pulse-shaping capabilities, both for AURORA target experiments and for demonstrating techniques required for future KrF systems. The remainder of this article addresses primarily the techniques that we envision for these longer-term goals. A discussion of the current front end can be found in Chapter V.B.

REQUIREMENTS FOR AN ADVANCED FRONT END

The front end of an advanced KrF ICF system must have the flexibility to produce pulses of complex and highly reproducible shapes, as well as a bandwidth that may need to be relatively large for optimum target coupling. Although experiments done on intermediate-scale facilities may help to define the importance of these parameters, it is likely that the need for a high degree of pulse shaping flexibility will persist throughout the useful life of the LMF facility as different target designs are studied. Reduction of prepulse to a very low level ($<10^{-7}$) is also a major consideration. Although the issue of pulse shaping is only beginning to be addressed experimentally, we see no major technological challenges to meeting these requirements for KrF at a cost that is an insignificant fraction of the total facility cost. In fact, this ability to pulse shape is one of the major potential performance advantages of this class of laser.

The requirement for a pulse shape with a long, low-level leading edge followed by a much shorter high-intensity spike (which may consist of a series of steps) or a pulse with a concave-rising front edge can be met either by stacking pulses of different lengths or by programming a Pockels cell to generate the desired input pulse to subsequent amplifiers. Propagation models discussed in Volume II, V.A indicate that the shape of individual pulses in a multiplexed train of pulses can be preserved with high fidelity, if the medium is kept nearly uniformly loaded. Some changes in pulse shape will occur if the spacing between pulses is much larger than the pulse width, but the pulse from the front end can (in principle) be tailored to compensate for these changes.

Pulse stacking can be accomplished either by beam splitting and recombining delayed versions of the same pulse, or by combining pulses of different lengths from different sources. It requires fairly stringent alignment between beams, but to no greater accuracy than a single front end beam must be aligned to the rest of the system, determined by the degree to which downstream optical masks are overfilled by the beam. Pulse stacking permits precision control of timing and amplitude ratios of different parts of the pulse, but it is probably best suited to step-function (staircase) pulse shapes. (Stacking of other shapes is certainly possible.) Pulses with sharp steps tend to undergo more significant shape changes under further amplification than continuous pulses.

Programmed Pockels cells can provide a more smoothly varying pulse and do not require alignment of multiple beams. However, control over the amplitude of different parts of the pulse is limited by the accuracy of the generation of the desired voltage pulse and by the rejection ratio that can be achieved with polarizers and Pockels cells. If the pulse shaping is done on the low-intensity pulse from a master oscillator, the effect of thermally induced birefringence is not a significant problem. (It was mentioned above that birefringence can limit the front-end repetition rate). Growth of prepulse and changes in the overall pulse shape through successive front-end amplifier stages will have to be carefully controlled, and some off-line experiments have begun to demonstrate the necessary techniques. We do not see any major problems with this approach that cannot be solved by careful staging of devices, which is discussed further below.

The ability to generate a wide bandwidth is presently believed to have important benefits for ICF lasers. A moderate bandwidth of ~30 cm^{-1} is easily produced by KrF. This bandwidth is required for induced spatial incoherence (ISI) smoothing of beams, which inhibits filamentation and leads to more uniform drive (Lehmberg and Obenschain 1983). A considerably larger bandwidth of ~200 to 400 cm^{-1} is believed to be beneficial for suppressing the growth of plasma instabilities that could lead to hot electron production. Investigation of the benefits of bandwidth on present and next-generation facilities will have an important role in defining the requirements for an LMF. Achieving large bandwidths will require some tailoring of the front end to produce a spectrum with a dip in the center, because even a flat spectrum would be narrowed to ~100 cm^{-1} after it was propagated through the full amplifier chain. We expect that a large bandwidth can be accomplished with a Fabry-Perot etalon in the initial amplifier to produce a loss at line center, with additional etalons used (if needed) after the oscillator or subsequent

amplifiers to further tailor the spectrum. Because the small-signal gain is down by only 16% at ± 100 cm^{-1} from line center, only a small increment of overall system gain will be needed in the case of 200 cm^{-1} bandwidth to drive the output to a saturation level comparable to the narrow band case. Achieving larger bandwidth will have an increasingly greater impact on system output energy unless additional amplification is added, but useful energy may be available for some AURORA experiments. It should be noted that the present optical configuration of AURORA will not allow small target spot sizes to be attained with this bandwidth because of chromatic aberration in the relay lenses. A complete validation and testing of the physics impact of broad bandwidth amplifier concepts for use on advanced lasers may require modification to the centered optical system to remove or correct these chromatic aberrations. Tests of simple laser performance should be possible with the existing AURORA optical configuration.

Advanced Front-End Conceptual Design

To produce on the order of 1 J of shaped, broadband radiation with the required contrast ratio, the front end will have some or all of the elements indicated in Fig. 1. The gain, size, and number of individual amplifiers is currently being examined. The characteristics of presently available commercial units are being considered versus the option of using in-house expertise to build amplifier units more suited to our own requirements.

Bandwidth Control

We envision starting with a long-pulse master oscillator with an intracavity etalon capable of generating a wide-band spectrum that peaks at ± 100 cm^{-1} (or more) from line center and gradually tapers down to a central spectral intensity of a few percent of the peak wing intensity. As noted above, some spectral tailoring can be done on the output of the oscillator if needed. The degree of contrast between the center and the displaced peaks is determined by the spectrally dependent system gain that follows and the flatness of the desired output spectrum. Although the overall system gain after the front end is $\sim 10^4$, the saturated amplifier gain will have to be approximately 10^2 times larger to account for splitting and aperturing losses in the encoders, and an additional gain of $\sim 10^3$ is needed between the master oscillator and the front-end output to provide useful output, taking into account optics losses and

discarded energy. For amplification of 10^9 at line center and an exponent that is 84% of this at ± 100 cm^{-1} from line center, a nearly flat-topped spectral distribution would be produced for a $\sim$4% ratio of central to peak wing intensity. For a higher-gain LMF, this ratio would decrease to $\sim$2%. At ± 150 cm^{-1} from line center, the gain is down to $\sim$68% of peak, and the central to peak wing intensity would have to be $\sim 10^{-3}$ to produce a nearly flat spectrum with a FWHM of $\sim$300 cm^{-1}. This large a ratio may be difficult to control accurately, and the lowered gain will require downstream enhancements to the system, but it is not out of the question to consider experiments at this bandwidth.

The input spectrum required to produce a given output spectrum is easy to calculate from the overall amplification and spectral gain profile, assuming that the line is homogeneously broadened so that any saturation occurs uniformly across the line profile. The input spectrum that produces a super-gaussian output spectrum strongly resembles the spectrum one would obtain by filtering a broadband spectrum through a Fabry-Perot etalon. Therefore, we have chosen to examine what happens when one amplifies the spectrum produced by this approach, which is readily amenable to experimental implementation. Figure 2(a) shows the output spectrum obtained after a gain of 10^8 for an input spectrum given by the transmission curve of an etalon with 50% reflectors and 200 cm^{-1} free spectral range (25-μm spacing). A relatively flat spectrum with a FWHM is obtained in this case. We have used a model Gaussian gain profile having a FWHM of 400 cm^{-1} (which closely approximates the gain near line center of the actual spectrum shown in Figs. 2 and 3 of Chapter V.A of Volume II).

If the etalon spacing is changed to obtain a free spectral range of 250 cm^{-1}, the ratio of the central to wing intensity must be decreased, which can be done either by increasing the etalon reflectivity or by double passage through an etalon. We find the latter procedure to be generally preferable, because high reflectivity etalons tend to give a spectral transmission that is too narrow in the wings and too flat in the center. Also, the transmission of low reflectivity etalons are not greatly affected by mirror losses, which are not accounted for in Fig. 2. The output after a gain of 10^8 and 2×10^9 is shown in Figs. 2(b) and 2(c) respectively, for an input spectrum obtained by double passage through a 50% reflectivity etalon with a 20-μm spacing. One again obtains a relatively flat spectrum, with a FWHM that is very close to the 250 cm^{-1} separation of the input peaks.
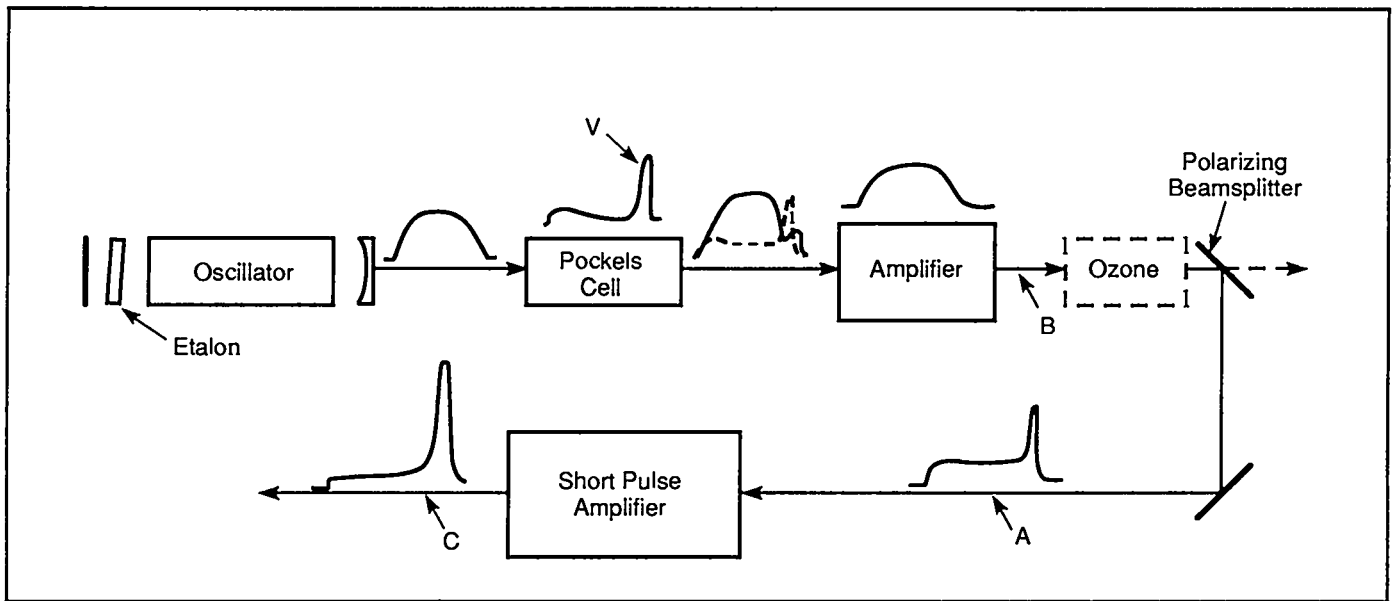
Fig. 1. Proposed experimental configuration for producing broadband shaped pulses. A, B, C are observation points referred to in discussion of preliminary experimental tests described in discussion of Figs. 4 and 5.

The impact of broad bandwidth operation on the performance of a final amplifier with a stage gain of 20 can be estimated from a comparison of the integration over the spectral distributions of these two outputs. We find that the stage gain is reduced to 15 in this case; i. e., to obtain the same output from the final amplifier without modifying it, the output of the previous amplifier must be increased by 33% to supply the additional energy needed to drive the wings of the line. The penalty in the 200 cm^{-1} case is only about 20%. In the design for the new system, the increased requirements do not impose a large cost burden. Even when an accounting is made for interstage coupling losses between the two amplifiers, the increase in the total energy that must be supplied to the system in the 250 cm^{-1} case is only ~3%, and the increase in cost is even smaller, because the amplifier, optics, and facilities costs will not scale proportionately to the energy of the penultimate amplifier. Additional enhancements will have to be made to each of the previous stages, but these represent even smaller fractions of the total system cost. It appears that the cost impact of a 250 cm^{-1} bandwidth will be under 1% of the total cost for a new system. In terms of retrofitting an existing system such as AURORA, one must either accept a decreased output or be willing to make improvements in the gain of each amplifier stage.

The actual gain profile is slightly asymmetric about line center and produces a small skewing of the spectrum, as shown in Fig. 3(a). Here we present the same calculation as Fig. 2(c) with the gain spectrum of Fig. 2 of Chap. V.A. of Vol II in place of the gaussian approximation. The

jaggedness of the output spectrum is an artifact of the courser grid on which this gain spectrum was calculated, but the skewing of the output is clearly evident. In Fig. 3(b), the input Fabry-Perot spectrum has been shifted by 5 cm^{-1} to compensate for the gain skewing. The difference between Figs 3(a) and 3(b) also indicates the sensitivity of the output spectrum to a change in the effective etalon spacing. We anticipate controlling this spacing by monitoring the output spectrum of a subsequent amplifier.

Pulse Shaping

The oscillator must be capable of generating a pulse with a duration slightly longer than the overall pulse length (foot plus spike), preferably with a flat intensity over most of this time (see Fig. 1), and a uniform spatial profile. Because the required energy is only on the order of 10 mJ, it should not be difficult to specify or design an oscillator to meet these requirements. The same basic concept can be used for echelon-free ISI, with some higher gain following the oscillator.

The polarized output of the oscillator is passed through a Pockels cell to which a programmed voltage pulse is applied to change the polarization of the pulse as a function of time. As shown schematically in Fig. 1, the voltage pulse consists of a long, low-level portion that turns on only a few nanoseconds after the beginning of laser oscillation and produces only a small perpendicular component of laser polarization, followed by a short, high-voltage spike that gives a full 90° rotation of polarization.
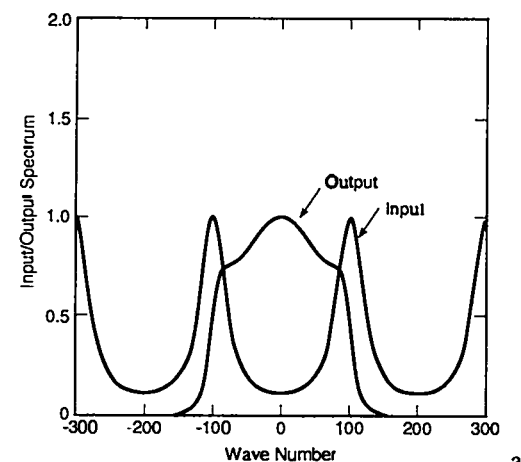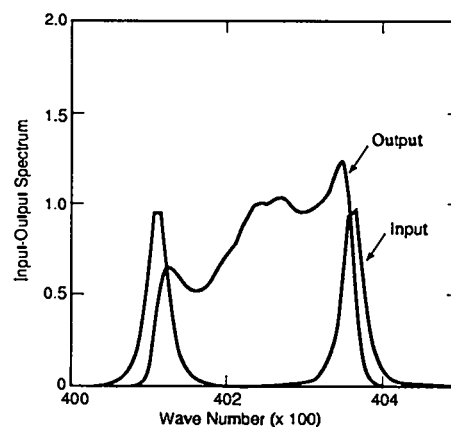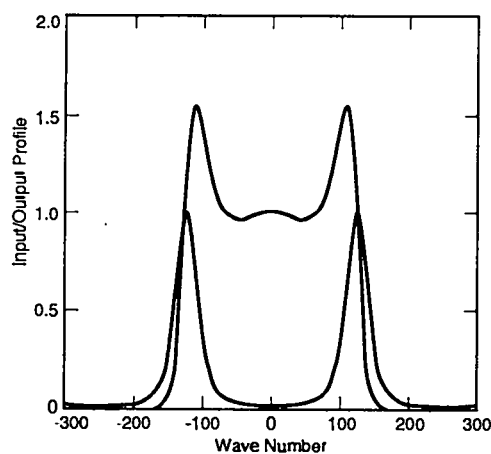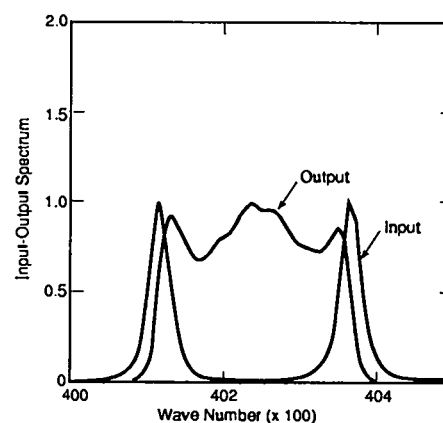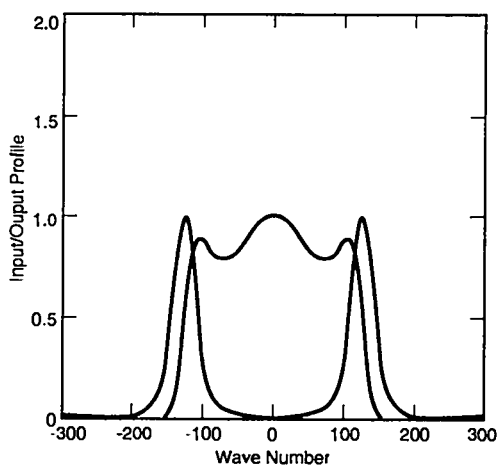
Fig. 2. Output spectrum produced by Gaussian approximation to KrF gain profile for input spectrum obtained by filtering a broad spectrum through a Fabry-Perot etalon having 50% reflectivity mirrors. a) 200 cm^{-1} free-spectral-range, 10^8 gain. b) 250 cm^{-1} free-spectral-range, etalon double-passed, 10^8 gain. c) Same, 2×10^9 gain.

Fig. 3. Same calculation as Fig. 2(c) with actual gain spectrum (computed, however, on a courser grid). a) Etalon centered at peak of gain spectrum. b) Etalon shifted by 5 cm^{-1}.

For convenience, the high voltage pulse may be applied to a second series Pockels cell, if it proves difficult to generate a single voltage pulse with the required characteristics. Because of the low level of the oscillator output, absorption in Pockels cells at this location does not impose a significant rep-rate limitation. The initial long voltage pulse can be shaped to compensate for gain rise times in the oscillator and amplifiers, as indicated in Fig. 1. It is turned on near the oscillator threshold to avoid significant prepulse from oscillator ASE.

At this point, the polarization components are not separated out; instead, the full beam is passed through a long-pulse amplifier. This amplifier is not pumped very hard in order to produce a uniform discharge over the required time, but it is of sufficient aperture and length to deliver several hundred millijoules when driven into saturation by

the input pulse. It is also turned on near the beginning of the input pulse to reduce prepulse ASE. Although strong saturation is desirable to minimize energy fluctuations, the small-signal gain should be kept as small as possible consistent with this to avoid excessive prepulse ASE. A polarizer located after this amplifier rejects the unwanted polarization. Because the two components are amplified together, the amplifier is kept uniformly saturated and the foot of the pulse does not grow significantly more than the peak. A birefringent wedge may be added after the Pockels cell to give a small angular separation to the two polarizations as well as to ensure high-contrast separation (Feng and Goldhar 1987).

At this point, we have discarded a large fraction of the energy we have produced, so further amplification is necessary. It is conceivable to do this additional amplification before separating the polarizations, most probably in an e-beam amplifier because in this case the total energy output must be ~10 J. To stay with easily rep-rated components and for a number of other reasons given below, we propose instead the following approach.

First, if it is necessary, the contrast ratio can be further improved by means of ozone saturable absorber. The saturable absorber can be used either before the polarizing beam splitter, as shown in Fig. 1, or after it. In the first location, the full energy of the amplifier is available for saturation, and relatively high absorber density can be used. In the second configuration (not shown), considerable (but reproducible) change in the shape of the leading foot would be experienced, but the well-defined polarization state of the beam would allow the absorption cell to be double-passed for better contrast. A polarizer and a quarter-wave plate would be used to separate the return beam.

The beam would then be amplified in a short-pulse amplifier that is timed to amplify the trailing, peak-power portion of the pulse. In this way, no ASE would be added before the foot. Also, the distortion of the front part of the foot that would result from amplification in an unsaturated gain medium would be avoided. Because only the high energy part of the pulse would be amplified, the amplifier need only be constructed to deliver the required output energy, not the much larger amount that would be required if the whole pulse were amplified. The one drawback of this approach is that the timing of the discharge must be controlled very precisely with respect to the rise of the high intensity pulse, so as not to greatly change the shape of the leading edge of this pulse. This requirement is most severe for lower-energy short-pulse driver facilities, but even in this case it should not be beyond the present state of the art.
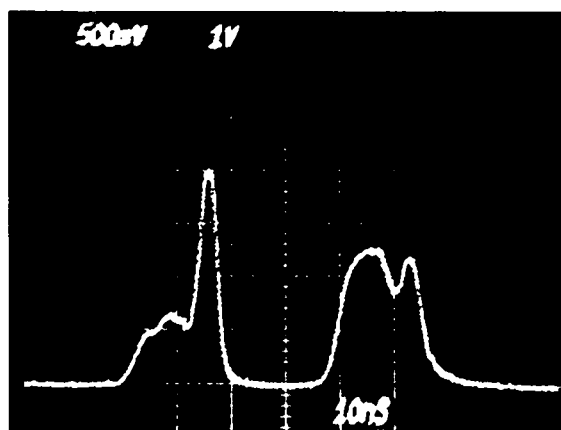
Demonstration of Prototype Pulse-Shaped Oscillator

Some of these concepts have been demonstrated with existing components on an off-line laser system. The oscillator section of a Lambda-Physik EMG 150 oscillator/amplifier similar to the one in the present AURORA front end serves as the oscillator indicated in Fig. 1. The ~20-ns pulse from this oscillator is sent through a Pockels cell as indicated in Fig. 1 and then through a rotatable quarter-wave plate (not shown). The quarter-wave plate, used in place of a long-pulse programmed Pockels cell, provides an adjustable component of crossed polarization over the whole pulse; a short voltage pulse is applied to the Pockels cell near the end of the oscillator pulse to switch the polarization by ~90°. This does not provide as much flexibility in pulse shaping as a programmed voltage pulse, but it is adequate for present demonstration purposes. The output is then single-passed through the amplifier section of the EMG 150, which serves as the first amplifier indicated in Fig. 1. The amplifier output is passed through a polarizing beam splitter, and the rotated component of polarization is fed into a similar amplifier timed to turn on just before the short spike, instead of to the short-pulse amplifier called for in Fig. 1.
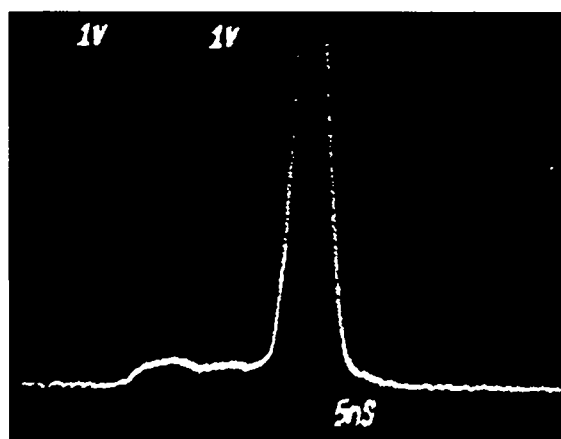
Figure 4 shows a series of laser pulses viewed at various points in the system. In Fig. 4(a), the leading pulse is the crossed component of the laser pulse viewed after the first amplifier and polarizing beam splitter ("A" in Fig. 1). The second pulse on this trace comes from a similar photodiode (60-ps rise time, limited by 1-GHz oscilloscope response) that views a portion of the amplifier output before the beam splitter ("B" in Fig. 1), with optical delay for display purposes. There are some depolarizing elements in the path to the second detector that provide higher sensitivity for the rotated component of polarization; the short spike is therefore overemphasized relative to the overall pulse amplitude. Nevertheless, one can see that this amplifier provides a relatively smooth output pulse in which the more complex pulse shape is contained. The relative amplitude of the two pulses is not significant, as it depends on beam splitter and attenuation factors that have been adjusted for convenient display with the photodiode kept in a linear response regime.

Figure 4(b) shows a pulse viewed at the output of the second amplifier ("C" in Fig. 1) under similar operating conditions. This amplifier is timed to turn on just before the sharp spike, so the ratio of spike to foot is greatly enhanced. (So that the foot of the pulse could be clearly seen, the peak has been allowed to go off screen.) This ratio can be varied by changing the amplifier gain or the

orientation of the quarter-wave plate. It can also be varied by changing the timing of the short voltage pulse with respect to the gain in the first EMG 150. This is shown in Fig. 5(a), in which the first pulse shows the cross-polarized output of the first amplifier with the Pockels cell voltage delayed into the low-level tail of the oscillator pulse. In this figure, the laser had a fresher gas fill than in Fig. 3 and had a somewhat longer pulse with a faster rise; it also has a slightly more prominent double-peaked feature characteristic of the ringing energy deposition circuit in this laser. The second pulse on this trace shows the output of the second amplifier. This picture shows two almost indistinguishable, overlapped sequential traces, indicating the inherent reproducibility of this technique. Figure 5(b) shows a similar pulse on an expanded scale. Some rounding of the transition region between the foot and spike that resulted from the turn-on of the amplifier gain is also evident in these pictures.
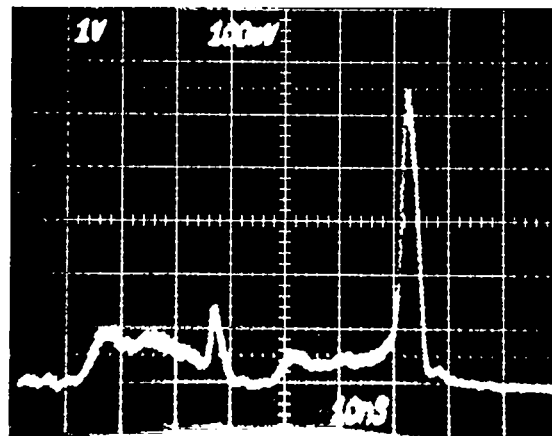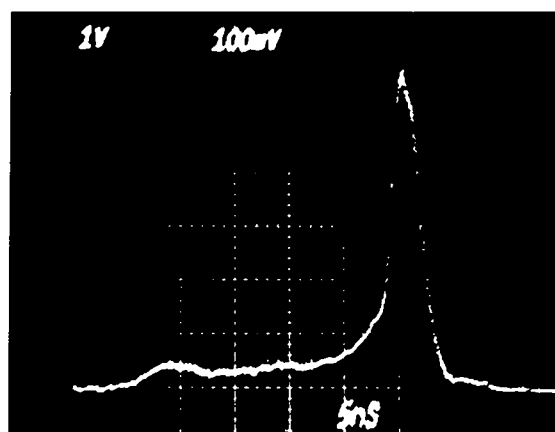
after polarizing beam splitter ("A" in Fig. 1), followed by optically delayed output observed before polarizing beam splitter ("B" in Fig. 1), 10 ns/div. b) Output of second amplifier ("C" in Fig. 1) timed to amplify only short spike, 5 ns/div.

a

b

Fig. 5. a) First pulse is the same as first pulse in Fig. 4 (a), with a fresh gas fill and Pockels cell voltage pulse delayed further into tail. Second pulse is output of second amplifier as in Fig. 4 (b). Two sequential traces are shown in this photograph. b) Same as second pulse in (a), time scale expanded to 5 ns/div.

a

b

Fig. 4. Pulse shapes obtained in off-line concept demonstration experiments. a) Output of first amplifier

Although no claim is made that this system has sufficiently low drift and jitter (and high enough energy and beam quality) to be immediately deployable, these initial results demonstrate the feasibility of producing complex, reproducible pulse shapes in KrF by some fairly simple

being usable in AURORA. With the use of some larger-
aperture amplifiers that have better medium homogeneity,
and in combination with some of the other techniques
discussed above, we are confident that pulses with the
required energy, bandwidth, and contrast ratio can be
generated.

REFERENCES

Kurnit, N. A. and S. J. Thomas, "Application of a Phase-
Conjugate Brillouin Mirror to Generation of High-Quality
Variable-Duration KrF Pulses," IEEE J. Quantum Electron,
QE-25, 421 (1989).

Thomas, S. J., K. W. Hosack, L. J. Lopez, I. J. Bigio, and
N. A. Kurnit, "Improved Performance of the AURORA
Front End with the Use of a Phase-Conjugate Mirror," Proc.
CLEO '88, Anaheim, CA, Apr. 26-29, 1988, paper TuM20.

Bigio, I. J. and S. J. Thomas, "Effective Saturable Absorber
for KrF Lasers," Appl. Phys. Lett. 49, 989 (1986).

Feng, S. T. and J. Goldhar, "KrF Laser Pulse Shaping in an
Oscillator-Amplifier Configuration," Proc. CLEO '87,
April 26-May 1, 1987, paper FC5.

Lehmberg, R. H. and S. P. Obenschain, "Use of Induced
Spatial Incoherence for Uniform Illumination of Laser
Fusion Targets," Opt. Commun. 46, 27 (1983).

ENDNOTE:
Figures 2 and 3 were provided by C. W. Patterson from
Vol. II, Chapter V.A of LA-UR-89-2675 (1989).

F. ELECTRON-BEAM PUMPING TECHNOLOGY FOR KrF LASERS

Garry R. Allen, Louis A. Rosocha,
Michael Kang, and Emanuel M. Honig

Historically, KrF lasers have been excited by three different means: electrical discharge pumping, direct electron-beam pumping, and a combination of the first two methods—discharge pumping sustained by an electron beam. For the excitation of large volumes, high energy electron beams have been shown to be more advantageous than the other two methods. Electrical discharges have a tendency to degenerate from a uniform glow discharge to a constricted arc discharge, causing nonuniform excitation of the laser gas, while electron-beam sustained discharges have shown limited effectiveness in KrF gas mixtures. The direct excitation of large volume KrF laser amplifiers by relativistic electron-beam pumping continues to be an effective, simple, and well-developed technology at the few kilojoule level. However, significant extension of this technology will be required to meet the cost and performance goals of future megajoule class systems.

The Electron-beam Pumping Technology component of the KrF Laser Development Program is structured to achieve these goals by addressing all technological elements required to deliver electron-beam energy to the laser gas. These elements include power conditioning, energy storage, electrical pulse shaping and compression, and electron-beam generation and transport. A schematic representation of a double-sided pumped KrF amplifier, showing the interrelationship of the various pumping system elements, is given in Fig. 1. In this section we will review the general pumping requirements of large KrF amplifiers, describe the basic features of the electron-beam diode and the power delivery system, identify the key pumping issues involved in scaling to larger amplifier sizes, and describe the development programs initiated to address the issues.
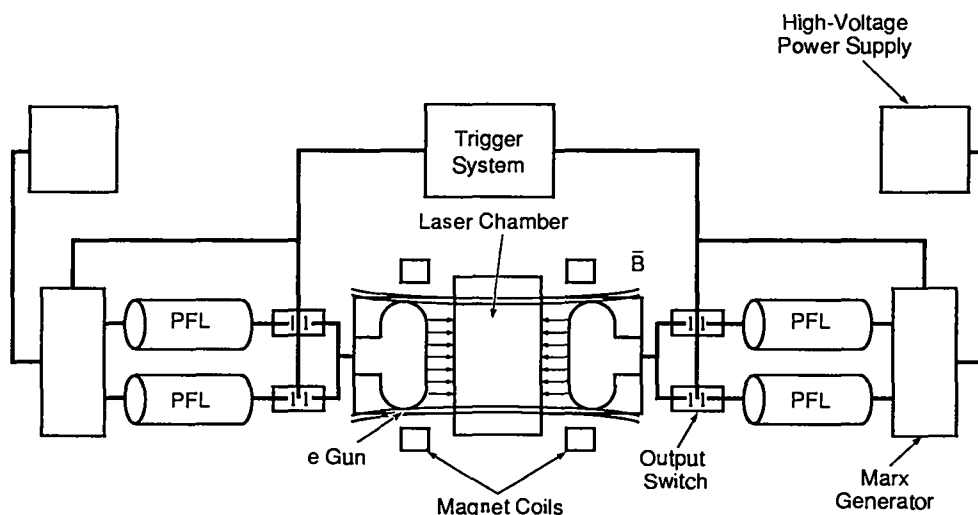

Fig. 1. Block diagram of a typical KrF laser amplifier using two-sided electron-beam pumping.

GENERAL AMPLIFIER PUMPING REQUIREMENTS

KrF lasers for ICF applications use a relatively long electron-beam pulse to excite the laser gas and efficiently extract laser energy over a period of time approaching a microsecond. Optical multiplexing then transforms the train of short optical pulses into a single high-energy laser pulse, about 5 ns long, on the target. A few stages of amplification are required to reach output energies in the kilojoule range. The electron-beam characteristics (voltage, current, specific pump power, and pulse length) of each amplifier stage are determined by a consideration of myriad interacting, and often conflicting, factors such as input fluence, saturated gain-length product, desired stage gain, number of optical channels, optical pulselength, laser chamber dimensions, laser gas mix and pressure, ASE and parasitic formation, voltage breakdown limits, optical component size limitations, diode impedance collapse, etc. Examining these various tradeoffs and limitations led to electron-beam energies at the MeV level, total diode current in the megampere range, and electrical pulselengths of hundreds of nanoseconds to a microsecond. A comparison of these operating parameters for the existing AURORA LAM amplifier and two conceptual designs for higher energy amplifiers is given in Table 1.

Energy deposition spatial and temporal uniformity are important pumping parameters, in addition to those given in Table 1. Design goals for these parameters are 10% peak-to-average variation for spatial uniformity and 25% peak-to-average variation for temporal uniformity.

Energy deposition spatial uniformity in the laser cavity is determined by the electron-beam voltage, cavity width, and laser gas mix and pressure. Spatial uniformity for double-sided pumped laser cavities is achieved by setting the electron energy to provide a practical range for a given laser gas mix and pressure that is equal to the cavity width. Choice of the appropriate beam energy is determined from Monte Carlo particle transport codes. This maximizes the electron energy fraction deposited in the laser gas and creates an energy deposition profile that rapidly drops to zero at the opposing cavity wall. Superposition of two opposing profiles results in a flat spatial deposition profile across the laser cavity. This approach works quite well for a constant energy electron beam.

However, spatial and temporal pumping uniformity of the laser gas also depend on the temporal evolution of the electron-beam pulse from the cold-cathode diode and its electrical driver. This dependance can be easily seen by considering two extreme cases. First, consider a

TABLE 1. A comparison of amplifier pumping parameters

Parameter	Units	AURORA LAM	50KJ amp	240KJ amp
Pumped Width	m	1.0	1.1	1.3
Pumped Height	m	1.0	2.2	3.9
Pumped Length	m	2.0	2.35	3.75
Pump Power	kW/cm^3	81	250	200
E-Beam Voltage	kV	675	800	1000
Gas Current Density	A/cm^2	6	21.5	13
Beam Transport	%	30	50	60
Cathode Current Density	A/cm^2	20	43	21.7
Diode Current per side	MA	.4	2.2	3.2

constant-voltage cold-cathode diode. Because all cold-cathode diodes that are operated for more than a few hundred nanoseconds exhibit an impedance collapse as a function of time, a constant-voltage electron beam will produce a rising current over the duration of the pulse. As a result, the power pulse increases with time, as shown in Fig. 2, but it provides a uniform spatial deposition profile across the cavity. The other extreme is a constant-power case in which the diode voltage is forced to droop severely over the pulse duration to compensate for the increasing current. The result is good temporal power deposition but extremely poor spatial uniformity across the cavity over the full pulse duration, as shown in Fig. 3. Thus, diode impedance collapse forces a tradeoff between spatial and temporal energy deposition uniformity.
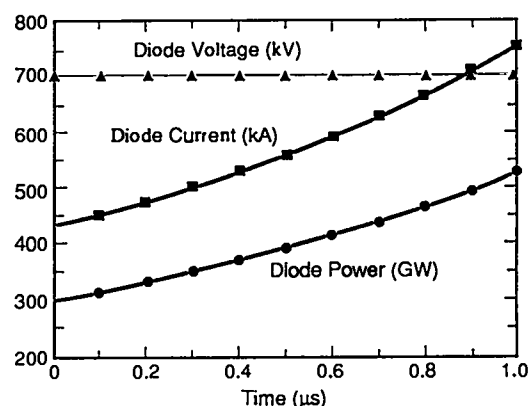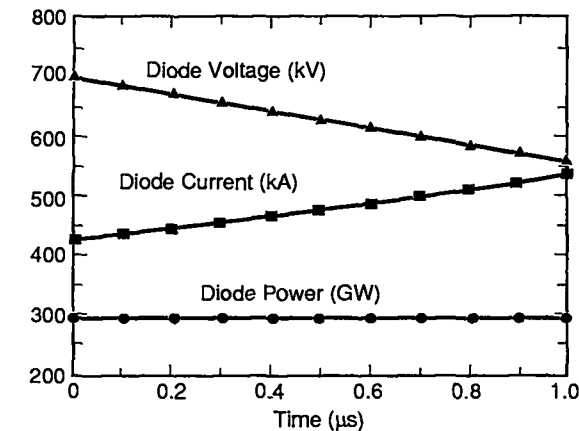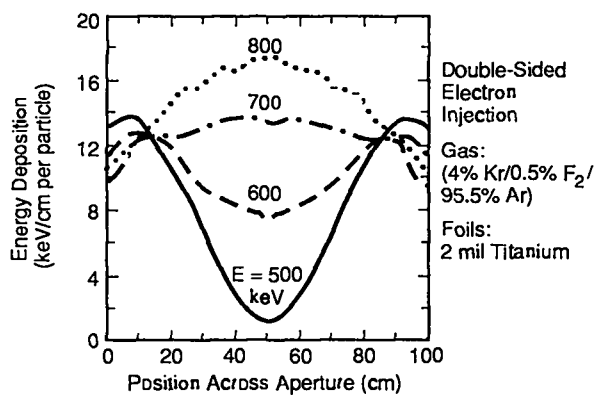

Fig. 2. Calculated diode current and output power of LAM-sized diode (2 m^2-cathode, 8-cm A-K gap) showing the effects of diode collapse (at 2 cm/μs) under constant-voltage operation.

a

b

Fig. 3. Effect of diode collapse on pumping uniformity under constant-power conditions: (a) Calculated diode current and voltage, and (b) Plot of energy deposition uniformity versus beam voltage.

Electron-Beam Diode

Because of its simplicity, the cold-cathode electron diode is commonly used to generate electron beams for single-shot devices, and it is the electron gun of choice for large, single shot KrF laser amplifiers. Hot-cathode electron guns do not experience the impedance collapse associated with cold-cathode guns and are generally chosen for rep-rate applications. However, they are expensive, require high voltage isolation of the heaters, and active foil cooling arrangements, and are subject to cathode contamination in the event of a foil rupture. The generic, planar cold-cathode diode, as shown in Fig. 4, consists of a vacuum chamber which contains a cathode with a contoured emitter surface, high voltage feedthrough bushing, anode, foil support structure (hibachi) and vacuum foil.
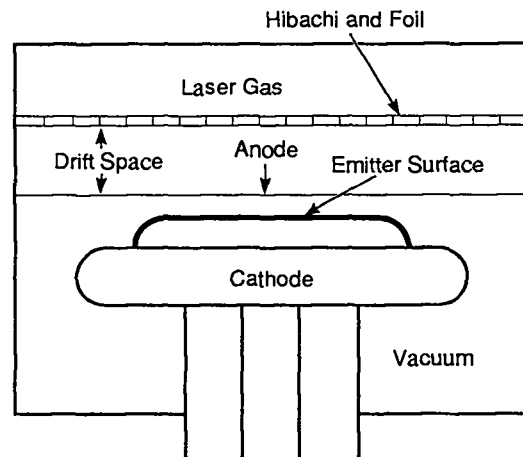

Fig. 4. Typical configuration for a monolithic cold-cathode e-beam diode.

Operation of a cold-cathode diode depends on localized field enhancement at the tips of microprotrusions on the emitter surface to produce field emission. Common emitter materials used in cold-cathode diodes include metal blades or punctured metal sheets, graphite felt, and velvet fabric, all of which provide an abundance of microprotrusions. As the field emission current increases, the microprotrusions heat up due to joule heating and explode, forming local plasma flares. These individual flares quickly expand and form a plasma sheath over the cathode emitter surface. The resulting plasma is an excellent source of electrons which are easily extracted up to the limit imposed by space charge buildup in the anode-cathode gap. For planar diodes, this limit is the Child-Langmuir space charge current given by,

$$J = k \; V^{3/2} / d^2$$

where J is current density in A/cm^2, V is the cathode potential in volts, d is the distance between the anode and the cathode in cm, and k = 2.34 × 10^{-6} A/V$^{3/2}$.

This field-generated plasma is the key feature that makes cold-cathode diodes relatively simple to engineer because the application of high voltage to the cathode serves the dual purpose of electron generation and acceleration. However, this same plasma is the source of cold-cathode diode impedance collapse because the plasma expansion is reducing the anode-cathode spacing, d, at a velocity of a few centimeters per microsecond throughout the pulse. The plasma velocity, and therefore the diode impedance collapse, have been empirically linked to external guide field magnitude as shown in Fig. 5.
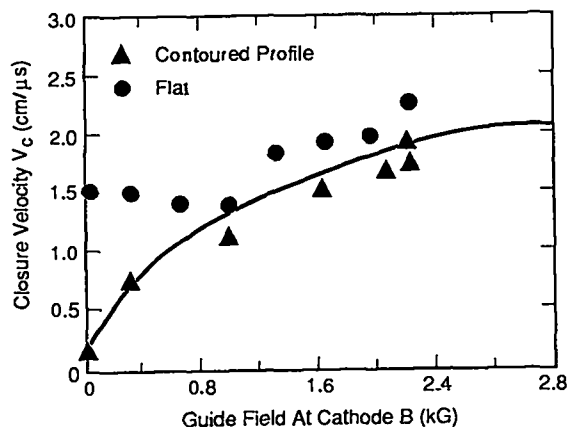
Fig. 5. Diode closure velocity for a cold cathode with a graphite felt emitter surface as a function of the applied guide magnetic field.

A major concern with large, high current cold-cathode diodes are the undesirable side effects that result from applying the external magnetic guide field, which is necessary to prevent beam pinching by the self-induced azimuthal magnetic field. Although the external guide field is essential for high energy, large area, monolithic diodes, it has these adverse effects. It

1. introduces beam rotation and beam shear as a result self and applied field interactions, as illustrated in Fig. 6;
2. inhibits the expansion of the initiating plasma flares, resulting in pencil-like cathode beamlets of high current density; (This not only produces less uniform pumping of the laser gas, but in extreme cases may create foil damage due to excessive localized heating.) and
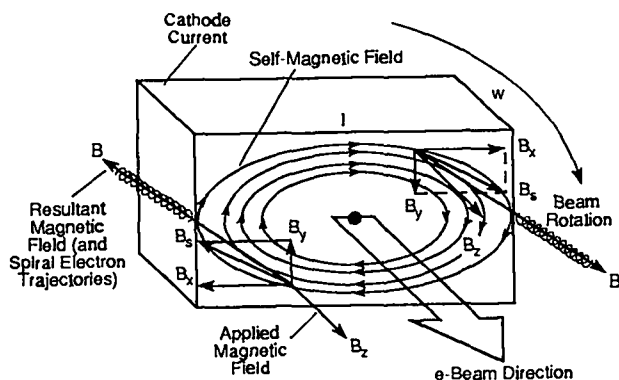3. increases diode impedance collapse, as mentioned above.

Fig. 6. Diagram showing combined effect of self and applied magnetic fields on the electron-beam trajectory for a rectangular cathode.

To adequately prevent beam pinching, the external guide field magnitude must be equal to or a few times the self field. For very large diodes with monolithic cathodes, the total diode current will be in the few megampere range, which places the external guide field in the kilogauss range. Note that item 1 above is improved with increasing guide field magnitude, but items 2 and 3 are made worse.

Beam rotation and distortion are offset somewhat by the beneficial effect of straightened electron trajectories through the foil support structure provided by the external axial magnetic field. The foil serves as the barrier between the laser gas and the diode vacuum. The foil in turn is supported by the foil support structure—a plate containing numerous slots—commonly referred to as a hibachi. The electron beam passes through open slots unobstructed at normal incidence but suffers angle-dependent shadowing losses at incident angles other than normal. These shadowing losses are spatially dependent: slots at or near beam center are hardly shadowed because contributions of azimuthal field from surrounding beam areas are largely self-cancelling by symmetry; however, slots further away from beam center shadow the beam heavily because the azimuthal field is pronounced at these locations.

Foil materials that are commonly used include metalized Kapton (polyimide), titanium, and aluminum. For a given thickness and pressure loading, foil tensile strength determines the maximum hibachi slot size that can be spanned. High foil tensile strength therefore maximizes hibachi geometric open area. A low mass number and surface mass density—the product of density and thickness—minimize energy deposition in the foil. Electron scattering by the foil is also minimized by using foil material with low mass numbers.

Materials used for hibachis include high-strength aluminum alloys and stainless steel. Nonmagnetic materials are required unless the external field can fully saturate the material, for field line trapping in the unsaturated media would block a high fraction of the beam. Hibachi slot sizes are totally dependent on foil strength. Their shape is typically rectangular and may be oriented for maximum transmission with the long dimension parallel to the azimuthal magnetic field. Hibachi material with a high tensile strength is required to minimize foil support rib and hibachi thickness, thereby minimizing beam shadowing.

Electron-Gun Power Delivery

Delivering high voltage, high peak power pulses to low impedance loads requires some means of voltage multiplication pulse shaping and power amplification. This is typically achieved through the use of a primary energy

store and a temporal energy compression circuit. Marx generators are commonly used to provide the primary energy storage. This technology is well understood and in widespread use today. A high-voltage pulse is generated by switching parallel charged capacitors into a series connected configuration. This voltage multiplication technique is a relatively easy and inexpensive method for generating a megavolt-level pulse for singe-shot machines. Capacitors are typically in the microfarad range, can be charged up to 100 kV, have good voltage reversal characteristics, and store tens of kilojoules. Marx banks for electron-beam pumped KrF lasers may have tens of stages and store up to hundreds of kilojoules.

Temporal energy compression circuits are used to improve energy transfer efficiency between the Marx generator and the diode. These circuits are typically pulse-charged by the Marx generator in a few microseconds and release the transferred energy in a well-defined pulselength in the hundreds of nanosecond range. Common examples of such circuits are the pulse forming line (PFL) and the Blumlein line. Energy transfer efficiency is maximized when the erected Marx generator capacitance is matched to that of the pulse compression line.

PFLs are preferable to Blumlein lines for low impedance loads for a number of reasons. Transmission lines become increasingly difficult to design for decreasing impedances. A load impedance, Z, would require a PFL of line impedance, Z, while a Blumlein line would require two transmission lines of impedance, Z/2. Furthermore, Blumlein lines require a much lower inductance Marx bank for the same charge time as a PFL. PFLs have the added advantages of simpler mechanical design and easier maintenance. Even though PFLs require twice the charging voltage as a Blumlein line, this is not a problem in our voltage range of interest, especially because the Marx inductance is less of a problem.

PFLs may be constructed in coaxial or flat (triplate) geometry. Vertical triplates with screened tops offer some slight advantages over their coaxial counterparts—visibility, ease of access, lower cost variable impedance option, and ease of impedance change. Water is commonly used as the PFL dielectric because its high dielectric constant results in relatively short lines for a given output pulselength (~18 ns/ft), and it provides reasonable energy density (~20 kJ/m^3). The use of water as the PFL dielectric requires that the lines be pulse-charged (<2 μs) to avoid excessive shunt resistive losses and to minimize breakdown probability while maintaining high stress levels.

A third option, pulse forming networks (PFNs), has the advantage of combining the energy storage and pulse shaping requirements into a common, lumped element circuit. This dual use of the primary energy storage element typically results in a smaller energy delivery package for the same total energy as compared to Marx generator-PFL systems. However, PFNs are best suited for higher impedance, longer pulse applications, and they are not cost effective for present diode designs for KrF laser systems.

The PFL output is coupled to the cathode of the diode through a triggered series output switch and a high voltage vacuum feedthrough bushing. A typical representation of this configuration is illustrated in Fig. 7, which shows a cross section of the AURORA LAM electron-gun assembly. A short rise time of the electron-beam power is desirable to minimize the electrical pulselength and associated energy storage and the required floor space, as well as to reduce foil heating by low energy electrons during the pulse rise time.
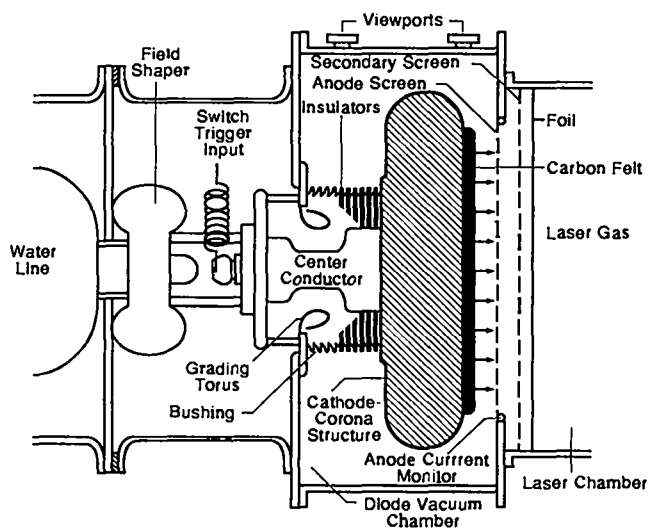

Fig. 7. Cross section of the electron-gun assembly in the LAM amplifier of the AURORA laser system.

Vacuum voltage breakdown is the final consideration in delivering power to the diode. Both the cathode structure and the bushing must be capable of holding off the high voltage for the duration of the pulse without emitting electrons, flashing over, or producing a vacuum arc. This is typically achieved by careful grading of the bushing insulation stack with field shapers, applying dielectric coatings to the cathode structure, and maintaining general cleanliness during assembly.
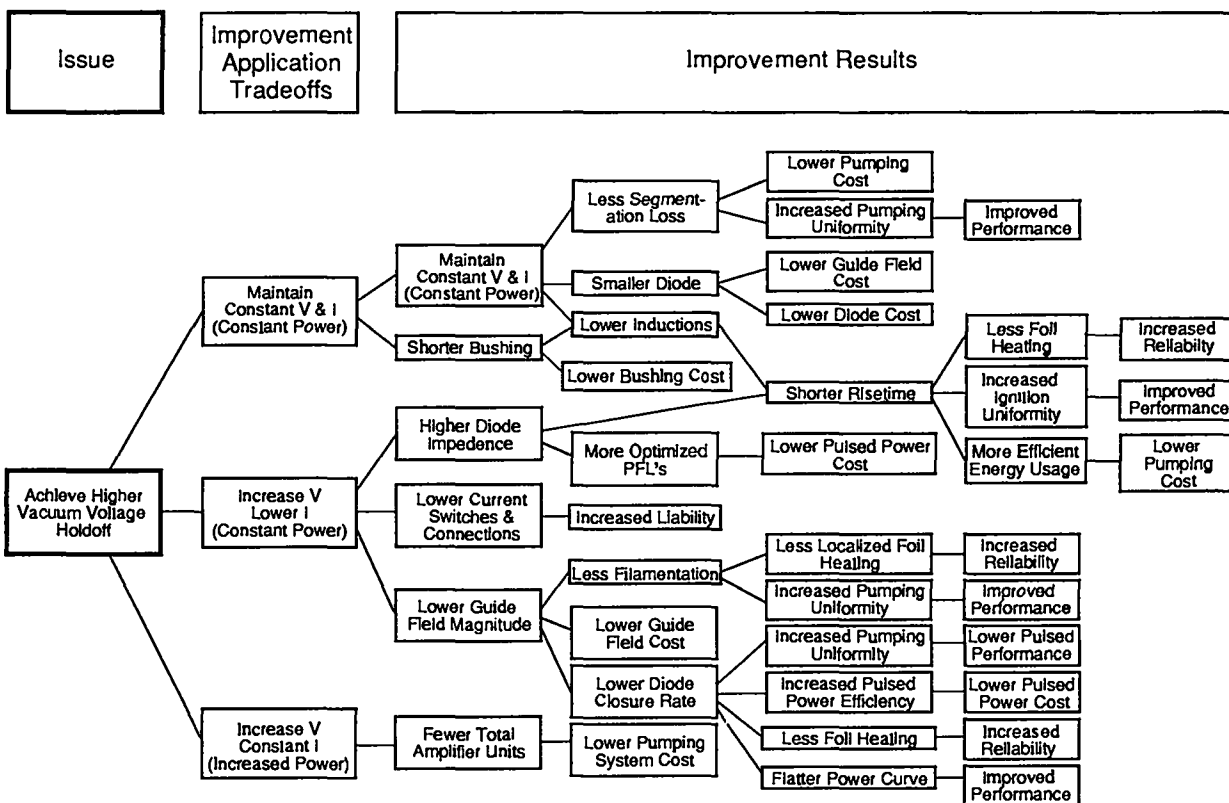
Fig. 8. Diagram showing e-beam pumping system improvements enabled by higher vacuum voltage holdoff capability.

Scaling to Megajoule Systems

Scaling to a megajoule-sized KrF laser system will require both a reduction of large amplifier cost and a significant improvement in the performance of the individual amplifier modules. The Los Alamos program plan projects that the 10-MJ LMF system can be reached by a two-staged increase in amplifier size, from the present 10-kJ AURORA LAM module to a 50-kJ module and finally to a 240-kJ module.

The increase in laser energy required in next-generation systems leads to a corresponding increase in the size of amplifier modules, to an increase in the operating voltage and current of the e-beam diodes, and to an increase in the magnetic guide field. The practicality of such systems depends greatly on increasing the system efficiency and reliability while reducing individual component costs. Better pumping efficiency requires improved e-beam transport from cathode to laser gas.

Increased amplifier size is driven by overall system cost issues. However, increased amplifier size presents challenging development requirements to the electron-beam pumping technology. The large total current (several MA

per diode) associated with very large amplifiers presents problems that must be addressed. First, large diode currents require large guide fields, which in turn lead to increased diode impedance collapse and electron-beam emission filamentation. Second, large diodes present problems with power flow to the emitter leading to possible nonuniform emission. Both of these issues indicate that the cathode needs to be segmented at some optimal size to reduce the total current in any one segment and thereby reduce the guide field and power flow problems. However, segmenting the cathode introduces other problems with vacuum voltage holdoff between segments and their return structure and nonuniform pumping of the laser gas that is produced by the unpumped regions between the segments. Thus, two primary development areas are readily apparent: a determination of the optimal cathode size and configuration and an improvement in the vacuum voltage holdoff of the cathode structure and feedthrough bushing. The improvement of vacuum voltage holdoff has a pervasive beneficial impact on the entire electron-beam pumping system as shown in Fig. 8; the improvement is not limited to the cathode segmentation issue.

The third key development area centers around improving the electron-beam transport efficiency. Because

the primary cost associated with any large KrF laser amplifier lies with the electron-beam pumping system, significant cost reduction leverage is associated with increasing electron-beam transport efficiency. Any improvement in this area has a direct impact on the entire electron-beam delivery system; that is, doubling the beam transport efficiency either cuts in half the cost of a given amplifier electron-beam pumping system or provides for an amplifier of twice the energy at the same pumping cost. Present transport efficiency of large, meter-scale amplifiers is on the order of 30-35%; thus, the potential for achieving a goal of 60-65% is clearly present. The cost leverage is especially apparent when one considers that any improvements in this area will be achieved through improved materials (foils and hibachi structures) and advanced designs (cathode shaping and emission mapping) rather than an increase in complexity or investment in additional hardware.

Other electron-beam pumping issues that deserve attention are diode impedance collapse, emission uniformity, energy deposition diagnostics, emitter material lifetime, vacuum foil lifetime, power delivery system inductance, energy density of the primary energy storage, electrical pulselength, etc. However, as important as these issues are, they do not have the global impact of the three primary development areas identified above: determination of optimal cathode size and configuration, improvement of vacuum voltage holdoff, and enhancement of the electron-beam transport efficiency.

Electron-Beam Pumping Technology Development

The objectives of the Electron-Beam Pumping Technology Development Program are to resolve the electron-beam pumping issues involved in scaling KrF amplifiers to the sizes required for modules characteristic of the LTTF and the LMF. Particular emphasis will be given to cost reduction and performance enhancement. The program has been planned to make use of appropriate LANL, university, and industry resources to meet the objectives.

The E-Beam Pumping Technology Development Program consists of the following major elements:
- pumping system architecture,
- diode physics,
- vacuum insulation, and
- energy deposition.

Pumping System Architecture

This element is targeted to answer the diode configuration question: At what size does the cathode need to be segmented to provide optimal cost and performance? In addition, What is the optimal segmentation arrangement—size, shape, presence/absence of guide field, etc.

Diode Physics

This element deals with enhancing the electron-beam transport efficiency in these ways: materials development (foils and hibachi support structures); trajectory code development and benchmarking; advanced cathode design (cathode shaping and emission mapping); and design verification testing. In addition, it is structured to investigate electron-beam uniformity and diode impedance collapse issues, predominantly through the use of new emitter materials.

Vacuum Insulation

This element is structured to accurately confirm the present vacuum breakdown limits in practical cold-cathode diode configurations (i.e., in the presence of uv-illumination, soft x rays, high energy electrons, and emitter generated conductive debris); investigate promising dielectric coatings for metal surfaces for improved holdoff capability; and demonstrate design improvements through control of field stress.

Energy Deposition

This element is chartered to increase the measurement accuracy of electron-beam energy deposition in the laser gas. Although this element will not directly increase the laser system performance or reduce its cost, it will provide the accurate knowledge of the laser efficiency that is prerequisite for making accurate laser system cost estimates. This effort consists of developing new diagnostic methods (spectroscopic techniques, fiber optic calorimetry); pursuing advancements of more traditional instruments (Faraday probes, standard calorimeter, radiographic film, Rogowski current probes); and benchmarking of Monte Carlo particle trajectory codes.

Each of these elements deal with specific technical areas that affect the scalability, cost, and performance of the e-beam pumping portion to the laser system. The technical efforts are supported by several development facilities at

LANL as well as through interactions with universities and industry. The LANL development facilities consist of the Amplifier Technology Unit, the Electron-Gun Test Facility, and the High Voltage Test Facility.

Amplifier Technology Unit (ATU)

This element is an amplifier development facility presently under construction with operating parameters (given in Table 2) and scale size sufficient to address future amplifier e-beam pumping issues without the need for significant extrapolation. Initially, the primary application of this facility will be restricted to addressing electron-beam transport efficiency and diode architecture issues.

TABLE 2. ATU operating parameters

Emitter Area	1.0 m × 0.5 m
Cathode Voltage	1.0 MV
Cathode Current	250 kA
Pulsewidth	650 ns
Current Density	50 A/cm^2
Guide Field	4 kG

Electron-Gun Test Facility (EGTF)

This element is a diode development facility operating at sub-scale parameters (given in Table 3) that employs a Marx generator, peaking capacitor, and diverter switch to provide the voltage, rise time and pulsewidth desired for a particular investigation. It is used for initial development of new materials (foils, emitters, dielectric coatings, etc.) prior to full-scale tests on the ATU. In addition, it is the primary research tool for investigating diode closure and emission uniformity.

TABLE 3. EGTF operating parameters

Emitter Area	200 cm^2
Cathode Voltage	500 kV
Cathode Current	15 kA
Pulsewidth	200 ns to several ms
Current Density	75 A/cm^2
Guide Field	3 kG

High Voltage Test Facility (HVTF)

This element consists of several test fixtures relating to the development and calibration of high voltage devices (vacuum bushings, high voltage switches, high voltage and high current probes, etc.). The most important of the various fixtures, the Bushing Test Fixture, allows full-scale testing and development of the critical vacuum feedthrough bushings along with the development of vacuum breakdown suppressing dielectric coatings. This fixture may operate up to 1.5 MV.

In addition to the internal development efforts and facilities outlined above, we have established ongoing collaborations with both universities and industrial organizations that address a subset of the key technical issues, and we plan to expand these interactions to encompass all the critical areas. The full scope of the developmental efforts are summarized in the experimental resources and technical development matrix shown in Table 4.

TABLE 4. Matrix of experimental resources and technical development areas

Experimental Resources	System Architecture	Technical Development Areas Energy Deposition	Vacuum Insulation	Beam Transport	Beam Generation
ATU	❑			❑	
EGTF		❑	❑		❑
HVTF			❑		
University	❑		❑	❑	❑
Industry	❑	❑	❑		
AURORA		❑		❑	

SUMMARY

Meeting the cost and performance goals of future KrF lasers systems will require significant extensions of existing e-beam technology because the performance and cost of any large KrF laser is intimately linked to the e-beam technology employed. To achieve these technology extensions we have identified the key cost and performance leverage areas, implemented development programs targeting these leverage areas, and made progress toward generating the information required to optimize the e-beam pumping system for megajoule class KrF lasers.

VIII. Plasma Physics for Light-Ion Program
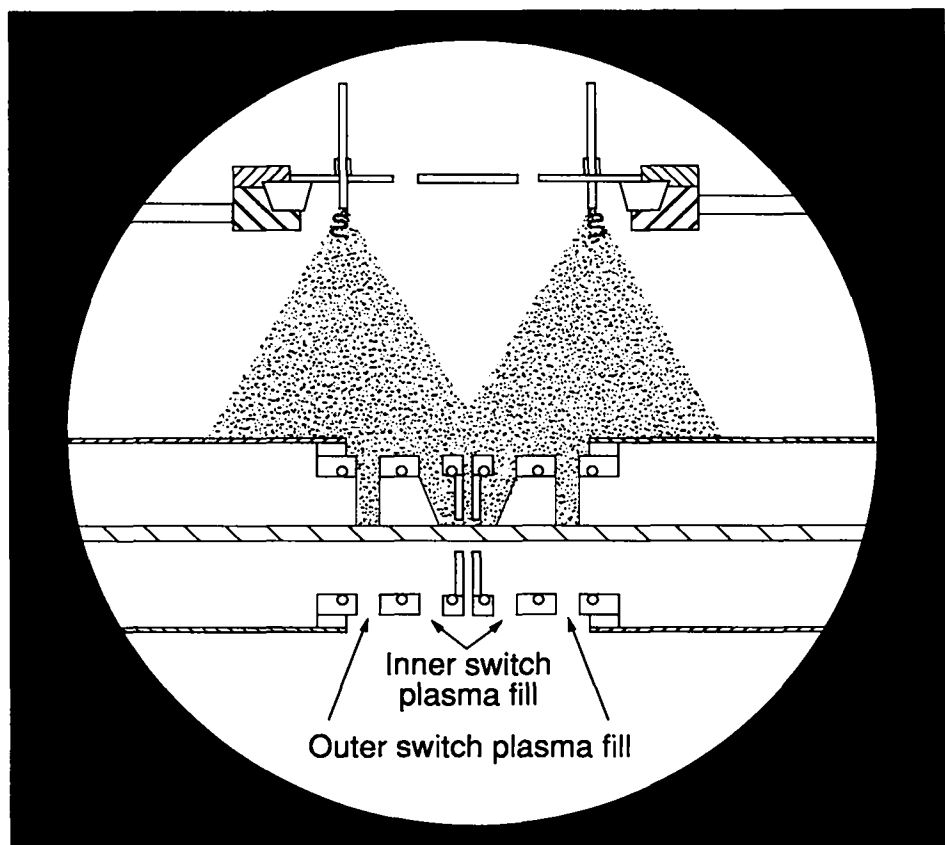
Simplified schematic of a plasma erosion opening switch.

VIII. PLASMA PHYSICS STUDIES FOR THE LIGHT-ION ICF DRIVER

Rodney J. Mason

The Particle Beam Fusion Accelerator (PBFA II) is the light ion driver at Sandia National Laboratory with the potential to deliver 1 to 2 MJ to a target in 10 ns. This report summarizes plasma physics research done by Los Alamos since 1986 to support two elements of this driver.

The PBFA II driver has a large system of Marx generators and transmission lines surrounding a central barrel diode region. The system is symmetrically replicated above and below the diode. The power flow is conditioned by a number of transmission line elements and switches and stored for a period of ~ 50 to 90 ns in bi-conical transmission lines just beyond the diode. In a final section of the lines, plasma is injected through the anode of the bi-conical region toward the cathode in the plasma opening switch (POS) (Fig. 1). ideally, current conduction through the switch is disrupted after about 50 ns. Voltage is multiplied by the rapid switch opening, and 4 MA at 28 MV is delivered in 7 ns to a barrel diode. Mastery of the plasma opening switch is identified as a crucial issue because the switch is needed to achieve the high diode voltages required to accelerate lithium. It is also clear that Los Alamos possesses unique modeling codes that could be used to understand the POS.

Computational Tools

The plasmas of interest are of moderate density and considerable physical extent. In the POS the fill plasma is typically 4- to 12-cm long and 4- to 8-cm wide. It may move during the opening process some 20 cm downstream toward the barrel diode load (Fig. 1). Its initial density ranges from 10^{12} to 10^{14} electrons/cm^3. The plasma dynamics obeys Newton's laws represented in the form of fluid and/or particle equations. But the plasmas are too collisionless and/or tenuous for reliable modeling through the magneto-hydrodynamic (MHD) representation of these laws and too extensive and too dense for an economical explicit particle-in-cell (PIC) treatment.
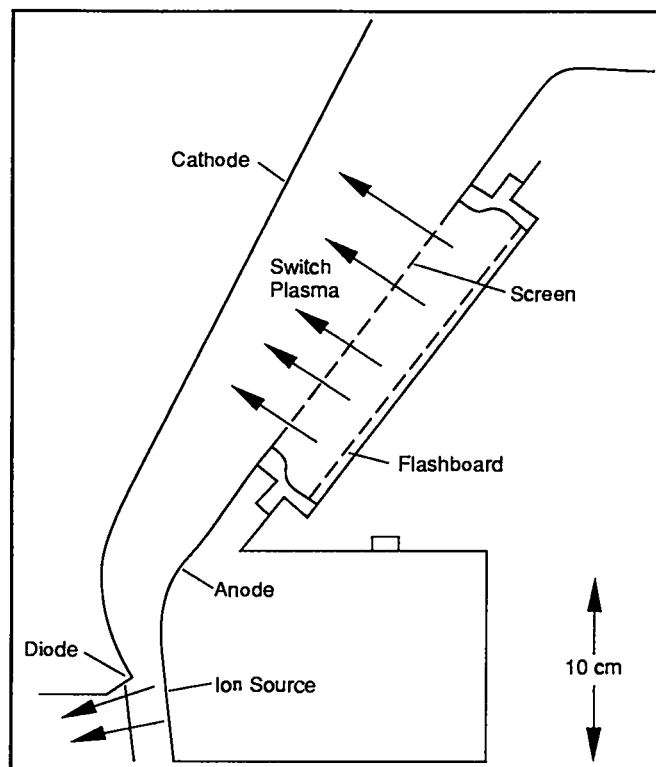

Fig. 1. The bi-conic plasma opening switches on PBFA II.

In traditional MHD codes and related hybrid codes (in which the electrons are inertialless fluids, and just the ions are particles), electron speeds are determined indirectly, through division of curl B in Ampere's law of Maxwell's equations (with displacement current neglected) by the local density. But in the POS, electrons are emitted in an intense stream from the cathode as field penetrates the switch plasma and accelerated to relativistic velocities. Electrons are separated from the main body of the plasma during the opening process and ejected toward the anode and through vacuum toward the load. These are non-neutral processes, beyond the scope of MHD and hybrid simulation.

On the other hand, the electromagnetic skin depth in the POS plasma is 0.2 cm at 10^{13} cm^{-3} fill density, and *the*

Debye length is correspondingly smaller for switch plasma initially colder than 0.5 keV temperature. (It is injected at 5 eV.) Explicit PIC codes require cells no wider than a Debye length. If adherence to this small cell restriction is ignored, the explicit PIC modeled rapidly heats by the finite grid instability, until the new plasma Debye length matches the condition. The noise in simulation during this numerical heating masks true physical processes and can suggest erroneous field penetration activity. The ultimate constraint is that the cost in time to simulate the large switch regions of interest can run to hundreds of CRAY-YMP hours for a single case.

Implicit plasma simulation codes use dynamical equations for the average properties of the plasma to predict advanced values of the current and charge density as sources to Maxwell's equations. In the Implicit Moment Method (Mason 1981; Brackbill and Forslund 1982), invented at Los Alamos, the additional dynamical equations are simply the lower two-fluid moment equations, that is, continuity and momentum. This can be solved algebraically with the full Ampere's law for new electric field values, E to apply at the end of a computational time step. Faraday's law gives the new magnetic field in terms of the derivatives of E, and thus closes the system of equations. Generally, one solves a resultant set of elliptic equations for B and then uses this in the combined moment equations and Ampere's law to extract an advanced E-field solution. The computational cycle is completed by advancing the true plasma dynamical equations (fluids or particles) in the advanced fields.

The use of time-advanced fields removes constraints that limit explicit codes to time steps less than the minimum plasma period on the mesh. The implicit codes can use the generally large Courant condition time step associated with the fastest electrons crossing the mesh. (This limit requires that the fastest electron should go no further than the minimum cell width in a time step.) Furthermore, with PIC simulation, implicitness suppresses the finite grid instability, if the time step remains close to the Courant value everywhere in the system. A fluid update of the plasma parameters will generally require considerable care in its temporal and spatial differencing. When auxiliary fluid equations are solved with the field equations, the need for such care in the fluid differencing is avoided. Generally, errors introduced by the use of simplified moment equations in the field solution can be subsequently corrected or iterated away. Furthermore, finite grid instability is totally avoided for arbitrary time step size with fluid modeling of the plasma. All this can be summarized as follows. Implicit differencing can provide a plasma model that allows for the large cells and large time steps requisite for the global modeling of the plasma systems that are now challenging

the future of light ion fusion. Implicit plasma simulation is a relatively new technology (and art).

Modeling of the POS was conducted chiefly with the implicit ANTHEM code (Mason 1987a). ANTHEM is a two dimensional model, originally built to resolve hot electron issues arising in the Los Alamos laser fusion program. Numerous modifications were required to apply ANTHEM to light ion problems:

1. The code was adjusted to allow for an external driving magnetic field to represent the input of electromagnetic energy from the PBFA II accelerator.
2. An option for surrounding conducting boundaries was added.
3. Allowance was made for plasma injection at the boundaries.
4. A rule for Child-Langmuir emission of electrons into the switch plasma was implemented.
5. The code had been cartesian; it was given a cylindrical geometry option.
6. ANTHEM allows for either multifluid or PIC plasma modeling. Both options were streamlined and vectorized.
7. The basis for the code was changed from velocity to momentum, and relativistic effects were added.
8. Circuitry for an external load was added.

Some POS calculations were conducted with the relativistic ISIS PIC simulation code (Jones and Gisler 1985). ISIS makes an implicit determination of electric fields but determines magnetic fields explicitly. Comparative solutions were obtained with both ANTHEM and ISIS, and general agreement was obtained with some important differences that are discussed later.

The Plasma Opening Switch

The POS is supposed to compress the power pulse arriving at the light ion diode in PBFA II. In recent experiments, a 4 MV, 50-ns pulse at 3 MA was to be steepened to an 8 MV, 7-ns pulse. Ultimately, the POS must steepen a voltage added 14-MV pulse to a 48-MV pulse. The pair of bi-conical switches for PBFA II is shown in Fig. 1. In addition to steepening the power pulse, the switches should also help to symmetrize the power flow in the azimuthal direction around the barrel diode. If the switch fails to give voltage multiplication and pulse shortening, the voltage will be too low to allow effective focusing of the lithium ions. A typical inertial confinement fusion (ICF) pellet implodes in 10 ns, so power and ions delivered after that time are wasted. So, instead of delivering 878 kJ in the 7-ns pulse, only 176 kJ would arrive from the

uncompressed pulse in the first 10 ns. Particles are deflected as they jet from the anode to the target. The lower voltage drop means slower ions that are more readily deflected by deficiencies in space and charge neutralization of the plasma surrounding the target. Protons can be used at the lower voltages, but their longer range spells a need for thicker walled targets, performing less ably with less than 200 kJ of deposition.

Figure 2 gives a schematic of the idealized switch used in ANTHEM and ISIS calculations. For PBFA II the inner (cathode) radius was set at 20 cm, and the outer (anode) radium was 28 cm. Initially, a current drive was assumed, supplied by the generator G to the left of the switch. At the right, the load L was first taken to be short circuit. More recently, resistive loads up to 28 Ω have been employed. At the start of a simulation run, plasma fills the test area between the electrodes for a distance along the cylindrical axis of 4 to 20 cm. It has been taken as uniform and typically given a drift velocity toward the cathode of 10 cm/μs. For early runs the electron density was taken as 10^{12} cm^{-3}. Later, 3×10^{13} cm^{-3} was employed. This is now believed to be the density present in experiments.
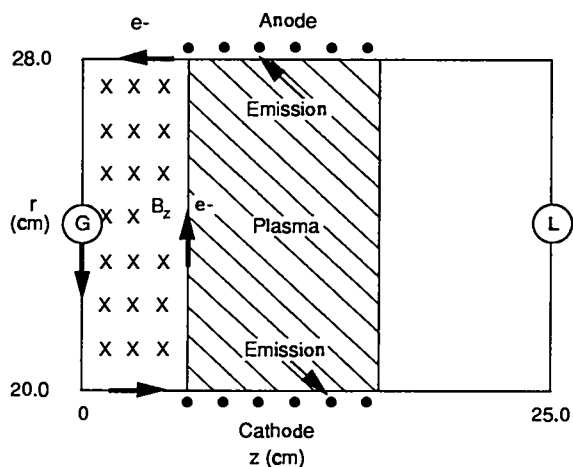

Fig. 2. Idealized POS used in simulation.

Much of the early theoretical work on the POS was done at the Naval Research Laboratories (NRL) in Washington, DC. NRL workers used the switch on their GAMBLE I and II accelerators. These were e-beam diode drivers that delivered approximately 1-MV, 50-ns pulses at 100 kA (GAMBLE I) and 300 kA (GAMBLE II), respectively. The NRL researchers had demonstrated that threefold voltage multiplication and 7-ns opening times after 40 ns of conduction through a POS. Experimentally, they had shown that these opening characteristics were possible with the switch attached to a 5-Ω load (Cooperstein and Ottinger 1987). The NRL machines used a cylindrical

switch of 2.5-cm inner (cathode) radius and 5-cm outer (anode) radius. The pulse power conditions for PBFA II are related to the NRL conditions but quite removed in scaling. At 3 MA the current level is at least 10 times greater than in the GAMBLE machines, as is the voltage pulse upon opening. The higher currents were thought to offer no problem because the radius of the inner conductor for PBFA II could be increased to maintain a similar value for the magnetic field intensity. Opening to such high voltages was a less easily resolved issue. In 1983 NRL workers were the first to use the POS to switch high power levels. Prior to this time it had only been employed as a prepulse suppressor. Weber et al. (1984) placed magnetic probes in the GAMBLE I plasma and charted the progress of the penetrating current sheet as it moved from the generator side to the load end of the plasma fill. The driver pulse rose to 100 kA over 50 ns. The probes indicated that the current sheet was broad, nearly 6 cm in width and propagating across 12 to 30 cm of fill plasma. There was no direct indication of gap formation (regions of lower plasma density) at either the cathode or the anode. The probe measurement was difficult and could not be duplicated on GAMBLE II because with its higher magnetic intensities the probes exploded. In any case, the results suggested that some anomalous mechanism was at work delivering the magnetic field to deep points in the plasma.

Classical collisions are too weak to explain the measurements. Anomalous resistivity from plasma instabilities could have been at work. With a judicious choice of anomalous collision rates, hybrid simulations by Hamasaki at JAYCOR and MHD calculations by Payne at MRC, Roderick at UNM, and Frese at Numerex have matched the experimental opening times for switches on both GAMBLE I and PBFA II and the GAMBLE field penetration history (Hamasaki et al. 1988). (An effective electron-ion scattering rate of $v_{eff} \cong 5\ \omega_{pi}$ was needed, where ω_{pi} is the ion plasma frequency). However, the 50-ns pulse rise time is possibly too short for the development of such mechanisms. Winske (1988) at Los Alamos has conducted a comprehensive analysis of the instabilities employed in the simulations – particularly the lower hybrid instability – and finds little likelihood that they are strong enough under switch conditions to provide the needed resistivity. Early theoretical ideas were at odds with the MHD-hybrid diffusing field picture. Cooperstein and Ottinger (1987) at NRL had concluded that electrons would be drawn from the cathode region, leaving an excess positively charged ions and creating a strong electric field to encourage acceleration of ions toward the cathode and their local depletion or "erosion" there. An erosion gap would open up along the cathode, and the driving magnetic field

would pass though this gap to the load region, opening the switch. The first particle simulations gave still another picture, in apparent variance with both the experimental indications of deep field penetration of the plasma and the theoretical predictions of erosion gap formation. For economy, these simulations were conducted for pulses rising to maxima in only 5 or 10 ns. A low ($\leq 4 \times 10^{12}$ electrons/cm^{-3}) density was assumed. The simulations of Waisman et al. (1985) for a 1-cm anode-cathode (A-K) gap showed flowing electrons in the plasma remaining close to the generator edge of the plasma but encountering magnetic insulation near the anode, which impeded their entry into this electrode. Electrons ran along the anode, entering it at a deep point in the plasma where the magnetic field was weak. Correspondingly, the field leaked through the switch plasma along the anode and accumulated in the load region to open the switch. According to this simulation, opening occurred via a penetration of magnetic field along the anode. The related MASK code PIC simulations of Grossman et al. (1986) for a 2.5-cm A-K gap showed the development of a thin diagonal current channel, with magnetic pressure (a magnetic piston) pushing plasma along the cathode toward the load. The thin current channel shifted right in the plasma and toward the load as the driving pulse continued to grow in amplitude. A diagonal gap was formed in behind the current sheet, and the magnetic field passed through this gap to the load, opening the switch. So the first PIC simulation predicted anode penetration of the drive field; the second predicted penetration through a diagonal plasma gap. Neither saw strong field diffusion or the development of a cathode erosion gap. This was the state of theoretical and experimental understanding, as the Los Alamos work began in 1986.

The first ANTHEM simulations were applied to model problems to check out the ability of the code's two- and three-fluid modes to replicate simple aspects of the POS physics. Field penetration through a switch for the NRL GAMBLE I machine was examined in the absence of wall emission (Mason et al. 1986; Mason et al. 1987). The first electron density explored was 4×10^{12} cm^{-3}. The driving field rose linearly to 8 kG (for 100 kA through a 2.5-cm inner conducting cathode radius) over 5 ns. A density gap quickly propagated along the cathode, allowing penetration of magnetic field from the drive side of the switch under the plasma along the cathode and out to the load region. Alternatively, when a 5-kG bias magnetic field was artificially imposed at the onset of the pulse, the emission was magnetically insulated. It remained trapped within 0.5 cm of the cathode. Multi-fluid calculations of the full GAMBLE I switch were then conducted for comparison with the PIC results from the MASK code. The fill electron

density was again taken as 4×10^{12} cm^{-3}, the upper limit for economy of the particle runs. Again, the magnetic field rose 1o 0.8 T over 5 ns. In the ANTHEM runs, the first fluid was the ions, and the second was the background electrons initially present in the fill plasma. The emission electrons constituted a third fluid. In each case the background plasma was pushed up toward the anode after a few nanoseconds, a diagonal gap appeared in the plasma, and emission electrons ran out below the gap toward the anode and load. At each time recorded, the two simulations - the PIC and multi-fluid results - were in general accord. Following these calibration runs, ANTHEM was applied to the PBFA II switch with a short circuit load for a fill density of 2×10^{13} cm^{-3}. The resolution was left at 50×50 cells, and a full calculation to switch opening was performed in about an hour of CRAY-XMP time. Much higher resolution would have been needed for explicit PIC modeling to avoid the finite grid instability, and more than 30 CRAY hours would have been demanded per run. This was the first POS collisionless simulation at a realistic density (Mason et al. 1987). It manifested several of the features seen in the earlier lower density runs. But significant modifications apparently followed from both the density rise and from the larger width (8 cm) of the PBFA II switch, compared to the GAMBLE I (2.5 cm) and Waisman (1 cm) switches.

At the anode there was, indeed, significant field penetration, but this was found to be coupled to large-scale ion motion away from the anode and toward the cathode, which opened an anode plasma gap to help let the field through. The body of the plasma in the center of the switch remained field free, shielded by diamagnetic currents running up the generator side of the fill. A second and larger plasma gap formed rapidly at the cathode. Opening of the switch was correlated principally with the propagation of this larger cathode gap to the load side of the fill plasma. The time spent creating the full cathode gap has been termed the "conduction phase" of POS operation by NRL workers. A rather high threshold (300 keV/cm) for electron emission had been imposed in this calculation. With it, the cathode gap reached the load side of the plasma in the first 20 ns of a 50-ns PBFA II drive pulse. Complete opening of the switch, such that the magnetic field at the load exceeded 85% of the drive field, then took another 8 ns. The voltage and current characteristics of this switch are summarized in Fig. 3.
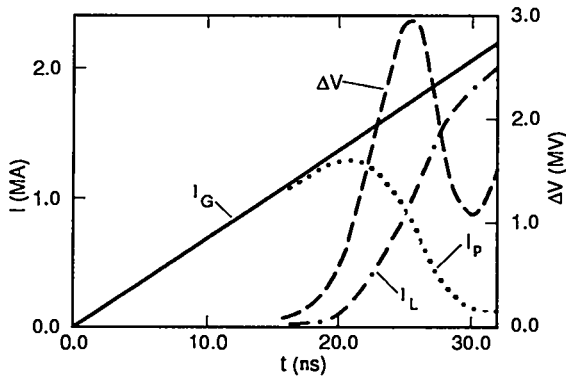
Fig. 3. Voltage and current characteristics of the PBFA II, 300- keV/cm emission threshold switch with a short circuit load.

Simulations were run over a range of densities from 10^{12} to the 2×10^{13} electrons/cm^3. It became clear that the diagonal current path seen at low densities gradually shifted down to run along the cathode as the density was increased. That is, "the erosion gap" of early theoretical discussions was a diagonal path at low densities and a true gap only for densities beyond $\sim 7 \times 10^{12}$ electrons/cm^3. Furthermore, the gap seemed to open largely by the removal of electrons from the cathode vicinity, as in a propagating wave along the cathode surface. The electron path was vertical (toward the anode) at the right of the gap, and then horizontal (parallel to the cathode) in the body of the plasma and over to its generator edge. After that, the electron path ran up the generator side of the plasma to the vicinity of the anode. Erosion of the ions (that is, their acceleration toward the cathode by electric fields) was active as an opening mechanism, but also active was a magnetic pressure effect from the v × B force pushing perpendicular to the electron path. In particular, this force acted like a piston driving the cathode gap toward the load. These results were for the 300 keV/cm emission threshold, and later it was determined that the results would change significantly for much lower thresholds. The Weber experiments (1984) had reported deep field penetration of the plasma. But the ANTHEM simulations at the high emission threshold had manifested good shielding of the collisionless plasma. The current sheet stayed on the generator side of the fill plasma during the opening process, and an island of field-free plasma remained even after full opening at 30 ns. This discrepancy was of considerable concern to the community of researchers studying the POS. Hamasaki et al. (1988) held the view that high levels of anomalous resistivity could be active to cause field diffusion (although Winske [1988] maintains that this is unlikely). Consequently, ANTHEM runs were made to examine the effects anomalous collisions might have on

switch opening. An anomalous collision rate derived for the lower hybrid instability was employed. That is, the electron velocity was relaxed to the ion velocity at the rate

$$v_{eff} = \min \; [(v_e/c_{i.a.}) \, \omega_{pi}, f\omega_p] \quad,$$

in which v_e is the electron drift speed, $c_{i.a.}$ is the local ion acoustic speed, and ω_{pi} and ω_p are the ion and electron plasma frequencies, respectively. The factor f was varied to set different limits on the maximal collisionality. The simulations showed that with f = 1 deep penetration of magnetic field could be achieved, and broad current sheets, $\sim$8 cm, consistent with the NRL experiments, would be set up. The problem with this was that theory limits f to about 0.05, and for this smaller f the results were essentially like the collisionless ones.

Some of the parameter settings for this first set of ANTHEM runs had been somewhat arbitrary, so in the next group of runs, these parameters were varied to examine the consequences (Mason et al. 1987; Mason et al. 1988a; Mason et al. 1988b). The anode had been run as a perfect conductor. That is, the electric field component parallel to it had been set to zero. Now the electric field gradient was set to zero at this boundary. This was done to mock up the large holes that can be present in the anode to allow for the injection of the fill plasma. The return path for electrons was assumed to close far above the test area. With this "open" boundary condition, the preferential penetration of magnetic field at the anode ceased. Collisionless opening followed entirely from the opening of the cathode gap.

The first simulations had used a 300 keV/cm emission threshold. This is appropriate for vacuum transmission lines. However, the fill plasma in the POS is available to ionize the outer layers of the cathode surface, converting them to a plasma with a very low emission threshold. With a zero electric field threshold, ANTHEM showed that during the conduction phase the emission electrons rose essentially vertically into the fill plasma. They no longer twisted back in a path toward the generator. A gap formed above the cathode, but it took considerably longer to open—35 instead of 20 ns—in PBFA II switches with comparable drive and injected plasma conditions. Development of the cathode gap (Mason et al. 1988b) was a most distinct opening feature. Magnetic pressure could only act at the right, load side of the gap. There, as a piston, it again helped to speed gap opening. However, in the absence of twist back for the electron path, no magnetic force was available to lift the plasma off the cathode, as in the high threshold case. Ions were seen to erode, accelerating electrostatically toward the cathode. Emitted electrons were clearly magnetically insulated late in the opening process, as the magnetic field

approached its peak value of 3 T. Then they deflected into the direction of the load upon emission eventually running up the load side of the fill plasma just prior to switch opening.

When the emission threshold was varied in a series of runs from zero to 300 keV/cm, or when the electron emission was "starved" by providing progressively smaller emission currents than those demanded to set the normal electric field to zero at the cathode (the Child-Langmuir condition), comparable results ensued. In each case the opening process switched from simple vertical emission of the electrons to the twist back of electrons toward the driver, with the accompanying development of a shielded plasma region free of penetrated magnetic field. A conclusion is that the intense stream of emission electrons in the low threshold cases, somehow carries magnetic field into the fill plasma, eliminating or minimizing the field-free region. The mechanism acting here has been identified as advective. Magnetic field is advected (equivalently—convected) into the plasma along with the stream of emission electrons. When the emission stream is stronger, as with lower electron thresholds, the advective effect is stronger. The field penetration is ascribed to advection, since at time scales much larger than a plasma period, the electron momentum equation reduces to $E \cong -v_e \times B/c$, from which Faraday's law yields

$$\partial B_\theta / \partial t = -\partial(v_{ez} B_\theta)\partial z - \partial(v_{er} B_\theta)\partial r \ ....$$

(The largest remaining terms represent a separation of the magnetic field lines from the electrons over several skin depths.) At large r this is analogous to the continuity equation for the advection of electron density. Thus, magnetic field B_θ is delivered by advection along the moving electron current channel, as it marches with the erosion gap along the cathode toward the load. In ANTHEM the magnetic advection terms were first modeled numerically by first order donor-cell differencing. This, in itself, resulted in some numerical smearing of the magnetic field. Recently, the advective differencing has been changed to an implicit second order scheme. Essentials of the field penetration process are unchanged with this improvement. The current sheet still rises vertically from the load end of a strong erosion gap. However, in the newer calculations some instability is noted along the current sheet as it rises in radius above the cathode. The new electron path from higher order differencing is more irregular, twisty, and convoluted (Mason 1989).

With these newer parameter settings ANTHEM was again used to examine the GAMBLE I field penetration experiment. It was determined that the choice of an open

anode boundary condition and a low emission threshold gave the most vertical current paths and magnetic field contours. With these choices, and assuming some anomalous collisionality, it was further sufficient to use f = 0.1 to yield broad current channels, in agreement with the Weber measurements. That is, field penetration, cathode gap formation, and switch opening time all follow from collisionless multi-fluid calculations. But, some low level of anomalous resistivity ($v_{eff} \cong 0.1 \ \omega_p$) is still needed to provide broad current channels (Mason 1987b; Mason et al. 1987).

From the outset, there was concern that the suppression electron gyro effects by ANTHEM's multifluid mode could be misleading. Individual particles, executing finite gyro orbits in a PIC model of the electron motion, could result in broader current sheets on the average. The electron particle routines in ANTHEM still need some developmental work. So, as an interim measure the full-particle ISIS code was used for a quick comparison of PIC and multifluid results (Mason and Jones 1987a). Indeed, the current sheets are much broader, matching the data. This is not the final word on this issue. However, since for the ISIS implicit algorithm to run with stability, the particle current accumulations must be smoothed repeatedly, each cycle, before their use as sources to Maxwell's equations. This smoothing could be the direct cause of the calculated broader channels. Planned application of the ANTHEM particle electron mode, may help to resolve this question at a future date. Particle ion, fluid electron runs have been completed with ANTHEM. General characteristics, gap formation, current channel width, B_θ field evolution are all quite similar to the corresponding results with fluid ions (Mason 1988; Mason and Jones 1988); that is, the current sheet remains thin.

In the spring of 1988, Sandia Laboratories conducted POS experiments on the BLACK-JACK 5 accelerator at Maxwell Laboratories, and in the Fall PBFA I was used for switch studies (Rochau 1989). Shots were made with short circuit loads and diode loads. Magnetic probes were placed at upstream (for power flow) and downstream of the switch. Much useful data was recorded. Unfortunately, the magnetic probes were not placed within the plasma or along the walls in such a way as to extract a field penetration history for the PBFA II plasma. So, important data to help calibrate the various models in the PBFA I environment is still lacking. Acquisition of this data is a high priority item, however. It should be forthcoming shortly. Typical results showed optimized switches on PBFA II with 4 cm of fill plasma conducting for 35 ns and opening in 7 ns, much as in the ANTHEM simulations. For these, the load was a short circuit. There were strong indications of ejected ions

downstream of the switch. ANTHEM indicates that the ions are generated by the j × B forces associated with the late time current sheet on the back side of the fill plasma. It predicts a low density $\sim 10^{12}$ cm^{-3} for these ions. No dependence on the anode structure was noted, in disagreement with ANTHEM predictions. However, a set of anode probes to search for preferred field penetration near the anode were lacking. The experiments found the best opening times on PBFA II occurred when the injected plasma flow was segmented. That is, the plasma was delivered in three distinct spokes, rather than uniformly. Strictly, this is a three dimensional problem. The azimuthal symmetry needed for 2D modeling has been removed. However, a 3D mockup run was made on ANTHEM by driving the fill plasma from the generator as usual, but also with an opposing magnetic field from the load side. The reverse field was to correspond to that locally present at the back a conducting segment of fill plasma. The reverse field was arbitrarily set at 50% of the generator magnitude. Its effect was to cancel penetration proceeding at the anode, reduce the ejection of ions on the back side of the fill plasma, and shorten the actual opening time, much as seen in experiment (Mason 1989).

Experimental difficulties were encountered when efforts were made to open the PBFA II switch into the 7-Ω load characteristic of the full systems barrel diode. ANTHEM simulations have been made with such a load. They show opening beginning after 35 ns (Figs. 4a and 4b). With a short circuit load the arrival of the current sheet on the back side of the fill plasma is nearly coincidental with POS opening. But the presence of a load with as little as 1-Ω resistance results in slower opening through the slow development of magnetic insulation of the emitted electron stream. For a time this stream passes along the anode and out through the anode region. Then later it bends in an arc back toward the cathode (Mason 1989; Mason 1988; Mason and Jones 1988). Magnetic insulation traps the electrons so they will be forced through the load for opening of the switch. An important conclusion from the ANTHEM loaded switch runs is that there is no need to push back the fill plasma, to provide space for magnetic insulation of the emission electrons. They are deflected upon emission and propelled into the free space between the plasma and the load. Thus, the magnetic insulation can proceed in this free space. The results with ANTHEM are interesting and at least qualitatively correct at the initiation of opening. However, the code is presently driven by a current boundary condition at the generator. It must be modified to allow for the induction of the drive circuitry and voltage drive. Then the relaxation of the drive current as the load voltage rises will be properly considered. At considerable expense Steen

and Wilson (1989) at Maxwell Laboratories have recently examined the voltage driven loaded switch with explicit PIC simulation. They predict rapid oscillations in the output pulse characteristics, as magnetic insulation of the current channel is periodically initiated and lost, interrupting the opening process. The addition of voltage drive circuitry will allow for an independent analysis of this conclusion, as well as opening the way to economical parameter studies of the loaded POS and its possible design variations.

For the success of PBFA II the POS must open into the barrel diode load, to set up the 28-MV diode voltage drop needed to focus the lithium ions. Researchers at Sandia are concerned that their original bi-conical POS will fail in this objective. Simple variations of the switch have been considered, such as the conversion from a bi-conic to a bi-cylindrical (coaxial) design, and the use of a smaller inner radius (Ottinger 1989) to raise the maximum magnetic field in the switch to 6 T. NRL has suggested 10 cm. The large field would strengthen the magnetic insulation, and Maxwell suggests that the larger POS impedance should aid opening into the fixed load. A reversal of polarity (making the outer electrode the cathode emitter) might also help, by allowing the large field near the inner anode to enhance the magnetic insulation. However, even these simple changes would require costly hardware, so there is no present plan for their implementation. With the addition of circuitry for voltage drive, ANTHEM will have the power to perform parameter studies to evaluate the benefits from such simple modifications. From such studies the potential savings in time and expense by the experimentalists could be great.

Instead of simple POS modifications, Sandia Laboratories has decided to make a very new switch their "baseline." This new POS has two creative elements (Mendel and Rochau 1989). The first is a magnetically injected plasma source, producing a magnetic injection plasma switch, a MIPS switch. The second is a "toggle" addition, by which an external field is triggered to help push back the fill plasma. Since November of 1988 the MIPS-toggle has been Sandia's new mainline approach. For the MIP source, an additional arc of B_r and B_2 magnetic field lines enters and leaves the switch through its inner (cathode) radius. Experiments of PBFA II have indicated that switch opening is faster and more reliable with a MIPS. Performance with the MIPS is as good as that obtained via segmentation of the injected plasma in the original POS. Experimentalists at Maxwell Labs have found no similar need for segmentation in POS studies on their ACE accelerator (Rix 1989). This probably derives from their use of a smaller inner radius, and correspondingly greater smoothing of the injected plasma reaching it. Such benefits could derive from the use of the smaller inner radius POS on
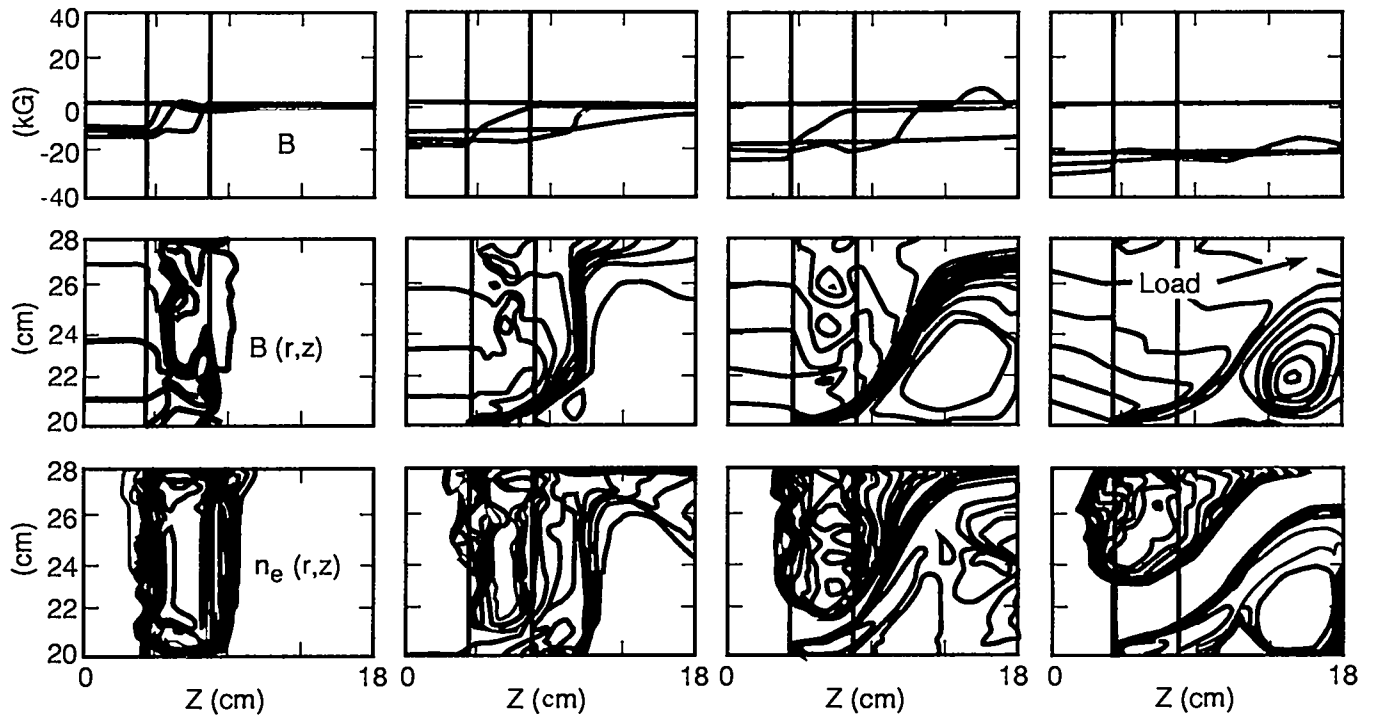
Fig. 4a. Late time magnetic field and plasma density contours showing magnetic insulation of the electrons, as the switch opens into a 7-Ω load. Top: B-field cuts at r = total electron density contours. Electrons are magnetically confined near the cathode at r = 20 cm.
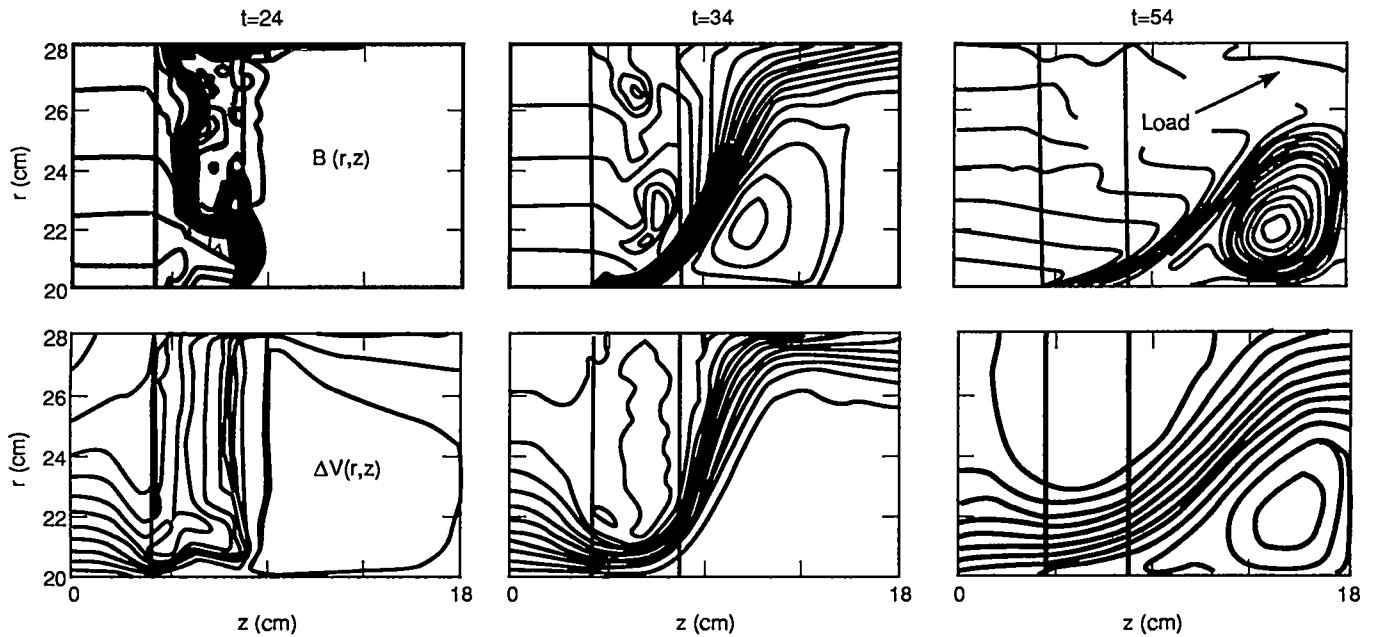

Fig. 4b. Contours of the evolving voltage in the -Ω switch. Top: penetrating B-field. Bottom: Voltage $\Delta V = - \int E(r,z)dr$.

PBFA II, as well. But MIPS-toggle is now the chosen PBFA II approach. Thus far, use of the toggle feature has shown no improvements in opening time.

Application of ANTHEM should be made to study the physics of POS opening into realistic loads. Parameter studies are needed to determine predicted conduction and opening times as functions of the load impedance, load structure, drive impedance, and plasma density and injection velocity. Switches with smaller inner diameters and altered polarity should be simulated. Dependence of the loaded opening characteristics on assumed levels of anomalous resistivity should be explored. Computational tests should be made of the long time dependence of results on zoning. In particular, higher resolution studies should be made of the switch opening characteristics in cathode (erosion) and anode (magnetic insulation) gaps. Reliable full-particle runs are needed to isolate effects arising from finite electron gyro orbits and ion multi-streaming (as in collisionless shocks). Further studies might still be made with finer resolution in search for anomalous resistivity mechanisms. Comprehensive efforts in these areas will help develop a sound scientific base for new practical switch developments.

The more complicated MIPS and toggle switches have become the mainline approach at Sandia. So, additional code development is urgently needed to allow for fundamental studies of magnetic injection along present external magnetic fields (MIPS) and to acquire knowledge of how the external toggle magnetic field can be used to enhance magnetic insulation, as this insulation competes with large voltages set up by a load. An understanding of the new options must be developed and knowledge of the simpler fundamental problems is deepened.

For broader application, studies must be made of both the old and new switch designs, operating in a long time scale ≥ 1 μs mode. Finally, for a generalized understanding of the emerging switch technology, extended concepts, such as staging (mounting a series of switches in parallel) and the use of plasma filled diode switch elements should be explored.

The Light Ion Source

Suppose that sufficient power does, indeed, arrive at the diode. Then how does one produce enough focusable lithium ions? The anode of the barrel diode is made of stainless steel. How does this become a Li^+ source? A favored approach is BOLVAPS-LIBORS, which stands for the boil-off of lithium vapor and its subsequent ionization by the absorption of laser light. This is described schematically in Fig. 5. Sandia is devoting several man-years to the investigation of this approach. By it, electrodes are used to

melt lithium metal. The liquid is then exposed to an ionizing laser beam. This creates a plasma composed primarily of Li^+ ions. Analytic estimates place its density at 10^{17} electrons/cm^3.
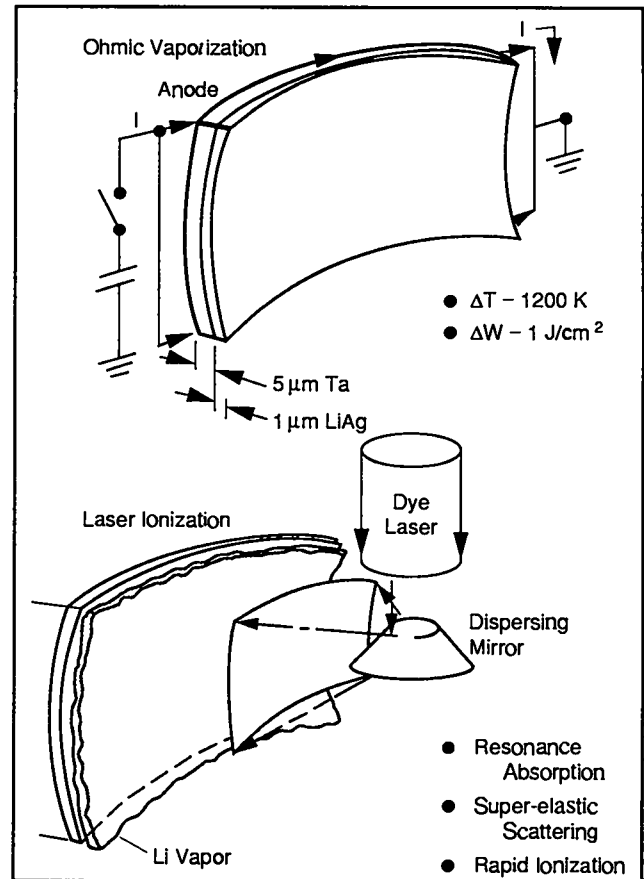

Fig. 5. Sketch of BOLVAPS-LIBORS lithium ion production.

Assuming this plasma can be created, the next questions arising are: can it remain pure and can it be focused on the target? ANTHEM was applied to the second of these questions. The ions coming from a solid metal surface will be launched, obeying the original curvature of the surface. But the focusing of ions pulled from a plasma may well suffer from dynamic nonuniformities in the plasma. Very preliminary calculation with ANTHEM gave only a hint of this possibility (Mason and Jones 1987b). The problem was investigated in cartesian geometry. Lithium plasma was set up in a block decaying exponentially in the y coordinate, but being uniform in the x direction over some 5 cm contiguous with the barrel diode anode. The initial density decayed by 7 orders of magnitude over a distance of 2 cm from the anode (see Fig. 6a). A B_2 magnetic field was supplied from the left, rising in a 7-ns pulse to 7 T. The drive pulse was then constant for 7 ns, followed by a 7-ns drop-off period to zero
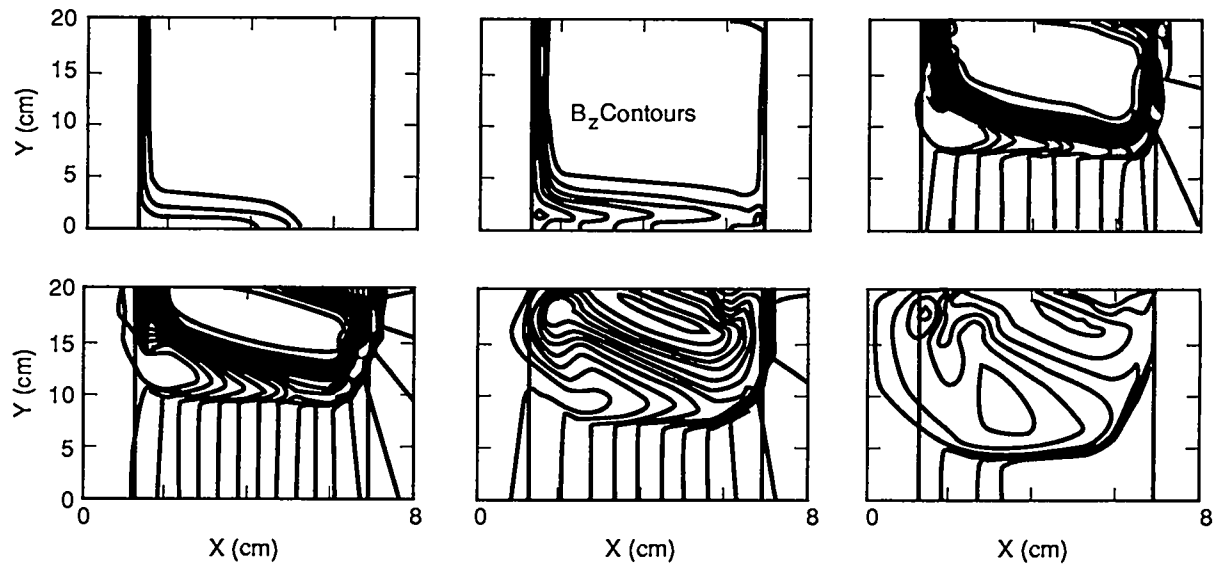
Fig. 6a. Magnetic field penetration history near the BOLVAPS-LIBORS plasma. From the left, the B-field sweeps under the exponentially decaying lithium plasma.
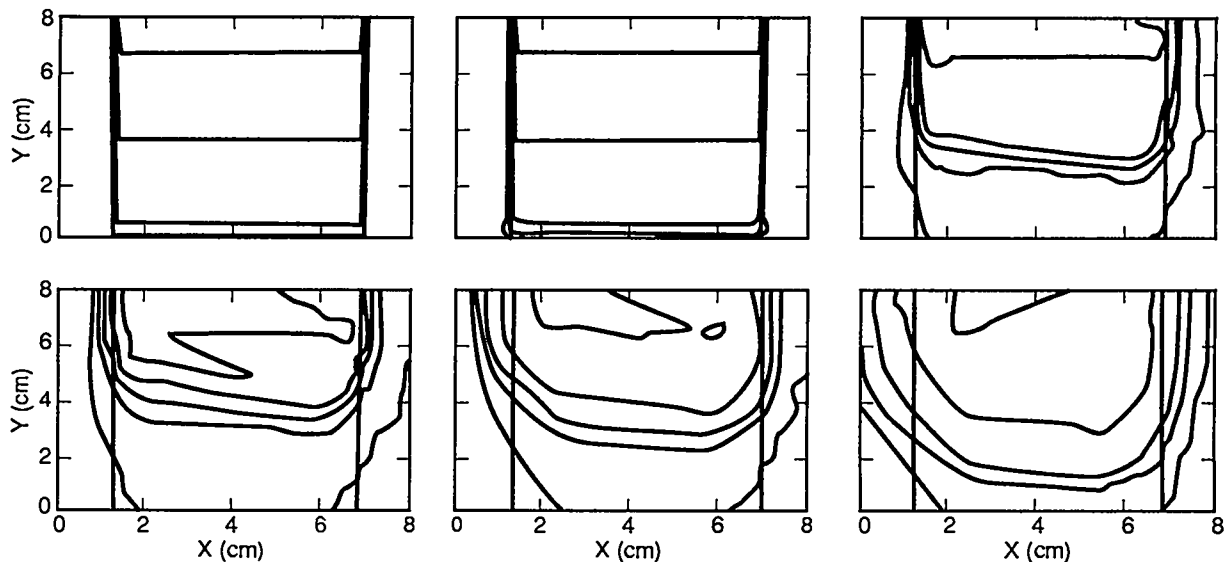

Fig. 6b. Contours of the evolving ion density from the BOLVAPS-LIBORS source.

intensity. The magnetic field swept through the lowest density plasma regions, pushing the electrons up into the high density plasma, and initiating the extraction of ions. A mirror boundary condition was imposed to the right of the problem, simulating the symmetric delivery of power. The main new result was that ions from the portion of plasma closest to the driver were accelerated first. Density dropped more quickly at the edge of the original plasma block. The resultant ion source was more isotropic than beam-like (see

Fig. 6b). It was clear that when the pulsed power arrives at the BOLVAPS-LIBORS plasma on the same time scale as the ion beam production, the two processes will interact. The interaction can lead to defocusing. An integrated simulation of pulsed power arrival and beam evolution may, indeed, be crucial to the design of an adequate lithium source.

However, ANTHEM had several deficiencies which may have biased the detailed outcome from simulation. Its load physics was incomplete at the time when these simulations

were run. So, a large voltage drop was never established. This would have aided focusing. No B_x and B_y field components were present, as they would be in the true barrel diode. These would have stiffened the plasma, also aiding focusing. Therefore, only the possibility of a problem can be registered. Additional and improved simulation runs, or experiment will be needed to determine the true extent of pulsed power transients on beam quality.

Conclusion

Los Alamos has provided substantial theoretical and computational support to the light ion fusion program at Sandia Laboratories. The joint interaction has been most productive. Much has been learned, particularly in the area of switch modeling . New switch configurations are under investigation, as well as the coupling to loads and extension of the plasma opening switch to long time scale switching. Challenging issues remain in the study of lithium ion sourcing, beam target interactions, and beam propagation.

REFERENCES

Brackbill, J. U., and D. W. Forslund, "An Implicit Method for Electromagnetic Plasma Simulation in Two Dimensions," J. Comput. Phys. 46, 271, 1982.

Cooperstein, G., and P. R. Ottinger, "Guest Editorial: Fast Opening Vacuum Switches for High-Power Inductive Energy Storage," IEEE Trans. Plasma Sci. PS-15, 629, 1987.

Grossmann, J. M., P. F. Ottinger, J. M. Neri, and A. T. Drobot, "Numerical Simulation of a Low-Density Plasma Erosion Opening Switch," Phys. Fluids 29, 2724, 1986.

Hamasaki, S., N. Krall, S. Payne, N. Roderick, and M. Frese, Respective Presentations, Plasma Opening Switch Workshop, Sandia National Laboratories, Albuquerque, NM, April 7-8, 1988 (unpublished).

Jones, M. E., and G. R. Gisler, "An Implicit Particle-in-Cell Algorithm for Intense Relativistic Beam Simulations," LA-UR-85-118, Los Alamos National Laboratory, Los Alamos, NM, 1985. (Also 11th International Conference on the Numerical Simulation of Plasmas, Montreal, Canada, July 25-27, 1985.)

Mason, R. J., Comments, Plasma Opening Switch Workshop, Sandia National Laboratories Albuquerque, NM, January 3-4, 1989 (unpublished).

Mason, R. J., "Dynamics of Opening Switch Plasmas," Bull. Am. Phys. Soc. 33, 2041, 1988.

Mason, R. J., "An Electromagnetic Field Algorithm for 2D Implicit Plasma Simulation," J. Comput. Phys. 71, 429, 1987a.

Mason, R. J., "Simulated Dynamics of Plasma Opening Switches," Talk 3C9-10, Procs. 1987 International Conference of Plasma Science, Arlington, VA, June 1-3, 1987b.

Mason, R. J., "Implicit Moment Particle Simulation of Plasmas," J. Comput. Phys. 41, 233, 1981.

Mason, R. J., and M. E. Jones, "Numerical Simulation of Plasma Opening Switches," LA-UR-88-4102, Los Alamos National Laboratory, Los Alamos, NM, 1988. (Also Proc. Opening Switch Workshop, Novosibirsk, USSR, July 1-2, 1989.)

Mason, R. J., and M. E. Jones, "Simulation of Plasma Opening Switches," LA-UR-87-4620, Los Alamos National Laboratory, Los Alamos, NM, 1987a . [Also Proc. 7th International Conference on High Power Particle Beams, Karlsruhe, FRG, July 4-8, 1988 (unpublished).]

Mason, R. J., and M. E. Jones, "Simulation of Lithium Ion Emission Hydrodynamic from a BOLVSPS-LIBORS System on PBFA II," Bull. Am. Phys. Soc, 32, 1878, 1987b.

Mason, R. J., M. E. Jones, J. M. Grossmann, and P. F. Ottinger, "Three-Fluid Simulation of the Plasma-Erosion-Opening Switch," J. Appl. Phys. 64, 4208, 1988a.

Mason, R. J., M. E. Jones, J. M. Grossmann, and P. F. Ottinger, "Magnetic Field Penetration of Erosion Switch Plasmas," Phys. Rev. Lett. 61, 1835, 1988b.

Mason, R. J., J. M. Wallace, J. Grossmann, and P. Ottinger, "Implicit Collisional Three-Fluid Simulation of the Plasma Erosion Opening Switch," IEEE Trans. Plasma Sci. PS-15, 715, 1987.

Mason, R. J., J. M. Wallace, and K. Lee, "Implicit Two-Fluid Simulation of Electron Transport in a Plasma Erosion Switch," Proc. 6th International Topical Conference on High Power Electron and Ion-Beam Research and Technology, Kobe, Japan, June 9-12, 1986. [Also Proc. 2nd International Topical Symposium on ICF Research by High Power Particle Beams, Nagoaka, Japan, June 16-18, 1986 (unpublished).]

Mendel, C., and G. Rochau, Comments, Plasma Opening Switch Workshop, Sandia National Laboratories, Albuquerque, NM, January 3-4, 1989 (unpublished).

Ottinger, P., Comments, Plasma Opening Switch Workshop, Sandia National Laboratories, Albuquerque, NM, January 3-4, 1989 (unpublished).

Rix, W., Comments, Plasma Opening Switch Workshop, Sandia National Laboratories, Albuquerque, NM, January 3-4, 1989 (unpublished).

Rochau, G., Comments, Plasma Opening Switch Workshop, Sandia National Laboratories, Albuquerque, NM, January 3-4, 1989 (unpublished).

Steen, P. and A. Wilson, Comments, Plasma Opening Switch Workshop, Sandia National Laboratories, Albuquerque, NM, January 3-4, 1989 (unpublished).

Waisman, E. M., P. G. Steen, D. E. Parks, and A. Wilson, "Switching of Low Density Diode Plasmas," Appl. Phys. Lett 46, 1045, 1985.

Weber, B. V., R. J. Commisso, R. A. Meger, J. M. Neri, W. F. Oliphant, and P. F. Ottinger, "Current Distribution in a Plasma Erosion Opening Switch," Appl. Phys. Lett. 45, 1043, 1984.

Winske, D., "Some Comments on Microinstabilities in Plasma Erosion Opening Switches," LA-UR-88-1038, Los Alamos National Laboratory, Los Alamos, NM, 1988. [Also Plasma Opening Switch Workshop, Sandia National Laboratories, Albuquerque, NM, April 7-8, 1988 (unpublished).]

IX. Selected Reprints of Research Supported by ICF

- ICF Program Overview
- Materials Technology
- Experimental Plasma Physics
- Theoretical Plasma Physics and Hydrodynamics
- ICF Systems Studies

LOS ALAMOS * NATIONAL LABORATORY PROGRESS AND PATH TO INERTIAL CONFINEMENT FUSION COMMERCIALIZATION **

David B. HARRIS and Donald J. DUDZIAK

University of California, Los Alamos National Laboratory, PO Box 1663, MS·F611, Los Alamos, New Mexico 87545, USA

KrF lasers appear to be an attractive driver for inertial confinement fusion commercial applications such as electric power production. Los Alamos National Laboratory is working to develop the technology required to demonstrate that KrF lasers can satisfy all of the driver requirements. The latest experimental and theoretical results indicate that cost currently appears to be the main issue for KrF lasers. The Los Alamos program is working to reduce the cost of KrF laser systems by developing damage-resistant optical coatings, low-cost optical blanks, high-intrinsic-efficiency gas mixtures, low-cost and high-efficiency pulsed power, and optimized system architectures. Other potential issues may cause problems after the 5 kJ Aurora KrF laser system becomes operational, such as amplified spontaneous emission, cross talk, or temporal pulse distortion. Design solutions to issues such as these have been identified and will be experimentally demonstrated on Aurora. Issues specific to commercial-applications drivers, such as cost, gas flow, repetitively pulsed power, and high reliability cannot be experimentally addressed at this time. Projections will be made on the ability of KrF lasers to satisfy these requirements. The path to commercialization of inertial fusion for KrF lasers is also described.

1. Introduction

In a recent study, KrF lasers were shown to be the most attractive laser driver for inertial confinement fusion (ICF) commercial applications [1]. The study evaluated six different laser candidates with respect to their perceived ability to satisfy eight different requirements for commercial applications. The eight requirements were efficiency, cost, target coupling, pulse shaping, focussing, repetition rate, energy scaling, and reliability and robustness. The study identified the outstanding issues and unknown quantities for KrF lasers. For example, is the cost of a 5 MJ, 5 Hz, 8%-efficient KrF laser affordable, and can the system be made reliable enough for commercial applications? The thrust of the Los Alamos National Laboratory ICF program is to address these issues for KrF lasers.

This paper is organized as follows. Section 2 examines the reasons why KrF lasers appear attractive for ICF commercial applications. Next, the Los Alamos program is discussed. Aurora, 5 kJ, 5 ns KrF laser currently under construction, is described in Section 3. Section 4 describes the technology development program at Low Alamos and Section 5 describes the commercial applications development plan as currently envisioned.

2. KrF lasers as commercial ICF drivers

To be considered as a candidate for an ICF commercial-applications driver, a laser must simultaneously satisfy eight major requirements.

(1) The laser must have an efficiency high enough such that the product of the driver efficiency and the target gain is greater than eight [2]. This means that the driver power recirculation fraction is acceptably small.

(2) The driver must have a low cost so as not to add significantly to the cost of electricity. The acceptable value of the cost depends on the driver efficiency and target gain, but typically needs to be less than about $300/J [3].

(3) The driver must efficiently couple to the target. For example, because of its poor coupling, the CO_2 laser has been found to be unsatisfactory for commercial applications.

ICF RESEARCH AT LOS ALAMOS

P. D. Goldstone, J. R. Ackerhalt, L. S. Blair, D. C. Cartwright, L. R. Foreman, C. A. Fenstermacher, A. Hauer, D. E. Hanson, J. K. Hoffer, R. Kristal, W. C. Mead, L. A. Rosocha, and D. C. Wilson

Los Alamos National Laboratory
Los Alamos, NM 87545

ABSTRACT

It is apparent that short wavelength lasers (< 500 nm) provide efficient coupling of laser energy into ICF target compression. KrF lasers (248 nm) operate at a near-optimum wavelength and provide other potential benefits to ICF target coupling (e.g., bandwidth) and applications (high wallplug efficiency and relatively low cost). However, no driver technology has yet been shown to meet all of the requirements for a high-gain ICF capability at a currently acceptable cost, and there are still significant uncertainties in the driver-target coupling and capsule hydrodynamics that must be addressed. The Los Alamos research program is designed to assess the potential of KrF lasers for ICF and to determine the feasibility of achieving high gain in the laboratory with a KrF laser driver. Major efforts in KrF laser development and technology, target fabrication and materials development, and laser-matter interaction and hydrodynamics research are discussed.

INTRODUCTION

It has become increasingly apparent that short wavelength lasers (< 500 nm) provide efficient coupling of laser energy into ICF target compression. However, no lasers or particle beam driver technology has yet been shown to meet all of the requirements for a high-gain ICF capability at a currently acceptable cost (– $1B). Furthermore, there are still significant uncertainties in the driver-target coupling and the effect of hydrodynamic instabilities on the implosion and burn performance of ICF capsules which must be addressed. Therefore, the goals of the Los Alamos ICF research program are:

(1) Develop driver technology to provide a cost-effective path toward a high-gain experimental capability and longer-term energy applications

(2) Address critical issues in driver-matter interaction physics and the physics and hydrodynamics of ICF capsule implosion and burn, to define the requirements for achieving high gain and reduce the risk and cost of a laboratory microfusion facility

AURORA STATUS AND PLANS

R. Kristal, L. S. Blair, M. D. Burrows, D. C. Cartwright,
P. D. Goldstone, D. P. Greene, J. A. Hanlon, A. Hauer,
M. Kang, B. L. Kortegaard, J. McLeod, W. C. Mead,
E. A. Rose, and L. A. Rosocha

Los Alamos National Laboratory
Los Alamos, NM

ABSTRACT

Aurora is a short wavelength (248 nm) 10 kJ KrF laser system in the ICF program at Los Alamos National Laboratory. It is both an experiment in driver technology and a means for studying target performance using KrF laser light. Both features will be used to help evaluate the uv excimer laser as a viable fusion driver.

The system has been designed to employ several electron-beam pumped amplifiers in series, with a final aperture of one meter square, to amplify 96 angularly multiplexed 5 ns beamlets to the 10 kJ level. In Phase I, 48 of these beamlets are brought to target by demultiplexing and focusing with f/26 optics. The beamlet ensemble, contained within an f/1.8 bundle, is focused as a single beam; however, pointing is done individually. Spot size in the target plane is variable from 0.1-4 mm, with maximum averaged intensity of $- 4 \times 10^{15}$ W/cm^2.

The illumination geometry is designed specifically for several classes of important target physics experiments. These include: (1) energy flow, symmetry and preheat studies related to indirectly driven targets; (2) x-ray conversion and plasma coupling characterization on disc targets, and (3) hydrodynamic instability studies in planar geometry.

System integration is proceeding toward initial target experiments in late 1988. Ninety-six beam amplification through the penultimate amplifier has been obtained at the sub-kJ level. Installation of beam train optics is proceeding, and the target system vacuum envelope is in place.

INTRODUCTION

Aurora is an ultraviolet laser fusion system under construction at Los Alamos National Laboratory.[1] It utilizes electron beam pumped krypton fluoride excimer laser technology and operates at a wavelength of 248 nm. The excimer lifetime is much shorter than the electrical pump time, preventing significant energy storage in the gain medium. Consequently, optical angular multiplexing is employed to effectively compress the relatively long (- 500 ns) laser gain pulse to a short (- 5 ns) light pulse required for fusion applications. The system is designed to ultimately produce 10 kJ in two sided illumination on target.

PLASMA PHYSICS
AND CONTROLLED
NUCLEAR FUSION RESEARCH
1986

PROCEEDINGS OF THE
ELEVENTH INTERNATIONAL CONFERENCE ON PLASMA PHYSICS
AND CONTROLLED NUCLEAR FUSION RESEARCH
HELD BY THE
INTERNATIONAL ATOMIC ENERGY AGENCY
IN KYOTO, 13-20 NOVEMBER 1986

In three volumes

VOLUME 3

INTERNATIONAL ATOMIC ENERGY AGENCY
VIENNA, 1987

IAEA-CN-47/B-II-2

INERTIAL CONFINEMENT FUSION PROGRAM
AT LOS ALAMOS NATIONAL LABORATORY

D.C. CARTWRIGHT, P.D. GOLDSTONE, J.A. HANLON,
A. HAUER, R. MAH, J. McLEOD, W.C. MEAD,
L.A. ROSOCHA, D.C. WILSON, C.A. WINGATE
Los Alamos National Laboratory,
Los Alamos, New Mexico,
United States of America

Abstract

INERTIAL CONFINEMENT FUSION PROGRAM AT LOS ALAMOS NATIONAL
LABORATORY.
   Los Alamos National Laboratory has completed a thorough evaluation of the CO_2 laser as a
driver for inertial confinement fusion (ICF) and concludes that in the case of a large driver the cost of
this laser is too high to be attractive. Recent studies, at Los Alamos and elsewhere, show that 0.25 μm
is near the optimum coupling wavelength, and Los Alamos is involved in experimental and theoretical
studies of laser-matter interaction near that wavelength. Since KrF lases at 0.25 μm and has the
potential for 10% wall plug efficiency and relatively low capital cost, Los Alamos investigates the
feasibility of the KrF laser as a future ICF driver.

SOLID FUEL TARGETS
FOR THE ICF REACTOR

L.R. FOREMAN, J.K. HOFFER (Los Alamos
National Laboratory, Los Alamos, New Mexico,
United States of America)

ABSTRACT. The discovery that radioactively induced
sublimation can drive a layer of frozen tritium to uniform thick-
ness strongly influences the fabrication of targets for inertial
confinement fusion (ICF) power reactors. Targets utilizing
solid fuel layers, made uniform by this process and incorporating
either a foam layer or a vapour barrier, offer clear fabrication
advantages over previous, similar designs incorporating liquid
fuel.

The recent verification [1] that the heat generated
by the radioactive beta decay of tritium will drive
frozen layers of tritium to uniformity will profoundly
influence the design of fusion targets for laser fusion
power reactors. The final uniformity of the tritium
layer is not yet known to the precision required by
implosion physics. Much remains to be done to
characterize the composition and density variations as
well. However, the implication is that a frozen lump
of tritium fuel will redistribute itself uniformly over
the interior of its spherical enclosure within hours.

In solid tritium, nearly all of the beta particle energy
is deposited within 20 μm of the emitting atom [2].
For layers thicker than 40 μm, 0.977 W per mole of
tritium is deposited in the frozen tritium itself [2].
Thus, a frozen lump of tritium self-heats and its tem-
perature elevates. This self-heating drives mass
redistribution in a target interior according to a model
by Martin et al. [3]. Simply, the tritium or a 50/50
deuterium/tritium mixture (D-T) sublimes from the
thicker, warmer layers and refreezes on colder, thinner
layers. The process is predicted to take place with a
time constant given by

$$\tau = H_s/\dot{q}$$

where H_s is the enthalpy of sublimation and $\dot{q}$ is the
heat generated by the beta decay per unit volume [1,3].
For T_2, the predicted time constant is $\tau = 14.4$ min at
19.6 K and it would be about 1.85 times as long for
D-T. Work by Hoffer and Foreman [1] demonstrated
that the process does indeed take place and at rates
that are not inconsistent with the model [3]. Cryogenic,
high gain targets for ICF power reactors based on this
concept would offer substantial fabrication advantages.

Some previous cryogenic designs [4] of capsules for
laser fusion power generation rely on spherical foam
shells wetted and soaked with liquid D-T. The foam
provides a matrix that prevents the liquid fuel from
slumping due to gravity or acceleration to high velocity

Radioactively Induced Sublimation in Solid Tritium

James K. Hoffer and Larry R. Foreman

Los Alamos National Laboratory, Los Alamos, New Mexico 87545

(Received 14 December 1987)

A horizontal cylindrical cavity bounded by isothermal walls was partially filled with liquid tritium which was then frozen by reduction of the temperature to 1.0 K below the triple point. Visual observations revealed that the solid subsequently redistributed itself into a layer of uniform thickness covering the complete interior of the cavity. The time constant for this effect depends on the age (or ^{3}He content) of the tritium and not on the initial filling fraction. Time constants of 14.9, 92, 219, and 234 min were measured for tritium 0.04, 7, 16, and 17 days old, respectively.

Radioactive isotopes are classic examples of materials which exhibit internal self-heating. Tritium decays to ^{3}He, emitting a β particle and an antineutrino. Because the β's are reabsorbed within approximately 10 μm, condensed tritium samples have a nearly uniform self-heating rate $\dot{q}$ and a quadratically increasing temperature profile in the direction away from the containing boundary. The interior surface of a thick layer of tritium can thus be warmer than the interior surface of a nearby, thinner layer, as long as the exterior surfaces of these layers are equal in temperature or are radiating with equal emissivities to an infinite thermal sink. Being warmer, the interior surface of the thicker layer has a higher vapor pressure than the interior of the thinner layer, and a preferential sublimation-condensation effect can occur, tending to make the layers uniform in thickness. This effect, dubbed the "β heating effect," was first proposed by Martin, Simms, and Musinski[1] as a method of preparing the "ideal" inertial-confinement fusion target, namely a uniform spherical shell of DT.

Martin and Simms[2] have constructed a one-dimensional model of the β heating effect which predicts that layer-thickness equilibration proceeds exponentially in time with a minimum time constant $\tau_{min} \equiv H_s/\dot{q}$, where H_s is the heat of sublimation of the solid. For pure T_2 at 19.6 K, $\tau_{min} \approx 14.4$ min, representing the rate constant for the hypothetical case where there is no impedance to the flow of vapor in the cavity. Without repeating the arguments used in Ref. 2, we can easily derive the above expression for one-dimensional slabs of material bounded by semi-infinite isothermal plane surfaces. Imagine a layer of radioactively heated solid completely filling a finite space between two such semi-infinite surfaces, both at the same temperature. At steady-state conditions, the solid will have a parabolic temperature profile with a maximum at the exact center. Take a thin sliver of the solid starting at a distance δ from the center and expand it many times its original width, turning the solid into vapor and simultaneously creating a space between two layers of solid of unequal thickness, as shown in Fig. 1. We now assume that the impedance to the flow of vapor

is so small that the process of sublimation and condensation can transport heat just as effectively as did the original solid sliver. In other words, the temperature drop across the vapor space is identical to the drop which was present in the original solid sliver. The temperature profile in each of the two opposing solid layers now will be identical to the original parabolic profile which existed in these sections before the split occurred. The heat flux transported in the vapor phase by the sublimation-condensation process is equal to $\rho H_s \dot{\delta}$, where ρ is the molar density and δ is the time rate of change of the "excess thickness" δ. We assume that the temperatures are at quasi steady state, i.e., all the heat generated internally is eventually deposited to the isothermal boundaries. Referring to Fig. 1, we note that no heat can flow past the point of the temperature maximum in the thicker layer, and therefore the heat being generated to the right of this maximum (in a solid layer of thickness
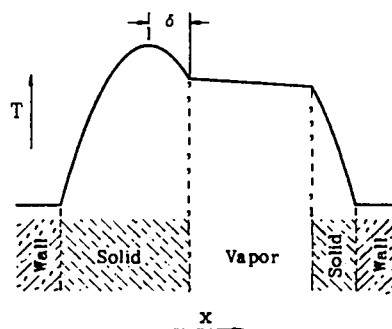

FIG. 1. One-dimensional slab model of the β heating effect. The temperature profiles in the solid, self-heated layers are parabolic. Sublimation-condensation across the vapor space results in the gradual erosion of the excess layer thickness δ. Heat balance at the solid-vapor boundary leads to the limiting rate constant $\tau_{min} = H_s/\dot{q}$, where H_s is the heat of sublimation and $\dot{q}$ is the self-heating rate.

Compression moduli of some PMP microcellular foams

JOEL M. WILLIAMS
Materials Science and Technology Division, Los Alamos National Laboratory, P.O. Box 1663, Los Alamos, New Mexico 87545, USA

The elastic moduli of poly(4-methyl-1-pentene) foams made by several processes are measured. The results reveal that several terms need to be added to the currently accepted mathematical representation. Thus, the amount of noncontributing mass and the efficiency of the contributing mass must be considered along with the isotropic reduction in total mass. The mathematical equation derived gives new insight into the structure and properties of microcellular foams.

1. Introduction

Over the past few years, Los Alamos National Laboratory has been making microcellular foams for inertial confinement fusion (ICF) targets [1, 2]. The foams are prepared by phase separation of poly(4-methyl-1-pentene), or PMP, from a cooling solution followed by removal of the solvent [3]. In the 0.01 to 0.08 g cm^{-3} range, these foams are friable and difficult to handle. This is very much unlike the character of polystyrene blown foams. To quantify the difference, the compression moduli of two series of these PMP foams, ranging from 0.02 to 0.09 g cm^{-3} were measured and related to that for a 0.031 g cm^{-3} polystyrene insulation board foam. The dependency of the compression modulus on bulk density was then compared with a current model describing porous materials. This comparison has lead to several important considerations overlooked in treating these very low-density materials; namely, the possible presence of noncontributing material and the change in the effective modulus of the contributing material.

2. Experimental details

2.1. Foam preparation

Foams were made from poly(4-methyl-1-pentene) by the phase separation technique [1–3]. Series A was prepared with a solvent consisting of bibenzyl, diphenylmethane, biphenyl, and stearic acid. The solidified mass was extracted with methanol to produce an open microcellular foam. Series B was prepared with 1,2,4,5-tetramethylbenzene. The solid mass from each of these mixtures was also extracted with methanol to yield an open microcellular foam.

2.2. Compression testing

Cubes of foam approximately 1 cm × 1 cm × 1 cm were tested. The probe was a 6.35 mm (0.25 in.) diameter, stainless stain, dowel rod. Samples above 0.020 g cm^{-3} were tested (Method A) with a table model Instron using a 50 lb (~22.7 kg) compression load cell. The load was applied to a depth of 2.5 mm (0.10 in.) at a rate of 1.3 mm sec^{-1} (0.05 in sec^{-1}).

Those samples below 0.034 g cm^{-3} were also tested (Method B) with a 100 g load cell assembly developed at our laboratory by Hoover and Petrovic for testing silicon carbide whiskers. Because of the slight resistance of the cell, the recorded displacement was larger than the actual value. The correction was linear with load and easily eliminated. Load/deflection data (Table 1) from each method were in very good agreement. Duplicate values were generally within 10% of one another. No sharp break in the load curve was observed up to 1.1 mm penetration.

The elastic modulus, E, was calculated by relating the stress, L_{sample}, at a given strain to the stress of a standard foam, L_{std}, measured at the same strain. Thus, the equation for the modulus is as

$$E = \left(\frac{L_{sample}}{L_{std}}\right) E_{std} \qquad (1)$$

The standard used was a 2.5 cm (1 in.) thick sheet of 0.031 g cm^{-3} extruded polystyrene insulation board (Classification D-369) made by Dow Chemical Co. The compression modulus was determined by ASTM Method D1621-73 using a 2.8 cm × 2.8 cm cross-section. The experimental E was 7.2 ± 0.2 MPa (1045 ± 25 p.s.i.). This compares favourably with the reported data [4]: 800 to 1000 p.s.i. (0.029 g cm^{-3}) and 1200 p.s.i. (0.036 g cm^{-3}).

Using Equation 1, the polystyrene standard and the 0.76 mm penetration data, the moduli of the tested examples (Table I) have been determined and plotted in Fig. 1.

3. Discussion

The compression moduli of the open microcellular poly(4-methyl-1-pentene) foams are indeed much less than that of a comparable density, closed cell, polystyrene blown foam. The moduli for the PMP foams are over an order of magnitude less although the modulus of bulk PMP polymer is only two to three times less than that of polystyrene (see Table II). Also the moduli of the PMP foams from the two processes are markedly different. The moduli of each foam type, however,

NEAR-REAL-TIME RADIOGRAPHY DETECTS VERY SMALL WIRES AND THICKNESS VARIATIONS

David M. Stupin and Grant H. Stokes

Materials Science and Technology Division
Los Alamos National Laboratory
Los Alamos, NM 87545

Judith Steven-Setchell

Atomic Weapons Establishment
Aldermaston, Reading, R647PR
United Kingdom

ABSTRACT

The author uses radiography with two simple image-processing techniques and 17 keV x-rays (45 kV pk) from a molybdenum anode to detect very small changes in areal density and very small-diameter wires These image-processing techniques will improve the performance of any digital-imaging x-ray system and can be performed in about 30 s Furthermore. the x-ray energy is nearly optimum for examining some plastic and ceramic parts This technique can be modified for examining materials at other energies

INTRODUCTION

Digital subtraction radiography serves angiography[1] and other medical applications successfully to extract minute x-ray signals from noisy backgrounds. Verhoeven[2] demonstrated that detecting surprisingly small changes in x-ray absorption makes this technique useful for industrial applications as well. We detect very small areal density differences and also wires as small as 2 μm in diameter although the spatial resolution of our x-ray apparatus is 1 mm.

Areal density is the product ρx. where ρ is the material density and x is the material thickness. Hence. an areal density change is caused by a variation in thickness or density. Using digital subtraction radiography. we detect a 0.1% change in areal density in a phantom. Therefore. it is possible to detect a 0.1% difference in density or thickness in unknown samples.

Toroidal Microstructures from Water-in-Oil Emulsions

Joel M. Williams

*Materials Science and Technology Division, Los Alamos National Laboratory,
Los Alamos, New Mexico 87545*

Polymerization of emulsions made from styrene–divinylbenzene–dodecane–water mixtures provides a useful route to open-microcellular rigid foams. The structures of the resulting foams demonstrate that the emulsions possess considerable segregation and alignment of each molecular species at the time of polymerization. Simple pictorial models are sufficient to explain the emulsion structures and the resulting foams. Toroidal microstructures are predictable and observed.

Introduction

Over the last decade, rigid open-microcellular polymeric foams have been needed for high-energy physics experiments, especially those for inertially confined fusion. The required foams needed densities less than 0.1 g/cm^3 and cell sizes of 30 μm or less. Los Alamos National Laboratory has investigated a variety of routes for producing these special foams. Successful routes have generally involved a polymer phase that separated from a hot solution and then removal of the solvent in a manner such that the polymer did not move.[1] Along with workers at Lawrence Livermore National Laboratory,[2] the Atomic Weapons Research Establishment (England),[3] and Case Western Reserve University,[4] we are now exploring the usefulness of emulsion technology in producing rigid microcellular foams.

Unilever[5] has described the production of a porous, homogeneous, cross-linked polymeric block material having a dry density of less than 0.1 g/cm^3 by a process in which monomer (styrene or substituted styrene plus comonomers) are polymerized after they have formed an emulsion having a high (at least 90%) internal phase comprised of water. The emulsion polymerization of styrene is not new, of course, and has been the subject of numerous patents because of the technical importance of polystyrene.[6] Monodispersed polystyrene latexes, for example, have been prepared by seeded-emulsion polymerizations and 3–5-μm particles were successfully prepared on a US space shuttle in 1982.[7] Styrene is readily polymerized in an emulsion

(1) Young, A. T. *J. Vac. Sci. Technol. A* **1986**, *A4*(3), 1128.

(2) Letts, S. A.; Lucht, L. M.; Morgan, R. J.; Cook, R. C.; Tillotson, T. M.; Mercer, M. B.; Miller, D. E. *Progress in Development of Low Density Polymer Foams for the ICF Program*; Lawrence Livermore National Laboratory Report UCID-20537, 1985.

(3) Gunn, T. Atomic Weapons Research Establishment, Aldermaston, England, 1985, private communication.

(4) Litt, M. L.; Hsieh, B. R.; Krieger, I. M.; Chen, T. T.; Lu, H. L. *J. Colloid Interface Sci.* **1987**, *115*(2), 312 (contains photomicrographs).

(5) Barby, D.; Haq, Z., *Low density porous cross-linked polymeric materials and their preparation and use as carriers for included liquids*, European Patent 0 060 138 (Unilever, applicant), September 1982.

(6) Sumner, C. G. *Clayton's The Theory of Emulsions and Their Technical Treatment*; Blakiston Co.: New York, 1954.

(7) Vanderhoff, J. W.; El-Aasser, M. S.; Micale, F. J.; Sudol, E. D.; Tseng, C. M.; Silwanowicz, A.; Kornfeld, D. M.; Vicente, F. A. *J. Dispersion Sci. Technol.* **1984**, *5*(3/4), 231.

REFRIGERATOR-COOLED CRYOSTATS FOR RESEARCH ON ICF TARGETS

by

James K. Hoffer and Robert J. Candler
Physics Division

Los Alamos National Laboratory
P. O. Box 1663
Los Alamos, New Mexico 87545

INTRODUCTION

It is becoming clear that cryogenics is a valuable tool for conduct-
ing research on inertial confinement fusion prototype targets.   The
increased density in the DT fuel afforded by cryogenic temperatures can not
be easily matched in room-temperature designs, and then only by utilizing
relatively thick walls to safely contain the high pressures needed.   To
achieve a density in DT equal to the liquid density at the triple point, a
room-temperature pressure of just over 3 kbar (44,550 psi) is necessary.[1]
However, providing the target with an environment near 20 K is generally
not accomplished without introducing and solving a number of problems
inherent to cryogenics. Many of these problems can be circumvented by
utilizing a closed-cycle-helium refrigerator as the cryogenic cooling
agent.

CONVENTIONAL CRYOSTATS

Before discussing these advantages, it will be instructive to review
briefly a conventional cryostat, i.e., one cooled with the use of liquid
cryogens nitrogen (LN_2) and helium (^4He).   (The use of liquid H_2 for tem-
peratures near 20 K was once standard practice.   However, the associated
hazards and current limited availability have prompted most researchers to
utilize other techniques.)   Such a cryostat is shown in Fig. 1.   This is
similar to a design used by one of us (JKH) for light scattering experi-
ments at very low temperatures[2].   The sample to be studied is suspended in
a sealed can immersed in a bath of liquid ^4He.   The bath is pumped to below

Spatial Distribution of the Phases in Water-in-Oil Emulsions. Open and Closed Microcellular Foams from Cross-Linked Polystyrene†

Joel M. Williams* and Debra A. Wrobleski

Materials Science and Technology Division, Los Alamos National Laboratory, Los Alamos, New Mexico 87545

The composition of styrene/divinylbenzene/sorbitan monooleate/water emulsions has a dramatic effect on the openness of the cells of the foam prepared by polymerizing the monomers and subsequently removing the water. Monomer concentrations were varied from 0.025 to 0.20 g/cm³, while the surfactant level was varied from 1.2% to 320% of the monomer. Most remarkably, the variation in cell openness, and hence the continuity of the oil phase, was insensitive to the amount of oil. The variation was, however, strongly related to the surfactant-to-oil ratio. The structures of the resulting foams provide further evidence that emulsions possess considerable spatial ordering of the phases and, hence, the molecular species associated with them at the time of polymerization.

Introduction

Unilever[1] has described the production of porous, homogeneous, cross-linked polymeric block material having a dry density of less than 0.1 g/cm³ by a process in which monomers (styrene or substituted styrene plus comonomers) are polymerized after they have formed an emulsion having a high fraction (at least 90%) of internal phase comprised of water. The rigid open microcellular foams made by this process have potential use in high-energy physics experiments.[2] Because of this interest, Los Alamos National Laboratory and workers at Lawrence Livermore National Laboratory,[3] the Atomic Weapons Establishment (England),[4] and Case Western Reserve University[5] are evaluating the influence of changes in emulsion parameters on the microstructure of the final foam. During our initial investigations of making foams by polymerizing water-in-oil (w/o) emulsions containing styrene/divinylbenzene as the oil phase, it appeared that the structure of the foam obtained could give significant information about the structure of the emulsion that led to it. In a previous paper,[2] this fact was vividly illustrated; the foams obtained demonstrated that considerable spatial ordering occurred in the oil phase at the micrometer level down to less than 1/100th of a micrometer (<100 Å). Consequently, foam structures can be a very useful and graphic tool for depicting the structures that must be addressed in any comprehensive theoretical description of emulsions. This paper utilizes this approach in a systematic evaluation of the foam structures and hence the accompanying emulsion structures, that are produced when the relative amounts of polymerizable monomers and surfactants are varied.

Experimental Section

Emulsion Preparation. Sorbitan monooleate surfactant (Lonzest SMO, HLB = 4.3) and organic components were mixed in a 120-mL (4-oz.), tall form Qorpak jar. While the mixture was stirred at approximately 1000 rpm with a 3.5-cm-diameter splashless Jiffy stirrer, an aqueous solution with 1.50 g/L of potassium persulfate was added dropwise from an addition funnel. The total addition time was 15 min and gave a total volume of 100 mL. The mixture was then vigorously stirred for an additional

5 min. Experimental details of the amounts of reactants and the consistencies of the emulsions are given in Table 1.

Polymerization. Each jar was capped and heated overnight in a 60 °C oven. Most samples produced a stiff white solid. Some of the samples with very high surfactant levels were soft and had a small amount of oil above the solid.

Foam Production. The solid masses were removed from the jars by cracking the glass jar and carefully removing the fragments. Each sample was set on a piece of plate glass and placed in a 83 °C forced-air convection oven for several days until dry. Since all the masses had the same dimensions, rates of water loss were determined by fitting the weight-loss data to a first-order rate expression and evaluating the half-life time about the 50% weight-loss point. Water-loss rate data and visual foam quality are listed in Table 1. The water-loss rate for a "0% SMO" foam was determined by placing 100 mL of water in a short, open glass container whose open surface area was equivalent to that of the exposed foams described above. The water-loss half-life for the "0% SMO" case, under the experimental conditions used (0.75 atm and 83 °C), was 100 min. Foam densities were determined from weight and volume measurements and are given in Table 1. Compression analyses were determined on 2.54-cm-diameter × 2.54-cm-high cylinders by using an Instron with a 454-kg (1000-lb) load cell and a platen speed of 0.127 cm/min (0.05 in./min). Results are reported in Table 1.

Microscopy. The dried foam was mounted on a metal stalk with DUCO cement. After the cement dried, a smooth surface was cut with a vibrating razor blade. The device used was a Vibratome Model 1000 sold by Ted Pella, Inc., of Tustin, CA. The sides of the foam and the mount were then coated with silver paint for conductivity. After the silver paint dried, the foam was coated with a few angstroms of gold. The prepared foam was then analyzed with a Hitachi Model S-520LB scanning electron microscope.

Results and Discussion

Foam and Emulsion Structures. While the monomer–surfactant–water tricomponent system can be for-

(1) Barby, D.; Haq, Z. Low density porous cross-linked polymeric materials and their preparation and use as carriers for included liquids; European Patent 0060138 (Unilever, applicant), September, 1982.
(2) Williams, J. M. *Langmuir* 1988, 4, 44-49.
(3) Letts, S. A.; Luebt, L. M.; Morgan, R. J.; Cook, R. C.; Tillotson, T. M.; Mercer, M. B.; Miller, D. E. *Progress in Development of Low Density Polymer Foams for the ICF Program*; Lawrence Livermore National Laboratory Report UCID-20537, 1985. Chen, C.; Cook, R. C.; Haendler, B. L.; Hair, L. M.; Kong, F. M.; Letts, S. A. *Low-Density Hydrocarbon Foams for Laser Fusion Targets*; Lawrence Livermore National Laboratory Report UCID-21080-86, 1987.
(4) Gunn, T.; private communication. Atomic Weapons Establishment, Aldermaston, England, 1985.
(5) Litt, M. M.; Hsieh, B. R.; Krieger, I. M.; Chen, T. T.; Lu, H. L. *J. Colloid Interface Sci.* 1987, 115(2), 312.

RADIOGRAPHIC DETECTION OF 100 Å THICKNESS VARIATIONS IN 1-μm-THICK

COATINGS ON SUBMILLIMETER-DIAMETER LASER FUSION TARGETS

David M. Stupin

Materials Science and Technology Division
Los Alamos National Laboratory
P.O. Box 1663
Los Alamos, NM 87545

INTRODUCTION

We have developed x-ray radiography to measure thickness variations
of coatings on laser fusion targets. Our technique is based on measur-
ing the variation in x-ray transmission through the targets. The sim-
plest targets are hollow glass microshells* or microballoons** 100 to
500 μm in diameter (Fig. 1), that have several layers of metals or plas-
tics, 1 to 100 μm thick (Fig. 2). Our goal is to examine these opaque
coatings for thickness variations as small as 1% or 0.1%, depending on
the type of defect. Using contact radiography we have obtained the
desired sensitivity for concentric and elliptical defects of 1%. This
percentage corresponds to thickness variations as small as 100 Å in a
1-μm-thick coating. For warts and dimples, the desired sensitivity is a
function of the area of the defect, and we are developing a system to
detect 0.1% thickness variations that cover an area 10 μm by 10 μm.

We must use computer analysis of contact radiographs to measure 1%
thickness variations in either concentricity or ellipticity. Because
this analysis takes so long on our minicomputer, we preselect the
radiographs by looking for defects at the 10% level on a video image
analysis system.

Detection of 0.1% warts or dimples requires a signal-to-noise ratio
of 700 to 1. This range exceeds the signal-to-noise ratio of photo-
graphic products, and we are therefore developing a point-projection
radiography system that uses an x-ray-sensitive television camera. The
video images from this system are digitized and summed in a computer
until the desired signal-to-noise ratio is obtained. Point-projection
radiography magnifies the x-ray image to match the spatial resolution of
the camera. All of these techniques can be used on other objects with
different sizes and shapes.

---

* Microshell is a registered trademark of KMS Fusion, Inc., Ann Arbor,
  MI 48106
** Microballoon is a registered trademark of Emerson and Cuming, Inc.,
  Canon, MA 02021. In this paper, microballoon and microshell are used
  interchangeably.

Microcellular foams: phase behaviour of poly(4-methyl-1-pentene) in diisopropylbenzene

Joel M. Williams and Joyce E. Moore

Materials Science and Technology Division. Los Alamos National Laboratory. Los Alamos. NM 87545. USA

Microcellular foams are an important component of Inertially Confined Fusion (ICF) targets. The spatial distribution of the material is critical as the target implodes. In an effort to improve the spatial uniformity, we have explored the phase separation behaviour of poly(4-methyl-1-pentene) solutions with diisopropylbenzene solvent. The cloud-point phase-separation diagram from pure solvent to pure polymer is discussed. Microstructures of the various density foams and the need for a three-dimensional phase diagram are presented.

(Keywords: polymer; poly(4-methyl-1-pentene); diisopropylbenzene; phase diagram; foam; microcellular)

INTRODUCTION

Low density materials continue to be needed as 'structural air' and cushions in ICF targets. In 1980[1], these low density materials needed to be in the 50 mg cm^{-3} range with cells about 25 μm in size, have low Z composition (mainly hydrogen to carbon), be structurally sound, and be fabricated to high tolerances. A foam meeting these requirements was developed at Los Alamos using a phase separation technique in which the dissolved polymer separated from a hot organic solvent as the temperature was lowered[1]. The organic solvent was leached from the separated polymer–solvent mass to leave a foam structure. The polymer used was poly(4-methyl-1-pentene) or PMP. The best solvent at that time was a 90/10 mixture of bibenzyl and paraffin[2]. The most significant feature of that polymer/solvent system was the soap-like texture of the solvent-filled polymer mass. This physical property allowed the mass to be readily machined to high tolerances with standard tooling before the solvent was leached and a fragile foam produced.

By 1985, the properties needed for low density materials had become more stringent. The basic 1980 requirements were still needed, but designers now wanted smaller cell sizes (1 μm or less) and a foam that could withstand much harsher conditions. Recently Aubert and Clough[3] have reported success at making low density, microcellular polystyrene foams directed at achieving these goals. Like them, we have explored new polymer/solvent systems and have found that poly(4-methyl-1-pentene) produces a strong 50 mg cm^{-3} foam with near 1 μm cells when prepared from diisopropylbenzene (DIPB) solvent. Unlike previous efforts, the microcellular structure is uniform over very large (at least 10 cm in every direction) three-dimensional structures. We believe that the information gained from studying this system points the way to achieving the more stringent requirements listed above while shedding new light on the phase behaviour of polymer solutions in general.

EXPERIMENTAL PROCEDURES

Sample preparation

Solid poly(4-methyl-1-pentene) and the appropriate amount of solvent to give the desired polymer weight fraction and a total of 5 ml mix were added to a pyrex test tube. Also known as TPX, the PMP polymer was used in bead form, containing less than 5% other polymer homologues, and was produced by Mitsui Petrochemical Industries, Ltd, Japan, or Aldrich Chemical Company. The DIPB was technical grade with an isomeric ratio $o/m/p$:10/50/40 from Kodak. (The large fraction of 1,3- and 1,4-isomers caused significant effects in the phase separation behaviour, as will be discussed.) The 20 cm long, 1.3 cm i.d., 1.5 cm o.d. test tubes used in the cloud point studies were previously necked down about 12 cm from the bottom. The contents of each test tubes were cooled externally with pulverized dry ice and the test tubes closed off with an oxygen–natural gas torch.

Observation of phase behaviour

A sealed tube containing polymer and solvent was placed in the tube holder of the assembly shown in *Figure 1*. The tube was rotated as the oil bath was heated. After the polymer was dissolved, the temperature was raised somewhat higher (typically 50°C above the cloud point) and maintained for a short period (generally 15–30 min) to ensure good dissolution. After this dissolution process, the test tube was stopped vertically in front of a high intensity fibre optics white light beam. The beam was viewed visually from low (5–10°) to right (90°) angles in the horizontal plane. The temperature of the oil near the tube was measured with a thermocouple and plotted *versus* time on a strip chart recorder. Observations were generally concerned with the earliest certainty of clouding, the degree of system opacity, the colour and nature of the separating system, and the temperature at which the polymer mass (gel) pulled away from the test

Polymer-Solvent Phase Separation as a Route to Low Density, Microcellular Plastic Foams

AINSLIE T. YOUNG

University of California
Materials Science and Technology Division
Los Alamos National Laboratory
P.O. Box 1663
Los Alamos, NM 87545

INTRODUCTION

High energy physics research and development programs at Los Alamos National Laboratory are extremely demanding on the nature and properties of materials for these programs. In particular, inertial fusion programs which are designed to conduct thermonuclear experiments in the laboratory by imploding deuterium-tritium capsules to high compression (more than one thousand times liquid density) using lasers, particle beams, or soft x-rays as drivers for the implosion have required whole new classes of materials for the construction of the capsules (referred to here as fusion targets) [1]. It is hoped that such studies can someday lead to commercial inertial fusion activities applied to electric power production.

Typical high gain fusion targets are simply a series of concentric spherical shells. It is at this point that simplicity disappears. These targets are generally very small with overall dimensions of one millimeter or less, and the tolerances put on these targets are on the micron scale. The components of a typical high gain fusion target are shown in Figure 1.

One of the critical elements of such a multishell target is a cushion layer situated between tamper and ablator layers. This cushion, ideally

Measurements of laser plasma coronal conditions and thermal transport with time-resolved x-ray spectroscopy

O. Willi, S. D. Tabatabaei, and D. Riley

The Blackett Laboratory, Imperial College of Science and Technology, London, SW7 2BZ, United Kingdom

A. Hauer and N. Delamater

Los Alamos National Laboratory, Los Alamos, New Mexico 87545

C. Chenais-Popovics

École Polytechnique, 91128 Palaiseau CEDEX, France

P. Apte and A. Cole

Rutherford Appleton Laboratory, United Kingdom Science Research Council.
Chilton, Didcot, Oxfordshire OX11 0QX, United Kingdom

This paper presents a detailed characterization of the plasma conditions near the critical density of a laser-produced plasma. Solid spherical plastic targets with small aluminum tracer dots buried below overcoated plastic layers have been uniformly illuminated with green laser light at irradiances of 10^{14}–10^{15} W/cm^{-2}. Time-resolved temperature and density profiles were obtained by using x-ray emission spectroscopy. Detailed comparisons with hydrodynamic simulations show that the thermal transport is well characterized by a flux limit of 0.1.

In laser-produced plasmas, the laser energy is absorbed below and up to the plasma critical density. The absorbed energy is transported, via electron thermal conduction, beyond the absorption region towards the colder, higher-density region of the target. A knowledge of the plasma conditions close to and above the critical-density surface is, therefore, crucial for an understanding of thermal transport in laser-produced plasmas. Measurements of plasma ablation rates in spherical geometry have indicated that the electron thermal transport is inhibited to 0.05–0.1 with respect to the classical flux streaming limit when compared to hydrodynamic computer simulations.[1-3] These experiments measured the average mass ablation at the ablation layer. No detailed time-resolved observations have, however, been made of the plasma conditions in the region where the transport processes take place.

This Rapid Communication reports on the first detailed time-resolved measurements of the plasma conditions above and close to the critical-density layer of uniformly laser irradiated spherical targets. The temporal histories of the electron density and temperature were obtained via simultaneous time-resolved measurements of x-ray line profiles and line ratios. Temporal resolution of both temperature and density (and spatial resolution of temperature) provide a new diagnostic method for evaluating coronal properties such as transport and ablation. Detailed comparisons of these observations, with hydrodynamic simulations were carried out.

The targets were made of solid plastic, to prevent implosion, and were approximately 150 μm in diameter. Aluminum tracer dots, 0.1 μm thick and ranging from 25 to 75 μm in diameter, were implanted beneath the target surface at depths of 0.24–2.0 μm. The use of microdots

has several advantages.[4] First, the emitting source is localized in space and time and so reflects plasma conditions locally. Hydrodynamic simulations indicated that the presence of the dot made no significant difference to the plasma conditions or heat flow. Second, the effect of opacity on line ratios and broadening due to source size are both greatly reduced by using a small source. In addition, the effects of large-scale nonuniformity of irradiance are reduced. In contrast to previous use of tracer dots[4] for measurement of temperature and density, the present work is in an irradiance regime more relevant to laser fusion ($\sim 1 \times 10^{14}$ W/cm^2) is temporally resolved, and is performed in spherical geometry [where two-dimensional (2D) lateral heat-flow effects are minimized].

Targets were symmetrically irradiated with the twelve beams of the Vulcan Nd-glass laser at the Rutherford Appleton Laboratory High Power Laser Facility. The beams were frequency doubled to 0.53-μm wavelength and had an approximately Gaussian temporal profile with an 800 ps full width at half maximum duration. The focusing on target was tangential with $f/2.5$ lenses. The beam profiles were found to have a 30% rms intensity variation due to small-scale structure. The overlap of the beams and energy imbalance resulted in a 50% peak-to-valley variation over large-scale length. Absorbed irradiances varied from 5×10^{13} to 3×10^{14} W/cm^2.

Several instruments were used to diagnose the x-ray radiation emitted from the heated aluminum tracer dot. The temporal history of the Stark profile for the He-like $1s^2$-$1s4p$ (He$_\gamma$) transition was measured with a novel toroidally focusing pentaerythritol (PET) crystal,[5] which was coupled to an x-ray streak camera to produce a high dispersion spectrum of the line. The time-dependent electron density was obtained from the line profile[6] by com-

Kilovolt x-ray spectroscopy of a subpicosecond-laser-excited source

J. A. Cobble, G. A. Kyrala, A, A. Hauer, A. J. Taylor, C. C. Gomez, N. D. Delamater, and G. T. Schappert

Los Alamos National Laboratory, Los Alamos, New Mexico 87545

(Received 18 April 1988)

A subpicosecond laser is focused to 10^{17} W/cm^2 to create an extremely transient Al plasma with a kV radiation time short compared to most of the excitation times. High-resolution spectroscopy is used to analyze the kV line emission from the He- and H-like ions and to determine that the plasma reaches a temperature near 1 keV and cools in less than 10 ps.

INTRODUCTION

The advent of high-intensity, picosecond lasers has introduced a new dimension for the study of laser-matter interactions.[1] Irradiance levels above 10^{17} W/cm^2, for which the electric field strength of the laser approaches 100 V/Å, are now available. This offers the possibility of studying a new regime of laser-plasma interactions in which plasma heating and cooling occur on a time scale that is short compared to the characteristic excitation and ionization times of the observed states. This is very different from the case of (0.1–1)-ns laser-driven plasmas in which equilibrium models may be applied.[2]

In the present work, we report on the observation and analysis of x-ray emission produced by high-intensity laser irradiation of a solid Al target. Copious x-ray emission is observed from 100 eV to 2 keV. We emphasize high-resolution spectroscopic analysis of the kV line radiation. This makes possible studies of the detailed atomic structure of highly stripped ions and the development of related time-dependent plasma diagnostics. Previous spectroscopic work with solid targets was at lower irradiance and dealt with much softer radiation.[3] In addition, in the present case, target ions are more highly stripped, e.g., He- and H-like Al.

EXPERIMENTAL CONDITIONS

The laser is a high-brightness, small-aperture, KrF-based system which routinely produces irradiances greater than 10^{17} W/cm^2 when focused on target.[4] Subpicosecond 248-nm seed pulses, generated by up-converting the output of a visible dye laser, are amplified at 3 Hz in two commercial KrF discharge lasers separated by a vacuum spatial filter. The amplified pulses have an energy up to 25 mJ and are 700 fs in duration. The output beam, expanded to 2.5 cm in diameter, is focused on target with an $f/3$ off-axis parabolic mirror. The spot diameter on target has been determined by several independent means[5] to be about 4 μm—twice the diffraction limit.

The main pulse is superimposed on a 10-ns pedestal of amplified spontaneous emission (ASE) which contains 5–10% of the total energy. The ASE produces a plasma with which the main pulse interacts. By adjusting the timing of the 700-fs pulse within the ASE window, the prepulse energy fraction can be reduced to as little as 2%—about 400 μJ.

The x-ray emission is studied with a variety of diagnostics. Spectroscopy is typically done at an angle of between 60° and 70° with respect to the target normal. A free-standing, gold-foil, transmission-grating spectrograph was employed to survey time-integrated plasma radiation between 100 and 4000 eV with a resolution of 1–2 Å. Typically, spectra are accumulated in several hundred shots. High-resolution, time-integrated spectra in the (1.5–2)-keV range were obtained with a flat pentaerythritol (PET) crystal spectrograph. The resolving power of this instrument is about 2000. The very small emission region in this work causes the source-size contribution to instrument broadening to be only about 0.3 eV. In addition, due to the very short duration of the keV radiation, there is no hydrodynamic expansion of the effective source size. The high resolution of the kV line spectra is a notable feature of this experiment.

A pinhole camera was used to characterize the emission region. It consists of a Be-filtered, 3-μm pinhole, and direct exposure film (DEF). The camera has a magnification of about 15 and a spatial resolution of 6 μm. The Al radiation above 1 keV is seen to come from a region limited by the spatial resolution of the camera, which is consistent with the focal spot size. Thus, the keV x-rays are emitted only from the region of highest laser intensity.
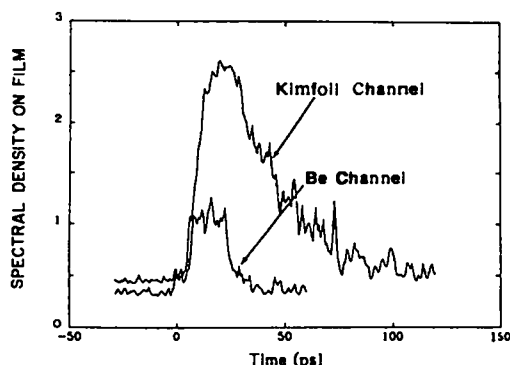

FIG. 1. Densitometered streak camera record of the Be and Kimfoil channels. The instrument broadening corresponds to about 20 ps.

Laser-Induced Plasmas and Applications

edited by

Leon J. Radziemski
Department of Physics
New Mexico State University
Las Cruces, New Mexico

David A. Cremers
Chemical and Laser Sciences Division
Los Alamos National Laboratory
Los Alamos, New Mexico

3
Introduction to Laser Plasma Diagnostics

Allan A. Hauer
Los Alamos National Laboratory
Los Alamos, New Mexico

Hector A. Baldis
National Research Council of Canada
Ottawa, Ontario, Canada

3.1 INTRODUCTION

The interaction of intense laser light with matter has been an active topic in the fields of plasma and atomic physics for more than 15 years. During this period, an amazingly rich diversity of plasma conditions has been investigated. As an indication of the interesting range of parameters, the following conditions have been encountered: (1) electron temperatures (T_e) from 10 eV to many keV; (2) scale lengths, e.g., $T_e/|\nabla T_e|$, as short as a few microns, (3) self-generated magnetic fields greater than a megagauss; (4) particles accelerated to energies as high as a megavolt/amu; (5) imploded compressed densities of > 30 g/cm^{-3} (while maintaining $T_i \sim 1$ keV); and (6) ionization stages as high as those of helium-like Kr. In this chapter, we will describe some of the methods that have been devised for diagnosing this wide range of plasma and atomic conditions.

A number of excellent review articles (Bekefi et al., 1976, Boiko et al., 1985, Key and Hutcheon, 1980; Peacock, 1980) and one book (Hughes, 1975) have addressed the subject of laser plasma diagnostics. Because of this wealth of available background material, we place emphasis on work that has been done over the last six years. We will also emphasize the underlying physical principles of measurement techniques as opposed to instrumentation. Several good reviews of instrumental methods have been published recently (Richardson et al., 1985; Hall, 1985). In addition, a somewhat earlier article by Attwood (1978) still is a very valuable source on

Laser-Induced
Plasmas
and
Applications

edited by

Leon J. Radziemski
Department of Physics
New Mexico State University
Las Cruces, New Mexico

David A. Cremers
Chemical and Laser Sciences Division
Los Alamos National Laboratory
Los Alamos, New Mexico

10
Current New Applications
of Laser Plasmas

Allen A. Hauer, David W. Forslund, and Colin J. McKinstrie*
Los Alamos National Laboratory
Los Alamos, New Mexico

Justin S. Wark[1]
Laboratory for Laser Energetics
University of Rochester
Rochester, New York

Philip J. Hargis, Jr. and Roy A. Hamil
Sandia National Laboratories
Albuquerque, New Mexico

Joseph M. Kindel
Mission Research Corporation
Los Alamos, New Mexico

10.1 INTRODUCTION

As the previous chapters have illustrated, the applications of laser-produced plasma (LP's) have been a wide-ranging field of investigation for more than two decades. In this final chapter, we will review several applications that (with one exception) have been active topics of investigation only for the last few years.

We deal first with the application of laser-generated particles and x-rays. This topic is largely an outgrowth of laser fusion research and primarily employs the higher flux regime with irradiances $> 10^{13}$ W/cm^2. This topic demonstrates a very satisfying diversity of practical applications ranging

Present affiliations:
*Laboratory for Laser Energetics, University of Rochester, Rochester, New York
[1]Royal Society University Fellow, Oxford University, Oxford, England

Dynamics of High-Z Plasmas Produced by a Short-Wavelength Laser

P. D. Goldstone, S. R. Goldman, W. C. Mead, J. A. Cobble, G. Stradling, R. H. Day, and A. Hauer

Los Alamos National Laboratory, University of California, Los Alamos, New Mexico 87545

and

M. C. Richardson, R. S. Marjoribanks, P. A. Jaanimagi, R. L. Keck, F. J. Marshall, W. Seka, O. Barnouin, B. Yaakobi, and S. A. Letzring

Laboratory for Laser Energetics, University of Rochester, Rochester, New York 14623

(Received 25 August 1986)

The dynamics and energy flow in Au plasmas produced by a 0.35-μm laser have been studied with layered targets with 6- and 24-beam spherical illumination from the Omega laser, to understand the processes leading to subkiloelectronvolt x-ray emission. A significant enhancement in x-ray conversion at low intensities is observed for the 24-beam irradiations with higher energy, greater uniformity, and larger targets. Results are interpreted by comparison with hydrodynamics-code calculations. The depth of energy penetration and x-ray emission in the plasma appears to be well understood, but some details of the x-ray time signature and spectra are not.

The efficiency with which energy absorbed in laser-produced high-Z plasmas is converted to soft x rays increases markedly at shorter laser wavelengths.[1-3] This results from laser-light deposition at higher plasma densities, yielding cooler plasmas with lower hydrodynamic losses, and can be important for some approaches to inertial-confinement fusion.[4] A similar increase in conversion efficiency is expected at lower laser intensities. However, early experiments with planar Au targets[1,2] showed a decrease of x-ray emission at low intensities, whereas the LASNEX[5] simulations code predicted an increase,[2] indicating that high-Z plasmas were not well understood. Thus we have sought more specific observations of the hydrodynamic, energy-transport, and atomic processes which affect x-ray emission.

Here, we report the first measurements of x-ray conversion performed in spherical geometry. This pseudo one-dimensional experiment simplifies integration of measurements over solid angle and allows a test of whether two-dimensionality inherent in previous planar experiments might have affected the results.[6,7] Also, we examine the dynamics of high-Z plasmas and the processes which affect x-ray emission, including the material depths associated with energy transport and x-ray generation, and the time dependence and spectra of the x-ray emission, at intensities of 4×10^{12} to 4×10^{15} W/cm^2. Finally, we compare similar experiments using two different laser-energy–target-size combinations at the 4×10^{13} and 4×10^{14} W/cm^2 intensities.

We have investigated some of the changes in plasma conditions which are expected as the $\lambda_L \approx 0.35$ μm irradiance is decreased from 4×10^{14} to 4×10^{13} W/cm^2 (where the emission discrepancy was first noted[2]). At 4×10^{14} W/cm^2, radiation cooling is weaker than laser deposition in the underdense plasma. Hence the corona

temperature rises, reducing the inverse-bremsstrahlung absorption opacity, so that the laser penetrates to the critical surface and deposits its energy locally. This produces strong steepening of the density and temperature profiles near the critical density. The x-ray emission originates in a localized region near and above the critical density, with electron transport carrying energy from the absorption region to the emitting region. At 4×10^{13} W/cm^2, radiation cools the corona at a rate nearly equal to the laser deposition, so that the deposition and the x-ray emission occur in an extended plasma well below the critical density. Electron transport is relatively unimportant in this case.

Specific predictions of the features of the x-ray–emission region are shown in Table I. The one-dimensional (1D) LASNEX[5] modeling used for this work

TABLE I. Calculated ($f_e = 0.08$, $\lambda_L = 0.35$, $\tau_L = 650$ ps) characteristics of the subkiloelectronvolt x-ray emission and burnthrough features for layered Au-on-(CH)$_x$ spheres.

	4×10^{13} W/cm^2	4×10^{14} W/cm^2
X-ray emission		
Radial extent (μm)	40	8
Density	$(0.04-0.5)n_c$	$(0.3-1.8)n_c$
Electron temperature (keV)	0.1–0.5	0.3–1.2
Average Z	25–30	35–45
E_{rad}/E_{abs}	0.85	0.72
$E_{M\ Vac}/E_{rad}$ (%)	<1	5
Burnthrough features		
Laser penetration depth (at peak of pulse) (Å)	350	750
X-ray–emission decrease (at burnthrough)	Negligible	Significant

Shock launching in silicon studied with use of pulsed x-ray diffraction

J. S. Wark

Laboratory for Laser Energetics, University of Rochester, Rochester, New York 14623

R. R. Whitlock

U.S. Naval Research Laboratory, Washington, D.C. 20375-5000

A. Hauer

Los Alamos National Laboratory, Los Alamos, New Mexico 87545

J. E. Swain and P. J. Solone

Lawrence Livermore National Laboratory, Livermore, California 94550

Multikilobar shocks were launched into a single crystal of (111) silicon coated with 1000 Å of aluminum and a 25-μm transparent plastic layer by irradiation with a 1-nsec pulse of 1.06-μm laser light at 0.8–8 J cm^{-2}. Peak lattice compressions were directly measured and shocked-lattice stresses inferred as a function of irradiance and time by Bragg-diffracting a short (< 100 psec) burst of probing x rays through the shock-launching region. Compressions of up to $\sim 4\%$ were measured, corresponding to stresses of the order of 70 kbar, at irradiances of $\sim 4 \times 10^9$ W cm^{-2}.

The laser generation of shocks encompasses a wide range of physical processes and effects,[1-3] since virtually every property of condensed matter can be altered with pressure. For the more conventional shock-driving mechanisms, the shock-launching region, i.e., the initial layer of compressed material, is obscured by the driving mechanism. While laser-driven shocks do not present this limitation, so far *direct* measurements of the lattice spacing of the impact surface have been interactable. Such measurements are of importance because many physical phenomena not in agreement with classical dislocation theory, such as elastic-plastic interactions, originate at this surface.

In this Rapid Communication we report results of an experiment in which, for the first time, we have probed the initial[4,5] micrometers of the shock-launching region in a crystal lattice with pulsed x rays, and directly observed the spatial and temporal evolution of lattice compression and subsequent relaxation in one dimension of Bragg x-ray diffractometry. We observe the existence of a range of compressions (lattice spacings) in the launch phase, and have also examined the experimentally determined peak compression as a function of laser irradiance.

The use of x rays to measure the compression of shocked materials was first performed by Johnson, Mitchel, Keeler, and Evans in the early 1970s.[4] They shocked LiF to several hundred kilobars using conventional explosive techniques,[5,6] and diffracted a 40–50-nsec pulse of x rays[7] off the shocked material. However, to our knowledge, the work presented here is the first of a similar nature to be presented since then, with a 500-fold improvement in temporal resolution, and it is the first time that either the spatial or temporal development of the compression within the launch region has been studied directly.

The experiment was performed on the JANUS research laser system at the Lawrence Livermore National Laboratory, California. The experimental setup is shown in schematic form in Fig. 1. The shocked targets consisted of 250-μm-thick (111) silicon wafers 5 cm in diameter, the surface of which had been coated first with 1000 Å of aluminum and then with 25 μm of plastic (CH). The motivation for such a target design is explained below. Half of the target was irradiated to a vacuum by a (1 ± 0.05)-nsec pulse of 1.06-μm laser light at an irradiance varying from 0.8 to 8 J cm^{-2} with a beam diameter on target of 3.9 cm. A beam block prevented irradiation of the other half of the target; diffraction from this unshocked region gave us a reference point from which to measure the changes in Bragg angle. After the shock had been launched in the silicon crystal, a second laser beam containing ~ 10 J of 0.53-μm light in 100 psec, which was synchronous with known and variable delay with respect to the shock-launching beam, was focused to a ~ 40-μm-diam spot on a second, calcium-containing target. The
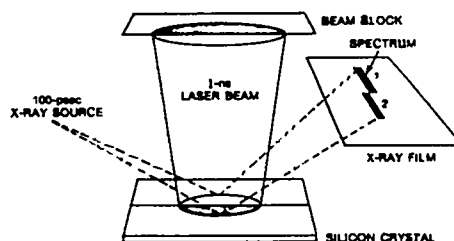

FIG. 1. The experimental setup showing schematically the x-ray diffraction from the (1) unshocked and (2) shocked crystal.

COMPUTERIZED 3-GHz MULTICHANNEL SOFT X-RAY DIODE SPECTROMETER FOR HIGH DENSITY PLASMA DIAGNOSIS *

G. PIEN and M.C. RICHARDSON

Laboratory for Laser Energetics, University of Rochester, 250 E. River Road, Rochester, NY 14623-1299, USA

P.D. GOLDSTONE, R.H. DAY, F. AMEDURI and G. EDEN

Los Alamos National Laboratory, University of California, P.O. Box 1663, Los Alamos, NM 87545, USA

Investigations of high density plasma conditions, particularly those used in laser fusion and X-ray laser schemes often demand a quantitative characterization of the X-ray spectral emission in the 100–2000 eV range covering the peak of the thermal radiation energy distribution. We describe a 3 GHz bandwidth, 4-channel soft X-ray diode spectrometer coupled to a computerized digital oscillographic system. The characteristics of this system, and examples of its use in high density plasma experiments are described in detail.

1. Introduction

The analysis of transient high density plasmas such as those produced by high power lasers and pulsed power systems often demand a precise quantitative characterization of the emitted soft X-ray emission. In many cases, such a characterization provides a reliable estimate of the total radiated X-ray flux, and this has important implications on the radiation and electron thermal transport within the plasma, and affects the mechanisms responsible for energy absorption, wave propagation, and hydrodynamic instabilities in the plasma. In high density plasmas these processes occur on a nanosecond time scale. These considerations are behind the need for a calibrated, broadband soft X-ray (100–2000 eV) spectrometer having a signal bandwidth sufficient to resolve subnanosecond emission features.

There are, in principle, two architectural approaches to satisfying this requirement for subnanosecond resolution broadband soft X-ray spectrometry on high density experiments. In many respects they are complimentary. The first approach, implemented at several major high density plasma facilities, involves the use of a number of calibrated X-ray diodes [1] separately filtered for

different bands of the soft X-ray region by the incorporation of either K-edge, L-edge, or M-edge filters [2–4] or specific bandpass X-ray mirrors coated with reflective multilayer structures [5]. The stability of the simple metal cathodes used in the X-ray diode has been studied in detail [6]. With a few exceptions the calibration stability of most metal cathodes has been found to be constant over lengthy periods of time (several months) under the typical experimental conditions necessitating frequent vacuum cycling and occasional exposure to oxygen, air, and other elements. Unless special care is taken to minimize the X-ray response time, such as with the diodes developed by Kornblum [7] and Day [8], the majority of X-ray diodes have response times of nanoseconds or longer. A spectrometer incorporating diodes having subnanosecond time resolution significantly increases the complexity of the overall system. The diodes themselves must be impedance matched to maintain the signal integrity, and a GHz signal detection system must be used. The fastest readily available commercial oscilloscopes have detection bandwidths of ~ 1 GHz [9], though a special system has been built in France by Intertechnique and Hyperlec with a bandwidth ~ 7 GHz [10].

An alternative approach to establishing time-resolved broadband soft X-ray spectrometry with much greater (~ 10 ps) temporal resolution is through the incorporation of an X-ray streak camera [11] with an X-ray energy filter system, such as a set of K-edge, L-edge, or M-edge filters [12] or an array of multilayer mirrors [13], or with a weak X-ray dispersive element

Fast ions and hot electrons in the laser–plasma interaction

S. J. Gitomer, R. D. Jones, F. Begay, A. W. Ehler, J. F. Kephart, and R. Kristal
University of California, Los Alamos National Laboratory, Los Alamos, New Mexico 87545

Data on the emission of energetic ions produced in laser–matter interactions have been analyzed for a wide variety of laser wavelengths, energies, and pulse lengths. Strong correlation has been found between the bulk energy per AMU for fast ions measured by charge cups and the x-ray-determined hot electron temperature. Five theoretical models have been used to explain this correlation. The models include (1) a steady-state spherically symmetric fluid model with classical electron heat conduction, (2) a steady-state spherically symmetric fluid model with flux limited electron heat conduction, (3) a simple analytic model of an isothermal rarefaction followed by a free expansion, (4) the LASNEX hydrodynamics code [Comments Plasma Phys. Controlled Fusion 2, 85 (1975)], calculations employing a spherical expansion and simple initial conditions, and (5) the LASNEX code with its full array of absorption, transport, and emission physics. The results obtained with these models are in good agreement with the experiments and indicate that the detailed shape of the correlation curve between mean fast ion energy and hot electron temperature is due to target surface impurities at the higher temperatures (higher laser intensities) and to the expansion of bulk target material at the lower temperatures (lower laser intensities).

I. INTRODUCTION

The emission of energetic ions from laser-produced plasmas has been a consistent observation in laser–matter interactions since the early 1960's.[1] As more powerful lasers were built and used as research tools, the amount of energy partitioning to fast ions was determined to be substantial, especially for longer wavelength lasers.[2] It has been proposed[3] that self-generated magnetic fields produced in laser–matter interactions effectively insulate fast electrons from the surface of the target, and the resulting space charge electric field produced away from the laser spot acts to accelerate large numbers of ions into the blow-off plasma. For direct drive laser fusion, this loss to fast ions can reduce useful absorption to low levels.[4–6] It has been suggested, however, that the energy in fast ions might be harnessed in targets specifically designed to recapture this ion energy.[7] It has also been suggested that laser-produced fast ions might be useful in plasma heating for some types of magnetic confinement fusion reactors.[8]

By energetic or fast ions we mean the most energetic ions found in a particular experiment, observed for example by charge or Faraday cups[9] or by Thomson ion spectrometers.[10] Observed energies are typically in the keV–MeV range. We confine our attention here to results obtained from charge cup or Faraday cup detectors in which the several peaks seen in the current versus time oscilloscope records can be roughly lumped into (a) a "fast ion peak" arriving at an early time and (b) a "plasma peak or series of peaks" arriving at later times.

In this paper, we examine measurements of energetic ions from the Los Alamos National Laboratory eight-beam Helios CO_2 laser facility[11] and from laser–matter interaction experiments carried out at 25 other laboratories to determine to what extent a correlation may be obtained between the measured mean fast ion energy (determined from the fast ion current peak), the laser intensity, and the electron

temperature as measured from the slope of the bremsstrahlung x-ray spectrum. When two or more slopes are present in the x-ray data, we take the electron temperature from the slope that would give the highest temperature. Specifically, we find (1) a strong correlation between the mean fast ion energy as determined from the time of peak fast ion current and the hot electron temperature and (2) that this correlation seems to be independent of target material, target size, laser wavelength, laser pulse length, and laser focal conditions.

The experimental data are compared with five theoretical models: (1) a steady-state fluid model in spherical coordinates with classical thermal conduction assumed,[12] (2) a steady-state fluid model in spherical coordinates with flux limited thermal conduction assumed,[13] (3) a simple analytic model involving an isothermal rarefaction allowed by a ballistic expansion, (4) the large scale hydrodynamics code LASNEX,[14] assuming a spherical expansion and simple initial conditions, and (5) a LASNEX model using a more complete physics model with laser light deposition, ponderomotive force, radiation emission, and hot electron transport. These models yield results that compare well with the experimental data presented.

II. EXPERIMENTAL RESULTS

A. Evidence for surface contamination of laser targets

Before discussing the experiments, we will first explore a number of studies that support the claim that there is important and measurable target surface contamination in laser–matter interaction experiments. As early as 1968, x-ray spectroscopic studies of laser produced plasma[15] showed the presence of hydrogen (from vacuum pump oil) and copper (from the extrusion fixture) in experiments on solid-deuterium targets. Ehler and Linlor,[10] using an electrostatic particle analyzer, were able to identify light element contaminants (carbon, nitrogen, and oxygen) in laser experiments on

Absorption-spectroscopy diagnosis of pusher conditions in laser-driven implosions

A. Hauer and R. D. Cowan

Los Alamos National Laboratory, University of California, Los Alamos, New Mexico 87545

B. Yaakobi, O. Barnouin, and R. Epstein

Laboratory for Laser Energetics, College of Engineering and Applied Science,
University of Rochester, 250 East River Road, Rochester, New York 14623-1299

Absorption spectroscopy has been used in this work to diagnose the conditions in the pusher of laser-imploded targets. Absorption lines are produced when continuum radiation from the hot central compressed gas passes out through the colder surrounding pusher. They can be used to determine both the temperature and the $\rho \Delta R$ product of the pusher around peak compression. Fair agreement is found between the experimental absorption spectra and simulations calculated by a hydrodynamic code. Applications of this work to the diagnosis of future, high-compression implosions is discussed.

I. INTRODUCTION

The use of emission spectroscopy for diagnosis of conditions in the compressed gas core of laser-imploded targets has received considerable attention.[1] Another important problem is the characterization of the pusher shell containing the fill gas. The temperature in the pusher is often too low (≤ 100 eV) for self-emission to be useful as a diagnostic. This is because to probe such low temperatures we would need to detect lines of low-Z species. However, these low-energy lines will be heavily absorbed by photoionization in a sufficiently dense or thick tamper, thereby preventing such a measurement. As an alternative we have investigated the use of absorption spectroscopy in pusher characterization. Experiments were performed with CO_2-laser-imploded targets which demonstrate the utility of this technique for future laser fusion experiments.

High temperatures (≥ 1 keV) are often obtained in the central gas core of laser-imploded targets. Under these conditions, the continuous x-ray emission from the core passes out through the pusher and undergoes absorption at wavelengths characteristic of atomic species in the tamper. A schematic diagram illustrating this effect is shown in Fig. 1. The resulting absorption lines can yield information on the temperature (T_e), density (ρ), and the $\rho \Delta R$ product (density times thickness) of the tamper.

Particularly, strong absorption can be caused by resonance line transitions of the type $1s$-$2p$ in ions which have one or more vacancies in the $n = 2$ shell; these are thus inner-shell transitions. The optimal choice of tamper species for this method is such that at the prevailing tamper temperature, ionization will remove some of the L-shell ($n = 2$) electrons, as well as all electrons of higher shells. For the present experiment, potassium and chlorine bracketed the range of anticipated temperatures, and therefore a KCl absorption layer was embedded within the tamper. Chlorine and potassium absorption lines were indeed observed and used to determine the con-

ditions within the KCl layer, and by inference, within the rest of the tamper.

The method of using pusher (tamper) absorption lines was previously reported by Yaakobi *et al.*[2] at the Laboratory for Laser Energetics (LLE) and by Hauer[3] and collaborators at Los Alamos National Laboratory. Bradley, Hares, and Kilkenny at Rutherford Appleton Laboratory reported on similar observations in planar targets. We discuss below the advantage of using absorption by higher-Z ions and analyze the results in more detail than has been previously done. The values of T_e and $\rho \Delta R$ derived from the experiment are in fair agreement with those predicted by the LASNEX laser-fusion code.

Absorption spectroscopy provides the same information as the neutron-activation technique[5] (such as that using ^{28}Si), namely the $\rho \Delta R$ product of the target pusher. Absorption spectroscopy, can, however, provide more detailed information on density and ρR. In addition, it can be used for temperature measurements. The method can be further enhanced by time resolving the spectra. Furthermore, the method can also be extended to the backlighting mode, by using an external continuum source. In this case, the parameters of the fuel can also be determined if a high-Z dopant is used. More importantly, the method
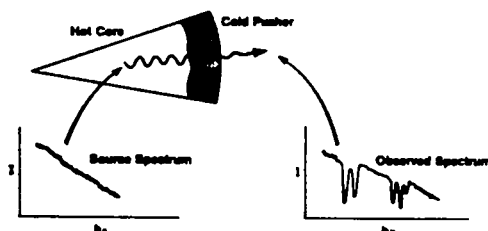

FIG. 1. Schematic representation of the measurement of cold-pusher parameters through the observation of absorption lines in a continuum emitted by the hot compressed core.

X-ray spectroscopic methods for the diagnosis of laser-imploded targets (invited)

B. Yaakobi, O. Barnouin, M. C. Richardson, and J. M. Soures

Laboratory for Laser Energetics, University of Rochester, 250 East River Road, Rochester, New York 14623-1299

A. Hauer

Los Alamos National Laboratory, Los Alamos, New Mexico 87545

Benjamin Post

Polytechnic Institute of New York, Physics Department, Brooklyn, New York 11201

(Presented on 13 March 1986)

Several methods involving x-ray spectroscopic methods for diagnosing laser-imploded targets are discussed. The first method involves the recording of absorption lines formed in the target tamper, out of the continuum emitted by a hotter compressed core. This method is applied to ablatively imploded targets having a thin KCl signature layer. The tamper $\rho\Delta R$ is deduced from the area within the absorption lines, whereas the tamper temperature is deduced from the intensity distribution among absorption lines of adjacent charge states. In a second method, doubly diffracting crystals can give two-dimensional monochromatic images of thin signature layers in spherical targets. Such information is useful in studying stability and mixing. Experimental results relevant to these methods will be shown and the limitations on their application to laser-target experiments will be discussed.

I. X-RAY ABSORPTION LINES IN LASER-IMPLODED TARGETS

High temperatures ($\gtrsim 1$ keV) are often obtained in the central gas core of laser-imploded targets. Under these conditions, the continuous x-ray emission from the core passes out through the pusher and undergoes absorption at wavelengths characteristic of atomic species in the tamper. The resulting absorption lines can yield information on the temperature (T_r), density (ρ), and the $\rho\Delta R$ product (density times thickness) of the tamper. Particularly, strong absorption can be caused by resonance line transitions of the type $1s$-$2p$ in ions which have one or more vacancies in the $n = 2$ shell; these are thus inner-shell transitions. The optimal choice of tamper species for this method is such that at the prevailing tamper temperature, ionization will remove some of the L-shell ($n = 2$) electrons, as well as all electrons of higher shells. For the present experiment, potassium and chlorine bracketed the range of anticipated temperatures, and therefore a KCl absorption layer was embedded within the tamper. Chlorine and potassium absorption lines were indeed observed and used to determine the conditions within the KCl layer, and by inference, within the rest of the tamper.[1]

The targets used in this study (see Fig. 1) were imploded with the eight-beam Helios CO_2 laser system at the Los Alamos National Laboratory. The total laser energy was about 4.5 kJ in a pulse of a FWHM of about 650 ps. The imploded gas core reaches electron temperatures of about 700 eV, which excites a strong continuum around 3 keV (as well as 3–4-keV argon lines), which is a prerequisite for observing chlorine absorption lines. The relative position of the embedded KCl layer within the target is such that by the

time of peak compression, most or all of the CH layer (but none of the KCl layer) has been ablated.

Figure 2 shows an example of the spectra emitted by these imploded targets. The contrast between strong Ar emission lines and strong Cl absorption lines vividly demonstrates a hot compressed core surrounded by a cooler shell.

Figure 3 shows in more detail the chlorine absorption structure. The identification of these line complexes was made by comparison with Hartree–Fock atomic structure calculations.[1] As an example, the line marked B in Fig. 3 corresponds to transitions of the type $1s$-$2p$ in boronlike chlorine (Cl^{+12}), i.e., $1s^2 2s^2 2p$-$1s 2s^2 2p^2$; we likewise refer to other lines as the Be or the C feature, etc. For each configuration there can be several atomic states. For example, the B feature includes 14 transitions, the C feature contains 35 transitions.

The tamper temperature at the time of strong continuum emission from the core can be inferred from the intensi-
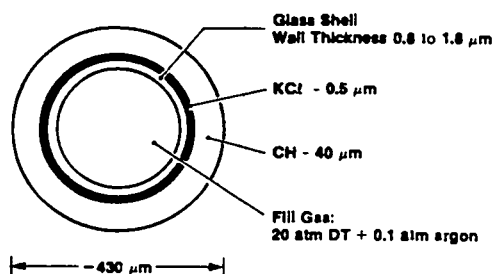

FIG. 1. Typical target parameters used in this experiment

Studies of x-ray switching and shuttering techniques

J. S. Wark

Laboratory for Laser Energetics, University of Rochester, New York 14623

A. Hauer

Los Alamos National Laboratory, Los Alamos, New Mexico 87545

J. D. Kilkenny

Lawrence Livermore National Laboratory, Livermore, California 94550

(Presented on 13 March 1986)

Experimental studies have been conducted on the changes in x-ray diffraction properties of crystals under intense subnanosecond laser heating. One beam of the PHOENIX laser system was used to create an intense source of x-ray line radiation. This radiation was, in turn, diffracted from a silicon crystal that was heated with the other beam of the laser. The diffracted radiation was temporally resolved with an x-ray streak camera. The diffracted lines are observed to broaden on a subnanosecond time scale. From the temporal structure of the diffracted radiation, information is derived on the nature of the laser heating process. We show that such interruption of the diffracting process is a potentially useful mechanism for x-ray switching and shuttering. Considerations for the design and construction of such devices are discussed.

INTRODUCTION

Several techniques for switching x rays have been known for several years.[1,2] Until now these techniques have only been experimentally demonstrated on the tens of nanoseconds time scale. We report on a method of switching x rays on the time scale of hundreds of picoseconds. An intense source of line radiation is produced for a period of 1 ns by focusing a high-power laser beam onto a target containing the appropriate element. The x-ray lines of interest are then Bragg reflected off the diffracting crystal. During the x-ray pulse a second laser beam, synchronous and delayed with respect to the first, illuminates the crystal. The subsequent large temperature gradient induced in the crystal gives rise to a thermal strain which significantly broadens the rocking curve of the crystal and reduces the peak reflectivity. The angular distribution of the diffracted radiation is thus altered, and with appropriate beam blocks, both on–off and off–on switching of x-ray line radiation should be obtained on the time scale of the thermal strain induction, as will be described below. Time resolved x-ray diffraction studies on the tens of nanoseconds time scale have previously been performed using a similar technique.[3]

In this article we shall report measurements of the broadening of the rocking curve of an illuminated silicon crystal, and from this infer the switching ratios that could be obtained.

I. EXPERIMENT

The experiment was performed using the PHOENIX laser system at the Lawrence Livermore National Laboratory, California. One beam of the laser, containing 25 J of 0.53-μm light in a pulse of FWHM 1 ns, was focused down to a spot of 30 μm diameter onto a PVC target. This produced an intense source of the resonance line of heliumlike chlorine at

4.44 Å. This radiation was diffracted off a silicon (111) crystal into a x-ray streak camera using a CsI photocathode. During the diffraction process the crystal was illuminated at an irradiance of about 1 J cm^{-2} of 1.05-μm light, covering approximately 10 cm^2 of the crystal surface.

The experimental data are shown in Fig. 1. Figure 1(a) shows the temporally resolved spectrum of the radiation diffracted from an unirradiated crystal. The two lines are the resonance and intercombination line of heliumlike chlorine.
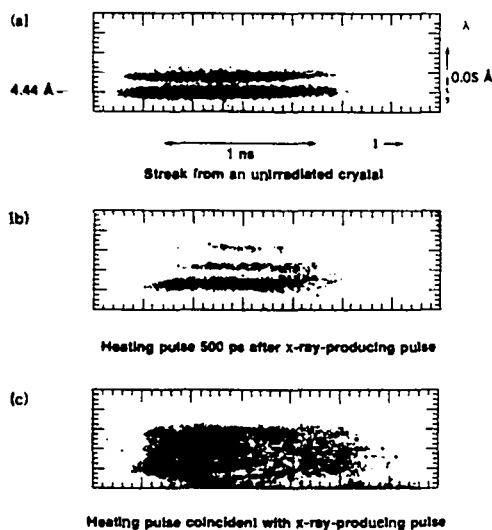

FIG. 1. (a) Time-resolved x-ray spectrum from a crystal with no heating pulse, (b) heating pulse 500 ps after x-ray producing pulse, and (c) heating and x-ray producing pulses coincident.

TIME-RESOLVED X-RAY DIAGNOSTICS FOR HIGH DENSITY PLASMA PHYSICS

STUDIES

M.C. Richardson, G.G. Gregory, R.L. Keck, S.A. Letzring
R.S. Marjoribanks, F.J. Marshall, G. Pien, J.S, Wark,
and B. Yaakobi
Laboratory for Laser Energetics
University of Rochester
250 East River Road
Rochester, New York 14623-1299

P.D. Goldstone, A. Hauer, G.S. Stradling, and F. Ameduri
Los Alamos National Laboratory
University of California

B.L. Henke and P.A. Jaanimagi
Lawrence Berkeley Laboratory
University of California

ABSTRACT

Investigations of the many transient features of the high density
plasmas produced in laser fusion and x-ray laser studies have stimulated
the development of many x-ray and XUV diagnostic techniques. We review
here a broad range of x-ray diagnostic instrumentation to spatially,
spectrally and temporarily resolve x-ray emission from plasmas of direct
interest to laser fusion, high density atomic physics studies and x-ray
laser investigations performed at the OMEGA irradiation facility over the
past few years.   Several categories of instruments are described,
including   time-resolving   x-ray   crystal   and   transmission   grating
spectrographs, soft and hard x-ray spectrometric systems, a streak x-ray
photographic   system,   and   approaches   to   fast-time   framing   x-ray
photography, radiography and spectroscopy.   The primary characteristics
of each approach are described and illustrated with typical data drawn
from experiments performed on the 24-beam IR (1054/nm) and UV (351 nm)
OMEGA system.

1.0 INTRODUCTION

The study of transient microscopic high density plasmas such as
those intrinsic to laser fusion and various x-ray laser schemes has for
many years, pressed the limits of x-ray diagnostic capabilities.   The
stiff requirements of micron (even submicron) spatial resolution,
picosecond time resolution, and calibrated recording sensitivity, in some

TURBULENCE IN MULTIPHASE FLOW [*]

D.C. BESNARD [x]

Centre d'Etudes de Limeil

BP 27, 94190 Villeneuve St Georges, France

F.H. HARLOW

Theoretical Division

The University of California

Los Alamos National Laboratory

Los Alamos, NM 87545

[x] Visiting Staff member, Los Alamos National Laboratory

ABSTRACT

We describe in this paper a two-field turbulent flow model, valid for dispersed particles in an incompressible carrier fluid. This model gives the required features, such as mass diffusion, damping of the turbulence in the second fluid due to the presence of the particles, and decay of the turbulent kinetic energy.

ANALYSIS OF SHOCK-INTERFACE AND SHOCK-TURBULENCE
INTERACTIONS BY DIRECT SIMULATION AND TURBULENCE
TRANSPORT MODELING

Didier Besnard and Jean-Francois Haas
Centre d'Etudes de Limeil-Valenton, BP 27,
94190, Villeneuve-St-Georges FRANCE
and
Rick Rauenzahn
Los Alamos National Laboratory, Group T-3, MS B216
Los Alamos N.M. 87545 USA

ABSTRACT:

We present three methods of analyzing shock-interface and shock-
turbulence interaction: direct simulation, turbulence transport with a
full Reynolds tensor, variable density transport model, and a newly
developed "k-ε-ρ'²" model. Using direct simulations performed with the
2D FCT code EAD, we discuss here the structure of the flow produced by a
shock-interface interaction as well as shock-mixed region interaction,
as obtained in shock-tube experiments. Boundary layer effects, a
prominent feature of such experiments, are examined using the 2D ALE
CAVEAT code, in which the simplified model mentioned above was
implemented.

I-INTRODUCTION

Turbulence modeling has long been an indispensible tool for
examining complex flows. More recently their applications have been
extended to circumstances involving several compressible materials. As a
result, Reynolds-stress transport closure models have evolved /1,2/.
Quantitative assessment of these models in general flows is still quite
limited, primarily due to their complexity and the questionable
improvement in performance over that of standard "k-ε" models and their
derivatives. This paper is an attempt to look at shock-interface and
shock-turbulence interaction by combining the two approaches of
turbulence modeling and highly resolved direct simulations.

ON THE MODELING OF TURBULENCE FOR MATERIAL MIXTURES.

D.C. BESNARD*
Commissariat à l'Energie Atomique, Centre d'Etudes de
LIMEIL-VALENTON, BP27, 94190, VILLENEUVE-St-GEORGES,
FRANCE

R.M. RAUENZAHN and F.H. HARLOW
Los Alamos National Laboratory, Theoretical Division.
Group T-3, MS B216, LOS ALAMOS N.M. 87545, USA

Normal acceleration and/or tangential slippage at a de-
formable interface can result in the unstable amplifica-
tion of pertubations, the creation of turbulence, and
considerable mixing of mass, momentum and energy. Analy-
sis of these processes is accomplished by means of single
field statistical transport theory for a material with
large density variations.

1. INTRODUCTION

Fluid dynamics instabilities can occur whenever there is an
excess of large-scale energy in the coordinate system of mean
flow. If this excess energy is kinetic, then it may transform
directly to heat, provided that viscous dissipation is sufficien-
tly large ; the creation of disordered energy is immediately ma-
nifested at the smallest possible scale, that of molecular fluc-
tuations. More commonly this inevitable transition from order to
disorder takes place through an intermediate set of length scales;
turbulence eddies are formed and the energy cascades through a
progression of smaller and smaller sizes on its way towards the
purely molecular fluctuations. When turbulence occurs, the mean-
flow profiles of mass, momentum, and energy density can be pro-
foundly altered. In particular, we investigate turbulence and its
effects near the interface between two different mean-flow
states.For some years,the use of turbulence models was devoted to
single fluid, incompressible flow. Although tensor models were
first proposed /1/, "k-ε" models, composed of equations for the
turbulent kinetic energy and its dissipation rate /2,3/ were soon
preferred, for the sake of simplicity and reducing computing
cost. These models were mostly used for shear layers. Recently,
models for instability-induced turbulence in mixtures have been
developed /4,5,6/ including the effect of large density gradients
in the mean flow. Our approach of interface turbulence problem
is based on the statistical transport equations for a single
field with the two material properties represented by a concen-
tration variable. This model is presented in Section 2 and its
theoretical analysis in Section 3. In particular, we show that it
can describe the different phases of instability-driven fluctua-
ting energy growth, exponential at first, then turning into a
late time, self-similar phase ; In the limit of well defined.
two-field interpenetration. (this occurs only if the local

_____

*Visiting Scientist, Los Alamos National Laboratory, Group T.3.

Modeling, measurements, and analysis of x-ray emission
from 0.26-μm-laser-irradiated gold disks

W. C. Mead and E. K. Stover

Los Alamos National Laboratory, Los Alamos, New Mexico 87545

R. L. Kauffman, H. N. Kornblum, and B. F. Lasinski

Lawrence Livermore National Laboratory, Livermore, California 94550

(Received 10 August 1987; revised manuscript received 18 July 1988)

We present modeling, measurements and analysis that extend our understanding of laser-plasma coupling and x-ray conversion processes to shorter laser wavelengths at kilojoule energies. We have studied the x-ray emission from gold-disk targets irradiated at 0.26-μm wavelength, using 0.5–1.5-kJ, 1-ns full width at half maximum Gaussian pulses at intensities of 1×10^{14}–2×10^{15} W/cm^2. We interpret measurements of the absolute broadband x-ray spectrum, the time history of sub-keV x-ray emission flux, and the broadband hard-x-ray spectrum. We find negligible hot-electron levels ($< 10^{-3} E_{inc}$). We infer increased conversion of incident light to soft x rays (72%±15% at 1×10^{14} and 38%±12% at 2×10^{15}), compared with longer wavelengths, as predicted. We find good overall agreement between the modeling and the data, but identify some areas that need to be better understood, including certain aspects of the x-ray emission spectrum and the decay rate of the emission pulse.

I. INTRODUCTION

The interaction of submicrometer laser light with high-Z plasmas presents a fascinating, complex interplay of diverse physical processes. Moreover, the efficiency of conversion of submicrometer laser light into soft x rays is important in determining the performance of x-ray driven inertial confinement fusion (ICF) targets.[1] As a result, considerable effort has been devoted to understanding the mechanisms involved in laser-plasma coupling and x-ray conversion.

When a laser is incident on a high-Z target at high intensities, a plasma corona quickly forms. For submicrometer-wavelength laser light at peak intensities below about 10^{15} W/cm^2 and for high-Z target plasmas, the light is efficiently absorbed near or below its critical density by strong inverse bremsstrahlung collisional absorption. Inverse bremsstrahlung primarily heats the bulk of the plasma electron distribution, leading to temperatures of several kilo-electron-volts (keV). The energy deposited into the electrons is then transported to the unheated, higher-density regions of the plasma, converted by electron-ion collisions into excitations that lead to x-ray emission, and converted hydrodynamically into convecting ion kinetic energy. The competition among these energy transport and conversion processes depends on the temperatures, scalelengths, and charge states of the plasma, which in turn are self-consistently determined by the irradiation conditions, i.e., intensity, pulse width, and spot diameter, and the laser-plasma coupling processes. Although a detailed understanding of these processes can best be obtained using computer simulations, behavior of the dominant processes can be readily understood by consideration of their basic scaling relationships, to which we shall return in a moment.

The earliest reported observations of laser-plasma coupling for high-intensity irradiations of high-Z targets were those of Shay et al.[2] at 1.06-μm wavelength. They reported efficient conversion of laser light to x rays and noted nonuniform x-ray-emission structures that correspond with structures in the incident laser beam. Rosen et al.[3] used greatly improved modeling and diagnostics, and were the first to discuss the importance of both thermal transport inhibition and non-local-thermodynamic-equilibrium (non-LTE) atomic physics in modeling high-Z target irradiations at 1.06-μm wavelength, for intensities of about 3×10^{14} W/cm^2 or higher. They also showed the first accurate scaling measurements for the intensity dependence of x-ray conversion processes, showing that x-ray conversion efficiency decreases as laser intensity increases. Nishimura et al.[4] performed experimental wavelength scaling studies and reported high-Z target measurements showing x-ray conversion efficiency increasing with shorter laser wavelength in the intensity range of 10^{13}–10^{14} W/cm^2. Their work also included high-Z thin-foil burn-through measurements. Mead et al.[5] reported extensive measurements and modeling of 0.53-μm irradiations of gold- and titanium-disk targets. They, too, found that x-ray conversion efficiency for gold-disk targets increased at shorter wavelengths. Further, Mead et al. found that the wavelength scaling agreed with computer hydrodynamics code predictions (using modeling similar to that of Rosen et al.), except at intensities below 3×10^{14} W/cm^2, where experiments suggested a rolloff, while calculations predicted continued increase.

Recently, experimental and modeling studies of laser-plasma coupling and x-ray conversion in high-Z plasmas have been extended and refined at several laboratories. Various spectrometers have been developed and used to

"Flicker" in small scale laser–plasma self-focusing

S. V. Coggeshall, W. C. Mead, and R. D. Jones

University of California, Los Alamos National Laboratory, Los Alamos, New Mexico 87545

Small amplitude, short wavelength ion acoustic waves in laser-produced plasmas cause fluctuations in the trajectories of light rays that can lead to time-dependent, self-sustaining shifting of focal spots and a somewhat random redistribution of the light near the critical surface. This flickering is seen in simulations involving small scale beam inhomogeneities over a uniform background laser profile, which model the center of a realistic laser beam. The effect can cause significant intensity multiplication in long scale length high-Z plasmas with only modest beam imperfections.

Recently, much effort has been applied to the study of ponderomotive and thermal filamentation of laser light in plasmas,[1] including numerical simulations[2-8] and experimental investigations.[9] Much of the numerical and theoretical work has addressed whole-beam thermal self-focusing, which might be important in large short wavelength laser-produced plasmas. The present paper concentrates on phenomena that can occur on smaller lateral scale lengths; in particular, the effects of small scale laser beam nonuniformities. We find that small scale beam structure can be the source of small amplitude ion sound waves that significantly modify the character of the interaction.[4]

The flicker cycle begins with some source of acoustic waves. In the present work, these are generated by thermal self-focusing of the imposed beam structure. These short wavelength acoustic waves (short compared with the beam size), which both propagate and convect, change the local index of refraction and alter the paths of the light rays. For long scale length plasmas, small-angle deflections can cause significant light trajectory changes deeper into the plasma. Focal spots shift in space, launching new sound waves that, under certain conditions described later, can continue the process. The light reaching the critical surface is somewhat randomly distributed because of the chaotic nature of the feedback mechanism. This "flicker," i.e., the *continually shifting focused intensity distribution with self-sustaining sonic feedback*, could have important implications for the interaction physics. Some transient focusing has been seen before,[3] but this is the first report of a persistent, self-perpetuating shifting of focal spots with a feedback process that causes significant light redistribution at the critical surface.

The calculations were performed using the laser fusion code LASNEX,[10] with two-dimensional Lagrangian hydrodynamics in cylindrical geometry. Maxwellian distributions of ions and electrons were used with flux limited thermal conduction. The laser light was represented through a ray trace technique with inverse bremsstrahlung absorption. Ponderomotive force, diffraction, radiation transport, and ion and electron Landau damping were neglected. The probable consequence of omitting these processes are discussed later.

As a reference case, we consider a gold disk illuminated with an axisymmetric, f/∞ laser at an average intensity of 3×10^{15} W/cm^2. Most previous simulations of this type assumed a smooth radial intensity profile. In reality, laser beams have a great deal of small scale spatial structure. To investigate the effects of this structure, we assume a spatially flat laser profile with a fine scale structure in the center.

Figure 1 shows the radial profile of the laser beam, which propagates in the negative z direction. The beam has a nonuniform section extending to radius $r = 400$ μm, then continues at constant intensity to a fixed boundary at $r \simeq 3000$ μm. This allows the development of the process in a nearly radially homogeneous plasma and minimizes boundary effects. The imposed intensity structure is characterized by a smallest scale size $\lambda_1 = 80$ μm, and a peak to average intensity of about 2:1.

The simplest expected evolution for this problem (using steady-state theory[1]) is that the "hot spots" in the laser profile would, under some circumstances, focus down into separate, steady, focal spots in the plasma. At early times (~ 400 psec), we do indeed see each of the five peaks of the laser structure focusing to high intensity in the plasma. However, at this point the evolution departs from the steady behavior.

As initial focusing occurs, small amplitude sound waves are launched from the focal spots and travel outward in all directions. Since the density perturbations are small (a few percent of the background), the light is refracted only slightly. After the perturbations have moved far enough in z away from the foci, the small-angle deflections of the light shift the focal spots, launching new density fluctuations. Once the flicker cycle is initiated, it becomes self-sustaining. Flicker persists for the entire 3–4 nsec simulation times, even if the nonuniform laser beam is replaced by a uniform beam after flicker begins. This is a long time scale, important for laser fusion applications.

Figure 2 contains three snapshots showing flicker in progress at 2.3, 2.4, and 2.5 nsec. The ray plots show the trajectories of light rays in the central plasma region. Below each ray plot is a contour plot of ion density deviation from
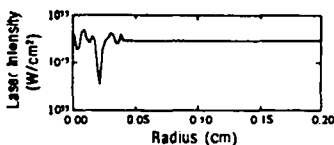

FIG. 1. Radial profile of the laser source.

Magnetic Field Penetration of Erosion-Switch Plasmas

Rodney J. Mason and Michael E. Jones

Applied Theoretical Physics Division, Los Alamos National Laboratory, Los Alamos, New Mexico 87545

John M. Grossmann and Paul F. Ottinger

Naval Research Laboratory, Washington, D.C. 20375-5000

Computer simulations demonstrate that the entrainment (or advection) of magnetic field with the flow of cathode-emitted electrons can constitute a dominant mechanism for the magnetic field penetration of erosion-switch plasmas. Cross-field drift in the accelerating electric field near the cathode starts the penetration process. Plasma erosion propagates the point for emission and magnetic field injection along the cathode toward the load—for the possibility of rapid switch opening.

Plasma-erosion-opening switches (PEOS)[1] are central elements in new inductive-pulsed-power technology that permits the storage of electrical energy magnetically in association with currents, rather than electrostatically. The switches must conduct for a long period, and then open quickly for maximal transfer of power to a load. They are of growing utility in light-ion inertial-confinement fusion and radiation-effects simulation,[2] yet the essential physics of their operation is still under investigation. Plasma convection has long been recognized as important in alternative switch concepts.[3] Our Letter gives new simulation results showing that magnetic advection with the emission electrons can constitute a dominant mechanism for the field penetration of a PEOS.

Experiments performed on the GAMBLE accelerators at the Naval Research Laboratory (NRL) have demonstrated that the magnetic field deeply penetrates the fill plasma in a PEOS prior to its opening.[4] A field equal to the driving intensity is measured at depths at least sixty skin depths within the plasma, and well above the cathode surface. Yet, at a typical density of 10^{13} electrons/cm^3 and an initial temperature of 5 eV the switch plasma is classically collisionless during the 50-ns rise time for the magnetic pulse that drives the experiments. This incongruity has motivated a strong interest in anomalous field-penetration mechanisms.[5]

Explicit particle-in-cell simulations at low densities ($\leq 4 \times 10^{12}$ cm^{-3}) have predicted that electrons cross switches in a narrow current channel.[6,7] Implicit plasma simulations[8] have been performed for more realistic densities,[9,10] with deep penetration of the driving magnetic field observed[10] for fill densities as high as 6×10^{13} cm^{-3}. In this Letter we demonstrate for the first time that such deep penetration of the collisionless plasma can be accomplished by advection (or entrainment) of the driving magnetic field with emitted electrons from the cathode.

Our simulations were performed with the implicit code ANTHEM, used in its three-fluid mode, with the initial plasma ions and electrons as the first two fluids, and the emission electrons as the third. The code's physics and equations are documented in Ref. 8; Ref. 9 describes our emission algorithm. Calculations were in cylindrical geometry. The azimuthal B_θ, axial E_z, and radial E_r electromagnetic fields were calculated by the implicit moment method.[8] We considered the behavior of switches constructed with a fully conducting anode, and so E_z was zero at this electrode. With a high emission threshold (e.g., 300 keV/cm) the PEOS can open rapidly through the formation of a gap by the action of magnetic pressure gradients normal to the cathode.[9] But with zero emission threshold (now thought to be most likely for a cathode bombarded by fill plasma) opening is slower, and accompanied by deeper plasma penetration by the magnetic field.[10] Here, we explain the mechanism for this penetration.

We have carried out global simulations of the Fig. 1 idealization of a switch in use on the PBFAII accelerator at the Sandia National Laboratories. The actual
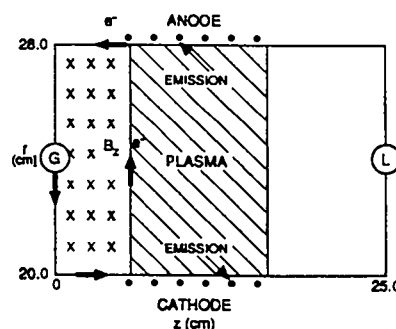

FIG. 1. A generic PEOS for inductive storage. Plasma initially fills the cross-hatched region. G denotes the generator and L the load, here a short circuit.

Three-fluid simulation of the plasma-erosion-opening switch

Rodney J. Mason and Michael E. Jones
Applied Theoretical Physics Division, Los Alamos National Laboratory, Los Alamos, New Mexico 87545

John M. Grossmann and Paul F. Ottinger
Naval Research Laboratory, Washington, DC 20357-5000

The dynamics of the plasma-erosion-opening switch is characterized with the aid of 2D three-fluid simulation using the ANTHEM implicit simulation code, for plasma fill densities ranging from 10^{12} to 6×10^{13} cm^{-3} with 45-ns pulse rise times. The switch behavior is found to depend sensitively on the threshold for electron emission at the cathode, on the detailed structure of the anode with its injection holes, and on the possible action of anomalous resistivity in the fill plasma. Closest agreement with NRL GAMBLE I experimental results is obtained with the combination of zero electric field threshold emission at the cathode, an "open" anode, and modest anomalous resistivity.

I. INTRODUCTION

Plasma-erosion-opening switches (PEOS) allow for the storage of energy in the magnetic field with currents which can be switched from flow through a load to flow through a switch plasma to flow through a load. Inductive storage facilities can be significantly more compact and economical than corresponding capacitive storage facilities. Consequently, the development of efficient plasma-opening switches is of growing importance for advances in pulsed power[1] and light ion inertial confinement fusion.[2] Although the technology of basic plasma-opening switches has existed for nearly 10 years,[3] a fundamental understanding of their operation has been lacking. Early models attributed opening to the formation of an erosion gap near the cathode.[3,4] Later, short-pulse particle simulations ascribed the opening of low-density switches to the $E \times B$ drift[5] of electrons in a diagonal channel across the plasma with magnetic insulation at the anode. Most recently several of us[6] produced a first calculation of a collisionless high density switch (2×10^{13} cm^{-3}) with a high electron emission threshold (300 keV/cm) that opened principally through the formation of a density gap along the cathode through the joint action of erosion and magnetic pressure.

The present paper demonstrates that while this mix of opening scenarios is possible, the actual behavior of a particular switch will depend sensitively on at least the following parameters: (1) the emission threshold for electrons at the cathode, (2) the detailed 3D structure of the anode with its guns and entrance holes for injected plasma, and (3) the action of instabilities in the fill plasma.

We have assumed that space-charge-limited emission prevails. We find that when the emission threshold exceeds 250 keV/cm a large density gap rapidly develops near the cathode (for switch plasma densities above 7×10^{12} cm^{-3}); shielding currents flow along the bottom of this gap, at first in the direction of the generator. Alternatively, for thresholds below 30 keV/cm gap formation is delayed, and emission currents are launched with an inclination in the direction of the load. When the anode is treated as a perfect conductor, we observe that the electrons are magnetically insulated from entering it, and a large density gap forms near the anode from the Z-pinchlike compression of the plasma.

But when we mock up the 3D presence of injection holes for the plasma as an "open" boundary by rendering the anode-parallel electric field component continuous (rather than zero), no magnetic insulation occurs, and no anode gap forms. Gap formation at either electrode allows for magnetic field penetration and eventual switch opening. Anomalous resistivity[6] can represent instabilities suppressed by the numerics in our calculations. We find that an effective anomalous collision rate no greater than $0.1\omega_p$, where ω_p is the local plasma frequency, significantly straightens and broadens the contours of the magnetic field penetrating the fill plasma.

At present there is no best choice for these parameters, so we have attempted to set them by simple comparison with the magnetic field penetration data from early experiments at the Naval Research Laboratories.[7] Best agreement is obtained with the combination of a zero-cathode-emission threshold, an open anode boundary condition, and the limited anomalous collision rate. These choices give rise to broad vertical current sheets across the switches, seen also in recent experiments.[8]

II. THE MODELING

Figure 1 is a sketch of the idealized switch examined. Current is provided by the generator "G" at the left. Electron flow runs along the cathode at the bottom, up across the generator side of the plasma, and back along the anode to G, following the arrows. The resultant magnetic field is directed into the page. The early-time electric field points down toward the cathode. Later, when the switch is an *open* state, the passage of electrons across the plasma is inhibited by magnetic insulation, so their flow is constrained to continue along the cathode, up through the load "L," then back along the anode to G. For the present calculations the load is a short circuit. The generator current rises linearly over 45 ns to 100 kA. For the actual cylindrical geometry the magnetic field $B(r,t)$ (T) $= 0.02I(t)$ [kA]/r(cm). This corresponds to a peak field of 0.8 T (8 kG) at the $r = 2.5$ cm cathode position. Our idealized geometry is Cartesian, so we set the magnetic field at the generator boundary to the cylindrical $B(r,t)$ at $r = 2.5$ cm. The fill plasma consisted of carbon

MAGNETIZED FUEL INERTIAL CONFINEMENT FUSION*

D.P. KILCREASE (University of Florida,
Miami, Florida, United States of America),
R.C. KIRKPATRICK (Los Alamos National
Laboratory, Los Alamos, New Mexico,
United States of America)

ABSTRACT. A more complete radiation treatment is
introduced into the zero-dimensional magnetized fuel inertial
confinement fusion (ICF) model of Lindemuth and Kirkpatrick.
In particular, the effects of synchrotron radiation and the inverse
Compton effect are considered. Only slight changes in the high
gain regions of initial shell velocity, initial fuel density parameter
space were observed. This more complete radiation treatment
removes some objections to the Lindemuth-Kirkpatrick model
and lends further support to the idea that magnetic thermal
insulation can significantly reduce driver requirements for
ICF targets.

1. INTRODUCTION

In 1945, Enrico Fermi reported in some Los Alamos
lectures on thermonuclear fusion about work done by
R. Landshoff [1] on a possible method of reducing
thermal conduction to the container walls in a
deuterium plasma. This heat loss was considered an
important impediment to producing thermonuclear

---

* This work was performed under the auspices of the
US Department of Energy, Contract No. W-7405-ENG-36.

burning. It was pointed out that by imposing a
sufficiently strong magnetic field parallel to the walls,
thermal transport to the walls could be impeded.
Since that early time the magnetic thermal insulation
technique has been employed in only a few ICF
studies [2–5]. The idea is to produce a central region
of preheated low density D-T fuel surrounded by a
dense shell (the pusher). In the preheated region an
azimuthal magnetic field is created, so that when the
target is imploded the magnetic field insulates the
central region from heat loss to the shell.

Lindemuth and Kirkpatrick [3] developed the com-
puter code MAGIT for a zero-dimensional model that
can survey the parameter space for these targets. Their
idea was to take a pessimistic view toward the physical
processes and look for regions of high gain in the
parameter space. These assumptions included low
shell ratio of specific heats, short thermal and
magnetic field gradient lengths, no magnetic
confinement of the fuel, no fusion product energy
deposition, and termination of the calculation
at the free fall limit. The system is described by six
coupled non-linear ordinary differential equations and
appropriate thermonuclear reaction rate equations.
Their approach consisted of fixing all initial para-
meters except the initial fuel density ρ_0 and the initial
shell velocity v_0. These two quantities were then
varied over several orders of magnitude, resulting in
contours of constant gain in (ρ_0, v_0) space. The
magnetic thermal insulation effect creates a region
where gain is greater than one at much lower density-
velocity conditions than the conventional ICF scenario.
This leads to greatly reduced driver requirements.

HEAVY ION BEAM TARGET CORONAL PHYSICS

G.R. MAGELSSEN
Los Alamos National Laboratory,
Los Alamos, New Mexico,
United States of America

ABSTRACT. Numerical calculations of the heavy ion beam interaction with the low density plasma (corona) surrounding a small fusion pellet are discussed. As heavy ions enter the coronal plasma, they lose some of their electrons. and these stripped electrons, called 'drop-offs', constitute an electron beam with approximately the velocity of the ions. The interaction among the heavy ions, the drop-off electrons and the background electrons is investigated. The coronal density and temperature profiles are determined from one-dimensional hydrodynamic calculations, assuming classical ion deposition. The electron–electron and ion–electron cold two-stream instabilities are examined with one-dimensional particle-in-cell calculations. The results suggest that a strong coupling among the heavy ions, the drop-off electrons and the background electrons can exist; this leads to the creation of a non-Maxwellian electron plasma and significant electron heating. The ion beam energy loss is sensitive to the emittance of the beam, to the saturation level of the electric fields generated and to the background density scale length; these effects are discussed. Estimates of ion energy coupling to the corona are made, including the possible impact of target charge buildup; also, the coronal coupling effect on target physics is addressed.

1. INTRODUCTION

In the last few years, serious attention has been given to the possibility of making beams of high energy heavy ions that are capable of producing thermonuclear burn by imploding small targets [1-4]. For a number of years, there have been significant efforts to use laser beams for inertial confinement fusion (ICF). Major laser research efforts in the USA are centred at Los Alamos and Lawrence Livermore National Laboratories, and at KMS Fusion and the University of Rochester; also, there are major research centres in the USSR, Japan and the Federal Republic of Germany. Understanding of laser-target interaction has been and still is a major difficulty for the laser programme. For KrF, CO_2 and neodymium lasers, the most important interaction occurs in the plasma corona — the low density plasma blown off the target surface. A low density corona also exists when heavy ions are used to implode and ignite small pellets. The purpose of this paper is to give a qualitative description of the many and varied physical processes to be expected in ion–coronal plasma interaction, and to examine in one dimension the electrostatic two-stream instabilities that can occur.

Swegle [5] examined the effect of the light ion beam-plasma interaction on ICF targets and found that all the streaming instabilities were benign. Unfortunately, he studied the interaction only for target ion

densities of 5.9×10^{22} and 5.9×10^{20}. At such high densities, the streaming instabilities are suppressed by collisions, by the beam momentum spread and by the small beam-to-background electron density ratio. At lower background densities, it is possible that these effects do not suppress the light ion streaming modes; therefore, the instabilities should be re-examined at lower densities. The most significant differences between light ions and heavy ions concern the beam momentum spread, the beam density and the atomic physics. The beam momentum spread ($\Delta P/P$) of heavy ions is at least an order of magnitude less than that of light ions ($\Delta P/P \sim 10^{-3}$). The heavy ion beam current at the focusing lens is of the order of one kiloampere, whereas the light ion beam current is of the order of one megaampere. For heavy ions, atomic physics plays an important role in evaluating instability growth rates that depend on the current. By stripping all the heavy ion electrons, the heavy ion current can increase by almost two orders of magnitude over its value at the focusing lens. The stripped electrons may also impact the target interaction. The light ions are fully stripped when they reach the propagation channel to the target.

Section 2 presents a calculation which suggests the presence of a plasma corona. An overview of the plasma physics problem is also given. Section 3 discusses the ion–coronal plasma streaming instabilities. One-dimensional particle-in-cell calculations have been performed to determine in a qualitative way the effects

Self-focusing and filamentation of laser light in high Z plasmas

R. D. Jones, W. C. Mead, S. V. Coggeshall, C. H. Aldrich, J. L. Norton, G. D. Pollak, and J. M. Wallace

University of California, Los Alamos National Laboratory, Los Alamos, New Mexico 87545

Self-focusing and filamentation of short wavelength laser light in high Z plasmas of interest to laser fusion are discussed. It is found that self-focusing behavior is very dependent on the details of the characteristics of the laser beam, the plasma conditions, and the energy transport processes. Laser light absorption and self-focusing are strongly competitive processes. At 0.26 μm wavelength the collisional absorption is often so great that there is no intensity amplification of the beam despite the fact that strong self-focusing is present. Wide variations are found in laser light penetration, affected by several factors. Diverging optics reduce the likelihood of self-focusing. Large scale length density gradients have little effect on focusing behavior. The self-focusing behavior is very dependent on beam shape. Large scale hot spots can have a significant effect on whole beam self-focusing early in the pulse. The behavior of small scale hot spots can be qualitatively different than the standard picture. The calculations indicate that small scale hot spots do not achieve a steady state in some cases. Sound waves cause chaotic interactions among neighboring hot spots. It is found that there is little qualitative change when nonlocal thermodynamic equilibrium (non-LTE) radiation and atomic physics are used in the calculations. The nature of the heat flux and thermoelectric magnetic field generation are examined with a kinetic model. Stimulated Raman backscattering levels in self-focused light are significantly reduced for short wavelengths and high Z plasmas. Landau damping plays an important role in determining the Raman levels. Implications for suprathermal electron production, symmetric illumination, x-ray conversion efficiency, and laser light absorption are discussed.

I. INTRODUCTION

The understanding of self-focusing and filamentation of laser light may be important to the success of laser fusion. In the long scale length plasmas envisioned for reactor targets, local intensity hot spots caused by self-focusing or laser light filamentation can drive the plasma above parametric instability thresholds. These instabilities tend to be saturated by the creation of suprathermal electrons.[1] The hot electrons can penetrate deeply into the pellet, heating the interior, making high compressions difficult. Directly driven targets require very uniform driving pressures. Filamentation could spoil this uniformity, making large compressions difficult. The laser light absorption, penetration, and conversion to x rays could also be affected by self-focusing and filamentation.

There are a number of mechanisms that can degrade the uniformity of a laser beam. At very high intensities, the relativistic mass variation of the electrons oscillating in the laser electric field can increase the index of refraction in the center of a beam or in a hot spot in the beam.[2] This leads to focusing that increases the mass variation further, causing the system to go unstable. At high intensities, the ponderomotive force of the laser can drive plasma from the interior of a beam thus raising the index of refraction there, leading to focusing and an instability.[3] Finally, at lower intensities, if the beam or hot spot width is large compared with an electron mean free path, inverse bremsstrahlung heating can raise the pressure in the interior of the beam. The increased pressure drives

plasma out of the beam, once again raising the index of refraction there, leading to instability.[4] The first mechanism, relativistic self-focusing is not of interest to laser fusion. With the intensities, wavelengths, and plasma scale lengths envisioned for reactor targets, little self-focusing is expected from this mechanism. Ponderomotive self-focusing could be important for small scale hot spots. The third mechanism, thermal self-focusing, is important in the focusing of whole beams and large scale hot spots.

There have been a number of experimental investigations of filamentation. Eidmann et al.[5] attributed the nonreproducibility of x-ray emissions to the filamentation instability. Haas et al.[6] were able to image x-ray hot spots and observe an intensity threshold for their formation. Baldis and Corkum[7] used Thomsom scattering and a 0.53 μm probe beam to examine filaments in structured and unstructured beams. Looking at x-ray, $3\omega_0/2$, and $2\omega_0$ emission, Herbst et al.[8] were able to observe four filamentation signatures: (1) localization of light on a finer spatial scale than incident beam nonuniformities; (2) locally higher intensities in these regions; (3) locally lower density in these regions; and (4) the appearance of these effects only at higher intensity. Lin et al[9] obtained time integrated $3\omega_0/2$ images of filamentary structures. Willi et al.[10] obtained Schlieren images and shadowgrams. Additionally, filaments as small as 5 μm have been observed to last for time scales on the order of a few picoseconds.[11] Hydrodynamic jetting,[12] which may be caused by filaments, has also been observed. Willi et al.[13] observed the breakup of an annular beam into a set of filaments with a periodic structure. Localized structures in back

Kinetic theory of electron drift vortex modes

Roger D. Jones

University of California, Los Alamos National Laboratory, Los Alamos, New Mexico 87545

Magnetic electron drift vortex modes are examined using a kinetic theory. The dispersion is found to be much different than that obtained from the fluid theory. For frequencies much smaller than the electron plasma frequency, the waves are heavily Landau damped. The modes are weakly damped at frequencies just below the plasma frequency and hence have an electromagnetic rather than magnetic character.

I. INTRODUCTION

Because of their applications to long wavelength laser fusion,[1] there has been a great deal of interest in plasma surface waves that generate magnetic fields. Electron surface modes that generate magnetic fields through compressional heating of fluid elements were first studied by Pert[2] over a decade ago using magnetohydrodynamic (MHD) theory. As Pert pointed out, however, MHD theory did not permit the propagation of the surface waves over great distances because the phase velocity depended locally on the plasma density. This defect was addressed by Jones[3] who noted that electron inertial effects made the dependence nonlocal and, consequently, distant propagation was permitted. The electron inertial effects manifested themselves in a finite electron fluid vorticity, hence the name "electron vortex mode." Subsequently, Amendt et al.[4] examined the stability of the modes in an accelerating plasma and Yu and Stenflo[5] looked at the stability in the presence of large temperature gradients. Stenflo and Yu[6] noted the similarities of these waves to gradient driven electron acoustic waves and observed that the two modes can be strongly coupled. Shukla et al.[7] studied the parametric excitation of these modes by Langmuir waves and Stenflo et al.[8] investigated the three wave decay into an ion acoustic mode. Nycander et al.[9] examined the nonlinear vortex versions of these surface waves.

To date, all theoretical work is based on a fluid approximation in which the internal electron energy is transported adiabatically. The properties of the surface waves are very dependent on the manner in which the energy equation is treated. If one assumes there is sufficient heat flux to make the plasma isothermal, for instance, the modes disappear. Since the mere existence of the waves depends upon the method of closure of the fluid equations, an examination of the waves using kinetic methods would seem worthwhile. This study attempts to do that. We find that the dispersion is quite different than predicted by the fluid theory. For frequencies much less than the electron plasma frequency, the waves are strongly Landau damped. The modes are weakly damped just below the plasma frequency and are found to have a strong electromagnetic character.

II. MODEL AND SOLUTION

We will assume that the background electron density varies in the x direction. The magnetic field lies in the z direction. The electric field and charge current density lie in the x-y plane. We will look for wave propagation in the y direction. It is assumed that no quantities vary in the z direction. With these assumptions, the linearized Vlasov equation yields for the charge current density

$$\mathbf{J}(\omega,\mathbf{k}) = \int d^3r' \exp(-i\mathbf{k}\cdot\mathbf{r'})\sigma_0(x')$$

$$\times \int d^3v \frac{\omega}{\omega - \mathbf{k}\cdot\mathbf{v}}\left(\frac{\mathbf{vv}}{v_e^2}\right)\cdot\mathbf{E}(\omega,\mathbf{r'})f_0(v), \quad (1)$$

where σ_0 is the collisionless high frequency conductivity given by

$$\sigma_0(x) = in(x)e^2/m\omega,$$

and the zeroth order distribution is taken to be Maxwellian:

$$f_0(v) = \frac{1}{(2\pi)^{3/2}}\frac{1}{v_e^3}\exp\left(-\frac{v^2}{2v_e^2}\right).$$

Here, $v_e = (T/m)^{1/2}$ is the electron thermal speed, e is the absolute value of the electronic charge, and m is the electron mass. The arguments indicate over which variables Fourier transformation has occurred. We are assuming a fixed background ion density. The electrostatic field is related to the density by

$$n(x) = n_0 \exp(e\phi/T).$$

Here, $e\phi$ can be of the order of T. This field has not been included in the particle trajectories, which are represented by the denominator in Eq. (1). We will show *a posteriori* that neglect of this term has no effect on the conclusions of the present paper. The magnetic field does not appear in Eq. (1) since the zeroth order distribution is isotropic.

Equation (1) can be written in terms of the plasma W function[10] as

$$\mathbf{J}(\omega,\mathbf{k}) = \int d^3r' \exp(-i\mathbf{k}\cdot\mathbf{r})$$

$$\times [\sigma_0(x')\mathbf{E}(\mathbf{r'}) - (1 - \hat{\mathbf{k}}\hat{\mathbf{k}})\cdot\sigma_0(x')\mathbf{E}(\mathbf{r'})W(Z)$$

$$- \hat{\mathbf{k}}\hat{\mathbf{k}}\cdot\sigma_0(x')\mathbf{E}(\mathbf{r'})[Z^2 W(Z) + 1]], \quad (2)$$

where $W(Z)$ is

$$W(Z) = \frac{1}{(2\pi)^{1/2}}\int du \frac{u}{u - Z}\exp\left(\frac{-u^2}{2}\right),$$

and Z is

$$Z = \omega/kv_e.$$

DERIVATION OF THE
ION SPHERE SLOWING-DOWN EXPRESSION
FOR INERTIAL CONFINEMENT FUSION

D.B. HARRIS*, G.H. MILEY
Fusion Studies Laboratory,
Nuclear Engineering Department,
University of Illinois,
Urbana, Illinois,
United States of America

ABSTRACT. In the early stages of the burn of an inertial confinement fusion (ICF) target, the plasma parameter g can be greater than one, indicating that the number of electrons in a Debye cube is less than one. Under these conditions, the assumptions used in the classical plasma treatment are not valid. A fusion product slowing-down model is derived for strongly coupled non-classical plasmas and is compared with the classical slowing-down expression. A simple expression for interpolation between the classical region and the non-classical region is proposed. The effect that this new slowing-down expression has on the burn of ICF targets is investigated in a companion paper.

1. INTRODUCTION

The classical treatment of plasmas breaks down when there are less than a few electrons in a Debye cube. Since the plasma parameter g is equal to the inverse of the number of electrons in a Debye cube, this situation is equivalent to plasmas with $g \gtrsim 1$ (Fig. 1). These plasmas are of interest in some special situations of fusion systems, for example the early stages of the burn of high density inertial confinement fusion (ICF) targets. It is important to understand the slowing-down of fusion products under such conditions in order to properly model the thermonuclear burn wave propagation in core ignited ICF targets.

It has recently been proposed [1, 2] that the microscopic electric potential of a high-g plasma can be described by the ion sphere potential [3]. This potential is calculated under the assumption that the ions in the plasma relax into a lattice-like structure while the electrons form a neutralizing cloud around the ions. The calculated potential is then the resultant field, which includes the effect of both ions and electrons. The potential itself has been devised previously [1], but it has not been used to formulate a slowing-down model.

* Present address: Los Alamos National Laboratory,
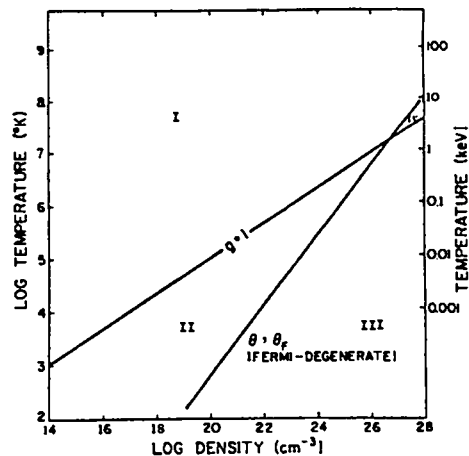 P.O. Box 1663, Los Alamos, NM 87545, USA.

FIG. 1. Plasmas can be divided into four types, depending on the value of the electron density and temperature (which determines the plasma parameter g) and the ratio of the kinetic temperature to the Fermi degenerate temperature. ICF plasmas can fall into any of the categories.

As shown in Fig. 1, the plasmas defined in the density–temperature space can fall into one of four regions, depending on the value of the plasma parameter g and the ratio of the kinetic temperature to the

BURN PERFORMANCE OF
INERTIAL CONFINEMENT FUSION TARGETS

D.B. HARRIS*, G.H. MILEY
Fusion Studies Laboratory,
Nuclear Engineering Department,
University of Illinois,
Urbana, Illinois,
United States of America

ABSTRACT. The effect of the slowing-down rate of fusion products on the burn wave propagation velocity and the inertial confinement fusion (ICF) target yield has been studied. The results indicate that the yield of strongly burning targets is relatively insensitive to the fusion product slowing-down expression. Marginally burning targets are much more sensitive to the fusion product slowing-down rate.

1. INTRODUCTION

In this study, the burn phase of bare D-T and D_2 targets is investigated, first to determine the compressed target conditions required for sufficient burnup of D-T and D_2 targets, and second to investigate the sensitivity of the target yields to variation in the slowing-down ratio dE/dx of the fission products. The first aspect is studied by varying the compressed target ρR, the spark ρR and the initial spark temperature, and by searching for the optimum conditions with respect to fuel gain (defined as the ratio of the yield to the initial thermal energy in the fuel). Two approaches are taken to investigate the sensitivity of the target burn to dE/dx. The first approach involves an analytic study of the effects of varying dE/dx on burn wave propagation. This is backed up by a parametric study of a fixed D-T target, with dE/dx artificially modified. The second approach examines the effect of using a new slowing-down model, the ion sphere interpolation model [1], in a hydrodynamics burn code.

It is easy to show that the yield from a solid density (uncompressed) D-T target is too small to be useful for energy production [2]. It was recognized in 1943 (as part of the fission weapons programme) that improved yields can be achieved by utilizing high compression in spherical geometry [2, 3]. The first mention of using lasers to compress targets to high densities for electrical energy production appears in a 1972 journal article by Nuckolls et al. [4]. After a

* Present address: Los Alamos National Laboratory,
   P.O. Box 1663, Los Alamos, NM 87545, USA.

publication on burn effects by Clarke et al. [2] in 1973, Fraley et al. [3] began the convention of studying the implosion phase and the burn phase separately. This was done in part because the burn phase is independent of the driver (laser or particle beam) and, to a certain degree, the target design. At about the same time, Brueckner and Jorna published an extensive review article [5]; they also separated the burn phase from the implosion phase and discussed the burn performance of a number of targets. Continuing this tradition, Jarvis [6] published in 1976 the results of target burn simulations, again starting from the compressed conditions. Jarvis compared his results with those of Refs [3] and [5]. We will compare the present results with those published in Refs [3, 5] and also with the results of Jarvis [6].

Burn propagation plays an even more crucial role in advanced fuel (non-equimolar D-T) ICF targets. The burn of two types of advanced fuel targets has been described previously. The first study [7] considered the burn of core-ignited targets, with an equimolar D-T mixture heated to 5 keV and a non-equimolar D-T mixture as the outer layer. The second study [8] considered AFLINT targets. These consist of a D-T core at the centre of a deuterium target, and the objective is to minimize the required driver energy while achieving tritium self-sufficiency without breeding tritium in a blanket.

Two types of targets will be considered in this paper. The first type is the equimolar D-T target with a shock-heated core. The other type is a pure deuterium target that is also spark-ignited. The performance of the two targets is first characterized with respect to the

SYNOPSIS OF RESULTS ON SELF FOCUSING AND FILAMENTATION

OF LASER LIGHT IN HIGH-Z PLASMAS

Roger D. Jones, W. C. Mead, S. V. Coggeshall,

J. L. Norton, G. D. Pollak, and J. M. Wallace

Los Alamos National Laboratory

Los Alamos, New Mexico 87545

A. INTRODUCTION

The understanding of self focusing and filamentation of laser light is important
for the success of laser fusion. Reactor plasmas will be very large. Sizes as large
as a centimeter are expected. The electron densities of these plasmas are expected
to be a tenth of the critical density for short wavelength (typically $\lambda \sim 0.25 \ \mu m$)
laser light. In some scenarios, the plasma material is heavy highly ionized material.
Temperatures are typically in the keV range. Stimulated Raman scattering (SRS) may
be important in plasmas of this sort. An unfortunate characteristic of SRS is that it
is often saturated by the production of suprathermal electrons.[1] Only a few kilojoules
of hot electrons can fatally degrade a targets performance by preheating the fuel,
preventing efficient compressions. An important question is whether filamentation and
self focusing can create plasma conditions favorable for the development of SRS and the
production of suprathermal electrons. Also of concern is the effect that filamentation
might have on drive symmetry in some schemes, as well as its effect on backscattering
and absorption. Additionally, beam quality is important for the efficient production
of x-rays.[2]

There are two self focusing mechanisms important for laser fusion, thermal and
ponderomotive. In thermal self focusing the laser creates a temperature gradient trans-
verse to the beam through inverse bremsstrahlung heating. This leads to a transverse
pressure gradient which drives plasma from the beam. The decreased density in the
beam raises the index of refraction which focuses the beam leading to instability.
The thermal instability is important for whole beam self focusing and the focusing of
large sub-beam structures. In ponderomotive self focusing, the laser creates a light
pressure which drives plasma from the beam leading to instability. This mechanism
is important for small sub-beam structure. These mechanisms have been studied
experimentally[3-12] and theoretically.[13-29]

In this paper, we take as a reference case the laser and plasma conditions examined

Collisional effects on the Weibel instability

J. M. Wallace, J. U. Brackbill, C. W. Cranfill, D. W. Forslund, and R. J. Mason

Los Alamos National Laboratory, Los Alamos, New Mexico 87545

The effects of electron Rutherford scattering on the Weibel instability are investigated using the implicit plasma simulation code VENUS [J. Comput. Phys. 46, 271 (1982); 63, 434 (1986)]. Collisions decrease the Weibel growth rate below the collisionless value, in agreement initially with simple linear theory. Likewise, collisions decrease the saturation level, in agreement with a magnetic trapping mechanism. When the collision rate exceeds the collisionless Weibel growth rate, the instability is suppressed altogether. The results provide benchmarks for analysis of proposed short-wavelength laser-fusion schemes.

I. INTRODUCTION

There has been considerable interest recently in inertial-fusion schemes employing submicron wavelength lasers, such as KrF, as there are obvious advantages to short wavelengths. Decreasing the laser wavelength increases the critical density of the target plasma, making possible increased energy deposition by the collisional inverse bremsstrahlung process outside the critical surface and correspondingly decreased energy absorption near the critical surface into suprathermal electrons by resonant absorption and parametric processes, e.g., Brillouin and stimulated Raman scattering. Consequently energy is deposited more deeply into the fusion target where it can produce the desired implosion more efficiently; and there are fewer deleterious long-range suprathermal electrons to preheat the target interior. The heat flow from the deposition region into the interior, where the energy is needed, results from a poorly understood, anomalous, electron-transport process. This process must be understood if a valid assessment of various inertial-fusion schemes is to be made. It is certain, however, that the transport process can be affected by the presence of strong magnetic fields, which are, in fact, known to be produced in laser irradiations at 1–10 μm wavelengths.[1] Magnetic fields are expected to influence heat flow when $\omega_c \tau > 1$, where ω_c is the electron-cyclotron frequency and τ is the scattering time for a 90° deflection. On the basis of theoretical considerations, first presented by Weibel,[2] any magnetic fluctuation present in the plasma and lying within a partial volume of k space, discussed in Sec. II, is unstable; and it will initially grow exponentially in the presence of an anisotropic electron distribution. The initial electron anisotropy necessary for growth of this instability can be produced directly by all known laser–plasma energy-deposition processes, or it can arise indirectly as a result of hot-electron drift[3] or the heat-flow process.[4] Thus any progress in understanding the heat flow in laser targets requires consideration of the Weibel growth of magnetic fields. This is true despite the lack of definitive experimental evidence for the Weibel instability in laser-produced plasmas at this time. Extensive theoretical studies of the Weibel instability in collisionless plasmas have been made using numerical simulation techniques.[5-7] As short-wavelength lasers come under consideration for inertial fusion, it becomes necessary to study the Weibel instability in the presence of collisions. The results of the first such study using the method of plasma simulation are reported here.

The tool for this investigation is the VENUS implicit plasma simulation code.[8,9] The implicit property of the code allows the use of much larger time steps than required by an explicit code, without introducing numerical instabilities, thus reducing computation time requirements significantly. The code solves self-consistently the Maxwell–Boltzmann equations for a system of electrons and ions of fixed Z. The electrons undergo Rutherford scattering off the ion distribution according to the model of Cranfill, Brackbill, and Goldman.[10,11] The collisions of electrons with each other are incorporated approximately with the replacement $Z \to (Z + 1)$ in the scattering formulation. The scattering frequency for a 90° deflection is

$$v_c(v) = \frac{e^2 \omega_{pe}^2 (Z+1)}{m_e c^3} \frac{N_e}{N_0} \left(\frac{c}{v}\right)^3$$

$$\times \ln\left[\frac{1.166 m_e c^2}{2\hbar\omega_{pe}} \sqrt{\frac{N_0}{N_e}} \left(\frac{v}{c}\right)^2\right], \qquad (1)$$

which provides a measure of the collisionality of the plasma ($v_c = \tau^{-1}$). Here N_e is the electron particle density, v the electron velocity, and ω_{pe} the electron plasma frequency at some reference density N_0.

II. SIMULATION AND ANALYSIS

All simulations are two dimensional employing a computational box of dimensions $x_{max} = 80c/\omega_{pe}$ and $y_{max} = 40c/\omega_{pe}$. The y direction, which corresponds to the spatial dimension in one-dimensional treatments, is zoned rather more finely than the x direction. Periodic boundary conditions for both particles and fields are applied in both dimensions. There is no z dependence, although all components of the vector quantities are incorporated. It should be noted that some of the early numerical simulations failed to give the correct late-time behavior of the instability, i.e., decay subsequent to saturation, because the computational box was too small, precluding coupling to the long-wavelength slowly growing modes.[8] Our computational box is adequate for this purpose. The simulations employ 250 000 computational particles of each species. We choose an initial average

Nonlinear Coupling of Stimulated Raman and Brillouin Scattering in Laser-Plasma Interactions

Harvey A. Rose, D. F. DuBois, and B. Bezzerides

Los Alamos National Laboratory, University of California, Los Alamos, New Mexico 87545

(Received 29 December 1986)

Detailed agreement with the experiments of Walsh, Villeneuve, and Baldis is obtained from a theory of the coupling of stimulated Raman scattering and stimulated Brillouin scattering which incorporates the nonlinear physics of the Zakharov model.

PACS numbers: 52.40.Nk, 42.65.−k, 52.35.Mw, 52.35.Ra

Two years ago Walsh, Villeneuve, and Baldis[1] (WVB) reported on experiments in which they observed the interaction of electron density fluctuations associated with stimulated Raman scattering (SRS) and stimulated Brillouin scattering (SBS). Fluctuations associated with SRS were observed to occur only in a narrow band of densities $0.01 < n_0/n_c < 0.05$, where n_c is the critical density for the CO_2 pump laser and n_0 is the plasma density at the top of the Gaussian profile; in the experiments n_0/n_c was always less than 0.25.

The equations for our model[2] were given by Aldrich et al.[3] and can be derived from standard plasma fluid equations. We assume spatial variation only in the x direction and represent the total electromagnetic vector potential A^T as

$$A^T = [\tfrac{1}{2} A \exp(-i\omega_0 t) + \tfrac{1}{2} A_R \exp(-i\omega_R t)] + \text{c.c.},$$

where $\omega_R = \omega_0 - \omega_p$ with ω_0 and ω_p the incident light frequency and electron plasma frequency of the background density, respectively. The slowly varying envelope amplitudes satisfy

$$[-2i\omega_0\partial_t + (\omega_p^2 - \omega_0^2) - c^2\partial_x^2]A = -\omega_p^2(n/n_0)A + (\omega_p^2/8\pi e n_0)(\partial_x E A_R), \tag{1}$$

$$[-2i\omega_R\partial_t + (\omega_p^2 - \omega_R^2) - c^2\partial_x^2]A_R = -\omega_p^2(n/n_0)A_R + (\omega_p^2/8\pi e n_0)A\partial_x E^*. \tag{2}$$

The nonlinear source terms on the right-hand sides of these equations contain the couplings responsible for SBS and SRS.

The slowly varying envelope E of the electrostatic field satisfies

$$(-2i\omega_p\partial_t + \omega_p^2 n/n_0 - 3r_e^2\partial_x^2)E = -\tfrac{1}{2}(\omega_p^2/c^2)(e/m)\partial_x(AA_R^*) + \delta S_E(x,t). \tag{3}$$

The conditions for validity of these equations are discussed in more detail in Ref. 3 and include the condition $n/n_0 \ll 1$. The low-frequency density *fluctuation, n*, obeys

$$(\partial_t^2 - c_s^2\partial_x^2)n = (16\pi m_i)^{-1}\partial_x^2[|E|^2 + (\omega_p^2/c^2)(|A|^2 + |A_R|^2)] + \delta S_n(x,t). \tag{4}$$

In the present study the left-hand sides of Eqs. (3) and (4) are augmented by collision operators $-2i\omega_p \times \nu_e(-i\partial_x)$ and $2\nu_i(-i\partial_x)\partial_t$, respectively. The function $\nu_e(k)$ is chosen to be a simple polynomial fit to the sum of collisional[4] plus Landau damping for Langmuir waves, and likewise $\nu_i(k)$ and c_s^2 [in Eq. (4)] are fitted by the ion acoustic roots of the collisionless-plasma dispersion relation for parameters of the experiment ($m_i/Zm_e = 5500$, $T_e/T_i \approx 1$, $Z \approx 4$).

An important departure from Ref. 3 and other works on Langmuir turbulence is that the calculations presented here are for *finite*, slab geometry. In this case we have found it useful to make a further decomposition of the vector potentials into slowly varying spatial envelopes $A = a_0\exp(ik_0 x) + a_B\exp(ik_B x)$ and $A_R = a_R\exp(ik_R x)$, where k_j's ($j = 0, B, R$) are wave vectors of the incoming laser pump and backscattered Brillouin and Raman light, respectively. The a_j's are assumed to be slowly

varying in space over a distance $2\pi/k_j$, and their second spatial derivatives are neglected. In the slab geometry considered here the pump wave is incident from the left at $x = 0$ with amplitude specified to by *an increasing function of time*: $a_0(x = 0, t) = a_{\max}(t/t_{\text{rise}})^{1/2}$ for $t < t_{\text{rise}}$. This corresponds to the WVB experiments where the pump power is a linearly increasing function of time with $t_{\text{rise}} \approx 500$ ps. The laser field then propagates[5] to the right through the region of uniform plasma $0 \leq x \leq L$. The boundary conditions are taken to be $a_B(x = L, t) = a_R(x = L, t) = 0$, outgoing ion and Langmuir waves; for the latter $\partial_x E = \pm i k_E E$ at $x = L, 0$, respectively, where k_E is the wave number of the fastest (linear) growing Langmuir mode with group velocity ν_E. These boundary conditions eliminate reflections in the mode k_E and have little effect on the nonlinear processes which are local in space. The equations are nu-

Lie group invariance properties of radiation hydrodynamics equations and their associated similarity solutions

Stephen V. Coggeshall
Applied Theoretical Physics Division, Los Alamos National Laboratory, Los Alamos, New Mexico 87545

Roy A. Axford
214 Nuclear Engineering Laboratory, University of Illinois, Urbana, Illinois 61801

The Lie group invariance properties of the one-dimensional radiation hydrodynamic equations with the equilibrium diffusion approximation, a local thermodynamical equilibrium assumption, and an arbitrary material equation of state are derived. These properties are used systematically to generate similarity solutions of these equations for a given form of the equation of state. A comprehensive list of allowed similarity solutions for a perfect gas is presented. Several special cases that have been found previously by other authors appear in the list. Many other cases not reported previously are also presented. An example numerical solution is given for a piston-driven shock with a thermal precursor.

I. INTRODUCTION

The determination and use of similarity solutions of sets of hydrodynamic and radiation hydrodynamic partial differential equations has been a successful technique in the past 45 years. Such solutions comprise special classes of solutions compatible with certain initial/boundary conditions, which can provide insight into the behavior of more general solutions. These special cases may also be taken as benchmark problems useful in the checking of various computer codes.

Two methods for finding similarity solutions to partial differential equations are described in the literature. A method often used is that of a dimensional analysis.[1-8] The second method is based on the transformation theory of differential equations originally introduced by Lie.[9-20] The dimensional analysis approach has been a very successful technique, but it has important limitations as described by Bluman and Cole.[17] Using Lie group methods one can systematically seek similarity solutions of the first and second types[7] to a given set of partial differential equations. This systematic determination by the group method makes it a very powerful technique for analyzing system evolution.

Lie group transformations fall into two classes: point and contact transformations. The elements of a set of Lie group transformations form a group with respect to the composition of transformations. The infinitesimal transformations of a group are represented by a differential operator called the group generator. When the coordinate functions of the group generator depend only on the independent and dependent variables, the group is said to be a point transformation. If the coordinate functions also depend on the derivatives of the dependent variables, it is called a contact transformation. One may speak of an nth-order contact transformation when the coordinate functions depend on up to the nth-order derivatives. In this sense a point transformation may be considered as a zeroth-order contact transformation.

The transformation theory of differential equations was originally developed by Lie to explain and unify apparently disparate and *ad hoc* methods for obtaining solutions of differential equations. It may be applied to systems of linear or nonlinear ordinary and partial differential equations that admit groups. Invariance under a one- or multi-parameter group of transformations allows for the following:

(i) a first-order ordinary differential equation to be reduced to quadratures,

(ii) an nth-order ordinary differential equation to be reduced to an $n-1$st-order ordinary differential equation,

(iii) an nth-order partial differential equation with two independent variables to be reduced to an nth-order ordinary differential equation, and

(iv) an nth-order partial differential equation with m independent variables to be reduced to an nth-order partial differential equation with $m-1$ independent variables.

For more detailed information of the application of this theory to differential equations see, for example, Refs. 11–19. Reference 20 contains a brief description of the history of the development and use of these techniques.

The present work concentrates on the transformation properties of a set of radiation hydrodynamics partial differential equations. It is easy to show that for a system of partial differential equations any contact transformation automatically collapses to a point transformation.[21,22] We therefore look only for point transformations that are admitted by this set of partial differential equations. Once these have been found we can introduce similarity variables as invariant functions of the group and reduce the partial differential equations to ordinary differential equations. Similarity solutions are a consequence of Lie group invariance properties of differential equations when invariant functions of the group are introduced as new variables.

The equations studied in this work are one-dimensional radiation hydrodynamic equations in which the flow of radiation is treated in the diffusion approximation. This results in a model referred to as the radiation conduction approximation. Similarity solutions for the hydrodynamic equations have been known for some time and are well documented. (See, for example, Refs. 1–8, 23–29.) Some similarity solutions for several cases of radiation hydrodynamics equations have also been found.[30-37] A short summary of these earlier works can be found in the concluding discussion.

Section II contains a brief review of how the application

SCALING OF HIGH-Z LASER PLASMAS
WITH ENERGY AND PULSELENGTH

S.R. GOLDMAN, W.C. MEAD
Los Alamos National Laboratory,
Los Alamos, New Mexico,
United States of America

ABSTRACT. The authors have used LASNEX modelling, which matches most current experiments, to study the scaling of high-Z laser-target interactions to the higher laser energies and longer pulses appropriate to future inertial fusion targets. Results are presented for the irradiation of gold disk targets with 0.26 μm light at a normal incident intensity of 3×10^{14} W·cm^{-2} and incident energy varying from 10^2 J to 10^7 J. For both low- and high-energy cases, steep plasma profiles develop near the critical density of the laser light. In the absence of filamentation, the combination of large electron density gradients at densities substantially below the critical density and strong collisionality due to the high-Z plasma appears to suppress stimulated Raman backscattering and the $2\omega_{pe}$ instability. There is some possibility of stimulated Raman sidescatter in the high-energy case. Using one-dimensional plasma contours, filament generation is strongest at early times for the 10^7 J case, and weak at all times for the 10^2 J case. The radiation emission is largely generated near the critical surface, and the conversion efficiencies are of the order of 0.6 and constant to within ±0.1. There is weak variation with energy in global flow parameters.

1. INTRODUCTION

The understanding of the interaction of submicron laser light with high-Z plasmas [1] is important for some classes of Inertial Confinement Fusion (ICF) reactor targets [2]. Considerable experimental and theoretical effort has been devoted to this goal. Experiments [3–6] at 0.53 μm and 0.35 μm wavelengths have shown absorption efficiencies of 80% or more, suprathermal energy fractions of the order of 1% or less, and X-ray conversion efficiencies exceeding 50%. Theoretical and experimental work has shown substantial benefits for laser plasma coupling processes in high-Z plasma at reactor scalelengths [7, 8].

We have used LASNEX modelling, which matches most recent experiments [3, 6, 9–12], to study the scaling of high-Z laser–target interactions to the higher laser energies and longer pulses appropriate to future ICF targets, such as might be driven by a 0.25 μm multi-megajoule KrF laser. In this work we survey the scaling of the interaction with increasing pulselength and target size at fixed peak pulse intensity. The essential adequacy of LASNEX at current laboratory energies has been established through a number of detailed comparisons with experiment [3, 6, 9]. The accuracy of code calculations at longer pulselengths is ultimately in question, especially in view of the lack of a detailed theory or experimental verification. However, simulations, based on the same components

whose usage has been authenticated by current experiments, provide guidance for further efforts.

In this work, we evaluate the scaling of plasma profiles and energetics for a gold disk irradiated by a circular spot of KrF light ($\lambda \cong 0.26$ μm) with a Gaussian pulse of peak intensity 3×10^{14} W·cm^{-2}. This intensity falls within the range of peak intensities for reactor designs [7] and is sufficiently low that, as shown below, suprathermal electron production and coronal plasma instabilities are generally suppressed. We vary the energy, E, from 100 J to 10 MJ, and the pulsewidth, τ (FWHM), from 0.5 ns to 23.2 ns. The value of 100 J corresponds to early Argus experiments; the value of 10 MJ corresponds to projected reactor designs. It is striking that, over the large range of parameter space surveyed, the main features of plasma development are qualitatively similar. We find strong steepening of the plasma temperature and density profiles near the critical surface in all cases. Global features of the flows scale slowly with energy. We find some striking modifications of scalings from simplest expectations which have significant impact on the expected behaviour of laser–plasma coupling processes.

Early estimates [13] and simple models [14], examining the scaling of high-Z plasmas with increasing laser energy and pulsewidth, assumed that the plasma profiles were not very different from an isothermal rarefaction. Using $c_s\tau$ as an estimate for the scalelength, with c_s the coronal sound speed and τ the laser pulse

ANALYSIS, MODELING, AND DESIGN OF

SHORT-WAVELENGTH LASER-PLASMA EXPERIMENTS

W. C. Mead, S. V. Coggeshall, S. R. Goldman, E. K. Stover,
P. D. Goldstone, J. Cobble, A. Hauer, G. Stradling,
J. M. Kindel, and L. Montierth[a]

Los Alamos National Laboratory
Los Alamos, N.M. 87545

M. C. Richardson, O. Barnouin, P. Jaanimagi,[b]
F. Marshall, and R. Marjoribanks

University of Rochester
Rochester, NY 14623

R. L. Kauffman, H. N. Kornblum, and B. F. Lasinski

Lawrence Livermore National Laboratory
Livermore, CA 94550

[a]University of Arizona, Tucson, AZ 85721
[b]Lawrence Berkeley Laboratory, Berkeley, CA 94720

ABSTRACT

We present analysis and LASNEX modeling of two experiments designed to explore
the mechanisms and scaling of laser-plasma coupling in high-Z plasmas. The first used
layered Au-on-CH spheres irradiated symmetrically using the Omega (Laboratory for
Laser Energetics) 0.35 μm laser to observe the x-ray emission and energy penetra-
tion in gold plasmas. Measurements of the subkilovolt and kilovolt emission from
targets with varying Au-coating thicknesses were made using diagnostics of varying
spectral, temporal, and spatial resolution. The results indicate that the x-ray conver-
sion efficiency is a function of target size, with larger targets yielding x-ray emission
in excellent agreement with calculations. The x-ray emission fall-off with decreasing
gold thickness agrees well with predictions. The second experiment used the Novette
(Lawrence Livermore National Laboratory) laser to irradiate solid gold disk targets,
examining wavelength scaling to 0.26 μm. The measured subkilovolt x-ray emission
is in good agreement with calculations using mildly inhibited thermal electron trans-
port, indicating enhanced target coupling, compared with previous experiments using
smaller spot sizes. The experiment also indicates very low suprathermal electron pop-
ulations, on the order of 0.1% at about 30 keV effective temperature. Finally, we
present preliminary plans and designs for experiments which will use the Aurora 5 kJ,
5 ns, 0.25 μm KrF laser now being constructed at Los Alamos.

An Implicit Moment Electromagnetic Plasma Simulation in Cylindrical Coordinates

JON M. WALLACE, JEREMIAH U. BRACKBILL, AND
DAVID W. FORSLUND

*Applied Theoretical Physics Division,
Los Alamos National Laboratory, Los Alamos, New Mexico 87545*

An electromagnetic PIC plasma simulation code incorporating the implicit moment method and a two-dimensional cylindrical mesh, with r- and z-coordinate dependence, has been developed The code is an extension of the VENUS code from the original two-dimensional Cartesian mesh. The physical model employed in the code will be discussed, with emphasis on aspects unique to cylindrical geometry. An application to self-generated magnetic fields and electron transport in a laser-irradiated disk is presented that highlights the usefulness of cylindrical coordinates. © 1986 Academic Press, Inc

INTRODUCTION

An implicit moment method for nonrelativistic electromagnetic plasma simulation in two dimensions has recently been developed [1]. The method, introduced by Mason [2] in an electrostatic context, employs a new way of advancing in time the coupled particle and field equations that eliminates many of the numerical constraints on time and space steps encountered in explicit plasma simulation codes. With the implicit method, it is not necessary to resolve the electron plasma oscillations or the propagation of light waves. Computations which follow in detail only the ions and still remain numerically stable are possible. Likewise, it is unnecessary to resolve the Debye length. The method makes accessible to simulation larger time and space scales than are practical with an explicit formulation of the Maxwell–Vlasov equations. This is especially useful when simulating low-frequency plasma phenomena in which the high-frequency component of the electron motion is physically insignificant and only the average electron motion, where the high-frequency component has been removed, need to be considered.

The implicit moment method has been employed in the VENUS PIC code using the usual Cartesian grid [1]. However, because the implicit method makes possible the simulation of an entire plasma, including boundary effects, one is lead to incorporate the option of another mesh geometry. The two-dimensional Cartesian mesh is appropriate for a system which is infinite and perfectly homogeneous along the

434

Electrostatic electron surface modes on a plasma–vacuum interface of finite width

Roger D. Jones

Applied Theoretical Physics Division, Los Alamos National Laboratory, Los Alamos, New Mexico 87545

The electron surface mode dispersion relation, including Landau damping, is obtained for a vacuum–plasma interface. Unlike previous work, the interface is permitted to have a finite width and no wall boundary conditions are assumed. When the density gradient scale length L_n is large compared with a Debye length k_D^{-1} and small compared with a surface mode wavelength $2\pi k^{-1}$, then the mode frequency is $\omega = (\omega_p/2^{1/2})(1 + kL_n/6)$, and the Landau damping rate is $\gamma = -[6/(2\pi)^{1/2}]\omega_p/(k_D L_n)$. These expressions are much different than the comparable expressions for a wall-confined plasma.

I. INTRODUCTION

All plasmas, whether classical or solid state, are in some sense bounded. The modes that can be supported by the surfaces of bounded plasmas have been a source of study for some time (for a recent review see Ref. 1]. The lateral transport of energy,[2] the acceleration of fast ions,[2] noncollisional absorption of radiation,[3] the generation of very high harmonics of incident laser light,[4] magnetic field generation,[2] and transition radiation[5] are phenomena whose existence has been attributed to electron surface waves. In the cold plasma limit, the frequency of both the electrostatic and p-polarized electromagnetic modes (in the absence of a static magnetic field) is $\omega = \omega_0/2^{1/2}$, where ω_0 is the plasma frequency of the upper density shelf. Using a cold plasma fluid theory, Kaw and McBride[6] have calculated the real part of the full electromagnetic dispersion for a semi-infinite plasma that has a density variation on the upper density shelf [see Fig. 1(a)]. They did not consider a surface of finite width. Additionally, since they used a fluid theory, they were unable to calculate the Landau damping. In calculations of the finite wavelength corrections to the surface wave Landau damping, attention has been restricted to plasmas that are confined by perfectly or specularly reflecting walls[7] [see Fig. 1(b)]. This is an idealization, at best, to wall-confined plas-

mas. Many important plasmas are not confined by walls at all, e.g., magnetic fusion plasmas, inertial confinement plasmas, astrophysical plasmas, and metals. In this paper, the dispersion and Landau damping of electrostatic surface waves will be calculated in the important situation in which the plasma is not confined by walls but is confined by the ion inertia (see Fig. 2). It will be shown that, in the case where the electron density scale length L_n at the plasma–vacuum interface is much larger than the Debye length k_0^{-1} of the upper density shelf and much smaller than a surface mode wavelength $2\pi k^{-1}$, the wave frequency is given by $\omega = \omega_0(1 + kL_n/6)/2^{1/2}$ and the Landau damping is given by $\gamma = -[6/(2\pi)^{1/2}]\omega_0/(k_0 L_n)$, where γ is the damping rate. These expressions are much different than the comparable expressions for wall-confined plasmas.

II. ELECTRON SURFACE MODE DISPERSION AND DAMPING

First consider a cold semi-infinite plasma. For $x < 0$, the electron density is n_0. For $x > 0$, the density is 0. Since we are considering electron time scales that are much faster than the ion time scales, we can neglect the expansion of the plasma into the vacuum and regard the ions as fixed. The dielectric response is

$$\epsilon \equiv \epsilon_0 = 1 - \omega_0^2/\omega^2, \qquad x < 0,$$

$$\epsilon = 1, \qquad x > 0, \tag{1}$$

where ω_0 is the plasma frequency at density n_0. Electrostatic
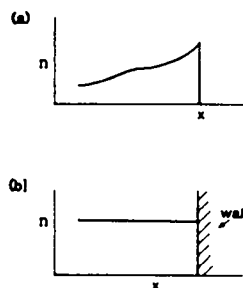

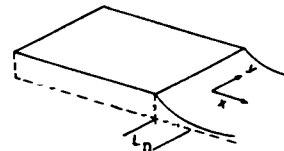FIG. 1.(a) Surface with density gradient on upper density shelf. (b) Wall-confined plasma.

FIG. 2. Surface of finite width.

THE PHYSICS OF BURN IN MAGNETIZED
DEUTERIUM-TRITIUM PLASMAS

Spherical geometry

R.D. JONES, W.C. MEAD
Los Alamos National Laboratory,
Los Alamos, New Mexico,
United States of America

ABSTRACT. There is a large region of density-temperature space in which the effects of a magnetic field on heat transport and alpha-particle mobility are significant and the magnetic pressure is small compared with the pressure of a deuterium-tritium plasma. Spherical fusion burn in this regime is examined. It is found that for volume burn, magnetic fields can greatly increase the yield. In regimes where propagating burn does not occur, the burn can be enhanced by a magnetic field. In regimes where propagating deflagration would normally occur in the absence of a magnetic field, magnetic fields actually degrade the cross-field propagation. A detonation wave is harder to ignite in the presence of a magnetic field. Once a detonation wave is ignited, no change in the propagation speed is produced by applying a magnetic field.

1. INTRODUCTION

Recently, Lindemuth and Kirkpatrick [1] suggested that magnetic fields might play a role in increasing the gain of laser targets and in reducing the power and focusing requirements of particle beam targets for inertial confinement fusion. Their conclusions were based on a simple zero-dimensional model in which the deuterium-tritium (DT) burn was included in a heuristic manner. Since they used a single zone to model the DT fuel in their numerical calculation, they were unable to examine propagating burn waves or the details of temperature and density gradients in volume burn. If inertial confinement fusion is to succeed, it must achieve high gain by using propagating burn in order to compensate for low driver efficiencies. Therefore, an important issue in the study of magnetized inertial fusion targets is the role that magnetic fields may play in enhancing or degrading propagating burn. This issue is discussed in the present paper. We use the hydrodynamics code LASNEX [2] to examine volume and propagating burn in spherical geometries. A model of the magnetic field is assumed in which the dynamics of the magnetic field are greatly simplified. This is necessary in order to discuss the role of the magnetic field in spherical geometry.

The conclusions reached in *spherical geometry* are as follows:

(a) In a volume burn regime, magnetic fields can greatly improve the burn.

(b) In regimes where propagating deflagration would normally occur in the absence of a magnetic field, the fields actually degrade the cross-field propagation.

(c) In the presence of a magnetic field, deflagration burn can be made to occur in a regime in which it would not occur otherwise. This regime, however, is not the high-gain regime of most interest to inertial fusion.

(d) A detonation wave is generally harder to ignite in the presence of a magnetic field.

(e) Once a detonation is ignited, there is no difference in the propagation speed between a wave with and a wave without a magnetic field.

(f) A consequence of point (a) is that the performance of low-gain targets, as might be used for particle beam drivers, may be enhanced.

(g) A consequence of point (b) is that magnetic fields are unlikely to be able to significantly improve the performance of high-gain targets *in one-dimensional burn geometries*.

The paper is organized as follows. Section 2 discusses the model used in arriving at the above conclusions. The volume burn regime is discussed in Section 3. In Section 4, propagating and non-propagating burn is discussed, together with a concept called magnetically enhanced tamping. In Section 5, the qualitative results of Section 4 are discussed in the context of achieving high fuel gains (yield per total internal energy).

Inertial Fusion in the Nineties

David B. Harris,[1] Donald J. Dudziak,[1] and David C. Cartwright[1]

The 1980s have proven to be an exciting time for the inertial confinement fusion (ICF) program. Major new laser and light-ion drivers have been constructed and have produced some encouraging results. The 1990s will be a crucial time for the ICF program. A decision for proceeding with the next facility is scheduled for the early 1990s. If the decision is positive, planning and construction of this facility will occur. Depending on the time required for design and construction, this next-generation facility could become operational near the turn of the century.

1. INTRODUCTION

The inertial confinement fusion (ICF) program has maintained level funding over the past few years and is currently active at national laboratories, universities, and industries. Recent experimental results in many areas have been very encouraging, giving indications that the ultimate success of ICF is achievable. The 1990s will most certainly provide even more progress toward achievement of the short-term military applications and the long-term civilian goal of energy production.

The U.S. ICF program currently has three major elements: capsule physics, driver technology, and driver-matter interactions. Other smaller components such as target fabrication and reactor studies are also being investigated at a lower level. The capsule physics effort is mainly in a classified program called Centurion/Halite, a theoretical and experimental effort to investigate the design characteristics of ICF targets. Excellent progress has recently been achieved and has been said to be a turning point in demonstrating target behavior [1].

[1]Los Alamos National Laboratory, Los Alamos, New Mexico 87545.

The 1980s have also seen new drivers being developed. At Lawrence Livermore National Laboratory (LLNL), the Nova solid-state laser has been constructed and is being used to implode targets. One significant result is the successful implosion of a target with a convergence ratio of 30 [1]. This demonstrates that compression of targets to high densities and small radius is achievable. At Los Alamos National Laboratory (LANL), the Aurora krypton fluoride laser system is currently under construction. When complete, this system will deliver ~5 kJ of 0.25-μm wavelength laser light to target. Aurora is the first end-to-end demonstration of an angularly multiplexed excimer laser for fusion. KrF lasers are an important laser driver because of, among other reasons, their unique attractiveness for ICF commercial applications such as electric power production [2,3]. At Sandia National Laboratory (SNL), the particle beam fusion accelerator PBFA II has made significant progress. Light-ion accelerators such as PBFA II are attractive for ICF because of their low cost. These drivers and others will be described in more detail in Section 2.

In 1986, the ICF program underwent a comprehensive review by a committee formed by the National Academy of Science (NAS) in response to a

163

SENSITIVITY OF ELECTRICITY COST TO HEAVY-ION FUSION TARGET CHARACTERISTICS

DOUGLAS C. WILSON, DONALD J. DUDZIAK, and
GLENN R. MAGELSSEN *Los Alamos National Laboratory*
Los Alamos, New Mexico 87545

DAVID S. ZUCKERMAN and DANIEL E. DRIEMEYER
McDonnell Douglas Astronautics Co., P.O. Box 516, St. Louis, Missouri 63166

The systems model for a commercial electric power facility produced by the Heavy-Ion Fusion System Assessment is used to study the sensitivity of electricity cost to various inertial confinement fusion target characteristics including gain, peak power, ion range, and target fabrication cost. Net electric power from the plant was fixed at 1000 MW(electric) to eliminate large effects caused by economies of scale. An improved target cost model is used and compared with earlier results. Although specific quantitative results changed, the earlier general conclusions remain valid. The system is moderately insensitive to target gain. A factor of 2.5 change in gain causes <10% change in electricity cost. Increased peak power needed to drive targets poses only a small cost risk but requires many more beamlets be transported to the target. Shortening the required ion range causes both cost and beamlet difficulties. A factor of 4 decrease in the required range at a fixed driver energy increases electricity cost by 43% and raises the number of beamlets from 34 to 330. Finally, the heavy-ion fusion system can accommodate large increases in target costs. While moderate target gain is required, to address the other major uncertainties target design should concentrate on understanding requirements for ion range and peak driver power.

I. INTRODUCTION

In this paper, we will use the model for a commercial electric power facility produced by the Heavy-Ion Fusion System Assessment[1] (HIFSA) to study the im-

pact of various inertial confinement fusion (ICF) target designs and characteristics on the cost of electricity (COE). Other papers in this issue address different aspects of this same model.[1-8] Previous system studies of heavy-ion fusion (HIF) for electricity production have focused on a point design system with a single target design.[9-11] By considering a variety of systems, we are able to identify which target designs and characteristics have the greatest impact on electricity cost.

Gain is one of the most uncertain target characteristics. Computer codes allow calculations of expected performance of inertial fusion reactor targets, but experimental verification must await the construction of large and expensive drivers. We expect that poorly known effects such as drive asymmetry, instability growth, mix, and fabrication imperfections will substantially degrade target performance. Therefore, the best-estimate gain curves of Lindl and Mark[12] differ from the ideal by as much as a factor of 10. In addition, gain curves are derived only for specific target designs. There are advanced concepts with higher gains for which curves have not been calculated. When high gain targets can be studied experimentally, measured gains will differ substantially from those predicted now. We can expect those gains to increase with driver energy, but little more can be said with confidence.

In addition to target gain, the actual beam pulse length, spot size, and ion range required by the target are uncertain. Target designs and performance span a multidimensional space including these and other variables. In this paper we will quantify the importance of each of these factors to the COE. The results can then be used to guide target designs toward the most important regions of the multidimensional space.

In Sec. II we briefly describe the HIFSA system model. A complete description is published elsewhere.[3] In Sec. III we cover general results from the system

HEAVY-ION FUSION TARGET COST MODEL

JOHN H. PENDERGRASS, DAVID B. HARRIS, and
DONALD J. DUDZIAK *University of California*
Los Alamos National Laboratory, P.O. Box 1663
Los Alamos, New Mexico 87545

A new model for the cost of production of heavy-ion fusion targets in dedicated on-site target factories is presented for power plants. The model treats single- and double-shell direct-drive and generic indirect-drive targets. Target factory capital costs, nontritium target materials costs, and target factory operations and maintenance costs are estimated for target substructures such as fuel capsules, radiation cases, and driver energy absorption regions. These individual estimates are combined to obtain the total target cost. Realistic scaling of target costs with variations of such important performance parameters as target factory production capacity and driver pulse energy is emphasized. The model can be modified and used for other inertial fusion drivers and fuels. Typical target cost estimates fall into the range of $0.25 to 0.45 per target. The estimated target cost contribution to the total cost of production of electric power is typically ~4 to 7 mill/kW·h.

I. INTRODUCTION

I.A. The Problem

Previous inertial confinement fusion (ICF) commercial applications studies used simple treatments of target costs even when target, driver, reactor plant, and balance-of-plant (BOP) performance parameters and repetition rates were varied over wide ranges.[1] Reasons for this include (a) optimism that target costs would be small and unimportant, (b) target and manufacturing process concepts were not completely defined, (c) resources for analysis of target costs were limited, and (d) the studies concentrated on point designs for ICF plants.[2] The following are two exam-

ples of such simple treatments. The first involves the assumption that targets are manufactured on-site, or by an off-site factory supplying many plants, at a cost per target that is independent of the target performance and the number of targets required annually. The second example includes an on-site target factory with a fixed capital cost, so that the capital-charge cost component per target is inversely proportional to the target manufacturing rate. The second example also involves the assumption of a fixed materials cost per target.

The simple treatments of target cost often assume no dependence of target cost on driver pulse energy, target concept, and number of targets required annually. They may involve the lumping of annual target factory operations and maintenance (O&M) costs with other annual plant O&M costs computed by multiplying the plant capital cost by a single fixed factor. The magnitudes of the target costs used in such studies have often been based on such simple rules of thumb as "the contribution of target or total fuel-cycle costs to total electric power production cost should not exceed 10%."

In general, ICF power plant cost studies indicate that a single driver pulse energy value corresponds to the lowest unit (in mills per kilowatt-hour) production cost for a fixed net plant electric power and specified driver, reactor plant, BOP, and target concept. The BOP systems include the turbine plant equipment for a plant using a steam cycle, the electric plant equipment, the ultimate heat rejection systems, and miscellaneous plant equipment. Such optima are illustrated by the graph in Fig. 1, which shows cost of electricity (COE) estimates as a function of driver pulse energy for a 1000-MW(electric) net heavy-ion fusion (HIF) power plant. Figure 1 was constructed using a simplified version of the cost model described in Ref. 3. Also shown in Fig. 1 are the contributions of target, driver, reactor plant, and BOP costs to the total COE. The

FUTURE DEVELOPMENTS AND APPLICATIONS OF KrF LASER-FUSION SYSTEMS

DAVID B. HARRIS and NORMAN A. KURNIT *University of California*
Los Alamos National Laboratory, P.O. Box 1663, MS F611
Los Alamos, New Mexico 87545

DENNIS D. LOWENTHAL, RUSSELL G. BERGER,
JOHN M. EGGLESTON, JAMES J. EWING, and MARK J. KUSHNER*
Spectra Technology, Inc., 2755 Northup Way, Bellevue, Washington 98004

LESTER M. WAGANER, DAVID A. BOWERS, and
DAVID S. ZUCKERMAN *McDonnell Douglas Astronautics Company*
P.O. Box 516, St. Louis, Missouri 63166

The development of KrF lasers has proceeded from the small lasers invented in 1975 to the 10-kJ large amplifier module at Los Alamos National Laboratory. The future KrF laser-fusion drivers required for inertial confinement fusion (ICF) development and commercial applications, starting with single-main-amplifier laser systems in the 100- to 300-kJ range, through multimegajoule single-pulse target demonstration facilities, to repetitively pulsed drivers for electric power plants are examined. Two different types of KrF lasers are currently being analyzed as potential laser-fusion drivers: large electron-beam (e-beam)-pumped amplifiers using pure optical multiplexing for pulse compression and small e-beam sustained discharge lasers using a hybrid pulse compression technique. Both types of KrF lasers appear able to satisfy all of the requirements for commercial-applications ICF drivers, including cost, efficiency, pulse shaping, energy scaling, repetition rate, reliability, and target coupling. The KrF driver can effectively operate at efficiencies >10% and can contribute <10 mill/kWh to the cost of electric power production, with the total estimated cost of electricity from either KrF laser system being comparable (25 to 50 mill/kWh, 1985 dollars) with the cost from other methods of electric power production.

I. INTRODUCTION

KrF lasers appear to be able to satisfy all of the driver requirements for commercial inertial confinement fusion (ICF) applications. This paper examines the different KrF laser systems required to go from the Aurora laser system (currently under construction)[1] to a commercial ICF electric power plant. This requires development in a wide range of technologies, including the KrF laser (optics, pulsed power, diodes, gas

*Present address: University of Illinois, Department of Electrical and Computer Engineering, Urbana, Illinois 61801.

flow, etc.), ICF target manufacturing (mass production techniques, quality control, automated systems, etc.), and ICF reactors (materials, tritium breeding and recovery, protection of final optical surfaces, etc.). The different stages of an integrated development plan for both KrF fusion lasers and inertial-fusion electric power plants are described. The driver for each stage is discussed, and the final product, the driver for an electric power plant, is analyzed in detail.

Los Alamos National Laboratory (LANL) is currently analyzing two different types of KrF laser-fusion drivers based on the methods used for laser pumping and pulse compression:

Directions for reactor target design based on the U.S. Heavy Ion Fusion Systems Assessment

By D. C. WILSON, D. DUDZIAK and G. MAGELSSEN

Los Alamos National Laboratory, Los Alamos, New Mexico, U.S.A.

AND

D. ZUCKERMAN and D. DRIEMEYER

McDonnell Douglas Astronautics Co., P.O. Box 516, St. Louis, Missouri, U.S.A.

The Heavy-Ion Fusion Systems Assessment project is nearing completion of a two-year effort. The resulting system model will be used to set directions for future target design work.

Major uncertainties in target design were studied using the cost of electricity as a figure of merit. Net electric power was fixed at 1000 MW to eliminate large effects due to economies of scale. The system is relatively insensitive to target gain, factors of three changes in gain resulting in 8 to 12% changes in electricity cost. Possible increased peak power requirements pose only a small cost risk, but require many more beamlets for transport. A shortening of the required ion range causes both cost and beamlet difficulties. A factor of 4 decrease in the required range at a fixed driver energy increases electricity cost by 44% and raises the number of beamlets to 240. Finally, the heavy ion fusion system can accommodate large increases in target costs. Thus, to address the major uncertainties, target design should concentrate on requirements for ion range and peak driver power.

---

1. Introduction

Although we attempt to calculate the performance of inertial fusion reactor targets, we are a long way from experimentally verifying their performance. In fact we expect that poorly known effects such as drive asymmetry, instability growth, mix, and fabrication imperfections can substantially degrade target performance. This is why the "best estimate" gain curves of Lindl and Mark (1984) differ from the "ideal" by as much as a factor of 10. On the other hand gain curves are derived for specific target designs. Advanced concepts do exist for which curves have not been calculated. When we are able to study targets experimentally, measured gains will differ substantially from those predicted now. We can expect the gain of these targets to increase with driver energy, but little more can be said with confidence.

In addition to target gain, the actual beam pulse length, spot size, and range required by the target are uncertain. Target designs and performance span a multidimensional space including these and other variables. In this paper we will use the results of the U.S. Heavy Ion Fusion Systems Assessment (HIFSA) to quantify the importance of each of these factors to the cost of electricity. This can then be used to guide target designs toward the most important regions of the multidimensional space. This project has been run over a two-year period and has joint participation from Los Alamos National Laboratory (LANL), Lawrence Berkeley Laboratory (LBL), and Lawrence Livermore National Laboratories (LLNL), the U.S. Department of Energy

IMPROVING INERTIAL CONFINEMENT FUSION POWER PLANT AND EFFECTIVE DRIVER EFFICIENCIES BY GENERATING ELECTRICITY FROM KrF LASER REJECT HEAT

JOHN H. PENDERGRASS *University of California*
Los Alamos National Laboratory, P.O. Box 1663
Mail Stop F611, Los Alamos, New Mexico 87544

KrF laser intrinsic efficiency increases modestly with increase in lasing medium temperature up to at least a few hundred degrees Celsius. Such temperatures are high enough to permit efficient generation of electric power from the large amounts of heat that must be continuously removed from the lasing medium of a repetitively pulsed KrF laser in an inertial confinement fusion power plant. The effects of power generation from lasing medium heat on net plant efficiency and effective laser efficiency were investigated in a generic systems analysis. Two approaches to efficient, cost-effective generation of electric power from lasing medium heat were analyzed in detail: (a) dedicated power generation systems that use lasing medium heat as the sole thermal energy source and (b) the use of lasing medium thermal energy to heat main-plant steam cycle feedwater. Feedwater heating gives higher generation efficiencies and is more cost-effective than a dedicated system. Electric power generated from lasing medium heat typically increases power plant efficiency by 2 to 3% absolute and the effective KrF laser efficiency by 2 to 3% absolute. Electric power from lasing medium can be used to reduce the fusion power required for a fixed net plant electric power typically by 4 to 5%.

I. INTRODUCTION

Lasers offer potentially crucial advantages as drivers for experimental and commercial inertial confinement fusion (ICF), including precise pulse shaping with large dynamic range and relatively inexpensive beam transport and turning that permit a wide range of target illumination geometries. A gaseous lasing medium allows the few-hertz pulse repetition rates currently projected as optimum for 1000-MW(electric) ICF power plants. A gaseous lasing medium can be circulated for removal of laser pump energy not extracted as light energy. KrF lasers provide an attractive combination of good efficiency, short wavelength, and broad bandwidth for good coupling with targets and a gaseous lasing medium for high repetition rate.[1]

Some lasers that are candidates for ICF commercial applications must be operated at or below ambient temperature to obtain best efficiency. However, experimental and theoretical studies[2] indicate that KrF laser intrinsic efficiency increases modestly with increase in lasing medium temperature up to at least a few hundred degrees Celsius due to decrease in absorption cross sections. The intrinsic efficiency is the product of the pumping efficiency and the extraction efficiency.[1] The pumping efficiency is the fraction of the pumping energy injected into a laser cavity that is actually converted to stored energy in the desired population inversion. The extraction efficiency is the fraction of the energy stored in the population inversion that can be converted to laser light when accessed by a low-energy extraction beam.

Such temperatures are high enough to permit efficient generation of electrical energy from the large amounts of heat deposited in the lasing medium by dissipation of electric power required to operate the laser. Significant amounts of power generated efficiently at acceptable cost from lasing medium heat can substantially enhance the attractiveness of KrF lasers as commercial ICF drivers.

Heat ends up in a KrF lasing medium as a consequence of numerous inefficiencies. These include inefficiencies in creating the population inversion required for lasing, in extracting the population inversion energy as laser light, in accessing the pumped

FUSION REACTOR DESIGN
AND TECHNOLOGY 1986

VOLUME 1

OVERVIEW OF THE UNITED STATES
HEAVY-ION FUSION COMMERCIAL
ELECTRIC POWER SYSTEMS
ASSESSMENT PROJECT

D.J. DUDZIAK, J.H. PENDERGRASS, W.W. SAYLOR
Los Alamos National Laboratory,
University of California,
Los Alamos, New Mexico,
United States of America

Abstract

The U.S. heavy-ion fusion (HIF) research program is oriented toward development of multiple-beam induction linacs. Over the last two years an assessment has been performed of the potential of HIF as a competitive commercial electric power source. This assessment involved several technology performance and cost issues (e.g., final beam transport system, target manufacturing, beam stability in reactor cavity environments, and reactor cavity clearing), as well as overall power plant systems integration and tradeoff studies. Results from parametric analyses using a systems code developed in the project show cost of electricity (COE) values comparable with COEs from other magnetic fusion and inertial confinement fusion (ICF) plant studies; viz, 50-60 mill/(kW·h) (1985 dollars) for 1-GWe plants. Also, significant COE insensitivity to major accelerator, target, and reactor parameters was demonstrated.

1. THE HIFSA PROJECT

The Heavy-Ion Fusion Systems Assessment (HIFSA) is a study of the prospects for successful commercial heavy-ion fusion electric power generation using induction linear accelerator (linac) drivers. Led by Los Alamos National Laboratory (LANL),

For more information, contact

David C. Cartwright
Program Director, ADNWT/ICF
MS F630
Los Alamos, NM 87545
(505) 667-3612